NUREG/CR-4391
EGG-2680

TRAC-BF1/MOD1 Models and Correlations

Edited by
J. A. Borkowski, N. L. Wade

Idaho National Engineering Laboratory
EG&G Idaho, Inc.

Prepared for
U.S. Nuclear Regulatory Commission

NUREG/CR-4391
EGG-2680
R4

TRAC-BF1/MOD1 Models and Correlations

Manuscript Completed: July 1992
Date Published: August 1992

Edited by
J. A. Borkowski, N. L. Wade

Contributing Authors
S. Z. Rouhani, R. W. Shumway, W. L. Weaver, W. H. Rettig*, C. L. Kullberg

Idaho National Engineering Laboratory
Managed by the U.S. Department of Energy

EG&G Idaho, Inc.
Idaho Falls, ID 83415

Prepared for
Division of Systems Research
Office of Nuclear Regulatory Research
U.S. Nuclear Regulatory Commission
Washington, DC 20555
NRC FIN L2031
Under DOE Contract No. DE-AC07-76ID01570

*Presently with the
Department of Energy
Idaho Field Office
Idaho Falls, ID 83401

AVAILABILITY NOTICE

Availability of Reference Materials Cited in NRC Publications

Most documents cited in NRC publications will be available from one of the following sources:

1. The NRC Public Document Room, 2120 L Street, NW., Lower Level, Washington, DC 20555

2. The Superintendent of Documents, U.S. Government Printing Office, P.O. Box 37082, Washington, DC 20013-7082

3. The National Technical Information Service, Springfield, VA 22161

Although the listing that follows represents the majority of documents cited in NRC publications, it is not intended to be exhaustive.

Referenced documents available for inspection and copying for a fee from the NRC Public Document Room include NRC correspondence and internal NRC memoranda; NRC bulletins, circulars, information notices, inspection and investigation notices; licensee event reports; vendor reports and correspondence; Commission papers; and applicant and licensee documents and correspondence.

The following documents in the NUREG series are available for purchase from the GPO Sales Program: formal NRC staff and contractor reports, NRC-sponsored conference proceedings, international agreement reports, grant publications, and NRC booklets and brochures. Also available are regulatory guides, NRC regulations in the *Code of Federal Regulations*, and *Nuclear Regulatory Commission Issuances*.

Documents available from the National Technical Information Service include NUREG-series reports and technical reports prepared by other Federal agencies and reports prepared by the Atomic Energy Commission, forerunner agency to the Nuclear Regulatory Commission.

Documents available from public and special technical libraries include all open literature items, such as books, journal articles, and transactions. *Federal Register* notices, Federal and State legislation, and congressional reports can usually be obtained from these libraries.

Documents such as theses, dissertations, foreign reports and translations, and non-NRC conference proceedings are available for purchase from the organization sponsoring the publication cited.

Single copies of NRC draft reports are available free, to the extent of supply, upon written request to the Office of Administration, Distribution and Mail Services Section, U.S. Nuclear Regulatory Commission, Washington, DC 20555.

Copies of industry codes and standards used in a substantive manner in the NRC regulatory process are maintained at the NRC Library, 7920 Norfolk Avenue, Bethesda, Maryland, for use by the public. Codes and standards are usually copyrighted and may be purchased from the originating organization or, if they are American National Standards, from the American National Standards Institute, 1430 Broadway, New York, NY 10018.

ABSTRACT

The TRAC-BWR code development program at the Idaho National Engineering Laboratory has developed versions of the Transient Reactor Analysis Code (TRAC) for the U.S. Nuclear Regulatory Commission and the public. The TRAC-BF1/MOD1 version of the computer code provides a best-estimate analysis capability for analyzing the full range of postulated accidents in boiling water reactor (BWR) systems and related facilities. This version provides a consistent and unified analysis capability for analyzing all areas of a large- or small-break loss-of-coolant accident (LOCA), beginning with the blowdown phase and continuing through heatup, reflood with quenching, and, finally, the refill phase of the accident. Also provided is a basic capability for the analysis of operational transients up to and including anticipated transients without scram (ATWS). The TRAC-BF1/MOD1 version produces results consistent with previous versions. Assessment calculations using the two TRAC-BF1 versions show overall improvements in agreement with data and computation times as compared to earlier versions of the TRAC-BWR series of computer codes.

CONTENTS

FIGURES

TABLES

SUMMARY

The TRAC-BWR Code Development Program at the Idaho National Engineering Laboratory (INEL) is developing versions of TRAC (Transient Reactor Analysis Code) to provide the U.S. Nuclear Regulatory Commission (NRC), and the public, a best-estimate capability for the analysis of postulated accidents and transients in boiling water reactor (BWR) systems and related experimental facilities. The first publicly released version of the code, TRAC-BD1, provided a basic capability for the analysis of design basis loss-of-coolant accidents (DBLOCAs). The second publicly released version of the code, TRAC-BD1/MOD1, was developed to provide an analysis capability for operational transients, including anticipated transients without scram (ATWS), as well as to provide an improved analysis capability for both large- and small-break LOCAs. The third release, TRAC-BF1, is a further improvement, particularly in the areas of computational speed and space-dependent (one-dimensional) neutron kinetics modeling capability. The fourth release, TRAC-BF1/MOD1, again improves the calculational speed, provides an improved steam separator-dryer model, and corrects many errors or omissions.

The code provides a consistent and unified analysis capability for an entire accident sequence. For a large break LOCA, this includes the blowdown phase, heatup, reflood with quenching, and, finally, the refill phase of the LOCA accident sequence. For an ATWS event initiated by the closure of the main steam isolation valve, the sequence includes the initiating event, the reactor power excursion caused by void collapse and terminated by reactivity feedback, periodic power excursion caused by cycling of the safety relief valves, and ultimate reactor shutdown though the injection of soluble boron poison.

Unique features of the code include (a) a full nonhomogeneous, nonequilibrium, two-fluid, thermal-hydraulic model of two-phase flow in all portions of a BWR system, including a three-dimensional thermal-hydraulic treatment of a BWR vessel; (b) detailed modeling of a BWR fuel bundle, including a thermal radiation heat transfer model for radiative heat transfer between multiple fuel rod groups, liquid and vapor phases, and the fuel channel wall, with quench front tracking on all fuel rod surfaces and inside and outside of the fuel channel wall for both bottom flooding and falling film quench fronts; (c) detailed models of BWR hardware, such as jet pumps and separator-dryers; and (d) a countercurrent flow limiting model for BWR-like geometries.

Other features of the code include a nonhomogeneous, thermal equilibrium critical flow model and flow-regime-dependent constitutive relations for the interchanges of mass, energy, and momentum between the fluid phases and between the phases and structure.

TRAC-BD1/MOD1 contained several upgrades and component enhancements. These include:

- Balance of plant component models, such as turbines, feedwater heaters, and steam condensers
- A simple lumped parameter containment model
- A comprehensive control system model
- Reactivity feedback model, including the effect of soluble boron
- Boron transport model
- Noncondensable gas transport model, including the effects of noncondensable gas on heat transfer
- Mechanistic separator-dryer model
- Two-phase level tracking model
- Generalized component-to-component heat and mass transfer models
- Moving mesh quench front tracking model for fuel rods and both inside and outside surfaces of fuel channel wall
- Improved constitutive relations for heat, mass, and momentum transfer between the fluid phases and between the fluid phases and structure
- A free-format input processor with extensive error checking.

New features of TRAC-BF1/MOD1 not available in the previously released version of the code include:

- Courant-limit-violating (fast-running) numerical solution for all one-dimensional hydraulic components
- Implicit steam separator/dryer model
- Implicit turbine model
- Improved interfacial package
- Condensation model for stratified vertical flow for realistic prediction of condensation in such cases
- One-dimensional neutron kinetic model (for space-dependent variations of power in ATWS-type transients)
- Improved control system solution logic
- Preload processor

- Conversion to ANSI standard FORTRAN 77.

From the very beginning of the TRAC-BF1/MOD1 development, adherence to a strict quality control program ensured that a well-documented, working version of the code would be available at all times. All changes to the code, however small, are given a program change label that appears on the modified FORTRAN statements and on all documentation that accompanies the changes. This ensures that all changes are traceable to documents that describe the basis for the change and the model developer making the change. A set of test cases was developed and executed after each successive working version of the code was assembled to ensure that recent changes did not affect changes or models inserted into previous versions of the code.

After the final working version of TRAC-BF1/MOD1 was assembled, a series of developmental assessment test cases was executed. These test cases provided insight into the code simulation capabilities for various separate effects hydrodynamic tests, separate effects heat transfer tests, and integral system effects tests. On the whole, agreement between the TRAC-BF1/MOD1 simulation of the various problems and measured test data is excellent.

The TRAC-BF1/MOD1 code is described by three documents: *TRAC-BF1/MOD1: An Advanced Best-Estimate Computer Program for Boiling Water Reactor Accident Analysis, Volumes 1 and 2, and TRAC-BF1/MOD1 Models and Correlations. Volume 1: Model Description* describes the thermal-hydraulic models, numerical methods, and component models available. *Volume 2: User's Guide* describes the input and output of the TRAC-BF1/MOD1 code and provides guidelines for use of the code modeling of BWR systems. *TRAC-BF1/MOD1 Models and Correlations* is designed for those users wishing a detailed mathematical description of each of the models and correlations available in TRAC-BF1/MOD1. This document reflects the as-coded configuration of the descriptive information provided in Volume 1.

ACKNOWLEDGMENT

This report has been prepared in response to and under the sponsorship of the Office of Nuclear Regulatory Research of the U. S. Nuclear Regulatory Commission. The authors wish to acknowledge the privilege of having the opportunity to contribute to this development. Also, the contributions of Dr. J. G. M. Andersen, of the General Electric Company, in clarifying several aspects in various sections of this document are sincerely appreciated.

NOMENCLATURE

A	flow area; interfacial area (Sections 4.1 and 6.1)
A_i	interfacial area between the liquid and gas phases
A_j	Flow area of cell j
$A_{j-1/2}$	Flow area at the junction (cell-edge) upstream of cell j
$A_{j+1/2}$	Flow area at the junction (cell-edge) downstream of cell j
A_o	Variable combination (Section 7.3)
A_w	geometric wall area
a	absorptivity
a_{HE}	homogeneous equilibrium mixture sound speed
a_s	sonic velocity
B	radiosity
B_k	radiation energy leaving surface k per unit area per unit time
$B2$	buckling squared
b	boron concentration
C	virtual mass coefficient (Section 7.2); reactivity coefficient (Section 9.4)
C_{bi}	Local average interfacial drag per unit volume
C_f	control rod fraction
C_f	Drag coefficient (dimensionless)
C_o	drift-flux model distribution parameter
C_p	specific heat constant pressure
C_v	specific heat constant volume

C_1	distribution parameter for the liquid phase (Section 6.1)
C_{wg}	wall shear coefficient for vapor flow
$C_{w\ell}$	wall shear coefficient for liquid flow
c_i	interfacial shear coefficient
c_{wg}	wall shear coefficient in the gas
$c_{w\ell}$	wall shear coefficient in the liquid
D	neutron diffusion coefficient
D_b	bubble diameter
D_d	droplet diameter
D_h	hydraulic diameter
D_h^*	nondimensional hydraulic diameter
D_H	hydraulic diameter
DZ	vessel cell axial length
DZL	two-phase level position within a vessel cell
dz	distance increment
E	fraction of the liquid flow entrained as droplets (Sections 4.1 and 6.1)
Ent	modified entrainment defined in Sections 4.1 and 6.1
Eψ2	void-interpolated entrainment defined in Section 6.1
e	relative roughness in relation to hydraulic diameter (Section 6.2); internal energy per mass (Section 7.2)
e_a	noncondensable gas internal energy
e_g	gas-mixture internal energy
e_ℓ	liquid internal energy
e_v	water-vapor internal energy

F_{kj}	view factor from surface k to surface j
$F_{\ell g}$	interfacial drag force per unit volume
FA	flow area in three-dimensional equations (subscript indicates direction)
$f_{1\phi}$	single-phase friction factor
$\vec{g}$	gravitational acceleration
G	mass velocity (Section 6.1 and 6.2); mass flux (Section 6.3)
G_{ave}	flow area averaged mass velocity
g	magnitude of the gravity vector
g_1	variable combination defined in Section 6.2
H	incident radiation heat flux
h	heat transfer coefficient
h_{ig}	interfacial HTC to the gas
$h_{i\ell}$	interfacial HTC to the liquid
h_{sg}	vapor enthalpy at saturation temperature
$h_{s\ell}$	liquid enthalpy at saturation temperature
h_v'	vapor enthalpy of the bulk vapor if the vapor is condensing or the vapor saturation enthalpy if liquid is vaporizing
h_ℓ'	liquid enthalpy of the bulk liquid if the liquid is vaporizing or the liquid saturation enthalpy if vapor is condensing
h_{wg}	wall HTC to the gas
$h_{w\ell}$	wall HTC to the liquid
J	volumetric flux

j	Total mass flux = $j_g + j_\ell$
j_g	Vapor volumetric flux density = αV_g
j_{go}	The limiting value of j_g (for $J_\ell = 0$) = $\frac{(g \sigma \Delta\rho)^{0.25}}{\sqrt{\rho_g}}$
j_ℓ	Liquid volumetric flux density = $(1 - \alpha) V_\ell$
$j_{\ell o}$	The limiting value of $j\ell$ (for $j_g = 0$) = $\frac{(g \sigma \Delta\rho)^{0.25}}{\sqrt{\rho_\ell}}$
K	utateladze number in the CCFL correlation (Section 7.3)
K_d	radiation absorption coefficient per unit length for droplets (Section 4.3)
K_g	radiation absorption coefficient per unit length for vapor (Section 4.3); vapor Kutateladze number (Section 7.3)
K_ℓ	liquid Kutateladze number (Section 7.3)
k	hydraulic loss coefficient (Section 6.2); neutron multiplication (Section 9.4)
k_g	thermal conductivity of vapor
k_ℓ	thermal conductivity of water
k_{vm}	virtual mass coefficient
L	hydraulic cell length
L_{kj}	length along the path kj
m	solute concentration in the liquid (mass of solute per unit mass of liquid); constant in CCFL correlation (Sections 6.1 and 7.3)
m	total mass flow

m'	sulute weight concentration in liquid (mass of solute per unit mass of mixture)
N	number of surfaces
Nu	Nusselt number = h/kD
n	neutron density
$\bar{n}$	nuclei density
P	pressure (Section 7.3); power density
$P_d(z)$	probability of absorption per unit length
P_w	Wetted perimeter
P_w^*	Dimensionless variable defined in Section 7.3
p	fluid pressure, or equivalently, total pressure
p_a	partial pressure of the noncondensable gas
p_v	partial pressure of the vapor
q	core property, fuel temperature, moderator temperature, or moderator void, etc.
q_{dg}	power deposited directly in the gas (without heat-conduction process)
$q_{d\ell}$	power deposited directly in the liquid (without heat-conduction process)
q_i	total heat transfer across liquid-vapor interface
q_{ig}	interfacial heat transfer to the gas
$q_{i\ell}$	interfacial heat transfer to the liquid
q_{wg}	wall heat transfer to the gas
$q_{w\ell}$	wall heat transfer to the liquid
Re	Reynolds number
Re_g	Reynolds number for vapor

Re_{gf}	Reynolds number for vapor in film flow
Re_{ℓ}	Reynolds number for liquid
$Re_{\ell f}$	Reynolds number for liquid in film flow
r	spatial location
S_g	vapor entropy
S_{ℓ}	liquid entropy
St	Stanton number = h/GC_p
s_c	plated-out solute density (mass of plated solute divided by cell volume)
s_m	source term in the solute-mass differential equation
T	temperature
T_g	gas temperature
T_{ℓ}	liquid temperature
T_{sv}	saturation temperature corresponding to the vapor partial pressure
t	time
V	volume
V_D	velocity of dispersed phase
$\vec{V}_g$	gas velocity vector
$\overline{V_g}$	cross-sectional average vapor velocity
$\overline{V_{gj}}$	cross-sectional average vapor drift velocity
$\overline{V_{\ell}}$	cross-sectional average liquid velocity
$\overline{V_r}$	void-weighted average relative velocity
$\overline{V_{\ell n}}$	$= - \lvert\overline{V_{\ell}}\rvert$

$\overline{V_{ix}}$	countercurrent liquid velocity (Section 7.3)
V_g	magnitude of the gas velocity (one-dimensional equations)
V_{gj}	drift flux model drift velocity
VLEV	two-phase level velocity within a vessel cell
V_j	average velocity in cell j (the phasic subscript is omitted for simplicity)
$V_{j-1/2}$	velocity at the junction upstream of cell j
$V_{j+1/2}$	velocity at the junction downstream of cell j
V_k	velocity of phase k (k = g for vapor and k = ℓ for liquid)
V_ℓ	magnitude of the liquid velocity (one-dimensional equations)
$V_{g\theta}$	component of the gas velocity vector in the θ direction
$\vec{V}_\ell$	liquid velocity vector
V_{gr}	component of the gas velocity vector in the r direction
V_{gz}	component of the gas velocity vector in the z direction
$V_{\ell r}$	component of the liquid velocity vector in the r direction
$V_{\ell z}$	component of the liquid velocity vector in the z direction
$V_{\ell\theta}$	component of the liquid velocity vector in the θ direction
V_m	mixture velocity
$V_{\ell})_j$	volume of cell j

Vol, vol	hydrodynamic-cell volume
W	weighting factor
We	Weber number = $\rho DV^2/\sigma$
X	steam quality = $A\ \alpha\ \rho_g\ \overline{V_g}$
X2	an interpolation variable defined in Section 4.1
x	steam quality
Z	length in axial direction
z	length in vertical direction

Greek Letters:

α	gas volume fraction or void fraction
α_g	vapor void fraction
α_ℓ	liquid void fraction
α_j	void volume fraction in cell j
α_{tran}	void fraction at transition from bubbly/churn to annular flow
ΔP	pressure difference across a junction
ΔX	axial length
$\Delta\rho$	$\rho_\ell - \rho_g (kg/m^3)$
ε	emissivity
ε_{gkj}	emissivity of the vapor phase along the path k to j
ε_{kj}	emissivity of the two-phase mixture along the path k to j
ϵ	absolute wall roughness height
η	variable defined in Section 6.1
ϕ	direct neutron flux

Γ	interfacial mass-transfer rate
Γ_j	rate of vapor mass generation per unit time in cell j.
$\Gamma 4$	defined in Section 6.1
γ	specific heat ratio (Section 7.2); square root of density ratio = $\sqrt{\rho_\ell/\rho_g}$ (Sections 6.1 and 7.3)
χ	an interpolation variable defined in Section 6.1; fission neutron spectrum (Section 9.4)
χ^2	an interpolation variable defined in Sections 6.1 and 7.3
μ_g	vapor viscosity
μ_ℓ	liquid viscosity
ν	wave number (Section 4.3); number of neutrons produced per fission (Section 9.4)
ξ	defined in Section 6.1
ρ	density or concentration
ρ_a	noncondensable gas density (microscopic)
ρ_c	density of continuous phase (microscopic)
ρ_g	gas-mixture density (microscopic)
ρ_j	physic density in cell j
ρ_ℓ	liquid-water density (microscopic)
ρ_m	liquid/gas mixture density (microscopic)
ρ_v	water-vapor density (microscopic)
∇P_s	pressure force per unit volume due to void gradient between adjacent cells in horizontal direction.
Σ	macroscopic neutron cross section
σ	surface tension
σ_{SB}	Stefan-Boltzmann constant

τ	shear stress at the wall
τ_{gkj}	transmissivity of the vapor phase along path k to j
τ_{kj}	transmissivity of the two-phase mixture along path k to j
$\tau_{\ell kj}$	transmissivity of the liquid phase along path k to j
ξ	relative roughness in relation to channel radius = $2\epsilon/D_h$
ξ_n	defined in Section 6.1
ξ_2	an interpolation variable defined in Section 4.1

Superscripts

T	transpose of vector or matrix
n	old time
n+1	new time
+	above two-phase level
-	below two-phase level

Subscripts

a	air or noncondensable gas (Section 2); absorption (Section 9.4)
B	boron
b	bubble
c	cell center
d	droplet
DMH	direct moderator heating
DOP	Doppler
eff	effective value

ent	entrained
F	fuel
f	liquid film (Section 4.1); fission (Section 9.4)
fb	feedback
g	mixture of water vapor and noncondensable gas (Section 2); group (Section 9.4)
HE	homogeneous equilibrium mixture
i	interface
ib	bubble interface
id	droplet interface
if	film interface
igt	total vapor to interface
ift	total liquid to interface
iftc	total liquid to interface in condensation
j	center
j±1/2	cell edges
k	surface number
kj	along the path kj
l or ℓ	liquid
M	moderator
m	mixture
NC	noncondensable
P	constant pressure
r	radiative (Section 4.3); removal
S	constant enthalpy
s	saturation state

t	total (Section 4.3); throat
T	constant temperature
TF	fuel temperature
TM	moderator temperature
U	upstream
v	water vapor
VD	void
w	wall
∞	infinite lattice or infinite reactor
1,2	fast and thermal neutron groups, respectively
1→2	neutron downscatter from fast into thermal group

TRAC-BF1/MOD1 MODELS AND CORRELATIONS

1. INTRODUCTION

The transient reactor analysis code for boiling water reactors (TRAC-B)[1-1,1-2] is a large and complex computer program for analyzing thermal-hydraulic transients in boiling water reactor (BWR) systems. Development of this code was initiated at the Idaho National Engineering Laboratory (INEL) in 1979 under the sponsorship of the U.S. Nuclear Regulatory Commission (NRC). The starting point for this development was an early version of the transient reactor analysis code for pressurized water reactors (TRAC-P)[1-3] developed at Los Alamos National Laboratory (LANL). For this reason, the basic equation system and the principal coding structure of TRAC-BF1/MOD1 are the same as in TRAC-PF1. However, many of the models representing physical phenomena or performance of certain components unique to BWRs are different in TRAC-BF1/MOD1. Furthermore, a number of programming changes that have been included in the evolving versions of TRAC-B, over several years, have made TRAC-BF1/MOD1 considerably different than TRAC-PF1. Table 1-1 gives a list of the released versions of TRAC-B and their main capabilities.

Because of basic differences between BWRs and pressurized water reactors (PWRs), specific models have been included in TRAC-B for treatment of important BWR components, such as fuel bundles with canisters, jet pumps, steam separators, and dryers.[1-4] The differences between the predecessor TRAC-P version and TRAC-B have increased in many respects with each new version. Two of the most important differences from the user's point of view are the input and output data structures. These are considerably different between TRAC-BF1/MOD1 and TRAC-PF1.

In spite of the many differences, there are still fundamental similarities between TRAC-BF1/MOD1 and TRAC-PF1 in the use of the two-fluid six-equation system, the discretization of the partial differential equations and, to a large extent, the numerical solution schemes. For this reason, a detailed description of these aspects of TRAC-PF1 is equally descriptive of the similar aspects of TRAC-BF1/MOD1, and a number of these features are identified in the following sections of this report. Typical examples of these are the basic set of one- and three-dimensional flow equations, steam-water properties, and remedies for water packing problems.

From the start, development of TRAC-B was technically coordinated with a similar development at General Electric (GE) in San Jose, California. Several models, solution approaches, and whole subroutines for TRAC-B versions have been exchanged between GE and INEL in this collaboration. Major examples of GE's contributions are the interfacial shear, jet pump, and interfacial heat transfer models that are described later. It may be observed that TRAC-BF1/MOD1 contains many models and features that were developed outside of

Table 1-1. Previously released versions of TRAC-BWR.

Code version	Release date	Major new or improved capabilities	Reference
TRAC-BD1	February 1981	Basic large break LOCA	a
TRAC-BD1/V12	June 1982	Improved large and small breaks, basic compatibility for operational transients and ATWS	
TRAC-BD1/MOD1	November 1983	Large and small breaks, balance of plant modeling, operational transient and ATWS (with point kinetics)	b
TRAC-BF1 (interim)	January 1985	Basic fast running numerics, one-dimensional neutron kinetics	c
TRAC-BF1	August 1986	Complete one-dimensional fast numerics, upgraded control system, improved hydraulics and heat transfer	d

a. J. Spore, *TRAC-BD1: An Advanced Best Estimate Computer Program for Boiling Water Reactor Loss-of-Coolant Analysis*, NUREG/CR-2178, October 1981.

b. D. D. Taylor et al., *TRAC-BD1/MOD1: An Advanced Best Estimate Computer Program for Boiling Water Reactor Transient Analysis*, NUREG/CR-3633, EGG-2294, April 1984.

c. Unpublished EG&G report, *TRAC-BF1 Manual: Extensions to TRAC-BD1/MOD1 (Draft)*, August 1985.

d. W. L. Weaver et al., *TRAC-BF1 Manual: Extensions to TRAC-BD1/MOD1*, EGG-2417, August 1986 (available from EG&G Technical Library).

the INEL. The aim of this report is to give a detailed documentation of all important features of TRAC-BF1/MOD1, regardless of their source of development. In particular, it is important to note that models and features received from other sources have often been revised, modified, or reprogrammed before inclusion in TRAC-B.

The code manuals published with different versions of TRAC-B include adequate descriptions of many models introduced in each version. However, a complete and detailed documentation of all features of TRAC-BF1/MOD1 has not been available in one publication. The present report is intended to fill

this gap.

The approach taken in preparation of this document has been guided by the following process:

1. Review the coding of different models.

2. Identify the source of models and formulations used in the coding.

3. Identify the data base used in the derivation of models or correlations.

4. Provide a thorough sequence of equations leading to the programmed equations.

5. Identify and explain any limitations, modifications, interpolations, or other treatments imposed in the coding.

6. Comment on the implementation of each model in the coding; in particular, on the numerical procedures in the preparation of inputs and numerical treatments of the calculation results when they are used in the main equations.

7. Identify errors, inconsistencies, or other shortcomings.

Due to limitations in time and resources, this report does not include any systematic assessment of the individual models. Only some specific model assessments that were found in earlier publications have been included in a few cases. The absence of some necessary assessments is also pointed out in several places. Although general assessment of TRAC-B versions with the use of system data (see Reference 1-5) have indicated good predictive capabilities, it is probable that a systematic assessment of individual models, followed by subsequent refinements in the code, would enhance the accuracy of TRAC-BF1/MOD1 for actual BWR transient analysis.

Adoption of the title "Quality Assurance Report" for this document has been avoided on the grounds that the identified inconsistencies and the systematic assessment of the models must be performed before such a report can be produced. The structure of this report has been coordinated as far as possible with similar documentation for TRAC-PF1[1-6] and RELAP5/MOD2.[1-7] The initial work on detailed documentation of TRAC-BF1/MOD1 models began early in FY-1987, and was intended to focus on the interfacial package and some other features that users had found influence reactor analysis calculations most significantly. However, the focus and extent of this documentation was later changed to achieve the above mentioned coordination.

A basic outline for the contents of the documentation of these codes was suggested by the Safety Code Development Group, Nuclear Technology and Engineering Division, LANL. This outline was slightly modified by inputs from

the INEL and the NRC and was finalized in July 1987.[a] The adopted outline was to a large extent oriented towards TRAC-PF1 features. For this reason, some of the main chapter headings are not quite relevant to a description of TRAC-BF1, and there are some additional features in the latter code that would require separate sections of their own. On this account, Sections 3 and 5 in this report are very brief because there is no centralized determination of flow-regime in TRAC-BF1 (subject of Section 3) and the different aspects of fluid mass conservation (subject of Section 5) are no different than those described in the interfacial heat transfer section (4.1) or wall heat transfer section (4.2). The same argument applies to many other sections, yet for consistency, LANL's suggested outline is preserved. Brief comments under some of the headings are included to lead the reader to where the relevant details are found in the report.

Coordination of documentation allowed exchanging write-ups of some identical features in TRAC-BF1/MOD1 and TRAC-PF1. On this basis, the contents of Section 2 (Field Equations) is to a large extent a reproduction of the same chapter in Reference 1-3. However, many changes and alterations have been included to describe the field equations, which are different in detail in TRAC-BF1 from those in TRAC-PF1. Several other sections from Reference 1-3 are used in the same manner. Each of these sections is identified appropriately with an acknowledgment of the source.

This report includes, also, some isolated sections from different TRAC-B manuals and completion reports, which were found to give an adequate description of the specific models. These insertions are identified with appropriate references.

1.1 REFERENCES

1-1. J. Spore et al., *TRAC-BD1: An Advanced Best Estimate Computer Program for Boiling Water Reactor Loss-of-Coolant Analysis*, NUREG/CR-2178, October 1981.

1-2. D. D. Taylor et al., *TRAC-BD1/MOD1: An Advanced Best Estimate Computer Program for Boiling Water Reactor Transient Analysis, Volumes 1 through 4*, NUREG/CR-3633, EGG-2294, April 1984.

1-3. D. R. Liles et al., *TRAC-PF1/MOD1: An Advanced Best Estimate Computer Program for Pressurized Water Reactor Thermal-Hydraulic Analysis*, NUREG/CR-3858, LA-10157-MS, July 1986.

1-4. W. H. Rettig and N. L. Wade, Eds., *TRAC-BF1/MOD1: An Advanced Best-Estimate Computer Program for Boiling Water Reactor Accident Analysis, Volume 2: User's Guide*, NUREG/CR-4356, EGG-2626, June 1992.

---

a. T. D. Knight, "Models and Correlations Document, An Outline," Memorandum, Los Alamos National Laboratory, July 28, 1987.

1-5. B. L. Charboneau, *Overview of TRAC-BD1/MOD1 Assessment Studies*, NUREG/CR-4428, EGG-2422, November 1985.

1-6. Safety Code Development Group, *TRAC-PF1/MOD1 Correlations and Models*, NUREG/CR-5069, LA-11208-MS, December 1988.

1-7. R. A. Dimenna et al., *RELAP5/MOD2 Models and Correlations*, NUREG/CR-5194, EGG-2531, August 1988.

2. FIELD EQUATIONS

The main purpose of the TRAC-BF1/MOD1 code is to solve a coupled set of field equations describing the thermal-hydraulic behavior of the fluid coolant in the BWR system, the flow of energy in the fuel and the structural components of the reactor, and the generation of the nuclear power in the reactor core. The following subsections briefly describe those field equations. The most difficult part of the solution is to solve the thermal-hydraulic behavior of the fluid and the coupling to the fuel/structural heat transfer through the heat transfer coefficients (HTCs); the code devotes most of the programming and most of the computer time to solving this part of the problem. This area is more complex because there are more coupled field equations associated with describing the fluid (more independent variables), more phenomena to be considered, and the HTCs are very dependent on the fluid properties and velocities. On the other hand, the field equations describing the energy field in the solid structures and the nuclear reaction are much simpler and involve fewer variables, although this statement is not intended to indicate that these fields are not as important as the thermal-hydraulic model to the overall solution of the problem.

We present the field equations here almost solely to provide a basis for understanding the required closure relations incorporated into TRAC-BF1/MOD1, although the equations help to express the coupling among the different parts of the overall code. Also, the discussion of the fluid field equations provides an indication of averaging processes and the time levels at which the variables are evaluated.

2.1 FLUID FIELD EQUATIONS

TRAC-BF1/MOD1 uses a two-fluid model for fluid flow in both the one- and three-dimensional components. These equations were derived at LANL and were coded into a developmental version of the TRAC-PF1 code, which was the code from which TRAC-PF1/MOD1 was developed (see Section 1).

There have been two additional terms added to the original equations of motion (momentum equations), which represent the virtual mass force and a pressure force due to the void fraction gradient between adjacent cells in the horizontal direction.

2.1.1 Nomenclature

Before presenting the fluid field equations, we need to define certain terminology. In our nomenclature, the term gas implies a general mixture of water vapor and the noncondensable gas. The subscript g will denote a property or parameter applying to the gas mixture; the subscript $\underline{v}$ indicates a

quantity applying specifically to water vapor (referred to as simply vapor); and the subscript a (for air) signifies a noncondensable-gas quantity. The term liquid implies pure liquid water, and the subscript ℓ denotes a quantity applying specifically to liquid water. In the discussion of the finite-difference equations, all quantities except for the velocities are centered in the hydrodynamic cell (cell-centered); the velocities are cell-edge quantities.

2.1.2 Gas/Liquid Equations

The basic two-phase two-fluid model consists of six partial differential equations.

Mixture Thermal Energy Equation

$$\frac{\partial[(1-\alpha)\rho_\ell e_\ell + \alpha\rho_g e_g]}{\partial t} + \nabla\cdot[(1-\alpha)\rho_\ell e_\ell \vec{V}_\ell + \alpha\rho_g e_g \vec{V}_g]$$

$$= p\nabla\cdot[(1-\alpha)\vec{V}_\ell + \alpha\vec{V}_g] + q_{w\ell} + q_{sg} + q_{d\ell} + q_{dg} . \qquad (2.1\text{-}1)$$

Combined-Gas Thermal Energy Equation

$$\frac{\partial(\alpha\rho_g e_g)}{\partial t} + \nabla\cdot\left(\alpha\rho_g e_g \vec{V}_g\right) = -p\frac{\partial\alpha}{\partial t} - p\nabla\cdot(\alpha\vec{V}_g) + q_{wg} + q_{dg} + q_{ig} + \Gamma h_v' , \qquad (2.1\text{-}2)$$

Liquid Mass Equation

$$\frac{\partial[(1-\alpha)\rho_\ell]}{\partial t} + \nabla\cdot[(1-\alpha)\rho_\ell\vec{V}_\ell] = -\Gamma . \qquad (2.1\text{-}3)$$

Combined-Gas Mass Equation

$$\frac{\partial(\alpha\rho_g)}{\partial t} + \nabla\cdot(\alpha\rho_g\vec{V}_g) = \Gamma . \qquad (2.1\text{-}4)$$

Liquid Equation of Motion

$$\frac{\partial\vec{V}_\ell}{\partial t} + \vec{V}_\ell\cdot\nabla\vec{V}_\ell + k_{vm}\frac{\rho_c}{(1-\alpha)\rho_\ell}\frac{\partial}{\partial t}(\vec{V}_\ell - \vec{V}_g) = -\frac{1}{\rho_\ell}\nabla p$$

$$+ \frac{c_i}{(1-\alpha)\rho_\ell}(\vec{V}_g - \vec{V}_\ell)\cdot|\vec{V}_g - \vec{V}_\ell| - \frac{c_{w\ell}}{(1-\alpha)\rho_\ell}\vec{V}_\ell|\vec{V}_\ell| + \vec{g}$$

$$- k_{vm}\frac{\rho_c}{(1-\alpha)\rho_\ell}\vec{V}_D\nabla(\vec{V}_\ell - \vec{V}_g) + \frac{\nabla p_s}{(1-\alpha)\rho_\ell} . \qquad (2.1\text{-}5)$$

Combined-Gas Equation of Motion

$$\frac{\partial\vec{V}_\ell}{\partial t} + \vec{V}_\ell\cdot\nabla\vec{V}_\ell + k_{vm}\frac{\rho_c}{(1-\alpha)\rho_\ell}\frac{\partial}{\partial t}(\vec{V}_\ell - \vec{V}_g) = -\frac{1}{\rho_\ell}\nabla p - \frac{c_i}{\alpha\rho_g}(\vec{V}_g - \vec{V}_\ell)|\vec{V}_g - \vec{V}_\ell|$$

$$- \frac{c_{wg}}{\alpha\rho_g}\vec{V}_g|\vec{V}_g| + \vec{g} - k_{vm}\frac{\rho_c}{\alpha\rho_g}\vec{V}_D\cdot\nabla(\vec{V}_g - \vec{V}_\ell) + \frac{\nabla p_s}{\alpha\rho_g} . \qquad (2.1\text{-}6)$$

An alternative to solving one of the phasic mass equations is to solve the total mass equation, which is obtained by summing Equations (2.1-3) and (2.1-4).

Total Mass Equation

$$\frac{\partial[(1-\alpha)\rho_\ell + \alpha\rho_g]}{\partial t} + \nabla\cdot\left[(1-\alpha)\rho_\ell\vec{V}_\ell + \alpha\rho_g\vec{V}_g\right] = 0 . \qquad (2.1\text{-}7)$$

Solving either Equation (2.1-3) or (2.1-4) together with Equation (2.1-7) is completely equivalent to solving both Equations (2.1-3) and (2.1-4).

The mass equations are written in fully conservative form to permit the construction of a numerical scheme that rigorously conserves some measure of the system mass. The energy equations are written in a partially conservative form to make numerical solution simpler than would be possible if the fully conservative form (bulk kinetic energy terms included) were used. The nonconservative form of the momentum equations also permits simpler numerical solution strategies and can generally be justified because the presence of wall friction makes the fully conservative form of the momentum equation far less useful. However, when sharp void fraction changes exist, numerical solution of the nonconservative motion equations can produce significant errors. In such instances, a version of the fully conservative momentum equation must be solved (see Section 2.1.7.2.).

Closure is obtained for these equations with normal thermodynamic relations, which for water are described in Appendix A, together with the transport properties and specifications for the interfacial drag coefficients (c_i), the interfacial heat transfer (q_{ig} and $q_{i\ell}$), the phase-change rate (Γ),

the wall-shear coefficients (c_{wg} and $c_{w\ell}$), and the wall heat flows (q_{wg} and $q_{w\ell}$). The phase-change rate is evaluated from a simple thermal-energy jump relation

$$\Gamma = \frac{-(q_{ig} + q_{i\ell})}{h_v' - h_\ell'} , \tag{2.1-8}$$

where

$$q_{ig} = h_{ig} A_i \frac{(T_{sv} - T_g)}{vol} , \tag{2.1-9}$$

and

$$q_{i\ell} = h_{i\ell} A_i \frac{(T_{sv} - T_\ell)}{vol} . \tag{2.1-10}$$

Here, A_i and the h_i terms are the interfacial area and HTCs, and T_{sv} is the saturation temperature corresponding to the partial steam pressure. The quantities h_v' and h_ℓ' are the appropriate enthalpies of the vapor and liquid, respectively; these enthalpies are the bulk fluid enthalpy for the phase moving to the interface and the saturation enthalpy for the product of the phase change.

Wall heat-transfer terms assume the form

$$q_{wg} = h_{wg} A_w \frac{(T_w - T_g)}{vol} \tag{2.1-11}$$

and

$$q_{w\ell} = h_{w\ell} A_w \frac{(T_w - T_\ell)}{vol} , \tag{2.1-12}$$

where A_w is the actual heated surface area. The h_{wg} and $h_{w\ell}$ of the cell include the information necessary for partitioning the wall heat transfer between the gas and the liquid.

2.1.3 Noncondensable Gas

A single noncondensable gas field may be followed with TRAC-BF1/MOD1. It is assumed to be in thermal equilibrium with any steam that is present and to

move with the same velocity as the steam. Hence, only a single field equation is needed to track the noncondensable gas.

Noncondensable Gas Mass Equation

$$\frac{\partial(\alpha\rho_a)}{\partial t} + \nabla \cdot (\alpha\rho_a\vec{V}_g) = 0 \ . \tag{2.1-13}$$

With this field present, the total gas density and energy are sums of the vapor and the noncondensable components

$$\rho_g = \rho_v + \rho_a \tag{2.1-14}$$

and

$$\rho_g e_g = \rho_v e_v + \rho_a e_a \ . \tag{2.1-15}$$

We assume Dalton's law applies; therefore,

$$p = p_v + p_a \ . \tag{2.1-16}$$

The subscripts v and a indicate, respectively, the steam and air properties; the code normally applies the thermodynamic properties for air to the noncondensable gas.

2.1.4 Liquid Solute

TRAC-BF1/MOD1 includes a mass continuity equation for a solute moving with the liquid field.

Liquid-Solute Mass Equation

$$\frac{\partial[(1-\alpha)m\rho_\ell]}{\partial t} + \nabla \cdot (1-\alpha)m\rho_\ell\vec{V}_\ell = S_m \ , \tag{2.1-17}$$

where m is the solute concentration (mass of solute/unit mass of liquid water) in the liquid phase.

This mass continuity equation is converted into a weight concentration equation by assuming that the mixture of liquid and solute is a dilute mixture. The assumption of a dilute mixture is appropriate for the boron concentration, which is measured in parts per million by weight. The weight

concentration is given by

$$m' = \frac{\text{mass of solute}}{\text{mass of solute + mass of liquid}}$$

$$= \frac{m(1-\alpha)\rho_\ell}{m(1-\alpha)\rho_\ell + (1-\alpha)\rho_\ell} \tag{2.1-18}$$

$$= \frac{m}{1+m} \approx m \text{ if } m \ll 1 .$$

Using this approximation, the liquid-solute concentration equation is

$$\frac{\partial_t[(1-\alpha)\rho_\ell m']}{\partial t} + \nabla \cdot [(1-\alpha)\rho_\ell m' \vec{V}_\ell] = S_{m'} \tag{2.1-19}$$

where m' is the weight concentration of solute (mass of solute/mass of mixture) in the liquid phase and the units of m' are parts per million (ppm).

The solute does not affect the hydrodynamics directly. If we assume that the solute represents boron, the amount of the dissolved and the plated-out boron in the core may affect the hydrodynamics indirectly through reactivity feedback. If the solute concentration exceeds the orthoboric-acid solubility at the liquid temperature in a specific hydrodynamic cell, we assume that the solute in that cell plates out. Plating can occur if the cell fluid flashes or boils and increases the concentration beyond the solubility limit. We also assume that any plated-out solute instantaneously redissolves to the maximum allowable concentration if more liquid enters the cell. Because the solute does not affect the hydrodynamics directly, the solute variable may be used as a tag to track the movement of fluid fro a specific source through the system.

2.1.5 One-Dimensional Finite-Difference Methods

For the one-dimensional components, the code solves Equations (2.1-1) through (2.1-6), (2.1-12), and (2.1-16) to provide a complete description of the fluid field, although Equation (2.1-12) and/or (2.1-16) can be turned off through input. The spatial mesh used for the difference equations is staggered with thermodynamic properties evaluated at the cell centers and velocities evaluated at the cell edges. For stability, flux terms at cell edges require donor-cell averages of the form

$$(YV)_{j+1/2} = \begin{cases} Y_j V_{j+1/2}, & \text{if } V_{j+1/2} \geq 0 \\ Y_{j+1} V_{j+1/2}, & \text{if } V_{j+1/2} < 0 \end{cases} \tag{2.1-20}$$

where Y can be any cell-center state variable or a combination of such variables, and V is either the liquid or vapor velocity, as appropriate. The subscript j+1/2 points to a cell interface, and the subscripts j and j+1 indicate the hydrodynamic cells on each side of the cell interface. With this notation, the finite-difference divergence operator for one-dimensional calculations is

$$\nabla_j \cdot (YV) = \frac{[A_{j+1/2}(YV)_{j+1/2} - A_{j-1/2}(YV)_{j-1/2}]}{vol_j} \tag{2.1-21}$$

where A is the local cell-interface cross-sectional area (flow area) and vol_j is the volume of the jth cell. For the equations of motion, the donor-cell form of any $V \cdot \nabla V$ term is

$$V_{j+1/2} \nabla_{j+1/2} V = \begin{cases} \dfrac{DV_{j+1/2}(E \cdot V_{j+1/2} - F \cdot V_{j-1/2})}{\overline{\Delta X}_{j+1/2}}, & \text{if } V_{j+1/2} \geq 0 \\ \dfrac{DV_{j+1/2}(E \cdot V_{j+3/2} - F \cdot V_{j+1/2})}{\overline{\Delta X}_{j+1/2}}, & \text{if } V_{j+1/2} < 0 \end{cases} \tag{2.1-22}$$

where $\overline{\Delta X}_{j+1/2}$ is half the sum of ΔX_j and ΔX_{j+1}, respectively the cell lengths of cells j and j+1, and

$$D = \frac{A_{j+1/2}}{A_{j+1}} + \frac{A_{j+1/2}}{A_j} \tag{2.1-23}$$

$$E = \begin{cases} \dfrac{A_{j-1/2}}{A_{j+1}} & ; V_{j+1/2} \geq 0 \\ \dfrac{A_{j+3/2}}{A_{j+1}} & ; V_{j+1/2} < 0 \end{cases} \tag{2.1-24}$$

$$F = \frac{A_{j+1/2}}{A_j} \tag{2.1-25}$$

$$A_j = \frac{vol_j}{\Delta X_j} \tag{2.1-26}$$

$$A_{j+1} = \frac{vol_{j+1}}{\Delta X_{j+1}} \tag{2.1-27}$$

The factors D, E, and F are used to obtain the correct Bernoulli (or reversible) pressure loss (gain) through area reductions (expansions). The formulations for D, E, and F yield exact results for single-phase flow and approximately correct results if the change in the void fraction through the area change is small. The derivation of the factors D, E, and F can be found in Section 7.1.

The code uses the following finite-difference equations. In these equations, the superscripts n and n+1 indicate current-time and new-time quantities, respectively. A tilde ($\tilde{}$) above a variable indicates that it is the result of an intermediate step and not a final value for the end of the time step. A horizontal line ($\bar{}$) above a quantity indicates that it is obtained from the arithmetic average of values at adjacent cells. If there are no subscripts denoting cell location, we assume subscript j for mass and energy equations and subscript j+1/2 for equations of motion. Finally, θ is the angle between a vector from the center of cell j to the center of cell j+1 and a vector directed against gravity; in the application of the code, θ is more generally the inverse cosine ($\cos^{-1}$) of the change in elevation between cell centers divided by the flow length between cell centers.

The source terms on the right-hand sides of the stabilizer mass and stabilizer energy equations have been eliminated by subtracting the basic equations from the stabilizer equations. This eliminates the recomputation of the source terms in the stabilizer phase of the time advancement.

2.1.5.1 Basic Equations of Motion

Combined Gas

$$\frac{\left(V_g^{n+1} - V_g^n\right)}{\Delta t} + V_g \nabla_{j+1/2} V_g + k_{vm} \frac{\rho_{c_{j+1/2}}}{\left(\overline{\alpha\rho_g}\right)^n_{j+1/2}} \frac{\left(V_g^{n+1} - V_\ell^{n+1}\right) - \left(V_g^n - V_\ell^n\right)}{\Delta t}$$

$$+ \frac{C_i^n |V_g^n - V_\ell^n| \left(V_g^{n+1} - V_\ell^{n+1}\right)}{\left(\overline{\alpha\rho_g}\right)^n_{j+1/2}} + \frac{p_{j+1}^{n+1} - p_j^n}{\left(\overline{\rho_g}\right)^n_{j+1/2} \overline{\Delta x}_{j+1/2}}$$

$$+ \frac{C_{wg} |V_g^n| V_g^{n+1}}{\left(\overline{\alpha\rho_g}\right)^n_{j+1/2}} + g \cos\theta + \frac{k_{vm} \rho^n_{c_{j+1/2}}}{\left(\overline{\alpha\rho_g}\right)^n_{j+1/2}} V_D^n \nabla_{j+1/2}(V_g - V_\ell)$$

$$+ \frac{\nabla p_s^n}{\overline{\alpha\rho_g}^n_{j+1/2}} = 0 . \qquad (2.1\text{-}28)$$

Liquid

$$\frac{V_\ell^{n+1} - V_\ell^n}{\Delta t} + V_\ell \nabla_{j+1/2} V_\ell$$

$$+ k_{vm} \frac{\rho^n_{c_{j+1/2}}}{\left(\overline{1 - \alpha_j \rho_\ell}\right)^n_{j+1/2}} \frac{\left(V_\ell^{n+1} - V_g^{n+1}\right) - \left(V_\ell^n - V_g^n\right)}{\Delta t}$$

$$+ \frac{C_i |V_g^n - V_\ell^n| \left(V_p^{n+1} - V_g^{n+1}\right)}{\left(\overline{1 - \alpha}\right) \overline{\rho_\ell}^n_{j+1/2}} + \frac{p_{j+1}^{n+1} - p_j^n}{\overline{\rho_\ell}^n_{j+1/2} \overline{\Delta x}_{j+1/2}}$$

$$+ \frac{C_{w\ell} |V_\ell^n| V_\ell^{n+1}}{\left(\overline{1 - \alpha}\right) \overline{\rho_\ell}^n_{j+1/2}} + g \cos\theta$$

$$+ C_{vm} \frac{\rho_{\ell_{j+1/2}}^{n}}{(1-\alpha)\rho_{\ell_{j+1/2}}^{n}} V_D^n \nabla_{j+1/2}(V_\ell - V_g)$$

$$+ \frac{\nabla p_g^n}{(1-\alpha)\rho_{\ell_{j+1/2}}^{n}} = 0 . \qquad (2.1\text{-}29)$$

2.1.5.2 Basic Mass Equations

Combined Gas

$$\frac{\left[\bar{\alpha}\bar{\rho}_g - (\alpha\rho_g)^n\right]}{\Delta t} + \nabla_j \left(\alpha\rho_g V_g^{n+1}\right) = \bar{\Gamma} . \qquad (2.1\text{-}30)$$

Noncondensable Gas

$$\frac{\left[\bar{\alpha}\bar{\rho}_a - \alpha\rho_a^n\right]}{\Delta t} + \nabla_j \left(\alpha\rho_a V_a^{n+1}\right) = 0 . \qquad (2.1\text{-}31)$$

Liquid

$$\frac{\left\{(1-\bar{\alpha})\bar{\rho}_\ell - [(1-\alpha)\rho_\ell]^n\right\}}{\Delta t} + \nabla_j \left[(1-\alpha)\rho_\ell V_\ell^{n+1}\right] = -\bar{\Gamma} . \qquad (2.1\text{-}32)$$

2.1.5.3 Basic Energy Equations

Combined Gas

$$\frac{\left[\bar{\alpha}\bar{\rho}_\ell \bar{e}_g - (\alpha\rho_g e_g)^n\right]}{\Delta t} + \nabla_j \left[(\alpha\rho_g e_g) V_g^{n+1}\right]$$

$$+ \bar{p}\left[\frac{(\bar{\alpha} - \alpha^n)}{\Delta t} + \nabla_j \left(\alpha^n V_g^{n+1}\right)\right] = \bar{q}_{wg} + \bar{q}_{dg} + \bar{q}_{ig} + \bar{\Gamma}\,\bar{h}_{sg} . \qquad (2.1\text{-}33)$$

Total

$$\frac{\left\{\bar{\alpha}\bar{\rho}_g\bar{e}_g + (1-\bar{\alpha})\bar{\rho}_\ell\bar{e}_\ell - (\alpha\rho_g e_g)^n - \left[(1-\alpha)\rho_\ell e_\ell\right]^n\right\}}{\Delta t}$$

$$+ \nabla_j\left[(\alpha\rho_g e_g)V_g^{n+1} + (1-\alpha)\bar{\rho}_\ell e_\ell V_\ell^{n+1}\right]$$

$$+ \theta\,\nabla_j\left[(\bar{\alpha}-\alpha^n)V_\ell^{n+1} + \alpha^n V_g^{n+1}\right] = \bar{q}_{wg} + q_{w\ell} + \bar{q}_{d\ell} + \bar{q}_{dg} \,. \qquad (2.1\text{-}34)$$

2.1.5.4 Stabilizing Mass Equations

Combined Gas

$$\frac{\left[(\alpha\rho_g)^{n+1} - \bar{\alpha}\bar{\rho}_g\right]}{\Delta t} + \nabla_j\left\{\left[(\alpha\rho_g)^{n+1} - \alpha\rho_g\right]V_g^{n+1}\right\} = 0 \,. \qquad (2.1\text{-}35)$$

Noncondensable Gas

$$\frac{\left[(\alpha\rho_a)^{n+1} - \bar{\alpha}\bar{\rho}_a\right]}{\Delta t} + \nabla_j\left\{\left[(\alpha\rho_a)^{n+1} - \alpha\rho_a\right]V_g^{n+1}\right\} = 0 \,. \qquad (2.1\text{-}36)$$

Liquid

$$\frac{\left\{\left[(1-\alpha)\rho_\ell\right]^{n+1} - \left[(1-\bar{\alpha})\bar{\rho}_\ell\right]\right\}}{\Delta t} + \nabla_j\left(\left\{\left[(1-\alpha)\rho_\ell\right]^{n+1}\right.\right.$$

$$\left.\left. - \left[(1-\alpha)\rho_\ell\right]\right\}V_\ell^{n+1}\right) = 0 \,. \qquad (2.1\text{-}37)$$

Liquid Solute

$$\frac{\left\{\left[\overline{(1-\alpha)\rho_\ell m'}\right] - \left[(1-\alpha)\rho_\ell\right]^n m'^n\right\}}{\Delta t}$$

$$+ \nabla_j\left\{\left[\overline{(1-\alpha)\rho_\ell m'}\right]V_\ell^{n+1}\right\} = 0 \,. \qquad (2.1\text{-}38)$$

and

$$(m')^{n+1} = \min \left\{ \frac{\overline{[(1-\alpha)\rho_\ell\, m']} + S_c^n}{[(1-\alpha)\rho_\ell]^{n+1}} \, , \, \dot{m}_{max} \right\} \tag{2.1-39}$$

$$S_c^{n+1} = S_c^n + \overline{[(1-\alpha)\rho_\ell m']} - (m')^{n+1}[(1-\alpha)\rho_\ell]^{n+1} \, . \tag{2.1-40}$$

2.1.5.5 Stabilizing Energy Equations

Combined Gas

$$\frac{\left[(\alpha\rho_g e_g)^{n+1} - \bar{\alpha}\bar{\rho}_g\bar{e}_g\right]}{\Delta t} + \nabla_j \left\{ \left[(\alpha\rho_g e_g)^{n+1} - \alpha\rho_g e_g\right] V_g^{n+1} \right\} = 0 \, . \tag{2.1-41}$$

Liquid

$$\frac{[(1-\alpha)\rho_\ell e_\ell]^{n+1} - (1-\bar{\alpha})\bar{\rho}_\ell\bar{e}_\ell}{\Delta t} + \nabla_j \Big[\left\{ [(1-\alpha)\rho_\ell e_\ell]^{n+1} \right.$$

$$\left. - (1-\alpha)\rho_\ell e_\ell \right\} V_\ell^{n+1} \Big] = 0 \, . \tag{2.1-42}$$

Time levels are omitted from some flux terms in Equations (2.1-30) through (2.1-42) because these terms contain both old and new time quantities. If X is a combination of state variables without a time superscript, then the correct definition for the divergence term in the mass and energy equations in which it appears is

$$\nabla_j(XV) = \left(\frac{1}{vol}\right)_j \left\{ A_{j+1/2} V_{j+1/2}^{n+1} \left[f_{j+1/2} \hat{X}_j + (1 - f_{j+1/2}) X_{j+1}^n \right] \right.$$

$$\left. - \left\{ A_{j-1/2} V_{j-1/2}^{n+1} \left[f_{j-1/2} X_{j-1}^n + (1 - f_{j-1/2}) \hat{X}_j \right] \right\} \right. \tag{2.1-43}$$

where

$$\hat{X}_j = g' X_j^n + (1 - g')\bar{X}_j \, . \tag{2.1-44}$$

The factor $f_{j+1/2}$ ($f_{j-1/2}$) is used to obtain donor-cell averaging (defined

in [Equation (2.1-20)] and has the value 1 when $V^{n+1}_{j+1/2}\left(V^{n+1}_{j+1/2}\right)$ is zero or positive and 0 when the velocity is negative. The weighting factor g' depends on the rate of phase change and goes to unity as the phase change disappears and to zero as the phase change approaches the total outflow of the phase created in the cell. For nonzero g', this form of the divergence operator is nonconservative, but total conservation is maintained by the stabilizer step.

The divergence operator for the equations of motion (i.e., momentum equations) uses a mixed time level so that the Courant stability limit may be exceeded without the use of the predictor and stabilizer equations of motion found in TRAC-PF1/MOD1. The divergence operator is

$$V \nabla V_{j+1/2} = \begin{cases} \dfrac{DV^{n}_{j+1/2}EV^{n+1}_{j+1/2} - FV^{n}_{j-1/2}}{\Delta x_j} ; V_{j+1/2} \geq 0 \\ \dfrac{DV^{n}_{j+1/2}EV^{n}_{j+3/2} - FV^{n+1}_{j+1/2}}{\Delta x_{j+1}} ; V_{j+1/2} < 0 \end{cases} \tag{2.1-45}$$

The modifying coefficients are D = E = F = 1 in the divergence of the relative velocity found in the virtual mass terms.

2.1.5.6 Additional Force Terms in Momentum Equations. In addition for the forces represented by wall friction, interfacial friction, gravity, and momentum flux terms in the momentum equations, two additional force terms have been added to the one-dimensional momentum equations. The two additional terms represent the virtual mass force and an additional gravity force due to the void gradient between cells.

2.1.5.7 Formulation of the Virtual Mass Term. A virtual mass force term has been included in the one-dimensional momentum equations. The magnitude of this term is small and does not affect the solution very much. However, it does affect the coupling between the phases and adds damping to the solution procedure, leading to a smoother and faster-running code. The product of the virtual mass coefficient and the continuous phase density is given by

$$k_{vm}\rho_\ell = \begin{cases} 0.5\alpha\left(\dfrac{1+2\alpha}{1-\alpha}\right)\rho_\ell ; 0 < \alpha < \alpha_{tr} \\ 0.5(1-\alpha)\left(\dfrac{3-2\alpha}{\alpha}\right)\rho_v + \left(\rho_\ell^{vm} - \rho_v^{vm}\right)\left(\dfrac{1-\alpha}{1-\alpha_{tr}}\right)^3 ; 1 > \alpha > \alpha_{tr} \end{cases} \tag{2.1-46}$$

$$\rho_\ell^{vm} = 0.5\alpha_{tr}\left(\frac{1 + 2\alpha_{tr}}{1 - \alpha_{tr}}\right)\rho_\ell \qquad (2.1\text{-}47)$$

$$\rho_v^{vm} = 0.5(1 - \alpha_{tr})\left(\frac{3 - 2\alpha_{tr}}{\alpha_{tr}}\right)\rho_v \qquad (2.1\text{-}48)$$

where α_{tr} represents the transition between liquid continuous flow regime and the vapor continuous flow regime. For simplicity, this transition void fraction is taken as

$$\alpha_{tr} = 0.5 \; . \qquad (2.1\text{-}49)$$

The formulation of the virtual mass coefficient is in agreement with Zuber's recommendation. The velocity of the dispersed phase is given by

$$V_D = (1 - \alpha)V_g + \alpha V_\ell \; . \qquad (2.1\text{-}50)$$

This formulation gives the correct limits for single-phase flows (i.e., $V_D = V_\ell$ at $\alpha = 1$ and $V_D = V_g$ at $\alpha = 0$). The velocity of the dispersed phase V_D should more rightly be the kinematic velocity associated with the virtual mass force. In the absence of a definitive derivation of this kinematic velocity, the simple form shown above was adopted, since it has the correct limits.

2.1.5.8 **Void Gradient Gravity Head Term.** The other term added to the momentum equation represents information lost in the derivation of the one-dimensional momentum equations by the integration over the cross-sectional area perpendicular to the flow direction. In a horizontal flow path at low flow rates, a horizontally stratified flow will develop with a force resulting from the difference in the hydrostatic heads in adjacent computational cells. This force term is given by

$$\nabla p_s = p_1 - p_2 = (\rho_\ell - \rho_g)g_c \; \Delta z(\alpha_2 - \alpha_1) \qquad (2.1\text{-}51)$$

where the subscripts 1 and 2 refer to the diagram in Figure 1-1.

This force is added to the liquid phase momentum equation (the liquid phase has the highest inertia) in such a way as to equalize the liquid levels between the two cells and is computed based an beginning of time step void fractions. The explicit formulation of this force term can result in the momentum equations being unstable if too large a time step is taken during the time advancement. The time step used by the stratifical force is given by

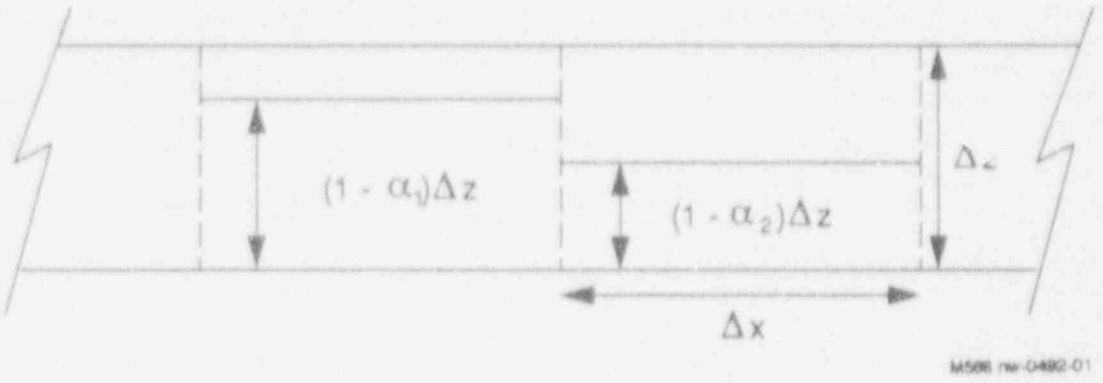

Figure 2.1-1. Void gradient gravity head term schematic.

$$\Delta t_s = \min \left[\Delta t, \frac{0.25}{\left\{ \overline{\Delta X} \sqrt{g_c \, \Delta z [1. - 0.5(\alpha_1 + \alpha_2)]} \right\}} \right] \tag{2.1-52}$$

where the time step associated with horizontal stratification force is determined by analyzing the flow between the two adjacent cells as if they were the two legs of a manometer. The stability limit for explicit integration of the manometer equations is given by

$$\Delta t \leq \frac{1}{\left\{ \Delta X \, g_c \, \Delta z [1 - 0.5(\alpha_1 + \alpha_2)] \right\}^{1/2}} \, . \tag{2.1-53}$$

The time step used by the code is one-fourth of the stability limit. Finally, the stratification force varies with the orientation of the flow path so that the final form of the horizontal stratification or void gradient force term is

$$\nabla p_s = (\rho_\ell - \rho_g) \, g_c \, \Delta z (\alpha_2 - \alpha_1) \sin \theta \, . \tag{2.1-54}$$

Equations (2.1-28) through-(2-34), combined with the necessary thermodynamic and constitutive equations, form a coupled system of nonlinear equations. Equations (2-28) and (2-29) are solved directly to obtain V_g^{n+1} and V_ℓ^{n+1} as dependent variables. After substituting these equations for velocity into Equations (2.1-30) through (2.1-34), the resulting system is solved for the independent variables

$\bar{p}^{n+1}$, $\bar{p}_g^{n+1}$, $\bar{T}_g^{n+1}$, and $\bar{\alpha}^{n+1}$

with a standard Newton iteration, including all coupling between cells. In practice, the linearized equations solved during this iteration can be reduced easily to a tridiagonal system involving only total pressures. The final six stabilizing equations (Equations (2.1-35) through (2.1-42)] also are simple

tridiagonal linear systems because V_g^{n+1} and V_ℓ^{n+1} are known after solving Equations (2.1-23) through (2.1-34). Because the pressure and fluid temperatures are used mainly as the starting point for the next iteration, the start of time-step values for these quantities are the tilde values from the end of the previous basic step. This approximation prevents an extra evaluation of the thermodynamic and transport properties. A void fraction consistent with the stabilizer mass and energy quantities is calculated by a simple linearization.

The basic momentum equations are set up in TF1E. Subroutine TF11 sets up the solution of the basic mass and energy equation, and FF1D completes the solution of the full basic equation set within a Newton iteration driven by subroutine OUTER. The stabilizer mass and energy equations are solved in STBME and BKSSTB.

2.1.6 Three-Dimensional Finite-Difference Methods

In the three-dimensional VESSEL component, the code solves the combined-gas mass equation (Equation (2.1-4)] and the total mass equation (Equation (2.1-7)] instead of the individual phasic mass equations solved in the one-dimensional components. However, for the three-dimensional component, the code solves the momentum and energy equations in the same form as for the one-dimensional components; i.e., individual liquid and combined-gas equations of motion (Equations (2.1-5) and (2.1-6)], and total and combined-gas energy equations (Equations (2.1-1) and (2.1-2)]. The momentum equations separate into three orthogonal-coordinate components. We discuss only the gas-phase equations, with the understanding that the liquid equations are treated analogously. For an orthogonal, right-handed cylindrical coordinate system in which the z axis is oriented vertically upwards, the three components of the vapor-momentum differential equation follow.

Momentum Equation Axial (z) Component

$$\frac{\partial V_{gz}}{\partial t} = -\left(v_{gr}\frac{\partial V_{gz}}{\partial r} + \frac{V_{g\theta}}{r}\frac{\partial V_{gz}}{\partial \theta} + V_{gz}\frac{\partial V_{gz}}{\partial z}\right) - \frac{1}{\rho_g}\frac{\partial p}{\partial z}$$

$$- \frac{C_{iz}}{\alpha\rho_g}(V_{gz} - V_{\ell z})|\vec{V}_g - \vec{V}_\ell| - \frac{C_{wgz}}{\alpha\rho_g}V_{gz}|\vec{V}_g| - g \quad . \qquad (2.1\text{-}55)$$

Momentum Equation Radial (r) Component

$$- \frac{C_{ir}}{\alpha\rho_g}(V_{gr} - V_{\ell r})|\vec{V}_g - \vec{V}_\ell| - \frac{C_{wgr}}{\alpha\rho_g}V_{gr}|\vec{V}_g| + \nabla p_{s,r} \qquad (2.1\text{-}56)$$

$$\frac{\partial V_{gr}}{\partial t} = -\left(V_{gr}\frac{\partial V_{gr}}{\partial r} + \frac{V_{g\theta}}{r}\frac{\partial V_{gr}}{\partial \theta} - \frac{V_{g\theta}^2}{r} + V_{gz}\frac{\partial V_{gr}}{\partial z} \right) - \frac{1}{\rho_g}\frac{\partial p}{\partial r}$$

Momentum Equation Azimuthal (θ) Component

$$\frac{\partial V_{g\theta}}{\partial \theta} = -\left(V_{gr}\frac{\partial V_{g\theta}}{\partial r} + \frac{\partial V_{g\theta}}{r}\frac{\partial V_{g\theta}}{\partial \theta} - \frac{V_{gr}V_{g\theta}}{r} + V_{gz}\frac{\partial V_{g\theta}}{\partial z} \right) - \frac{1}{\rho_{gr}}\frac{\partial p}{\partial \theta}$$

$$- \frac{C_{i\theta}}{\alpha\rho_g}(V_{g\theta} - V_{\ell\theta})\,|\bar{V}_g - \bar{V}_\ell| - \frac{C_{wg\theta}}{\alpha\rho_g}V_{g\theta}|\bar{V}_g| + \nabla p_{s,\theta} \,. \qquad (2.1\text{-}57)$$

TRAC-BF1/MOD1 uses a staggered-mesh scheme in which the velocities V are defined at the mesh-cell surfaces as opposed to the volume properties of pressure p, gas volume fraction α, temperature T, internal energy e, and density ρ, which are defined at the mesh-cell center. The scalar field equations (mass and energy) apply to a given mesh cell, whereas the momentum equations apply at the interfaces between mesh cells, a staggered mesh, in the three component directions.

The difference scheme for each of the momentum equations is lengthy because of the cross-derivative terms. Therefore, to illustrate the procedure, we describe only the gas z-direction momentum finite-difference equation for a typical mesh-cell interface, together with the gas mass and energy equations for a typical mesh cell. The gas component momentum equations in the r and r directions along with the all of the liquid equations are similar in form. The superscript n indicates a current-time quantity; the superscript n+1, a new-time quantity. The functional dependence (r,θ,z) points to the cell center. By incrementing r or θ or z by ±1, one moves to the adjacent cell in the direction based on which coordinate is incremented and on the sign of the increment. The functional dependencies (r-1/2,θ,z) and (r+1/2,θ,z) point to the inside and outside radial faces of the cell, respectively; (r,θ-1/2,z) and (r,θ+1/2,z), the right and left azimuthal faces of the cell (based on a perspective of looking radially out of the cell), respectively; (r,θ,z-1/2) and (r,θ,z+1/2), the bottom and top axial faces of the cell, respectively. The subscript g (for gas) is dropped unless it is needed for clarity. The three-dimensional finite-difference equations do not contain stabilizer steps and are simple generalizations of the one-dimensional basic equations.

2.1.6.1 Gas Momentum Equation in the z Direction. Using these conventions, the finite-difference gas-momentum equation in the z direction is where Δt is the time-step size.

$$V_z^{n+1}(r,\theta,z+1/2) = V_z^n(r,\theta,z+1/2) - \Delta t \left[\frac{\overline{V_r \Delta_r V_z}^n}{\Delta r} + \frac{\overline{V_r \Delta_\theta V_z}^n}{r \Delta \theta} \right.$$

$$+ \frac{DV_z^n(r,\theta,z+1/2)}{\Delta z} [V_z(r,\theta,z+1) - V_z(r,\theta,z)]^n$$

$$- \frac{p(r,\theta,z+1) - p(r,\theta,z)^{n+1}}{\rho^n(r,\theta,z+1/2)\ \Delta z}$$

$$- \frac{C_{iz}^n(r,\theta,z+1/2)}{\alpha^n(r,\theta,z+1/2)\ \rho^n(r,\theta,z+1/2)} \left\{ \left| V_\theta^n(r,\theta,z+1/2) \right| \right.$$

$$\left. - V_\ell^n(r,\theta,z+1/2) \left| \left[V_\theta^{n+1}(r,\theta,z+1/2) - V_\ell^{n+1}(r,\theta,z+1/2) \right] \right| \right\}$$

$$- \frac{C_{wz}^n(r,\theta,z+1/2)}{\alpha^n(r,\theta,z+1/2)\ \rho^n(r,\theta,z+1/2)} \left| \left| V_\ell^n(r,\theta,z+1/2) \right| \right.$$

$$\left. V^{n+1}(r,\theta,z+1/2) - g + \Delta p_s \right] \qquad (2.1\text{-}58)$$

Any finite-difference scheme requires certain quantities at locations where they are not defined formally; therefore, additional relations are needed. TRAC-BF1/MOD1 obtains the volume properties α and ρ_g at the cell axial interface from a cell-level weighted average. For example,

$$\alpha(r,\theta,z+1/2) = \frac{\Delta z(z)\alpha(r,\theta,z) + \Delta z(z+1)\alpha(r,\theta,z+1)}{\Delta z(z) + \Delta z(z+1)} \ . \qquad (2.1\text{-}59)$$

This averaging is necessary to compute accurately the gravitational pressure heads.

The cross-derivative term $\overline{V_r \Delta_r V_z}$ reflects a donor-cell average

$$\overline{V_r \Delta_r V_z} = V_r(r+1/2,\theta,z+1/2)[\ V_z(r+1,\theta,z+1/2) - V_z(r,\theta,z+1/2)]$$

$$+ V_r(r-1/2,\theta,z+1/2)\ [V_z(r,\theta,z+1/2) - V_z(r-1,\theta,z+1/2)] \qquad (2.1\text{-}60)$$

where

$$V_r(r+1/2,\theta,z+1/2) = \min\left[\frac{V_r(r+1/2,\theta,z+1)\ \Delta z(z) + V_r(r+1/2,\theta,z)\ \Delta z(z+1)}{\Delta z(z) + \Delta z(z+1)}\ ,\ 0\right] \qquad (2.1\text{-}61)$$

and

$$V_r(r-1/2,\theta,z+1/2) = \max\left[\frac{V_r(r-1/2,\theta,z+1)\ \Delta z(z) + V_r(r-1/2,\theta,z)\ \Delta z(z+1)}{\Delta z(z) + \Delta z(z+1)}\ ,\ 0\right]. \qquad (2.1\text{-}62)$$

In the above equations, min and max are the mathematical functions of minimum and maximum of the terms inside the brackets. An analogous expression holds for the $\overline{V_\theta \Delta_\theta V_z}$ term. The usage of central differences was dropped because of problems with numerical instabilities.

The radial component of the velocity at the axial location $(z+1/2)$ is obtained from

$$V_r(r,\theta,z+1/2) = \frac{1}{4}\ [V_r(r+1/2,\theta,z) + V_r(r-1/2,\theta,z)$$

$$+ V_r(r+1/2,\theta,z+1) + V_r(r-1/2,\theta,z+1)]\ ; \qquad (2.1\text{-}63)$$

a similar expression applies to $V_\theta(r,\theta,z+1/2)$.

The axial difference of V_z includes some cross-sectional area weighting to eliminate problems with pressure drops across area changes and is similar to the gradient terms in the one-dimensional component.

$$V_z(r,\theta,z+1) - V_z(r,\theta,z) = \begin{cases} \dfrac{V_z(r,\theta,z+1/2)\ FA_{z+1/2}}{FA_{z+1}} \\ - \dfrac{V_z(r,\theta,z-1/2)\ FA_{z-1/2}}{FA_z} \quad \text{if } V_z(r,\theta,z+1/2) \geq 0; \\ \dfrac{V_z(r,\theta,z+3/2)\ FA_{z+3/2}}{FA_{z+1}} \\ - \dfrac{V_z(r,\theta,z+1/2)\ FA_{z+1/2}}{FA_z} \quad \text{if } V_z(r,\theta,z+1/2) < 0 \end{cases} \tag{2.1-64}$$

where

$$FA_{z+1} = \frac{vol(r,\theta,z+1)}{\Delta z(z+1)} \tag{2.1-65}$$

and

$$FA_z = \frac{vol(r,\theta,z)}{\Delta z(z)} \ . \tag{2.1-66}$$

The spatial differences for V_z are, in the r direction,

$$V_z(r+1/2,\theta,z+1/2) - V_z(r-1/2,\theta,z-1/2) = \begin{cases} V_z(r,\theta,z+1/2) \\ - V_z(r-1,\theta,z+1/2) \quad \text{if } V_r(r,\theta,z+1/2) \geq 0 \\ V_z(r+1,\theta,z+1/2) \\ - V_z(r,\theta,z+1/2) \quad \text{if } V_r(r,\theta,z+1/2 < 0 \end{cases} \tag{2.1-67}$$

and, in the θ direction,

$$V_z(r,\theta+1/2,z+1/2) - V_z(r,\theta-1/2,z+1/2) = \begin{cases} V_z(r,\theta,z+1/2) \\ - V_z(r,\theta-1,z+1/2) \text{ if } V_\theta(r,\theta,z+1/2) \geq 0 \\ V_z(r,\theta+1,z+1/2) \\ - V_z(r,\theta,z+1/2) \text{ if } V_\theta(r,\theta,z+1/2 < 0 \end{cases}$$

(2.1-68)

Note that the V_z differences in the r and θ directions do not contain the flow-area weighting of the z-direction difference.

2.1.6.2 **Combined-Gas Mass Equation.** The convective terms in the finite-difference relations for the scalar field equations are in conservative form. The finite-difference form of the combined-gas mass equation is

$$\alpha^{n+1}\rho_g^{n+1} = \alpha^n\rho_g^n - \left(\frac{\Delta t}{vol}\right)\left[FA_{z+1/2}\left(\alpha^n\rho_g^n V_{gz}^{n+1}\right)_{z+1/2} - FA_{z-1/2}\left(\alpha^n\rho_g^n V_{gz}^{n+1}\right)_{z-1/2}\right.$$

$$+ FA_{r+1/2}\left(\alpha^n\rho_g^n V_{gr}^{n+1}\right)_{r+1/2} - FA_{r-1/2}\left(\alpha^n\rho_g^n V_{gr}^{n+1}\right)_{r-1/2} \quad FA_{\theta+1/2}\left(\alpha^n\rho_g^n V_{g\theta}^{n+1}\right)_{\theta+1/2}$$

$$\left. - FA_{\theta-1/2}\left(\alpha^n\rho_g^n V_{g\theta}^{n+1}\right)_{\theta-1/2}\right] + \Delta t\ \Gamma^{n+1} + SM_g^{n+1} \qquad (2.1\text{-}69)$$

where vol is the hydrodynamic cell volume, FA is the flow area at the mesh-cell edge, and SM_g is the gas source term for all one-dimensional components connected to the cell.

2.1.6.3 **Combined-Gas Energy Equation.** The combined-gas energy equation is

$$\alpha^{n+1}\rho_g^{n+1}e_g^{n+1} = \alpha^n\rho_g^n e_g^n - \left(\frac{\Delta t}{vol}\right)\left[FA_{z+1/2}\left(\alpha^n\rho_g^n e_g^n V_g^{n+1}\right)_{z+1/2}\right.$$

$$\left. - FA_{z-1/2}\left(\alpha^n\rho_g^n e_g^n V_g^{n+1}\right)_{z-1/2} + FA_{r+1/2}\left(\alpha^n\rho_g^n e_g^n V_g^{n+1}\right)_{r+1/2} - FA_{r-1/2}\left(\alpha^n\rho_g^n e_g^n V_j^{n+1}\right)_{r-1/2}\right.$$

$$- FA_{\theta+1/2}\left(\alpha^n \rho_g^n e_g^n V_g^{n+1}\right)_{\theta+1/2} - FA_{\theta-1/2}\left(\alpha^n \rho_g^n e_g^n V_g^{n+1}\right)_{\theta-1/2}\Big] - p^{n+1}(\alpha^{n+1} - \alpha^n)$$

$$- \left(\frac{p^{n+1}\Delta t}{VOL}\right)\Big[\left(FA\alpha^n V_g^{n+1}\right)_{z+1/2} - \left(FA\alpha^n V_g^{n+1}\right)_{z-1/2} + \left(FA\alpha^n V_g^{n+1}\right)_{r+1/2} - \left(FA\alpha^n V_g^{n+1}\right)_{r-1/2}$$

$$+ \left(FA\alpha^n V_g^{n+1}\right)_{\theta+1/2} - \left(FA\alpha^n V_g^{r+1}\right)_{\theta-1/2}\Big] + \Delta t\left(q_{wg}^{n+1} + q_{ig}^{n+1} + \Gamma^{n+1} h_v^{n+1}\right) . \qquad (2.1\text{-}70)$$

The differencing of the other scalar equations (the total mass and energy equations, the noncondensable-gas mass equation, and the liquid-solute mass equation) is similar.

2.1.6.4 Source Terms. All of the field equations in the three-dimensional VESSEL can have additional source terms to allow piping to be connected anywhere in the three-dimensional mesh. The source terms in the mass and energy equations follow below. The subscripts 1D and VESSEL indicate that quantities are obtained from the attached 1D components and the VESSEL, respectively; the subscript D represents the donor based on the velocity g; and the summation is over all one-dimensional components connected to a given vessel cell.

Overall Mass-Continuity Source Term

$$SM_T^{n+1} = \sum_{k=1}^{K} (\alpha\rho_g)_D^n \left(V_g^{n+1} FA\right)_{1D} + [(1 - \alpha)\ \rho_\ell]_D^n \left(V_\ell^{n+1}\ FA\right)_{1D} \qquad (2.1\text{-}71)$$

Combined Gas Mass Continuity Source Term

$$SM_g^{n+1} = \sum_{k=1}^{K} (\alpha\rho_g)_D^n \left(V_g^{n+1} FA\right)_{1D} \qquad (2.1\text{-}72)$$

Overall Energy Source Term

$$SE_T = \sum_{k=1}^{K} [(1 - \alpha)\rho_\ell e_\ell]_D^n \left(V_\ell^{n+1} FA\right)_{1D} + (\alpha\rho_g e_g)_D^n \left(V_g^{n+1} FA\right)_{1D}$$

$$+ p_{VESSEL} \cdot \left[\left(\alpha_D^n V_g^{n+1} FA\right)_{1D} + (1 - \alpha_D)^n \left(V_\ell^{n+1} FA\right)_{1D}\right] \qquad (2.1\text{-}73)$$

Combined Gas Energy Source Term

$$SE_g^{n+1} = \sum_{k=1}^{K} (\alpha\rho_g e_g)_D^n \left(V_g^{n+1} FA\right)_{1D} + P_{VESSEL}\alpha_D^n \left(V_g^{n+1} FA\right)_{1D} \quad (2.1\text{-}74)$$

Noncondensable Gas Mass Continuity Source Term

$$SA^{n+1} = \sum_{k=1}^{K} (\alpha\rho_a)_D^n \left(V_g^{n+1} FA\right)_{1D} \quad (2.1\text{-}75)$$

Liquid Solute Mass Continuity Source Term

$$SC^{n+1} = \sum_{k=1}^{K} \left[(1 - \alpha)\ \rho_\ell m'\right]_D^n \left(V_\ell^{n+1} FA\right)_{1D} \quad (2.1\text{-}76)$$

The momentum source terms are complicated by the staggered differencing and by the fact that allowable one-dimensional components may enter at an arbitrary angle. For TRAC-BF1/MOD1, we have assumed that the one-dimensional component attaches normal to the VESSEL mesh-cell face. The basic forms for the liquid and vapor momentum source terms follow.

Liquid-Momentum Source Term

$$\sum_{k=1}^{K} \frac{\left[(1 - \alpha)\ \rho_\ell V_\ell FA\right]_{1D,k}^n}{(1 - \alpha)\rho_\ell]_{VESSEL}^n} \cdot \frac{(V_\ell FA)_{1D,k}^n + (V_\ell FA)_{VESSEL}^n}{\left(\frac{vol}{\Delta z}\right)_{VESSEL}^2 \overline{\Delta z}}$$

Vapor-Momentum Source Term

$$\sum_{k=1}^{K} \frac{\left[\alpha\rho_v V_g FA\right]_{1D,k}^n}{(\alpha\rho_v)_{VESSEL}^n} \cdot \frac{(V_g FA)_{1D,k}^n + (V_g FA)_{VESSEL}^n}{\left(\frac{vol}{\Delta z}\right)_{VESSEL}^2 \overline{\Delta z}} \cdot$$

The $\overline{\Delta z}$ in the two previous terms is the distance between the centers of the two cells separated by the mesh-cell face under consideration. The $(V_g\ FA)_{VESSEL}$ is the product of the velocity and the flow area at the cell face opposite to the one of attachment, and these momentum source terms are applied to the momentum equations written at this opposite face.

The existence of the momentum source terms is dependent on the sign of the velocities in the VESSEL to keep the VESSEL donor-cell momentum equations consistent. For example, if the nearest VESSEL liquid velocity indicates that the flow is into the one-dimensional component from the VESSEL, then the source term is set equal to zero.

The finite-difference equations thus formed for the VESSEL component are semi-implicit, because the pressure gradient terms in the vapor and liquid momentum equations are treated at the new time. A Courant stability criterion,

$$\Delta t < \frac{L}{V} = \min\left[\frac{\Delta z}{V_{gz}}, \frac{r\Delta\theta}{V_{gr}}, \frac{\Delta z}{V_{\ell z}}, \frac{r\Delta\theta}{V_{\ell r}}, \frac{\Delta r}{V_{\ell r}}\right] \tag{2.1-77}$$

is necessary.

If hardware structure exists in the mesh cell, the hydrodynamic FA and vol are reduced from their geometric mesh-cell values. Thus, FA may be less than or equal to the geometric mesh-cell area, and vol may be less than or equal to the geometric mesh-cell volume. When FA is zero, all fluxes across that plane, as well as the individual velocities of each phase, are suppressed. This procedure allows large obstacles, such as the downcomer walls, to be modeled properly. The user specifies the flow and volume restrictions. (There are no constraints in the code to restrict FA and vol to be less than or equal to the geometric values, although the code user should adhere to such constraints.)

The number of independent variables is limited to V_ℓ, V_g, T_ℓ, T_g, a, and p by using the thermal equations of state,

$$\rho_\ell = \rho_\ell(p, T_\ell) \tag{2.1-78}$$

$$\rho_v = \rho_v(p_v, T_g) \tag{2.1-79}$$

$$\rho_a = \rho_a(p_a, T_g) \tag{2.1-80}$$

the caloric equations of state,

$$e_\ell = e_\ell(p, T_\ell) \tag{2.1-81}$$

$$e_v = e_v(p_v, T_g) \tag{2.1-81}$$

$$e_a = e_a(p_a, T_g) \tag{2.1-83}$$

and the definitions for ρ_g, e_g, and p (Equations (2.1-14), (2.1-15), and

(2.1-16)].

The horizontal stratification or void gradient force in the radial and azimuthal momentum equations is computed in the same way as in the one-dimensional components. The force is partitioned between the two phase based on the relative inertias of the phases rather than being added to the liquid momentum equation as in the one-dimensional components.

The full set of momentum equations is evaluated in subroutine TF3E. The mass and energy equations are set up and linearized in TF3I. Final solution of the equations occurs in FF3D.

2.1.7 Modifications to the Field Equation Set

Because of the choice of independent variables in the solution of the one-dimensional field equations (total pressure, air partial pressure, void fraction, and liquid and vapor temperatures), the basic equation set becomes singular at void fractions of 0 and 1. To avoid this problem, we replace the liquid mass equation with a mean mass equation at these extremes. At a void fraction of zero, the gas mass and energy equations are replaced with equations setting the void fraction equal to zero and the gas temperature equal to the saturation temperature based on the total pressure. At the other extreme, the replacement equations set void fraction equal to one and the liquid temperature to the saturation temperature based on the partial pressure of the water vapor. When a transition first occurs from pure gas to a two-phase mixture, the proper mass equations are used; but the replacement of the vapor energy equations is maintained for one time step to avoid numerical problems.

These equation replacements are avoided in the three-dimensional formulation by using α^{n+1}, p^{n+1}, $(1 - \alpha)^{n+1}$, T_ℓ^{n+1}, and $\alpha^{n+1}T_g^{n+1}$ as independent variables in the solution procedure. However, this approach was found to be inadequate when applied to the iterative equation solution used for one-dimensional flow.

When the pressure exceeds the critical point, the field equations are also singular, and a replacement might be expected. However, to model this regime with minimal code changes, we have chosen to slightly modify the thermal properties of steam. The code limits the calculated steam density to never exceed 0.999 times the liquid density, thus preventing a singularity from arising. Also, at pressures above the critical point, the calculated saturation temperature is forced quickly to a high value to drive a phase change to a pure liquid system.

2.1.7.1 Modifications to the Regular Momentum Solution. There are many situations and places in the code where the regular momentum equations as discussed in the previous sections are modified or are not used. These

situations and places are

- Water packing
- Counter-current flow limiting (CCFL)
- Choking
- First face in separator component side arm
- Location of turbine blades in turbine component
- Turbine separator
- Pump impeller
- Leak paths
- TEE component joining cell.

Most of these situations will be discussed in subsequent sections of this report. The water packing modifications will be discussed here, since the modifications to the regular momentum solution are the same in the one-dimensional and three-dimensional component models.

2.1.7.2 **Water Packing.** The water-packing logic in the code is triggered under certain conditions (but not all conditions) when the code attempts during a time step to overfill (pack) a liquid-full finite-difference mesh cell or to over-extract (stretch) liquid from a liquid-full cell. The physical analog to water packing is a water hammer; when cold water surges down a dead-end pipe filled with steam, a large pressure spike occurs when the last steam collapses and the water fills the pipe. Because of the low compressibility of liquid water, the spike has a very short duration.

In any Eulerian finite-difference scheme, the boundary of a mesh cell behaves like the dead end of a pipe in a water hammer. This is especially true when condensation is present. Consider a one-dimensional mesh cell with pure liquid entering from the left and pure vapor flowing in from the right to condense on the liquid. It is not possible for a standard finite-difference momentum equation to produce a liquid mass flow out of the right cell face that exactly balances the flow in the left cell face at the instant when the cell fills with liquid. In fact, when strong condensation is present, the momentum equation generally will predict a liquid velocity into the cell on the right face. This circumstance produces a numerical dead end for the liquid. Unlike the water hammer, the final solution is not to halt the flow but to push the liquid on through the right cell face. As with a hammer, this is accomplished with an abrupt increase in pressure.

The simplest way to remove these packing spikes is to run with a higher time-step size. The large time-step size helps, because the change in momentum in a time step is the product of the time-step size and the change in

the pressure. At larger time steps, the same change in momentum can be accomplished with a proportionally smaller change in pressure.

During the calculation of a reactor transient, it is often not possible to force the time step to high enough values to solve the packing problem. In TRAC-BF1/MOD1, we have adopted a method for mitigating water-packing, which is similar in spirit to shock-fitting techniques. Logic has been installed that detects pressure excursions caused by water packing. When they occur, it is clear that the finite-difference momentum equation is producing invalid results. Therefore, we modify the equation at those locations and times to obtain a better solution. A standard motion equation at a cell edge can be written as

$$V_{j+1/2}^{n+1} = V_{j+1/2}^{n} + a + b\left(p_j^{n+1} - p_{j+1}^{n+1}\right) . \qquad (2.1\text{-}84)$$

Additional force terms are incorporated in the term a, and b includes the time-step size and inverse of mesh length and density. If packing is detected in cell j, the equation is modified to the form

$$V_{j+1/2}^{n+1} = V_{j+1/2}^{n} + a + b\left(cp_j^{n+1} - p_{j+1}^{n+1}\right) . \qquad (2.1\text{-}85)$$

The constant c multiplying p_j^{n+1} is taken to be a large number (10^6) so that only small changes in the pressure of the j^{th} cell are required to obtain the appropriate velocity for the liquid outflow. To prevent excessively large vapor velocities, the value of the coefficient b in the vapor equation is set equal to the corresponding coefficient in the liquid equation.

In a given cell of a component (either one- or three-dimensional), the code does not consider the water-packing logic if the cell void fraction is greater than 0.15, if the liquid in the cell is superheated, or if the net mass flow is out of the cell. Also, the code cannot make adjustments at a cell interface or test across that interface if the associated flow area is less than or equal to 10^{-10} m^2. Further, the code does not consider adjacent cells in which the void fraction is less than 0.1. The code predicts the change in the current cell pressure to give a new pressure; if the predicted pressure change is negative, the code transfers to logic to detect stretching. If the pressure rise is greater than or equal to 0. then the new pressure is compared to a maximum value P_{max} which is computed as

$$p_{max} = \max\left[p_j^n,\ p_a^n\right] + \max\left[p_j^n - p_a^n,\ 0.02\ p_j^n\right] \qquad (2.1\text{-}86)$$

where p_a^n equals the pressures in all adjacent cells. If the new pressure is greater than P_{max}, the momentum equation for the face meeting the void fraction tests is modified, as shown in Equation (2.1-85).

The void-fraction tests ensure that the water-packing logic will not

smooth out a true water-hammer-type phenomenon in the calculation, while the pressure checks prevent the logic from being triggered too often. If, through the tests, more than one interface of a given cell permits the water-packing correction, the code applies the correction only at the interface across which the void fraction difference is highest. The code does not permit the water-packing correction at the interface opposite a FILL component if the velocities at both interfaces have the same sign or at the interface at which the PUMP component source is applied.

The stretching logic is similar, although the code looks for a pressure drop in the current cell that reduces its pressure to less than

P_{min}

where

$$P_{min} = \max\left(1., P_s^{n+1}, P\right) \tag{2.1-87}$$

$$P_s^{n+1} = \text{saturation pressure based on } T_\ell^{n+1} - 5K \tag{2.1-88}$$

$$P = \min\left(P_j^n, P_a^n\right) - \max\left(P_j^n - P_a^n, 0.02\, P_j^n\right) \tag{2.1-89}$$

with the additional constraint that the projected pressure must be less than the saturation pressure corresponding to the current liquid temperature minus 5 K. The final constraint for stretching is that the test pressure cannot be below the lower pressure limit for the equation of state (see Appendix A). For a stretch, the code does not make an adjustment at a given interface if the void fraction on the other side of the interface is less than or equal to 0.1, if the liquid velocity at the interface is into the cell in which the stretch is detected, or if the PUMP component source is applied at the interface.

The first criteria ensures that the test pressure will not be lower than the lower pressure limit for the equation of state, while the second criterion ensures that the test pressure will be no lower than the estimated saturation pressure in the cell based on the liquid temperature minus 5 K.

The search over all adjacent cells and the use of the maximum pressure difference between adjacent cells in determining P_{max} and P_{min} attempts to determine if the pressure in the cell sticks out relative to the cells around it.

2.2 HEAT CONDUCTION IN SOLID MATERIALS

Because the nuclear reaction in the core of a PWR generates energy inside the fuel, which moves to the primary fluid and crosses the steam-generator tubes to the secondary fluid, the code must calculate the heat conduction in the fuel and the steam-generator tubes to simulate correctly the heat transfer processes involved in thermal energy transport. Also, the passive solid structures, such as piping walls, vessel walls, and the internal vessel structures, represent significant metal masses that either can store or release large amounts of thermal energy, depending upon the reactor coolant temperature. Therefore, the code needs to model these additional structures, also.

Because the heat flux in a solid material is a vector quantity, the following general equation describes the heat conduction process in an arbitrary geometry:

$$\frac{\partial(\rho c_p T)}{\partial t} + \nabla \cdot \bar{q} = q''' \qquad (2.2\text{-}1)$$

where ρ is the local density of the solid; c_p, the specific heat at constant pressure of the material; T, the local temperature; $\bar{q}$, the heat flux; q''', the local volumetric heat generation rate; and t, time. In practice, the product ρc_p is assumed to be constant for purposes of taking the time derivative.

The heat flux $\bar{q}$ can be expressed in terms of the temperature gradient by Fourier's law of conduction:

$$\bar{q} = -k \nabla T \qquad (2.2\text{-}2)$$

where k is the thermal conductivity of the material. Therefore, Equation (2.2-1) becomes

$$\rho c_p \frac{\partial T}{\partial t} = \nabla(k \nabla T) + q''' \ . \qquad (2.2\text{-}3)$$

Writing this equation for one or two dimensions in Cartesian and cylindrical coordinates is a straightforward task described in Section 9. The code solves the one-dimensional conduction equation implicitly, although the solution of the two-dimensional cylindrical conduction equations for the fuel rod modeling is implicit in the radial direction and explicit in the axial direction. This explicit solution of the axial conduction in the fuel rod introduces an additional time-step limit for the code, which generally is important only when the axial increments in the conduction mesh become small. We will not discuss here the finite-difference forms of these equations, because they shed little light on the main purpose of this document.

Equation (2.2-3) does require boundary conditions on the inside and outside surfaces of the heat structure. The code permits two types of boundary conditions. The first is an adiabatic boundary

$$\left.\frac{\partial T}{\partial \zeta}\right|_{surface} = 0 , \qquad (2.2\text{-}4)$$

where ζ is length measured in the direction normal to the surface. The second boundary condition permits active heating or cooling of the surface by convection

$$-k \left.\frac{\partial T}{\partial \zeta}\right|_{surface} = h \left(T_{surface} - T_{fluid}\right) \qquad (2.2\text{-}5)$$

where Newton's law of cooling is used to describe the convective transport of thermal energy into the fluids.

Appendix B discusses the solid material properties required by the heat conduction equation.

3. FLOW REGIME MAP

The two-fluid model used in TRAC-BF1/MOD1 requires using some auxiliary relations for the source terms in the basic six equations. The auxiliary relations that express the rates of exchange of mass, momentum, and energy between each phase and its surroundings take on different forms for different flow patterns. As an example, two-phase flow patterns affect the rate of vapor generation in direct contact with the walls, and this term is important in determining mass exchange between liquid and vapor. Both the exchange of energy and momentum at the interface between vapor and liquid depend on the interfacial area per unit volume and the topology of the two-phase flow. For these reasons, it is important to identify the flow regime in each hydraulic cell before proceeding with the solution of the flow equations for that cell.

3.1 BASIS FOR FLOW REGIME MAP IN TRAC-BF1/MOD1

The interfacial package and wall heat transfer routines of TRAC-BF1 use a relatively simple flow regime map, which consists basically of two distinct patterns--liquid-continuous at low void fractions and vapor-continuous at high void fractions--with a transition zone in between. The liquid-continuous regime applies to the single-phase liquid flow, bubbly/churn, and inverted annular flows. The vapor-continuous regime applies to the dispersed droplet flow and single-phase vapor flow. The transition regime involves annular-droplet and film flow situations, depending on the void fraction and other flow variables.

The criterion for transition from the liquid-continuous zone is defined in terms of a transition void fraction, α_{tran}, that is a function of flow conditions and channel geometry. The criterion for transition to dispersed droplet flow is a void fraction that is 25% above α_{tran}.

This flow regime map is based on Andersen and Chu's work.[3-1] It is a modified flow regime map that was originally suggested by Ishii.[3-2] In his derivations of the drift-flux model, Ishii[3-2] suggested two simple flow regime transition criteria that, in his words, "are based on the relative motion between phases and are consistent with the concept of drift-flux model".

Andersen and Chu modified Ishii's criteria for transition between the different regime and stated its basis in the following terms:

- Transition between bubbly/churn and annular flow takes place when the liquid in the film (or entrained droplets) can be lifted relative to the liquid velocity in the bubbly/churn flow regime. This criterion is mathematically expressed as a relationship between void fraction, α, the distribution parameter, C_o, and the density ratio of liquid and vapor.

- Transition between annular flow and dispersed droplet flow is given

by the onset of entrainment. This is expressed mathematically by the entrainment correlation, in terms of the superficial phasic velocities, j_g and j_ℓ, hydraulic diameter, D_h , and physical properties.

3.2 IMPLEMENTING ASSUMPTIONS

The flow regime map that was originally developed for vertical flow is assumed to be usable for both vertical and horizontal flow components. Hence, the same set of flow transition criteria are used for all flow directions with no variation.

While the interfacial package and wall heat transfer calculations use similar logic for flow regime identification (with the exception of the interfacial shear model), the wall friction calculation uses a different logic that is an integral part of the Hancox[3-3] two-phase flow multiplier.

3.3 CONSTANT VOID FRACTION INTERVAL FOR TRANSITION REGION

The criterion for transition between annular-dispersed and dispersed droplet flows is not observed strictly in the coding. Instead of using the onset of entrainment as the criterion for this transition, a 25% window of void fraction above the transition from bubbly/churn to annular flow is used for indication of complete transition to dispersed droplet flow. This approach is based on the assumption that droplet entrainment may exist even in the bubbly/churn flow regime, and certainly will exist as soon as annular flow is initiated. As the void fraction increases, the intensity of entrainment will also increase and, at the end of the transition region, droplet entrainment becomes 100%. This is a helpful assumption in the calculations, and it appears to be logically reasonable. However, no assessment has been made of the effect of changing the 25% void window to another value.

The 25% void fraction window used in TRAC-BF1/MOD1 is different than the 10% void window implied in Reference 3-1. Repeated calculations in different cases have shown that the 25% window provides a smoother changeover and less discontinuity in computations.

3.4 AS-CODED FLOW REGIME MAP

TRAC-BF1/MOD1 does not feature a central and separate flow regime calculation scheme. Instead, the subroutines dealing with interfacial heat transfer, wall heat transfer, and interfacial friction include similar coding for determining flow regimes internally.

The prevailing range of the different flow regimes and the identical

features of the flow regime determination logic in different subroutines of TRAC-BF1/MOD1 are the following (see Reference 3-1):

- Bubbly/churn flow for $\alpha < \alpha_{tran}$
- Annular flow for $\alpha_{tran} < \alpha < \alpha_{tran} + 0.25$, and
- Dispersed droplet flow for $\alpha > \alpha_{tran} + 0.25$.

where

$$\alpha_{tran} = \left(1 + \frac{4}{\gamma}\right)\frac{1}{C_o} - \frac{4}{\gamma} - 0.15 \qquad (3\text{-}1)$$

in which

$$\gamma = \sqrt{\frac{\rho_\ell}{\rho_g}} \qquad (3\text{-}2)$$

$$C_o = C_\infty - \frac{C_\infty - 1}{\gamma} \, . \qquad (3\text{-}3)$$

The C_∞ factor is calculated differently in different routines, as will be discussed in the next section. Further remarks regarding the actual coding of the flow regime transition criteria are discussed in the sections for the models where the criteria are applied.

3.5 VARIATIONS IN APPLICATION

Calculations of C_∞ are done identically in the interfacial heat transfer and in the wall heat transfer models, while a different formula is used in the interfacial shear model.

3.5.1 Bubbly/Churn to Annular Transition in Interfacial Heat Transfer

In interfacial and wall heat transfer calculations, the C_∞ in Equation (3-3) is calculated by using Nikuradse's[3-4] correlation for peak-to-average velocity ratio in single-phase flow (see References 3-1 and 3-2). This correlation gives

$$C_\infty = 1.393 - 0.0155 \log (Re) \qquad (3\text{-}4)$$

where

$$Re = \frac{GD_h}{\mu_\ell} \quad . \tag{3-5}$$

As may be seen, Equation (3-4) is a weak function of the Reynolds number; this makes the flow transition criterion almost independent of flow velocity and hydraulic diameter.

3.5.2 Bubbly/Churn to Annular Transition in Interfacial Shear.

In the interfacial shear model, C_∞ is calculated with the following equation

$$C_\infty = 1.0 + 0.2 \left[\frac{\rho_\ell}{G} \sqrt{gD_h} \right]^{0.5} \quad . \tag{3-6}$$

This is a slightly modified version of the C_0 correlation suggested by Rouhani.[3-5] The original correlation was based on a wide range of experimental data from void measurements in different geometries, including several rod bundles. Equation (3-6), which is derived from two-phase flow data, gives better agreement of the overall computation results with data when compared to the same computations performed with Nikuradse's single-phase velocity ratio.

It may be observed that, according to Equation (3-6), C_∞ has a stronger dependence on flow velocity and hydraulic diameter than is indicated by Equation (3-4). This difference in C_∞ calculations leads to noticeably different trends of void fraction at the transition from bubbly/churn to annular flow regimes. Equation (3-4), which is used in interfacial heat transfer, makes α_{trpn} almost independent of mass velocity, while Equation (3-6), which is used in the interfacial shear model, shows a considerable variation of mass velocity with α_{tran}, or vice-versa.

3.6 ASSESSMENT

No isolated assessment of the flow regime maps in TRAC-BF1/MOD1 has yet been performed.

3.7 SCALING CONSIDERATIONS

The rationale used for calculating void fraction at transition between

bubbly/churn and annular flow is based on using the non-dimensional quantities γ and C_o. The density ratio, γ, is quite independent of geometric scale; and C_o has been correlated in terms of flow and hydraulic diameter. The data base used by Ishii[3-2] for comparing his derivations for C_o with experiments, covers a range of hydraulic diameters from 0.006 to 0.168 m (see Appendix C). However, as will be shown in Section 6.1, the procedures for C_o calculations are based on logical derivations and non-dimensional quantities and not on any set of experimental data. With these considerations, it may be claimed that the flow regime transition criteria in TRAC-BF1/MOD1 have no scale-dependent limitations.

3.8 CONCLUSIONS REGARDING FLOW REGIME MAP AND IMPLEMENTATION

A single flow regime map is used for all flow directions in TRAC-BF1/MOD1. This flow regime map considers only three zones, namely, a liquid-continuous region, a transition zone, and a vapor-continuous zone. The continuous-liquid and continuous-vapor flow zones are clearly definable in terms of phasic drift velocities and the distribution parameter. A mathematical relationship between these parameters gives the void fraction for transition between bubbly/churn and annular flow regimes. The onset of dispersed droplet flow is also defined with the entrainment correlation. Although the extent of the transition zone is taken arbitrarily to exist over a range of 25% in void fraction, the overall scheme seems to provide logically acceptable results with simple computational steps. Due to the use of different correlations for C_∞, there is considerable difference among the transition void fractions calculated in the interfacial friction model and in other routines that use these transition criteria. No assessment has been made to determine which one of the two C_∞ equations provides a better match to experimental data regarding heat transfer.

3.9. REFERENCES

3-1. J. G. M. Andersen and K. H. Chu, *BWR Refill-Reflood Program, Task 4.7 - Constitutive Correlations for Shear and Heat Transfer for the BWR Version of TRAC*, NUREG/CR-2134, EPRI NP-1582, GEAP-24940, December 1981.

3-2. M. Ishii, *One-Dimensional Drift-Flux Model and Constitutive Equations for Relative Motion Between Phases in Various Two-Phase Flow Regimes*, ANL-77-47, October 1977.

3-3. W. T. Hancox and W. B. Nicoll, "Prediction of Time Dependent Diabatic Two-Phase Water Flows," *Progress in Heat and Mass Transfer*, 6, Pergamon Press, 1972, pp. 119-135.

3-4. J. Nikuradse, "Principles of Turbulent Flow in Smooth Tubes," *Forschung auf dem Gebeite des Ingenieurwesens (Research at the Request of Engineers)*, 3, September-October 1932, p. 356.

3-5. S. Z. Rouhani, *Modified Correlations for Void and Pressure Drop*, AE-RTV 841, March 1969.

4. CLOSURE RELATIONS REQUIRED BY FLUID-ENERGY FIELD EQUATIONS

Closure relations required by the fluid-energy field equations are described in the following sections.

4.1 INTERFACIAL HEAT TRANSFER

Interfacial heat transfer calculation is a necessary part of the two-fluid equation system solution. The particular focus of the models used for these calculations is to obtain the variable products $(hA)_{if}$ and $(hA)_{ig}$, which are the liquid and vapor heat transfer coefficient times interfacial area, respectively. As in the case of interfacial friction in TRAC-BF1/MOD1, the interfacial heat transfer variables are dependent on flow regime and local void fraction.

The interfacial heat transfer calculations, for both one- and three-dimensional components, are performed in the HEATIF subroutine of TRAC-BF1/MOD1. This section describes the correlations used in HEATIF, their basis, and their relationship to the interfacial friction model.

4.1.1 Background

The interfacial heat transfer model of TRAC-BF1/MOD1 is closely related to the interfacial friction model described in Section 6.1, and it is based on the derivations of Ishii[4.1-1] and Andersen and Chu[4.1-2,3], which are discussed in that section. The data base for the working correlations, regarding drift flux parameters and interfacial area, are basically the same as for interfacial friction. Due to the logical relation of these two models and identical derivations, some of the equations derived in Section 6.1 are reproduced here with only a reference to their derivation. Each equation that is used in the coding is marked with an asterisk (*), followed by the variable name used for the left-hand side of that equation in the coding.

4.1.2 Components of the Interfacial Heat and Mass Transfer

The basic assumptions in the calculations of interfacial heat and mass transfer are:

- The interface is always at saturation temperature corresponding to the local pressure
- Steam and water exchange energy with the interface at a rate which

defines any necessary mass exchange for maintaining the interface at saturation temperature.

The total rate of heat exchange at the interface is

$$q_i = (hA)_{i\ell}(T_\ell - T_s) + (hA)_{ig}(T_g - T_s) \qquad (4.1\text{-}1)$$

and the net mass transfer rate in a hydraulic cell is

$$\Gamma = \Gamma_{wall} + \frac{q_i}{h_{sg} - h_{s\ell}} \qquad (4.1\text{-}2)$$

where Γ_{wall} is the rate of mass exchange produced at the channel walls.

According to Equation (4.1-1), the components of interfacial heat transfer are the interfacial area and the heat transfer coefficients between each phase and the interface. The temperature differences are obtained from the heat balance for each phase.

4.1.3 Flow Regime Transitions

As in the case of interfacial friction, the interfacial heat transfer model recognizes three different flow regimes--namely, bubbly/churn, annular (transition), and dispersed droplet flows. This scheme of flow patterns and the criteria for transitions between them are according to the works of Ishii[4.1-1] and Andersen and Chu.[4.1-2,3] Different correlations for the interfacial area and heat transfer coefficients are used in different flow regimes. The transitions between different flow regimes are defined in terms of void fraction:

- Bubbly/churn flow for $\alpha < \alpha_{tran}$,
- Annular flow for $\alpha_{tran} < \alpha < \alpha_{tran} + 0.25$, and
- Dispersed droplet flow for $\alpha > \alpha_{tran} + 0.25$.

where

$$\alpha_{tran} = \left(1 + \frac{4}{\gamma}\right)\frac{1}{C_o} - \frac{4}{\gamma} - 0.15 \qquad \text{*, ACA} \quad (4.1\text{-}3)$$

$$\gamma = \sqrt{\frac{\rho_\ell}{\rho_g}} \qquad \text{*, GAMMA} \quad (4.1\text{-}4)$$

$$C_o = C_\infty - \frac{C_\infty - 1}{\gamma} \qquad *, \text{CO} \quad (4.1\text{-}5)$$

$$C_\infty = 1.393 - 0.0155 \log (Re) \qquad *, \text{COINF} \quad (4.1\text{-}6)$$

$$Re = \frac{GD_h}{\mu_f} . \qquad *, \text{RE} \quad (4.1\text{-}7)$$

A few points may be observed considering the actual coding of these equations. Firstly, Re in Equation (4.1-6) is replaced by 1 + Re to make sure that the logarithm is always positive. Then, C_∞ is limited to a lower bound of 1.0; and, finally, C_o is limited to an upper bound of 1.3333, which is the experimentally observed maximum value of this variable (see Reference 4.1-1).

Note that the transition void fraction, α_{tran}, is calculated in a manner similar to that of the interfacial friction case. However, in this model, C_∞ is calculated according to Nikuradse's[4.1-4] equation for the maximum-to-average velocity ratio in single-phase flow. This is different than the equation used in the case of interfacial friction. As a result, transitions between different flow regimes are at different void fractions for interfacial shear and interfacial heat transfer models. For heat transfer, α_{tran} changes very slightly with pressure, mass velocity, or hydraulic diameter. But, in the shear model, α_{tran} shows a strong dependence on these variables. An example of the different trends of αtran in the shear and heat transfer models is given in Figure 4.1-1.

In the transition region, where $\alpha_{tran} < \alpha < \alpha_{tran} + 0.25$, an interpolation variable, X2, is used for interpolating drift flux variables between bubbly and dispersed droplet conditions. This variable, which depends on void fraction, is calculated according to the following:

$$X2 = \xi_2(3\xi_2 - 2\xi_2^2) \qquad *, \text{X2} \quad (4.1\text{-}8)$$

where

$$\xi_2 = \frac{\alpha - \alpha_{tran}}{0.25} . \qquad *, \text{X2} \quad (4.1\text{-}9)$$

Note that Equation (4.1-8) is different than the simple relation used for the same variable in FRCIF (Section 6.1). The advantage of this formulation is in providing a smooth changeover of variables at both ends of the transition region, as the derivative of X2 with respect to ξ_2 (or α) vanishes at $\alpha = \alpha_{tran}$ and at $\alpha = (\alpha_{tran} + 0.25)$. For consistency, it is advisable to

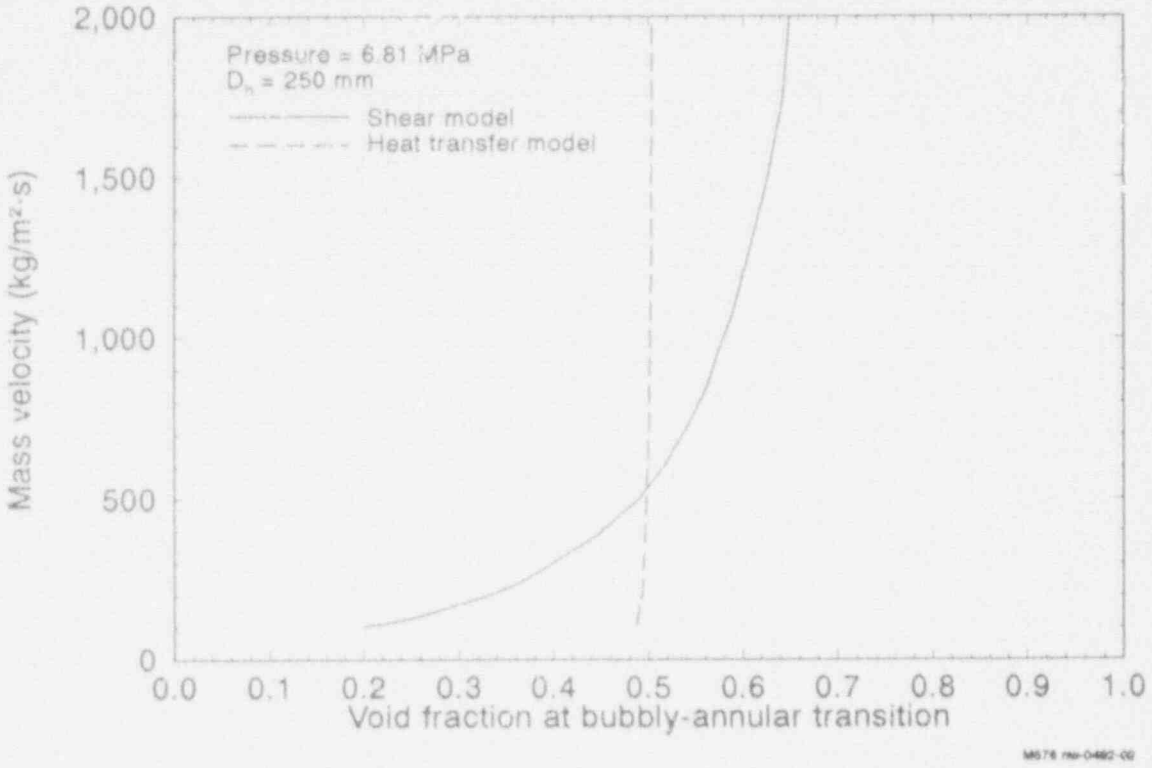

Figure 4.1-1. Comparison of flow regime boundaries between bubbly/churn and annular patterns in the interfacial shear and heat transfer models for a hydraulic diameter of 0.0145 m.

implement Equation (4.1-8) in the interfacial shear model.

4.1.4 Data Base For Interfacial Heat Transfer

The phenomena related to the interfacial heat transfer, such as the extent of interfacial area in each flow regime or the local rates of phasic heat transfer at the interface, are not measurable; thus, there are no data available for a direct comparison with theories or correlations. The different formulas presented in this chapter, particularly those concerning the interfacial areas, are derived on theoretical basis, using the same arguments that were employed in the case of interfacial friction. For this reason, as far as the interfacial areas are concerned, the data base that was used to confirm the drift flux parameters for the interfacial shear model (Section 6.1) is applicable to the interfacial heat transfer model as well. The heat transfer correlations for different flow geometries are based on data from measurements performed on heat transfer between similar solid geometries and a fluid. In some cases, additional numerical multipliers are introduced to take into account the difference between rigid and fluid particles. These

multipliers are identified following the equations where they are introduced. The data base for some of the heat transfer correlations that are not yet a part of the classical literature in this field are given in Table 4.1-1.

4.1.5 Entrainment

In the interfacial heat transfer model, a contribution of droplet entrainment to the interface is a considered in all flow regimes, including bubbly/churn flow. The extent of entrainment changes with phasic velocities and void fraction. The entrainment calculation in this model is done according to the same procedure that is described for the interfacial friction model [Equations (6.1.43) through (6.1.50) in Section 6.1.8]. These equations are

$$E = (X_E - 0.03)\left[1 + (X_E + 0.1)^2\right]^{-0.5} \qquad \text{*, ENT} \quad (4.1\text{-}10)$$

where

$$X_E = 10^{-4}(J_g^*)^{2.5}(D^*)^{1.25}Re_\ell^{0.25} \qquad \text{*, XE} \quad (4.1\text{-}11)$$

$$J_g^* = \frac{J_g}{\left[\frac{\sigma\Delta\rho g}{\rho_g^2}\left(\frac{\rho_g}{\Delta\rho}\right)^{2/3}\right]^{1/4}} \qquad \text{*, XJGS} \quad (4.1\text{-}12)$$

$$D^* = D_h\sqrt{\frac{g\Delta\rho}{\sigma}} \qquad \text{*, DS} \quad (4.1\text{-}13)$$

$$Re_\ell = \frac{\rho_\ell J_\ell D_h}{\mu_\ell} \; . \qquad \text{*, REL} \quad (4.1\text{-}14)$$

As in the interfacial shear model, the calculated entrainment is modified in two occasions--when $X_E < 0.03$ and when there are some wetted walls and some dry walls in the same cell. These modifications are

$$Ent = 0.1 \;, \; if \; X_E < 0.03 \qquad \text{*, ENT} \quad (4.1\text{-}15)$$

and

Table 4.1-1. Data base for heat transfer correlations.

Data Description	Lee-Ryley	Cook et al.
Test apparatus	Horizontal glass fiber in a horizontal duct	Vertical rectangular channel
Dimensions:		
Cross section (m)	0.025 x 0.025	0.381 x 0.038
Length (m)	0.229	-
Height (m)	-	0.965
Droplet diameter (μm)	230 - 1126	-
Droplet Reynolds number	64 - 250	-
Pressure (Mpa)	0.1 - 0.2	Slightly above atmospheric
Steam superheat (°C)	2.8 - 33.9	-
Inlet steam velocity (m/s)	2.68 - 11.95	-
Inlet mass flow rate (kg/s)		
Water	-	0.8 - 1.78
Steam	-	0.066 - 0.104
Inlet temperature (°C)		
Water	-	73 - 94
Steam	-	130 - 141

$$Ent = E + (1 - E)(1 - W_{wet}) \quad *, \text{ENT} \quad (4.1\text{-}16)$$

Here again, as in FRCIF, $W_{wet} = WA_f/WA_{tot}$ is the fraction of the channel walls that are in contact with a liquid film. If all the walls are wet, Ent = E; if all the walls are dry, Ent = 100%, which means all the liquid phase is entrained as droplets.

Note that in the coding of HEATIF, no void-dependent restriction is imposed on entrainment. While in FRCIF (for interfacial friction), the calculated entrainment was modified by using the void-dependent χ^2 multiplier [see Equations (6.1.51) and (6.1.61)]. As a result, there is no entrainment in the bubbly/churn flow regime for interfacial friction, while some entrainment is considered in the same flow regime for interfacial heat transfer. Although this appears to be a discrepancy between the two models, its effect on the results is not expected to be considerable, as the entrainment may only have a minute contribution to the interface in

bubbly/churn flow.

4.1.6 Interfacial Area

The relationship between interfacial area and relative phasic velocity in different flow regimes is discussed in Section 6.1.6. The resulting equations from that section are employed here for the interfacial heat transfer. However, for heat transfer, one should consider the entire interfacial contact area. (In the case of friction, only the projected area of the particles had to be considered.) This has a particular bearing in bubbly and droplet flows, but it makes no difference in the case of annular (or film) flow.

4.1.6.1 Interfacial Area in Bubbly/Churn Flow. Equation (6.1.33) of Section 6.1.6 is employed, with a critical Weber number of $We_c = 6.5$ for bubbly flow, to calculate the average bubble size, interfacial area, and the number of bubbles per unit volume (see Reference 4.1-3). These calculations begin with determining the relative phasic velocity in each flow regime. In bubbly/churn flow,

$$\bar{V}_{rob} = \frac{1.53}{1-\alpha}\left[\frac{g\Delta\rho\sigma}{\rho_\ell^2}\right]^{0.25} . \qquad \text{*, VROB (4.1-17)}$$

[Note that in the interfacial shear model, an exact equivalent of Equation (4.1-17) is used for bubbly/churn flow in pipes, while Equation (6.1.40), with a $(1-\alpha)$ divider, is used for rodded bundles.]

Substituting $\bar{V}_r$ with V_{rob} from Equation (4.1-17) and using $We_c = 6.5$ (see Reference 4.1-2) yields the inversed bubble diameter as

$$\frac{1}{d_{ib}} = \frac{\rho_\ell \bar{V}_{rob}^2}{6.5\sigma} . \qquad \text{*, DIAB (4.1-18)}$$

This inversed diameter is limited to 10^{-1} m^{-1} in the coding, and an average bubble diameter is calculated, using the largest of d_{ib}^{-1} or 10^{-1}. (Normally, d_{ib}^{-1} is very large compared to 10^{-1}, and d_{ib} turns out to be a small number.)

$$d_{ib} = \frac{1}{Max\ [d_{ib}^{-1},\ 10^{-1}]} . \qquad \text{*, DIAB (4.1-19)}$$

This bubble diameter is checked against three criteria and adjusted, if

necessary, in order to keep its value within physically meaningful bounds. The limiting values are a minimum diameter of 0.0005 m, an upper limit of 0.5 D_h, and a void-dependent maximum average diameter of

$$d_{bmx} = \left(\frac{6\alpha}{10^7 \pi} \right)^{1/3} . \qquad \text{*, DIABMX} \quad (4.1\text{-}20)$$

This maximum diameter is based on assuming a limit of 10^7 bubbles per unit volume (m^3). Hence,

if $d_{ib} < 0.0005$, then d_{ib} is reset to 0.0005;
if $d_{ib} > 0.5\ D_h$, then d_{ib} is reset to $0.5\ D_h$, and
if d_{ib} (or $0.5\ D_h$) $> d_{bmx}$, then d_{ib} is reset to d_{bmx}.

The final d_{ib} is used to calculate the interfacial area of bubbles per unit volume of the hydraulic cell

$$A_{ib} = \frac{6\alpha}{d_{ib}} . \qquad \text{*, AREAB} \quad (4.1\text{-}21)$$

This final d_{ib} is also used to obtain a corresponding number of average bubbles per unit volume

$$N_b = \frac{6\alpha}{\pi d_{ib}^3} . \qquad \text{*, CNB} \quad (4.1\text{-}22)$$

Variations of A_{ib} with void fraction for three different mass velocities at a pressure of 7.0 MPa are shown in Figure 4.1-2. There is no effect of mass velocity on the interfacial area of the bubbles, as might be expected, since the bubble diameter is not affected by this variable.

4.1.6.2 Interfacial Area in Annular Droplet Flow. The interfacial area in this flow regime may include contributions from a liquid film on the walls and from droplets in the gaseous core. Each of these areas is used with a different heat transfer coefficient that is relevant to its regime.

The interfacial area per unit cell volume for the droplets is calculated in a manner analogous to that of the bubbles.

$$A_{id} = \frac{6(1 - \alpha_d)}{D_d} \qquad \text{*, AREAD} \quad (4.1\text{-}23)$$

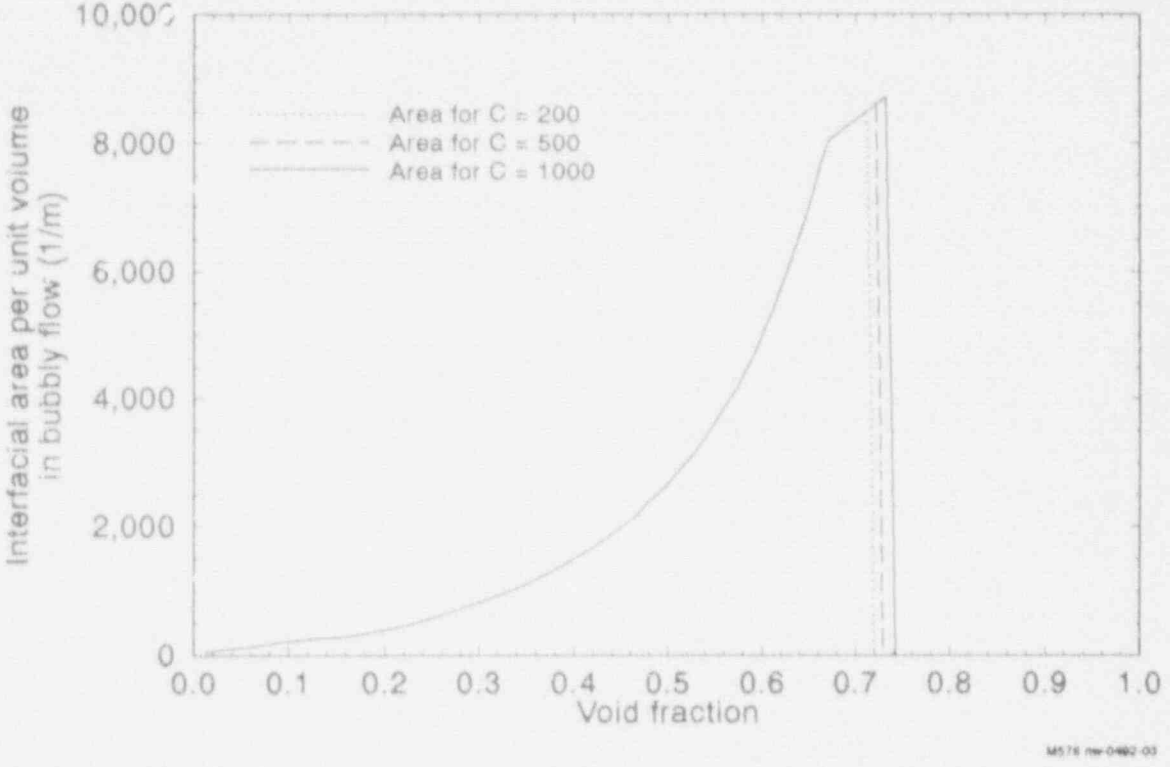

Figure 4.1-2. Variations of the interfacial area per unit volume in bubbly flow (p = 6.81 MPa; mass velocities in $kg/m^2 \cdot s$).

where α_d is the void fraction corresponding to the annular core of vapor and droplets

$$\alpha_d = 1. - (1 - \alpha) Ent \qquad *, \text{ALPD} \quad (4.1\text{-}24)$$

and D_d is the average droplet diameter calculated from

$$D_d = \frac{\sigma We_d}{\rho_g \, Max\left[V_{rod}^2, j^2\right]} . \qquad *, \text{DIAD} \quad (4.1\text{-}25)$$

We_d in Equation (4.1-25) is the critical Weber number for droplets; its numerical value is set at 2.7 for these calculations.[4.1-2]

V_{rod} is the relative droplet velocity that is calculated according to one of the following equations:

$$V_{rod} = 1.414 \left(\frac{g\sigma\Delta\rho}{\rho_g^2} \right)^{0.25} \qquad *, \text{VROD} \quad (4.1\text{-}26)$$

or

$$V_{rod} = \frac{3\sigma}{\rho_g} \left[\frac{(g\Delta\rho)^2}{\mu_g \rho_g} \right]^{0.333} j^{-2} , \qquad *, \text{VROD} \quad (4.1\text{-}27)$$

Equation (4.1-27) is used only if the following condition is satisfied:

$$1.456 \left(\frac{g\sigma\Delta\rho}{\rho_g^2} \right)^{0.25} \left(\frac{\mu_g^2}{\sigma\rho_g \sqrt{\frac{\sigma}{g\Delta\rho}}} \right)^{-1/12} < j . \qquad *, \text{XJCD} \quad (4.1\text{-}28)$$

Equations (4.1-26) through (4.1-28) are based on Ishii's work[4.1-1] and represent $V_r = v_{jg}/(1 - \alpha)$ for dispersed liquid flow. Figure 4.1-3 shows typical variations of the droplet interface area per unit volume as a function of void fraction. In comparison with the interface area per volume for the bubbles, the droplet interface has a much stronger dependence on the mass velocity, and peaks at higher void fractions, where the entrainment is at its maximum.

Note that although V_{rod} should be identical for interfacial heat and interfacial shear calculations, Equations (6.1.55) through (6.1.59), which are used for calculating this variable in the shear model, are somewhat different as they include a $\alpha^{1.5}$ multiplier and some dependence on Re_g. Since those equations are the result of a more recent development, it might be advisable to change V_{rod} calculations in HEATIF to match those in FRCIF.

In the HEATIF coding, a number of limitations are imposed on D_d to make sure its calculated value is within physically meaningful limits. The droplet diameter is bound between a minimum limit of 0.2 mm and a maximum limit that is the least of 0.25 D_h, or a droplet diameter calculated for the given void and the assumption of 10^6 droplets per m^3 of the vapor phase, which yields

$$D_{d,max} = \left[\frac{6(1 - \alpha)}{(10^6\pi + 1)} \right]^{0.333} . \qquad *, \text{DIADMX} \quad (4.1\text{-}29)$$

Contribution of the liquid film to the interfacial area is described in the following.

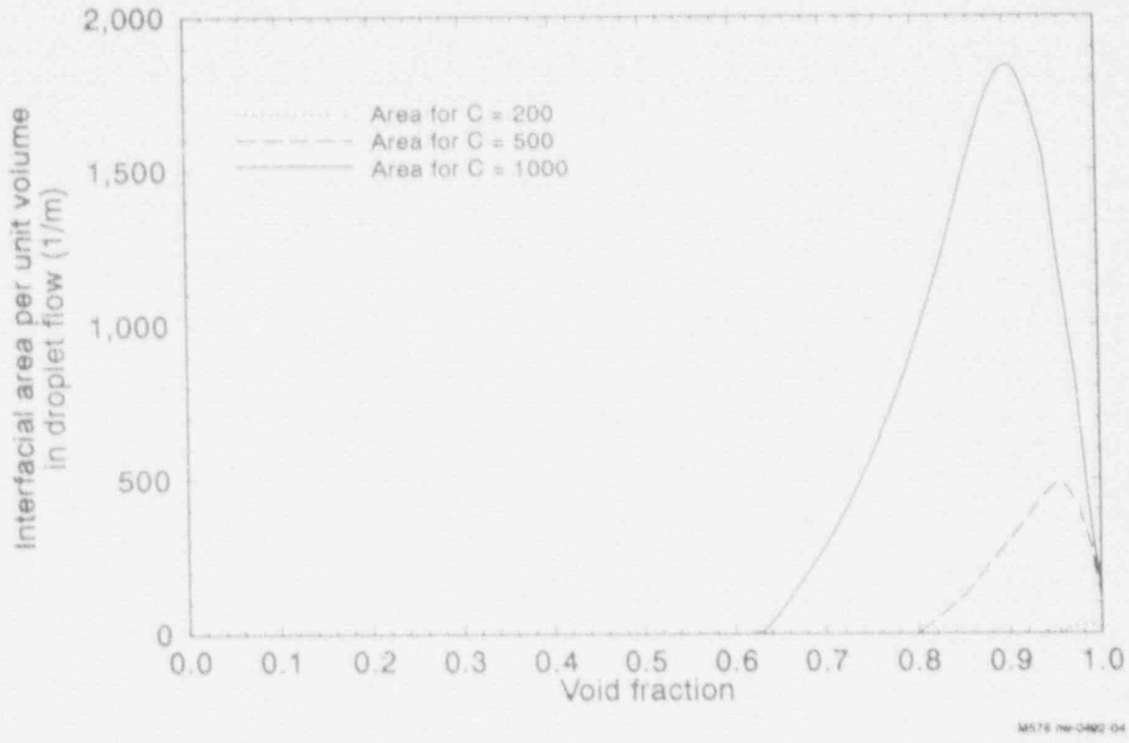

Figure 4.1-3. Variations of the interfacial area per unit volume in droplet flow (p = 6.81 MPa; mass velocities in $kg/m^2 \cdot s$).

4.1.6.3 **Interfacial Area in Annular Film Flow.** The interfacial area per unit volume due to the liquid film depends on the film thickness, which is obtained from the film liquid fraction, $1 - \alpha_f$, in which α_f is the fraction of liquid flow area that is not occupied by the liquid film.

$$\alpha_f = 1 - (1 - \alpha)(1 - E) \; . \qquad \text{*, ALPF} \quad (4.1\text{-}30)$$

In terms of this void fraction, the average film thickness may be expressed as

$$\delta_f = 0.5 D_h \left(1 - \sqrt{\alpha_f}\right) . \qquad \text{*, DIAF} \quad (4.1\text{-}31)$$

A minimum film thickness is established from a force balance on the creeping film, which yields

$$\delta_{f,min} = \left(\frac{18\sigma\mu_\ell^2}{g^2\rho_\ell^3} \right)^{0.2} . \qquad \text{*, DIAFMN (4.1-32)}$$

In the coding, the film thickness is chosen as the larger of δ_f and $\delta_{f,min}$.

The core void fraction corresponding to the minimum film thickness is

$$\alpha_{f,min} = \left(1 - \frac{2\delta_{f,min}}{D_h} \right)^2 . \qquad \text{*, ALPFMN (4.1-33)}$$

It should be noted that if there is any liquid entrainment in the vapor core, $\alpha < \alpha_{f,min}$, and if the liquid film is thick, then $\alpha > \alpha_{f,min}$. With these considerations, the film-vapor interfacial area per unit volume is

$$A_{if} = \begin{cases} \frac{4}{D_h}\sqrt{\alpha_f} & \text{for } \alpha \le \alpha_{f,min} \\ \frac{4}{D_h}\sqrt{\alpha_f}\,\frac{1-\alpha_f}{1-\alpha_{f,min}} & \text{for } \alpha > \alpha_{f,min} \end{cases} . \qquad \text{*, AREAF (4.1-34)}$$

Figure 4.1-4 shows variations of the interfacial area per unit volume in film flow for three different mass velocities at 6.91 MPa pressure. As Equation (4.1-34) indicates, the interfacial area in this flow regime is insensitive to the variations in mass velocity.

4.1.7 Interfacial Heat Transfer Coefficients

The heat transfer coefficients for liquid to interface and vapor to interface are dependent an the flow topology, and different correlations are used for the different flow components in each flow regime.

4.1.7.1 Heat Transfer in Bubbly/Churn Flow. For heat transfer between the continuous liquid phase and the interface with bubbles, the Lee-Ryley[4.1-5] correlation for Nusselt number is used.

$$Nu_{\ell b} = 2.0 + 0.7\sqrt{\frac{\rho_\ell D_b V_{rb}}{\mu_\ell}} . \qquad \text{*, CNUB (4.1-35)}$$

Note that a factor of $Pr^{0.33}$ that should be a part of this correlation (after

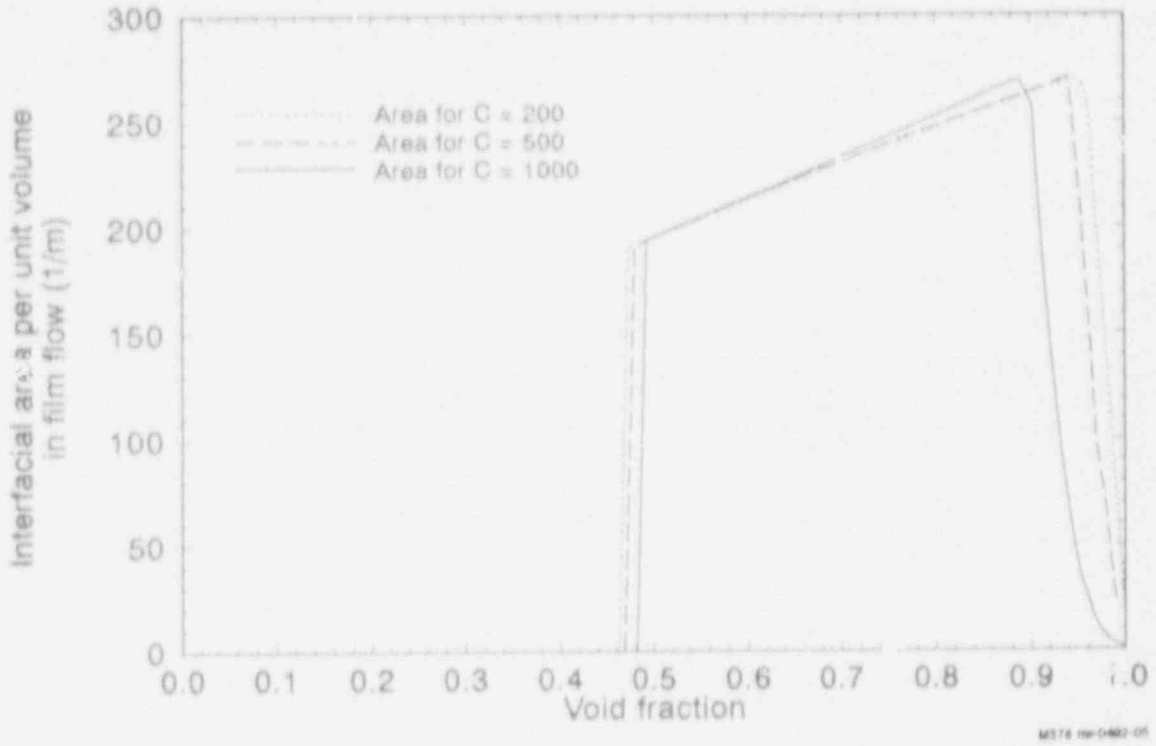

Figure 4.1-4. Variations of the interfacial area per unit volume in film flow (p = 6.81 MPa; mass velocities in $kg/m^2 \cdot s$).

the square root) is left out in the coding. The impact of this omission is an underestimation of the Nusselt number by a maximum of about 50% for very low water temperatures (around 50 K) and an overestimation of the same variable by about 5% in the extreme cases. The liquid-to-interface heat transfer rates calculated on the basis of these Nusselt numbers will be off by the same fractions.

This correlation is based on data from measured rates of evaporation on the surface of small droplets, due to heat transfer from hot air or superheated steam. A summary of Lee-Ryley's test conditions is given in Table 4.1-1.

Equation (4.1-35) is used to obtain the heat transfer coefficient in the following form:

$$h_{i\ell b} = \frac{Nu_{\ell b} k_\ell}{D_b} \quad . \qquad \text{*. HIL} \quad (4.1\text{-}36)$$

For the heat transfer between the vapor-phase and bubble surface, the following correlation is employed:

$$h_{igb} = \frac{2}{3}\pi^2 \frac{k_g}{D_b}\left(2.7\frac{\mu_\ell}{\mu_g}\right) . \qquad *, \text{HIV} \quad (4.1\text{-}37)$$

This equation is suggested by Andersen and Abe'-Larsen,[4.1-6] based on COREC?OL-II code development wor?. The factor 2.7 μ_ℓ/μ_g is used for the effect of internal circulation inside the bubbles on heat convection to the surface.

As stated earlier, the interfacial heat transfer model assumes the existence of some entrainment even in bubbly/churn flow. Heat transfer coefficients for vapor-to-droplet surfaces are calculated according to the Lee-Ryley correlation[4.1-5] in the following form:

$$Nu_{igd} = 2.0 + 0.74\sqrt{\frac{\rho_g D_d V_{rod}}{\mu_g}}\, Pr_g^{0.333} \qquad *, \text{CNUD} \quad (4.1\text{-}38)$$

$$h_{igd} = \frac{k_g Nu_{igd}}{D_d} . \qquad *, \text{HIV} \quad (4.1\text{-}39)$$

For heat transfer between liquid and droplet surface, the following correlation, which is a modified form of Equation (4.1-37), is used:[4.1-6]

$$h_{i\ell d} = \frac{2}{3}\pi^2 \frac{k_\ell}{D_d}(2.7) . \qquad *, \text{HIL} \quad (4.1\text{-}40)$$

The numerical factor of 2.7 is used for the effect of internal turbulence inside the droplet.[4.1-6] The overall heat transfer coefficient in bubbly/churn flow for each phase in the cell volume is obtained from the individual interfacial areas per unit volume and their specific heat transfer coefficients. For the liquid phase,

$$(hA)_{i\ell b} = Vol(A_{ib} H_{i\ell b} + A_{id} h_{i\ell d}) \qquad *, \text{HAIL} \quad (4.1\text{-}41)$$

and, for the vapor phase,

$$(hA)_{igb} = Vol(A_{ib} H_{igb} + A_{id} h_{igd}) . \qquad *, \text{HAIV} \quad (4.1\text{-}42)$$

4.1.7.2 Heat Transfer in Dispersed Droplet Flow Regime. In this regime (for $\alpha > \alpha_\ell + 0.25$), the interface is only between droplets and vapor. The heat transfer coefficient for vapor to interface is calculated with the

Lee-Ryley correlation[4.1-5] in the following form:

$$h_{igd} = \frac{k_g Nu_{gd}}{D_d} \qquad \text{*, HIV (4.1-43)}$$

where

$$Nu_{gd} = 2.0 + 0.74 \sqrt{\frac{\rho_g D_d \, Max[V_{rod}, j]}{\mu_g}} \, Pr_g^{0.333} \qquad \text{*, CNUD (4.1-44)}$$

and Equation (4.1-40) is used again for droplet-to-interface heat transfer.

The overall heat transfer rate for each phase in the cell volume is given by

$$(hA)_{itd} = Vol \, A_{id} h_{itd} \qquad \text{*, HAILD (4.1-45)}$$

$$(hA)_{igd} = Vol \, A_{id} h_{igd} \, . \qquad \text{*, HAIVD (4.1-46)}$$

4.1.7.3 Heat Transfer in Film Flow Region. The interface between vapor and liquid film is defined in terms of the film thickness and hydraulic diameter of the channel

$$D_{if} = D_h - 2\delta_f \, . \qquad \text{*, HDMID (4.1-47)}$$

In the HEATIF coding, a minimum limit of 10^{-6} (m) is imposed on D_{if}. This diameter is then used in the well-known Dittus-Boelter correlation for heat transfer between vapor and interface

$$h_{igf} = 0.023 \, \frac{k_g}{D_{if}} \, Re_{gf}^{0.8} \, Pr_g^{0.333} \qquad \text{*, HIV (4.1-48)}$$

where

$$Re_{gf} = \frac{\rho_g V_g D_{if}}{\mu_g} \, . \qquad \text{*, REV (4.1-49)}$$

Equation (4.1-48) is used for turbulent vapor flow. However, if D_{if} is very small, vapor flow may be laminar. In lieu of checking the Reynolds number for laminar flow and then using the laminar flow heat transfer, the vapor-to-interface heat transfer is set as follows:

$$h_{igf} = Max\left[h_{igf}\ ,\ 4.0\frac{k_g}{D_{if}}\right] \qquad *,\ \text{HIV} \quad (4.1\text{-}50)$$

in which the term $4.0\frac{k_g}{D_{if}}$ is the heat transfer for laminar vapor flow. This is based on the classical heat transfer relation in laminar flow (see Kays[4.1-7]) that is expressed as Nu = 4.364, with the constant value reduced from 4.364 to 4.

The liquid film-to-interface heat transfer is calculated according to a correlation suggested by Megahed.[4.1-8] If the liquid is subcooled, then the local film-to-interface heat transfer is

$$h_{iff} = \frac{0.771\,C_{pf}m\left(g\ \nu_f^{-2}\right)^{1/3}}{\pi D_i\,(Jax\ Re_{ff})^{2/3}} \qquad *,\ \text{HIL} \quad (4.1\text{-}51)$$

where m_f is the total mass flow rate of the liquid film given by

$$m_f = \frac{(1 - Ent)(1 - \alpha)\rho_f V_f Vol}{dZ} \qquad *,\ \text{FLOFLM} \quad (4.1\text{-}52)$$

$$Jax = \left[\frac{C_{pf}(T_s - T_f)}{h_{fg}}\sqrt{\frac{\rho_f}{\rho_g}}\right]^{2/3} \qquad *,\ \text{XJACOB} \quad (4.1\text{-}53)$$

$$Re_{ff} = \frac{4\ m_f}{\mu_f \pi D_h}\ . \qquad *,\ \text{REYF} \quad (4.1\text{-}54)$$

However, if $(T_s - T_f) = 0$ or $Re_{ff} = 0$, then the above calculation is skipped and a constant heat transfer rate of 10^8 is used (based on the experimental value of condensation heat transfer).

Equation (4.1-51) is based on Megahed's derivation of the heat transfer between steam and water in countercurrent flows.[4.1-8] His derivations suggest a Stanton number that is given as

$$St = 0.0922\ (\lambda Re_{\ell\ell})^{-0.6} \left(\frac{gL^3}{\nu^2}\right)^{0.3} \tag{4.1-55}$$

where L is the length (height) of the channel,

$$\lambda = Ja \left(\frac{\rho_\ell}{\rho_g}\right)^{1/2} = C_{p\ell}(T_s - T_\ell) \left(\frac{\rho_\ell}{\rho_g}\right)^{1/2} \tag{4.1-56}$$

$$\nu = \frac{\mu_\ell}{\rho_\ell} \ . \tag{4.1-57}$$

The numerical constant 0.0771 that is used in Equation (4.1-51) was obtained from experimental data by Cook et al.[4.1-9] The data were obtained from measured rates of steam condensation in countercurrent flow inside a vertical test section with rectangular cross section. A summary of the test conditions of Cook et al. was given in Table 4.1-1.

It should be noted that, in implementing Equation (4.1-55) in the code, the height dimension, L, has been replaced by πD_h, which is the periphery of the channel. The correct application of the original equation would require a lengthy logic to reevaluate the effective height of the channel for the film-to-interface heat transfer calculation, regardless of nodalization changes and changes in the actual zone of film flow, from one time-step to the next. Without such logic, the calculation results would be unnecessarily sensitive to the nodalization changes and the course of the transient.

Having established the local heat transfer coefficients for vapor and liquid in the film flow regime, the total rates of heat transfer for the cell volume are given by

$$(hA)_{i\ell f} = Vol\ A_f h_{i\ell f} \qquad *, \text{HAILF} \quad (4.1\text{-}58)$$

$$(hA)_{igf} = Vol\ A_f h_{igf} \ . \qquad *, \text{HAIVF} \quad (4.1\text{-}59)$$

The overall liquid-to-interface heat transfer in the cell volume is then obtained by adding the contributions from the droplet and the film components

$$(hA)_{i\ell tot} = (hA)_{i\ell d} + (hA)_{i\ell f} \qquad *, \text{HAIL} \quad (4.1\text{-}60)$$

and, similarly, for vapor-to-interface

$$(hA)_{igdf} = (hA)_{igd} + (hA)_{igf} \quad \text{*, HAIV (4.1-61)}$$

4.1.7.4 **Heat Transfer in the Transition Zone.** A final interpolation procedure is employed to cover the variations in the overall interfacial heat transfer from bubbly/churn and annular-droplet to the dispersed droplet flow regimes. This interpolation is done with the void-dependent X2 variable that was defined by Equation (4.1-8). This interpolation takes into account the fractions of each phase that are present in any of the named flow regimes. The overall interfacial heat transfer coefficient for the liquid phase is

$$(hA)_{ift} = (1 - X2)\left[(hA)_{ifb} + (hA)_{ifd}\right] + X2\left[(hA)_{ifd} + (hA)_{iff}\right] \quad \text{*, HAIL (4.1-62)}$$

and the corresponding coefficient for the vapor phase is

$$(hA)_{igt} = (1 - X2)\left[(hA)_{igb} + (hA)_{igd}\right] + X2\left[(hA)_{igd} + (hA)_{igf}\right] . \quad \text{*, HAIV (4.1-63)}$$

In the transition region, where $\alpha_{tran} < \alpha < \alpha_{tran} + 0.25$, the X2 variable changes from 0 to 1; and this interpolation scheme adjusts the heat transfer rates accordingly.

4.1.8 Effect of Noncondensable Gas

Presence of a noncondensable gas, such as air, affects the heat transfer coefficient in condensation. The HEATIF subroutine includes some logic for this purpose. If the logic indicates presence of air (noncondensable), the following modification is made on the liquid-side heat transfer, $(hA)_{ift}$:

$$(hA)_{iftc} = C_{ncg}\,(hA)_{ift} \quad \text{*, HAIL (4.1-64)}$$

where

$$C_{ncg} = Min\left[1.0,\ C_{ncf}\right] \quad \text{*, CNCG (4.1-65)}$$

$$C_{ncf} = 0.168\left[\frac{C_{ncg1}}{C_{ncg2}}\right]^{0.1} \quad \text{*, CNCG (4.1-66)}$$

$$C_{ncg1} = Max\left[10^{-8},\ \alpha\rho_v^2\right] \quad \text{*, CNCG1 (4.1-67)}$$

$$C_{ncg2} = Max\left[10^{-8},\ (1-\alpha)\rho_a\rho_\ell\right] \quad *,\ CNCG2 \quad (4.1\text{-}68)$$

$$\rho_v = \rho_g - \rho_a \ . \quad *,\ ROS \quad (4.1\text{-}69)$$

ρ_a is the local density of the noncondensable gas that is a component in the total vapor density, ρ_g.

The logic for correction of heat transfer due to noncondensable gas was introduced in TRAC-P[4.1-10] at LANL. It has not been possible to find the original source of these equations in the technical literature. Furthermore, one may argue that the presence of noncondensable gas should affect the vapor-side heat transfer, $(hA)_{igt}$, rather than the liquid-side heat transfer, as is done in the coding. However, this may be a more effective way of adequately reducing the overall heat transfer across the interface.

4.1.9 Effect of Horizontally Stratified Liquid Interface

In situations where vapor and liquid are separated due to gravity (at very low axial phasic velocities), the interfacial contact area may be limited to the quiescent liquid surface and the heat exchange may be restricted, regardless of void fraction in that volume. The existence of such a separated liquid level in a volume is detected independently by the level tracking model in the code. In these situations, when the void fraction above the liquid level is > 0.999, interfacial heat transfer in the steam volume above the level is ignored, the $(hA)_{igt}$ and $(hA)_{ift}$ terms are proportioned to the liquid height in the volume, and the contribution of the heat exchange over the liquid level is added to these components.

Calculation of the interfacial heat transfer components across the liquid level is based on a correlation given by Holman[4.1-11] for free natural convection in air above a horizontal surface. The original form of this correlation, given in British units, is

$$h_{si} = 0.22(\Delta T)^{1/3} \ . \quad (4.1\text{-}70)$$

This correlation was converted to S.I. units and modified by Chu[a] to take into account the heat conductivity of vapor instead of air, for which the correlation was suggested, by using the ratio of the two conductivities. The result is

---

a. Private communication, K. H. Chu, General Electric Company, San Jose, CA, October 7, 1987.

$$h_{gi} = 1.027 \left(\frac{k_g}{0.0305} \right) (\Delta T)^{1/3} \qquad (4.1\text{-}71)$$

in which k_g is the local heat conductivity of the vapor and 0.0305 is the heat conductivity of air at standard conditions.

The overall interfacial heat transfer rates for liquid and vapor in a volume with stratified liquid level are then calculated as

$$(hA)_{i\ell s} = \left[(hA)_{i\ell o} Dz_\ell + 1.027\ k_g\ 32.79 (|T_\ell - T_g|)^{1/3} \right] DZ_1 \qquad \text{*, HAIL} \quad (4.1\text{-}72)$$

and

$$(hA)_{igs} = \left[(hA)_{igo} Dz_\ell + 1.027\ k_g\ 32.79 (|T_\ell - T_g|)^{1/3} \right] DZ_1 \qquad \text{*, HAIV} \quad (4.1\text{-}73)$$

for liquid and vapor, respectively. In these equations, $(hA)_{i\ell o}$ and $(hA)_{igo}$ represent the overall heat transfer rates for liquid and vapor that may include contribution from different flow regimes, Dz_ℓ is the height of the stratified liquid in the volume, 32.79 is 1/0.305, and DZ_1 is the area per unit volume of the cell.

4.1.10 Implementation in Coding

The coding of the HEATIF subroutine is very close to the equations described in Sections 4.1.3 through 4.1.9. Most of the numerical values or limits imposed on the variables have been indicated in connection with the equations to which they apply. There are, however, two sets of adjustments made near the end of the HEATIF subroutine to the calculated overall rates of heat transfer, that should be discussed here. In addition, the procedures involved in calculating the initial variables before HEATIF is called are described below.

4.1.10.1 Volume-Dependent Limits. Before the modifications of $(hA)_{i\ell o}$ and $(hA)_{igo}$ for stratified liquid level (described in Section 4.1.9), the calculated values of these variables are compared to the cell volume for which they have been evaluated (Vol) and the larger of the two numbers is chosen as the minimum rate of phasic heat transfer to the interface; i.e.,

$$(hA)_{i\ell o} = Max \left[(hA)_{i\ell o}, Vol \right] \qquad \text{*, HAIL} \quad (4.1\text{-}74)$$

and

$$(hA)_{igo} = Max\left[(hA)_{igo}, Vol\right] . \qquad *, \text{HAIV} \quad (4.1\text{-}75)$$

The logical meaning of these operations is simply setting the minimum rate of heat transfer per unit volume equal to 1.

In order to cover the other extreme, maximum limits of $2\times10^{8}\cdot$Vol and $10^{8}\cdot$Vol are imposed on the $(hA)_{ito}$ and $(hA)_{igo}$ terms, respectively. These upper numerical limits have been found adequate in preventing disruption of computations due to occurrence of some abnormally high numbers for the rate of heat transfer during iterations.

4.1.10.2 Adjustments for Metastable States. A correction in $(hA)_{ito}$ is made if the liquid is superheated. Similarly, $(hA)_{igo}$ is corrected if the vapor is subcooled. These corrections are simply a ten-fold increase in the calculated value for the phase that is in the metastable state, if the temperature difference exceeds one degree, and proportionally less if the temperature excess is below one degree. These operations are expressed by the following relations:

If $T_\ell > T_s$, the liquid is superheated; hence,

$$(hA)_{itm} = (hA)_{ito}\left[1. + 9.X_{1\ell}^{2}(3. - 2.X_{1\ell})\right] \qquad *, \text{HAIL} \quad (4.1\text{-}76)$$

where

$(hA)_{itm}$ = modified rate of liquid heat transfer in metastable state, and

$$X_{1\ell} = Min\left[(T_\ell - T_s), 1.0\right] . \qquad *, \text{X1} \quad (4.1\text{-}77)$$

If $T_g < T_s$, the vapor is subcooled; hence,

$$(hA)_{igm} = (hA)_{igo}\left[1. + 9.X_{1g}^{2}(3. - 2.X_{1g})\right] \qquad *, \text{HAIV} \quad (4.1\text{-}78)$$

where

$(hA)_{igm}$ = modified rate of vapor heat transfer in metastable state, and

$$X_{1g} = Min\left[(T_s - T_g), 1.0\right] . \qquad *, \text{X1} \quad (4.1\text{-}79)$$

There are no comparisons of these modified correlations with data, and there are no known data from any measurements of the interfacial heat transfer in metastable conditions.

4.1.10.3 Calculation of Initial Variables. The interfacial heat transfer subroutine HEATIF computes the two cell-centered interfacial heat transfer coefficients and the cell-centered interfacial area using a combination of cell-centered variables, edge-centered variables, and mixed variables that are products of cell-centered and edge-centered variables. All but one of the cell-centered variables, as computed by the numerical solution scheme, can be used directly to calculate several thermodynamic and transport properties, such as density and viscosity; cell geometry (i.e., cell volume and length); and stratified level parameters. The void fraction used in the calculation of the interfacial heat transfer parameters is the cell-centered value but is subject to modification, as discussed below. The other variables that are input to subroutine HEATIF are variables whose values are computed by the numerical solution scheme at the cell edges or are variables that are products of cell-centered and edge-centered variables.

The values of these variables are computed for each cell by subroutines TFIE and TF3E before subroutine HEATIF is called to determine the interfacial heat transfer parameters for cells in the one- and three-dimensional components, respectively. The variables whose value at the cell center must be computed from edge-centered values include hydraulic diameter, phasic velocities, and phasic mass fluxes. Because the calculation of the unknown cell-centered variables is somewhat different in the one-dimensional and three-dimensional components, they will be discussed separately.

4.1.10.3.1 Computation of Cell-Centered Variables for One-Dimensional Components--As stated above, the void fraction (which is a cell-centered variable) is modified from the value computed by the numerical solution scheme in several special circumstances. These circumstances are (a) presence of stratified mixture level, (b) presence of subcooled vapor at high void fraction, (c) presence of superheated liquid at low void fraction, and (d) presence of subcooled boiling in the cell. The code first sets the void fractions to be used in the computation of the interfacial heat transfer parameters equal to the cell-centered void fraction

$$\alpha_j^i = \alpha_j \qquad (4.1\text{-}80)$$

where

α_j^i = void fraction to be used in computation of interfacial heat transfer parameters in cell j, and

α_j = void fraction in cell j computed by numerical solution scheme.

Next, the code tests the above-level void fraction variable to determine the presence of a highly stratified, two-phase mixture level in the cell. If a highly stratified mixture level is present, the void fraction to be used in the calculation of the interfacial parameters is set equal to the below-level

void fraction

$$\alpha_j^i = \alpha_{j,B} \text{ if } \alpha_{j,A} > 0.999 \tag{4.1-81}$$

where

$\alpha_{j,A}$ = above-level void fraction in cell j, and

$\alpha_{j,B}$ = below-level void-fraction in cell j.

The above-level void fraction $\alpha_{j,A}$ will be identically zero if no two-phase mixture level exists in the cell.

The next modification is made if the cell-centered void fraction is less than 0.5 and the liquid temperature is above the local saturation temperature. The void fraction to be used in the calculation of the interfacial heat transfer parameters is the maximum of the previously selected void fraction and a void fraction based on the amount of liquid superheat

$$\alpha_j^i = Max\ [\alpha_j^i,\ 0.001 \cdot (T_{\ell j} - T_{sj})] \tag{4.1-82}$$

where

$T_{\ell j}$ = liquid temperature in cell j, and

T_{sj} = saturation temperature in cell j.

This modification is an attempt to limit the amount of superheat in the liquid phase at low void fraction by increasing the interfacial heat transfer area if superheat exists. The coefficient 0.001 was chosen from experience.

The next modification is made if the cell-centered void fraction is less than 0.5 and saturated or subcooled liquid and subcooled boiling are present in the cell.

The amount of vapor that will be created by subcooled boiling during the time step is estimated from

$$\Delta\alpha_j = \frac{QEVAP_j \cdot DELT}{H_{fgj} \cdot Vol_j \cdot \rho_{vj}} \tag{4.1-83}$$

where

$\Delta\alpha_j$ = change in void fraction due to subcooled boiling in cell j

$QEVAP_j$ = subcooled boiling power in cell j

DELT = time step

H_{fgj} = heat of vaporization based on pressure in cell j

Vol_j = volume of cell j

ρ_{vj} = vapor density in cell j.

The estimated void fraction change due to subcooled boiling is limited by the maximum change in void fraction allowed during a time step (which is based on the void fraction in the cell)

$$\Delta\alpha_j = Min\ [\Delta\alpha_j,\ \Delta\alpha_{M,j}] \tag{4.1-84}$$

where $\Delta\alpha_{M,j}$ is the maximum allowed change in void fraction during a time step.

The void fraction used for the calculation of the interfacial heat transfer parameters is the maximum of the void fraction chosen on the basis of the previous modifications and the void fraction in the cell at the end of the time step predicted from the production of vapor due to subcooled boiling,

$$\alpha_j^1 = Max\left[\alpha_j^1,\ (\alpha_j + \Delta\alpha)\right]. \tag{4.1-85}$$

The subcooled boiling modification was implemented to cover the case where void first appears in a cell. In this situation, the unmodified void fraction used to compute the interfacial heat transfer parameters would be zero, leading to a saturation where the interfacial area would be zero but the void fraction would be non-zero due to the production of vapor by subcooled boiling. The inconsistency between the void fraction and interfacial area causes the solution procedure to fail due to excessive iterations or leads to incorrect phasic temperatures due to the lack of an interfacial energy exchange mechanism. The modification anticipates the creation of void due to subcooled boiling and adjusts the interfacial area accordingly.

The final modification to the void fraction used to compute the interfacial heat transfer parameters is activated whenever the cell-centered void fraction is greater than 0.5 and the vapor temperature is below the saturation temperature based on the pressure in the cell. In this situation, the liquid fraction, which is defined as one minus the void fraction, is set to the maximum of the liquid fraction, as computed using the void fraction obtained using the previous steps, and a liquid fraction based on the vapor subcooling,

$$\alpha_{\ell j}^1 = Max\left[1. - \alpha_j^1,\ 0.0001\ (T_{s,j} - T_{v,j})\right] \tag{4.1-86}$$

where

$\alpha_{\ell,j}^1$ = liquid fraction to be used in the calculation of interfacial parameters for cell j

$T_{s,j}$ = saturation temperature in cell j, and

$T_{v,j}$ = vapor temperature in cell j.

The void fraction used in the computation of the interfacial heat transfer parameters is computed from the liquid fraction as

$$\alpha_j^i = 1. - \alpha_{\ell j}^i \quad . \tag{4.1-87}$$

This final modification attempts to limit the amount of vapor subcooling at high void fractions. The factor 0.0001 in the expression for the liquid fraction was chosen based on experience with the interfacial heat transfer model at high void fraction. This completes the computation of the void fraction for use by subroutine HEATIF.

The edge-centered properties whose values must be computed at the cell center for use in subroutine HEATIF are the hydraulic diameter, the phasic velocities, and the phasic mass fluxes. The computation of these parameters depends upon whether a highly stratified, two-phase mixture level exists in the cell [see Equation (4.1-81)]. If no two-phase level exists in the cell or if the above level void fraction does not satisfy the criterion, then the cell-centered parameters are computed by

$$HD_j = 0.5 \left[HD_{j-1/2} + HD_{j+1/2} \right] \tag{4.1-88}$$

and the average liquid and mixture mass velocities are calculated by

$$GL_j = (1 - \alpha_j) \rho_{\ell j} \bar{V}\bar{L}_j \tag{4.1-89}$$

for the liquid, and

$$GM_j = \alpha_j \rho_{vj} \bar{V}\bar{V}_j + (1 - \alpha_j) \rho_{\ell j} \bar{V}\bar{L}_j \tag{4.1-90}$$

for the mixture. In these equations,

$$\bar{V}\bar{V}_j = \begin{cases} \dfrac{0.5}{A_j} \left[A_{j-1/2} \cdot VV_{j-1/2} + A_{j+1/2} \cdot VV_{j+1/2} \right] & \text{if } VV_{j-1/2} \cdot VV_{j+1/2} \geq 0 \\ \dfrac{A_{j-1/2}}{A_j} \cdot Min \left[|VV_{j-1/2}|, |VV_{j+1/2}| \right] & \text{if } VV_{j-1/2} \cdot VV_{j+1/2} < 0 \end{cases} \tag{4.1-91}$$

and

$$\bar{VL}_j = \begin{cases} \frac{0.5}{A_j}\left[A_{j-1/2}\cdot VL_{j-1/2} + A_{j+1/2}\cdot VL_{j+1/2}\right] & \text{if } VL_{j-1/2}\cdot VL_{j+1/2} \geq 0 \\ \frac{A_{j-1/2}}{A_j}\cdot Min\left[|VL_{j-1/2}|, |VL_{j+1/2}|\right] & \text{if } VL_{j-1/2}\cdot VL_{j+1/2} < 0 \end{cases} \quad (4.1\text{-}92)$$

where

$$A_j = \frac{Vol_j}{DX_j} . \quad (4.1\text{-}93)$$

The linear phasic velocities are calculated with the following relations;

$$VL_j = Max\left[0.1\ m/s,\ |\bar{V}\bar{L}_j|\right] \quad (4.1\text{-}94)$$

$$VV_j = Max\left[0.1\ m/s,\ |\bar{V}\bar{V}_j|\right] . \quad (4.1\text{-}95)$$

The cell-centered hydraulic diameter is computed as the average of the edge-centered hydraulic diameters at the two edges of the cell. The cell-centered phasic velocities depend upon whether the velocities at the two ends of the cell are in the same direction or not. If the velocities are in the same direction, then a simple edge flow area weighted average is computed, where the cell centered flow area is computed as the ratio of the cell volume to the cell length. If the velocities at the two ends of the cell are in opposite directions, the velocity that has the lowest absolute value is multiplied by the ratio of the flow area at the low numbered edge of the cell to the cell-centered flow area.

Note that the method used to compute the phase velocity when the velocities at the two edges of the cell are in opposite directions is inconsistent with the method used when the edge velocities are in the same direction. For total accuracy, the method for the case of opposite directions should be changed to

$$VL_j = Min\left[A_{j-1/2}\ |VL_{j-1/2}|,\ A_{j+1/2}\ |VL_{j+1/2}|\right]\frac{1}{A_j} \quad (4.1\text{-}95)$$
$$for\ VL_{j-1/2}\cdot VL_{j+1/2} < 0$$

and

$$VV_j = Min\left[A_{j-1/2}\,|VV_{j-1/2}|,\ A_{j+1/2}\,|VV_{j+1/2}|\right]\frac{1}{A_j} \qquad (4.1\text{-}97)$$

$$for\ VV_{j-1/2}\cdot VV_{j+1/2} < 0$$

so that the minimum function chooses the smallest area-weighted velocity rather than the smallest velocity. This is a small point, which would only change the results of the computation if the three flow areas associated with the cell have very different values.

Once the cell-centered phasic velocities are computed, the phasic mass fluxes are computed using the cell-centered void fraction and phasic densities.

If the highly stratified, two-phase level criterion is satisfied, the cell-centered phasic velocities and mass fluxes are computed as

$$HD_j = HD_{j-1/2} \qquad (4.1\text{-}98)$$

$$VV_j = |VV_{j-1/2}| \qquad (4.1\text{-}99)$$

$$VL_j = |VL_{j-1/2}| \qquad (4.1\text{-}100)$$

$$GL_j = (1. - \alpha_{j,B})\rho_{\ell j} VL_j \qquad (4.1\text{-}101)$$

$$GM_j = \alpha_{j,B}\rho_{vj} VV_j + (1. - \alpha_{j,B})\rho_{\ell j} VL_j \qquad (4.1\text{-}102)$$

This computation uses the edge-centered values at the low-numbered edge of the cell as the cell-centered value that is appropriate if the component is upright with the low-numbered end of the component at a lower elevation than the high-numbered end of the component. The cell-centered velocities and mass fluxes are then computed from the cell edge below the stratified mixture level. However, the model for the computation of the phasic velocities in the presence of a stratified two-phase level appears inappropriate when the user has oriented the component with the high-numbered end at the lower elevation. In that event, the cell-centered phasic velocities will be computed from the values at the cell edge above the stratified mixture level, while the void fraction used in the computation of the interfacial heat transfer parameters will be the below-level void fraction. The model should be changed so that the closest edge values below the two-phase level are used regardless of the orientation of the component.

One final comment is appropriate. The cell-centered phase velocities are computed as positive values to be consistent with the correlations used in subroutine HEATIF, which were all developed from upflow data, and are limited to be greater in magnitude than 0.1 m/s to give finite values of the interfacial heat transfer parameters at low flows.

4.1.10.3.2 Computation of Cell-Centered Variables for Three-Dimensional Components. The computation of the void fraction to be used in the computation of the interfacial heat transfer parameter is the same in three-dimensional components except that there is no modification for subcooled boiling since subcooled boiling is not allowed in three-dimensional components.

The computation of the cell-centered phase velocities is quite different in three-dimensional components. First, average velocities are computed for each of the three coordinate directions

$$\bar{V}_{z,ijk} = \begin{cases} V_{(i+1/2)jk} & \text{if } A_{z,i+1/2} \geq 10^{-10}\ m^2 \\ V_{(i-1/2)jk} & \text{if } A_{z,i+1/2} < 10^{-10}\ m^2 \end{cases} \quad (4.1\text{-}103)$$

$$\bar{V}_{R,ijk} = 0.5\left[V_{i(j-1/2)k} + V_{i(j+1/2)k}\right] \quad (4.1\text{-}104)$$

$$\bar{V}_{\theta,ijk} = 0.5\left[V_{ij(k-1/2)} + V_{ij(k+1/2)}\right] \quad (4.1\text{-}105)$$

where

$V_{(i+1/2)jk}$ = velocity in axial (z) directions on upper axial face of cell ijk

$V_{(i-1/2)jk}$ = velocity in axial direction (z) on lower axial face of cell ijk

$\bar{V}_{z,ijk}$ = average velocity in axial (z) direction for cell ijk

$\bar{V}_{R,ijk}$ = average velocity in radial (R) direction for cell ijk

$\bar{V}_{\theta,ijk}$ = average velocity in azimuthal (θ) direction for cell ijk

and the other velocities with half-integer subscripts have their usual definitions.

The cell-centered phase velocity is the maximum of 0.1 m/s and the vector

sum of the three average velocities in the individual directions, i.e.,

$$\bar{V}_{ijk} = Max\left[0.1\ m/s,\ \left(\bar{V}_{z,ijk}\cdot\bar{V}_{z,ijk} + \bar{V}_{R,ijk}\cdot\bar{V}_{R,ijk} + \bar{V}_{T,ijk}\cdot\bar{V}_{T,ijk}\right)^{1/2}\right] . \quad (4.1\text{-}106)$$

This algorithm is used for both the liquid and vapor velocities.

The cell-centered mass fluxes are then computed as

$$G_{\ell,ijk} = (1 - \alpha^{i}_{ijk})\rho_{\ell,ijk}\bar{V}_{\ell,ijk} \quad (4.1\text{-}107)$$

$$G_{m,ijk} = \alpha^{i}_{ijk}\rho_{g,ijk}\bar{V}_{g,ijk} + G_{\ell,ijk} \quad (4.1\text{-}108)$$

where α^{i}_{ijk} is the cell-centered void fraction to be used in the calculation of the interfacial heat transfer parameters.

4.1.11 Mass Exchange Across the Interface

Calculations of the heat and mass exchanges across the interface, according to Equations (4.1.1) and (4.1-2), are performed in the TF1E and TF3E subroutines of TRAC-BF1/MOD1 for one- and three-dimensional components, respectively.

4.1.12 Summary and Conclusions

The interfacial heat transfer calculation in TRAC-BF1/MOD1 is based on a mechanistic model that calculates the interfacial contact areas for vapor and liquid in different flow regimes and applies appropriate heat transfer correlations for heat exchange between each phase and the interface over those areas. The flow regime map for this model consists mainly of two distinct regions, bubbly/churn and dispersed droplets, with a transition zone, called annular-droplet, between them.

The boundary between bubbly/churn and annular-droplet flows is identified with a transition void fraction, α_{tran}, which is calculated as a function of the flow, pressure, and system variables. The dependence of α_{tran} on these variables in this model is much weaker compared to α_{tran} in the interfacial shear model. The transition from annular-droplet to fully dispersed droplets is set arbitrarily at a void fraction of 0.25 + α_{tran}. This is the same as in the interfacial shear model.

Calculation of the interfacial area for each flow pattern is according to the drift flux formulas suggested by Ishii,[4.1-1] with some variations according

to Andersen et al.[4.1-2,3]. There are some minor differences in the correlations used for bubble drift velocity in fuel bundles and for droplet drift velocity in general between this model and the interfacial shear model. The impact of these differences has not been evaluated. There are also some other minor differences between these two models that may need to be harmonized in the future.

Calculations of the heat transfer coefficients are based on published correlations for overall heat transfer obtained from studies of heat transfer on solid geometries of different kinds. In some cases, such as in heat transfer between a bubble or droplet and the interface, modifications have been made to include the effects of local circulation inside the fluid particle.

Finally, the effects of noncondensable gas and horizontal stratification of liquid in a volume on the condensation heat transfer have been considered.

4.1.13 References

4.1-1. M. Ishii, *One-Dimensional Drift-Flux Model and Constitutive Equations for Relative Motion Between Phases in Various Two-Phase Flow Regimes*, ANL-77-47, October 1977.

4.1-2. J. G. M. Andersen and K. H. Chu, *BWR Refill-Reflood Program, Task 4.7 - Constitutive Correlations for Shear and Heat Transfer for the BWR Version of TRAC*, NUREG/CR-2134, EPRI NP-1582, GEAP-24940, December 1981.

4.1-3. J. G. M. Andersen, K. H. Chu, J. C. Shaug, *BWR Refill-Reflood Program, Task 4.7 -Model Development, Basic Models for the BWR Version of TRAC*, NUREG/CR-2573, EPRI NP-2375, GEAP-22051, September 1983.

4.1-4. J. Nikuradse, "Principles of Turbulent Flow in Smooth Tubes," *Forschung auf dem Gebeite des Ingenieurwesens (Research at the Request of Engineers)*, 3, September-October 1932, p. 356.

4.1-5. K. Lee and D. J. Ryley, "The Evaporation of Water Droplets in Superheated Steam," *Journal of Heat Transfer*, November 1968, pp. 445-451.

4.1-6. J. G. M. Andersen and H. Abel-Larsen, *CORECOOL-Model Description of the Program*, RISO-M-21380, November 1980.

4.1-7. W. M. Kays, *Convective Heat and Mass Transfer*, New York: McGraw-Hill Book Company, 1966, pp. 109-110.

4.1-8. M. M. Megahed, *Interfacial Heat Transfer in Countercurrent Flows of Steam and Water*, EGG-RTH-2495, January 1987.

4.1-9. D. Cook et al., *Countercurrent Steam-Water Flow in a Vertical Channel*, NUREG/CR-2056, April 1981.

4.1-10. Los Alamos National Laboratory Safety Code Development Group, *TRAC-PD2, An Advanced Best Estimate Computer Program for Pressurized Water Reactor Loss-of-Coolant Accident Analysis*, NUREG/CR-2054, LA-8709-MS, April 1981.

4.1-11. J. P. Holman, *Heat Transfer*, 3rd Ed, New York: McGraw-Hill, Inc., 1972, Table 7-2.

4.2 WALL HEAT TRANSFER

Wall heat transfer in TRAC-BF1/MOD1 involves all processes of energy exchange between the fluid and the solid walls of each hydraulic volume. The calculation results from wall heat transfer provide the Q_{wg} and Q_{wf} terms that are used in the energy balance equations for the mixture and vapor. The main part of wall heat transfer calculations in TRAC-BF1/MOD1 is performed by the HTCOR subroutine. This subroutine was originally developed as a part of TRAC-PD2 at Los Alamos National Laboratory, but it includes a number of modifications that were introduced in the course of TRAC-BWR development at the INEL.

HTCOR is called within nine different subroutines in TRAC-BF1/MOD1; and, in turn, HTCOR calls a few other subroutines for some specific calculations that will be discussed later. This section describes the correlations used in HTCOR and its related subroutines, their basis, and the situations in which they apply. In the following sections, each equation that is actually used in the coding is marked with an asterisk (*), followed by the variable name used in the code for the left-hand side of that equation.

4.2.1 Background

Numerous experimental studies have shown that the mechanism of heat transfer from a solid wall to a mass of water and steam varies as the temperature difference between the wall and the bulk of fluid passes trough some certain limits. The intensity of heat transfer, known as heat flux, shows dramatic variations with changes in the temperature difference between the wall and fluid. The diagram showing these variations is known as the boiling curve, an example of which is shown in Figure 4.2-1.

In general, the boiling curve displays the following modes of heat transfer:

- Forced or natural convection to single-phase (sub-cooled) liquid
- Nucleate boiling, up to the point of departure from nucleate boiling (DNB), or critical heat flux (CHF), at which the heat flux passes a maximum and begins to drop
- Transition boiling, with reduced heat flux, as intensive evaporation prevents adequate contact between the wall and liquid
- Film boiling, where thermal radiation from the wall to the two-phase mixture begins to enhance the heat transfer
- Forced or natural convection to single-phase (super-heated) steam.

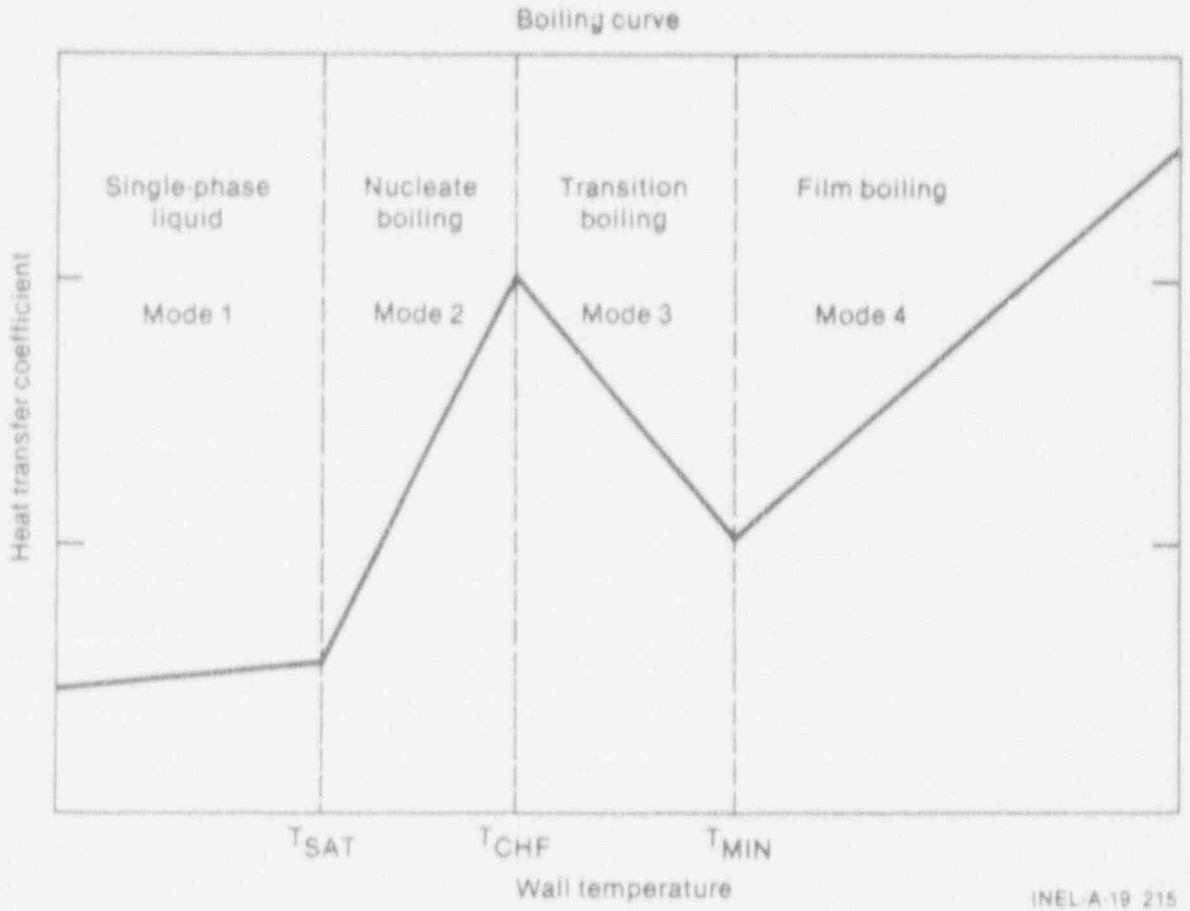

Figure 4.2-1. TRAC-BF1/MOD1 boiling curve.

The true shape of the boiling curve in each case will depend on the channel geometry, mass velocity and fluid properties.

Wall heat transfer may also involve cooling of the fluid through the walls. Heat transfer from the fluid to a solid wall may involve one of the following processes:

- Forced or natural convection in single-phase water
- Condensation of vapor or two-phase mixture
- Forced or natural convection in single-phase vapor.

The overall structure of the wall heat transfer model in TRAC-BF1/MOD1 is based on the processes involved in the boiling curve and flow cooling.

4.2.2 Different Modes Of Heat Transfer In HTCOR

The wall heat transfer calculations in TRAC-BF1/MOD1 include all phases of the boiling curve and fluid cooling processes. In order to apply proper correlations for heat transfer coefficients in different situations, each phase is identified with a mode number that will direct the path of calculations to the right correlation. The mode numbers and their interpretations are given in Table 4.2-1.

Table 4.2-1. Modes of heat transfer in subroutine HTCOR.

Mode No.	Heat transfer calculation form
0	Vapor condensation (if $\alpha > 0.5$)
1	Convection to single-phase liquid
2	Nucleate boiling (both subcooled and quality boiling)
3	Transition boiling (both subcooled and quality boiling)
4	Film boiling
5	Convection to single-phase vapor
6	Not used for any mode
7	Convection to two-phase mixture with no detailed CHF calculation

Each of these modes comprises a number of subsets, representing different flow or system conditions, which require application of specific heat transfer correlations. Example of these subsets are single-phase convection in laminar or turbulent flows, each one to be calculated with a different correlation. The subsets of each mode are identified by a combination of the mode number and some decimal points, such as 1.0 for convection in laminar flow and 1.1 for natural convection.

4.2.3 Effect Of Flow Regimes On Wall Heat Transfer

Two-phase flow patterns affect the rate of vapor generation in direct contact with the walls, and this term is important in determining mass exchange between liquid and vapor. Variations in two-phase flow regimes are considered in nucleate boiling and in transition boiling modes, as the steam quality and void fraction experience their widest range of variations in these

two modes of heat transfer.

4.2.3.1 Flow Regime Transitions. As in the cases of interfacial shear and interfacial heat transfer, three flow patterns are considered--namely, bubbly/churn, annular (transition), and dispersed droplet. The transitions between these flow regimes are defined in terms of void fraction. This scheme of flow pattern definition is based on the derivations of Ishii[4.2-1] and Andersen and Chu[4.2-2] with a slight modification. The transition range is expanded from 10% in void to 25% in void (for a more smooth change). The prevailing range of the different flow regimes are:

- Bubbly/churn flow for $\alpha < \alpha_{tran}$
- Annular flow for $\alpha_{tran} < \alpha < \alpha_{tran} + 0.25$, and
- Dispersed droplet flow for $\alpha > \alpha_{tran} + 0.25$

where

$$\alpha_{tran} = \left(1 + \frac{4}{\Upsilon}\right)\frac{1}{C_o} - \frac{4}{\Upsilon} - 0.15 \qquad \text{*, ACA} \quad (4.2\text{-}1)$$

$$\Upsilon = \sqrt{\frac{\rho_f}{\rho_g}} \qquad \text{*, GAMMA} \quad (4.2\text{-}2)$$

$$C_o = C_\infty - \frac{C_\infty - 1}{\Upsilon} \qquad \text{*, CO} \quad (4.2\text{-}3)$$

$$C_\infty = 1.393 - 0.0155 \log (Re) \qquad \text{*, COINF} \quad (4.2\text{-}4)$$

$$Re = \frac{GH_d}{\mu_f} . \qquad \text{*, RE} \quad (4.2\text{-}5)$$

A few points may be observed considering the actual coding of these equations. First, Re in Equation (4.2-5) is replaced by 1 + Re to make sure that the logarithm is always positive. Then, C_∞ is limited to a lower bound of 1.0; and, finally, C_o is limited to an upper bound of 1.3333, which is the experimentally observed maximum value of this variable (see Reference 4.2-1).

Note that the transition void fraction, α_{tran}, is calculated in a manner

that is identical to that of the interfacial heat transfer and similar to that of the interfacial friction case. As explained in Sections 6 and 4.1, there is a difference between Equation (4.2-4) and the formula used for calculating C_w in the interfacial shear model. As a result, transitions between different flow regimes are at different void fractions for wall heat transfer and interfacial shear. An example of the difference in transition from bubbly/churn to annular flow is given in Section 6.

4.2.4 Determination Of Heat Transfer Mode

Within subroutine HTCOR, a decision is made that determines the heat transfer mode that will be used for the following time interval. This mode selection logic is shown in Figure 4.2-2.

First, certain conditions of the fluid are calculated. These include the velocities, slip, mass flux, and equilibrium quality. The slip is set equal to one for countercurrent flow or when either phase velocity is zero.

4.2.4.1 Mode Selection in the Containment. Three modes can be chosen for a heat transfer surface in the containment; subcooled convection (mode 1), forced convection to vapor (mode 5), and film condensation from two-phase fluid (mode 0). Subcooled convection is chosen if the surface is below the water level. If the surface is above the water level, forced convection to vapor is chosen when the surface temperature is greater than or equal to saturation temperature. Film condensation from two-phase is chosen when the surface temperature is less than saturation temperature.

4.2.4.2 Mode 7--Simplified Boiling Curve. For each heat transfer surface, either the full-selection logic (modes 0 through 5) or the simplified boiling curve (mode 7) will always be used as preselected by the user. For surfaces where an accurate prediction of transition boiling is required, the full-selection logic should be chosen. The full-selection logic is recommended for fuel elements and heated structures that are likely to develop critical heat fluxes. Using the simplified boiling curve will result in faster calculations and is recommended for the heat transfer calculations from surfaces such as piping or unheated structures.

4.2.4.3 Mode 5--Convection to Vapor. The forced convection to vapor correlations (mode 5) are selected whenever the fluid contains little or no liquid and the wall temperature is greater than the saturation temperature. Under these conditions, wall condensation cannot occur.

4.2.4.4 Mode 4--Film Boiling. The first way in which the film boiling correlations (mode 4) are selected is if the wall temperature is greater than minimum stable film boiling temperature. If the wall temperature is less than

Figure 4.2-2. Heat transfer mode selection logic.

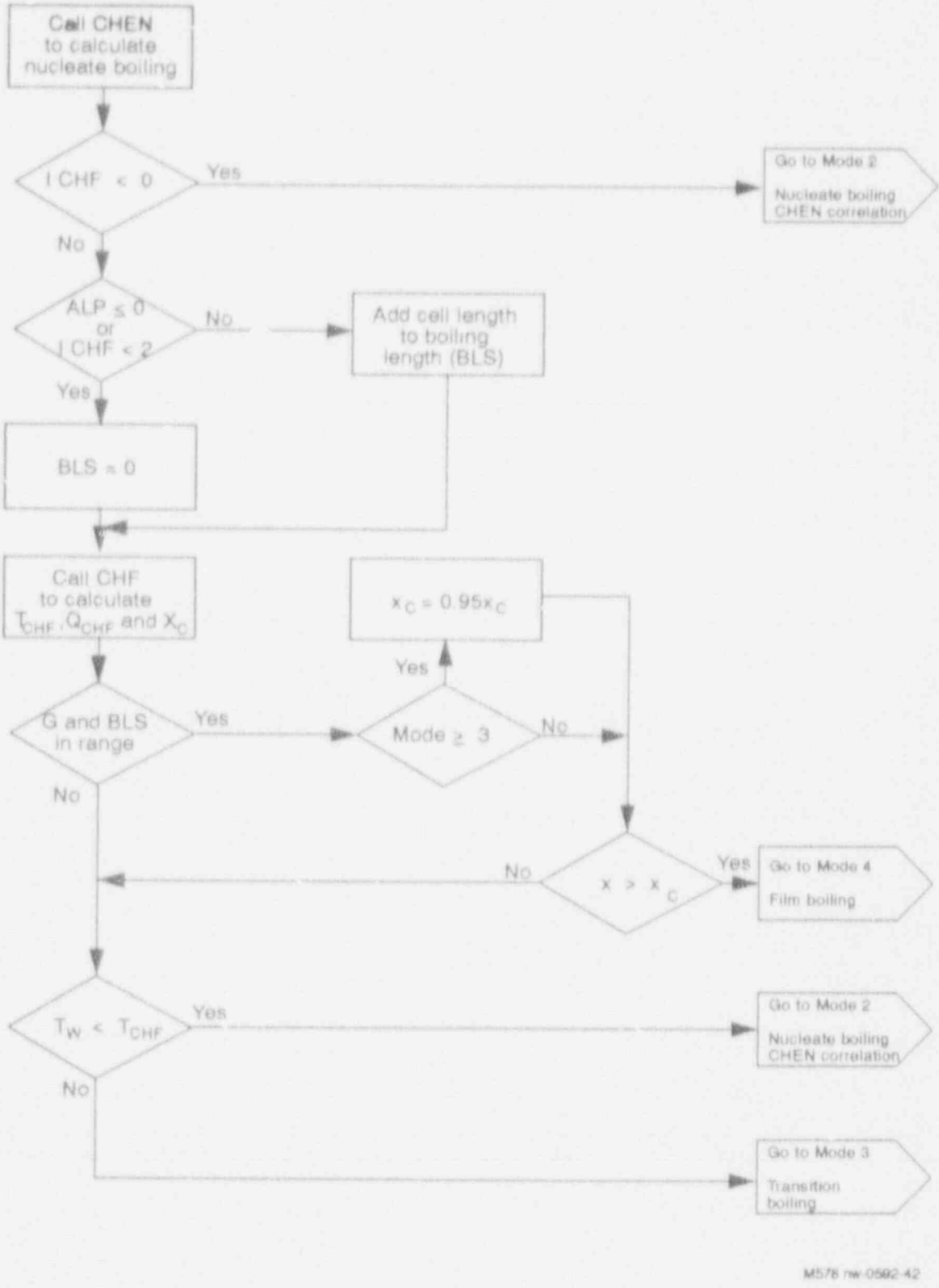

Figure 4.2-2. (continued)

minimum stable film boiling temperature, the selection procedure continues.

4.2.4.5 Mode 0--Film Condensation from Two-Phase Fluid. The correlations for film condensation from two-phase fluid (mode 0) are selected if the wall temperature is less than saturation temperature and the void fraction is greater than 0.5.

4.2.4.6 Mode 1--Convection to Liquid. The correlations for subcooled convection are used when either (a) the wall temperature is less than saturation temperature and the void fraction is less than or equal to 0.5; or (b) the wall temperature is less than or equal to the liquid temperature.

4.2.4.7 Mode 2--Nucleate Boiling (Path 1). There are two paths that lead to using the Chen[4.2-3] correlations for the nucleate boiling regime. The first is simply that the user has determined that the chance of going into transition boiling or film boiling can be ruled out for this particular heat transfer surface and transient. Using the option to not calculate a boiling transition will result in faster calculations and is recommended for the heat transfer calculations from surfaces such as piping or unheated structures. This choice should definitely be made for calculations that are being performed to establish a reactor steady state, since even the heated structures are known to be below the critical heat flux point. If this choice is not made in attempting to reach steady state, it is possible that the TRAC-BF1/MOD1 calculation will undergo a transient that enters transition boiling and then film boiling before recovering or attempting to recover.

4.2.4.8 Calculation of the Critical Heat Flux. The boiling length is initialized to zero. For each cell thereafter, the length of the cell is added to the boiling length if the cell quality is greater than 0.0 and if the user has chosen to use a critical quality correlation. If a cell quality is less than or equal to 0.0 or the user has chosen not to use a critical quality correlation, the boiling length is reinitialized to zero.

A critical heat flux (departure from nucleate boiling) calculation is performed to establish the heat flux, wall temperature, and fluid quality at the point of maximum heat transfer during nucleate boiling and beyond which transition boiling occurs.

4.2.4.9 Mode 4--Film Boiling. If the fluid quality is greater than the critical quality and the mass flux and the boiling length are within the correlation bounds (200 kg/m^2-s and 1 m, respectively), the film boiling heat transfer correlations are chosen. In order to reduce hunting between the film boiling, transition boiling, and nucleate boiling regimes, a hysteresis factor of 0.95 is applied to the calculated critical quality when the previously determined heat transfer regime was either film boiling or transition boiling.

If film boiling is eliminated as a possibility by one of the above tests, either transition boiling or nucleate boiling is selected by testing the old wall temperature against the wall temperature at critical heat flux.

4.2.4.10 Mode 3--Transition Boiling. If, after eliminating film boiling from consideration, the wall temperature is greater than or equal to the wall temperature at critical heat flux, the transition boiling correlations are selected.

4.2.4.11 Mode 2--Nucleate Boiling (Path 2). If, after eliminating film boiling from consideration, the wall temperature is less than the wall temperature at critical heat flux, the Chen[4.2-3] nucleate boiling correlations are selected.

4.2.5 Mode 0--Vapor Condensation

Figure 4.2-3 shows the logic used to select among four models that are used in the vapor condensation regime of surface heat transfer. The four models that are possible are the Nusselt[4.2-4] horizontal tube equation, the Dittus-Boelter[4.2-5] correlation, the McAdams[4.2-6] turbulent natural convection model, and the Chen[4.2-3] forced-convection model.

4.2.5.1 Mode 0.2--Nusselt Horizontal Tube Equation. As shown in Figure 4.2-3, the Nusselt[4.2-4] horizontal tube equation is always used to get an initial value for the liquid and vapor heat transfer coefficients

$$H_\ell = 0.725 \left[\frac{\rho_\ell^2 g_c h_{fg} K_\ell^3}{\mu_\ell D_H (T_s - T_w)} \right]^{1/4} \qquad *, \text{HL (4.2-6)}$$

$$H_v = 0.0 \; . \qquad *, \text{HV (4.2-7)}$$

If the quality is less than 0.71, these coefficients will be used unless adjusted for a high void fraction, as discussed in Sections 4.2.5.4 and 4.2.5.5.

4.2.5.2 Mode 0.4, Dittus-Boelter, McAdams, or Modified Kays. At higher qualities (greater than 0.71), the liquid film becomes thin and H_ℓ from the Nusselt equation above is linearly decreased from its value calculated at $X = 0.71$ to zero at $X = 0.999$. For these high qualities, HV is obtained by interpolation between zero at $X = 0.71$ and the maximum of the Dittus-Boelter,[4.2-5] McAdams,[4.2-6] and modified Kays[4.2-7] correlations at $X = 0.999$. The equations for the three correlations are

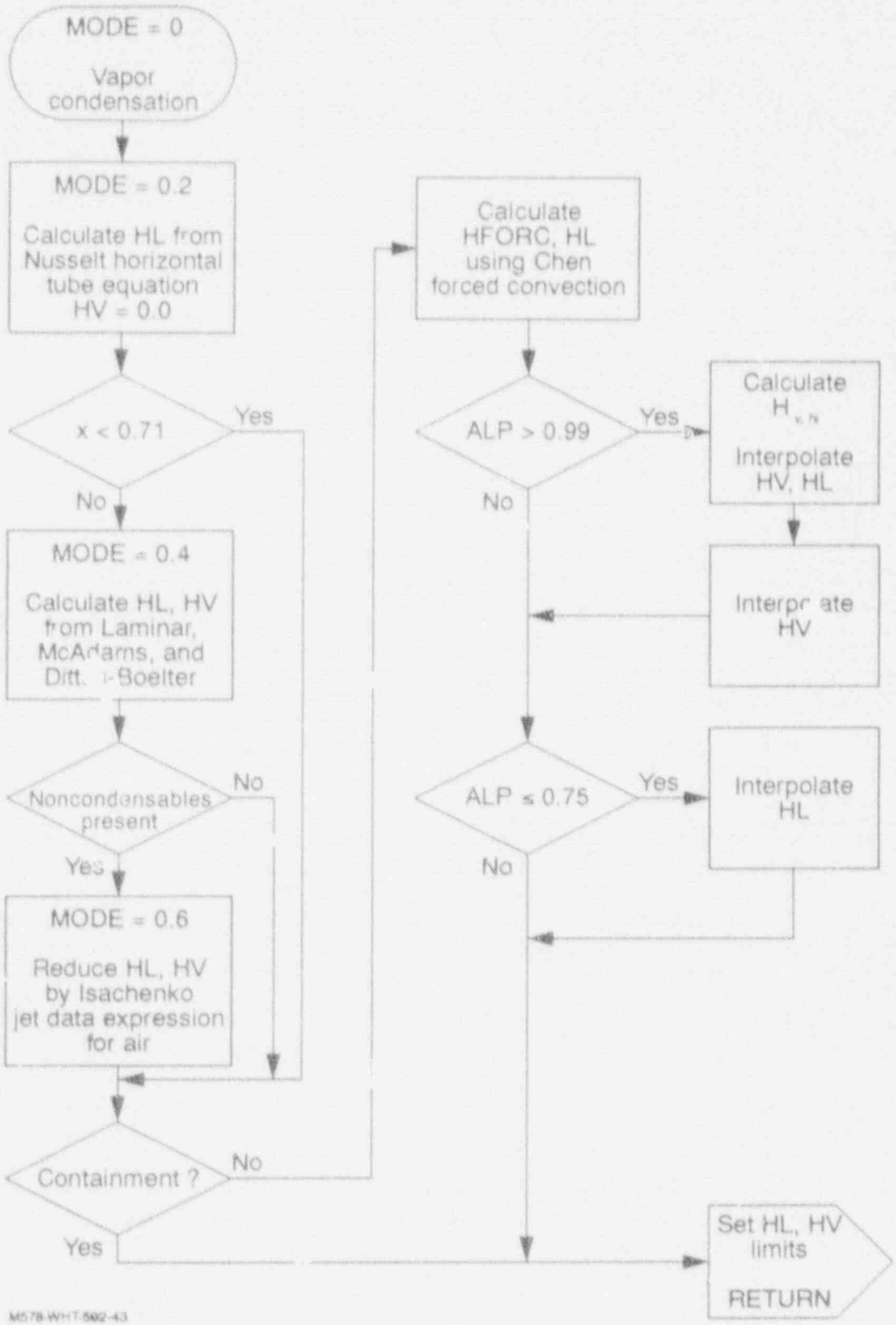

Figure 4.2-3. Mode 0--vapor condensation.

$$H_{v,turb} = 0.023 \frac{k_v}{D_H} Re_v^{0.8} Pr_v^{1/3} \qquad *, \text{HV (4.2-8)}$$

$$H_{v,nc} = 0.13 \frac{k_v}{D_H} \left(\frac{Gr_v}{Pr_v} \right)^{1/3} \qquad *, \text{HV (4.2-9)}$$

$$H_{v,lam} = 4 \frac{k_v}{D_H} \qquad *, \text{HV (4.2-10)}$$

where

$$Re_v = \frac{\rho_v \alpha V_v D_h}{\mu_v} \qquad (4.2\text{-}11)$$

$$Pr_v = \frac{\mu_v C_{pv}}{k_v} \qquad (4.2\text{-}12)$$

$$Gr_v = \frac{g_c \rho_v^2 |T_w - T_v| D_H^3}{\mu_v^2 T_v} \qquad (4.2\text{-}13)$$

and $1/T_v$ approximates the coefficient of thermal expansion. Note that the power on the Prandtl number in the Dittus-Boelter[4.2-5] correlation has been decreased to 1/3 from the original value of 0.4.

4.2.5.3 Isachenko's Jet Data Correction. If any noncondensables are present, the heat transfer coefficients are reduced by multiplying by a factor based on the Russian jet data expression by Isachenko.[4.2-8] The factor is

$$F_{ISA} = 0.168 \left[\frac{\alpha(\rho_v - \rho_a)^2}{(1-\alpha)\rho_a \rho_\ell} \right]^{0.1} . \qquad *, \text{CNDM (4.2-14)}$$

4.2.5.4 Chen Forced Convection. If the particular fluid volume represents the containment, the heat transfer coefficients calculated above are used with no further tests or corrections applied. For normal fluid

volumes, assuming that the void fraction is greater than 0.05 and the quality is greater than 10^{-5}, the Chen[4.2-3] forced convection correlations are used. In order to begin this calculation, the Lockhart-Martinelli[4.2-9] factor is first calculated as follows:

$$\chi_{TT}^{-1} = \left(\frac{X}{1-X}\right)^{0.9}\left(\frac{\rho_\ell}{\rho_g}\right)^{0.5}\left(\frac{\mu_g}{\mu_\ell}\right)^{0.1} . \qquad *, \text{XXTT (4.2-15)}$$

The Lockhart-Martinelli factor is limited to the range $0.10 \le \chi_{TT}^{-1} \le 100$. A Reynolds number factor is then calculated as

$$F = 2.35\left(\chi_{TT}^{-1} + 0.213\right)^{0.736} . \qquad *, \text{F (4.2-16)}$$

The three correlations (Dittus-Boelter,[4.2-5] McAdams,[4.2-6] and modified Kays[4.2-7]) are then used to calculate three heat transfer coefficients:

$$H_{\ell,turb} = 0.023\,\frac{k_\ell}{D_H}\,(F^{1.25}Re_\ell)^{0.8}Pr_\ell^{1/3} \qquad *, \text{HL (4.2-17)}$$

$$H_{\ell,nc} = 0.13\,\frac{k_\ell}{D_H}\left(\frac{Gr_\ell}{Pr_\ell}\right)^{1/3} \qquad *, \text{HL (4.2-18)}$$

$$H_{\ell,lam} = 4\frac{k_\ell}{D_H} \qquad *, \text{HL (4.2-19)}$$

where

$$Re_\ell = \frac{\rho_\ell \alpha V_\ell D_H}{\mu_\ell} \qquad (4.2\text{-}20)$$

$$Pr_\ell = \frac{\mu_\ell C_{p\ell}}{k_\ell} \qquad (4.2\text{-}21)$$

$$Gr_\ell = -\,g_c\rho_\ell\left(\frac{d\rho_\ell}{dT}\right)|T_w - T_\ell|\,\frac{D_H^3}{\mu^2} . \qquad (4.2\text{-}22)$$

The highest of the three heat transfer coefficients is then chosen as H_{forc}. H_{forc} and $H_{\ell,old}$, the liquid heat transfer coefficient calculated from Section 4.5.2.1, 4.5.2.2, or 4.5.2.3, as appropriate, are then used to calculate a modified liquid heat transfer coefficient

$$H_\ell = \begin{cases} (1-\alpha)H_{forc} + \alpha H_{\ell,old} \text{ for } T_s - T_w \geq 5 \\ \dfrac{1-\alpha(T_s-T_w)}{5}H_{forc} + \dfrac{\alpha(T_s-T_w)}{5}H_{\ell,old} \text{ for } T_s - T_w < 5 \end{cases} \quad *, \text{ HL (4.2-23)}$$

The second equation for the modified H_ℓ is a linear interpolation between the first equation at $T_s - T_w = 5$ and H_{forc} at $T_s - T_w = 0$.

The vapor heat transfer coefficient, H_v, from Section 4.2.5.1, 4.2.5.2, or 4.2.5.3 is unmodified.

4.2.5.5 Void Fraction Range Corrections. The correlations used in Section 4.2.5.4 above are applied when the void fraction is in the range $0.75 \leq \alpha \leq 0.99$. Above and below this range, the heat transfer coefficients are modified to match correlations used for $0.99 < \alpha \leq 0.999$ and for $0.5 \leq \alpha < 0.75$. The modifications to the liquid-to-wall heat transfer coefficient are

$$H_\ell = \begin{cases} \left(\dfrac{0.999-\alpha}{0.009}\right)H_{\ell,old}, \text{ for } 0.99 < \alpha \leq 0.999 \\ 1.0H_{\ell,old} \text{ for } 0.75 \leq \alpha \leq 0.99 \\ \left(\dfrac{\alpha-0.5}{0.25}\right)\left(\dfrac{0.999-\alpha}{0.009}\right)H_{\ell,old} + \left(\dfrac{0.75-\alpha}{0.25}\right)H_{forc}, \text{ for } 0.50 < \alpha < 0.75 \end{cases}$$

*, HL (4.2-24)

The wall-to-vapor heat transfer coefficient, $H_{v,lo}$, calculated in Sections 4.2.5.1, 4.2.5.2, and 4.2.5.3 above, is used in the range $0.5 < \alpha \leq 0.99$. The equations of Section 4.2.5.2 are used to calculate the vapor-to-wall heat transfer coefficient, $H_{v,hi}$, that would be used in the range $\alpha \geq 0.999$. The resulting heat transfer coefficient, H_v, is

$$H_v = \begin{cases} H_{v,lo}, \text{ for } 0.50 < \alpha \leq 0.99 \\ \left(\dfrac{0.999-\alpha}{0.009}H_{v,lo} + \dfrac{\alpha-0.99}{0.009}\right)H_{v,hi} \text{ for } 0.99 < \alpha \leq 0.999 \end{cases} \quad *, \text{ HV, (4.2-25)}$$

4.2.6 Mode 1--Convection to Liquid

Figure 4.2-4 shows the logic used to select among four models that are used in the convection-to-liquid regime of surface heat transfer. The four models that are possible are the Dittus-Boelter[4.2-5] turbulent flow correlation, the Chen[4.2-3] forced convection model, the McAdams[4.2-6] natural convection model, and the modified Kays[4.2-7] laminar flow equation.

4.2.6.1 Lockhart-Martinelli Factor for Forced Convection. The quality and void fractions are tested to determine whether the Chen[4.2-3] forced convection heat transfer coefficient will be calculated. If the void fraction is greater than 0.5 or the quality is less than 10^{-5}, the unmodified Dittus-Boelter[4.2-5] correlation will be used to obtain a turbulent flow heat transfer coefficient. If the void fraction is less than or equal to 0.5 and the quality is greater than or equal to 10^{-5}, the Lockhart-Martinelli[4.2-9] factor will be used to modify the Dittus-Boelter correlation used in obtaining the turbulent flow heat transfer coefficient. When called for, the Lockhart-Martinelli factor is calculated by Equation (4.2-15). Since the Lockhart-Martinelli factor, χ_{TT}^{-1}, is limited to be in the range $0.1 \le \chi_{TT}^{-1} \le 100$, a Reynolds number factor is then calculated as

$$F = \begin{cases} 2.35(0.1 + 0.213)^{0.736} = 1.0, \text{ for } \alpha \ge 0.05,\ X \ge 10^{-5}, \\ \qquad \text{and } \chi_{TT}^{-1} \le 0.1 \\ 2.35(\chi_{TT}^{-1} + 0.213)^{0.736}, \text{ for } \alpha \ge 0.05,\ X \ge 10^{-5}, \\ \qquad \text{and } 0.1 \le \chi_{TT}^{-1} \le 100 \\ 2.35(100 + 0.213)^{0.736} = 69.8, \text{ for } \alpha \ge 0.05,\ X \ge 10^{-5}, \\ \qquad \text{and } \chi_{TT}^{-1} \ge 100 \\ 1.0, \text{ for } \alpha < 0.05 \text{ or } X < 10^{-5} \end{cases} \quad *, F \quad (4.2\text{-}26)$$

This factor will be used to modify the Reynolds number in the Dittus-Boelter turbulent flow heat transfer coefficient.

4.2.6.2 Liquid Heat Transfer Coefficients. The three correlations (Dittus-Boelter,[4.2-5] McAdams,[4.2-6] and modified Kays[4.2-7]) defined as Equations (4.2-17), (4.2-18), and (4.2-19) are then used to calculate three heat transfer coefficients. The highest of the three heat transfer coefficients is then chosen as $H_{\ell,max}$. If the void fraction < 0.99, $H_{\ell,max}$ is used for the value of H_ℓ with no further modifications. If the void fraction $\ge$ 0.99, H_ℓ is decreased linearly with void fraction until reaching zero at a void fraction of 0.999

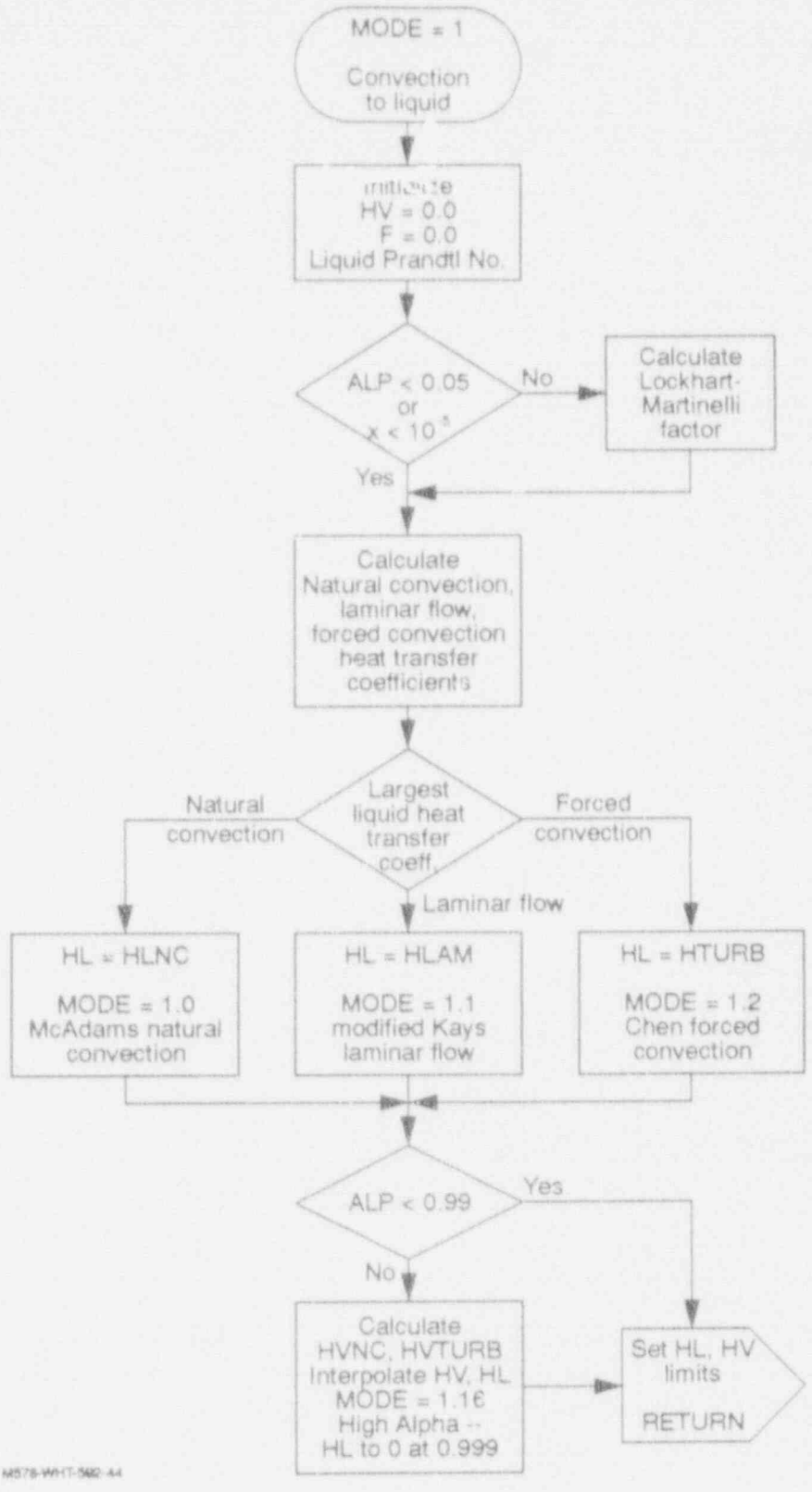

Figure 4.2-4. Mode 1--convection to single-phase liquid.

$$H_\ell = \begin{cases} H_{\ell,max}, \text{ for } \alpha < 0.99 \\ \left(\dfrac{0.999 - \alpha}{0.009}\right) H_{\ell,max}, \text{ for } 0.99 \le \alpha \le 0.999 \\ 0, \text{ for } \alpha > 0.999 \end{cases} \quad *, \text{ HL, } (4.2\text{-}27)$$

4.2.6.3 Vapor Heat Transfer Coefficients. For void fractions, $\alpha \le 0.9$, the heat transfer to the vapor is neglected by setting $H_v = 0$ and only the heat transfer to the liquid is considered. For void fractions, $\alpha \ge 0.999$, the vapor heat transfer coefficient is taken to be the highest of the turbulent flow, natural convection, and laminar flow heat transfer coefficients for vapor. For void fractions, $0.99 < \alpha < 0.999$, the coefficient is varied linearly between zero at $\alpha = 0.99$ and the highest of the turbulent flow, natural convection, and laminar flow heat transfer coefficients for the vapor at $\alpha = 0.999$. The three correlations (Dittus-Boelter,[4.2-5] McAdams,[4.2-6] and modified Kays[4.2-7]) are defined by Equations (4.2-8), (4.2-9), and (4.2-10).

The highest of the three heat transfer coefficients is then chosen as $H_{v,max}$. If the void fraction < 0.99, zero is used for the value of H_v with no further modifications. If the void fraction ≥ 0.99, H_v is decreased linearly with void fraction until reaching $H_{v,max}$ at a void fraction of 0.999

$$H_v = \begin{cases} H_{v,max}, \text{ for } \alpha < 0.99 \\ \left(\dfrac{\alpha - 0.99}{0.009}\right) H_{v,max}, \text{ for } 0.99 \le \alpha \le 0.999 \\ 0, \text{ for } \alpha > 0.999 \end{cases} \quad *, \text{ HV, } (4.2\text{-}28)$$

4.2.7 Mode 2--Nucleate Boiling

Figure 4.2-5 shows the logic used to select among models that are used in the nucleate boiling regime of surface heat transfer. It also shows the order of the various tests and calculations that need to be performed.

4.2.7.1 Chen Correlation for Nucleate Boiling. Figure 4.2-6 shows the logic used in the module to calculate the Chen[4.2-3] model for nucleate boiling. The Chen correlation is composed of two parts; a forced convection term and a nucleate boiling term that contains a suppression factor, S.

As described in section 4.2.6.1, the quality and void fractions are tested to determine whether the Chen[4.2-3] forced convection heat transfer coefficient will be calculated. If the void fraction is greater than 0.5 or the quality is less than 10^{-5}, the unmodified Dittus-Boelter[4.2-5] correlation will be used to obtain a turbulent flow heat transfer coefficient. If the

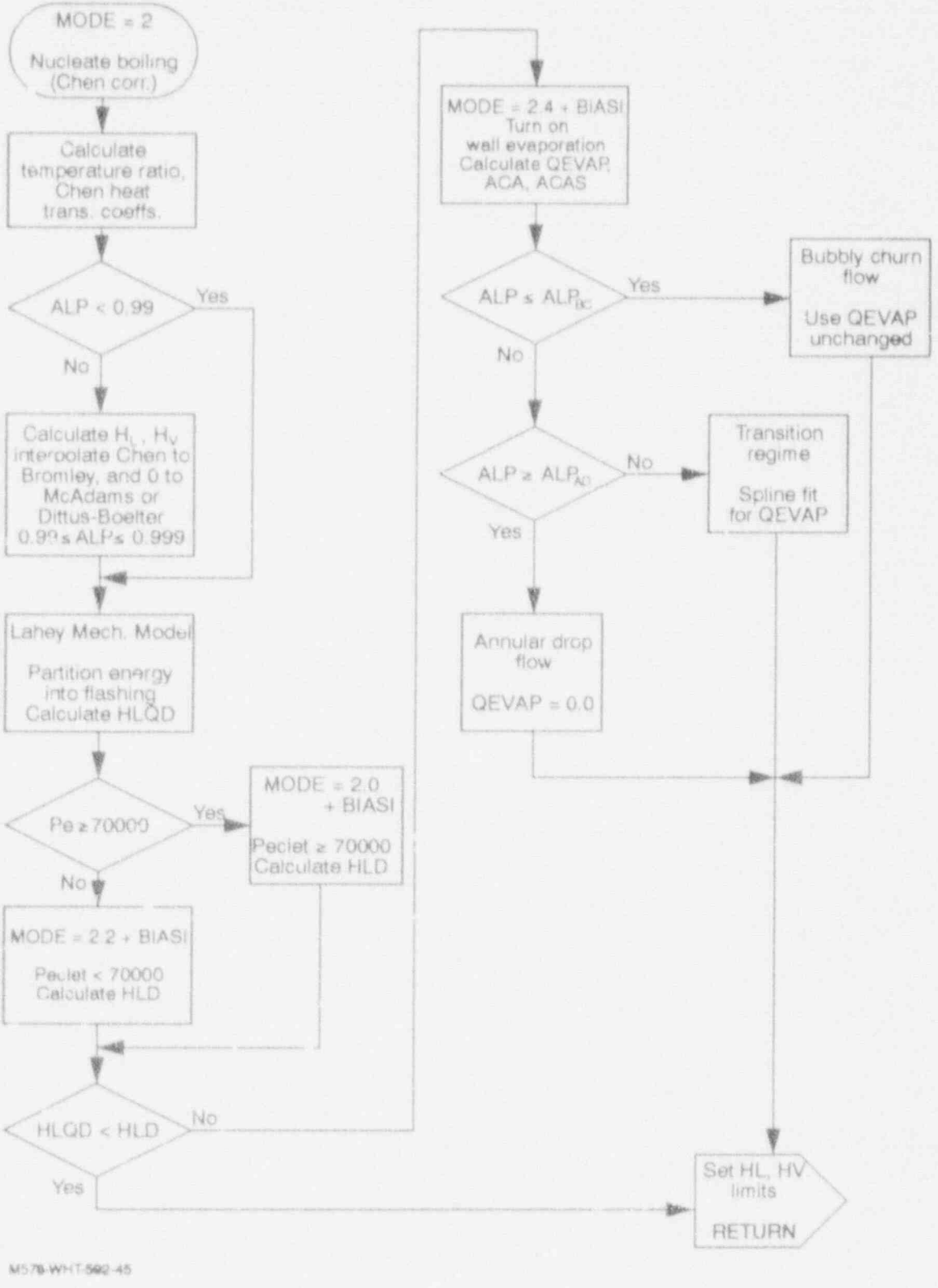

Figure 4.2-5. Mode 2--nucleate boiling.

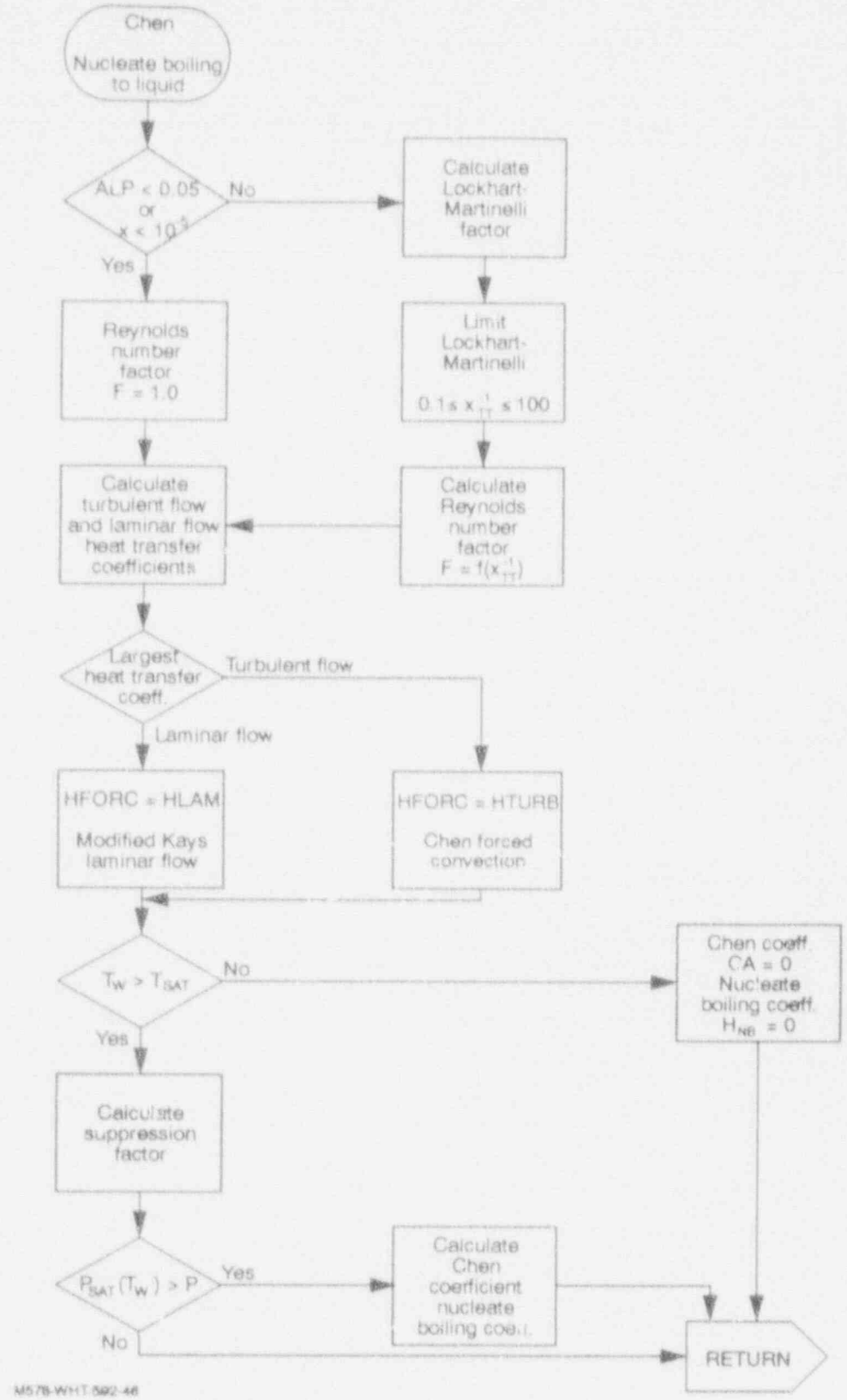

Figure 4.2-6. Chen model for nucleate boiling.

void fraction is less than or equal to 0.5 and the quality is greater than or equal to 10^{-5}, the Lockhart-Martinelli[4.2-6] factor [Equation (4.2-15)] is used to modify the Dittus-Boelter[4.2-5] correlation used in obtaining the turbulent flow heat transfer coefficient. A Reynolds number factor is then calculated according to Equation (4.2-26). Two correlations (Dittus-Boelter and modified Kays[4.2-7]) are then used to calculate two heat transfer coefficients:

$$H_{turb} = 0.023 \frac{k_\ell}{D_H} Re_{tp}^{0.8} Pr_\ell^{0.4} \qquad *, \text{HTURB (4.2-29)}$$

$$H_{lam} = 4 \frac{k_\ell}{D_H} \qquad *, \text{HLAM (4.2-30)}$$

where

$$Re_{tp} = Re_\ell F^{1.25} \qquad (4.2\text{-}31)$$

and Re_ℓ and Pr_ℓ are as defined in Equations (4.2-21) and (4.2-22). The higher of the two heat transfer coefficients is then chosen as H_{forc}. If the wall temperature is less than or equal to saturation temperature, no nucleate boiling can occur. In this case, the Chen[4.2-3] coefficient and the nuclear boiling coefficient are both set equal to zero and the calculation is ended. If the wall temperature is greater than saturation temperature, a suppression factor is calculated

$$S = \begin{cases} \dfrac{1}{1 + 0.12(Re_{tp} \times 10^{-4})^{1.14}}, & \text{for } Re_{tp} < 32.5 \times 10^4 \\ \dfrac{1}{1 + 0.42(Re_{tp} \times 10^{-4})^{0.78}}, & \text{for } 32.5 \times 10^4 \le Re_{tp} < 70 \times 10^4 \\ \dfrac{1}{1 + 0.42(70)^{0.78}} = 0.0797, & \text{for } 70 \times 10^4 \le Re_{tp} \end{cases} \qquad *S, (4.2\text{-}32)$$

If the saturation pressure at the wall temperature is greater than the fluid pressure, the Chen[4.2-3] coefficient, C_p, and the nucleate boiling heat transfer coefficient, H_{nb}, are then calculated:

$$C_a = \frac{0.00122\ S\left(k_\ell^{0.79} C_{p\ell}^{0.45} \rho_\ell^{0.49}\right)}{\sigma^{0.5} \mu_\ell^{0.29} h_{fg}^{0.24} \rho_g^{0.24}} \qquad \text{*, CA (4.2-33)}$$

$$H_{nb} = C_a (T_w - T_s)^{0.24} (P_{sw} - P)^{0.75} . \qquad \text{*, HNUCB (4.2-34)}$$

If the saturation pressure at the wall temperature is less than the fluid pressure, no nucleate boiling can occur.

4.2.7.2 **Non-equilibrium Temperature Adjustment**. The properties are evaluated at the liquid and vapor temperatures; X_ℓ is the equilibrium quality and V_ℓ is the liquid quality parallel to the surface. Because the nucleate boiling contribution to the Chen[4.2-3] correlation was developed for saturated conditions, H_{nb} is multiplied by a temperature ratio to adjust the heat transfer coefficient to the actual liquid temperature, T_ℓ. Since TRAC-BF1/MOD1 can tolerate superheated liquids, the adjustment factor is restricted to a maximum value of 1.0, restricting the adjustment to subcooled liquid.

For qualities less than or equal to 0.99, the heat transfer to the vapor is ignored by setting the vapor heat transfer coefficient equal to zero, and the Chen[4.2-3] calculation is used for the liquid heat transfer coefficient

$$H_\ell = \begin{cases} H_{forc} + H_{nb}\dfrac{T_w - T_s}{T_w - T_\ell}, & \text{for } T_\ell \le T_s \\ H_{forc} + H_{nb}, & \text{for } T_\ell \ge T_s \end{cases} \qquad \text{*, HL (4.2-35)}$$

$$H_v = 0 . \qquad \text{*, HV (4.2-36)}$$

For qualities greater than or equal to 0.999, the heat transfer coefficient to the liquid is calculated using the Bromley[4.2-10] correlation for film boiling, while the coefficient for vapor is chosen as the larger of that calculated using McAdams[4.2-7] natural convection and the modified Dittus-Boelter[4.2-5] turbulent flow. The Bromley correlation

$$H_\ell = 0.62 \left[\frac{k_v^3 (\rho_\ell - \rho_v) \rho_v g_c h'_{fg}}{\mu_v (T_w - T_s) \lambda} \right]^{1/4} \qquad \text{*, HL (4.2-37)}$$

uses two expressions, a modified heat of vaporization, h'_{fg}, and a

characteristic length, λ.

$$h'_{fg} = h_{fg} + 0.5C_{pv}(T_v - T_s) \qquad \text{*, HFGP (4.2-38)}$$

$$\lambda = 2\pi \left[\frac{\sigma}{g_c(\rho_\ell - \rho_v)} \right]^{1/2} . \qquad \text{*, WL (4.2-39)}$$

The modified Dittus-Boelter turbulent flow and the McAdams natural convection correlations are defined by Equations (4.2-8) and (4.2-9).

For qualities between 0.99 and 0.999, both the Chen[4.2-3] and Bromley[4.2-10] calculations are performed; and H_ℓ and H_v are linearly interpolated according to the fluid quality.

4.2.7.3 Flashing Energy using Lahey Mechanistic Model. The possibility of net vapor generation is considered even though the liquid may be subcooled. Accurate estimates of the axial core void profile are needed for reactor transients without scram because core power is very sensitive to void changes. Estimates of the bulk enthalpy needed are suggested by the mechanistic model proposed by Lahey.[4.2-11]

The enthalpy needed to produce net vapor is expressed as

$$h_{\ell d} = \begin{cases} h_f - Nu' \dfrac{C_{p\ell}}{455}, & for\ Pe \le 70000 \\ h_f - St \dfrac{C_{p\ell}}{0.0065}, & for\ Pe > 70000 \end{cases} \qquad \text{*, HLD (4.2-40)}$$

where the modified Nusselt, Peclet, and Stanton numbers (Nu', Pe, and St, respectively) are given by

$$Nu' = q \frac{D_H}{k_\ell} \qquad \text{*, XNUMOD (4.2-41)}$$

$$Pe = \frac{GD_H C_{p\ell}}{k_\ell} \qquad \text{*, PE (4.2-42)}$$

$$St = \frac{Nu'}{Pe} . \qquad \text{*, ST (4.2-43)}$$

The heat flux transferred to the liquid is approximated by

$$q = 0.5(H_\ell + H_{\ell,old})(T_w - T_\ell) \quad \text{*, QPPW (4.2-44)}$$

The parameter $h_{\ell qd}$ is the smaller of the actual liquid enthalpy, h_ℓ, and the saturated liquid enthalpy, h_f. When the net vapor generation enthalpy, $h_{\ell d}$, is greater than $h_{\ell qd}$, no bubbles will be generated and the bubble generation flux, q_{evap}, used in the energy equation is zero.

4.2.7.4 Calculating the Wall Evaporation. When the net vapor generation enthalpy, h_w, is less than $h_{\ell qd}$, bubbles will be generated. The heat flux used for bubble generation is

$$q_{bc} = q \frac{h_{\ell dq} - h_{\ell d}}{h_f - h_{\ell d}} . \quad (4.2\text{-}45)$$

When the quality is low enough, the bubbly churn flow is maintained and the Bromley[4.2-10] correlation is used without modification. For high-quality flows, the flow will be annular and the bubble generation will be zero. Between these two extremes, q_{evap} is interpolated using the quality in a spline function. The high-quality end of the bubbly churn regime and the low end of the transition to annular drop flow regime is calculated by

$$\gamma = \left(\frac{\rho_\ell}{\rho_v}\right)^{1/2} \quad \text{*, GAMMA (4.2-46)}$$

$$Re_{mix} = \frac{|G_{mix}| D_H}{\mu_\ell} \quad \text{*, REMIX (4.2-47)}$$

$$C_{o,\infty} = Max\ (1,\ [1.393 - 0.155\ Log\ (1 + Re_{mix})]) \quad \text{*, CO (4.2-48)}$$

$$C_o = Min \left[1.33,\ C_{o,\infty} - \frac{C_{o,\infty} - 1}{\gamma}\right] \quad \text{*, CO (4.2-49)}$$

$$\alpha_{bc} = \frac{1 + \frac{4}{\gamma}}{C_o} - \frac{4}{\gamma} - 0.15 \ . \qquad \text{*, ACA (4.2-50)}$$

The low end of the annular drop flow regime and the high end of the transition regime is taken as 0.25 higher in quality unless this would be greater than 1.

$$\alpha_{ad} = Min\ [1,\ (\alpha_{bc} + 0.25)] \ . \qquad (4.2\text{-}51)$$

Finally, q_{evap} is fitted by a spline function from the bubbly churn correlation for $\alpha \leq \alpha_{bc}$ to zero for $\alpha \geq \alpha_{ad}$.

$$q_{evap} = \begin{cases} q_{bc},\ for\ \alpha \leq \alpha_{bc} \\ q_{bc}(3X_2^2 - 2X_2^3),\ for\ \alpha_{bc} < \alpha < \alpha_{ad} \\ 0,\ for\ \alpha_{ad} \leq \alpha \end{cases} \qquad \text{*, QEVAP (4.2-52)}$$

where

$$X_2 = \frac{\alpha_{ad} - \alpha}{\alpha_{ad} - \alpha_{bc}} \ . \qquad (4.2\text{-}53)$$

4.2.8 Mode 3--Transition Boiling

Transition boiling may be considered as a combination of nucleate and film boiling. A given spot on the wall surface is wet part of the time and dry during the remainder of the time. Therefore, contributions to both the liquid and the vapor heat transfer coefficients exist for all conditions.

Figure 4.2-7 shows the logic used to calculate the transition boiling heat transfer coefficients. The logic diagram shows both the selection criteria and the correlations and models that are used for various combinations of fluid conditions and wall temperatures.

4.2.8.1 Minimum Stable Film Boiling Temperature. The minimum stable film boiling temperature, T_{min}, is calculated using the TMSFB subroutine (see Figure 4.2-8) whenever the wall temperature, T_w, is no more than 50 degrees above the saturation temperature, T_s. The user may choose to use either the homogeneous nucleation model, by setting ITMIN $\leq$ 0, or the Shumway[4.2-12] model, by setting ITMIN > 0.

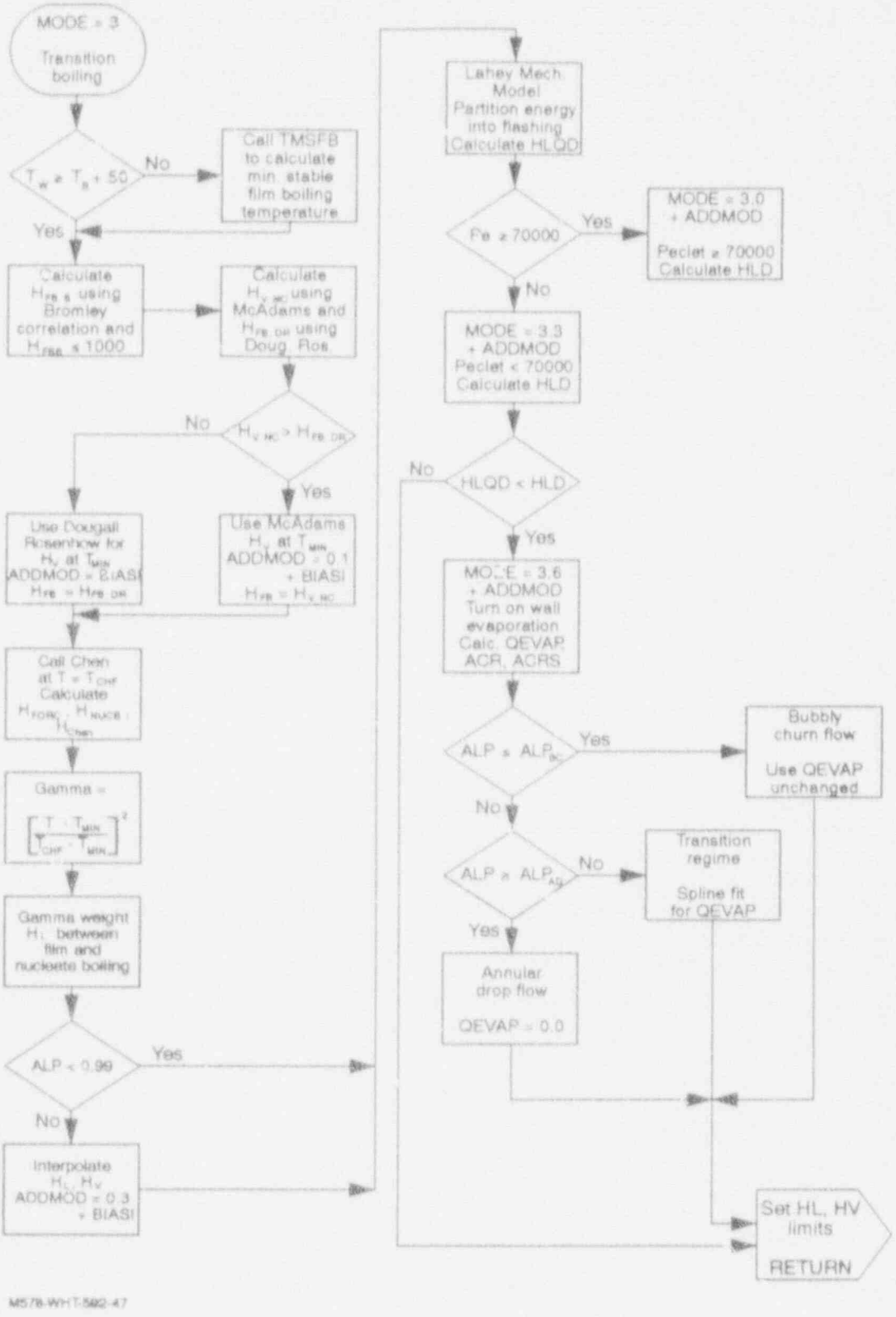

Figure 4.2-7. Mode 3--transition boiling.

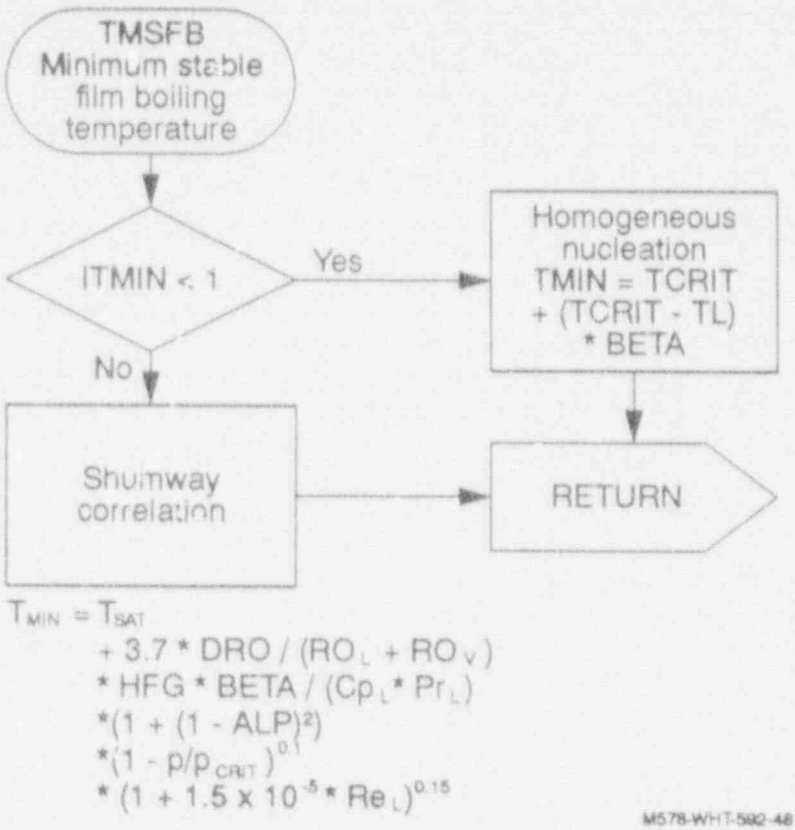

Figure 4.2-8. Minimum stable film boiling temperature.

$$T_{min} = \begin{cases} T_{crit} + (T_{crit} - T_\ell)\,\beta, \text{ for ITMIN} \le 0 \\ T_s + 3.7\left(\dfrac{\rho_\ell - \rho_v}{\rho_\ell + \rho_v}\right)\left(\dfrac{h_{fg}\beta}{C_{p\ell}Pr_\ell}\right) \\ [1 + (1 - \alpha)^2]\left(1 - \dfrac{p}{p_{crit}}\right)^{0.1} \\ (1 + 1.5 \times 10^{-5} Re_\ell)^{0.15}, \text{ for ITMIN} > 0 \end{cases} \quad *, \text{ TMIN} \quad (4.2\text{-}54)$$

where

$$\beta = \sqrt{\frac{(k\rho C_p)_\ell}{(k\rho c)_w}} \quad . \tag{4.2-55}$$

4.2.8.2 Heat Transfer Coefficients at T_{min}. The heat transfer coefficient to the liquid at T_{min} is calculated using the Bromley[4.2-10] correlation for film boiling, while the coefficient for vapor is chosen as the larger of that calculated using McAdams[4.2-6] natural convection and the Dougall-Rosenhow[4.2-13] turbulent flow correlations. The Bromley correlation uses two expressions, a modified heat of vaporization, h'_{fg}, and a characteristic length, λ, as defined in Equations (4.2-38) and (4.2-39).

$$H_{fb,b} = 0.62 \left[\frac{k_v^3 (\rho_\ell - \rho_v) \rho_v g_c h'_{fg}}{\mu_v (T_w - T_s) \lambda} \right]^{1/4} \quad . \qquad \text{*, HFBB (4.2-56)}$$

The Bromley heat transfer coefficient used for the liquid is limited to a value of 1000, as spurious large values can sometimes be calculated when a volume becomes liquid filled after having been two-phase.

$$h_{\ell,tmin} = \begin{cases} (1 - \alpha) h_{fb,b}, & \text{for } h_{fb,b} \le 1000 \\ (1 - \alpha) 1000, & \text{for } h_{fb,b} > 1000 \end{cases} \quad . \tag{4.2-57}$$

The Dougall-Rosenhow turbulent flow and the McAdams natural convection correlations are calculated for the vapor

$$H_{v,dr} = 0.023 \frac{k_v}{D_H} Re_{tp}^{0.8} Pr_v^{1/3} \qquad \text{*, HV (4.2-58)}$$

$$H_{v,nc} = 0.13 \frac{k_v}{D_H} \left(\frac{Gr_v}{Pr_v} \right)^{1/3} \qquad \text{*, HV (4.2-9)}$$

where

$$Re_{tp} = \rho_v [\alpha |V_v| + (1-\alpha) |V_\ell|] \frac{D_H}{\mu_v} \tag{4.2-59}$$

Pr_v and Gr_v are as defined in Equations (4.2-12) and (4.2-13), and $1/T_v$ approximates the coefficient of thermal expansion.

The higher of these two vapor heat transfer coefficients is used for the vapor at the minimum stable film boiling temperature

$$H_{v,tmin} = \begin{cases} H_{v,dr}, \text{ for } h_{v,dr} \geq h_{v,nc} \\ H_{v,nc}, \text{ for } h_{v,nc} > h_{v,dr} \end{cases} . \quad (4.2\text{-}60)$$

4.2.8.3 Chen Correlation for Nucleate Boiling. As shown in Figure 4.2-6 and described in Section 4.2.7.1, the Chen[4.2-3] model is used for nucleate boiling in the liquid phase.

4.2.9 Mode 4--Film Boiling

Film boiling is composed of a forced convection component, a pool boiling component, and transitional components. The logic is shown in Figure 4.2-9. The forced convection component is taken as the maximum of the Dougall-Rohsenow[4.2-13] correlation and natural convection to steam, defined in Equations (4.2-58) and (4.2-9). The pool boiling component is taken from the Bromley correlation defined in Equation (4.2-55).

4.2.10 Mode 5--Single-Phase Vapor

Single-phase vapor is assigned a wall heat transfer coefficient equal to the maximum obtained from the laminar, turbulent, and natural convection correlations defined in Equations (4.2-8), (4.2-9), and (4.2-10). The logic is shown in Figure 4.2-10.

4.2.11 Mode 7--Simple Boiling Curve

The seventh heat transfer mode is specifically for nonreactor core structures or for situations where accurate values of CHF are not desired. This simplified logic allows nucleate boiling up to a wall superheat of 25 K if the quality is not greater than one and the void fraction is not > 0.999. This logic is shown in Figure 4.2-11. At very dry steam conditions, h_ℓ is set to zero and h_v is the maximum of the natural convection, laminar flow, and Dittus-Boelter[4.2-5] correlations given by Equations (4.2-8), (4.2-9), and (4.2-10), respectively. For nucleate boiling, the CHEN correlation is used; and transition boiling uses the Loomis-Shumway[4.2-14] correlation

$$h_\ell = HTB = 2000(1 - \alpha)([62.36 + 8.804 \times 10^{-5}(P)]$$

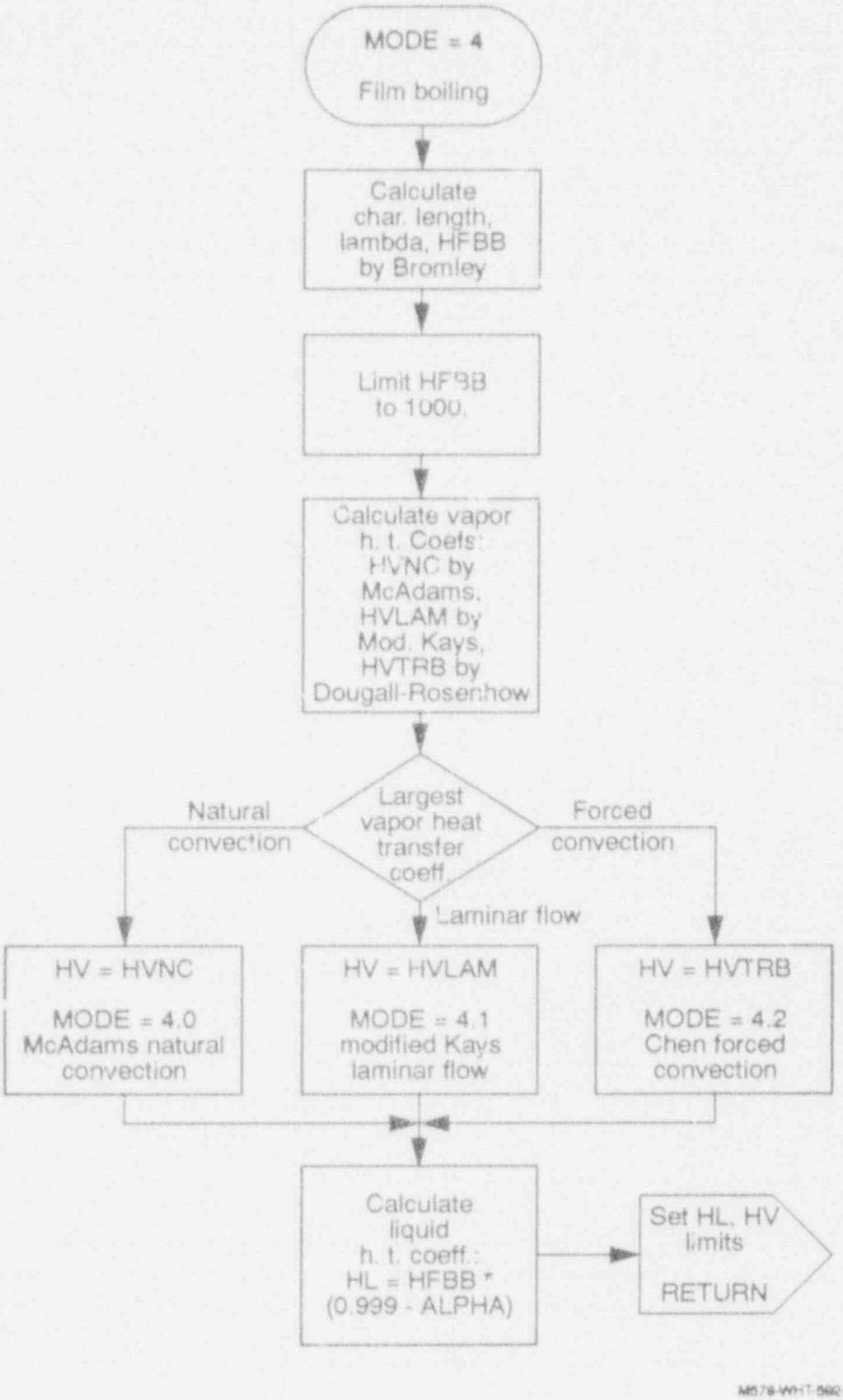

Figure 4.2-9. Mode 4--film boiling.

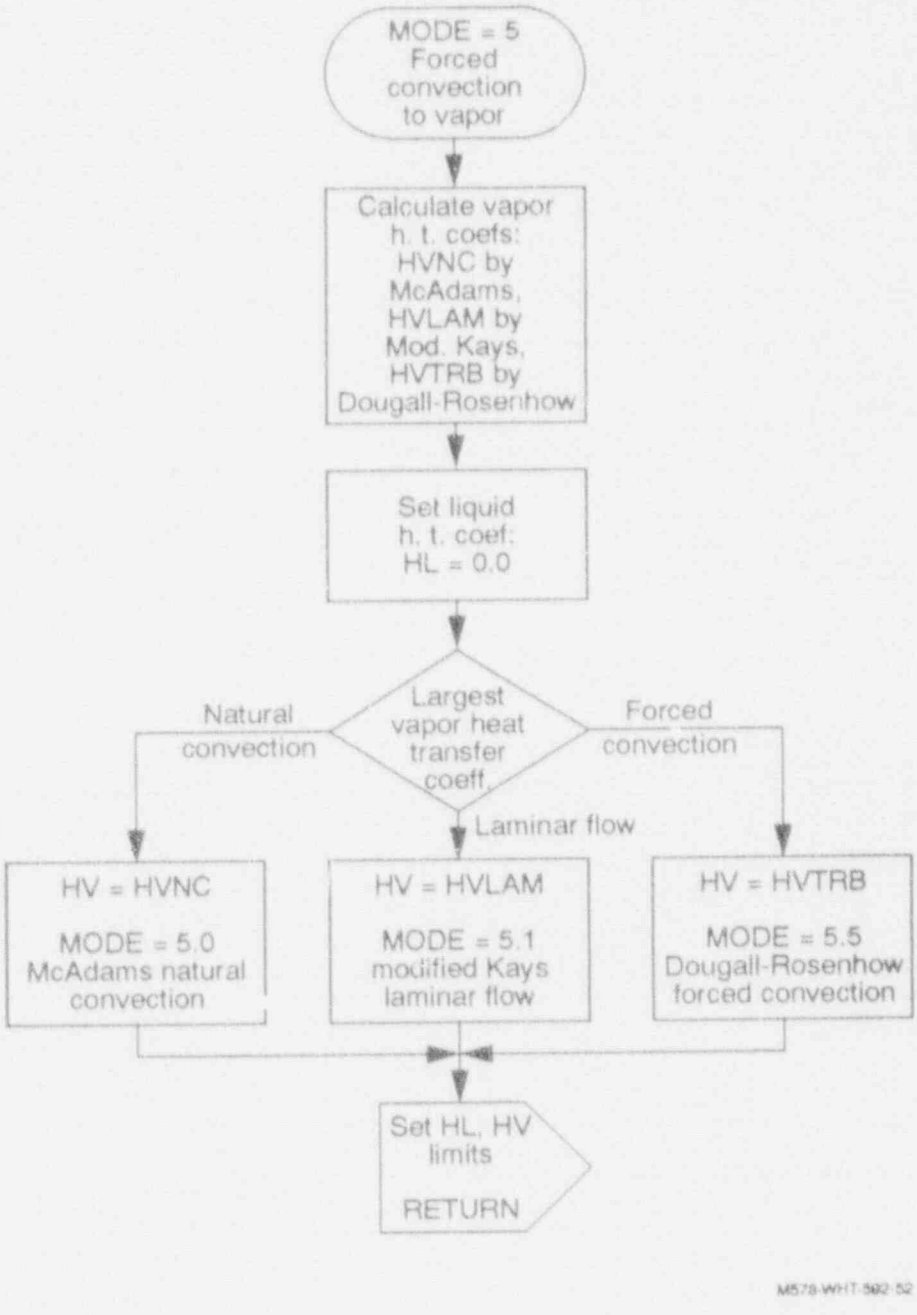

Figure 4.2-10. Mode 5--forced convection to vapor.

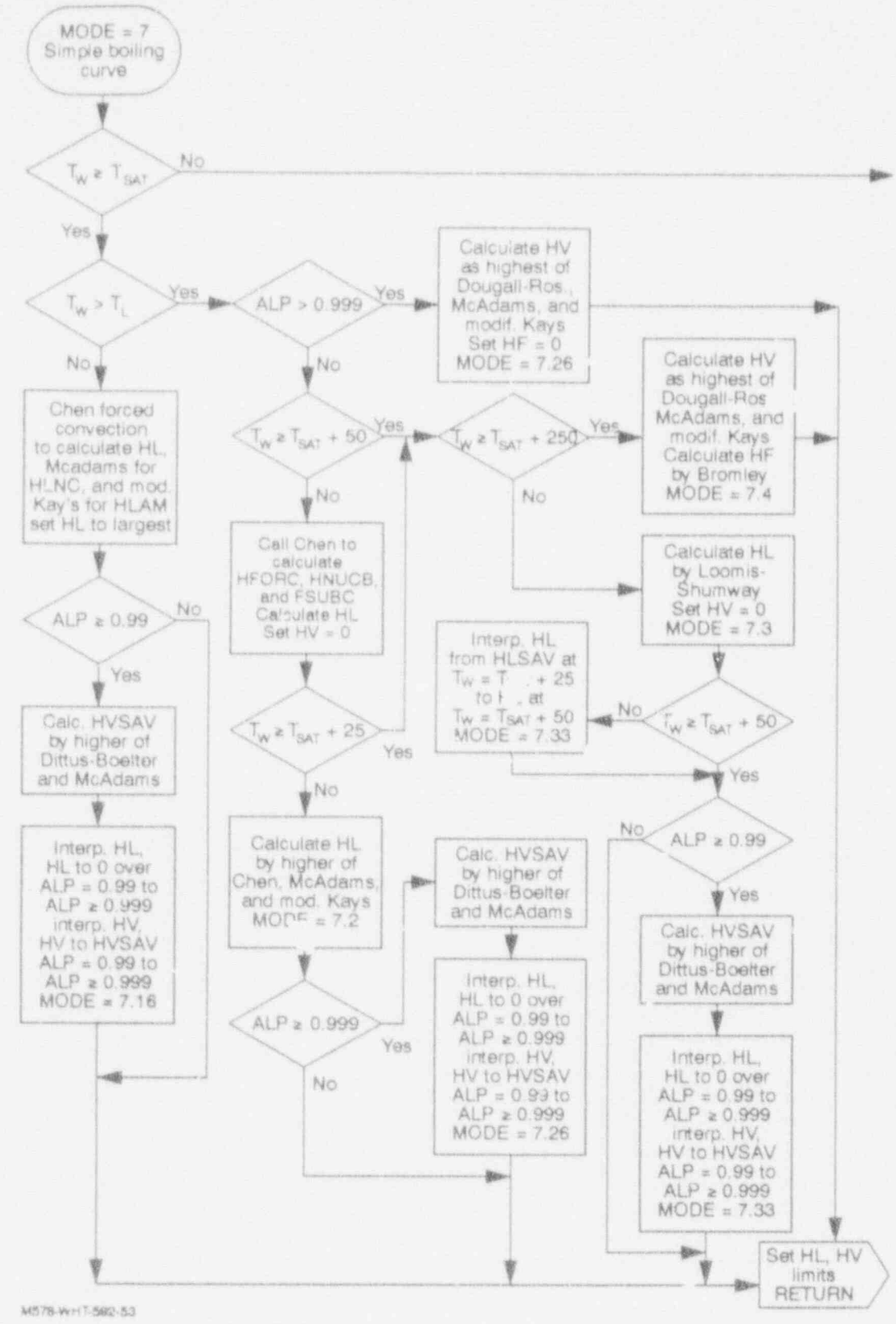

Figure 4.2-11. Mode 7--simple boiling curve.

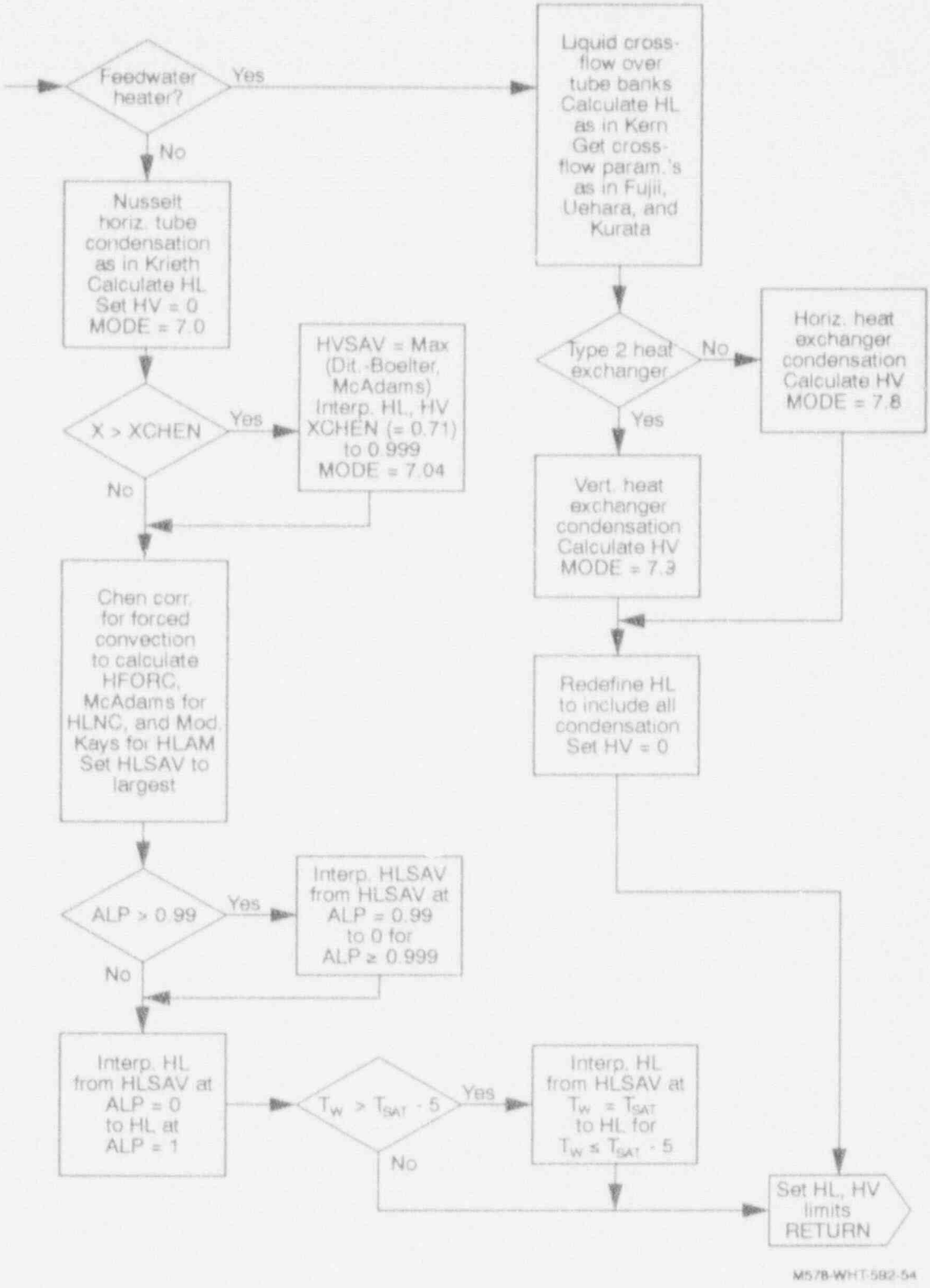

Figure 4.2-11. (continued)

$$- [11.3 + 1.59 \times 10^{-5}(P) \ln(N)) \quad . \tag{4.2-61}$$

Figure 4.2-11 diagrams the condensation logic. Mode 7 through 7.5 follow closely Mode 0 through Mode 5; Modes 7.8 and 7.9 have been added for heat exchangers that have horizontal and vertical tubes, respectively. The equations used for horizontal and vertical tubes are related such that differences disappear as the steam flow increases. The equation is

$$Nu = FL\ Nu_1 + (1 - FL) Nu_2 \frac{T_s - T_w}{T_L - T_w} \tag{4.2-62}$$

where FL is the fraction of tube surface beneath the water pool. Nu_1 is the Nusselt number[2.2-15] below the pool surface.

$$Nu_1 = 0.36 Re_\ell^{0.55} Pr_\ell^{1/3} \quad . \tag{4.2-63}$$

Nu_2 is the Nusselt number in the steam region. For horizontal tubes[2.2-16]

$$Nu_2 = XF \left[1 + \frac{0.276}{XF^4\ Fr\ HF}\right]^{1/4} Re^{1/2} \tag{4.2-64}$$

where

$$XF = 0.9 \left[1 + \frac{1}{RF\ HF}\right]^{1/3} \tag{4.2-65}$$

$$HF = \frac{K_\ell (T_s - T_w)}{\mu_\ell h_{fg}} \tag{4.2-66}$$

$$RF = \left(\frac{\rho_\ell \mu_\ell}{\rho_v \mu_v}\right)^{1/2} \quad . \tag{4.2-67}$$

Fr is the Froude number based on the volumetric vapor velocity perpendicular to the tubes in the steam region.

Vertical tubes use Equation (4.2-6) plus the first term in Equation (4.2-63). The coefficient in Equation (4.2-6) is 0.943, as recommended by Chen[2.2-17], and the length is the distance between baffle plates instead of the hydraulic diameter. The first term of Equation (4.2-63)

$$Nu_z = XF\ Re^{1/2} \qquad (4.2\text{-}68)$$

is the only velocity-dependent term and becomes dominant at normal flow rates so that the tube orientation makes little difference.

4.2.12 Nucleate Boiling Transition

Pressurized water reactor safety codes have predicted the onset of nucleate boiling transition by using an empirical correlation to determine the local CHF. Using this transition criteria alone is inadequate for boiling water reactors since the high-quality, high-mass-flux conditions may introduce memory effects when the heat flux is nonuniform.[4.2-18]

Several methods exist for correlating CHF data for nonuniform heat fluxes. Perhaps the two most widely accepted for analyzing BWR-like phenomena are the Tong F-factor and CISE critical quality correlations.[4.2-19] Since the critical quality correlation is a simpler function to evaluate and has been used by General Electric Corporation (GE) to correlate CHF data in BWR rod bundle simulation, it has been chosen for use in TRAC-BF1/MOD1. The general form of the correlation is

$$X_c = \frac{AL_B}{B + L_B} \qquad *, XC \quad (4.2\text{-}69)$$

where

X_c = critical quality

L_B = boiling length

and A and B are functions of pressure and mass flux (see Table 4.2-2).

Implemented into the code are two versions of this correlation, as shown in Table 4.2-2. The first is based upon the Biasi correlation[4.2-20] originally used in TRAC-BF1/MOD1. This correlation has been converted from a local CHF to a critical quality correlation, as described in Reference 4.2-18. The second is the CISE-GE correlation derived from data taken from experiments performed at GE. The Biasi X_c correlation gives larger values than the CISE-GE correlation.

Both correlations are included, since each has distinctive advantages. The improved Biasi correlation is based on a broad data base of CHF experiments. It is, however, subject to the assumptions used in converting to a critical quality. The CISE-GE correlation, on the other hand, is based on data from rod bundle experiments and includes effects of local peaking factors. The data base from which it is derived is limited to mass fluxes in

Table 4.2-2. Critical quality correlation options.

Improved Biasi (ICHF = 2)	CISE-GE (ICHF = 3)
$A_1 = 1.0$	$A = 1.055 - 0.013 \dfrac{(P - 4.137 \cdot 10^6)^2}{2.758 \cdot 10^6}$
$B_1 = 1.048 \times 10^{-8} G^{1.6} D_h^{1.4} h_{fg} / H(P)$	$- 1.233(7.37 \times 10^{-4} G) + 0.907(7.37 \cdot 10^{-4} G)$
$X_{cr_1} = \dfrac{A_1 L_B}{B_1 + L_B} \cdot \dfrac{P_h}{P_w} \cdot R_f^{1/2}$	$- 1.233(7.37 \times 10^{-4} G) + 0.907(7.37 \cdot 10^{-4} G)^2$
	$- 0.285(7.37 \cdot 10^{-4} G)^3$
$A_2 = F(P)/G^{1/6}$	$B = 0.457 + 2.003(7.37 \cdot 10\ G)^{-4}$
$B_2 = G^{7/6} D_n^{1/4} h_{fg} (5.707 \cdot 10^{-8})$	$- 0.901(7.37 \cdot 10^{-4} G)^2$
$X_{cr_2} = \dfrac{A_2 L_B}{B_2 + L_B} \cdot \dfrac{P_h}{P_w} \cdot R_f^{1/2}$	If Bundle is 8 x 8, B = B/1.12
$X_c = \text{Max}(X_{cr_1}, X_{cr_2})$	$X_c = \dfrac{AL_B}{B + L_B} \dfrac{1.24}{R_f}$
$H(P) = -1.159 + 0.149(P \cdot 10^{-5}) \exp(-.019\ P) + \dfrac{8.99}{10 + (P \cdot 10^{-5})^2}$	
$F(P) = 0.7249 + 0.099\ (P \cdot 10^{-5}) \exp(03.2 \cdot 10^{-7} P)$	

the range 300 kg/m^2-s $\leq$ G $\leq$ 1400 kg/m^2-s.

The local CHF Biasi correlation has a data base that covers the mass flux (G) range between 100 and 6000 kg/m^2-s. The local flux Biasi correlation logic uses the maximum of

$$q_{CHF} = \frac{1.883 \times 10^7}{D_H^n G^{1/6}} \left(\frac{f_p}{G^{1/6}} - X \right) \qquad *, \text{QPPCHF (4.2-70)}$$

$$q'_{CHF} = \frac{3.78 \times 10^7}{D_H^n G^{0.6}} h_p (1 - X) \qquad *, \text{QCHF1 (4.2-71)}$$

where

$$n = \begin{cases} 0.4 \text{ for } D \geq 1 \text{ cm} \\ 0.6 \text{ for } D < 1 \text{ cm} \end{cases} \qquad (4.2\text{-}72)$$

$$f_p = 0.7249 + (0.099)(P)[\exp^{-0.032P}] \qquad (4.2\text{-}73)$$

D_H = hydraulic diameter (cm)

G = mass flux (g/cm^2-s)

$$h_p = -1.159 + (0.149)(P)[\exp] + 8.99(P)/(10. + P^2) \qquad (4.2\text{-}74)$$

P = pressure (bars).

Note that the Biasi correlation uses cgs units, but the constants in Equations (4.2-70) and (4.2-71) have been changed so that Q_{CHF} is in W/m^2.

If Equation (4.2-70) is used, 0.02 is added to the heat transfer mode number. If Equation (4.2-71) is used, 0.01 is added to the mode number. Below a mass flux of 200 kg/m^2-s, the critical quality correlations are not used. Above 200, departure from nucleate boiling will occur if the local wall flux exceeds the Biasi CHF or the local quality exceeds either critical quality correlation specified by the user.

Between a mass flux of 200 and -700 kg/m^2-s, the local flux Biasi correlation is linearly interpolated with the Zuber[4.2-21] pool boiling correlation at a mass flux of zero and the Biasi correlation evaluated at G = 200 for positive flow and G = 700 for negative flow. The modified Zuber correlation is

$$q_{CHF} = (1 - \alpha)(0.9 \times 0.131\, h_{fg} \rho_v\, BRAC + QSUB) \qquad *, \text{QPPPB (4.2-75)}$$

where

$$BRAC = \left[\frac{\sigma g (\rho_\ell - \rho_v)}{\rho_v^2} \right]^{1/4} \qquad (4.2\text{-}76)$$

$$QSUB = \begin{cases} 0, \text{ if } T_\ell \geq T_s \\ \dfrac{2\kappa_\ell (T_s - T_\ell)}{\left(\dfrac{\pi TAUk_\ell}{\rho_\ell c p_\ell}\right)^{1/2}}, \text{ otherwise} \end{cases} \quad (4.2\text{-}77)$$

$$T_{ZUB} = 2.625 \frac{\left(\dfrac{\sigma}{g(\rho_\ell - \rho_v)}\right)^{1/2}}{BRAC} . \quad (4.2\text{-}78)$$

If the flow is countercurrent, the Zuber correlation is used; if the mass flux is less than -700 kg/m^2-s, the absolute value of the flux is used in the Biasi correlation.

Once q_{CHF} has been obtained from the Biasi correlation, the temperature corresponding to the CHF point, T_{CHF}, is calculated using a Newton-Raphson iteration[4.2-22] to determine the intersection of the heat flux found by using the nucleate boiling HTC and CHF. An iteration is required because $T_w = T_{CHF}$ must be known to evaluate the CHEN correlation; in turn, the CHEN HTC must be known to calculate the wall temperature. The expression thus becomes

$$q_{CHF} = h(T_w - T_s) . \quad (4.2\text{-}79)$$

The equation for T_{CHF} is

$$T_{CHF}^{n+1} = T_{CHF}^{n} - \frac{T_{CHF}^{n} - T_s - \dfrac{q_{CHF}}{h}}{1 + \dfrac{q_{CHF}}{h^2}\dfrac{dh}{dT_w}} \quad *, \text{ TCHF} \quad (4.2\text{-}80)$$

where T_{CHF}^{n} is the CHF temperature for the nth iteration, h is the HTC evaluated using the CHEN correlation, and $\dfrac{dh}{dT_w}$ is the derivative of the HTC with respect to the wall temperature.

Convergence occurs when $T_{CHF}^{n+1} - T_{CHF}^{n} < 1.0$. A maximum of ten iterations is allowed; if convergence does not occur, a message is printed and a fatal error

results.

The CHF temperature is restricted to the range, $(T_s + 0.5) \leq T \leq (T_s + 100)$. The options available to the user are

ICHF = negative, no CHF allowed

= 0, use simplified boiling curve (Mode 7)

= 1, use Biasi local CHF

= 2, use Biasi critical quality plus Biasi local CHF

= 3, use CISE-GE critical quality plus Biasi local CHF.

To assist in understanding the nature of the nucleate boiling transition for CHAN components, the output variable, FILMTRIP has been added, where

FILMTRIP = 0 implies no nucleate boiling transition

= 1 implies local CHF transition

= 2 implies critical quality transition.

Logic diagrams of both correlations are given in Figures 4.2-12 and 4.2-13.

4.2.13 References

4.2-1. M. Ishii, *One-Dimensional Drift-Flux Model and Constitutive Equations for Relative Motion Between Phases in Various Two-Phase Flow Regimes*, ANL-77-47, October 1977.

4.2-2. J. G. M. Andersen and K. H. Chu, *BWR Refill-Reflood Program Task 4.7--Constitutive Correlations for Shear and Heat Transfer for the BWR Version of TRAC*, NUREG/CR-2134, EPRI NP-1582, 1981.

4.2-3. J. Chen, "A Correlation for Boiling Heat Transfer of Saturated Fluids in Convective Flow," *ASME paper 63-HT-34*, 1963.

4.2-4. F. Kreith, *Principles of Heat Transfer*, International Textbook Company, 1973, p. 442.

4.2-5. F. W. Dittus and L. K. Boelter, "Heat Transfer in Automobile Radiators of Tubular Type," *Publications in Engineering*, University of California, Berkeley, CA, 1930, pp 443-461.

4.2-6. W. H. McAdams, *Heat Transmission*, Third Edition, New York: McGraw-Hill Book Company, Inc., 1954.

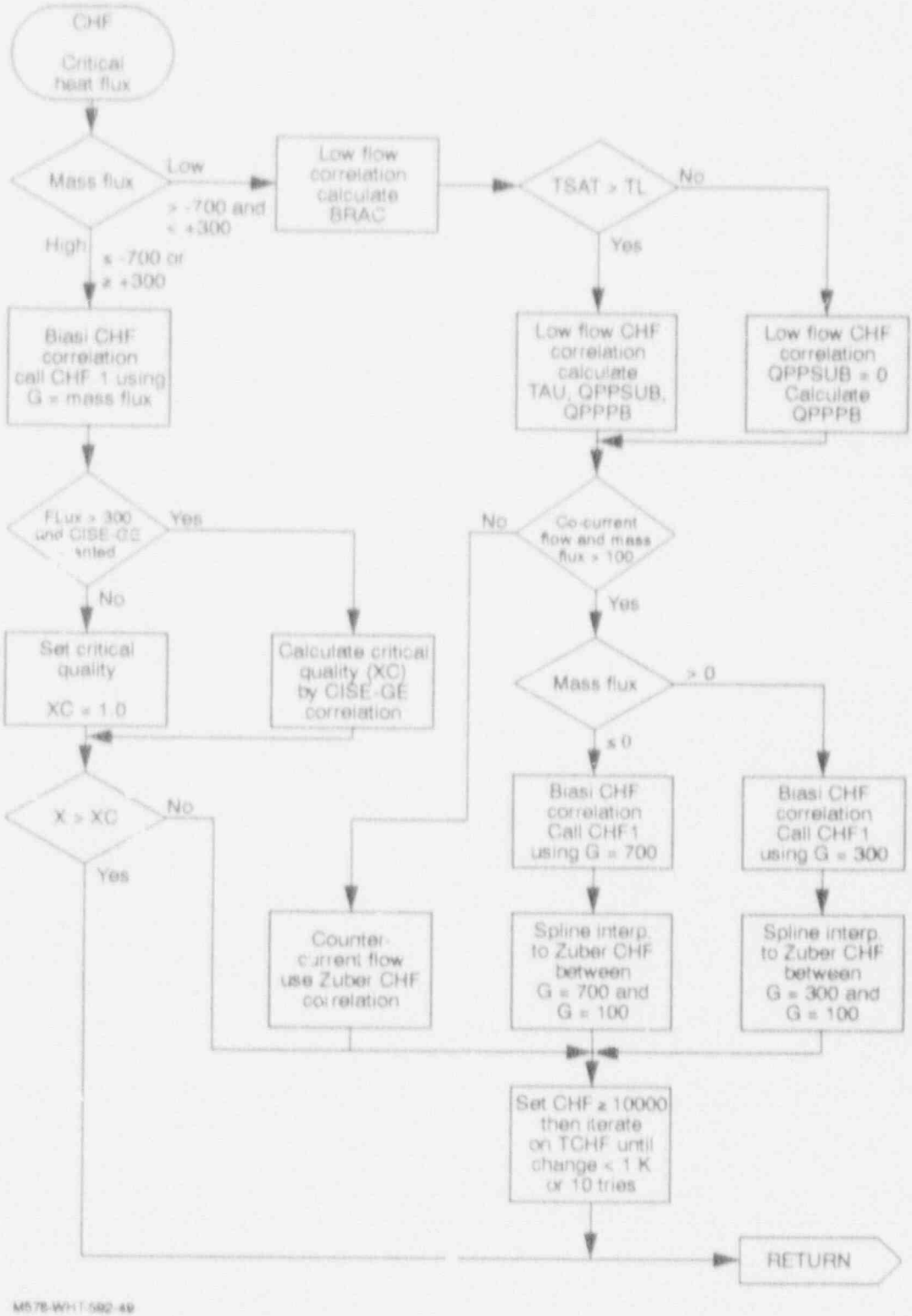

Figure 4.2-12. Critical heat flux calculation.

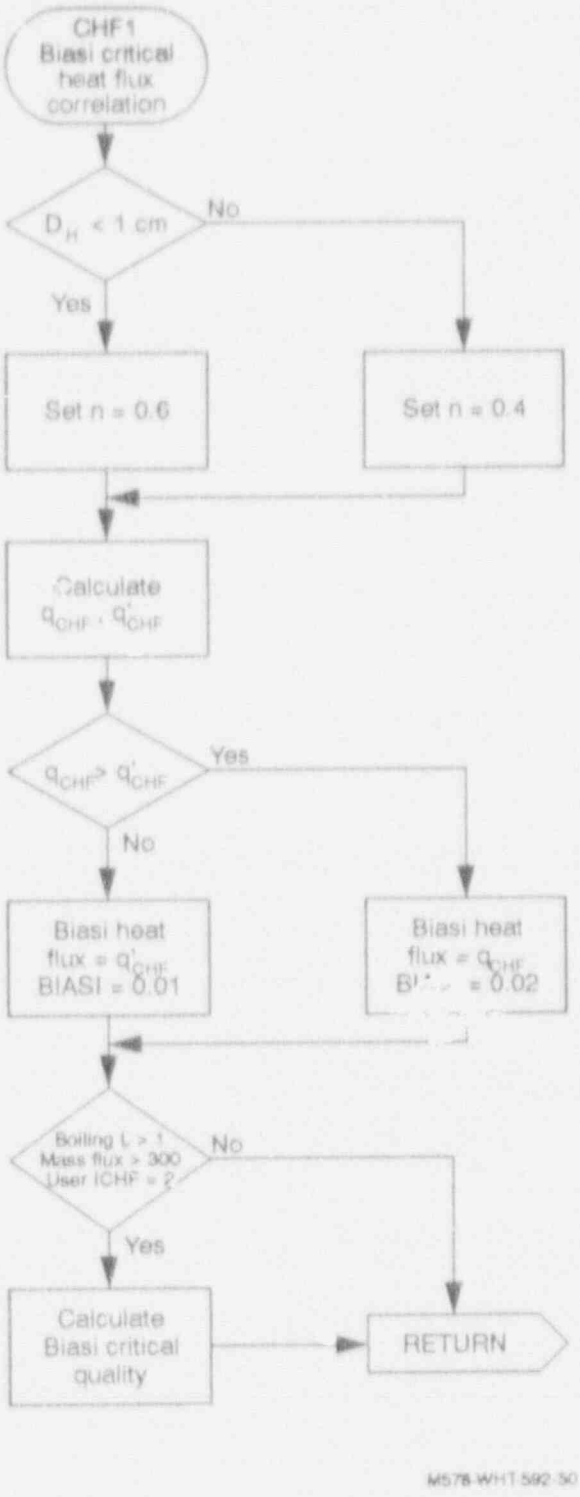

Figure 4.2-13. Biasi critical heat flux correlation.

4.2-7. W. M. Rohsenow and H. Y. Choi, *Heat, Mass, and Momentum Transfer*, Englewood Cliffs: Prentice-Hall, Inc., 1961.

4.2-8. V. P. Isachenko, "Heat Transfer in Condensation in Turbulent Jets," *Teploenergetika*, *2*, 1976, pp. 7-10.

4.2-9. R. W. Lockhart and R. C. Martinelli, "Proposed Correlation of Data for Isothermal Two-Phase, Two-Component Flow in Pipes," *Chemical Engineering Progress*, *45*, 1949, p. 39.

4.2-10. L. A. Bromley, "Heat Transfer in Stable Film Boiling," *Chemical Engineering Progress*, *46*, May 1950, pp. 221-227.

4.2-11. R. T. Lahey, "A Mechanistic Subcooled Boiling Model," *Proceedings of the Sixth International Heat Transfer Conference, 1, Toronto, Canada, 1978*, pp. 293-295.

4.2-12. R. W. Shumway, "Return to Nucleate Boiling," *Proceedings of the American Nuclear Society National Heat Transfer Conference, Denver, CO, August 1985.*

4.2-13. R. S. Dougall and W. M. Rohsenow, *Film Boiling on the Inside of Vertical Tubes with Upward Flow of the Fluid at Low Qualities*, Massachusetts Institute of Technology, Mechanical Engineering, 9079-26, 1963.

4.2-14. G. G. Loomis and R. W. Shumway, "Transition Boiling Heat Transfer in the Semiscale Mod-3 Core During Reflood," *Nuclear Technology*, *56*, 3, March 1982, p. 426.

4.2-15. D. Q. Kern, *Process Heat Transfer*, New York: McGraw-Hill Book Company, Inc., 1950.

4.2-16. T. Fujii, H. Vehara, and C. Kurato, "Laminar Filmwise Condensation of Flowing Vapour on a Horizonial Cylinder," *International Journal of Heat and Mass Transactions*, *14*, Great Britain: Pergamon Press, 1972, pp. 235-246.

4.2-17. M. M. Chen, "An Analytical Study of Laminar Film Condensation: Part 1--Flat Plates," *Transactions of the ASME*, February 1961, p. 48.

4.2-18. R. E. Phillips, R. W. Shumway, and K. H. Chu, "Improvements to the Prediction of Boiling Transition in BWR Transient Calculations," *Proceedings of the 20th ASME/AIChE National Heat Transfer Conference, Milwaukee, WI, August 2-5, 1981.*

4.2-19. R. T. Lahey, Jr., and F. Moody, *The Thermal Hydraulics of a Boiling Water Nuclear Reactor*, ANS, 1977.

4.2-20. L. Biasi et al., "Studies on Burnout: Part 3," *Energia Nucleare*,

14, 1967, pp. 530-536.

4.2-21. N. Zuber, M. Tribus, and J. W. Westwater, "The Hydrodynamic Crisis in Pool Boiling of Saturated and Subcooled Liquids, *International Developments in Heat Transfer*, 2, 1961, pp. 230-236.

4.2-22. F. B. Hildebrand, *Introduction to Numerical Analysis*, New York: McGraw-Hill Book Company, Inc., 1972.

4.3 RADIATION HEAT TRANSFER

It is known that the contribution of radiation to the overall heat transfer in LWR systems is negligible in normal operations. However, in a hypothetical accident situation in a BWR system that might lead to some core heatup, thermal radiation would contribute to the heat transfer from the fuel cladding to the shroud. This heat transfer by radiation is both directly, from surface to surface, and indirectly, through absorption by steam and water droplets inside the bundle. Radiation heat transfer may be appreciable only if the emitting surface is considerably hotter than its surroundings and if it is not directly in contact with an evaporating liquid. For these reasons, radiation heat transfer is neglected in all components except the fuel bundle (CHAN component in TRAC-BF1/MOD1 computations). In the case of the CHAN component, the user specifies a cutoff void fraction (ALPTST) below which radiation heat transfer is, again, neglected. (A value of 0.9 for the cutoff void fraction is suggested in the TRAC-BF1/MOD1 User's Guide.) For void fractions above ALPTST, radiation heat transfer in the CHAN is modeled as described below.[4.3-1]

4.3.1 Radiation Heat Transfer Model

The governing equations for radiative heat transfer within an absorbing, emitting, and scattering medium are a set of integro-differential equations for which only a few solutions for simple geometries are available.[4.3-2]. Numerical solutions to these equations are also impractical in terms of cost and effort. For engineering applications, approximate methods are typically chosen. A lumped-system approximation with uniform radiosity at the surfaces has been the traditional approach.[4.3-3,4,5,6].

The lumped-system approximation of the net-radiation method has been presented in Reference 4.3-2. The governing radiation exchange equations can be obtained for the k^{th} surface of area A_{tk} of an arbitrary enclosure of N discrete, diffuse, gray surfaces, as illustrated in Figure 4.3-1, by considering the incident and outgoing radiation components. As illustrated in Figure 4.3-2, the total radiation leaving surface k is

$$B_k A_{tk} = \epsilon_k \sigma_{SB} T_k^4 A_{tk} + (1 - \epsilon_k) H_k A_{tk} \qquad (4.3\text{-}1)$$

or

$$B_k = \epsilon_k \sigma_{SB} T_k^4 + (1 - \epsilon_k) H_k \ . \qquad (4.3\text{-}2)$$

As illustrated in Figure 4.3-3, the total incident radiation for surface k, assuming a transparent medium between surfaces, is

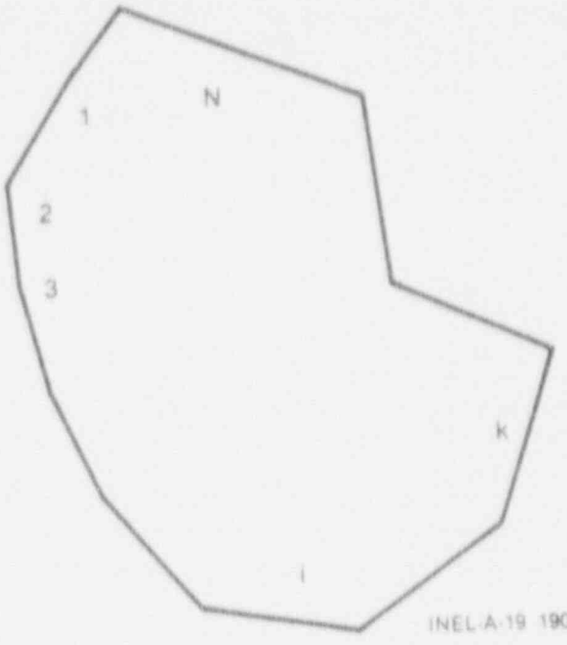

Figure 4.3-1. Enclosure of N discrete surfaces.

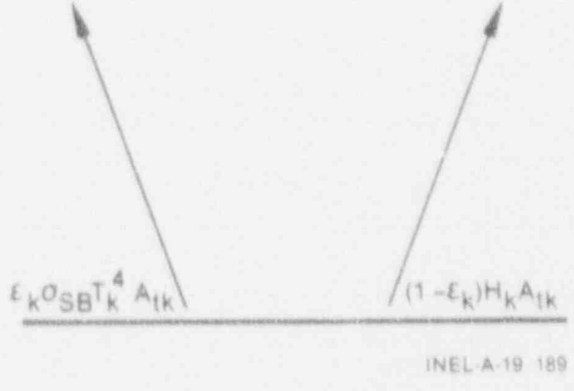

Figure 4 3-2. Radiation energy leaving surface k.

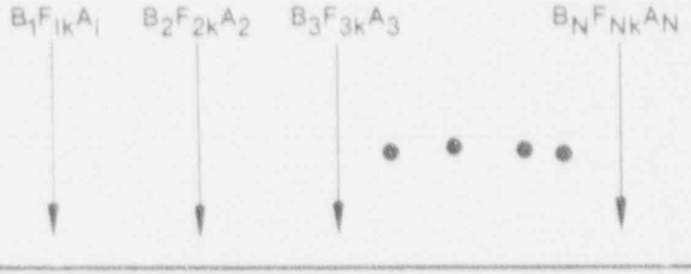

Figure 4.3-3. Radiant energy incident on surface i.

$$H_k A_{tk} = \sum_{j=1}^{N} B_j A_{tj} F_{jk} \quad . \tag{4.3-3}$$

Given the surface temperature, surface emissivities, and geometric view factors, Equations (4.3-2) and (4.3-3) can be solved for B_i and H_i. The net radiation from surface k is

$$q_k = B_k - H_k = \frac{e_k(\sigma_{SB} T_k - B_k)}{1 - e_k} \quad . \tag{4.3-4}$$

If a two-phase mixture is present, the governing radiative exchange equations would appear as

$$B_k = e_k \sigma_{SB} T_k^4 + (1 - e_k) H_k \tag{4.3-5}$$

$$H_k = \frac{1}{A_{tk}} \sum_{j=1}^{N} (B_j \tau_{jk} + e_{gjk} \tau_{\ell jk} \sigma_{SB} T_g^4 + e_{\ell jk} \tau_{gjk} \sigma_{SB} T_\ell^4) A_{tj} F_{jk} \tag{4.3-6}$$

where

$$\tau_{gjk} = (1 - a_{gjk}) \tag{4.3-7}$$

$$\tau_{\ell jk} = (1 - a_{\ell jk}) \tag{4.3-8}$$

$$\tau_{jk} = \tau_{gjk} \tau_{\ell jk} \tag{4.3-9}$$

and where the following assumptions have been made:

- All surfaces are gray and diffused.
- Each rod is one surface at one temperature, and the channel wall is one surface at one temperature.
- Axial radiative heat transfer is negligible.
- The droplets and vapor are gray.
- Scattering is negligible.
- The vapor and liquid temperatures are independent of the radial

dimension.

- The view factor of the two-phase mixture of surface j along the path k to j is given by the view factor from surface k to j (F_{kj}).

Equation (4.3-5) implies that the radiosity at surface k (B_k) is composed of two components,

1. $e_k \sigma_{SB} T_k^4$ - radiant heat flux emitted by surface k.

2. $(1 - e_k) H_k$ - radiation heat flux reflected from surface k due to the incident radiation heat flux on surface k (H_k).

Equation (4.3-6) gives three components to the incident radiant heat flux at surface k:

1. $\frac{1}{A_k} \sum_{j=1}^{N} B_j A_{tj} F_{jk} \tau_{jk}$ - radiation transferred from all surfaces to surface k without being absorbed by two-phase mixture.

2. $e_{gjk} \tau_{\ell jk} A_{tj} F_{jk} \sigma_{SB} T_v^4$ - radiation reemitted by the vapor phase along the path j to k and transferred to surface k without being reabsorbed by the liquid.

3. $e_{\ell jk} \tau_{gjk} A_{tk} F_{jk} \sigma_{SB} T_\ell^4$ - radiation reemitted by the liquid phase along the path j to k and transferred to surface k without being reabsorbed in the vapor phase.

Equation (4.3-5) and (4.3-6) can be combined to yield a system of linear equations if the surface temperatures, surface emissivities, view factors, and fluid radiation properties are known and can be solved for the radiosities for each surface

$$\sum_{j=1}^{N} \left[\delta_{jk} - (1 - e)\tau_{jk} F_{kj}\right] B_j = e_k \sigma_{SB} T_k^4 + (1 - e_k)$$

$$\sum_{j=1}^{N} \left(e_{gjk} \tau_{\ell jk} \sigma_{SB} T_g^4 + e_{\ell jk} \tau_{gjk} \sigma_{SB} T_\ell^4\right) F_{kj} \qquad (4.3\text{-}10)$$

where

$$\delta_{jk} = \begin{cases} 0. & \text{if } j \neq k \\ 1. & \text{if } j = k \end{cases} . \qquad (4.3\text{-}11)$$

Given the solution from Equation (4.3-10), a solution to Equation (4.3-4) can be determined to yield the net radiation heat flux from surface k. Equation (4.3-4) provides the radiation heat transfer boundary condition used for the conduction solution for surface k. However, additional calculations are required to determine the portion of radiant energy leaving surface k that is eventually absorbed into either the vapor, droplet, or film phases of the two-phase mixture.

The total radiation absorbed by the two-phase mixture is given by

$$\sum_{k=1}^{N} QABS_k = \sum_{k=1}^{N} \sum_{j=1}^{N} \left\{ A_{tk} f_{kj} \left[B_k (1 - \tau_{kj}) - \tau_{gkj} \epsilon_{\ell kj} \sigma_{sB} T_\ell^4 - \tau_{\ell jk} \epsilon_{gkj} \sigma_{sB} T_g^4 \right] \right\} . \qquad (4.3\text{-}12)$$

It can be shown that Equations (4.3-10) and (4.3-12) form a system of radiative exchange equations that conserve radiation energy

$$\sum_{k=1}^{N} (q_k A_{tk} - QABS_k) = 0 . \qquad (4.3\text{-}13)$$

However, since TRAC-BF1/MOD1 is a nonequilibrium two-fluid code, it is necessary to determine how much of the total radiant energy absorbed by the two-mixture phase is absorbed by the vapor phase and how much by the liquid phase.

The first term on the right side of Equation (4.3-12) is the amount of radiation absorbed by the two-phase mixture along the path k to j. The second term is the amount of radiation emitted by the liquid phase along the path k to j and not reabsorbed by the vapor phase. The third term is the amount of radiant energy emitted by the vapor phase along the path k to j and not reabsorbed by the liquid phase.

One method for splitting the first term on the right side into vapor/liquid components is to consider the probability that radiation will travel a distance z along a path L from k and then to j and be absorbed in the vapor phase in the next dz of path length, $P_g(z)dz$ or

$$P_g(z)\, dz = K_g e^{-(K_g + K_d)z}\, dz . \qquad (4.3\text{-}14)$$

Equation (4.3-14) assumes that the radiation absorption mechanism of the two-phase mixture can be expressed as an exponential function.[4.3-7,8] If Equation (4.3-14) is integrated from 0 to L, $P_g(L)$ can be determined, which is the probability that radiation traveling along the path L will be absorbed by the vapor phase

$$P_d(L) = \frac{K_g}{K_g + K_d}\left[1 - e^{-(K_g + K_d)L}\right] . \qquad (4.3\text{-}15)$$

The term of one minus the exponential can be recognized as one minus the transmissivity, since

$$\tau_{kj} = (1 - a_{gkj})(1 - a_{\ell kj})$$

$$= \left[1 - \left(1 - e^{-K_{gkj}L_{kj}}\right)\right]\left[1 - \left(1 - e^{-K_{dkj}L_{kj}}\right)\right]$$

$$= e^{-(K_{gkj} + K_{dkj})L_{kj}} . \qquad (4.3\text{-}16)$$

Equation (4.3-15) can now be written as

$$P_d(L_{kj}) = \frac{K_{gkj}}{K_{gkj} + K_{dkj}}(1 - \tau_{kj}) . \qquad (4.3\text{-}17)$$

Comparing Equations (4.3-12) and (4.3-14) yields the following equation for the net radiation absorbed by the vapor phase:

$$\sum_{k=1}^{N} QABSV_k = \sum_{k=1}^{N}\sum_{j=1}^{N}\left\{A_{tk}F_{kj}\left[B_k(1 - \tau_{kj})\ \frac{K_{gkj}}{K_{gkj} + K_{dkj}}\cdots\right.\right.$$

$$\left.\left. - \varepsilon_{gkj}\tau_{\ell kj}\sigma_{SB}T_g^4 + \varepsilon_{gkj}\varepsilon_{\ell kj}\sigma_{SB}\left(T_\ell^4 - T_g^4\right)\right]\right\} . \qquad (4.3\text{-}18)$$

The last term on the right side of Equation (4.3-18) is a correction proposed by Sun et al.[4.3-7] to account for radiation heat transfer between the droplet phase and the vapor phase. The radiation absorbed by the liquid phase can be obtained in a similar manner

$$\sum_{k=1}^{N} QABSL_k = \sum_{k=1}^{N}\sum_{j=1}^{N}\left\{A_{tk}F_{kj}\left[B_k(1 - \tau_{kj})\ \frac{K_{dkj}}{K_{dkj} + K_{gkj}}\right.\right.$$

$$- e_{\ell k j}\tau_{g k j}\sigma_{SB}T_{\ell}^{4} - e_{g k j}e_{\ell k j}\sigma_{SB}\left(T_{\ell}^{4} - T_{g}^{4}\right)\Big\}\Big\} \quad (4.3\text{-}19)$$

The sum of Equations (4.3-18) and (4.3-19) are solved in the routine RADSLAB, once B_k has been determined. The results of Equations (4.3-18) and (4.3-19) are used to determine a radiation heat transfer coefficient from the rod or channel wall surface k to the liquid phase and a radiation heat-transfer coefficient from the rod or channel wall surface k to the vapor phase.

$$h_{r\ell k} = \frac{QABSL_k}{(T_{k\ell} - T_{\ell})A_{tk}} \quad (4.3\text{-}20)$$

$$h_{rgk} = \frac{QABSV_k}{(T_{kg} - T_g)A_{tk}} \quad (4.3\text{-}21)$$

Before Equations (4.3-4), (4.3-5), (4.3-18), and (4.3-19) can be solved by RADSLAB,, the quantities e_k, e_{gkj}, $e_{\ell kj}$, $a_{\ell kj}$, and a_{gkj} must be determined. The emissivity of steam, e_g, is calculated taking into account the absorption and emission spectrum of water vapor. In physics, the emissivity and absorptivity of absorbing gaseous media are expressed as functions of radiation number v (the inverse of the radiation wave length). The total emissivity, e, for steam is obtained by integrating the emissivity equation over all wave numbers, with the Plank black body radiation distribution, B(v,T), as a weighting factor. Thus,

$$e_g = \frac{\int_0^{\infty} e_g(v,3(v,T_g)\ dv}{\int_0^{\infty} B(v,T_g)\ dv} \quad (4.3\text{-}22)$$

where

$$B(v,T) = \frac{2\pi hc^2v^3}{e^{\frac{hcv}{kT}} - 1} \quad (4.3\text{-}23)$$

h = Plank's constant

c = velocity of light

k = Boltzmann's constant.

In a similar procedure, the absorptivity for the vapor phase can be calculated as

$$a_g = \frac{\int_0^\infty a_g(\nu) B(\nu, T_g)\, d\nu}{\int_0^\infty B(\nu, T_g)\, d\nu} \quad . \tag{4.3-24}$$

where

T_k = surface temperature

$a_g(\nu)$ = $\epsilon_g(\nu)$ (4.3-25)

by Kirchoff's law (hence, $a_g = \epsilon_g$)

ν = wave number of radiation (cm^{-1}).

The absorption spectrum of water/vapor is generally considered to consist of six major absorption bands. The wave numbers and absorption coefficients associated with these bands are given in Reference 4.3-8 and Table 4.3-1. The values given in this table were obtained for the Thomson model of emissivity described in Reference 4.3-9, which is essentially the model utilized for the present calculation. The absorption coefficient values in Table 4.3-1 were obtained for a reference temperature of 300 K. These values are assumed to vary inversely with water/vapor temperature to account for various line broadening phenomena, or

$$K(\nu) = K_0(\nu) \frac{T_0}{T} \tag{4.3-26}$$

where T_0 = 300 K and K_0 (ν) is the tabular value of K(ν). The values of K(ν) used in the present model were assumed to be constant within each band, and zero in the region between bands.

Using data in Table 4.3-1, the integrals in Equations (4.3-22) and (4.3-24) can be approximately evaluated as sums over the six bands

$$\epsilon = \frac{\sum_{i=1}^{6} \epsilon(\bar{\nu}_i) \overline{B(\nu_i, T)}\, \Delta\nu_i}{\sigma_{SB} T^4} \tag{4.3-27}$$

$$a = \frac{\sum_{i=1}^{6} \epsilon(\bar{\nu}_i) \overline{B(\nu_i, T_w)}\, \Delta\nu_i}{\sigma_{SB} T^4} \tag{4.3-28}$$

Table 4.3-1. Water vapor absorption data.

Wave Length of Band Center (μ)	Minimum Wave Number (cm^{-1})	Maximum Wave Number (cm^{-1})	Absorption Coefficient $K(\nu)(Atm^{-1}cm^{-1})$
20.0	195.5	804.5	0.0959
1.0	1283.0	1892.0	0.2874
2.7	3399.0	4008.0	0.2069
1.87	5043.0	5652.0	0.0166
1.38	6942.0	7551.0	0.0136
1.1	8468.0	9077.0	0.00053

where i is the band index and $\overline{B(\nu_i,T)}$ is the average value of the Planck black body function over band i.

In the Thomson model, the value is obtained by integrating B(ν,T) over the entire band; while in the present model, it is obtained by evaluating B(ν,T) at the mean wave number ν_i of the band, or

$$\overline{B(\nu_i,T)} = B(\bar{\nu}_i,T) \quad . \tag{4.3-29}$$

4.3.2 Implementation In Coding

The model for water/vapor emissivity is incorporated into TRAC-BD1/MOD1 in Subroutine EMISS. To test the implementation of this model, EMISS was used to evaluate the emissivity of water/vapor for an applicable range of vapor temperatures and optical path lengths (PL products). The results of these calculations are compared in Figure 4.3-4 with experimental data and Thomson model results, both presented in Reference 4.3-8. Though the Thomson model gives better agreement with data than the present model, it is judged that the faster computational scheme used in the present model justifies the observed decrease in accuracy.

The droplet properties, $e_{\ell kj}$ and $a_{\ell kj}$, are also calculated in EMISS. The model developed in Reference 4.3-7 is

$$e_{dkj} = a_{dkj} = 1 - e^{-1.11 a_d \frac{l_{kj}}{D_d}} \quad . \tag{4.3-30}$$

Equation (4.3-30) also gives the absorption coefficient for the droplets (K_{dkj})

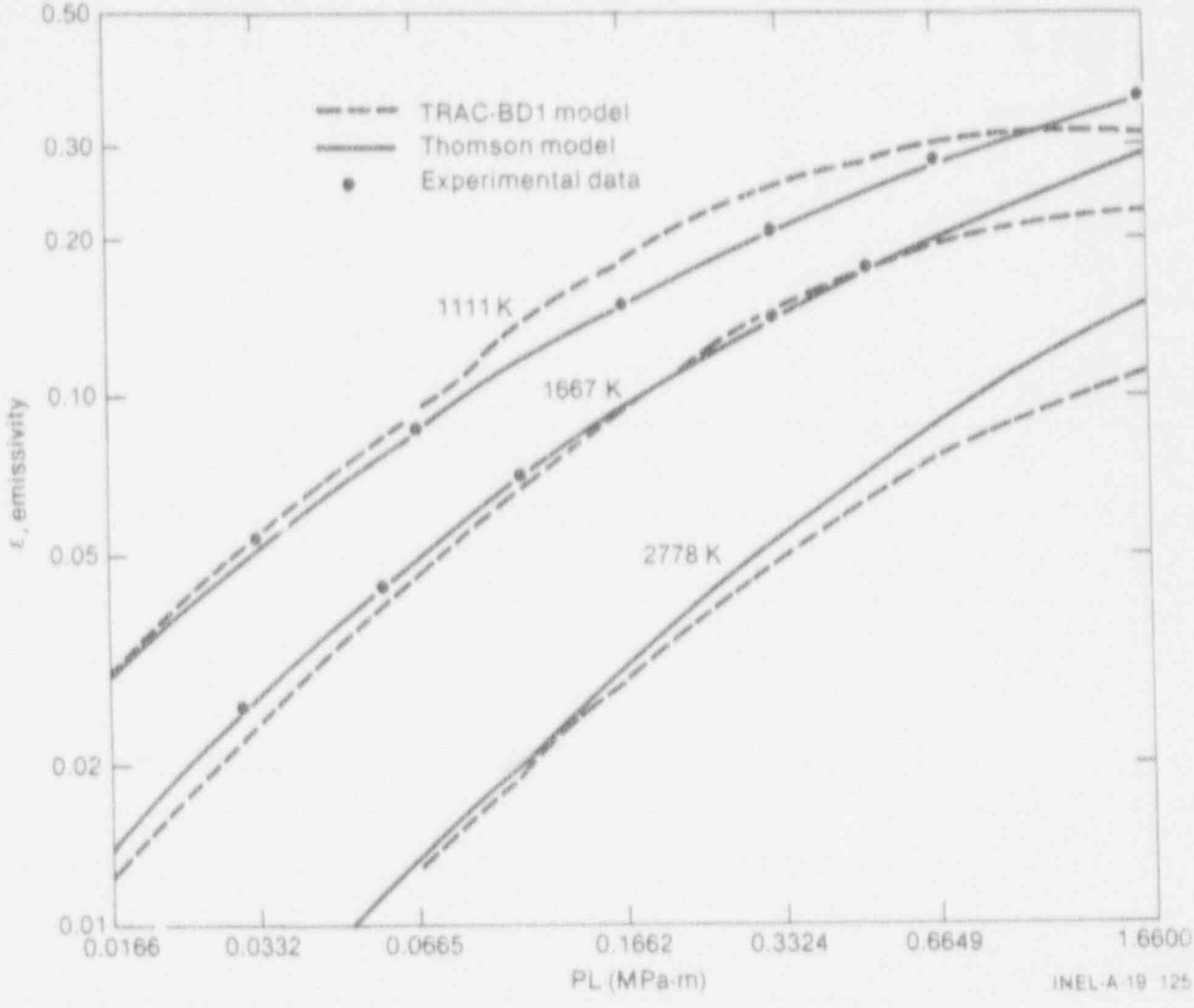

Figure 4.3-4. Water vapor emissivity.

$$K_{dkj} = \frac{1.11 a_d}{D_d} \quad . \tag{4.3-31}$$

The model for the steam absorptivity does not assume the form of Equation (4.3-18); therefore, K_{gkj} is calculated from

$$K_{gkj} = \frac{-\ln(1 - a_{gkj})}{L_{kj}} \quad . \tag{4.3-32}$$

The surface emissivities are input for the CHAN component and held constant over the transient. This completes information required by RADSLAB to calculate the radiation boundary conditions required by the TRAC-BF1/MOD1 hydrodynamics and heat transfer solution, if all involved surfaces are dry and the geometric data, F_{kj} and L_{kj}, are known.

If a surface involved in the radiation heat transfer calculation quenches, the radiation heat transfer calculation performed by RADSLAB is modified to account for the change in effective surface emissivity for the wetted or quenched surface. If a surface is quenched, the surface emissivity is set to 0.96^{10} (= 0.6648), and the calculated radiation heat flux at that surface is treated as an additional energy inflow to the liquid phase, since it is the liquid film absorbing the radiant energy and not the surface.

The quenched fraction for each axial node (for each rod group) and channel wall within a given CHAN component is calculated by CHAN1 and passed to RADSLAB. RADSLAB uses the fraction of quenched surface to linearly partition radiation at the quenching surface between the liquid phase and surface. CHAN1 also uses the fraction of quenched surface to linearly weight the dry surface emissivity with the wet surface emissivity and an effective wetted surface temperature with an effective dry surface temperature for the rods. Linear weighting may not be adequate. Additional work in this area may be required, depending on how the CHAN radiation model compares with data.

Calculation of the geometric quantities, F_{kj} and L_{kj}, required by the radiation model are performed in ICHAN by calls to CFIJ, GRPFIJ, and GRPLIJ. These routines were obtained from Reference 4.3-5. The method employed to calculate view factors between individual surfaces before grouping is the crossed-string method given in Reference 4.3-9. The method employed to calculate mean beam lengths between individual surfaces is the equivalent flat plate method proposed in Reference 4.3-3. The method employed in grouping of the individual view factors is the angle-factor algebra method given in Reference 4.3-8.

The CFIJ routine has been modified from that given in Reference 4.3-5. To reduce storage requirements, the channel wall is treated as one surface, rather than broken into segments and treated as 4-NROD surfaces, where NROD is the number of rods on a row. For calculation of the view factor from each rod to the channel wall, conservation of radiant energy can be used. The view factor from any given rod to the channel wall is given by

$$F_{kN} = 1 - \sum_{j=1}^{N-1} F_{kj} \quad . \tag{4.3-33}$$

The reciprocity rule[4.3-8] can be used to calculate the view factor from the wall to the rod surface K

$$F_{Nk} = \frac{A_{tk} F_{kN}}{A_{tN}} \quad . \tag{4.3-34}$$

The calculation of the path length from the rod surfaces to the channel wall uses the path length from the rod surface to the nearest channel wall. This is an approximation; however, it appears adequate for the outer row of rods in the bundle and is not a major factor for the inner rows of rods, since the view of the channel wall by the inner rows of rods is small. Work should

be performed in the area of improving these calculations and reducing the storage requirements at the same time.

An anisotropic reflection model has been developed for TRAC-BF1/MOD1, which modifies the view factors to account for anisotropic reflection effects from the rods and channel walls in a BWR bundle. Comparisons with experimental data indicate that the effect can be significant. The view factors are modified by the method suggested by Andersen,[4.3-10] in which a fraction μ_j of the radiation incident on rod i from rod j is directly reflected back to rod j, and a fraction $(1 - \mu_j)$ is reflected isotropically. This has the effect of reducing the effective view factor from rod j to rod i and increasing the effective view factor from rod j to itself, since a fraction μ_j of all radiation sent from rod j to rod i is immediately returned.

The anisotropic factor μ_j is used to modify the view factors used in Equations (4.3-3) through (4.3-12) in accordance with Equations (4.3-35) and (4.3-36):

$$F'_{ij} = \begin{cases} F_{ij}(1 - \mu_{ij}) \text{ for } i \neq j \\ F_{ii} + \sum_{\substack{j=1 \\ j \neq i}}^{N} F_{ij}\mu_{ij} \end{cases} \quad (4.3\text{-}35)$$

These new effective view factors conserve radiant energy and satisfy the reciprocity relationship if $\mu_{ij} = \mu_{ji}$. In accordance with the recommendations of Tien et al.,[4.3-11] values of 0.5 and 0.15, respectively, are used for μ_{ij} for rod-to-rod and channel-wall-to-rod radiation.

In an effort to reduce computation time for the radiation model, RADSLAB is called every NRADth time step, where NRAD is a user-supplied input. This has the disadvantage that if wall temperatures and fluid temperatures, or both, are rapidly changing, the radiation heat transfer boundary conditions (q_k, h_{rvk}, $h_{r\ell k}$) calculated by RADSLAB may not be consistent with

$$\sum_{k=1}^{N} q_k A_k - QABS_k = 0 . \quad (4.3\text{-}36)$$

Additional work should be done in this area of determining how often to call RADSLAB and what information to calculate at each time step.

4.3.3 Assessment

As reported in Volume 4 of Reference 4.3-1, the radiation model of TRAC-BF1/MOD1 has been compared to the data obtained in a simulated full-scale 8x8 BWR fuel bundle. The experimental data, reported by Nilsson et al.,[4.3-12] were obtained in the GOTA test facility at Studsvik, Sweden. Test No. 27 of

GÖTA experiments was used for this assessment. In this test, the electrically heated 64-rod bundle was filled with stagnant steam at near atmospheric pressure and operated at a high temperature in the middle with steep temperature gradients towards the periphery. The peak rod temperature in the middle of the bundle was 1224 K. The bundle shroud walls were maintained at 373 K by cooling water on the outside. Heating of the rods (radial power factors) was diagonally symmetrical, and over half of the 64 rods were instrumented.

The TRAC-BD1 model used a one-cell CHAN simulation of the bundle mid-section. Modeling the rods in one-half of the bundle plus the half rods along the diagonal requires 36 different rod types, as input to the CHAN component. A zero velocity FILL component was connected to the bottom of the CHAN, and a BREAK component with set pressure was connected to the top.

Figure 4.3-5 (from Ref. 4.3-1) shows a comparison of the calculated and measured data along the diagonal. A summation of the differences between the calculated and measured data for all the 36 rods, divided by 36 yields only 1.3 K error. This error is extremely small considering that the temperature gradient from the canister wall to the central rod is 600 times larger than the error. Performing the same calculation with the steam absorption set to zero has shown a negligible effect on the results. However, switching to uniform (isotropic) reflection reduces the peak temperature by about 100 K. The emissivity used for all surfaces was 0.7.

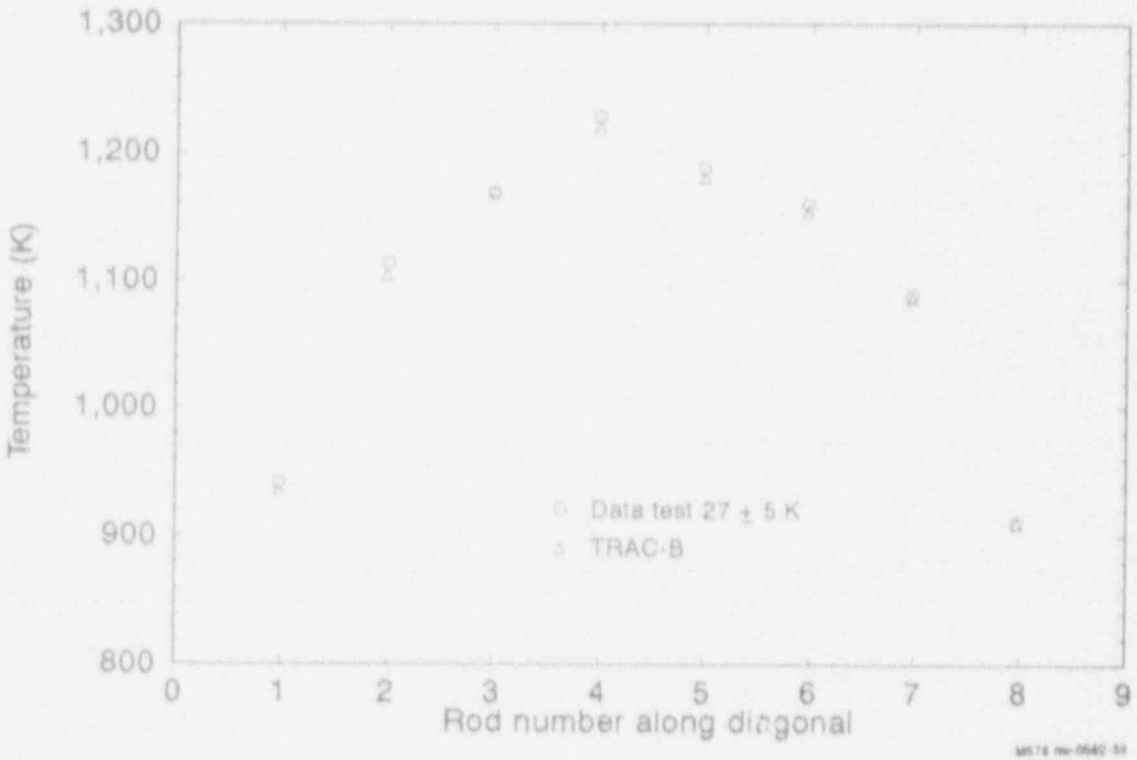

Figure 4.3-5. GÖTA radiation test data comparison.

4.3.4 References

4.3-1. D. D. Taylor et al., *TRAC-BD1/MOD1: An Advanced Best Estimate Computer Program for Boiling Water Reactor Transient Analysis*, Volumes 1 and 4, NUREG/CR-3633, EGG-2294, April 1984.

4.3-2. R. Seigle and J. R. Howell, *Thermal Radiation Heat Transfer*, New York: McGraw-Hill Book Co. Inc., 1972.

4.3-3. J. G. M. Andersen et al., *NORCOOL 1, A Model for Analysis of a BWR Under LOCA Conditions*, Riso National Laboratory, NORHAV-D-47, Denmark, August 1977.

4.3-4. M. M. Giles, "A Radiation to Steam Model for Reactor Core Thermal Analysis," *ANS Transactions, Sun Valley, Idaho, 1977.*

4.3-5. D. A. Mandell, *A Radiative Heat Transfer Model for the TRAC Code*, NUREG/CR-0994, LA-7965-MS, November 1979.

4.3-6. G. E. McCreery and C. E. Hendrix, "RELAP4/MOD7 Version 1 BWR Spray Cooling Calculations Compared with Data," *ANS Transactions, San Diego, California, June 1978.*

4.3-7. K. H. Sun et al., Calculation of Combined Radiation and Convection Heat Transfer in Rod Bundles Under Emergency Cooling Conditions," *Journal of Heat Transfer*, August 1976, p. 414.

4.3-8. E. M. Sparrow and R. P. Cess, *Radiative Heat Transfer*, Monterey: Books/Cole Publishing Co., 1967.

4.3-9. H. C. Hottel and A. F. Sarofim, *Radiative Heat Transfer*, New York: McGraw-Hill Book Co., Inc., 1967.

4.3-10. J. G. M. Andersen and C. L. Tien, "Radiation Heat Transfer in a BWR Bundle Under LOCA Conditions," *ASME Winter Annual Meeting, New York, New York, December 2-7, 1979*, ASME 79-WA/XX-00.

4.3-11. C. L. Tien et al., "Surface Radiation Exchange in Rod Bundles," *Transactions of ASME, 101*, 1979, p. 378.

4.3-12. L. Nilsson, L. Gustafson, and R. Harju, *Experimental Investigation of Cooling by Top Spray and Bottom Flooding of a Simulated 64 Rod Bundle for a BWR*, STUDSVIC/RL-78/59, Norhav S-406, June 30, 1978.

5. CLOSURE RELATIONS REQUIRED BY FLUID-MASS CONSERVATION EQUATIONS

Treatment of fluid-mass conservations equations in TRAC-BF1/MOD1 is very closely related to the energy exchange equations described in Section 4.1. For this reason, a separate section on this topic is not necessary.

6. CLOSURE RELATIONS REQUIRED BY FLUID-MOMENTUM FIELD EQUATIONS

Closure relations required by the fluid-momentum field equation are described in the following sections.

6.1 INTERFACIAL SHEAR

Calculation of interfacial shear and momentum exchange across the interface is a necessary part of the two-fluid equation system solution. In specific terms, the interfacial shear model calculates the variable $F_{\ell g}$ in equations of motion for vapor and liquid. $F_{\ell g}$ represents the drag force, per unit volume, between the phases; and it is expressed in terms of phasic velocity difference

$$F_{\ell g} = \bar{C}_i |\bar{V}_r| \bar{V}_r \qquad (6.1\text{-}1)$$

where $\bar{C}_i$ is the local average interfacial drag coefficient between phases (per unit volume) and $\bar{V}_r$ is the void-weighted average velocity difference between vapor and liquid. The local values of $\bar{C}_i$ and $\bar{V}_r$ are dependent on flow regime, void fraction, and properties of vapor and liquid. Furthermore, C_i is a function of $\bar{V}_r$. Equation (6.1-1) gives only the generic form of $F_{\ell g}$; its specific forms are described later. The basic principle of these calculations is to identify the prevailing flow pattern at each hydraulic junction and then apply specific correlations for relative phasic velocity and interfacial drag to determine the momentum exchange across the interface at that junction. However, to satisfy the requirements of hydraulic modeling with numerical solution, a two-stage interpolation scheme is used to obtain representative values of the relative velocity and interfacial drag that include the effects of drift velocity and distribution parameters in all possible flow regimes. This aspect is further clarified after the main variables have been discussed.

The interfacial friction is calculated mainly in the FRCIF subroutine in TRAC-BF1/MOD1. The present section is intended to provide a complete documentation of the actual equations used in that subroutine and to disc the background and origins of the basic relations used in these calculati , as well as the effects of coding on the results. The order of presenting different equations in the main text has been arranged, as closely as possible, to reflect the order of application of those equations in the flow chart of the FRCIF subroutine. In order to distinguish between the main variable computations and their derivations in this report, each equation that is used in the coding of FRCIF, either exactly or in successive steps, is

marked with an asterisk (*), followed by the variable name used in the coding for the left-hand side of that equation.

6.1.1 Background

The interfacial shear model in TRAC-BF1/MOD1 is based mainly on the drift-flux correlations derived by Ishii,[6.1-1] Andersen and Chu,[6.1-2] and Andersen et al.,[6.1-3] with some modifications that are specific to the INEL version of the code. These include some additional correlations by Ishii[6.1-4] and others, as will be specified later.

According to Andersen et al.,[6.1-2,6.1-3] the basic assumptions in the derivation of the present interfacial shear model are:

- For adiabatic and steady-state conditions, the two-fluid model and the drift flux model are equivalent, and the drift flux parameters can be used to characterize the relative velocity and the phase and flow distributions.

- The correlations for interfacial shear and drag and wall friction, as derived from adiabatic steady-state conditions, are applicable for transient conditions.

On these bases, an existing collection of data from two-phase flow pressure drop and average void fraction measurements has been analyzed to derive correlations for relative phasic velocity and interfacial drag in different flow regimes. These correlations are then employed in the two-fluid interfacial shear model. The data base for these derivations covers a large number of experiments. A detailed reference to these will be given later.

6.1.2 Flow Regime Transitions

The interfacial shear model distinguishes three regimes in two-phase flow. These are:

- Bubbly/churn flow

- Annular flow, including dispersed annular flow

- Dispersed droplet flow

Except for the extreme cases of zero or 100% void, each one of these flow regimes may involve either cocurrent or countercurrent flows.

Figure 6.1-1 shows a schematic diagram of the flow regime boundaries and two of the void-dependent variables calculated for a mass velocity of 500

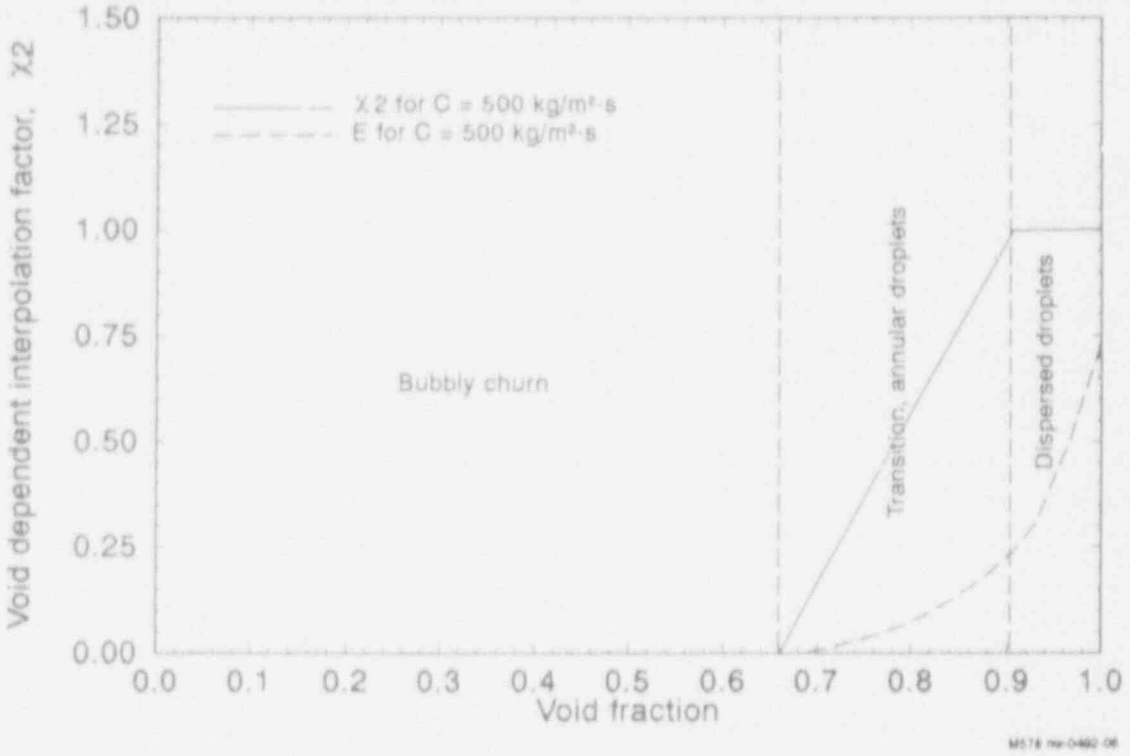

Figure 6.1-1. Flow regime map for a mass velocity of 500 kg/m^2·s at p = 7 MPa, showing the void-dependent limits of different flow patterns, the void-dependent interpolation factor $\chi 2$, and liquid entrainment.

kg/m^2·s, in a channel with a hydraulic diameter of 0.0145 m (typical of BWR fuel bundles) at a pressure of 7.0 MPa. As stated earlier, all variables calculated for each one of these flow regimes, including countercurrent flows, are used in an interpolation scheme with respect to void fraction and entrainment. The interpolation variables that are shown in Figure 6.1-1 will be discussed later. The void fraction at transition between different flow regimes depends on flow and system variables, as will be explained later. It should be noted that some of the correlations for flow regime transitions, relative velocity, and entrainment in different flow regimes that are derived for interfacial shear are also applied to the interfacial heat transfer calculations. These were discussed in Section 4.2.

6.1.3 Basic Definitions

Before presenting the equations used for interfacial exchange calculations, it is useful to review some of the specific notations used in drift flux formulation, as initially defined by Zuber and Findlay.[6.1-5]

Interfacial Shear

Simple area-averaged quantity of a locally varying property, f(A), is defined as

$$\langle f \rangle = \frac{1}{A}\int_A f(A)\, dA \qquad (6.1\text{-}2)$$

Void-weighted area-averaged quantities are defined as

$$\bar{f} = \frac{\langle \alpha f \rangle}{\langle \alpha \rangle} \qquad (6.1\text{-}3)$$

Local volumetric liquid flux:

$$j_\ell(A) = [1 - \alpha(A)]V_\ell(A) \qquad (6.1\text{-}4)$$

Local volumetric vapor flux:

$$j_g(A) = \alpha(A)V_g(A) \qquad (6.1\text{-}5)$$

Total volumetric flux at a point:

$$j(A) = j_g(A) + j_\ell(A) \qquad (6.1\text{-}6)$$

Average volumetric liquid flux:

$$\langle j_\ell \rangle = G\frac{(1. - X)}{\rho_\ell} \qquad (6.1\text{-}7)$$

Average volumetric vapor flux:

$$\langle j_g \rangle = G\frac{X}{\rho_g} \qquad (6.1\text{-}8)$$

Total average volumetric flux:

$$\langle j \rangle = \langle j_g \rangle + \langle j_\ell \rangle \qquad (6.1\text{-}9)$$

Distribution parameter:

$$C_o = \frac{\langle \alpha j \rangle}{\langle \alpha \rangle \langle j \rangle} \tag{6.1-10}$$

Void-weighted average liquid velocity:

$$\bar{V}_\ell = \frac{\langle \alpha V_\ell \rangle}{\langle \alpha \rangle} \tag{6.1-11}$$

Void-weighted average vapor velocity:

$$\bar{V}_g = \frac{\langle \alpha V_g \rangle}{\langle \alpha \rangle} \tag{6.1-12}$$

Local drift velocity of vapor with respect to volumetric flux:

$$V_{gj}(A) = V_g(A) - j(A) \tag{6.1-13}$$

Void-weighted average vapor drift velocity:

$$\bar{V}_{gj} = \frac{\langle \alpha V_{gj} \rangle}{\langle \alpha \rangle} = \bar{V}_g - C_o \langle j \rangle \tag{6.1-14}$$

This relation is employed to calculate C_o from $\bar{V}_g$, $\langle j \rangle$, and $\bar{V}_{gj}$. The distribution parameter C_o is an indicator of the nonuniform distribution of void, $\alpha(A)$ and phasic velocities, $V_{fj}(A)$ and $V_\ell(A)$, over flow area.

Note: In vertical flows, $\bar{V}_{gj}$ is related to the rising velocity of bubbles in a continuous liquid phase, or to the falling velocity of droplets in a continuous vapor phase.

Local relative velocity:

$$V_r(A) = \frac{V_{gj}(A)}{1 - \alpha(A)} \tag{6.1-15}$$

Void-weighted relative velocity (see Reference 6.1-2):

$$\bar{V}_r = \frac{1}{\eta} \frac{\bar{V}_{gj}}{\langle 1 - \alpha \rangle} \tag{6.1-16}$$

where

$$\eta = \frac{\langle \alpha(1-\alpha) \rangle}{\langle \alpha \rangle \langle 1-\alpha \rangle} = 1 \ , \qquad (6.1\text{-}17)$$

It should be noted that both $\bar{V}_{gj}$ and $\bar{V}_r$ depend on flow regime and the distribution parameter C_o as well as on the local void fraction, α.

For simplicity in the following equations, all area-averaged quantities are presented without the symbols, $\langle\ \rangle$ and the void-weighted average quantities are presented as defined. Hence, $\alpha = \langle\alpha\rangle$ and $\bar{V}$ = void-weighted average velocity. A complete list of other symbols used in the equations is given in the nomenclature.

6.1.4 Flow Transition Criteria

The criteria for transition between different flow regimes are given in terms of an average void fraction, α_{tran}, that is calculated in terms of phasic densities and flow the distribution parameter for bubbly/churn flow, C_o.

$$\alpha_{tran} = \left(1 + \frac{4}{\gamma}\right)\frac{1}{C_{ob}} - \frac{4}{\gamma} - 0.15 \qquad \text{*, ACA (6.1-18)}$$

where

$$\gamma = \sqrt{\frac{\rho_\ell}{\rho_g}} \qquad \text{*, GAMMA (6.1-19)}$$

$$C_{ob} = C_\infty - \frac{C_\infty - 1}{\gamma} \qquad \text{*, CO (6.1-20)}$$

$$C_\infty = 1.0 + 0.2\left(\frac{\rho_\ell}{G}\sqrt{gD_h}\right)^{0.5} \ . \qquad \text{*, COINF (6.1-21)}$$

The latter equation, which is specific to the interfacial shear model in TRAC-BF1/MOD1 (in deviation from Reference 6.1-3), is a slightly modified form of C_o formula that was recommended by Rouhani [6.1-6]. The original formula, which includes a factor of $(1 - X)$ in the second term, was derived from analyzing a large data base of measured void fractions in different geometries. Dropping the $(1 - X)$ term in this case is quite justified (for

simplicity), as the steam quality, X, is close to zero at low α values, where Equation (6.1-21) is applied. Equation (6.1-20) gives the distribution parameter for bubbly/churn flow.

Note that there is a difference between the C_o calculation in this model and the calculation of the same variable for interfacial heat transfer in the HEATIF subroutine (see Section 4.3).

Comparison of drift flux equations with experimental data indicates that, in most cases, C_o has a value slightly more than 1.0, and it never exceeds 1.33 (see Reference 6.1-1). In subcooled boiling, C_o may even reduce to less than 1. These restrictions are observed in the programming, as will be described later.

The flow transition criteria are:

Liquid continuous flow (including single-phase liquid, bubbly, and churn flows), when

$$\alpha \leq \alpha_{tran} \tag{6.1-22}$$

Transition flow (including annular and film flows), when

$$\alpha_{tran} < \alpha < \alpha_{tran} + 0.25 \tag{6.1-23}$$

Vapor continuous flow, (including dispersed droplet and single-phase vapor flow), when

$$\alpha > \alpha_{tran} + 0.25 \ . \tag{6.1-24}$$

Figure 6.1-2 shows variations of α_{tran} (boundary between bubbly/churn and annular dispersed flows) with mass velocity for three different hydraulic diameters, at a constant pressure of 6.81 Mpa. These are according to Equations (6.1-18) through (6.1-21), which are used in the FRCIF subroutine.

Note that the transition criteria given by Equations (6.1-22) through (6.1-24) are simplified forms of the criteria given by Ishii.[6.1-1] In particular, assumption of a band of 25% void for the transition from bubbly/churn to dispersed droplet flow is a computational convenience (a good practical approximation) for this region.

The original derivations by Ishii[6.1-1] suggest two transition criteria based on C_o, j_g, Re_ℓ, and the variable group

$$\left(\frac{\sigma g \Delta\rho}{\rho_g^2}\right)^{0.25} .$$

These are:

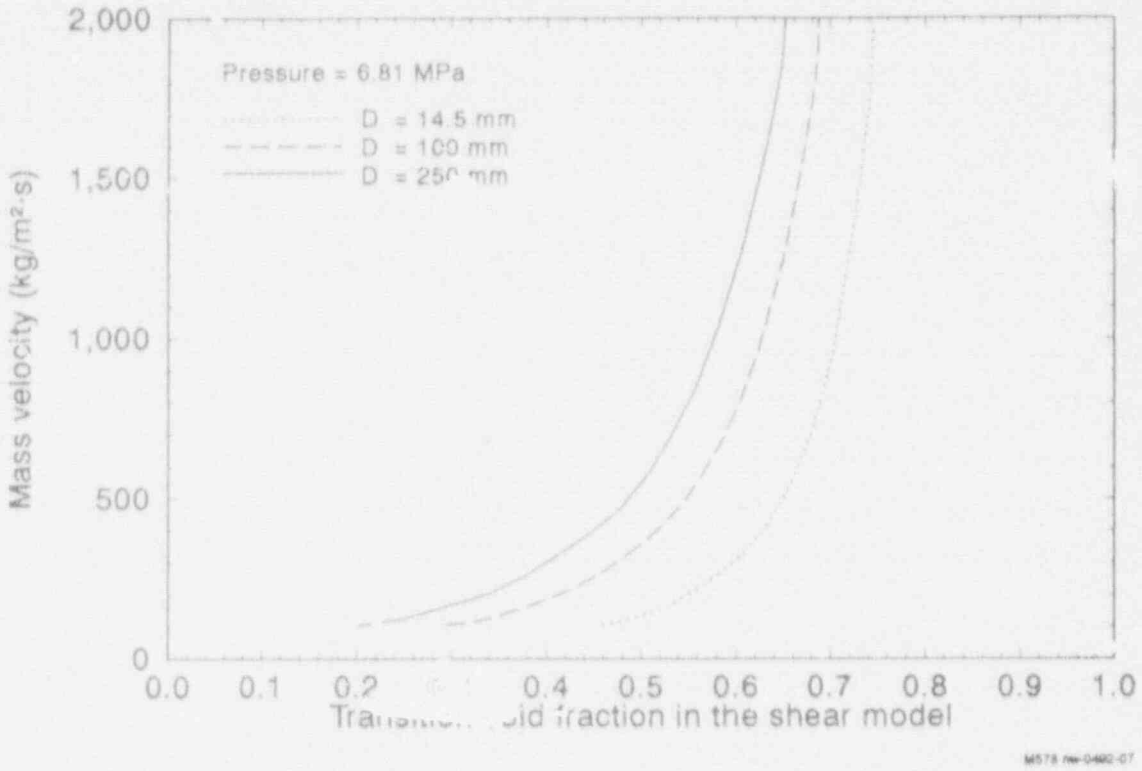

Figure 6.1-2. Relationship between mass velocity and void fraction at transition from bubbly/churn to annular-dispersed liquid flow

Transition from bubbly to annular when

$$\frac{j_g}{\frac{\sqrt{D_h G \Delta\rho}}{\rho_g}} \geq \frac{1}{C_o} - 0.1 \qquad (6.1\text{-}25)$$

and transition from annular to dispersed droplet flow when

$$|j_g| > \left(\frac{\sigma g \Delta\rho}{\rho_g^2}\right)^{0.25} N_{\mu\ell}^{-0.2} \begin{cases} \ldots 78\ Re_\ell^{-1/3} & \text{if } Re_\ell \leq 1635 \\ 1.0 & \text{if } Re_\ell > 1635 \end{cases} \qquad (6.1\text{-}26)$$

where

$$N_{\mu f} = \frac{\mu_f}{\sqrt{\rho_f \sigma \sqrt{\frac{\sigma}{g\Delta\rho}}}} \quad . \tag{6.1-27}$$

It should be noted that these derivations are for adiabatic flow, and the bubbly-annular transition is actually for the case of $j_f = 0$. For this reason (according to References 6.1-2 and 6.1-3), Equation (6.1-24) represents a modified version of Ishii's criteria, which includes the effect of non-zero liquid velocity (no proof has been given).

In reality, transition from annular to droplet flow is a gradual process that starts with the onset of liquid entrainment and is completed when 100% of the liquid flow is entrained. This process is dramatically affected by the onset of dry-out in heated channels. Both of these features are observed in the calculations of entrainment and drift flux variables, as will be discussed in the following sections.

6.1.5 Correlations For Interfacial Drag

In the derivations of References 6.1-1, 6.1-2 and 6.1-3, steady-state momentum equations for vapor and liquid in adiabatic flow are employed to show that the interfacial force may be expressed in terms of phasic density differences and void fraction. This is expressed as

$$F_{fg} = \bar{C}_i \frac{|\bar{V}_{gj}|\bar{V}_{gj}}{\langle 1 - \alpha \rangle^2} = \Delta\rho g \langle \alpha(1 - \alpha) \rangle \tag{6.1-28}$$

in which $\bar{C}_i$ includes $1/\eta^2$, which is a factor in relating $\bar{V}_{gj}$ to $\bar{V}_r$ (see Reference 6.1-3). The coefficient $\bar{C}_i$ represents the drag force per unit volume per unit velocity squared. Its components are interfacial area per unit volume and drag coefficient per unit area. Hence, $\bar{C}_i$ has the following general form

$$\bar{C}_i = \frac{1}{2} C_D \left(\frac{3}{2} \frac{1}{d_i} \right) \rho_c \frac{1}{\eta^2} \quad . \tag{6.1-29}$$

Here, $\frac{3}{2} d_i^{-1}$ is the frictional area per unit volume and ρ_c is the density of

the continuous phase. As will be shown later, the d_i^{-1} depends on $\bar{V}_{gj}$ in bubbly and dispersed droplet flow regimes. This makes C_i and $F_{\ell g}$ strongly dependent on the phasic velocity differences in these flow regimes.

By using known correlations for $\bar{V}_{gj}$, in terms of α and material properties of steam and water, suitable correlations for $\bar{C}_i$ are obtained from Equation (6.1-29) in comparison with data. The general form of this correlation is expressed as

$$F_{\ell g} = \bar{C}\left[\bar{V}_r\right]^N = \bar{C}_i|C_1\bar{V}_g - C_o\bar{V}_\ell|(C_1\bar{V}_g - C_o\bar{V}_\ell) \ . \qquad (6.1\text{-}30)$$

The exponent N varies between 2 and 4, due to the effect of the flow regime on the interfacial area. This effect is implied in the variable $\bar{C}_i$, as will be seen later. With this formulation, the calculations involve specifying the coefficients C_o, C_1, and $\bar{C}_i$. Here, C_o and C_1 account for the effects of vapor and liquid velocity distributions, respectively. C_o was defined earlier, and C_1 is given by

$$C_1 = \frac{1 - \alpha C_o}{1 - \alpha} \ . \qquad \text{*, C1B (6.1-31)}$$

In computation of the interfacial friction factor, the product of $\bar{C}_i$ and the absolute value of relative velocity is considered as a single variable, C_i, and expressed as

$$C_i = \bar{C}_i|C_1\bar{V}_g - C_o\bar{V}_\ell| \ . \qquad (6.1\text{-}32)$$

This product is readily usable in the integration of momentum equations that are linearized in terms of velocity difference.

Different correlations are used for C_o, C_1, and C_i in different flow regimes. These coefficients are computed in the FRCIP subroutine in TRAC-BF1/MOD1 and returned to the momentum solution routine, where FRCIF is called in each iteration.

6.1.6 Drag Coefficient and Interfacial Area Relations

In particulate flow regimes, such as bubbly or dispersed droplets, the total interfacial area per unit volume is related to a critical Weber number, We_c that is expressed in terms of $\bar{V}_{gj}$.[6.1-3]

For bubbly flow, the interfacial area per unit volume is

$$\frac{1}{d_i} = 6\alpha \frac{\rho_\ell \bar{V}_{gj}^2}{\sigma We_c (1 - \alpha)^2} \tag{6.1-33}$$

where

$$We_c = \frac{\rho_\ell D_b \bar{V}_r^2}{\sigma} . \tag{6.1-34}$$

This critical Weber number signifies the limiting value of $\bar{V}_r$ beyond which the bubbles may deform and break up. Equation (6.1-33) is obtained by considering that the void fraction, α, corresponds to n bubbles of diameter D_b per unit volume. The void volume is $\frac{1}{6} n\pi D_b^3$, and the total interfacial area is $n\pi D_b^2$. These give a ratio of area per unit volume that is $6\alpha/D_b$. By substituting D_b from Equation (6.1-34) and setting $\bar{V}_r = \frac{\bar{V}_{jg}}{1 - \alpha}$, one obtains Equation (6.1-33). However, for friction calculations, one should use the projected area--1/4 of the total surface area for the spherical particles.

In annular flow, the interfacial area per unit volume for both friction and heat transfer is independent of the relative velocity, as expressed by the following relation:[6.1-3]

$$\frac{1}{d_i} = \frac{4}{D_h}\sqrt{\alpha} . \tag{6.1-35}$$

This is obtained with the assumption of a vapor core surrounded by a smooth liquid film on the walls.

In bubbly flow, the interfacial drag coefficient $\bar{C}_D$ and the frictional area per unit volume are related to $\bar{V}_{gj}$ and the Weber number by[6.1-2,3]

$$\frac{3}{4}\alpha \frac{\bar{C}_D}{We_c} \frac{\rho_\ell^2}{\sigma} \frac{\bar{V}_{gj}^4}{(1 - \alpha)^4} = \Delta\rho g \alpha (1 - \alpha) . \tag{6.1-36}$$

A similar argument for dispersed droplet flow, in which the liquid fraction, $(1 - \alpha)$, corresponds to n droplets per unit volume, gives the

following relation between the drag coefficient and the drift velocity of droplets:

$$\frac{3}{4}(1-\alpha)\frac{\bar{C}_D}{We_c}\frac{\rho_g^2}{\sigma}\frac{\bar{V}_{gj}^4}{(1-\alpha)^4} = \Delta\rho g\alpha(1-\alpha) \quad . \tag{6.1-37}$$

The Weber number in this equation is

$$We_c = \frac{\rho_g D_d \bar{V}_r^2}{\sigma} \quad . \tag{6.1-38}$$

Equations (6.1-36) and (6.1-37) are employed to evaluate $\bar{C}_D$, as will be seen later.

6.1.7 Data Base For Interfacial Friction

It should be noted that the interfacial friction in two-phase flow is not measurable directly and, as yet, there is no measuring technique developed for this effect. The derivations of the interfacial friction factor, as well as phasic drift velocity and the phasic distribution parameter, are done on theoretical basis and verified indirectly through comparison with measurable data, such as void fraction and pressure drop, in two-phase flow. Some data from simultaneous measurements of radial and axial void distribution and axial pressure gradients, as reported by Zuber et al.,[6.1-5,7] have been very useful in the development and application of the drift flux theory. However, the fundamental task of deriving mathematical expressions for the drift flux parameters and comparing them with a wide range of measured data was performed by Ishii.[6.1-1,4] The data base used by Ishii in those comparisons is given in Appendix C. The data sources are organized in tabular form to show the range of variables for the different parameters. The appendix also includes a list of publication references.

Andersen et al.[6.1-2,3] adopted Ishii's correlations to the concept of two-fluid models and added some new ones of their own, particularly for interfacial friction in bubbly flow. For a final check on the interfacial shear in the two-fluid model, they used adiabatic void measurement data reported by Agostini et al. The data base for these derivations and assessment are also documented in Appendix C. Finally, the experimental data employed in the derivation of other correlations that are used in this model are also included in Appendix C.

6.1.8 Drift Velocity and Distribution Parameters in Different Flow Regimes

6.1.8.1 Bubbly/Churn Flow. The commonly used expression for $\bar{V}_{gj}$ in co-current bubbly flow[6.1-1,2,5] is

$$\bar{V}_{gj} = k\left[\frac{\Delta\rho g\sigma}{\rho_\ell^2}\right]^{0.25} \qquad *, \text{ VRB (6.1-39)}$$

where k has been given values ranging from 1.18 to 1.53. TRAC-BF1/MOD1 uses k = 1.53.

However, for bubbly flow between the fuel rods in a rod bundle, TRAC-BF1/MOD1 uses a different correlation for $\bar{V}_{gj}$ that is recommended by Bestion[6.1-8] on the basis of experimental data from void measurement in different rod bundles. This correlation is

$$\bar{V}_{gj} = 0.188\left(\frac{g\Delta\rho D_h}{\rho_g}\right)^{0.5} \qquad *, \text{ VRB (6.1-40)}$$

in which D_h is the hydraulic diameter of the bundle.

In either case, the relative velocity is calculated according to

$$\bar{V}_r = \frac{\bar{V}_{gj}}{1-\alpha} \; . \qquad *, \text{ VROB (6.1-41)}$$

In the absence of subcooled boiling, the distribution parameter, C_o for this bubbly/churn flow is calculated according to Equations (6.1-20) and 6.1-21).

In subcooled boiling, the bubbles are mostly concentrated within a layer close to the heated walls, where the liquid velocity approaches zero. For this reason, the distribution parameter, C_o, is modified to accommodate this difference from regular two-phase flow situations. The modification is done by applying a multiplier to C_o that is a function of liquid enthalpy and heat transfer parameters (see Reference 6.1-3). Hence, for subcooled boiling,

$$C_{o,s} = C_o\frac{h_\ell - h_{\ell d}}{h_f - h_{\ell d}} \qquad *, \text{ CO (6.1-42)}$$

where h_ℓ is the local liquid enthalpy, h_f is the saturation liquid enthalpy, and $h_{\ell d}$ is the liquid enthalpy at the point of net vapor generation according to the Saha-Zuber subcooled boiling model.[6.1-9] This enthalpy, which is a function of pressure and wall heat flux, is always less than h_f. Calculation of this variable is reviewed in the next section.

6.1.8.2 Transition Region, Annular Flow, and Entrainment

6.1.8.2.1 Entrainment--Beyond the bubbly/churn flow regime, that is, in the annular and dispersed droplet flow regimes, liquid entrainment as droplets in vapor must be considered. The general expression for entrainment is[6.1-3]

$$E = (X_E - 0.03)\left[1 + (X_E + 0.1)^2\right]^{-0.5} \quad \text{*, ENT (6.1-43)}$$

where

$$X_E = 10^{-6}\,(j_g^*)^{2.5}(D^*)^{1.25}(Re_\ell)^{0.25} \quad \text{*, XE (6.1-44)}$$

$$j_g^* = \frac{j_g}{\left[\frac{\sigma\Delta\rho g}{\rho_g^2}\left(\frac{\rho_g}{\Delta\rho}\right)^{2/3}\right]^{1/4}} \quad \text{*, XJGS (6.1-45)}$$

$$D^* = D_h\sqrt{\frac{g\Delta\rho}{\sigma}} \quad \text{*, DS (6.1-46)}$$

$$Re_\ell = \frac{\rho_\ell j_\ell D_h}{\mu_\ell}\,. \quad \text{*, REL (6.1-47)}$$

Equation (6.1-43) is a modified version of an empirical correlation for entrainment that was derived by Ishii from experimental data.[6.1-1] The constant 10^{-6} in Equation (6.1-44) is slightly higher than 8.0×10^{-7} that is given in Reference 6.1-3.

The calculated entrainment from Equation (6.1-43) is modified to Ent in two occasions; when $X_E < 0.03$ and when there are some wetted walls and some dry walls in the same segment of a channel. These modifications are

$$Ent = 0.0, \text{ if } X_E < 0.03 \quad \text{*, ENT (6.1-48)}$$

and

$$Ent = E + (1 - E)(1 - W_{wet}) \quad \text{*, ENT (6.1-49)}$$

where

$$W_{wet} = \frac{WA_f}{WA_{tot}} \qquad (6.1\text{-}50)$$

in which WA_f is the sum of the rod and wall areas in the cell that are covered with a liquid film, and WA_{tot} is the total rod and wall area in the cell, including the portions that are in film boiling or steam cooling process. It may be observed that if all walls are wet, Ent = E and if all walls are dry Ent = 1. (100% of the liquid flow is entrained). The variables WA_f and W_{wet} are calculated based on the wall heat transfer mode number. (These are discussed in the section on interfacial heat transfer.)

6.1.8.2.2 **Drift Velocity in Transition Region**--The vapor drift velocity in the transition region does not have a unique expression of its own. Instead, the drift velocity is calculated by interpolation between $\bar{V}_{gj}$ values for bubbly/churn and for annular flows. This interpolation is one in terms of the average void fraction in the cell, α, using

$$\chi 2 = \frac{\alpha - \alpha_{tran}}{0.25}, \text{ for } \alpha_{tran} < \alpha < \alpha_{tran} + 0.25 . \qquad *, X2 \ (6.1\text{-}51)$$

This interpolation factor is also used for calculating droplet entrainment in the transition region, as the entrainment should be zero at the end of bubbly/churn regime and it should reach 100% at the start of dispersed droplet flow. Examples of $\chi 2$ and Ent variations with void are shown in Figure 6-1.1, and variations of Ent with void for three different mass velocities are shown in Figure 6-1.3.

Generally, the liquid velocity in the transition and annular flow regimes will include two components, namely, $\bar{V}_{ra}$ for the annular film on the wall and $\bar{V}_{rd}$ for the droplets in a continuous vapor phase. In each case, an average relative velocity is obtained by interpolation between the velocities of the different components.

The drift velocity in annular film flow, $\bar{V}_{ra}$, is calculated from steady-state mass balance for the liquid film and the theory of minimum stable film flow.[6.1-3] The minimum film thickness is given by

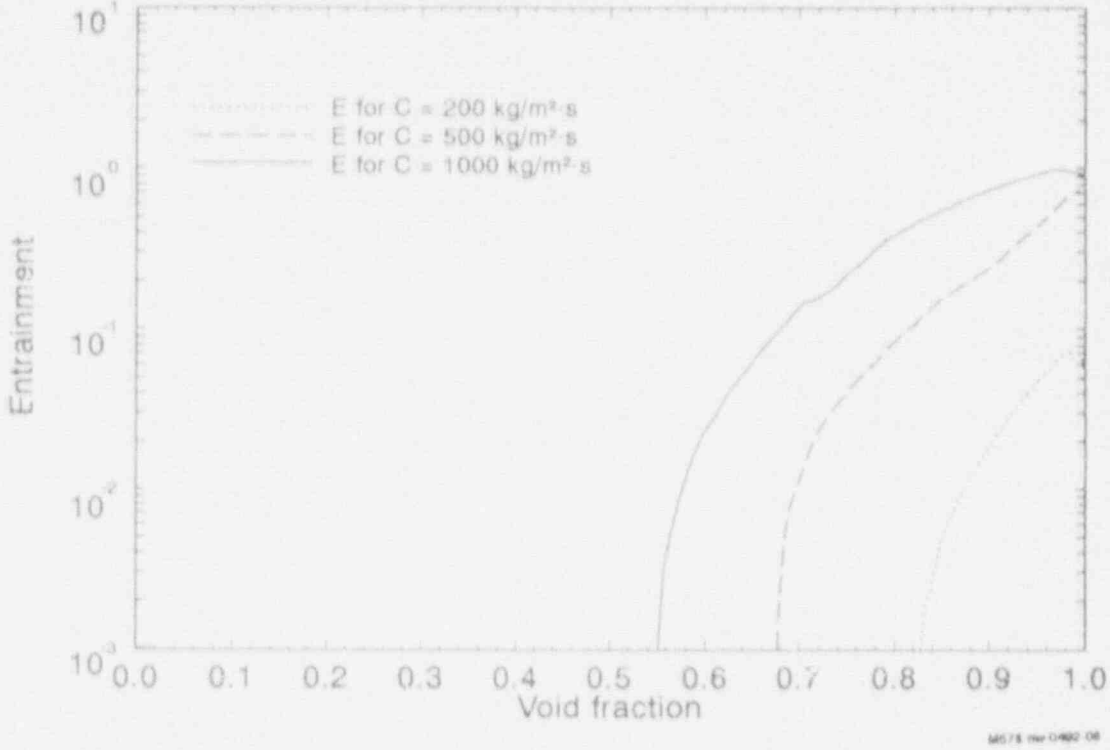

Figure 6.1-3. Variations of entrainment (Ent) with void fraction at different mass velocities.

$$D_{f,min} = \left[18 \frac{\sigma \mu_f^2}{g^2 \rho_f^3} \right]^{0.2} \qquad \text{*, DIAFMN (6.1-52)}$$

and the absolute velocity of the liquid film is

$$\bar{V}_{ra} = \frac{D_{f,min}^2 g \Delta\rho}{3\mu_f} \; . \qquad \text{*, VROA (6.1-53)}$$

This equation is from a simple force balance on a creeping film, assuming viscous flow and linear velocity distribution in the film.

The interpolated drift velocity, based on this $\bar{V}_{ra}$ and $\bar{V}_{rb}$ of Equation (6.1-41) is

$$\bar{V}_{rba} = (1 - \chi^2)\bar{V}_{rb} + \chi 2 \bar{V}_{ra} \; . \qquad \text{*, VROBA (6.1-54)}$$

It should be noted that Equation (6.1-54) gives, also, the relative velocity in annular film flow when $\alpha > \alpha_{tran} + 0.25$. In this region, $\chi 2 = 1$ and $\bar{V}_{rba} = \bar{V}_{ra}$.

For the dispersed droplet flow regime, TRAC-BF1/MOD1 uses some more recent correlations suggested by Ishii.[6.1-4] In this regime, the drift velocity, $\bar{V}_{rd}$, depends on the pattern of liquid flow. This may be either a wake regime or a distorted particle regime. In the wake regime, that is, when chunks of liquid are dragged behind very large bubbles or when large waves are fanned on the wall, the relative liquid velocity is

$$\bar{V}_{rd} = 0.5 R_d \alpha^{1.5} \left[\frac{(\Delta\rho g)^2}{\rho_g \mu_g} \right]^{1/3} \qquad \text{*, VROD (6.1-55)}$$

in which R_d is the droplet radius and is given by

$$R_d = 0.005 \frac{\sigma}{\rho_g J_g^2} \left[\frac{\rho_\ell}{\rho_g} \left(Re_g \frac{\mu_g}{\mu_\ell} \right)^2 \right]^{1/3} \qquad \text{*, RDISH (6.1-56)}$$

where

$$Re_g = \frac{\rho_g J_g D_h}{\mu_g} . \qquad \text{*, REG (6.1-57)}$$

However, if the liquid flow is in the form of distorted particles, the relative velocity is given by

$$\bar{V}_{rd} = \sqrt{2} \left(\frac{\sigma g \Delta\rho}{\rho_g^2} \right)^{1/4} \alpha^{1.5} . \qquad \text{*, VROD (6.1-58)}$$

The criterion for applying Equation (6.1-55) or Equation (6.1-58) for $\bar{V}_{rd}$ is set by comparing R_d of Equation (6.1-56) with a critical droplet radius that is defined by the following equation:[6.1-4]

$$R_{dc} = 2 \sqrt{\frac{2\sigma}{g\Delta\rho}} N_{\mu g}^{1/3} \qquad \text{*, RDCRIT (6.1-59)}$$

where

$$N_{\mu g} = \frac{\mu_g}{\sqrt{\rho_g \sigma \sqrt{\frac{\sigma}{g\Delta\rho}}}} \quad \text{*, VISNUM (6.1-60)}$$

The wake regime equation (6.1-55) is used whenever $R_d \leq R_{dc}$. In coding these equations, some numerical limitations are imposed on R_d, as will be described in Section 6.1.10.

Since the actual two-phase flow in the transition region involves a combination of liquid film and dispersed droplet flow (carried as entrainment), a relevant value of the relative velocity is obtained from an entrainment-dependent interpolation between $\bar{V}_{rba}$ of Equation (6.1-54) and $\bar{V}_{rd}$. The interpolation parameter is $E\chi 2$, that is defined in terms of Ent from Equations (6.1-48) or (6.1-49), and $\chi 2$, which is a function of α.

$$E\chi 2 = \chi 2 \; Ent \; . \quad \text{*, ENT (6.1-61)}$$

Figure 6.1-4 shows typical trends of $E\chi 2$ variations with void for three different mass velocities. Although entrainment, Ent, starts at lower void fractions for G = 1000 compared to G = 500 (see Figure 6.1-3), $E\chi 2$ values are lower for the higher mass velocity at the beginning. This is caused by the $\chi 2$ factor, which remains zero over a wider range of void fraction for higher mass velocities, as the transition from bubbly to annular flow takes place at increasingly higher voids.

With this $E\chi 2$ as a new interpolation parameter, the relative velocity in the transition region is given by

$$\bar{V}_{ro} = (1 - E\chi 2)\bar{V}_{rba} + E\chi 2 \bar{V}_{rd} \; . \quad \text{*, VRO (6.1-62)}$$

This relative velocity is then used to calculate the average drift velocity

$$\bar{V}_{gj} = \bar{V}_{ro}(1 - \alpha) \; . \quad \text{*, VGJ (6.1-63)}$$

Calculation of the distribution parameter, C_o, for the annular flow regime is described later.

6.1.8.3 Dispersed Droplet Flow. As was pointed out under Equation (6.1-54), the relative velocity in annual film flow is given by $\bar{V}_{ra}$ of Equation (6.1-53). In the case of dispersed droplet flow, where $\chi 2 = 1$, Equation (6.1-61) results in $E\chi 2 = Ent$ and, since Ent = 100% in this regime,

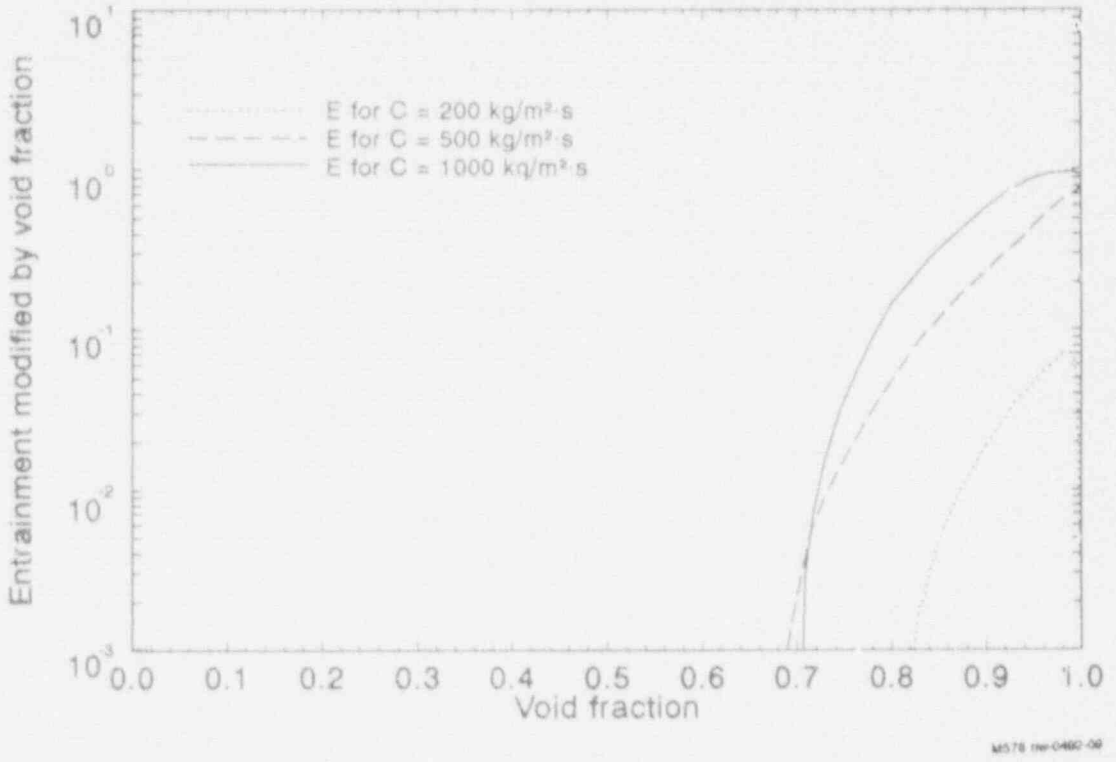

Figure 6.1-4. Variations of modified entrainment (Eχ2) with void fraction at different mass velocities.

Equation (6.1-62) yields $\bar{V}_{ro} = \bar{V}_{rd}$.

Calculation of the distribution parameter, C_o, for dispersed droplet flow is described later.

6.1.8.4 **Countercurrent Flow**. Countercurrent flows of vapor and liquid that may occur at some hydraulic restrictions can lead to flooding situations known as countercurrent flow limitation (CCFL). In this process, the rising vapor flow prevents downflow of liquid. This phenomenon is important in the penetration and distribution of the emergency core cooling (ECC) water in BWRs. CCFL may affect the liquid penetration through the upper core tie plate, and it may also affect outpouring of liquid from the fuel bundles, through the side entry orifices at the bottom of the bundles.

Experimental investigations[6.1-10] have shown that the CCFL behavior depends on the geometry of hydraulic restriction and the properties of the two phases. The CCFL model in TRAC-BF1/MOD1 employs a Kutateladze type correlation[6.1-11] in which two empirical constants, m and K, must be specified

(see Section 7.3).

TRAC-BF1/MOD1 employs the CCFL model in two different contexts:

a. as a regular part of the interfacial shear calculations within the FRCIF subroutine with a built-in set of constants, and

b. as a special option evoked by the user at any flagged hydraulic junction with the user-specified values of m and K.

A detailed discussion of the CCFL model of TRAC-BF1/MOD1, including the derivation of equations and features of the CCFLCK subroutine where the optional uses are performed, will be given in Section 7.3. In the following, only the equations that are coded in FRCIF are presented briefly.

The CCFL calculations in FRCIF are initiated by defining an interpolation variable, χ, that depends on phasic velocities. First, the absolute value of the larger phasic velocity, V_g or V_ℓ, is identified and used for calculating a normalized (nondimensional) relative velocity, χ_c

$$\chi_c = \frac{|V_g - V_\ell|}{Max\ [|V_g|, |V_\ell|]} \quad \text{*, X (6.1-64)}$$

If χ_c is larger than 1, it is set equal to 1 and, in either case, it is used to calculate another variable, χ_{c1}

$$\chi_{c1} = \frac{\chi_c - 0.8}{0.2} \quad \text{*, X (6.1-65)}$$

If χ_{c1} is negative, there is no countercurrent flow to be considered. In this case, χ_{c1} is set to zero and the CCFL calculations are skipped. However, if χ_{c1} is positive, it indicates the existence of a CCFL situation. In this case, χ_{c1} is used in Equation (6.1-81) for χ, and the following equation is used for the distribution parameter (see Section 7.3):

$$(C_o)_{ccfl} = A_o + (2\chi 2 - 1)\sqrt{A_o^2 - \frac{Fm^2}{\alpha}} \quad \text{*, COCCFL (6.1-66)}$$

in which

$$A_o = 0.5\left[\frac{1}{\alpha} + F\left(m^2 - \sqrt{\frac{\rho_g}{\rho_\ell}}\right)\right] \quad \text{*, AO (6.1-67)}$$

and

$$F = \frac{\bar{V}_{gj}}{Kj_{\ell o}} \quad . \qquad \text{*, F (6.1-68)}$$

For reasons that are explained in Section 7.3, the variable F is limited to a maximum defined by

$$F = F_{max} = \frac{\gamma}{\alpha\left(1 + \sqrt{m^2\gamma}\right)^2} \quad . \qquad \text{*, FMAX (6.1-69)}$$

As stated earlier, the CCFL constants m and K are dependent on geometry and flow properties. TRAC-BF1/MOD1 employs one set of default values of m and K in the FRCIF subroutine. These constants that are recommended for the upper tie-plate and general pipe calculations are: m = 1.0 and K = 4.2. Another set of default values are used for the side entry orifice of the BWR bundles (see Section 7.3).

In CCFL situations, the C_1 factor of Equation (6.1-30) is calculated with the following formula:

$$(C_1)_{ccfl} = \frac{1 - \alpha(C_o)_{ccfl}}{1 - \alpha} \quad . \qquad \text{*, C1CCFL (6.1-70)}$$

In cases of very high void fractions ($\alpha > 0.999999$), the above relation is replaced by the following:

$$(C_1)_{ccfl} = \frac{\bar{V}_{ro}}{K\bar{V}_{rd}} \quad . \qquad \text{*, C1CCFL (611-71)}$$

6.1.9 Calculation of C_o, C_1, and C_i Parameters

As stated earlier, two-phase flow beyond the bubbly/churn flow regime must be considered as a mixture of annular and dispersed droplet flows. In particular, for smoothness of the numerical solutions, it is important to ramp all changeovers of the variables from one flow regime to the next one. Hence, the final values of C_o, C_1, and C_i that are returned from the FRCIF subroutine in TRAC-BF1/MOD1 are obtained by interpolations with respect to void and entrainment. These interpolations are shown diagrammatically in Figure 6.1-5. Each of the elements, COB, COA, and COD, is obtained by a separate interpolation between its cocurrent and countercurrent components.

In the remainder of this section, a series of correlations for C_o, C_1, and C_i in different flow regimes are described and, finally, the interpolated

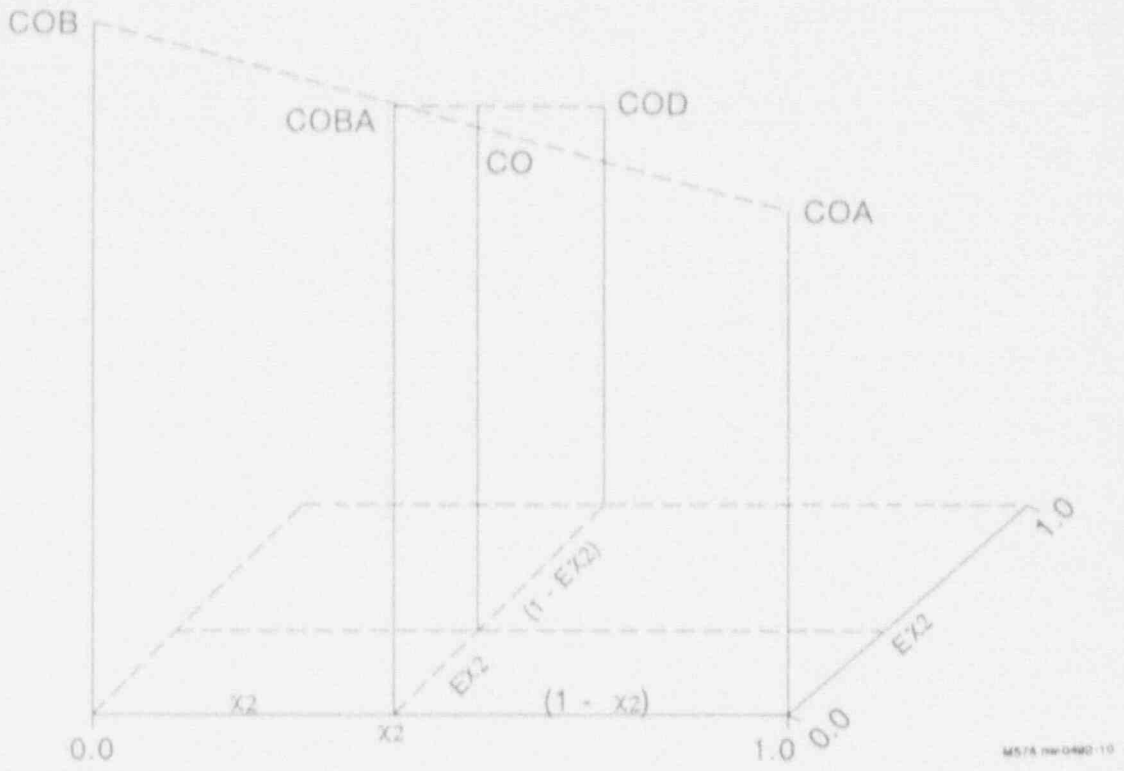

Figure 6.1-5. Schematic of interpolations for Co with respect to χ2 and Eχ2 in the transition region.

form of these variables will be presented, following the same order as in the coding.

6.1.9.1 Bubbly/Churn Cocurrent Flow. When $\alpha < \alpha_{tran}$ and flows of vapor and liquid are cocurrent, the following relations are used.

C_{ob} is calculated according to Equation (6.1-20) or $C_{o,s}$ of Equation (6.1-42), for subcooled boiling, depending on the prevailing thermal-hydraulic conditions. C_1 is given by the following relation:

$$C_{1b} = \frac{1 - \alpha C_o}{1 - \alpha} \quad *, \text{C1B (6.1-72)}$$

The interfacial friction factor for bubbly flow, C_{ib}, is derived from Equation (6.1-36) and a modified correlation for drift velocity, $\bar{V}_{gjm}$, based on bubble rise data of Wilson et al.[6.1-12] The modified drift velocity is

$$\bar{V}_{gjm} = \bar{V}_{gj} + (1 - F_a)|J|(C_{o,} - C_{ob}) \quad (6.1\text{-}73)$$

in which $\bar{V}_{gj}$ and C_{ob} are given by Equations (6.1-40) and (6.1-20), respectively,

$$F_\alpha = \frac{\alpha - 0.3}{\alpha_{tran} - 0.3} \qquad *, \text{XL (6.1-74)}$$

and

$$C_V = 0.73(D^*)^{0.121}\left(\frac{\Delta\rho}{\rho_g}\right)^{0.203}(j_g^*)^{-0.365} \qquad (6.1\text{-}75)$$

where D* is given by Equation (4.1.13) and

$$j_g^* = \frac{|j_g|\sqrt{\rho_\ell}}{(\Delta\rho g\sigma)^{0.25}} . \qquad *, \text{BB (6.1-76)}$$

C_{pr} is the distribution parameter for bubble rise in a mass of stagnant water based on Wilson's data.[6.1-3]

Using $\bar{V}_{gjm}$ for $\bar{V}_{gj}$ in Equation (6.1-36) and rewriting it as

$$\bar{C}_i\frac{\bar{V}_{gjm}^4}{(1-\alpha)^4} = \Delta\rho g\alpha(1-\alpha) \qquad (6.1\text{-}77)$$

gives

$$C_{ib} = \frac{\rho_\ell^2\alpha(1-\alpha)^5}{\alpha\xi^4}\left(|C_{ib}V_g - C_{ob}V_\ell|\right)^3 \qquad *, \text{CIB (6.1-78)}$$

where

$$\xi = 1.53 + \left(\zeta_a(j_g^*)^{0.635} - C_{ob}j_g^*\right)(1 - F_\alpha) \qquad *, \text{XX (6.1-79)}$$

$$\zeta_a = 0.73(D^*)^{0.121}\left(\frac{\Delta\rho}{\rho_g}\right)^{0.203} . \qquad *, \text{AA (6.1-80)}$$

As expressed earlier in Equation (6.1-32), C_i represents a product of the interfacial friction factor and the absolute value of relative velocity; also, for the dispersed flow, the interfacial area is proportional to the

relative velocity squared. Combining these two features leads to the third-power dependence of C_{ib} on relative velocity in Equation (6.1-78).

F_α in Equation (6.1-79) is a void-dependent interpolation factor. For $\alpha < 0.3$, the variable F_α is set equal to 0.0; and for $\alpha > \alpha_{tran}$, $F_\alpha = 1.0$. Inclusion of $(1 - F_\alpha)$ in Equation (6.1-79) is only a facility to ramp the ξ factor from bubbly to the start of transition region. The contribution of the second term in Equation (6.1-79) is maximum for void fractions less than 0.3, and there is no contribution from that term for void fractions greater than $\alpha = \alpha_{tran}$ (close to the transition region).

An exception to the use of Equation (6.1-78) for C_{ib} in bubbly/churn flow is in the case of flow in the rodded portion of fuel bundles. A special formula for this geometry that covers both bubbly/churn and transition flow regimes will be discussed later.

6.1.9.2 Bubbly/Churn Countercurrent Flows. When $\alpha < \alpha_{tran}$ and flows are countercurrent, the following relations are used.

First, a new interpolation variable, χ, is defined as

$$\chi = \chi_{-1} Min\left[\frac{\alpha}{\alpha_{tran}}, 1\right], \qquad *, X\ (6.1\text{-}81)$$

This interpolation variable, whose value is limited between zero and one in the coding, is used to obtain C_{oc}, C_{1c}, and C_{ic} according to the following relations:

$$C_{oc} = (1 - \chi)C_{ob} + \chi(C_o)_{ccfb} \qquad *, COB\ (6.1\text{-}82)$$

and

$$C_{1c} = (1 - \chi)C_{1b} + \chi(C_1)_{ccfb}, \qquad *, C1B\ (6.1\text{-}83)$$

In these equations, $(C_o)_{ccfl}$, and $(C_1)_{ccfl}$ are chosen from the corresponding parameter values for cocurrent and countercurrent flow situations according to the following comparisons:

$$(C_o)_{ccfb} = Max\left[C_{ob}, (C_o)_{ccfl}\right] \qquad *, COCCFB\ (6.1\text{-}84)$$

and

$$(C_i)_{ccfb} = Min\left[C_{ib}, (C_i)_{ccfl}\right] . \qquad \text{*, CICCFB (6.1-85)}$$

It may be observed that, with a few exceptions, if there is no countercurrent flow, $\chi = 0.0$ and Equations (6.1-82) and (6.1-83) reduce to their equivalents for cocurrent bubbly/churn flow. The interpolation procedure is needed to avoid strong discontinuities and numerical oscillations.

The interfacial friction factor, C_i, for the case of countercurrent flow is the same as given by Equation (6.1-78) that covers both cocurrent and countercurrent flows.

If the entrainment, $E\chi 2$, is less than 90%, Equation (6.1-78) is used as it is. But, for $E\chi 2 > 90\%$, Equation (6.1-78) is modified in the following manner:

$$C_{ibm} = \frac{\rho_\ell^2 \alpha (1-\alpha)^5}{\sigma \xi^4} \left(|C_{ib} V_g - C_{ob} V_\ell|\right)^3 [10(1 - E\chi 2)] . \qquad (6.1\text{-}86)$$

As may be observed, the last term in this equation ramps C_{ibm} smoothly to zero as the entrainment approaches 100%.

6.1.9.3 Special Case of Rodded Channels. In this type of geometry, C_{ib} is given by

$$C_{ib} = \frac{\rho_g \alpha (1-\alpha)^3}{(0.188)^2 D_h} |C_{ib} V_g - C_{ob} V_\ell| \qquad \text{*, CIB (6.1-87)}$$

which is based on Equation (6.1-40) for $\bar{V}_{gj}$.

6.1.9.4 Annular Flow. The distribution parameter, C_o, and C_i for this flow regime are

$$C_{oa} = 1 + \frac{(1-\alpha)(1 - E\chi 2)}{\alpha + \Gamma_4} \qquad \text{*, COA (6.1-88)}$$

and

$$C_{ia} = 1 - \frac{\alpha(1-\alpha)(1 - E\chi 2)}{\alpha + \Gamma_4} \qquad \text{*, CIA (6.1-89)}$$

where

$$\Gamma_4 = \sqrt{\frac{1 + 75(1 - \alpha)}{\sqrt{\alpha}}} \left(\frac{\rho_g}{\rho_\ell}\right) . \qquad \text{*, GAMMA4 (6.1-90)}$$

The origin of these equations is a correlation for interfacial friction factor in annular flow by Wallis.[6.1-13] That correlation is based on annular flow measurements in vertical tubes, with inside diameters of 0.051 and 0.076 m, and in a horizontal tube with 0.025-m diameter. Ishii employed Wallis' correlation to develop expressions for $\bar{V}_{gj}$, C_o, and C_{ia}.[6.1-1] These were then modified for the effect of entrainment by including the term (1 - Ent) and used in TRAC-BF1/MOD1. The interfacial friction term that is derived from the same source is given later.

In order to cover the cases of countercurrent flow with large void fractions, just as in the case of bubbly/churn flow, a comparison is made between the C_o and C_1 values of countercurrent flow and those given by Equations (6.1-88) and (6.1-89), respectively. The countercurrent interpolation factor, χ of Equation (6.1-81) is then used to combine the corresponding variables for the two flow regimes. These are expressed as

$$C_{oaf} = (1 - \chi)C_{oa} + \chi(C_o)_{ccfa} \qquad \text{*, COA (6.1-91)}$$

and

$$C_{1af} = (1 - \chi)C_{1a} + \chi(C_1)_{ccfa} \qquad \text{*, C1A (6.1-92)}$$

where

$$(C_o)_{ccfa} = Max\left[C_{oa}, (C_o)_{ccfl}\right] \qquad \text{*, COCCFA (6.1-93)}$$

and

$$(C_1)_{ccfa} = Min\left[C_{1a}, (C_1)_{ccfl}\right] . \qquad \text{*, C1CCFA (6.1-94)}$$

The interfacial friction factor, combined with $|\bar{V}_r|$ is given by

$$C_{ia} = \frac{0.015}{D_h}\rho_\ell\alpha(\alpha + \Gamma_4)^2\frac{|C_{1a}V_g - C_{oa}V_\ell|}{1 - E\chi 2} \qquad \text{*, CIA (6.1-95)}$$

in which Γ_4 is defined by Equation (6.1-90).

In order to make C_{ia} vanish smoothly when the liquid phase disappears,

whenever $\alpha > 90\%$, the C_{ia} of Equation (6.1-95) is modified according to the following:

$$C_{iam} = 10(1 - \alpha)C_{ia} \ . \qquad \text{*, CIA (6.1-96)}$$

Also, in order to ramp C_{ia} or C_{iam} to a limiting value as $E\chi 2$ approaches 100%, these terms are further modified, as shown below, whenever $E\chi 2 > 90\%$.

$$C_{ia} = 10(1 - E\chi 2)C_{ia} \qquad \text{*, CIA (6.1-97)}$$

$$C_{iam} = 10(1 - E\chi 2)C_{iam} \ . \qquad \text{*, CIA (6.1-98)}$$

6.1.9.5 **Dispersed Droplet Flow.** If flow is cocurrent, both C_o and C_1 are unity, because of the assumption of uniform distribution of the droplets. However, even in this regime, the flows may be countercurrent. In order to allow for either possibility and provide a smooth changeover between the two cases, the following interpolation scheme is employed.

$$C_{od} = (1 - \chi) + \chi(C_o)_{ccfd} \qquad \text{*, COD (6.1-99)}$$

and

$$C_{1d} = (1 - \chi) + \chi(C_1)_{cffd} \qquad \text{*, C1D (6.1-100)}$$

where

$$(C_o)_{ccfd} = Max\left[1.0, (C_o)_{ccfl}\right] \qquad \text{*, COCCFD (6.1-101)}$$

and

$$(C_1)_{ccfd} = Min\left[1.0, (C_1)_{ccfl}\right] \ . \qquad \text{*, C1CCFD (6.1-102)}$$

The product of the interfacial friction coefficient and $|\bar{V}_r|$ in this case is

$$C_{id} = \frac{\alpha(1 - \alpha)}{V_{rod}^4} \Delta\rho g \left(|C_{1d}V_g - C_{od}V_\ell|\right)^3 \ . \qquad \text{*, CID (6.1-103)}$$

6.1.9.6 **Final Interpolations.** The final instructions in the FRCIF

subroutine are some simple interpolations that give C_o, C_j, and C_i, to be used for F_{fg}, in the phasic momentum equations. These interpolations combine the corresponding values of each variable calculated for the three flow regimes, bubbly, annular, and dispersed droplets.

$$C_o = (1 - EX2)C_{oba} + EX2C_{od} \qquad \text{*, CO (6.1-104)}$$

$$C_j = (1 - EX2)C_{jba} + EX2C_{jd} \qquad \text{*, CJ (6.1-105)}$$

$$C_i = (1 - EX2)C_{iba} + EX2C_{id} \qquad \text{*, CI (6.1-106)}$$

where

$$C_{oba} = (1 - X^2)C_{ob} + X^2C_{oa} \qquad \text{*, COBA (6.1-107)}$$

$$C_{jba} = (1 - X^2)C_{jb} + X^2C_{ja} \qquad \text{*, CJBA (6.1-108)}$$

$$C_{iba} = (1 - X^2)C_{ib} + X^2C_{ia} \; . \qquad \text{*, CIBA (6.1-109)}$$

Another factor that is calculated in FRCIF and returned to the momentum solution routine is an interpolated exponent, F_{ac} [or N in Equation 6.1-30)], for the relative velocity in the friction formula. Due to the effect of flow regime on the interfacial area (see Section 6.1.6), the dependence of interfacial friction factor on the relative phasic velocity varies with the flow pattern. In bubbly/churn and droplet flow regimes, the interfacial friction varies with the fourth power of the relative velocity; while in the annular flow regime, it varies with the square of the relative velocity. In the transition zone, an interpolated value of the exponent is used in the numerical integration scheme. The interpolated exponent is obtained with the use of X2, (1- X2), ENT, and (1 - ENT), variables that were described earlier. The following formula is used for the calculation of F_{ac} within FRCIF:

$$F_{ac} = (1 - X2)F_{acb} + X2[(1 - ENT)F_{aca} + ENT\ F_{acd}] \qquad \text{*, FAC (6.1-110)}$$

where

F_{acb} = 2.0, the $\bar{V}$ exponent in Equation (6.1-30) for annular flow

F_{acb} = the $\bar{V}$ exponent in Equation (6.1-30) for bubbly/churn flow

= 4.0 for bubbly flow in pipes, and
= 2.0 for bubbly flow in rodded bundles.

F_{acd} = 4.0, the $\bar{V}$ exponent in Equation (6.1-30) for dispersed droplet flow.

F_{ac} is returned with C_o, C_1, and C_i to the subroutine where the call to FRCIP was initiated.

Variations of C_0, C_1, and C_i with void volume fraction are shown in Figures 6.1-6, 6.1-7, and 6.1-8, respectively. The calculated values are according to Equations (6.1-104), (6.1-105), and (6.1-106) for three different mass velocities at a pressure of 7.0 MPa.

6.1.10 Implementation in Coding

As mentioned at the beginning, presentation of the different equations in this section follow the order of their coding in the FRCIF subroutine rather closely. Hence, as far as the models and correlations are concerned, the coding implementation is already covered to a large extent. However, an important aspect of the coding concerns preparation of variables that are used to initiate a call to FRCIF and the numerical manipulation of the results returned from this subroutine. These aspects, that are different for one-dimensional and three-dimensional cases, are discussed in this section. There are, also, some minor aspects in the coding within FRCIF that are not mentioned in describing the equations. These are elaborated upon here.

6.1.10.1 Coding Aspects within FRCIF. A majority of the coding aspects within the FRCIF subroutine concern inclusion of finite limits for some of the variables in order to avoid division by zero or other discontinuities. Some remedies of this kind were presented as Equations (6.1-79), (6.1-86), (6.1-96), and (6.1-97), all of which provide a smooth ramping to zero for the involved variables. Some of the other noteworthy manipulations in the coding are stated below.

6.1.10.1.1 Comments on C_o.--In the coding after Equation (6.1-20), the calculated value of C_o is limited between that of Equation (6.1-20) and a maximum of 1.33. Furthermore, if the void fraction, α, is larger than 1/1.33, C_o is set equal to $1/\alpha$. These restrictions together make it certain that in no case the calculated C_o exceeds 1.33, a limit that is set by experimental observations.

Also, in coding Equation (6.1-21), the actual mass velocity, G, is increased by 10^{-4} kg/m^2 in order to avoid division by zero. This incremental change in G is completely negligible in all practical cases. There are a number of similar changes in the denominators of other equations. They will not be mentioned individually because of the obvious necessity of these operations.

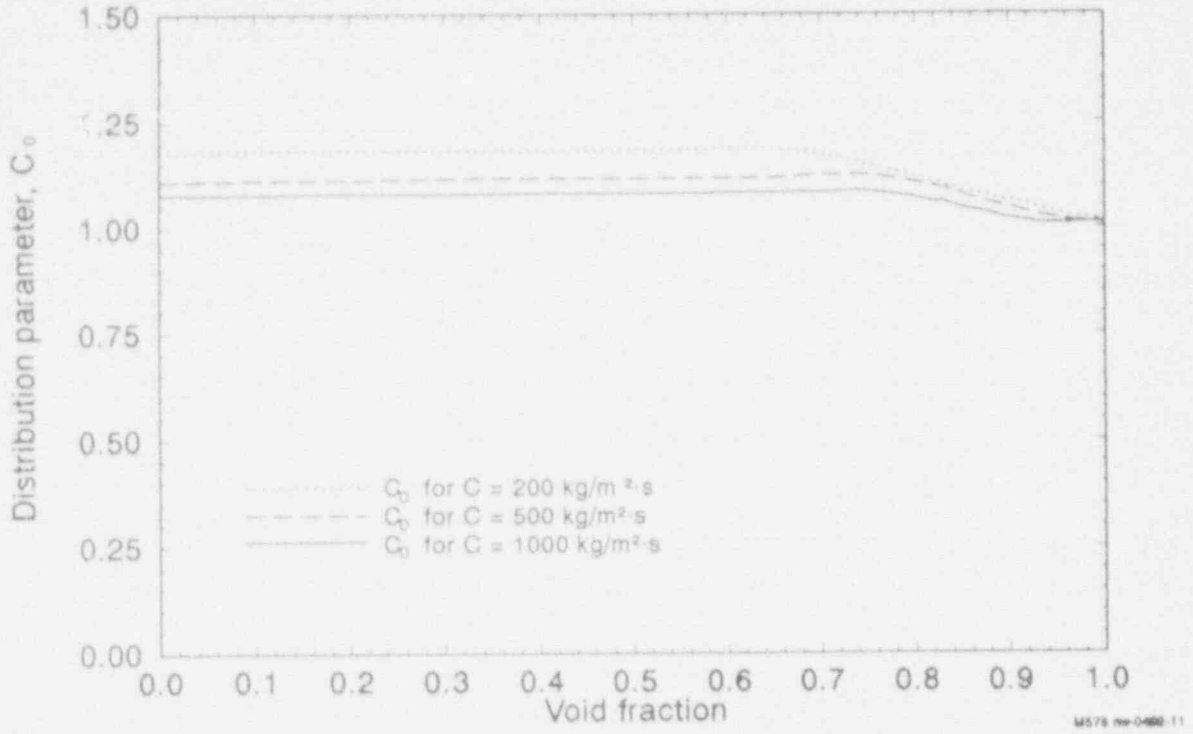

Figure 6.1-6. Variations of the distribution parameter (C_o) with void fraction at different mass velocities, as calculated in the FRCIF subroutine.

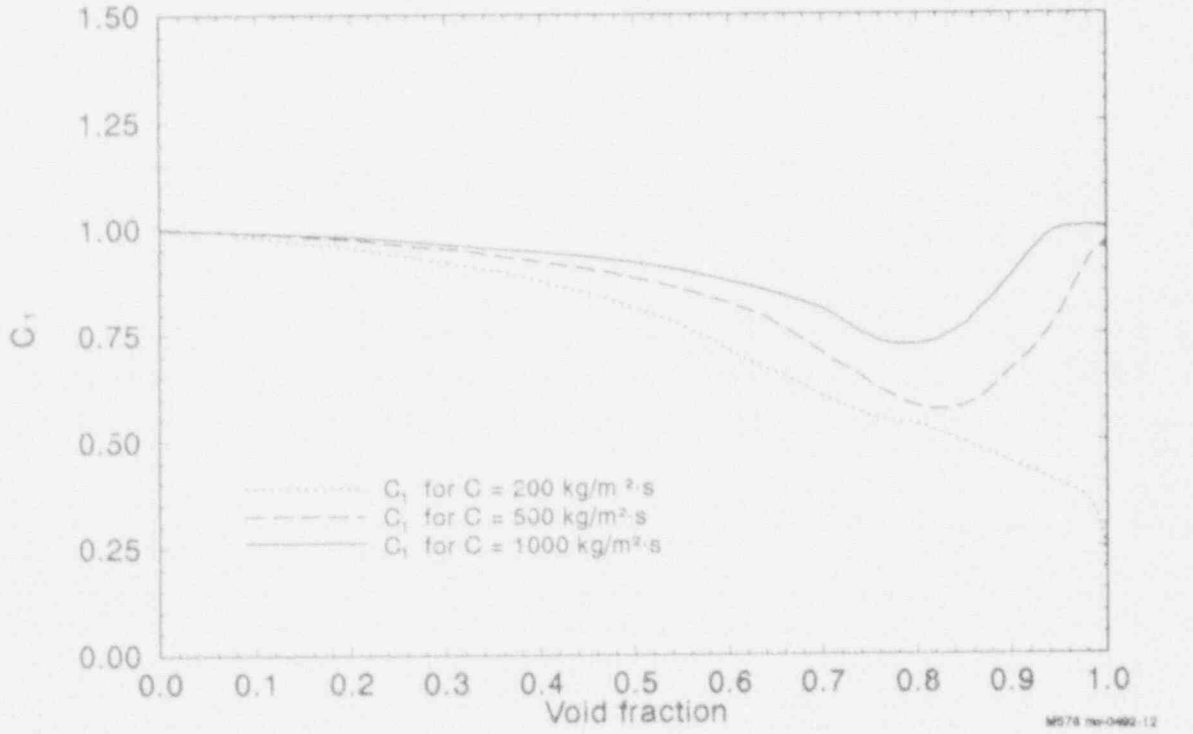

Figure 6.1-7. Variations of the vapor velocity distribution parameter (C_1) with void fraction at different mass velocities, as calculated in the FRCIF subroutine.

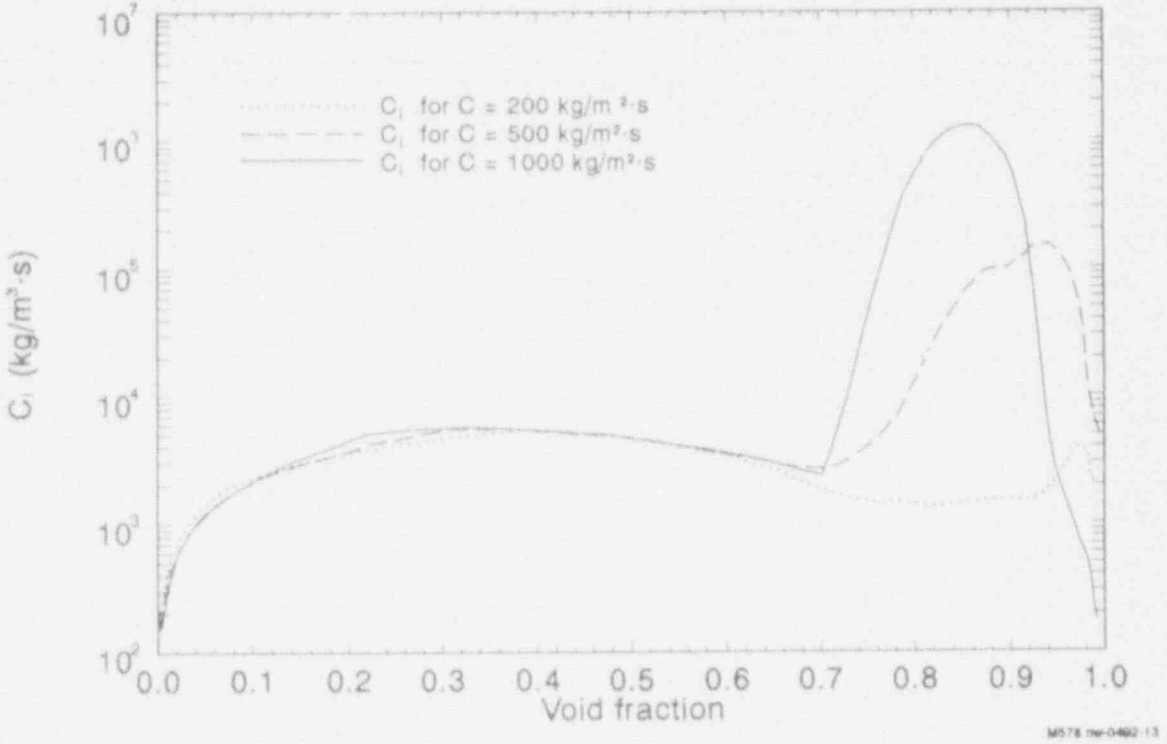

Figure 6.1-8. Variations of the linearized interfacial friction coefficient (C_i) with void fraction at different mass velocities, as calculated in the FRCIF subroutine.

6.1.10.1.2 **Limitation of Re_ℓ**--The Reynolds number for liquid, Re_ℓ, that is used in Equation (6.1-44) for entrainment, has been limited to $(Re_\ell)_{min} = 370$, and lower values of Re_ℓ are replaced with 370. This is in accordance with the source of data used in deriving the entrainment correlation, as reported by Ishii and Mishima.[6.1-14]

6.1.10.1.3 **CCFL Implementation**--For very low void fractions, $\alpha < 10^{-3}$, $(C_o)_{ccfl}$ calculation is bypassed and the following relation is used instead.

$$(C_o)_{ccfl} = Fm^2 \qquad (6.1\text{-}111)$$

where F is defined by Equation (6.1-68).

All other aspects of implementation in coding were included in the discussion of the equations.

6.1.10.2 Preparation of the Input Variables and Numerical Processing of the Results.

6.1.10.2.1 Edge-Centered and Cell-Centered Quantities--The interfacial shear model as described above computes the edge-centered interfacial shear parameters CO, C1, FAC, and CI in subroutine FRCIF using a combination of cell- and edge-centered variables for both one- and three-dimensional component models in TRAC-BWR/MOD1. The edge-centered variables used in the interfacial shear model for both the one- and three-dimensional component models include the cell edge hydraulic diameter and the cell edge phasic velocities. The other variables that are input to subroutine FRCIF are variables whose values are computed by the numerical solution scheme at the cell centers. The values of these variables at the cell edges are computed by subroutines TF1E and TF3E, which call FRCIF for the one- and three-dimensional cells, respectively.

Since the computation of the unknown cell edge parameters is somewhat different for the one- and three-dimensional cells, they will be explained separately.

6.1.10.2.2 Computation of Cell-Centered Properties for One-Dimensional Components--Several of the cell-centered properties whose values at the cell edges must be computed are thermodynamic properties. The phasic densities ($RL = \rho_\ell$) and $RV = (\rho_g)$ at the cell edges are computed by linear interpolation between the values in the center of the cells on either side of the cell edge as

$$RL_{j+1/2} = \frac{DX_j RL_j + DX_{j+1} RL_{j+1}}{DX_j + DX_{j+1}} \tag{6.1-112}$$

where RL is liquid density, DX is the cell length, and where the interpolation is based on the cell lengths. The interpolation for the vapor density is the same.

The cell edge phasic viscosities are computed from the donor cell value based on the direction of the phasic velocity as

$$XMYL_{j+1/2} = WL_{j+1/2} XMYL_j + (1. - WL_{j+1/2}) XMYL_{j+1} \tag{6.1-113}$$

where

$$WL_{j+1/2} = \begin{cases} 1.0 \text{ if } VL_{j+1/2} > 0.3 \text{ m/s} \\ 0.0 \text{ if } VL_{j+1/2} < -0.3 \text{m/s} \\ 0.0 \text{ if } |VL_{j+1/2}| < 0.3 \text{ and } DP_{j+1/2} > 0. \\ 1.0 \text{ if } |VL_{j+1/2} < 0.3 \text{ and } DP_{j+1/2} < 0. \end{cases} \tag{6.1-114}$$

$$DP_{j+1/2} = P_{j+1/2} - P_j \qquad (6.1\text{-}115)$$

and XMYL is the liquid viscosity. The vapor viscosity XMYV at the cell edge is computed in a similar manner, using the donor direction computed using the vapor velocity at the cell edge. The surface tension at the cell edge is computed using the liquid velocity to compute the donor direction in a similar manner to the computation of the cell edge liquid viscosity.

The parameter WAWET, which was defined under Equation (6.1-49), is a cell-centered parameter whose value is the fraction of the total structural surface area in a cell that is wetted by the liquid phase. The surface of a structure (i.e., pipe wall, fuel rod, channel wall) is wetted if the surface is not in the film boiling heat transfer mode (Mode 4), as determined by the surface heat transfer subroutine HTCOR. If a conduction solution is not being performed for a given structure (i.e., NODES = 0 for that structure), the surface is assumed to be wetted. The value of WAWET in the cell on the higher-numbered side of the cell edge is used for all cell edges in a component

$$WAWET_{j+1/2} = WAWET_{j+1} \qquad (6.1\text{-}116)$$

except the last (or highest-numbered) cell edge in the component, which uses the value of WAWET in the cell on the lower-numbered side

$$WAWET_{j+1/2} = WAWET_j \ . \qquad (6.1\text{-}117)$$

The variable CO (C_o notation in coding) is used to pass the subcooled boiling parameter into subroutine FRCIF, where the distribution parameter CO as computed by FRCIF is modified to account for subcooled boiling effects on the cross-sectional distribution of void. The modification as determined by Ishii (see Reference 6.1-1) is

$$CO = CO_{NB,j+1/2}\left(1. - e^{-18\alpha_{j+1/2}}\right) \qquad (6.1\text{-}118)$$

where

CO_{NB} = distribution parameter with no subcooled boiling effect,

C_o = distribution parameter after subcooled modification, and

$\alpha_{j+1/2}$ = void fraction at cell edge j+1/2.

The code uses the variable CO as both an input and as an output variable to subroutine FRCIF. On input,

$$CO_{j+1/2} = 1. - e^{-18\alpha_{j+1/2}} \tag{6.1-119}$$

for all interior cell edges in a component and

$$CO_{j+1/2} = 1.0 \tag{6.1-120}$$

for the cell edges at the ends of a component. In addition, for the interior cell edges, the void fraction is donored, based on the direction of the vapor velocity, and there must be subcooled boiling (QEVAP ≠ 0) on at least one structural surface in the donor cell, as determined by the vapor velocity direction. If the previous conditions are not met for interior cell edges, then CO = 1.0 as for the cell edges at the ends of the component.

Finally, there are three void fractions input to subroutine FRCIF. These void fractions are the void fractions to be convected across the cell edge based on the direction of the phasic velocities and the void fraction at the interface itself. The convected void fractions on either side of the cell edge are the cell-centered void fractions in the cells on either side of the cell edge unless there is a stratified two-phase level in either one of the cells, in which case the level model determines the void fraction to be convected across a given cell edge. The convected void fractions are used in subroutine FRCIF to determine the phasic superficial velocities and mass fluxes at the cell edge. The void fraction at the cell edge is used in subroutine FRCIF to determine the interfacial force per unit volume, the flow regime, and the interfacial shear coefficients.

The cell edge void fraction is computed as the donored value of the convected void fractions using the donor direction based on the mixture superficial velocity when the absolute value of the superficial mixture velocity is greater than 0.3 m/s.

$$\alpha_{j+1/2} = WM_{j+1/2}\alpha^{c}_{j,j+1/2} + (1 - WM_{j+1/2})\alpha^{c}_{j+1,j+1/2} \tag{6.1-121}$$

where

$\alpha_{j+1/2}$ = void fraction at cell edge,

$\alpha^{c}_{j,j+1/2}$ = void fraction to be convected from cell j at cell face j+1/2.

$\alpha^{c}_{j+1,j+1/2}$ = void fraction to be convected from cell j+1 at cell face j+1/2.

$$WM_{j+1/2} = \begin{cases} 1.0 \text{ if } jm_{j+1/2} > 0.3 \text{ m/s} \\ 0.0 \text{ if } jm_{j+1/2} < -0.3 \text{ m/s} \end{cases} \quad (6.1\text{-}122)$$

$$jm_{j+1/2} = VL_{j+1/2}\left[1 - WL_{j+1/2}\alpha_j - (1 - WL_{j+1/2})\alpha_{j+1}\right]$$

$$+ VV_{j+1/2}\left[WV_{j+1/2}\alpha_j + (1 - WV_{j+1/2})\alpha_{j+1}\right] \quad (6.1\text{-}123)$$

and where

$$WM_{j+1/2} = XI^2(3.0 - 2XI) \text{ if } |jm_{j+1/2}| < 0.3 \quad (6.1\text{-}124)$$

$$XI = \left|\frac{jm_{j+1/2} + 0.3}{0.6}\right| \quad (6.1\text{-}125)$$

when the absolute value of the mixture superficial velocity is less than 0.3 m/s. Since the phasic momentum equations are solved simultaneously even in the limit of single-phase flow, the three void fractions input to subroutine FRCIF are limited to be in the range $0.01 < a < 0.999$, so that the interfacial shear does not go to zero as the flow becomes single phase. This is done so that the velocity of the missing phase will be approximately correct when the phase reappears and will not cause a pressure disturbance due to phase reappearance.

6.1.10.2.3 **Computation of Cell-Edge Properties**--There are three cell edges (axial, radial, and azimuthal) associated with each cell in the three-dimensional component, leading to three calls to the subroutine FRCIF for each cell. The phasic densities used in each call are interpolated values as in the one-dimensional component, where the interpolation is based on the distance between cell centers in the appropriate direction. The viscosities and surface tension are not donored, as in the one-dimensional component; rather, the cell-centered value is used for all three cell edges associated with the cell. The fraction of the structural surface in a cell wetted by liquid (WAWET) is likewise used for all three cell edges (axial, radial, and azimuthal) associated with that cell.

A structural surface is assumed to be wetted if its temperature is below the minimum stable film boiling temperature, T_{min}, where T_{min} is set to the critical temperature for water (T_{crit} = 647.30 K) for simplicity. The subcooled boiling modification is disabled (i.e., input CO = 1.0) in the

three-dimensional component for all three cell edges, since subcooled boiling is deactivated for all structural surfaces in contact with fluid in the three-dimensional component by the surface heat transfer logic. The three void fractions for each of the three cell edges associated with each cell in the three-dimensional case are computed in exactly the same way as in the one-dimensional components.

6.1.10.2.4 **Integration Scheme**--The interfacial shear subroutine FRCIF computes four parameters, CI, CO, C1, and FAC, from given input variables, the flow regime selection logic, and the correlations for the average relative velocities between the phases, as described above. This section describes how these four parameters are used to compute the interfacial force per unit volume at the end of a time step in terms of the unknown phasic velocities (at the end of the time step). The interfacial force per unit volume is assumed to obey a force law given by

$$F_{\ell g} = \bar{C} \left(\bar{V}_r\right)^N \tag{6.1-126}$$

where

$F_{\ell g}$ = interfacial force per unit volume

$\bar{C}$ = coefficient

$\bar{V}_r$ = average relative velocity between the phases

$$= C_1 V_v - C_0 V1 \tag{6.1-127}$$

N = flow-regime-dependent exponent.

Expanding this force law into a first-order Taylor expansion to determine interfacial force per unit volume in terms of the known properties at the beginning of the time step gives

$$F_{\ell g}^{n+1} = F_{\ell g}^{n} + \left(\frac{\delta F_{\ell g}}{\delta \bar{V}_r}\right)^n \left(\bar{V}_r^{n+1} - \bar{V}_r^{n}\right) \tag{6.1-128}$$

where the superscripts n and n+1 represent the values at the beginning and end of the time step, respectively. Differentiating the interfacial force law [Equation (6.1-126)] with respect to the average relative velocity between the phases gives

$$\left(\frac{\delta F_{\ell g}}{\delta \bar{V}_r}\right)^n = N\bar{C}\left(\bar{V}_r^{n}\right)^{N-1} = N\frac{\delta F_{\ell g}^{n}}{\delta \bar{V}_r} . \tag{6.1-129}$$

Substituting this into the Taylor expansion for the interfacial force per unit volume gives

$$F_{\ell g}^{n+1} = (1 - N)F_{\ell g}^{n} + N\frac{F_{\ell g}^{n}}{\bar{V}_r^{n}}\bar{V}_r^{n+1} \quad . \tag{6.1-130}$$

The variable CI as computed by subroutine FCIF is defined as

$$CI \triangleq \frac{F_{\ell g}^{n}}{\bar{V}_r^{n}} \tag{6.1-131}$$

and the power N in the interfacial force law is computed as FAC.

Substituting these variables into the expression for the interfacial force per unit volume gives

$$F_{\ell g}^{n+1} = (1 - FAC)CI\left(CI\ V_v^{n} - CO\ V_\ell^{n}\right) + N\ CI\left(CI\ V_v^{n+1} - CO\ V_\ell^{n+1}\right) \tag{6.1-132}$$

which defines the interfacial force per unit volume in terms of the known phasic velocities at the beginning of the time step and the unknown phasic velocities at the end of the time step. This relation is simplified by defining

$$CI' = -(1 - FAC)\ CI\left(CI\ V_v^{n} - CO\ V_\ell^{n}\right) \tag{6.1-133}$$

$$CI' = FAC\ CI\ CI \tag{6.1-134}$$

$$CO' = FAC\ CI\ CO \tag{6.1-135}$$

so that the interfacial force per unit volume is given by

$$F_{\ell g}^{n+1} = -CI' + CI'V_v^{n+1} - CO'V_\ell^{n+1} \quad . \tag{6.1-136}$$

In order to smooth the transitions between flow regimes and to allow larger time steps to be taken, the parameter CI as computed by subroutine FACIF is averaged using an exponential weight factor

$$\overline{CI} = (1 - FFCI)\ CI + FFCI\ CI^{n} \tag{6.1-137}$$

where

$\overline{CI}$ = average value of CI

$$CI = \text{value computed by subroutine FRCIF}$$

$$CI^n = \text{value used during last time step}$$

$$FFCI = EXP(-DELT/0.010) \qquad (6.1\text{-}138)$$

$$DELT = \text{time step size.}$$

This averaging function assumes a time constant of 10 msec for the rate of change of interfacial shear. The averaged value of CI is used to compute the final interfacial coefficients in Equation (6.1-136). Finally, the argument in the exponential weighting function is limited to be less than 20 to prevent an underflow of the exponential function on the computer.

6.1.11 References

6.1-1. M. Ishii, *One-Dimensional Drift-Flux Model and Constitutive Equations for Relative Motion Between Phases in Various Two-Phase Flow Regimes*, ANL-77-47, October 1977.

6.1-2. J. G. M. Andersen and K. H. Chu, *BWR Refill-Reflood Program, Task 4.7 - Constitutive Correlations for Shear and Heat Transfer for the BWR Version of TRAC*, NUREG/CR-2134, EPRI NP-1582, GEAP-24940, December 1981.

6.1-3. J. G. M. Andersen, K. H. Chu, and J. C. Shaug, *BWR Refill-Reflood Program, Task 4.7 - Model Development, Basic Models for the BWR Version of TRAC, NUREG/CR-2573*, EPRI NP-2375, GEAP-22051, September 1983.

6.1-4. M. Ishii, "Recommended Correlations for Interfacial Shear in Post CHF Regime," Letter to Dr. M. W. Young, of U.S. NRC, from Argonne National Laboratory, May 12, 1983.

6.1-5. N. Zuber and J. A. Findlay, "Average Volumetric Concentration in Two-Phase Flow Systems," *Journal of Heat Transfer*, November 1965.

6.1-6. S. Z. Rouhani, *Modified Correlations for Void and Pressure Drop*, AB Atomenergi, Sweden, Internal Report No. AE-RTV 841, March 1969.

6.1-7. N. Zuber, F. W. Staub, G. Bijwaard, and P.G. Kroeger, *Steady State and Transient Void Fraction in Two-Phase Flow Systems*, GEAP-5417, Vol. 1, 1967.

6.1-8. D. Bestion, "Interfacial Friction Determination for the 1D-6 Equations Two Fluid Model Used in the CATHARE Code," *European Two-Phase Flow Group Meeting, Southampton, U. K., June 3-7, 1985.*

6.1-9. P. Saha and N. Zuber, "Point of Net Vapor Generation and Vapor Void

Fraction in Subcooled Boiling," *Proceedings of the 5th International Heat and Mass Transfer Conference, Tokyo, Japan. 1974.*

6.1-11. G. B. Wallis et al., *Countercurrent Annular Flow Regimes in Steam and Subcooled Water in a Vertical Tube*, EPRI NP-1336, January 1980.

6.1-12. K. H. Sun, "Flooding Correlations for BWR Bundle Upper Tie Plates and Side-Entry Orifices," *Second Multi-Phase Flow and Heat Transfer Symposium-Workshop, Miami Beach, Florida, April 16-19, 1979.*

6.1-12. J. F. Wilson, R. J. Grenda and J. P. Patterson, "The Velocity of Rising Steam in a Bubbling Two-Phase Mixture", *ANS Transactions, 5*, 1, 1962, pp. 151-152.

6.1-13. G. B. Wallis, *One Dimensional Two-Phase Flow*, New York: McGraw-Hill Book Co., 1969.

6.1-14. M. Ishii and K. Mishima, *Correlation for Liquid Entrainment in Annular Two-Phase Flow of Low Viscous Fluid*, ANL/RAS/LWR 81-2, March 1981.

6.2 WALL FRICTION CORRELATIONS

Like most other models in TRAC-BF1/MOD1, wall friction correlations are applied to both one-dimensional and three-dimensional calculations.

The general forms of wall shear coefficients for vapor and liquid are:

$$C_{wg} = \frac{\left.\frac{\partial P}{\partial z}\right|_w}{\rho_g (V_g)^2} \qquad (6.2\text{-}1)$$

for vapor, and

$$C_{w\ell} = \frac{\left.\frac{\partial P}{\partial z}\right|_w}{\rho_\ell (V_\ell)^2} \qquad (6.2\text{-}2)$$

for liquid.

The term $\left.\frac{\partial P}{\partial z}\right|_w$ is the static pressure gradient due to friction alone at the wall. The magnitude of this term is obtained from two basic correlations for single-phase and two-phase flows. The nature and origins of these correlations are discussed in this section. The calculated variables C_{wg} and $C_{w\ell}$ are used in the solution of momentum equations for vapor and liquid.

6.2.1 Single-Phase Friction Correlation

TRAC-BF1/MOD1 employs a set of four correlations for single-phase friction factor, depending on Reynolds number and relative wall roughness, $\xi = 2\epsilon/D_h$. These are:

For laminar flow, the single-phase Darcy friction factor is

$$f_{1\varphi} = \frac{64}{Re}, \text{ where } Re < 2300 . \qquad (6.2\text{-}3)$$

For turbulent flow in hydraulically smooth pipes,

$$f_{1\varphi} = \left(\frac{0.28}{\log Re - 0.82}\right)^2 \quad where \quad 2300 < Re < \frac{60}{\xi^{1.111}} \ . \tag{6.2-4}$$

For the transition region between laminar and turbulent flows,

$$f_{1\varphi} = \left|\frac{0.25}{(3.393 - 0.805\, g_1)g_1 - 2.477 - \log \xi}\right|^2 \tag{6.2-5}$$

where $\frac{60}{\xi^{1.111}} < Re < 424\frac{0.87 - \log \xi}{\xi}$; and, finally,

for turbulent flow in effectively rough tubes,

$$f_{1\varphi} = \left(\frac{0.25}{0.87 - \log \xi}\right)^2 \quad where \quad Re \geq 424\frac{0.87 - \log \xi}{\xi} \ . \tag{6.2-6}$$

In these equations,

$$Re = \frac{\rho_m V_m D_h}{\mu_f} \tag{6.2-7}$$

$$g_1 = \log\left(\frac{Re\ \xi}{0.87 - \log \xi}\right) . \tag{6.2-8}$$

Equation (6.2-3) is a classical formula for laminar flow that is found in all hydraulic text books. Equations (6.2-4) through (6.2-6) are due to Pfann[6.2-1] and have been chosen for their accuracy and single-valued form of f that does not require an iterative solution.

6.2.2 The Basis of Pfann Friction Correlations

In an article entitled "A New Description of Liquid Metal Heat Transfer in Closed Conduits," J. Pfann[6.2-1] elaborates on the different formulas used for friction factor calculations. Among these, he compares the well-known correlations of Colebrook and Frenkel with the original works of Nikuradse and the theoretical derivations of Von Karman, regarding the relationship between wall friction and velocity distribution in different conduits. Nikuradse results are given by two equations, one for hydraulically smooth tubes and another one for rough tubes. These are

$$\frac{1}{\sqrt{f}} = 4.0 \log (Re \sqrt{f}) - 0.40 \qquad (6.2\text{-}9)$$

for smooth tubes and,

$$\frac{1}{\sqrt{f}} = 3.48 - 4.0 \log e \qquad (6.2\text{-}10)$$

for fully turbulent flows in rough tubes, where $(e\ Re \sqrt{f})^{-1} > 0.01$. In these equations, e = relative roughness of the tube = e/D_h.

Equations (6.2-9) and (6.2-10) are the basis of many other correlations and charts that have been suggested for friction factor calculation in single-phase flow. According to Pfann,[6.2-1] the Colebrook formula[6.2-2] is obtained analytically as the simplest interpolation between equations (6.2-9) and (6.2-10). Also, a review of Moody's paper[6.2-3] on friction factors for pipe flow indicates that the well-known Moody chart for friction factor in smooth and rough tubes is created essentially with the use of Colebrook's formula that is based on Nikuradse's equations. Following is a brief review of the data base of Nikuradse equations, that is also the basis for Pfann correlations. The aim of this review is to find out whether the data base is relevant to channel geometries encountered in light water reactors.

6.2.3 The Data Base and Range of Applications of Nikuradse Friction Formulas

Equations (6.2-9) and (6.2-10), which are the basis for Pfann's friction factor correlations, were derived on the basis of experimental studies of radial velocity distribution and frictional pressure loss in pipes of different sizes. A review of Nikuradse's experimental studies and range of parameters is given in a brief report entitled "The Laws of Flow in Rough Pipes."[6.2-4] Table 6.2-1 gives a summary of the range of variables in Nikuradse's experiments.

Realizing that the hydraulic diameters of most reactor components, with the exception of the main vessel (the steam dome) and the downcomer, vary from 0.014 to about 0.30 m, it appears that the range of pipe diameters in Table 6.2-1 does cover the dimensions encountered in most parts of light water reactors. Besides, the nondimensional form of the relationships for friction factors provides a logical basis for its extrapolation to larger pipes. In particular, very large diameters and high mass velocities contribute to very large Reynolds numbers that indicate completely turbulent flow for which the friction factor is only a function of the relative wall roughness (e/D_h), regardless of the Reynolds number (see Reference 6.2-3).

Table 6.2-1. Range of variables in Nikuradse experiments on friction factors.

Variable	Description	Range of data base	Remarks
D_h, m	Hydraulic diameter	0.025, 0.050, and 0.10	Channel lengths from 1.0 to 2.5
R_e	Reynolds number	from 600 to 10^6	Water flow
$\xi=2e/D_h$	Relative roughness	from 0.0197 to 0.067	

6.2.4 Comparison of Pfann's Correlations with Other Forms of Friction Factor Formulas

Pfann's article[6.2-1] provides a basic review of the formulas for friction factors with no limitations to liquid metals (not withstanding the title and the main topic of the article). In particular, the appendix in Pfann's article includes some approximations to the original Nikuradse equations that simplify the computation procedure. These were given by Equations (6.2-4) to (6.2-6) above. A study of the effect of the simplified formulations is presented below.

Equation (6.2-3) for laminar flow is the classical formula for laminar flow situations and needs no further qualification in this report.

Equation (6.2-4) for smooth tubes is a close approximation to Nikuradse experimental results for smooth tubes, expressed by Equation (6.2-9). A comparison of these two equations over a wide range of Reynolds numbers is given by Pfann[6.2-1] and reproduced in Table 6.2-2. The table also gives friction factors calculated by Von Karman's theoretical equation for smooth pipes.

Table 6.2-2. Comparison of Pfann friction factors with Nikuradse and Von Karman equations for smooth pipes.[6.2-1]

Re =	$5*10^3$	10^4	$5*10^4$	10^5	$5*10^5$	10^6	10^7	10^8
Pfann	.009458	.007753	.005211	.004467	.003294	.002922	.002052	.001521
Nikur.	.009357	.007727	.005227	.004500	.003281	.002913	.002027	.001486
V. K.	.009417	.007754	.005217	.004484	.003268	.002889	.002003	.001465

It may be observed that the largest relative difference between the Pfann and Nikuradse correlations is about 2.36% at the largest Reynolds number in this table.

For turbulent flow in rough tubes, beyond the limiting values of Reynolds number specified in Equation (6.2-6), the Pfann correlation is analytically

identical to the Nikuradse formula given by Equation (6.2-10), and they need no numerical comparison.

For turbulent flow in the transition region, spanning between hydraulically smooth and rough tubes, an assessment of the Pfann correlation as expressed by Equation (6.2-5) is more difficult. There is a shortage of data in this area, and the literature reflects some dispute over validity of the different correlations. The contradictions over this region may be illustrated by comparing the charts in Figures 6.2-1a and 6.2-1b. Figure 6-2.1a, which is based on the Colebrook formula just like the Moody chart,[6.2-5] shows gradual single-valued transitions of friction factors in going from smooth to rough tubes. However, Figure 6.2-1b, which is generated according to the Pfann correlations, shows a dip in friction factors over the transition region.

Nikuradse has presented experimental data for artificially roughened tubes in the transition region, and those data do reflect the initial dip and the subsequent rise in the friction factors over this area. However, according to some comments in Reference 6.2-3, such trends have not been observed for commercial tubes (without artificial roughening). On the other hand, these comments are not supported by a comparison that is presented in the following.

Except for the original data reported by Nikuradse, there is not a large data base for comparison of friction factor formulas over the turbulent transition region, and a comparison of the Pfann correlation with Nikuradse data in this region would not provide any new information, since Pfann's correlation is based on Nikuradse results. However, some relatively recent data from single-phase friction factor measurements reported by Adorni et al.[6.2-5] do support Nikuradse data and agree fairly well with Pfann's correlation for this region. In Table 6.2-3, two numerical comparisons of the friction factors according to the Pfann and Colebrook correlations (or Moody chart) are presented first; and then the same two correlations are compared with the reported data. Note that the combinations of ξ and Re marked by N/A are outside of the transition region, and this Pfann correlation is not applicable.

As may be observed, Table 6.2-3 indicates some noticeable differences between Pfann and Colebrook correlations over the transition region. The deviations change considerably over a small range of Reynolds numbers for each roughness. A graphical comparison of TRAC-BF1/MOD1 single-phase friction factors with the Colebrook equation over a wide range of Reynolds numbers is provided in Section 6.2.8.

Adorni et al.[6.2-5] has reported some single-phase friction factor measurements for flows of cold and hot water with superheated steam in a round tube of 5.08 mm inside diameter with a surface roughness of ϵ = 4.3 μm. The data, which are presented only graphically in Reference 6.2-5, indicate that measured friction factors go through a minimum value in the turbulent transition region and then increase with increasing Reynolds numbers. Figure 6.2-2 shows a reproduction of Adorni's data in the Von Karman system of

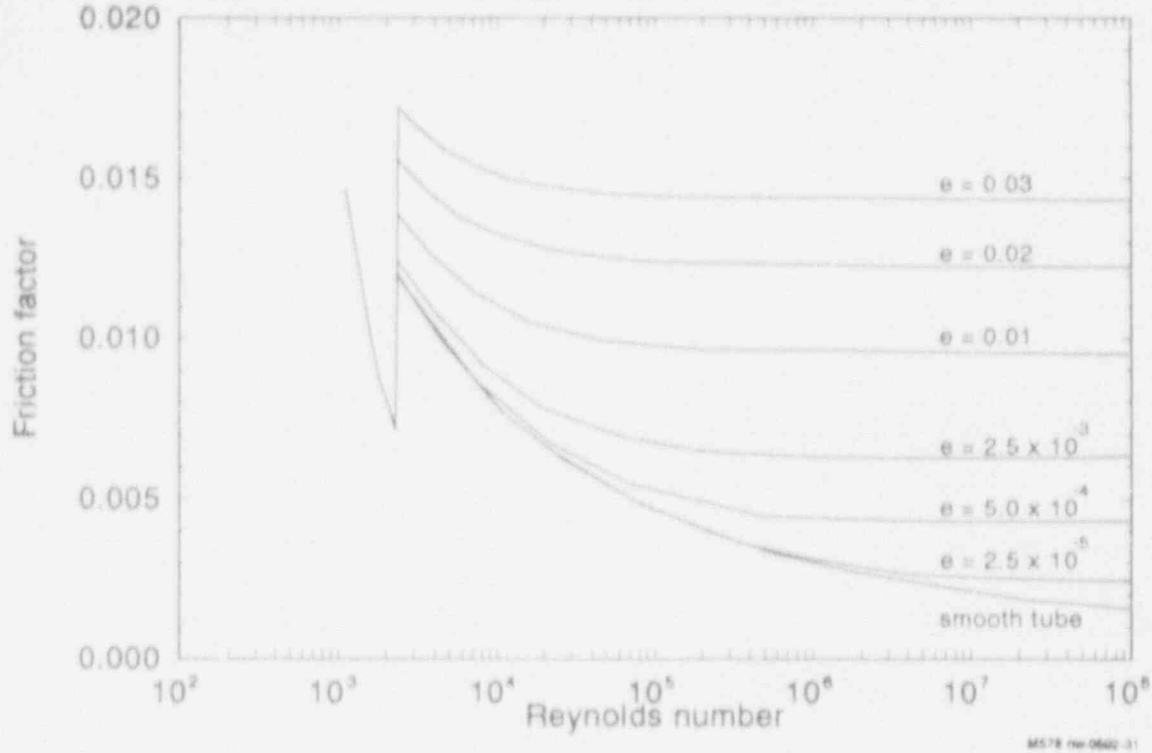

a. Colebrook formula.

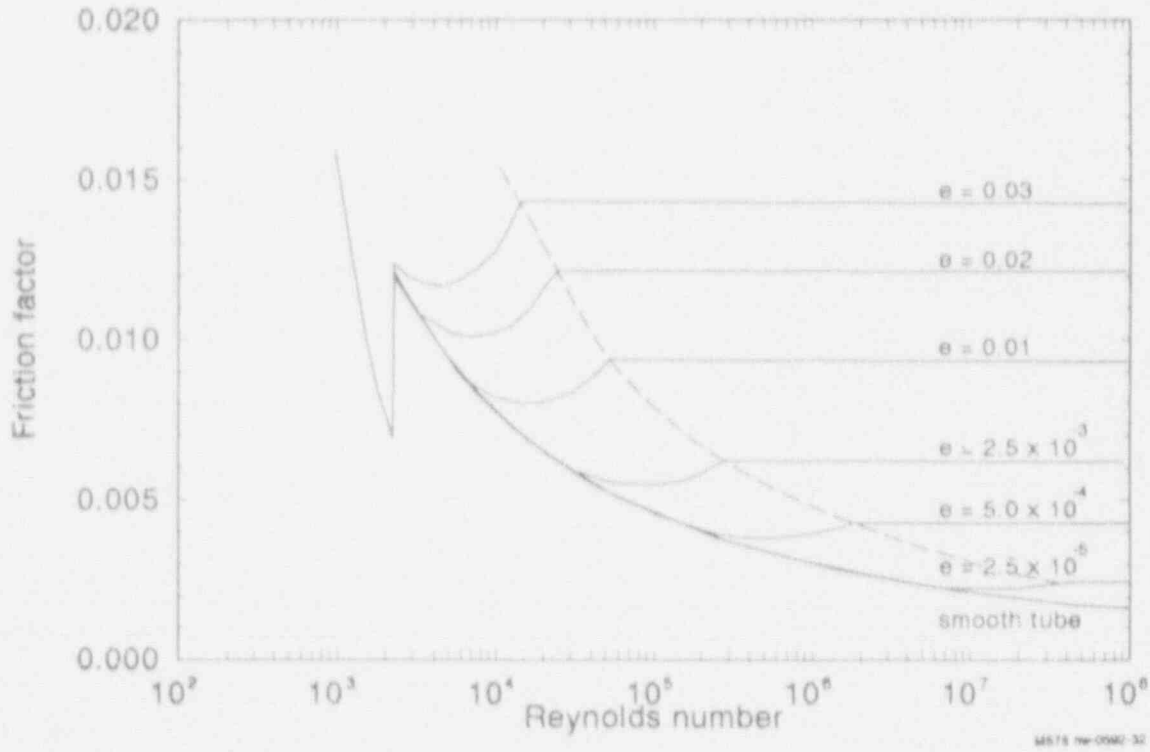

b. Pfann correlations.

Figure 6.2-1. Fanning friction factors.

Table 6.2-3. Comparison of the Pfann correlation with Moody's chart (or Colebrook formula) for rough tubes with relative roughnesses $\xi_1 = 10^{-2}$ and $\xi_2 = 10^{-4}$.

	Re =	$2*10^4$	$3.6*10^4$	$5*10^4$	10^5	$2*10^6$	$5*10^6$	10^7	$5*10^7$
ξ_1	Pf.	0.00678	0.00654	0.00660	0.00725	N/A	N/A	N/A	N/A
	Mo.	0.00862	0.00820	0.00804	0.00782				
	% Diff.	-21.3	-20.2	-21.8	-7.3				
ξ_2	Pf.	N/A	N/A	N/A	N/A	0.00261	0.00242	0.00244	0.00246
	Mo.					0.00295	0.00278	0.00271	0.00265
	% Diff.					-11.5	-13.0	-10.0	-7.7

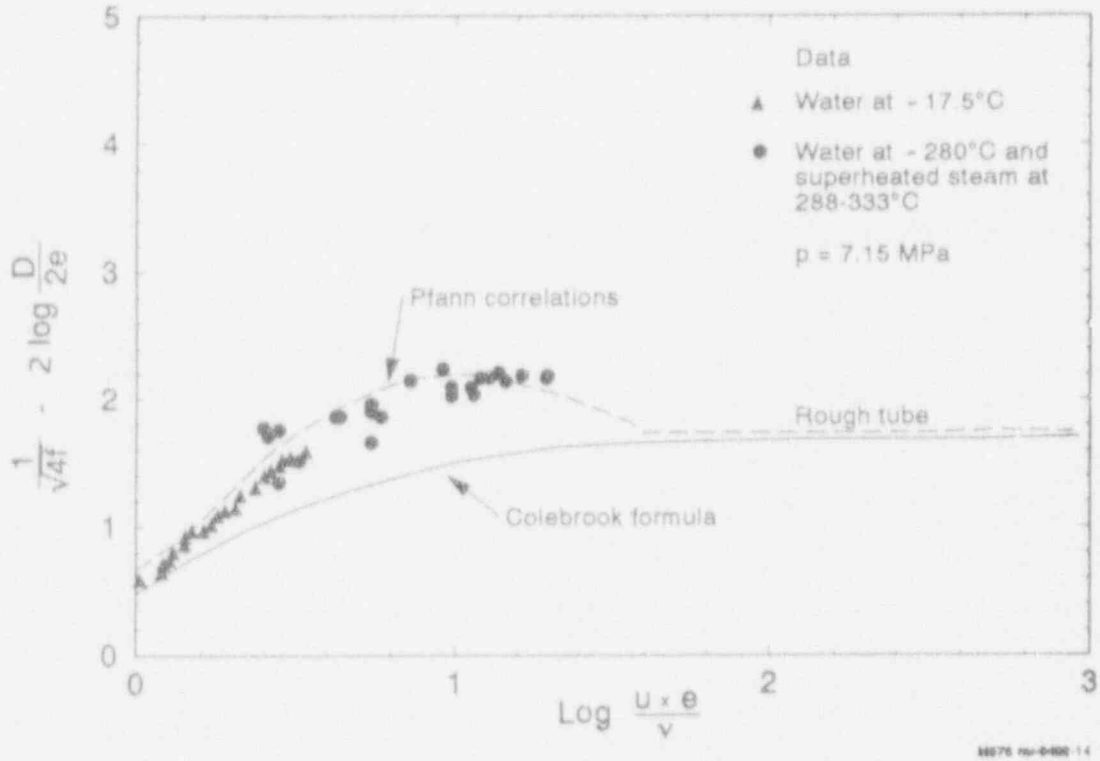

Figure 6.2-2. Comparison of Pfann correlations and Colebrook formula with Adorni's wall friction data from Reference 6.2-5.

coordinates, superimposed by calculations according to the Pfann and Colebrook correlations. As it appears, the Pfann correlation follows the data points rather closely, while the Colebrook formula undershoots the experimental curve considerably (indicating higher friction factors). This comparison provides some confidence in the validity of the Pfann correlation for this region.

6.2.5 Local Friction Losses

Local hydraulic resistances, such as abrupt area contractions or flow restrictions, can be modeled by specifying their form loss coefficients among the inputs. Each restriction may have different loss coefficients for flow in forward and reverse directions; hence, the user may specify separate loss coefficients, k_f and k_g, for forward and reverse directions, respectively. These local loss factors are usually given in terms of Darcy's pressure loss formula, that is

$$\Delta P_k = \frac{1}{2} k \rho V^2 \quad . \tag{6.2-11}$$

The given k values are converted internally in the code to correspond to an equivalent addition to the distributed friction factor over the length of the component. Further explanation is given in Section 6.2.7.

6.2.6 Two-Phase Friction Factor Multipliers

TRAC-BF1/MOD1 calculates two-phase frictional pressure drop as a product of the single-phase friction and a two-phase multiplier. This is the common Martinelli-Nelson[6.2-6] approach. The formula used for calculating the two-phase multiplier depends on the nature of the single-phase frictional pressure loss. For the normal friction along a conduit, the Hancox[6.2-7] multiplier is used; while for local losses, such as in abrupt area changes or across hydraulic restrictions, the two-phase multiplier is simply the ratio of the liquid density to the average mixture density, ρ_ℓ/ρ_m. Further details about these two types of two-phase multipliers are given in the following.

6.2.6.1 Hancox Two-Phase Multiplier. In a paper on prediction of time-dependent diabatic two-phase flows, Hancox and Nicoll[6.2-7] suggest the following correlation for the two-phase multiplier:

$$\phi_\ell^2 = \frac{\tau}{\tau_\ell} = \left\{ 1 + \left[\left(\frac{\rho_\ell}{\rho_g} \right) \left(\frac{\mu_g}{\mu_\ell} \right)^{1/5} - 1 \right] X \right\} \left[1 + RX^{1/2}(1 - X)^{1/4} \right] \tag{6.2-12}$$

where

$$R = 3.1\left(1 - \frac{P_s}{P_c}\right)\exp(-0.000565\ G) \qquad (6.2\text{-}13)$$

τ_ℓ = equivalent single-phase liquid shear stress.

The Hancox correlation has been derived[6.2-8] on the basis of a large number of data from two-phase flow measurements reported by Gaspari et al.,[6.2-9] Adorni et al.,[6.2-5] and Alessandrini et al.[6.2-10]. According to Hancox,[6.2-8] experimental data were used to determine the necessary constants in a generic function that was chosen to embody the following asymptotic behavior:

- $\frac{\tau}{\tau_\ell}$ must approach 1. as X approaches 0.
- $\frac{\tau}{\tau_\ell}$ must approach $\left(\frac{\rho_\ell}{\rho_g}\right)\left(\frac{\mu_g}{\mu_\ell}\right)$ as X approaches 1.
- $\frac{\tau}{\tau_\ell}$ must approach 1. for all values of X as the critical pressure is approached.

The selected functional form includes a dependence on Reynolds number in single-phase friction (expressed as $Re^{-0.2}$), and the final form of his correlation is given by Equation (6.2-1). It should be noted that the constant multiplier in the exponent term of R in Equation (6.2-1) has been wrongly given as 0.0135 in the article, but the correct value is as given above. (The constant is obtained by dividi.g -.00276 in Hancox original report by 4.885, which is the conversion factor for mass velocity from $lb/ft^2 \cdot s$ to $kg/m^2 \cdot s$.)

An advantage of the Hancox correlation over previous two-phase multipliers is its dependence on mass velocity. A comparison of Hancox two-phase multiplier with data from the cited references indicates a mean absolute error of 12%. The data range regarding pressure, flow, and steam quality are summarized in Table 6.2-4.

6.2.6.2 **Homogeneous Two-Phase Multiplier.** The two-phase friction factor multiplier for local restrictions is calculated according to a homogeneous flow model. The formula for this multiplier is

$$\Phi^2_{HOM} = \frac{\rho_\ell}{\rho_m} \qquad (6.2\text{-}14)$$

Table 6.2-4. Ranges of data used in the derivation of the Hancox two-phase multiplier.

	Ref. 6.2-9		Ref. 6.2-5		Ref. 6.2-10	
Parameter	Min	Max	Min	Max	Min	Max
Pressure (MPa)	4.9	8.83	7.12	7.12	5.00	5.00
Mass velocity ($kg/m^2 \cdot s$)	1000	4000	1066	3803	1100	3600
Steam quality (%)	0.0	100.0	0.0	100.	0.0	60.0
Channel diameter (m)	0.005	0.025	0.0051	0.0051	0.015	0.025

where

$$\rho_m = \alpha\rho_g + (1 - \alpha)\rho_\ell \ . \qquad (6.2\text{-}15)$$

This is an empirical relation, suggested by Kay and London,[6.2-11] that applies particularly to the case of abrupt area contractions. Its application to other types of local restrictions is very approximate but provides simplicity in computations.

6.2.7 Implementation in Coding

Wall friction calculations are performed in subroutine FRCW in TRAC-BF1/MOD1. This subroutine employs Equations (6.2-3) through (6.2-6) and Equation (6.2-11) for single-phase and Equations (6.2-12) and (6.2-14) for two-phase multipliers. There are, however, a number of other considerations regarding the way those equations are implemented in the program. These considerations are (a) limitations of variable ranges imposed within the FRIF subroutine, (b) the procedures employed in the preparation of the initial variables before a call to FRCIF, and finally, (c) the way the calculated results are used in one-dimensional and three-dimensional components. These aspects are discussed below.

6.2.7.1 Limitations Imposed within FRCIF. In order to guard against discontinuities and numerical oscillations, it has been necessary to include the following limitations on the extent of variables and range of correlations:

1. Hydraulic diameter values below 10^{-5} m are not used in the friction factor correlations. Instead, the friction factors are set to $f = 0.32$ for both liquid and vapor. This limitation will hardly affect any reactor calculations, since there are no such small diameters in any PWR system.

2. The lowest value of the relative roughness, ξ, is set at 10^{-10}. For

all practical purposes, this represents a very smooth surface; hence, it poses no restrictions on reactor calculations.

3. If a calculated Reynolds number is less than 1.0, it is set equal to 1.0. This limitation poses no restriction in any reactor calculations.

4. The laminar friction factor is not allowed to go below a limiting value corresponding to the turbulent friction factor at Re = 2300. For Reynolds numbers between the useful range of Equation (6.2-3) and Re = 2300, the friction factors are set to a constant determined from the turbulent transition correlation at Re = 2300. This feature is shown graphically as the first flat portion of the f curves in Figure 6.2-3. This modification prevents endless iterations in flow calculations that would result otherwise, due to considerable changes in the friction factors with some slight changes in Reynolds number. The adverse effects of this modification is minimal in reactor calculations, as laminar flow and low Reynolds numbers are seldom encountered. Even when flows diminish in a transient, the switchover to laminar flow is not immediate; hence, the turbulent friction factors apply in reality. The solid curves in Figure 6.2-3 are single-phase friction factors for three different roughnesses, calculated according to the procedure used in the FRCW subroutine in TRAC-BF1/MOD1. For comparison, friction factors according to the Colebrook formula (or Moody chart) are also shown in Figure 6.2-3 for the same roughnesses. The largest differences between the two sets are observed over the transition zone, as discussed in Section 6.2.1, with the quantitative examples given in Table 6.2-3.

5. Local loss coefficients are normalized over the length of corresponding hydraulic cells and, after multiplying by their homogeneous two-phase factors (see Section 6.2.2), they are added to the friction factors of the straight segments. This is expressed by the following relations:

$$f_{add} = 0.25\, k_i \frac{D_h}{L} \tag{6.2-16}$$

representing the local loss factor k_i in terms of an added friction factor along the cell length, L. k_i represents the local loss factor for forward or reverse flow directions, and,

$$f_{tot} = f_{1\phi}\Phi_{fl}^2 + f_{add}\Phi_{hom} \,. \tag{6.2-17}$$

Finally, the total frictional pressure drop is obtained by the following expression in the code.

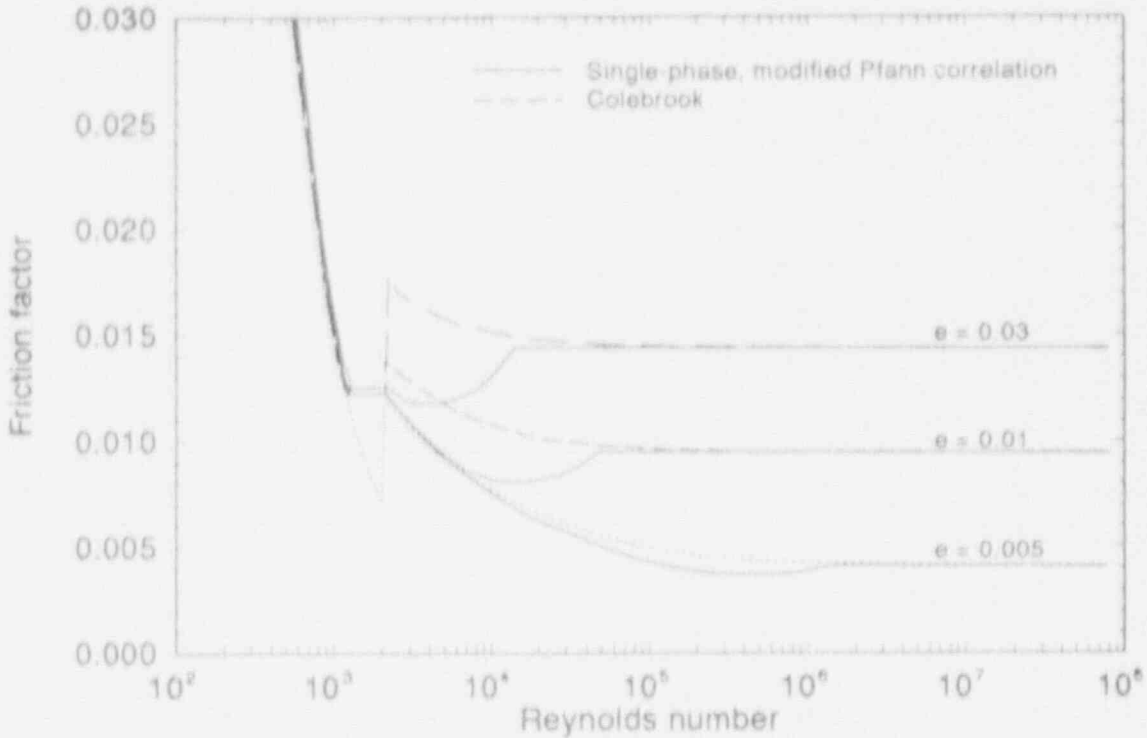

Figure 6.2-3. Single-phase friction factors according to the Pfann correlations as modified in TRAC-BF1/MOD1 (solid lines). Colebrook friction factors are shown with dashed lines for comparison.

$$\left(\frac{dP}{dz}\right)_{tot} = \frac{2f_{tot}G_{ave}^2}{\rho_\ell} \quad . \tag{6.2-18}$$

6. In the final calculations of C_{wg} and $C_{w\ell}$, according to Equations (6.2-1) and (6.2-2), a lower limit is imposed on the absolute values of V_g and V_ℓ to avoid division by zero. This minimum limit of velocity is 10^{-10} m/s; and, for all practical purposes, it has no influence on reactor calculations.

6.2.7.2 Calculation of Initial Variables. The wall shear model as described in the sections above computes the edge-centered phasic wall shear coefficients, using a combination of cell-centered and edge-centered variables. The edge-centered variables can be used directly and include the surface roughness, the hydraulic diameter, the phasic velocities, the singular loss coefficient, and the additive pressure gradient (only used by the mechanistic separator model). Cell-centered variables whose value at the cell

edge must be computed are the void fractions, pressure, phasic viscosities, phasic densities, and the mixture mass flux. The final input variable for the wall friction subroutine is the distance between the centers of the two cells that are separated by the cell edge under consideration. This distance is computed from the user-input cell geometry.

The computation of the unknown edge variables is different in the one-dimensional and three-dimensional components and will be discussed separately.

6.2.7.2.1. Computation of Cell-Edge Variables for One-Dimensional Components--The void fraction used in the wall shear routine has the same value as the void fraction used in the interfacial shear model and will not be described here (see Section 6.1).

The pressure at the cell-edge is a donor weighted value based on the vapor velocity direction

$$P_{j+1/2} = P_j WV_{j+1/2} + P_{j+1}(1. - WV_{j+1/2}) \tag{6.2-19}$$

where the donoring parameter is given by

$$WV_{j+1/2} = \begin{cases} 1.0 & \text{if } V_{g(j+1/2)} \geq 0.3\ m/s \\ 0.0 & \text{if } V_{g(j+1/2)} \leq 0.3\ m/s \\ 0.5 - SIGN\ (0.5,\ DP_{j+1/2}) & \text{if } |V_{g(j+1/2)}| < 0.3\ m/s \end{cases} \tag{6.2-20}$$

and

$$DP_{j+1/2} = P_{j+1} - P_j \ . \tag{6.2-21}$$

The phasic viscosities at the cell edge are the donor-weighted values where the donoring parameter is computed for each phase using its own velocity.

The phasic densities at the cell edges are linearly interpolated values based on the lengths of the cells on each side of the cell edge under consideration

$$\rho_{g(j+1/2)} = \frac{DX_j \rho_{gj} + DX_{j+1} \rho_{g(j+1)}}{DX_j + DX_{j+1}} \ . \tag{6.2-22}$$

A similar equation calculates liquid density. The mixture mass flux is the sum of the phasic mass fluxes, which are in turn computed as the product of the macroscopic density of each phase at the cell edge and the phasic velocity at the cell edge. Like the phasic densities, the macroscopic densities at the cell edge are linearly interpolated based on the lengths of the cells on

either side of the cell edges under consideration.

$$(\alpha\rho_g)_{j+1/2} = \frac{(\overline{\alpha\rho_g})_{j+1/2}DX_j + (\overline{\alpha\rho_g})_{(j+1),(j+1/2)}DX_{j+1}}{DX_j + DX_{j+1}} . \quad (6.2\text{-}23)$$

Again, a similar equation is used for the liquid phase. The average macroscopic phase density used in the linear interpolation is the cell-centered macroscopic phase density unless a stratified two-phase level exists between the center of the cell and the cell edge under consideration.

If a two-phase level exists, then the average macroscopic phase density is computed using the above-level and below-level void fractions as determined by the level model and the relative position of the level between the cell center and the edge under consideration to determine an average void fraction in the space between the cell center and the cell edge. This average void fraction is then multiplied by the cell-centered phasic density to give the average macroscopic phase density to be used in the interpolation scheme.

$$(\overline{\alpha\rho_g})_{j,j+1/2} = (\rho_g)_j \frac{(DX_j - DL_j)\alpha_{A,j} + DL_j\alpha_{B,j}}{0.5\ DX_j} \quad (6.2\text{-}24)$$

where

DX_j = cell length

DL_j = distance between level position and cell center.

For the liquid phase, the liquid fraction is used rather than the vapor fraction.

The mixture mass flux is computed from the phasic mass fluxes as

$$GM_{j+1/2} = GL_{j+1/2} + GV_{j+1/2} \quad (6.2\text{-}25)$$

$$GL_{j+1/2} = \overline{(1-\alpha)}\overline{\rho}_{\ell(j+1/2)}V_{\ell(j+1/2)} \quad (6.2\text{-}26)$$

$$GV_{j+1/2} = \overline{\alpha\rho}_{g(j+1/2)}V_{g(j+1/2)} . \quad (6.2\text{-}27)$$

The sign of the mixture mass flux is then used to choose which of the two input singular loss coefficients will be used at the cell edge

$$K_{j+1/2} = \begin{cases} K_{f,j+1/2} \text{ if } GM_{j+1/2} \geq 0 \\ K_{r,j+1/2} \text{ if } GM_{j+1/2} < 0 \end{cases} \quad (6.2\text{-}28)$$

where

$K_{j+1/2}$ = singular loss coefficient to be used in the calculation of the wall friction parameters,

$K_{f,(j+1/2)}$ = user-input singular loss coefficient for forward flow at cell edge j+1/2

$K_{r,(j+1/2)}$ = user-input singular loss coefficient for reverse flow at cell edge j+1/2.

6.2.7.2.2 Computation of Edge Variables for Three-Dimensional Components--The calculation of the edge variables in the three-dimensional components is identical to those in the one-dimensional components for the three cell edges (axial, radial, and azimuthal) associated with cells in the three-dimensional components with the following exceptions.

The pressure and phasic viscosities in the cell are used instead of donor-weighted values as in the one-dimensional components, and the presence of a stratified two-phase level is only taken into account in the computation of the mixture mass flux in the axial direction. All of the other variables are computed in the same way as in the one-dimensional components.

6.2.7.3 Implementation of the Calculated Results in Momentum Equations. The previous sections have described the wall friction subroutine FRCW and the computation of the input quantities for this subroutine. This section describes how the quantities computed by subroutine FRCW are manipulated to obtain the wall frictional force on each phase for use in the momentum equation. The implementation of the wall friction in the one-dimensional and three-dimensional components is different and will be discussed separately for the two types of components.

6.2.7.3.1 Implementation in One-Dimensional Components--The wall shear subroutine FRCW first computes the total pressure gradient due to shear at the wall as a function of the conditions at the beginning of the time step. The wall shear coefficients are then computed as the ratio of the total wall pressure gradient to the kinetic energy of each phase

$$CFWL = \frac{\left.\frac{dP}{dz}\right|_w^n}{\rho_\ell^n \left(V_\ell^n\right)^2} \tag{6.2-29}$$

$$CFWV = \frac{\left.\frac{dP}{dz}\right|_w^n}{\rho_g^n \left(V_g^n\right)^2} \tag{6.2-30}$$

and the wall shear coefficients are returned to the subroutine that called FRCW. We want to linearize the wall friction in such a way as to make it a function of the mixture mass flux, which itself is a function of both of the unknown phasic velocities. One way to do this is to write the end-of-time-step total pressure gradient due to wall friction as

$$\left.\frac{dP}{dz}\right|_w^{n+1} = \alpha^n \rho_g^n CFWV \left|V_g^n\right| V_g^{n+1} + (1. - \alpha^n) \rho_\ell CFWL \left|V_\ell^n\right| V_\ell^{n+1} . \tag{6.2-31}$$

This force is divided between the phases using the void fraction as a measure of the surface area in the cell melted by each phase. (The void fraction is used to be consistent with the assumptions used to convert the drift flux correlations into interfacial drag coefficients.) We obtain

$$\left.\frac{dP}{dz}\right|_{w,g}^{n+1} = \alpha \left.\frac{dP}{dz}\right|_w^{n+1} = (\alpha^n)^2 \rho_g^n \, CFWV \left|V_g^n\right| V_g^{n+1} + \alpha^n (1. - \alpha^n) \rho_\ell^n CFWL \left|V_\ell^n\right| V_\ell^{n+1} \tag{6.2-32}$$

and

$$\left.\frac{dP}{dz}\right|_{w,\ell}^{n+1} = (1. - \alpha) \left.\frac{dP}{dz}\right|_w^{n+1} = (\alpha^n)(1. - \alpha^n) \rho_g^n \, CFWV \left|V_g^n\right| V_g^{n+1} + (1. - \alpha^n)^2 \rho_\ell^n CFWL \left|V_\ell^n\right| V_\ell^{n+1} \tag{6.2-33}$$

The wall shear force appears in the momentum equations as a force divided by an inertia (to obtain the acceleration due to the force) for the gaseous and liquid phases, respectively, which can be written as

$$\frac{C_{wg} \left|V_g\right| V_g}{\left[\overline{\alpha \rho_g}\right]}$$

and

$$\frac{C_{wi}\,|V_i|\,V_i}{\left[(1.-\alpha)\rho_i\right]}$$

for the gaseous and liquid phases, respectively, which can be written as

$$\alpha^n\ CFWV\ \left|V_g^n\right|V_g^{n+1} + (1.-\alpha^n)\frac{\rho_i^n}{\rho_g^n}CFWL\ \left|V_i^n\right|V_i^{n+1}$$

and

$$\alpha^n\ \frac{\rho_g^n}{\rho_i^n}CFWV\ \left|V_g^n\right|V_g^{n+1} + (1.-\alpha^n)CFWL\ \left|V_i^n\right|V_i^{n+1}\ .$$

6.2.7.3.2 **Implementation in Three-Dimensional Components**--The implementation of the wall shear in the three-dimensional components is simpler than in the one-dimensional components. As for the one-dimensional components, the total wall shear is split between the phase using the void fraction, but the linearization is simpler. The wall shear on each phase is written as

$$\left.\frac{dP}{dz}\right|_{w,g}^{n+1} = \alpha\left.\frac{dP}{dz}\right|_{w}^{n+1} = \alpha^n\rho_g^n\ CFWL\ \left|V_g^n\right|V_g^{n+1} \qquad (6.2\text{-}34)$$

and

$$\left.\frac{dP}{dz}\right|_{w,i}^{n+1} = (1.-\alpha)\left.\frac{dP}{dz}\right|_{w}^{n+1} = (1.-\alpha^n)\rho_i^n\ CFWL\ \left|V_i^n\right|V_i^{n+1}\ . \qquad (6.2\text{-}35)$$

6.2.8 Conclusions

The detailed review of the wall friction calculation in TRAC-BF1/MOD1 that is presented in this section shows that there is a solid basis for the choice of formulas used for those calculations. The correlations used for single-phase friction factors include the classical formulas given in the technical literature for laminar flow, turbulent flow in smooth pipes, and fully developed turbulent flow in rough pipes. The correlation used for turbulent transition region shows deviations from Colebrook formula and Moody chart over a short range of Reynolds numbers. However, it gives considerably better agreement with the limited data available in this region. The chosen correlations are also very suitable for rapid calculations.

Hydraulic loss coefficients due to local restrictions are normalized over the hydraulic cell length and used as an added friction factor along the length of that cell.

WALL FRICTION

The effect of two-phase flow on friction losses is calculated by using two-phase multipliers. The Hancox correlation is used for straight channel parts, and the homogeneous two-phase multiplier is used for local restrictions. Both of these correlations are supported by considerable experimental observations.

The coding of wall friction calculations follows the nature of equations exactly, except for a few restrictions imposed on the range of parameters to be used in the equations (such as hydraulic diameters or absolute phase velocities). These restrictions are necessary for stability of numerical solutions, and none of them has any noticeable effect on reactor calculations.

6.2.9 References

6-2.1. J. Pfann, "A New Description of Liquid Metal Heat Transfer in Closed Conduits," *Nuclear Engineering and Design, 41*, 1977, pp. 149-163.

6-2.2. F. Colebrook, "Turbulent Flow in Pipes with Particular Reference to the Transition Region Between the Smooth and Rough Pipe Laws," *Journal of the Institution of Civil Engineers, 11*, 1938-1939, pp. 133- 156.

6-2.3. L. F. Moody, "Friction Factors For Pipe Flow," *Transactions of the ASME, 66*, 8, November 1944, pp. 671-684.

6-2.4. J. Nikuradse, "Laws of Flow in Rough Pipes," *Mechanical World, 95*, 2464, March 23, 1934, p 274.

6-2.5. N. Adorni et al., *Description of a Loop for Heat Transfer Experiments with Steam-water Mixtures (Part I), and of Pressure Drop Measurements in Diabatic Conditions (Part II)*, CISE-R-62, 1962.

6-2.6. R. C. Martinelli and D. B. Nelson, "Prediction of Pressure Drop Forced-Circulation Boiling of Water," *Transactions of the ASME, 70*, 1948, p. 695.

6-2.7. W. T. Hancox and W. B. Nicoll, "Prediction of Time Dependent Diabatic Two-phase Water Flows," *Progress in Heat and Mass Transfer, 6*, 1972, pp. 119-135.

6-2.8. T. W. Hancox, *Prediction of Oscillating Diabatic Steam-water Flow*, Ph. D. Thesis, University of Waterloo, 1971.

6-2.9. G. P. Gaspari et al., *Pressure Drops in Steam-Water Mixtures, Round Tubes-Vertical Upflow*, CISE-R-83, 1964.

6-2.10. A. Alessandrini et al., *Critical Heat Flux and Pressure Drop Measurements in Round Vertical Tubes*, CISE-R-86, 1963.

6-2.11. W. M. Kay and A. L. London, *Compact Heat Exchanger*, Palo Alto, CA: National Press, 1958.

6.3 LEVEL TRACKING MODEL

This section documents the liquid level tracking model presently used in the TRAC-BF1/MOD1 computer code. In early versions of TRAC-B, the cell void fraction was assumed to be uniformly distributed throughout each hydrodynamic volume. In many cases (in particular, vertically oriented cells), this can result in numerical solutions to the governing equations that overcalculate cell-to-cell fluid mass convection. To address this problem, a level tracking model originally developed by General Electric and subsequently modified by INEL was installed in the TRAC-BF1/MOD1 code.[6.3-1,2] This model has been shown to be capable of simulating a sharp void fraction gradient, which characterizes a two-phase mixture level. Level tracking models have been developed for both three-dimensional and one-dimensional components.

The remainder of this chapter is outlined as follows: Section 6.3.1 summarizes the TRAC-BF1/MOD1 level modeling methodology and implementation. Section 6.3.2 documents the details of the criteria used to detect a mixture level in a particular cell. Section 6.3.3 documents the models and correlations used to calculate the position of a mixture level if it exists. Section 6.3.4 documents the criteria for determining when a mixture level will cross a cell boundary. Section 6.3.5 gives conclusions relative to the applicability of the TRAC-BF1/MOD1 level tracking model.

6.3.1 Summary of Level Tracking Methodology and Implementation

The TRAC-BF1/MOD1 level tracking model was integrated into the code via two subroutines, LEV1D and LEV3D, for the one- and three-dimensional components, respectively. Both tracking models are programmed to work in the following sequence:

1. For each vertically oriented cell, the coding first searches for the presence of a two-phase mixture level from criteria based on the axial void profile around that particular cell.

2. If the presence of a mixture level is found in a particular cell, TRAC-BF1/MOD1 calculates the position of the mixture level and mixture level velocity.

3. Additional tests are performed to see if the mixture level will propagate across a cell edge in the next computational time step.

4. If either conditions 2 or 3 apply, the coding uses updated cell void and/or cell phasic velocities in the TRAC-BF1/MOD1 momentum solution solver.

The logic used in the one-dimensional level tracking model is nearly identical to the three-dimensional model. Because the TRAC-BF1/MOD1 and network solver allows the user to orient one-dimensional components in any

direction (unlike the VESSEL component, which is always assumed to be vertically oriented), allowances have been made to preclude the use of the level tracking model when a one-dimensional component is not vertically oriented.

Presented in Table 6.3-1 is a summary of the physical parameters that are passed to the LEV1D and LEV3D subroutines and the calculated output parameters, which are, in turn, passed back to the routines that solve for the two-phase conversion of mass, momentum, and energy. The parameter definitions in Table 6.3-1 do not necessarily correspond to the actual argument names used in the coding. In addition, there are user-selected option flags to independently activate the one-dimensional or three-dimensional models.[6.3-3] The user can also use level tracking parameters on a global basis for all one-dimensional or three-dimensional components. This information is summarized in Table 6.3-2. How these parameters are implemented in the code level tracking logic is discussed in the following subsections.

A number of the TRAC-BF1/MOD1 level tracking features are considered to be empirical rather than based on first-principal physics derivations. The reader should be cautioned that even though the level tracking model can successfully suppress numerical diffusion or unrealistic cell-to-cell mass convection, this is a necessary but not sufficient condition to guarantee accurate numerical results. The level tracking option is an alternative to employing finely noded cells in a TRAC-BF1/MOD1 computer simulation. The accuracy achieved with finely noded cells may be offset by high computational costs.[6.3-4]

6.3.2 Criteria for Calculating Cell Mixture Level

The logic used by TRAC-BF1/MOD1 to test for the presence of mixture level in a computational cell is based on a certain BWR experimental test data and numerical experiments.[6.3-1,2] The initial step in detecting a two-phase level is to evaluate the axial void profile around a particular hydrodynamic cell. The level detection logic required for a normal (increasing in the upward axial direction) void profile is not the same as the logic required for an inverted (increasing in the downward axial direction) void profile. In general, a level is assumed to exist in cell j if the calculated cell centered void distribution satisfies the following criteria:

$$(\alpha_{j+1} - \alpha_j) > DALPC \text{ or } (\alpha_j - \alpha_{j-1}) > DALPC \text{ and } \alpha_{j+1} > ALPCUT \qquad (6.3\text{-}1)$$

provided that no level exists in cell j+1 or cell j-1 (Figure 6.3-1). Here, DALPC and ALPCUT are predetermined cut off values (Table 6.3-2), which have default values of .2 and .7 or can be specified by the code user.

The criteria for a void profile inversion depends on whether a particular cell is above or below a void inversion. A two-phase level is defined as being below a void profile inversion if

Table 6.3-1. Summary of input and output parameters for TRAC-BF1/MOD1 level tracking routines.

Parameter name	Parameter description
Input Parameters:	
ILEV	Current two-phase level indicator
DZLEV	Current two-phase level position
VLEV	Current two-phase level velocity
ALPP	Current void fraction above two-phase level
ALPH	Current void fraction below two-phase level
ILEVB	Previous two-phase level indicator
ALPN	New-time cell-average void fraction
ALP	Old-time cell-average void fraction
VLN	Liquid velocity
VLV	Vapor velocity
DX	Cell axial length
FA	Cell boundary flow area
VCL	Cell volume
DH	Hydraulic diameter
Output Parameters:	
ILEV	New-time two-phase level indicator
DZLEV	New-time two-phase level position
VLEV	New-time two-phase level velocity
ALPP	New-time void fraction above two-phase level
ALPM	New-time void fraction below two-phase level
VLN	Junction cell liquid velocity
VVN	Junction cell vapor velocity

Table 6.3-2. User-input-specified level tracking parameters

Parameter name	Parameter description
LEVI	Level tracking option flag 1 implies level tracking option on 0 implies level tracking option off
ALPCUT	Minimum allowable cell average void fraction in cell above for a two-phase level to be detected in a cell.
DALPC	Minimum change in cell average void fraction between adjacent cells to detect a two-phase level in a cell.
DALPCI	Minimum change in cell average void fraction between adjacent cells to constitute a void inversion in the level tracking logic.
EPSALPL	Minimum allowable difference between cell average void fraction and above- and below-leve void fraction to allow level to persist. (level will be propagated out of cell if $\alpha_j - \alpha_j^- < EPSALPL$ or $\alpha_j^+ - \alpha_j < EPSALPL$.)

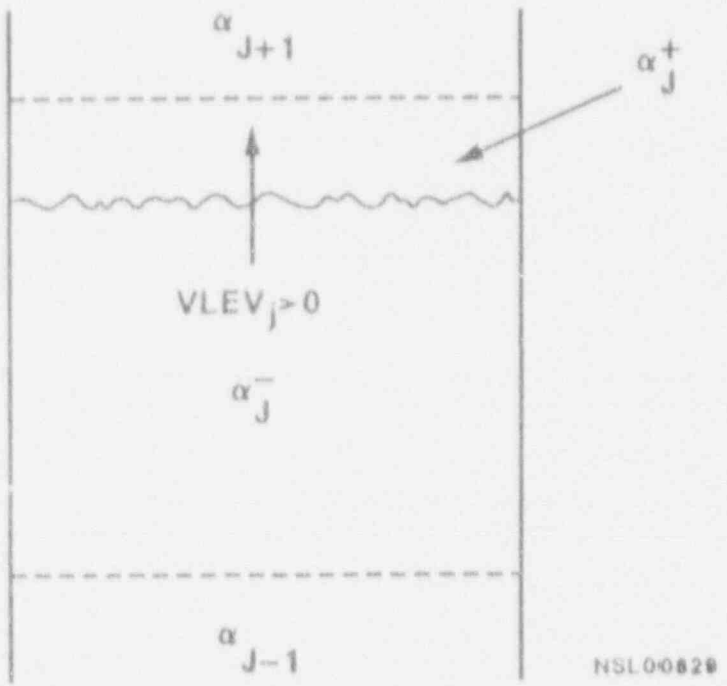

Figure 6.3-1. Two-phase level with normal void profile.

$$\alpha_j - \alpha_{j+1} > DALPCI \quad . \tag{6.3-2}$$

If a void inversion is above a cell, the criteria becomes

$$\alpha_{j-1} - \alpha_j > DALPCI \tag{6.3-3}$$

where DALPCI (Table 6.3-2) is a user-inputted predetermined cut-off value that defaults at .1.

These void inversions are typically the result of liquid pooling in the upper or lower tie plates in a BWR reactor pressure vessel. The coding in the LEV1D and LEV3D subroutines checks for the presence of flow restrictions by calculating the ratioed areas for a cell-to-cell junction:

$$Test\ E = \frac{A_{j+1/2} - A_{j+3/2}}{A_{j+3/2}} \tag{6.3-4}$$

$$Test\ B = \frac{A_{j+1/2} - A_{j-1/2}}{A_{j-1/2}} \quad . \tag{6.3-5}$$

If Test E > .5, the flag is set for an area reduction above cell j; if Test B > .5, a flag is set for a area reduction below cell j. In either case, the code logic automatically initiates a search for a void profile inversion.

If the inlet or outlet cell flow area is less than 1.E-10 m^2, the void profile inversion logic is also automatically activated. The subroutine logic automatically initiates a search for void inversion above or below that particular cell. The level detection logic is further explained in block diagrams given in Figures 6.3-2 through 6.3-5.

6.3.3 Models and Correlations Used to Calculate a Cell Two-Phase Mixture Level Location

Once the TRAC-BF1/MOD1 model logic determines the presence of a level in a particular cell, a level flag is switched on and the parameters necessary to define the level behavior are calculated. The position of the level in cell j of length DZ_j is calculated as

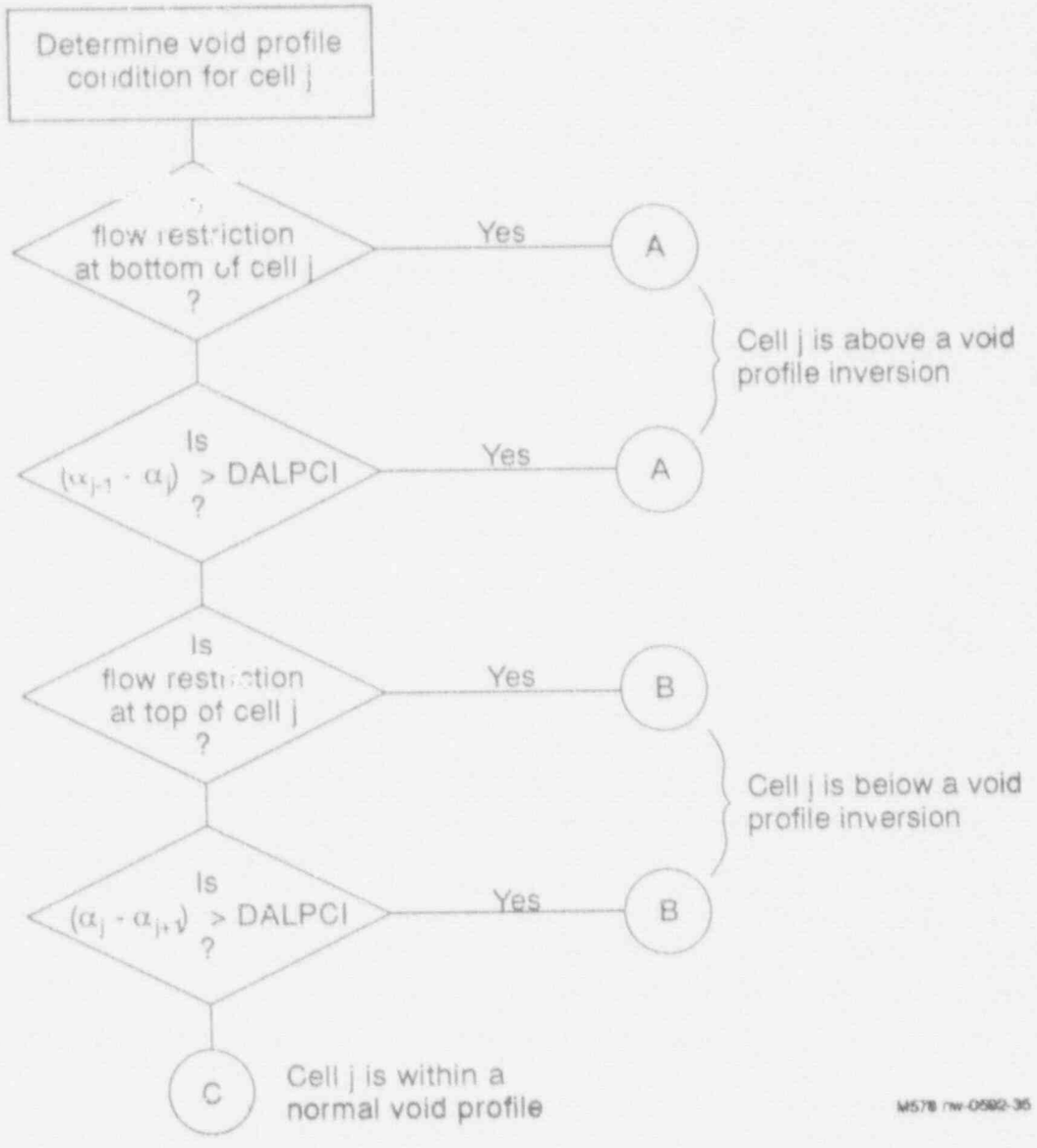

Figure 6.3-2. Level detection logic diagram.

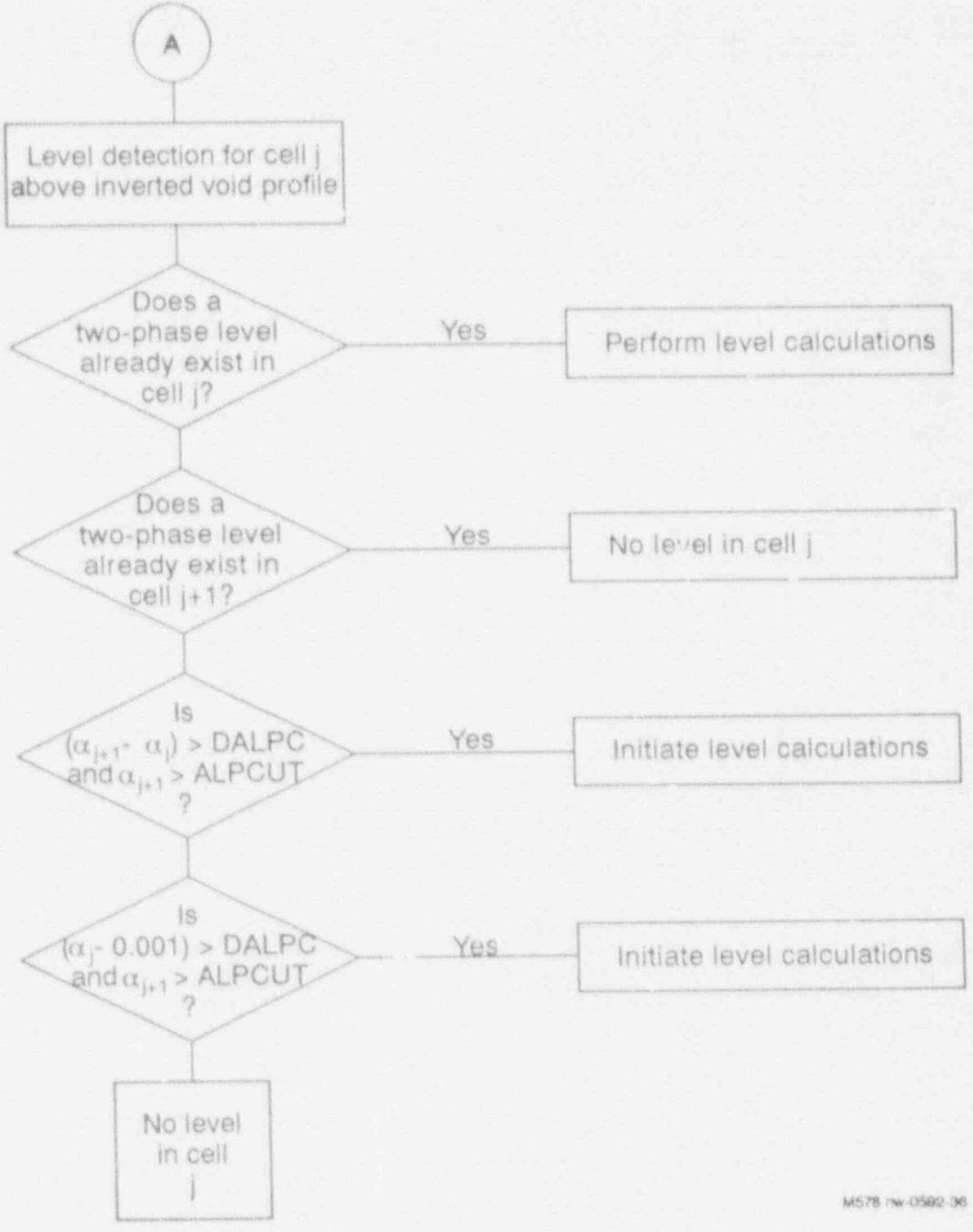

Figure 6.3-3. Level detection logic diagram for cell j above an inverted profile.

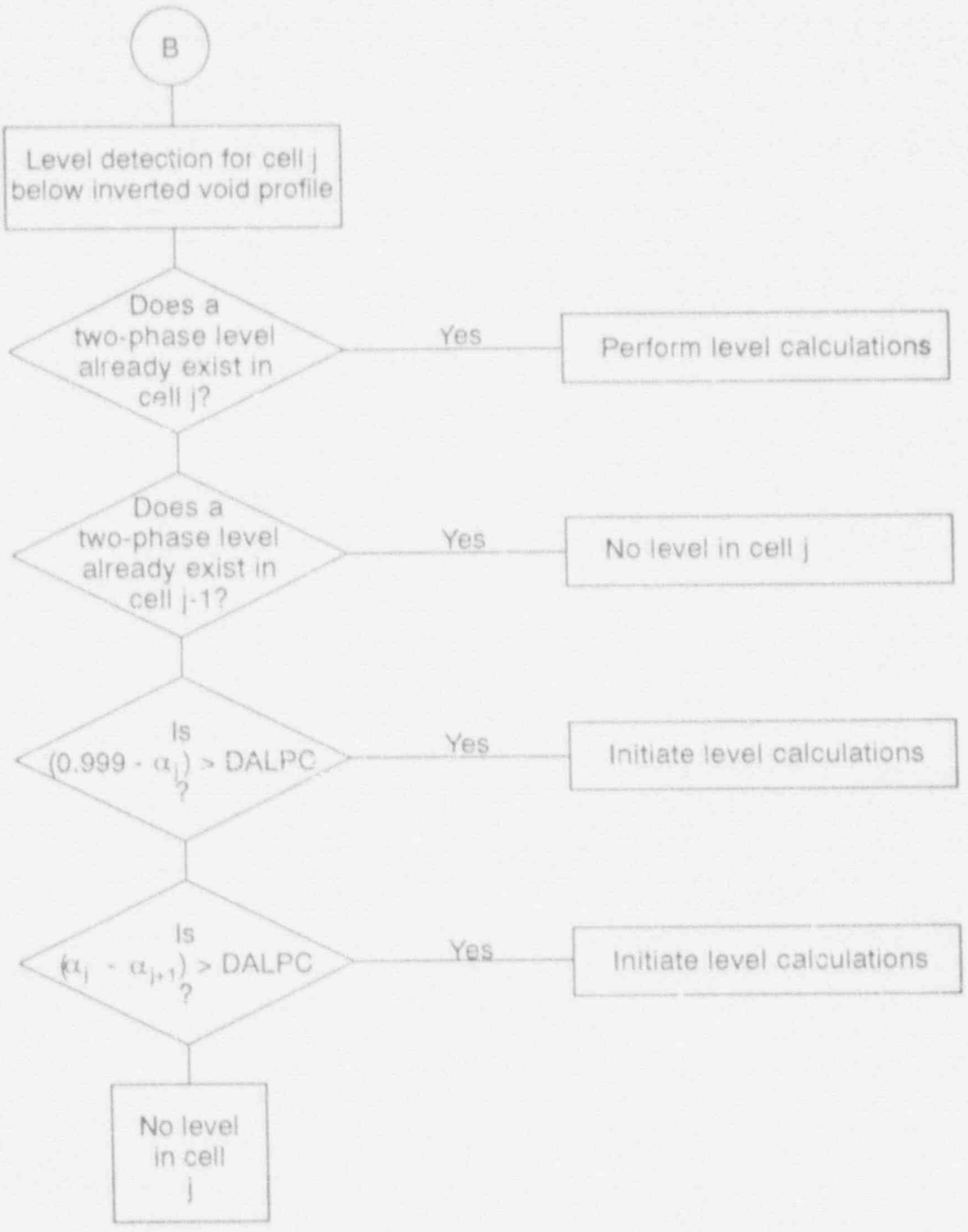

Figure 6.3-4. Level detection logic diagram for cell j below an inverted profile.

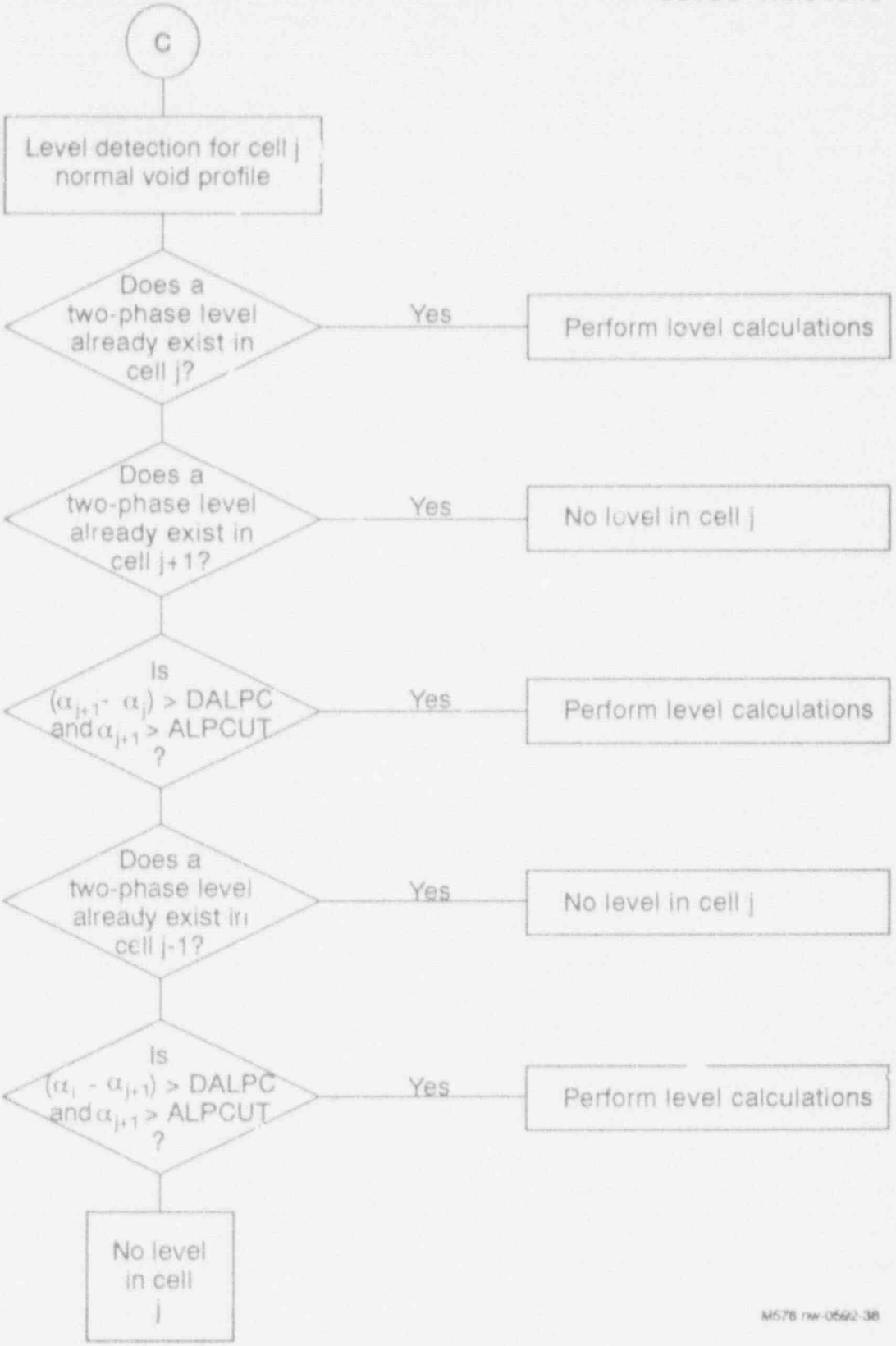

Figure 6.3-5. Level detection logic diagram for normal profile.

$$DZL_j = DZ_j \left(\frac{\alpha_j^+ - \alpha_j}{\alpha_j^+ - \alpha_j^-} \right) \tag{6.3-6}$$

where α_j^+ and α_j^- are the void fractions above and below the mixture level (Figure 6.3-1). The α_j^+ and α_j^- void fractions are calculated on the basis of whether j is part of a normal or inverted void profile. For a normal void profile, the void fraction below the level α is assumed to equal the void fraction in the cell j-1, which is below cell j

$$\alpha_j^- = \alpha_{j-1} \, . \tag{6.3-7}$$

In the absence of liquid entrainment in cell j, the value of α_j^+ would be

$$\alpha_j^+ = \alpha_{j+1} \, . \tag{6.3-8}$$

If the velocity from the previous time step at the top of cell j (Figure 6.3-1) is downward, then no liquid is assumed to be entrained and Equation (6.3-8) is used. If, on the other hand, the velocity at the cell junction is upward, an entrainment correlation developed by Rosen[6.3-5] is used. Liquid entrainment will tend to lower the vapor void fraction above the mixture level. The entrained liquid mass flux is expressed as follows:

$$G_{lent} = \left[3. \times 10^{-5} (CK^{0.5} + 530. \, CK^{2.1}) \left(\frac{\rho_\ell - \rho_g}{\rho_g} \right)^{0.5} \right] J_g \rho_g \tag{6.3-9}$$

where

$$CK = \frac{2. \, DMAX \, J_g}{\left[VCRIT \, g \left(\frac{\sigma}{\rho_\ell - \rho_g} \right)^{0.5} \right]} \tag{6.3-10}$$

$$VCRIT = 2. \left(\frac{\sigma g (\rho_\ell - \rho_g)}{\rho_g^2} \right)^{0.25} \tag{6.3-11}$$

$$DMAX = 0.3375 \frac{\rho_g V_g^2}{g(\rho_\ell - \rho_g)} . \quad (6.3\text{-}12)$$

In the above expression, G_{lent} is calculated using donor cell-averaged values for ρ_j, ρ_g, and α at cell j. The value of J_g is set equal to the trial value (for positive v_g)

$$J_g = \alpha_{j+1} V_g \quad (6.3\text{-}13)$$

where

$$V_g = V_{g,j+1/2} \left(\frac{A_{j+1/2}}{A_j} \right) \quad (6.3\text{-}14)$$

and $v_{g,j+1/2}$ is the junction vapor phasic velocity calculated by the TRAC-BF1/MOD1 momentum solution solver and passed to the level tracking subroutine. The value for the cross-sectional area A_j is calculated by simply dividing the cell j volume by the cell length.

The vapor velocity is weighted by the ratio $A_{j+1/2}/A_j$ to account for velocity field corrections inside the cell j, since the cell outlet area $A_{j-1/2}$ and cell average flow area A_j may not be equal.

By conservation of mass, the liquid mass flux out of the top of the cell j is equal to

$$G_{lent} = (1 - \alpha_j^*) \rho_\ell V_\ell \quad (6.3\text{-}15)$$

from which the above-level void fraction, α_j^*, is computed to be

$$\alpha_j^* = 1 - \frac{G_{lent}}{\rho_\ell V_\ell} \quad (6.3\text{-}16)$$

and

$$V_\ell = V_{\ell,j+1/2} \left(\frac{A_{j+1/2}}{A_j} \right) . \quad (6.3\text{-}17)$$

Again, if either $v_{\ell,j+1/2}$ or $v_{g,j+1/2}$ are negative, α_j^* is automatically set equal

to α_{j+1} and the above computational procedure is bypassed in the calculation.

When the level logic detects a void inversion below cell j (Equation (6.3-2)] or a flow area reduction at the top of cell j, the solution scheme for α_j^* is modified. In this case, the trial volumetric vapor flux used in Equation (6.3-9) becomes

$$J_g = .999\, v_g \tag{6.3-18}$$

where v_g was previously defined by Equation (6.3-14). This trial expression is substituted into Equation (6.3.6), G_{lent} is calculated, and α_j^* is subsequently calculated from Equation (6.3-16). Then, α_j^- and the two-phase level are then calculated using Equations (6.3-7 and 6.3-6). If $v_{g,j+1/2}$ is negative, α_j^* is set equal to .999.

For a cell two-phase level occurring above a void fraction inversion [Equation (6.3-3)] or bottom cell area reduction, the void fraction below the cell mixture level is calculated using the drift flux approximation[6.3-6]

$$\alpha_j^- = \frac{J_g^-}{C_o J^- + V_{gj}} \tag{6.3-19}$$

where

$$V_{gj} = 1.41\left(\frac{\Delta\rho g \sigma}{\rho_\ell^2}\right)^{1/4} \tag{6.3-20}$$

$$C_o = C_\infty - (C_\infty - 1)\sqrt{\frac{\rho_g}{\rho_\ell}} \tag{6.3-21}$$

$$C_\infty = 1.395 - 0.15 \ln (Re) . \tag{6.3-22}$$

These coefficients are calculated assuming a bubbly/churn flow map.[6.3-1,2] The parameters in the coding (C_o and v_g) are based on cell-centered (cell j) quantities. A further discussion of the drift flux formulation is given in Section 4.6.

The volumetric fluxes J_g^- and J^- are calculated using junction-donored velocities from the bottom of cell j and void fractions of either α_{j-1} or α_j^- (old time), depending on whether or not the phasic velocities are positive or negative, respectively. The values of the volumetric fluxes are

$$J_g^- = \frac{1}{2} v'_{g,j-1/2}[(\alpha_{j-1} + \alpha^-) + sgn\ v_g(\alpha_{j-1} - \alpha^-)] \tag{6.3-23}$$

$$J_\ell^- = \frac{1}{2} v'_{\ell,j-1/2}[(\alpha_{j-1} + \alpha^-) + sgn\ v_\ell(\alpha_{j-1} - \alpha^-)] \tag{6.3-24}$$

$$J^- = J_g^- + J_\ell^- \tag{6.3-25}$$

where sgn v_g and v_ℓ are the signs for the vapor and liquid cell-edge phasic velocities at j-1/2,

$$V'_{g,j-1/2} = V_{g,j-1/2}\left(\frac{A_{j-1/2}}{A_j}\right) \tag{6.3-26}$$

$$V'_{\ell,j-1/2} = V_{\ell,j-1/2}\left(\frac{A_{j-1/2}}{A_j}\right) . \tag{6.3-27}$$

The phasic velocities $V'_{g,j-1/2}$ and $V'_{\ell,j-1/2}$ are calculated using the phasic junction velocities $v_{g,j-1/2}$ and $v_{\ell,j-1/2}$ calculated from the TRAC-BF1/MOD1 momentum solution scheme and passed to the level tracking routines (LEV1D and LEV3D). The primed velocities are calculated using the same weighting scheme as for Equation (6.3-14) but with the inlet instead of outlet junction cell junction areas. The logic and correlations used to calculate α_j^* are the same used for the normal void profile scheme.

Once α_j^* and α_j^- have been calculated using the above methodology (assuming a level flag has been activated for that particular cell), these void fractions are passed back to the code's momentum finite-differencing solution scheme. It is the substituted cell mixture level void fractions, rather than the cell-averaged void fractions, which are then employed for void donoring to the adjacent cell volumes in the TRAC-BF1/MOD1 momentum solution solver. When a two-phase mixture level approaches a cell boundary, the cell junction

velocities are also recalculated in the level tracking routines and passed back to the code's general momentum solution scheme. The code methodology for this is discussed in the next section.

6.3.4 Criteria for Calculating Cell Mixture Level Velocities and Cell Boundary Crossings

This section summarizes the code methodology used to calculate cell mixture level velocities when a mixture level crosses a cell boundary and how junction phase velocities are recalculated under these circumstances.

The level velocity VLEV is calculated by taking the time derivative of Equation (6.3-6)

$$VLEV_j = \frac{DZ_j \frac{d\alpha_j}{dt} - DZL_j \frac{d\alpha_j^-}{dt} - (DZ_j - DZL_j)\frac{d\alpha_j^+}{dt}}{\alpha_j^- - \alpha_j^+} \quad . \tag{6.3-28}$$

The derivatives in Equation (6.3-28) are numerically approximated by taking the difference between the new-time and old-time void fractions and dividing by the thermal-hydraulic time step. The denominator in Equation (6.3-28) uses new-time mixture level void fractions.

The two-phase level tracking model uses two criteria to determine if a level will cross an axial cell boundary. For a rising level, VLEV > 0, the condition is

$$(\alpha_j - \alpha_j^-) < EPSALPL \quad . \tag{6.3-29}$$

If VLEV < 0, the criteria for a falling level is

$$(\alpha_j^+ - \alpha_j) < EPSALPL \quad . \tag{6.3-30}$$

Equations (6.3-29) and (6.3-30) comprise the first test for cell boundary level crossing. The level tracking void parameter EPSALPL is defined in Table 6.3-2 as a user-specified value that defaults to .02. Again, the above criteria are empirical. The reader is cautioned that using a larger nondefault value of EPSALPL may induce numerical instabilities.[6.3-4]

When a two-phase level approaches a boundary, a second test is also employed to see if the mixture level during the next computational time step will be advanced into the next adjoining cell for a rising or falling level. The level is advanced into an adjoining cell if the level transit time is less than the current hydraulic computational time step, Δt.

The criteria for a rising level to advance to the next cell is

$$\frac{DZ_j - DZL_j^n}{VLEV_j} < \Delta t \quad . \tag{6.3-31}$$

For a falling level, the criteria is

$$\frac{DZL_j^n}{VLEV_j} < \Delta t \quad . \tag{6.3-32}$$

When a two-phase level crosses a cell boundary, there is a discontinuous change in the void fraction and phase velocity at the cell boundary. To stabilize the numerics, the level model calculates modified phasic velocities that are used in the new-time solution to the momentum equation when a level crossing occurs. The modified velocities are determined from the jump conditions

$$VLEV = \frac{J_g^- - J_g^+}{\alpha_j^- - \alpha_j^+} \tag{6.3.33}$$

or

$$VLEV = \frac{J_\ell^- - J_\ell^+}{\alpha_j^+ - \alpha_j^-} \quad . \tag{6.3.34}$$

For a rising level that will cross a cell boundary at the next time step (as shown in Figure 6.3-6), the liquid velocity at the boundary after the level crosses can be calculated using Equation (6.3-34). The modified old-time junction liquid velocity becomes

$$(V_\ell)_{j-1/2}^n = \frac{(\alpha_j^+ - \alpha_j^-)\ VLEV_j + (1 - \alpha_j^+)(v_\ell)_{j+1/2}^n}{\left(1 - \alpha_j^-\right)} \quad . \tag{6.3-35}$$

For a falling level that will cross a cell boundary at the next time step (as shown in Figure 6.3-7), the modified old-time junction vapor velocity at the boundary after the level crosses can be calculated using Equation (6.3-33).

$$(V_g)_{j-1/2}^n = \frac{\alpha_j^-(v_g)_{j-1/2}^n - (\alpha)_j^- - \alpha_j^n)VLEV_j}{\alpha_j^+} \quad . \tag{6.3-36}$$

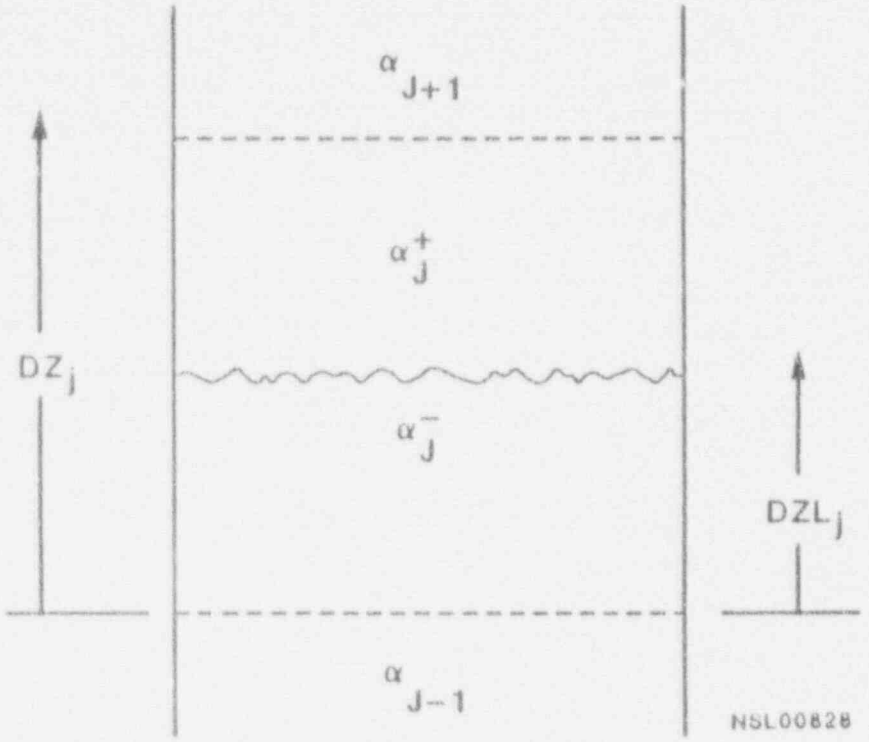

Figure 6.3-6. Rising two-phase level at a cell boundary.

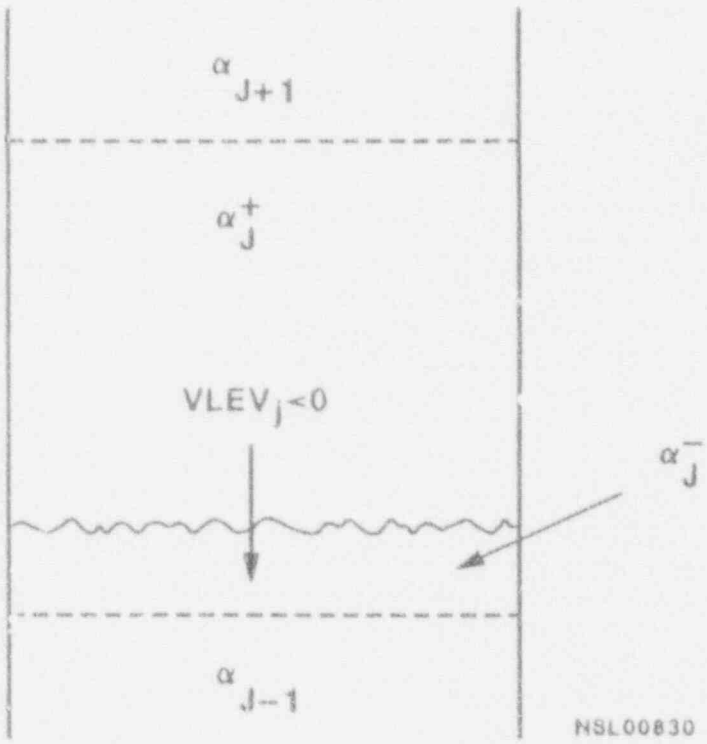

Figure 6.3-7. Falling two-phase level at a cell boundary.

If the junction velocities are recalculated by the one-dimensional or three-dimensional level tracking routines, these modified velocities are transferred back to the code's one- or three-dimensional momentum solution subroutines for solution advancement to the next time step.

It was discovered during the development of the level tracking models that computational instabilities may develop when a level is propagated to an adjacent cell where the void fraction is very near 0.0 or 1.0. For this reason, it was necessary to slightly adjust the void fraction in a cell to which a two-phase level is propagated if the initial void in the cell is near 0.0 or 1.0. System mass is still strictly conserved in this case by transferring mass to or from the cell from which the level originates.

6.3.5 Conclusions

The following conclusions are made with respect to the level tracking models which are currently used in TRAC-BF1/MOD1:

- The TRAC-BF1/MOD1 level tracking model has been shown to produce physically realistic results in thermal-hydraulic transients by suppressing artificial cell-to-cell mass convection.
- The level tracking model is designed to compensate for inherent limitations of the TRAC-BF1/MOD1 finite-differencing scheme.
- The use of this model has also allowed for coarser nodalization and a substantial savings in computational costs.
- The level tracking parameters supplied to the user should be employed with caution. The nature of the hypothesized transient may affect the range of validity of these default parameters.

6.3.6 References

1. D. D. Taylor, *Improvements to G.E. Level Tracking Model for 3-D Components*, WR-NSMD-83-007, February 1983.

2. D. D. Taylor, *1-D Level Tracking Model*, IS-NSMD-83-011, April 1983.

3. W. L. Weaver et al., TRAC-BF1 Manual: Extensions to TRAC-BD1/MOD1, NUREG/CR-4391, EGG-2417, August 1986.

4. B. L. Charboneau, *Overview of TRAC-BD1/MOD1 Assessment Studies*, NUREG/CR-4428, EGG-2422, November 1985.

5. A. Rosen et al., *Teploenergetikia, 11*, p. 59, 1976.

6. J. G. M. Andersen and K. H. Chu, *Constitutive Correlations for Shear and Heat Transfer for the BWR Version of TRAC*, NUREG/CR-2134, EPRI NP-1582, GEAP-24940, December 1981.

7. FLOW PROCESS MODELS

The following sections describe flow process models in TRAC-BF1/MOD1.

7.1 PRESSURE DROPS DUE TO AREA CHANGES

7.1.1 Velocity Divergence

In the TRAC-BF1/MOD1 momentum equations, the velocity divergence operator is written in terms of a backward spatial difference, which gives the correct pressure drop for a straight duct of constant cross-sectional area. In order to compute the pressure drop between cells j and j+1 for the case of a nonconstant cross-sectional area duct, the velocity divergence should be written in terms of the difference in the squares of the cell-centered velocities as

$$\begin{aligned}(V_k \nabla V_k)_{j+1/2} &= \frac{1}{2\Delta\bar{x}} \left(V_{k,j+1}^2 - V_{k,j}^2\right) \\ &= \frac{1}{2\Delta\bar{x}} \left(V_{k,j+1} + V_{k,j}\right)\left(V_{k,j+1} - V_{k,j}\right)\end{aligned} \tag{7.1-1}$$

Modifying the terms in the backward spatial difference results in an approximate form of the correct cell-center-to-cell-center velocity difference and the correct pressure drop between cell centers for a duct with changing cross-sectional area. The mass flow rates at the cell centers are written as the average of the mass flow rates at the cell edges (where the phasic subscript has been suppressed)

$$\alpha_j \rho_j A_j V_j = \frac{1}{2}\left(\alpha_j \rho_j A_{j+1/2} V_{j+1/2} + \alpha_{j-1} \rho_{j-1} A_{j-1/2} V_{j-1/2}\right); \quad V_{j+1/2} > 0,\ V_{j-1/2} > 0 \tag{7.1-2}$$

$$\alpha_{j+1} \rho_{j+1} A_{j+1} V_{j+1} = \frac{1}{2}\left(\alpha_{j+1} \rho_{j+1} A_{j+3/2} V_{j+3/2} + \alpha_j \rho_j A_{j+1/2} V_{j+1/2}\right); \quad V_{j+3/2} > 0,\ V_{j+1/2} > 0 \tag{7.1-3}$$

where the donor conversion has been used to express the phasic densities and void fractions at the cell edges. Analogous equations may be written for various combinations of positive and negative velocities at the cell edges.

These equations are combined in various ways with the steady-state phasic

continuity equations

$$\alpha_{j-1}\rho_{j-1}A_{j-1/2}V_{j-1/2} + \Gamma_j = \alpha_j\rho_j A_{j+1/2}V_{j+1/2} \tag{7.1-4}$$

$$\alpha_j\rho_j A_{j+1/2}V_{j+1/2} + \Gamma_{j+1} = \alpha_{j+1}\rho_{j+1}A_{j+3/2}V_{j+3/2} \tag{7.1-5}$$

to determine the cell-centered velocities. Substituting Equation (7.1-5) into Equation (7.1-3) to eliminate $V_{k,j+3/2}$, we obtain

$$V_{j+1} = \frac{\alpha_j\rho_j A_{j+1/2}V_{j+1/2}}{\alpha_{j+1}\rho_{j+1}A_{j+1}} + \frac{0.5\,\Gamma_j}{\alpha_{j+1}\rho_{j+1}A_{j+1}} . \tag{7.1-6}$$

Substitution of Equation (7.1-4) into Equation (7.1-2) results in two forms of the cell-centered phasic velocity in the upstream cell in terms of the phasic velocity at each cell edge

$$V_j^{(j+1/2)} = \frac{\alpha_j\rho_j A_{j+1/2}V_{j+1/2}}{\alpha_j\rho_j A_j} - \frac{0.5\,\Gamma_j}{\alpha_j\rho_j A_j} \tag{7.1-7}$$

$$V_j^{(j-1/2)} = \frac{\alpha_{j-1}\rho_{j-1}A_{j-1/2}V_{j-1/2}}{\alpha_j\rho_j A_j} + \frac{0.5\,\Gamma_j}{\alpha_j\rho_j A_j} . \tag{7.1-8}$$

Substitution of Equations (7.1-6), (7.1-7), and (7.1-8) into Equation (7.1-1) gives

$$\begin{aligned}(V\,\nabla V)_{j+1/2} &= \frac{1}{2\Delta X}\left[V_{j+1} + V_j^{(j+1/2)}\right]\cdot\left[V_{j+1} - V_j^{(j-1/2)}\right] \\ &= \frac{1}{2\Delta X}\left(AV_{j+1/2} + B\right)\left(CV_{j+1/2} - DV_{j-1/2} + B\right)\end{aligned} \tag{7.1-9}$$

where

$$A = \frac{\alpha_j\rho_j A_{j+1/2}}{\alpha_{j+1}\rho_{j+1}A_{j+1}} + \frac{\alpha_j\rho_j A_{j+1/2}}{\alpha_j\rho_j A_j} \tag{7.1-10}$$

$$B = \frac{0.5\,\Gamma_{j+1}}{\alpha_{j+1}\rho_{j+1}A_{j+1}} - \frac{0.5\,\Gamma_j}{\alpha_j\rho_j A_j} \tag{7.1-11}$$

$$C = \frac{\alpha\rho_j A_{j+1/2}}{\alpha_{j+1}\rho_{j+1}A_{j+1}} \tag{7.1-12}$$

$$D = \frac{\alpha_{j-1}\rho_{j-1}A_{j-1/2}}{\alpha_j\rho_j A_j} \tag{7.1-13}$$

It should be noted that setting A = C = D = 1.0 and B = 0 results in the uncorrected form of the velocity divergence operator.

This form of the velocity divergence will be numerically stable as long as it has the form of the corresponding backward difference (corresponding form in the sense that the two terms in parentheses have the same signs as the uncorrected form at the backward difference). Since A, C, and D are always greater than zero, the only situation that can cause instability is whenever $B > AV_{j+1/2}$ or $B > -(CV_{j+1/2} - DV_{j+1/2})$. These criteria come from the fact that the values of A, B, C, and D should not change the sign of the two terms in parenthesis in Equation (7.1-9) relative to the uncorrected form of the velocity divergence operator.

Rather than test for every combination of the coefficients, the coefficients A, B, C, and D are simplified to give

$$A = \frac{A_{j+1/2}}{A_{j+1}} + \frac{A_{j+1/2}}{A_j} \tag{7.1-16}$$

$$B = 0 \tag{7.1-17}$$

$$C = \frac{A_{j+1/2}}{A_{j+1}} \tag{7.1-18}$$

$$D = \frac{A_{j-1/2}}{A_j} \tag{7.1-19}$$

where

$$A_{j+1} = \frac{Vol_{j+1}}{\Delta X_{j+1}} \tag{7.1-20}$$

$$A_j = \frac{Vol_j}{\Delta X_j} . \qquad (7.1\text{-}21)$$

Since A, C, and D are always positive, the corrected velocity divergence has the form of a backward velocity divergence with modified coefficients. This form of the coefficients will give the correct pressure drop for single-phase flow in a duct with varying cross-sectional area and should be adequate for two-phase flow.

7.2 CRITICAL FLOW

This section details the equilibrium critical flow model presently employed in the TRAC-BF1/MOD1 computer code. The critical flow model used in TRAC-BF1/MOD1 is applicable for coarse-mesh nodalization and is based on a semi-empirical approximation of the choking criteria derived from the general one-dimensional, two-phase fluid field equations. The critical flow model also allows for the simulation of choking with a noncondensable gas phase. The principal motivation of using a choked flow limitation model was to improve code efficiency and run times. In the past, it was found that modeling choked flow using the TRAC-BF1/MOD1 finite-difference approximation to the basic conservation equations required extremely fine cell nodalization in the vicinity of the break plane. As a consequence, simulating break transients generally led to prohibitively costly calculations. The choked flow model was developed in several stages and was implemented into the code by a number of individuals.[7.2-1,2,3,4]

The remainder of this chapter is outlined as follows. Section 7.2.1 documents the basic assumptions used to formulate the choking criteria in TRAC-BF1 and how the choking model is implemented. Section 7.2.2 documents the general methodology used to calculate thermodynamic properties at the choke plane. Sections 7.2.3, 7.2.4, and 7.2.5 document the two-phase/two-component, single phase/two-component vapor, and single-phase liquid critical flow models, respectively. Section 7.2.6 documents the closure relations needed to calculate the choke plane phasic velocities. Section 7.2.7 gives conclusions relative to applicability and areas for further study relative to the present TRAC-BF1/MOD1 choking model.

7.2.1 Background

Choking occurs when the mass flow in a pipe becomes independent of the downstream conditions. Therefore, a further reduction in the downstream pressure will not change the mass flow rate. The reason choking occurs is that acoustic signals can no longer propagate upstream to affect the boundary conditions that determine the mass flow rate at the choke plane. The choking model employs a flow-limiting scheme that uses a linear function of the cell junction phasic velocities and compares this expression to the calculated local junction sound speed. If this linear function exceeds the local sound speed, the choking model is employed to limit flow at that particular junction. The quantitative details of how this is done will be identified later in this section. The choking model used in TRAC-BF1/MOD1 is based on the RELAP5/MOD1 model originally developed by Ransom and Trapp.[7.2-5,6,7,8]

Originally, the TRAC-BF1/MOD1 choking model was based on a characteristic analysis of the partial differential equations governing the flow response. However, it has been found empirically that a much simplified criterion relating the throat homogenous equilibrium mixture (HEM) sonic velocity and throat phasic velocities void fractions, and densities

$$\left| \frac{\alpha_g \rho_f V_g + \alpha_f \rho_g V_f}{\alpha_g \rho_f + \alpha_f \rho_g} \right| \geq a_{HE} \qquad (7.2\text{-}1)$$

may be used in place of the detailed theoretical expression and still yield good code/data comparisons.

The choking model consists of four different regimes, identified in Table 7.2-1. These regimes are presently based on cell-centered void conditions immediately upstream of the choke plane. Each of these regimes is simulated in the TRAC-BF1/MOD1 subroutine CHOKE. Figure 7.2-1 is a flow chart of the current logic for selecting these flow regimes. In each case, the method used to calculate the homogeneous sound speed a_{HE} is slightly different. The presence of noncondensables introduces an additional degree of complexity in the approximation of a_{HE}. At present, only air is modeled with the noncondensable option. The presence of air is accounted for in all of the break flow regimes with one exception. Noncondensables at the break choke plane are ignored for the low void regime (Table 7.2-1) when the Alamgir-Jones-Lienhard (AJL) correlation is used. In the subcooled blowdown regime the effects of noncondensables on the local sound speed are assumed to be small and are therefore ignored.

Table 7.2-1. Equilibrium critical flow regimes.

Void Fraction	Regime	Correlation
$\alpha < 0.01$	liquid	Alamgir-Jones-Lienhard
$0.01 < \alpha < 0.1$	transition	Interpolate
$0.1 < \alpha < 0.999999$	two-phase	Homogeneous equilibrium sound speed
$0.999999 < \alpha$	gas only	HEM with adiabatic gas approximation

We shall now summarize how the choking model is implemented into TRAC-BF1/MOD1. The choking model is presently implemented in only one-dimensional components. The critical flow model is called by the subroutine TF1E, which is the subroutine to solve the governing equations for one-dimensional TRAC-BF1/MOD1 components. TF1E passes donor cell parameters based on new-time velocities to CHOKE. Tables 7.2-2 and 7.2-3 summarize the principal variables passed to CHOKE and the calculated output variables. The alphanumeric identifiers in Tables 7.2-2 and 7.2-3 should not be necessarily interpreted as subroutine call arguments. After CHOKE has been entered,

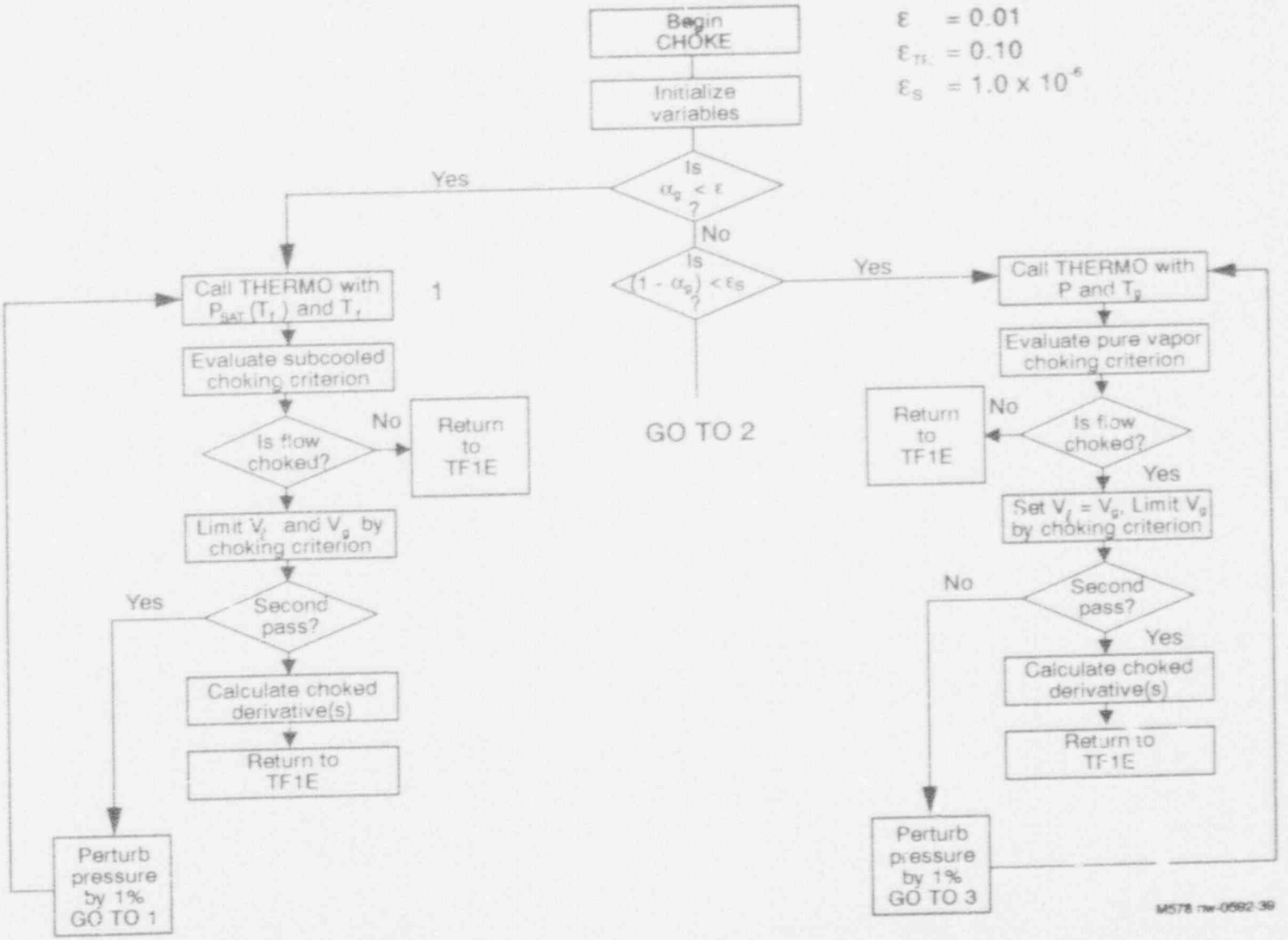

Figure 7.2-1. TRAC-BF1/MOD1 choke logic.

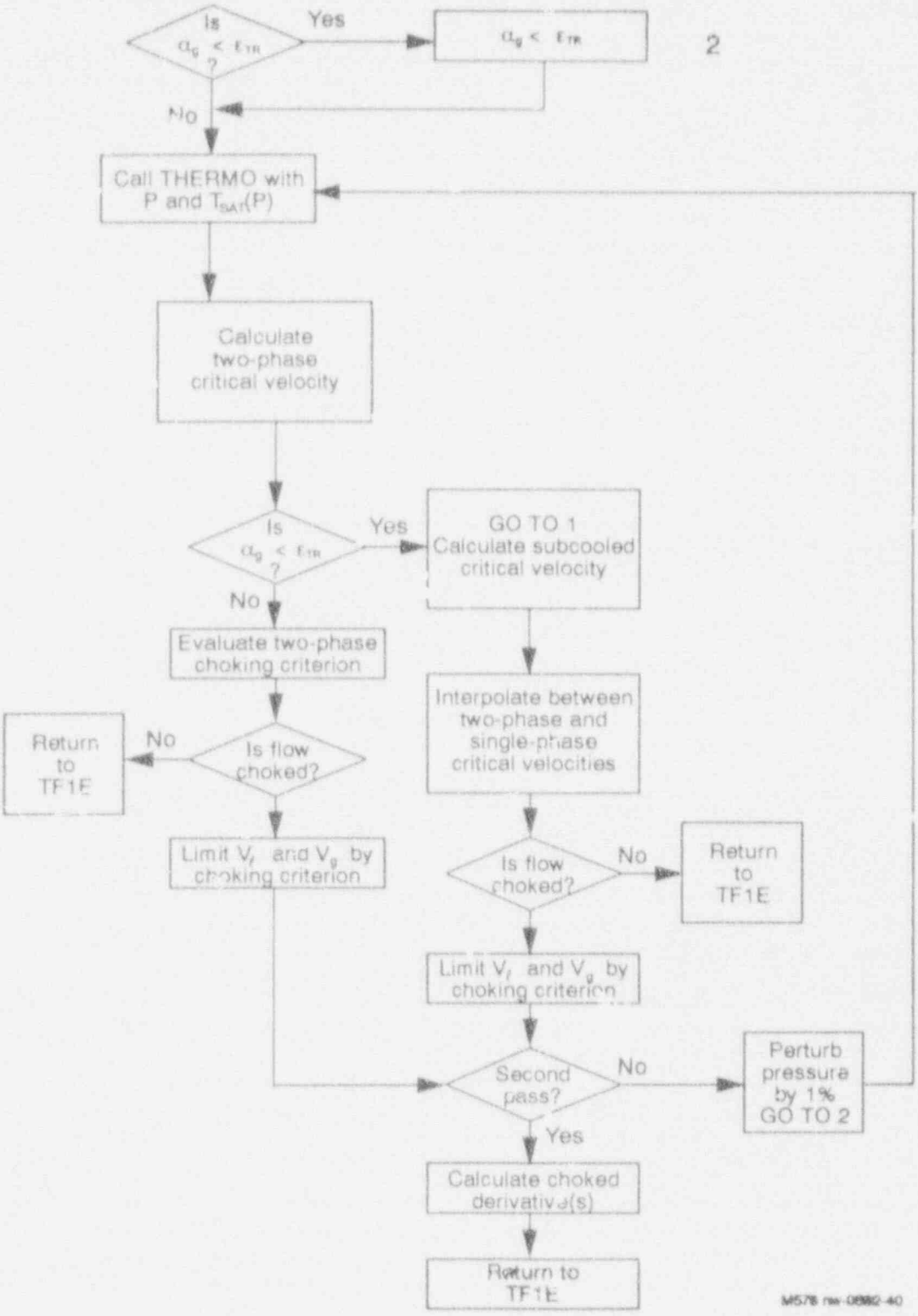

Figure 7.2-1. (continued)

Table 7.2-2. Input call parameters to CHOKE subroutine.

Variable	Parameter
DXC	Donor cell length
HD	Hydraulic diameter
WFL	Wall friction factor, liquid
WFV	Wall friction factor, vapor
ALP	Donor cell void fraction
PC	Donor cell upsteam pressure
PD	Donor cell downstream pressure
RL	Donor cell density, liquid
RV	Donor cell density, vapor
SIGMA	Donor cell surface tension
TL	Donor cell temperature, liquid
TV	Donor cell temperature, vapor
VMC	Donor cell mixture velocity
VMO	Old-time mixture velocity
VL	Throat junction velocity, liquid
VV	Throat junction velocity, vapor
DFLDP	Derivative of VL with respect to pressure
DFVDP	Derivative of VV with respect to pressure
ICHOKE	Choking flag
ROAIR	Donor cell air density
IEOS	Gaseous phase equation-of-state flag
AVMO	Old-time HE sonic velocity
RHOCK	Throat-to-cell-center mixture density ratio
CV	Coefficient of VVN in combined momentum equation. Obtain in IFIE by eliminating the pressure gradient term from the liquid and vapor momentum equations.
CL	Coefficient of VLN in combined momentum equation above
RHSN	RHS of combined momentum equation above
DADZ	Derivative of flow area with respect to axial distance (set to 0.0 if DADZ is non-negative)
AT	Flow area at current junction (choking plane)
AU	Flow area at upstream junction

Table 7.2-3. Output to subroutine CHOKE.

Variable	Parameter
VL	Throat liquid velocity
VV	Throat vapor velocity
DFLDP	Derivative of VL with respect to pressure
DFVDP	Derivative of VV with respect to pressure
ICHOKE	Choking status flag

control is passed to a particular model, depending on the void conditions defined in Table 7.2-1. Each model that is invoked follows the same computational sequence:

1. The throat pressure and temperature conditions are calculated. The subroutine THERMO is called to calculate additional thermodynamic throat conditions.

2. The throat sonic speed is calculated and the choking criteria are evaluated.

3. If the choking criteria are not met, control is returned to TF1E.

4. If choking criteria are met, new-time throat velocities and derivatives are recalculated. To calculate the derivatives, the throat pressure is perturbed by 1% and a second pass is made to calculate the liquid and vapor velocities. The choked derivatives are calculated by dividing the change in the choked velocity calculated between passes by the pressure perturbation.

5. Control is returned to TF1E with the new calculated junction phasic velocities and derivatives.

The above process is illustrated in the logic flow in Figure 7.2-1. We shall now detail how CHOKE calculates the throat conditions, the details of particular models that are invoked, and how they are implemented into the code.

7.2.2 Methodology for the Calculation of Choke Plane Thermodynamic Properties

This section details the principal method used to calculate choke plane thermodynamic properties and how this method is implemented in the TRAC-BF1/MOD1 code. In order to calculate a_{HE}, the cell break plane conditions must first be approximated. In the TRAC-BF1/MOD1 finite-differencing scheme, fluid properties are calculated as cell-centered quantities. As a consequence, approximation techniques must be employed to

estimate gradients in fluid conditions between the cell center and cell edge choke plane. In TRAC-BF1/MOD1, a half cell momentum (see Figure 7.2-2) balance approximation is used to estimate the junction pressure. It is assumed that the area change from the cell center to the cell face is not too abrupt. Hence, form loss effects are not accounted for in the approximation. The throat pressure becomes, using Bernoulli's theorem,

$$P_t = P_c - \frac{\rho_{mt} V_{mt}^2}{2} + 0.5 \left[\rho_{mc} - (\alpha_{gc}\rho_{gc} f_{gc} + \alpha_{\ell c}\rho_{\ell c} f_{\ell c}) \frac{L}{D_H} \right] V_{mc}^2 \qquad (7.2\text{-}2)$$

where the subscripts t and c designate cell throat and center locations. The m subscript designates mixture conditions. The parameters V_{mc}, V_{mt}, ρ_{mc}, and ρ_{mt} are mixture velocities and densities at the cell center and throat, respectively (Figure 7.2-2). The parameters f_{gc} and $f_{\ell c}$ are the liquid and vapor phasic friction factors. The L and OH parameters are the upstream cell half length and throat hydraulic diameter, respectively.

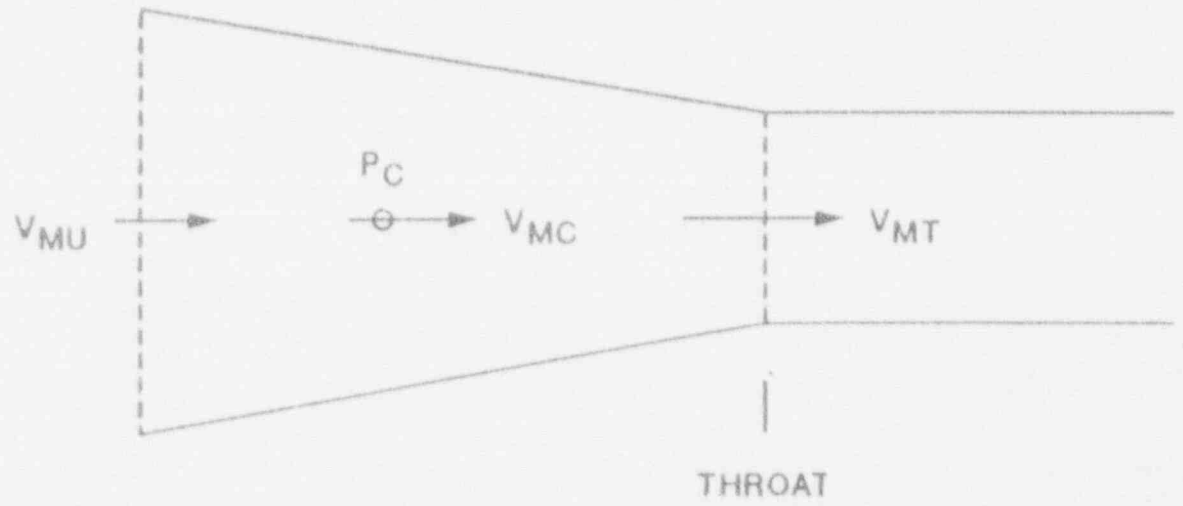

Figure 7.2-2. Choking cell configuration.

The above Bernoulli approximation has been done by assuming that the mixture velocities rather than the phasic velocities are sufficient to calculate throat properties. The wall phasic friction factors, f_ℓ and f_g, are passed from the TRAC-BF1/MOD1 momentum solution routine TF1E to the CHOKE routine. The frictional loss terms are neglected for the throat pressure calculation in the liquid regime and vapor regime (Table 7.2-1). A further elaboration of the above corrections is given in Sections 7.2.3 and 7.2.5.

Because of inherent limitations in the TRAC-BF1/MOD1 finite-difference solution scheme, additional approximations have been made to evaluate V_{mc}, V_{mt}, and ρ_{mt}. In particular, the finite-difference scheme solves the field equations so that the phasic velocities are calculated only at cell edges.

Cell-donored quantities, including the pressure, phase densities, temperatures and void fractions, are calculated only as cell-centered parameters. The mixture densities and velocities in Equation (7.2-2) are calculated as follows:

$$\rho_{mc} = \alpha_{gc}\rho_{gc} + \alpha_{\ell c}\rho_{\ell c} \tag{7.2-3}$$

$$RHOCK = \frac{\rho_{mt}}{\rho_{mc}} \tag{7.2-4}$$

$$V'_{mt} = \frac{\alpha_{gc}\rho_{gc}V_{gt} + \alpha_{\ell c}\rho_{\ell c}V_{\ell t}}{\alpha_{gc}\rho_{gc} + \alpha_{\ell c}\rho_{\ell c}} \tag{7.2-5}$$

$$V_{mt} = \frac{V'_{mt}}{RHOCK} \tag{7.2-6}$$

$$V_{mc} = \frac{4V_{mu}A_u}{A_u + 2\left(A_uA_t\right)^{1/2} + A_t} \tag{7.2-7}$$

$$V_{mu} = \frac{\alpha_{gu}\rho_{gu}V_{gu} + \alpha_{\ell u}\rho_{\ell u}V_{\ell u}}{\alpha_{gu}\rho_{gu} + \alpha_{\ell u}\rho_{\ell u}} \,. \tag{7.2-8}$$

The cell edge velocities and cell-centered densities and void functions are quantities calculated at the previous computational time step that are passed to the CHOKE subroutine, where the expressions (7.2-3) through (7.2-8) are calculated and substituted into Equation (7.2-2). The density ratio ρ_{mt}/ρ_{mc} is calculated at the previous time step, with ρ_{mt} being estimated using CHOKE. The expression for the throat mixture velocity V_{mt} is a logical consequence of the code finite-differencing scheme. The approximation for V_{mt} is done by equating the mass fluxes with cell and throat-donored densities so that $\rho_{mc}V'_{mc} = \rho_{mt}V_{mt}$. The mixture velocity V'_{mt} is the effective velocity weighted with the cell-centered mixture density, whereas V_{mt} is weighted with the throat mixture density. If compressibility effects are important, the approximation for V_{mt} will give more accurate results in calculating the throat pressure P_t.

The expression used to approximate the cell-centered mixture velocity V_{mc} is based on the assumption (Figure 7.2-2) that the break geometry upstream of the choke plane approximates a conical pathway. By assuming constant

volumetric flow, we have the following relationship between the cell-centered and upstream mixture velocities:

$$A_c V_{mc} = A_u V_{mu} \qquad (7.2\text{-}9)$$

where

$$A_c = \frac{A_u + 2(A_u A_t)^{1/2} + A_t}{4} , \qquad (7.2\text{-}10)$$

which gives us Equation (7.2-7). The value of A_c is the result of calculating the cross-sectional area of a frustrum at the half-cell length (cross-sectional area at P_c in Figure 7.2-2).

Once P_t has been calculated at the choke plane, the phasic temperatures at this location are calculated using assumptions dependent on the break upstream void fraction conditions and whether noncondensables are present. Once the phasic temperatures and throat pressure have been calculated at the break plane, these properties are passed to the subroutine THERMO, which calculates the remaining thermodynamic properties needed to calculate the sonic speed. THERMO passes the parameters back to CHOKE, where a_{HE} is calculated and the appropriate tests for choking using Equation (7.2-1) can be performed.

The current TRAC-BF1/MOD1 choking model assumes that the throat void fraction is equal to the calculated void fraction of the cell immediately upstream of the choke plane. In future versions of TRAC-BF1/MOD1, it may prove useful to investigate ways of accounting for void gradient changes between the choke plane and the upstream donor cell.

Table 7.2-4 summarizes the assumptions used in TRAC-BF1/MOD1 to calculate the key throat parameters (pressure and phasic temperatures) and the associated sonic models used in the code. This table also makes reference to the presence of noncondensables, which will be discussed in later sections. Additional details of the assumptions used to calculate the break plane thermodynamic conditions and corresponding sonic velocity are detailed in Sections 7.2.3 through 7.2.5.

7.2.3 Two-Phase/Two-Component Critical Flow Models

The two-component/two-phase (TCTP) HEM critical flow model used in TRAC-BF1/MOD1 was developed by Phillips et. al.[7.2-3,7] This model is based exclusively on theoretical grounds and employs several simplifying assumptions to enable one to derive an expression for the equilibrium sonic mixture velocity. This section will deal with several variations of the TCTP model employed in the TRAC-BF1/MOD1 code. The variations include the following:

Table 7.2-4. Summary of TRAC-BF1/MOD1 choking correlations and throat conditions.

Void fraction range	Two-phase liquid steam throat conditions	Two-phase two-component throat conditions	Water with noncondensable throat conditions	Steam with or without noncondensable throat conditions	Sonic velocity correlation
$\alpha_g \leq .01$	$P_T = SATPRS(T_{LC})$ $T_\ell = T_{SAT}(P_T)$ $T_g = T_\ell$	Noncondensable gas effects ignored throat conditioning same as left box.	Noncondensable gas effects ignored throat conditioning same as left box.	N/A	Use maximum of AJL and HEM correlation
$.1 \leq \alpha_g \leq .01$	Throat conditions based on information in box above or box below.	Throat conditions based on information in box above or box below.	Throat conditions based on information in box above or box below.	N/A	Use HEM sonic model (with α_g reset to .1) or AJL model. Interpolate with cubic spline.
$.1 \leq \alpha_g \leq 1-E-6$	P_T calculated from Bernoulli equation $T_g = T_{SAT}(P_T)$ $T_g = T_\ell$ Assume $\frac{d\alpha_g}{dP} \neq 0$	P_T calculated from Bernoulli equation equilibrium throat temperature T_{EQ} calculated with Taylor series approx. $T_{EQ} = T_\ell = T_{NC} = T_g$ Assume $\frac{d\alpha_g}{dP} \neq 0$	P_T calculated from Bernoulli equation liquid throat temp. set equal to cell center liquid temp $T_{NC} = T_\ell$ Assume $\frac{d\alpha_{NC}}{dP} = 0$	N/A	HEM sonic velocity model
$1.-E-6 < \alpha_g$	N/A	N/A	N/A	For perfect gas P_T-T_g calculated from Adiabatic law $T_g = T_{NC}$ For HEM case P_T is same value but. $T_g = T_{NC} = T_{SAT}(P_T)$	Max [HEM model with $\frac{d\alpha_g}{dP} = 0$., HEM model with $\frac{d\alpha_g}{dP} \neq 0$]

- Air/water mixture covering same void regimes as 1.
- Water/steam mixture covers same void regime as 1.
- General TCTP model with steam/water/air mixture applied to void fraction regimes

  $.1 \leq \alpha_g \leq .01$
  $.1 \leq \alpha_g \leq .999999.$

- Air/steam mixture formulation covers void regime $\alpha_g \geq .999999.$

Section 7.2.3 will deal with the first three cases. The last case is separately discussed in Section 7.2.4, dealing with single-phase one and two-component gas/vapor choking models.

The general expression for the local HEM sonic velocity is

$$a_{HE} = \left(\frac{\partial P}{\partial \rho}\right)_S^{1/2} \qquad (7.2\text{-}11)$$

where the subscript S corresponds to constant entropy of the derivative P with respect to ρ. In order to derive a tractable expression for a_{HE} in terms of thermodynamic quantities and derivatives, a number of simplifying assumptions have been made.

1. For an arbitrary steam-liquid-noncondensable mixture, each component is in temperature equilibrium.
2. Since the flow process is assumed to be isentropic in the formulation of Equation (7.2-11), nonequilibrium interfacial heat and mass transfer are not directly considered in the formulation.
3. If a noncondensable gas component is present, it is assumed that the noncondensable and vapor occupy the same volume and obey the Gibbs-Dalton law of partial pressures.
4. If a noncondensable is present, it is considered chemically inert; i.e., the noncondensable cannot dissolve in the liquid, come out of solution, or form new compounds with the water molecules.
5. If a noncondensable is present, its equation of state is assumed to obey the perfect gas law.
6. Multi-dimensional and turbulence effects are not considered.
7. The assumption that the liquid-steam-noncondensable is homogenous precludes formulation of stratification or other flow-map-dependent phenomena on the sonic velocity.

The above assumptions, with some exceptions, also apply to the critical flow models documented in Sections 7.2.4 and 7.2.5. With regard to assumptions 1 and 2, TRAC-BF1/MOD1 assumes a mixture equilibrium temperature at the choke plane that is calculated according to which break flow regime (Table 7.2-4) is considered. Under certain circumstances, the equilibrium assumption may break down.[7.2-1,2,3] In particular, for break assemblies of very short length, nonequilibrium transport behavior may be important. This occurs when the liquid and vapor phase at the choke plane have not had adequate time to relax to thermal equilibrium. However, it was judged that, in most cases, the equilibrium assumption is reasonable except in the low liquid void regime (Table 7.2-1). Modifications to assumption 2 under these circumstances are detailed in Section 7.2.5.

With respect to assumptions 3-5, we have confined the class of problems to situations where noncondensable gases cannot interact chemically with the liquid-steam mixture. This assumption may not produce accurate results for certain classes of problems where significant quantities of dissolved gases are hypothesized to come out of solution as the liquid decompresses at the choke plane.[7.2-9] Assumption 6 may require code input adjustments to account for break flow geometry effects. The effects of break geometry near the choke plane is discussed by a number of authors.[7.2-9 through 15] In general, the use of a one-dimensional critical flow model approximation requires that a discharge coefficient be employed to account for two- or three-dimensional geometry effects.[7.2-10] Since there is a wide range of possible break flow geometries, there is no particular universal discharge coefficient that is applicable to all situations.

With regard to assumption 7, flow stratification effects may be important under certain circumstances. The TRAC-BF1/MOD1 user is cautioned to be aware of the situations where stratification upstream of the break plane may exist. Critical flow models with stratification have been implemented in other thermal-hydraulic codes, such as RELAP5.[7.2-7] It may prove useful to incorporate stratification modeling in future versions of the critical flow model.

Using the formulation detailed in Appendix D and E, we shall now show how the HEM sonic speed is derived for either a steam-air or air-steam mixture. The general form of the isentropic derivative for the reciprocal of the sonic velocity squared is

$$a_{wt}^2 = \left(\frac{\partial p}{\partial \rho}\right)_s$$

$$= \alpha_g \left(\frac{\partial \rho_{nc}}{\partial p}\right)_s + \alpha_g \left(\frac{\partial \rho_g}{\partial p}\right)_s + \alpha_\ell \left(\frac{\partial \rho_\ell}{\partial p}\right)_s - (\rho_{nc} + \rho_g - \rho_\ell)\left(\frac{\partial \alpha_g}{\partial p}\right)_s \cdot \qquad (7.2\text{-}12)$$

In the liquid/noncondensable regime, $\left(\frac{\partial \alpha_g}{\partial p}\right)_s = 0$ so that Equation (7.2-12) reduces to

$$a_{wt} = \left/ \alpha_g \left(\frac{\partial \rho_{nc}}{\partial p}\right)_s + \alpha_\ell \left(\frac{\partial \rho_\ell}{\partial p}\right)_s \right]^{-1/2} .$$

The individual isentropic derivatives in Equation (7.2-13) are given by the general formula for a pure substance derived in Appendix D and is

$$\left(\frac{\partial p}{\partial \rho}\right)_s = \left(\frac{\partial p}{\partial \rho}\right)_T - \frac{T\left(\frac{\partial p}{\partial T}\right)_\rho^2}{\rho^2\left[\left(\frac{\partial e}{\partial T}\right)_\rho - \frac{p}{\rho^2}\left(\frac{\partial p}{\partial T}\right)_\rho\right]} \qquad (7.2\text{-}13)$$

where the state variables, such as p, are for the liquid or noncondensable. For the case where we are modeling a single-phase vapor/noncondensable mixture, Equation (7.2-14) becomes ($\alpha = 1$)

$$\left/ \left(\frac{\partial \rho_{nc}}{\partial p}\right)_s + \left(\frac{\partial \rho_g}{\partial p}\right)_s \right]^{-1/2} \qquad (7.2\text{-}14)$$

dual isentropic derivatives are again evaluated using Equation

re the steam/liquid phases coexist, the general

enous sound speed can be expanded using Equation (7.2-

sentropic derivative $\left(\frac{\partial \alpha_g}{\partial p}\right)_s \neq 0$; and we have a

sion. The expansion of the individual

ic expressions containing non-isentropic

13

LOW

tives is somewhat long and is detailed in Appendix E. In the limit
the noncondensable gas density becomes zero, Equation (7.2-12) can be
ressed as

$$a_{wf} = \left(\frac{\partial p}{\partial \rho}\right)_s = \left(\frac{\rho_f \rho_g}{\rho - \rho_g}\right)^{1/2} \tag{7.2-16}$$

where

$$\Omega = a_g \rho_f \left(\frac{\partial \rho_g}{\partial P}\right)_s + a_f \rho_g \left(\frac{\partial \rho_f}{\partial P}\right)_s - \Lambda \tag{7.2-17}$$

$$\Lambda = \frac{\rho_g - \rho_f}{s_g - s_f}\left[a_f \rho_g \left(\frac{\partial s_g}{\partial P}\right)_s + a_f \rho_f \left(\frac{\partial s_f}{\partial P}\right)_s\right]. \tag{7.2-18}$$

Prior to calculating the value of the sonic velocity, the throat
thermodynamic conditions must be evaluated. The general outline for
calculating the throat pressure was given in Section 7.2.2, using
Equation (7.2-2). We shall now give further details as to how the throat
temperature and partial pressures are calculated. The methodology used
depends on the particular break flow regime. We shall now consider cases 1-3;
Case 4 will be documented separately in Section 7.2.4. Table 7.2-4 summarize
how the throat conditions are calculated for cases 1-4.

Relative to the steam-water case, P_t is calculated with Equation (7.2-2).
The throat temperature of the liquid is assumed to be the upstream cell-
centered liquid temperature. The noncondensable gas throat temperature is set
equal to the liquid temperature. In the situation where there is a
steam-liquid mixture at the cell center upstream of the break plane,
Equation (7.2-2) is again used; and the steam-liquid mixture is assumed to be
in equilibrium with the throat steam and liquid temperatures set equal to the
saturation temperature at the throat pressure, P_t.

For the steam-liquid-noncondensable situation, the total throat pressure
P_t is again calculated with Equation (7.2-2). However, the effect due to
partial pressure corrections matters for estimating the throat temperature.
The steam-liquid-noncondensable temperature is calculated using a Taylor
series approximation to account for the steam partial pressure. 7.2-3 Gi
cell-centered pressure PC, which is the sum of the vapor and nonconde
partial pressures, the steam partial pressure P_g at the throat is e

$$a_{HE}^{-2} = \left(\frac{\partial \rho}{\partial P}\right)_s$$

$$= \alpha_g \left(\frac{\partial \rho_{NC}}{\partial P}\right)_s + \alpha_g \left(\frac{\partial \rho_g}{\partial P}\right)_s + \alpha_\ell \left(\frac{\partial \rho_\ell}{\partial P}\right)_s - (\rho_{NC} + \rho_g - \rho_\ell) \left(\frac{\partial \alpha_g}{\partial P}\right)_s \tag{7.2-12}$$

In the liquid/noncondensable regime, $\left(\frac{\partial \alpha_g}{\partial P}\right)_s = 0$ so that Equation (7.2-12) reduces to

$$a_{HE} = \left[\alpha_g \left(\frac{\partial \rho_{NC}}{\partial P}\right)_s + \alpha_\ell \left(\frac{\partial \rho_\ell}{\partial P}\right)_s\right]^{-1/2} . \tag{7.2-13}$$

The individual isentropic derivatives in Equation (7.2-13) are given by the general formula for a pure substance derived in Appendix D and is

$$\left(\frac{\partial \rho}{\partial P}\right)_s = \left(\frac{\partial \rho}{\partial P}\right)_T - \frac{T\left(\frac{\partial \rho}{\partial T}\right)_P^2}{\rho^2\left[\left(\frac{\partial e}{\partial T}\right)_P - \frac{P}{\rho^2}\left(\frac{\partial \rho}{\partial T}\right)_P\right]} \tag{7.2-14}$$

where the state variables, such as ρ, are for the liquid or noncondensable. In the case where we are modeling a single-phase vapor/noncondensable mixture, Equation (7.2-14) becomes ($\alpha = 1$)

$$a_{HE} = \left[\left(\frac{\partial \rho_{NC}}{\partial P}\right)_s + \left(\frac{\partial \rho_g}{\partial P}\right)_s\right]^{-1/2} \tag{7.2-15}$$

where the individual isentropic derivatives are again evaluated using Equation (7.2-14).

In situations where the steam/liquid phases coexist, the general expression for the homogenous sound speed can be expanded using Equation (7.2-12). In this situation, the isentropic derivative $\left(\frac{\partial \alpha_g}{\partial P}\right)_s \neq 0$; and we have a significantly more complex expression. The expansion of the individual isentropic derivatives into algebraic expressions containing non-isentropic

derivatives is somewhat long and is detailed in Appendix E. In the limit where the noncondensable gas density becomes zero, Equation (7.2-12) can be expressed as

$$a_{HE} = \left(\frac{\partial \rho}{\partial P}\right)_s^{-1/2} = \left(\frac{\rho}{\rho_\ell \rho_g}\Omega\right)^{-1/2} \tag{7.2-16}$$

where

$$\Omega = \alpha_g \rho_\ell \left(\frac{\partial \rho_g}{\partial P}\right)_s + \alpha_\ell \rho_g \left(\frac{\partial \rho_\ell}{\partial P}\right)_s - \Lambda \tag{7.2-17}$$

$$\Lambda = \frac{\rho_g - \rho_\ell}{S_g - S_\ell}\left[\alpha_g \rho_g \left(\frac{\partial S_g}{\partial P}\right)_s + \alpha_\ell \rho_\ell \left(\frac{\partial S_\ell}{\partial P}\right)_s\right]. \tag{7.2-18}$$

Prior to calculating the value of the sonic velocity, the throat thermodynamic conditions must be evaluated. The general outline for calculating the throat pressure was given in Section 7.2.2, using Equation (7.2-2). We shall now give further details as to how the throat temperature and partial pressures are calculated. The methodology used depends on the particular break flow regime. We shall now consider cases 1-3; Case 4 will be documented separately in Section 7.2.4. Table 7.2-4 summarizes how the throat conditions are calculated for cases 1-4.

Relative to the steam-water case, P_t is calculated with Equation (7.2-2). The throat temperature of the liquid is assumed to be the upstream cell-centered liquid temperature. The noncondensable gas throat temperature is set equal to the liquid temperature. In the situation where there is a steam-liquid mixture at the cell center upstream of the break plane, Equation (7.2-2) is again used; and the steam-liquid mixture is assumed to be in equilibrium with the throat steam and liquid temperatures set equal to the saturation temperature at the throat pressure, P_t.

For the steam-liquid-noncondensable situation, the total throat pressure P_t is again calculated with Equation (7.2-2). However, the effect due to partial pressure complicates matters for estimating the throat temperature. The steam-liquid-noncondensable temperature is calculated using a Taylor series approximation to account for the steam partial pressure.[7.2-3] Given the cell-centered pressure PC, which is the sum of the vapor and noncondensable partial pressures, the steam partial pressure P_g at the throat is expanded as

$$P_{gT}(P_c + \Delta P) = P_g(P_c) + \Delta P \left(\frac{\partial P_g}{\partial P} \right)_{P=P_c} \tag{7.2-19}$$

where from Dalton's law, the cell-centered pressure upstream of the throat is

$$P_c = P_{NC} + P_g \tag{7.2-20}$$

and the pressure increment to the throat is

$$\Delta P = P_t - P_c \ . \tag{7.2-21}$$

In the above expansion, we have calculated the steam throat partial pressure with a Taylor series expansion, where P_g is the dependent variable and P_c is the independent variable. The derivative $\left(\frac{\partial P_g}{\partial P} \right)$ is expressed as

$$\left(\frac{\partial P_g}{\partial P} \right) = \left(\frac{\partial T}{\partial P} \right)_s \left(\frac{dP_g}{dT} \right)_{\substack{P=P_c \\ T=T_{sat}(P_c)}} \ . \tag{7.2-22}$$

The isentropic part of the derivative $\left(\frac{\partial T}{\partial P} \right)_s$ is a fairly complex expression. Its expansion into its basic components is detailed in Appendix E. The equilibrium throat steam-liquid-noncondensable temperature is then

$$T_{eq} = PSAT\ (P_{gT}) \tag{7.2-23}$$

where PSAT is the saturation temperature function at the pressure P_{gT}.

7.2.4 Single-Phase One- or Two-Component Vapor Choking Models

The seven principal simplifying assumptions employed in Section 7.2.3 to calculate a_{He} are also employed in the single-phase, one/two-component vapor choking formulation. This choking model presently employs two methods for calculating the sonic speed. The first approximation models the steam as a "perfect gas" (in the sense that there is no potential for vapor condensation). This is a valid approximation when the throat temperature of the steam is well above saturation conditions so that the isentropic

derivative $\left(\frac{\partial \alpha_g}{\partial P}\right)_s = 0$. The second approximation employs the generalized HE formulation from Section 7.2.3. In this formulation, the isentropic derivative $\left(\frac{d\alpha}{dP}\right)_s$ is not equal to zero. This formulation fully accounts for vapor equation of state deviations from the "perfect gas" approximation when the calculated throat temperature is near saturation conditions.

In the first approximation, the steam and noncondensable mixture are assumed to approximate a perfect gas with zero friction losses between the cell center and downstream choke plane. Under these conditions, the cell-centered total pressure, temperature, and density are approximated within the adiabatic choked flow perfect gas formulation. The throat, pressure, temperature, and density become[7.2-17]

$$P_t = P_c^* \left(1 + \frac{\gamma - 1}{2}\right)^{-\left(\frac{\gamma}{\gamma - 1}\right)} \tag{7.2-24}$$

$$P_c^* = P_c + \frac{\rho_c V_c^2}{2} \tag{7.2-25}$$

$$T_t = T_c \left(1 + \frac{\gamma - 1}{2}\right)^{-1} \tag{7.2-26}$$

$$\rho_t = \rho_c \left(1 + \frac{\gamma - 1}{2}\right)^{-\left(\frac{\gamma}{\gamma - 1}\right)} \tag{7.2-27}$$

where the specific heat ratio is density-averaged

$$\gamma = \frac{\bar{C}_f}{\bar{C}_v} = \frac{X_{NC} C_{P_{NC}} + (1 - X_{NC}) C_{P_g}}{X_{NC} C_{V_{NC}} + (1 + X_{NC}) C_{V_g}} \tag{7.2-28}$$

and

$$X_{NC} = \frac{\rho_{NC}}{\rho_t} . \tag{7.2-29}$$

Assuming constant noncondensable mass fraction, X_{NC}, gives a noncondensable throat density

$$\rho_{NC_t} = X_{NC}\rho_t \quad . \tag{7.2-30}$$

The throat partial pressure of the steam becomes

$$P_{gt} = P_t - \rho_{NCt}RT_{NC} \quad . \tag{7.2-31}$$

The conditions at the throat are thus completely specified.

The above throat pressure and temperature conditions are then used by THERMO to calculate the remaining thermodynamic parameters and derivatives to evaluate the equations for the isentropic sound speed. In the limit $\alpha_g = 1$, Equation (7.2-12) reduces to

$$a_{HE} = \left[\left(\frac{\partial \rho_{NC}}{\partial P}\right)_s + \left(\frac{\partial \rho_s}{\partial P}\right)_s\right]^{-1/2} \tag{7.2-32}$$

where the individual isentropic derivatives are evaluated at $T_t = T_{NC} = T_G$.

In the second formulation of the sonic speed, the vapor and noncondensable temperature are set equal to TSAT (P_gT), or the saturation temperature at the partial steam pressure. Since the vapor state is now on the saturation curve, the isentropic derivative $\left(\frac{d\alpha_g}{dF}\right)_s$ is not equal to zero even though $\alpha_\ell = 0$. From Appendix E, the generalized HEM sonic velocity in the limit $\alpha_g = 1$ reduces to

$$a_{HE}^{-2} = \frac{\rho}{\rho_\ell \rho_g}\left\{\rho_g\left(\frac{\partial \rho_{NC}}{\partial P}\right)_s + (\rho_\ell - \rho_{NC})\left(\frac{\partial \rho_g}{\partial P}\right)_s - \frac{\rho_{NC} + \rho_g - \rho_\ell}{S_g - S_\ell}\left[\rho_{NC}\left(\frac{\partial S_{NC}}{\partial P}\right)_s + \rho_g\left(\frac{\partial S_g}{\partial P}\right)_s\right]\right\} . \tag{7.2-33}$$

The current version of TRAC-BF1/MOD1 calculates the sonic speed using both Equations (7.2-32) and (7.2-33) and uses the maximum value in the criteria for choking.

7.2.5 Single-Phase Liquid Critical Flow Models

This section documents the single-phase liquid critical flow model used in TRAC-BF1/MOD1. The terminology single-phase liquid is used in the sense that the vapor and/or noncondensable void fraction is either small or nonexistent. The single-phase liquid critical flow model presently employs two approximations for calculating the sonic velocity. The first method employs the ALJ sonic correlation, while the second method employs a modified HEM approximation. After the sonic speed for each scheme is calculated, the maximum value is used in the choking criterion formulation. The single-phase liquid model is activated when the cell vapor void fraction immediately upstream of the break plane satisfies the criteria $\alpha_g \leq .01$.

The seven principal assumptions employed to calculate the choke plane a_{HE} in Sections 7.2.3 and 7.2.4 are modified for the single-phase liquid critical flow model. These modifications are:

1. Vapor or noncondensables immediately upstream of the break plane are assumed to be insignificant and are not donored to the cell choke plane.

2. The ALJ model formulation quantifies turbulent fluctuations and nonequilibrium nucleation phenomena at the choke plane.

When high-pressure, high-temperature water is suddenly decompressed, it transitions from a subcooled or saturated state to a superheated state. As a consequence, the throat pressure of the flashing liquid can be much lower than the choke plane saturation pressure. Such enhanced depressurization can be driven by turbulent fluctuations or by bubble nucleation effects as the liquid exits the choke plane. The pressure undershoot $\Delta P(a_s)$ at the throat is related to the sonic speed a_s via the correlation

$$P_{sat}(T_\ell) - P_t = \Delta P(a_s) \tag{7.2-34}$$

$$\Delta P(a_s) = (CA + CB\ a_s^{2.4})^{1/2} - CC\ a_s^2 \tag{7.2-35}$$

where

$$CA = \frac{0.258\ \sigma^{3/2} \left(\frac{T_\ell}{T_{crit}}\right)^{13.76}}{(kT_{crit})^{1/2} \left(1 - \frac{\rho_g}{\rho_\ell}\right)} \tag{7.2-36}$$

$$CB = \left| \frac{(13.25)(9.866\ E\text{-}12)\rho_\ell \left(\frac{dA}{dx}\right)_t}{A_t} \right|^{0.8} \qquad (7.2\text{-}37)$$

$$CC = 0.072\ \rho_\ell \left(\frac{A_t}{A_u}\right)^2 \qquad (7.2\text{-}38)$$

σ = surface tension

k = Boltzmann constant

$\left(\frac{dA}{dx}\right)_t$ = rate of area change.

T_{crit} = critical fluid temperature

$P_{sat}\ (T_\ell)$ = saturation pressure at the liquid temperature in the cell adjacent to the choking plane.

The first term in Equation (7.2-33) represents the depressurization driven by nucleation effects formulated by Alamgir and Lienhard.[7.2-18] The second term represents effects of depressurization driven by turbulent driven flashing and was developed by Jones.[7.2-19,20] In the formulation implemented in TRAC-BF1/MOD1, code turbulence driven by acceleration effects (break geometry area gradients) is assumed to be much larger than wall friction effects. As a consequence, wall friction is ignored in the implementation of the AJL correlation in TRAC-BF1/MOD1. The .072 coefficient is a best estimate of the turbulent intensity index in Equation (7.2-35). This number is recommended unless there is a clear and substantially different value known *a priori* for a particular break geometry.[7.2-20]

For closure, the second equation used to equate the throat pressure with sonic speed is the Bernoulli equation (see Section 7.2.2).

$$P_c + \frac{\rho_m V_{mc}^2}{2} = P_t + \frac{\rho_m a_s^2}{2} . \qquad (7.2\text{-}39)$$

Equations (7.2-35) and (7.2-39) are solved in the TRAC-BF1/MOD1 solution scheme by eliminating P_t and finding a_s from the transcendental equation

$$a_s - \sqrt{\frac{2}{\rho_\ell}[DPP + \Delta P(a_s)] + V_{mc}^2} = 0 \qquad (7.2\text{-}40)$$

where

$$DPP = Max\,[0,\ PC - P_{sat}(T_\ell)]\ . \qquad (7.2\text{-}41)$$

Equation (7.2-40) is solved iteratively using a standard Newton-Raphson technique.

The sonic speed is calculated using a second approximation with Equation (7.2-14). Here, the throat temperature is set equal to T and the pressure is set equal to $P_{sat}(T_\ell)$, where T_ℓ is the cell-centered liquid temperature upstream of the throat. In the second approximation, it is assumed that the liquid has decompressed to a saturated state at the break plane. The final sonic velocity becomes Max $[a_s,\ a_{HE}]$, where a_{HE} is the liquid single phase homogenous sound speed from Equation (7.2-14).

In the course of doing simulations with early versions of the TRAC-B choking model, numerical oscillations in the break mass flow rate were observed when the throat conditions were near the subcooled sonic regime.[7.2-4] If the conditions upstream of the break plane transition from subcooled to saturated conditions, large reductions in the throat sonic velocity will occur. To prevent large discontinuous changes in the sonic velocity, a cubic spline interpolation scheme has been employed in the transition region $.01 \leq \alpha_g \leq .1$. In this α_g range, both the TCTF homogeneous equilibrium and single-phase liquid models are separately used to calculate the break plane sonic speed. The cubic spline interpolation yields the transition sonic speed

$$a_T = W a_{HE} + (1 - W) a_s \qquad (7.2\text{-}42)$$

where

$$W = 3\alpha_T^2 - 2\alpha_T^3 \qquad (7.2\text{-}43)$$

$$\alpha_T = \frac{\alpha_g - .01}{.1 - .01}\ . \qquad (7.2\text{-}44)$$

7.2.6 Choking Criteria and Phasic Velocity Formulation Implementation Into TRAC-BF1/MOD1

Once a particular regime has been picked and the corresponding sonic speed calculated, Equation (7.2-1) is employed to test for choking conditions. Because of the half-cell donoring scheme, Equation (7.2-1) is implemented into TRAC-BF1/MOD1 with the following modifications.

The sonic speed calculated from cell edge throat properties is first multiplied by the throat mixture density ratio so that

$$a'_s = a_s \left(\frac{\rho_{mt}}{\rho_{mc}} \right) . \qquad (7.2\text{-}45)$$

This modification was used to partially account for the difference in throat mass flux used in the cell continuity equation (due to cell-centered donoring) and the velocity that would exit if the throat density were used instead. If the choking criteria are satisfied, the new-time throat mixture velocity is set equal to the sonic velocity and then calculated using a relaxation scheme

$$a'^{n+1}_s = a'^{n}_s + RELAX\ (a'^{n}_s - a'^{n+1}_s) \qquad (7.2\text{-}46)$$

where n and n+1 refer to old and new times respectively. A RELAX = .9 is used except in the interpolation region, where RELAX = .1. The relaxation algorithm is used to ensure numerical stability. Calculating the throat sonic velocity is not sufficient to advance the momentum solution for the next time step.

Since there are two unknowns, the throat edge velocities, a second governing equation must be used to solve for two unknowns. The present solution scheme (except for single-phase vapor choking) uses the following two equations:

$$a'_s = \frac{\alpha_g \rho_\ell V_g + \alpha_\ell \rho_g V_\ell}{\alpha_g \rho_\ell + \alpha_\ell \rho_g} \qquad (7.2\text{-}47)$$

$$C_g V_g + C_\ell V_\ell = RHS \qquad (7.2\text{-}48)$$

where

a'_s = calculated sonic speed

V_ℓ, V_g = choke plane cell edge liquid and vapor velocities

C_ℓ, C_g, RHS = TRAC-BF1/MOD1 momentum equation solution constants calculated from TF1E.

For single phase one or two component vapor choking,

$$v_\ell = v_g = a_g' \quad . \tag{7.2-49}$$

In general, the above formulation allows for slip between the phases at the choke plane. In order to advance the TRAC-BF1/MOD1 momentum solution scheme in time, the velocity derivatives with respect to pressure must be calculated. The derivatives are calculated by perturbing the previously calculated throat pressure by 1% in the subroutine CHOKE. The sonic speed and junction velocities are then recalculated. The phasic velocity derivatives are then calculated as follows:

$$\frac{\Delta v_\ell}{\Delta P_t} = \frac{v_\ell(P_t + \Delta P_t) - v_\ell(P)}{\Delta P_t} \tag{7.2-50}$$

$$\frac{\Delta v_g}{\Delta P_t} = \frac{v_g(P_t + \Delta P_t) - v_g(P)}{\Delta P_t} \tag{7.2-51}$$

where ΔP_t is the 1% throat pressure variation. It should be noted that the phasic velocities calculated by CHOKE (if choking criteria are satisfied) that are passed back to TF1E are calculated at P_t and not $P_t + \Delta P_t$.

The current methodology for calculating the choke plane phasic velocities has generally yielded adequate results for comparisons calculated versus experimental data relative to calculated mass flow rates and system depressurization responses.[7.2-1,2,3,4,21]

7.2.7 Conclusions

The two-phase critical flow model detailed in Section 7.1 contains a number of simplifying assumptions that require the code user to understand where the break flow model is applicable. In particular, break flow geometry must be considered as a factor in simulating a particular scenario. If the modeled break configuration is suspected to be strongly effected by multi-dimensional hydrodynamic phenomena (TRAC-BF1/MOD1 choking model is inherently one-dimensional), the code user must determine if the input used for the one-dimensional modeling approximation needs modifications. In a number of circumstances, the use of a discharge coefficient in the break modeling is sufficient to approximate geometric effects.

The TRAC-BF1/MOD1 sonic speed formulation (with the exception of the ALJ correlation, which considers turbulence and nucleation) assumes that inhomogeneous or nonequilibrium processes are not significant. As a

consequence, the sonic speed at the choke plane is derived with the assumption that the liquid and vapor phases have relaxed to thermodynamic equilibrium. The degree of break plane nonhomogeneity is dependent on the flow map, while the degree of nonequilibrium is determined by interfacial transport processes and the time needed to relax to equilibrium. Further studies of these nonequilibrium-inhomogeneous effects on the local choke plane sonic speed may prove fruitful.

Assessment work using the TRAC-BF1/MOD1 critical flow model has generally yielded adequate results with regard to calculated versus measured data and associated system depressurization responses. Because there is still a fairly scarce experimental data base using noncondensables, the validity of the TRAC-BF1/MOD1 formulation with noncondensables is yet to be extensively tested.

7.2.8 References

7.2-1. S. T. Free, *Equilibrium Critical Flow Model Development*, WR-CD-024, June 1980.

7.2-2. J. W. Spore, *Improvements in the TRAC-RD1 Choking Model*, WR-CD-81-053, July 1981.

7.2-3. R. E. Phillips, *Two-Phase Two-Component Choking Model*, EGG-CDD-5977, August 1982.

7.2-4. D. D. Taylor, *Improvements to Subcooled Choking Model*, IS-SAAM-80-025, August 1983.

7.2-5. V. H. Ransom and J. A. Trapp, *RELAP5 Progress Summary Analytical Choking Criterion for Two-Phase Flow*, CDAP-TR-013, 1978.

7.2-6. V. H. Ransom and J. A. Trapp, "The RELAP5 Choked Flow Model and Application to a Large Scale Flow Test," *Proceedings of the ANS/ASME/NRC International Topical Meeting on Nuclear Reactor Thermal-Hydraulics, Saratoga Springs, NY, October 508, 1980*, pp. 799-819.

7.2-7. V. H. Ransom et al., *RELAP5/MOD2 Code Manual, Volume 1*, NUREG/CR-4312, EGG-2396, August 1985.

7.2-8. J. A. Trapp and V. H. Ransom, "A Choked-Flow Calculation Criterion for Nonhomogeneous, Nonequilibrium Two-Phase Flows," *International Journal of Multiphase Flow*, 8, 6, 1982, pp. 669-681.

7.2-9. Y. Y. Hsu et al., *Transport Processes in Boiling and Two-Phase Systems*, American Nuclear Society, La Grange Park, IL, 1986.

7.2-10. J. R. Travis et al., "Multidimensional Effects in Critical Two-Phase

Flow," *Nuclear Science and Engineering*, *68*, 1978.

7.2-11. G. L. Sozzi and W. A. Sutherland, *Critical Flow of Saturated and Subcooled Water at High Pressure*, NEDO-13418, 1975.

7.2-12. R. E. Henry et al., "The Two-Phase Critical Flow of One Component Mixtures in Nozzles, Orifices, and Short Tubes," *Journal of Heat Transfer*, May 1981.

7.2-13. R. E. Henry, "The Two-Phase Critical Discharge of Initially Saturated Subcooled Liquid," *Nuclear Science Engineering*, *41*, 3, 1970, pp. 336-343.

7.2-14. H. K. Fauske, "The Discharge of Saturated Water Through Tubes," *Chemical Engineering Progress Series*, *61*, 59, 1965, pp. 210-216.

7.2-15. D. K. Edmonds and R. V. Smith, "Comparison of Mass Limiting Two-Phase Flow in a Straight Tube and in a Nozzle," *Symposium on Two-Phase Flow*, *1*, *University of Exeter, England, 1966*, pp. G401-G414.

7.2-16. R. E. Henry, *A Study of One- and Two-Component, Two-Phase Critical Flows at Low Qualities*, ANL-7430, March 1968.

7.2-17. A. H. Shapiro, *The Dynamics and Thermodynamics of Compressible Flow*, *1*, New York: Ranald Press, 1953.

7.2-18. M. D. Alamgir and J. H. Lienhard, "Correlation of Pressure Undershoot During Hot Water Depressurization," *ASME Journal of Heat Transfer*, *103*, 1981, pp. 52-73.

7.2-19. N. Abuaf, O. C. Jones, Jr., and B. J. C. Wu, *Critical Flashing Flow in Nozzles with Subcooled Inlet Conditions*, BNL-NUREG-27512, 1980.

7.2-20. O. C. Jones, Jr., "Flashing Inception in Flowing Liquids," *ASME Journal of Heat Transfer*, *102*, 1980, pp. 439-444.

7.2-21. B. L. Charboneau, *Overview of TRAC-BD1/MOD1 Assessment Studies*, NUREG/CR-4428, EGG-2422, November 1985.

7.3 COUNTERCURRENT FLOW LIMITATION

Countercurrent flows of vapor and liquid, that may occur at some hydraulic restrictions, can lead to flooding situations, known as countercurrent flow limitation (CCFL), in which the rising vapor retards downflow of liquid. This phenomenon is important in the penetration and distribution of the emergency core cooling (ECC) water in BWRs. Countercurrent flow limitation may affect the liquid penetration through the upper core tie plate, and it may also affect outpouring of liquid from the fuel bundles through the side entry orifices at the bottom of the bundles. However, CCFL may occur at any hydraulic restriction in the vertical flow paths of a system, depending on the geometry of the restriction, vapor velocity, and the properties of water and steam at that point.

The CCFL formulation used in TRAC-BF1/MOD1 is a part of the inter-facial shear model according to Andersen et al.[7.3-1,2] The present section gives the derivation of the CCFL model, equations that are used in the FRCIF subroutine, and a review of the CCFLCK subroutine, where the user-specified applications of the CCFL model are performed. Equations that are used in the coding of the CCFLCK subroutine are marked with an asterisk, followed by the symbolic variable name used for the left-hand side of that equation in the coding.

7.3.1 The CCFL Model

Experimental investigations have shown that CCFL depends on properties of the two phases and on the geometry of the hydraulic restriction.[7.3-1] The limiting liquid flow rates may be correlated to the rising vapor flow rates either by a Wallis-type correlation[7.3-3] or through a Kutateladze correlation, as suggested by Sun,[7.3-1] with the following general expression

$$\sqrt{K_g} + m\sqrt{K_\ell} = \sqrt{K} \qquad (7.3\text{-}1)$$

in which

$$K_g = \frac{j_g}{j_{go}} = \alpha \bar{V}_g \frac{\sqrt{\rho_g}}{(\sigma \Delta\rho g)^{0.25}} \quad , \text{KG} \qquad (7.3\text{-}2)$$

$$K_\ell = \frac{j_\ell}{j_{\ell o}} = (1-\alpha)\bar{V} \frac{\sqrt{\rho_\ell}}{(\sigma \Delta\rho g)^{0.25}} \qquad (7.3\text{-}3)$$

where m is a constant and K, which is known as Kutateladze number, depends on geometry and flow properties (see Nomenclature for the other symbols). J_g^* and J_{fo} are the variable groups that are found useful in making the volumetric fluxes j_g and j_f nondimensional in Equation (7.3-1).

TRAC-BF1/MOD1 employs Equation (7.3-1) in two different contexts: (a) as a regular part of the interfacial shear model (described in Section 6.1) with a built-in set of constants, m and K, and (b) as a special option evoked by the user at any flagged hydraulic junction, with the user-specified constants, m and K. In the following, the general approach is discussed first and the special applications are mentioned later.

7.3.2 Distribution Parameter for CCFL

In order to employ the CCFL model in regular momentum solutions according to the interfacial friction model, one has to define the distribution parameter, C_o, and the interfacial friction coefficient, C_i, that match the CCFL situation. Referring to the variables j_g and j_f of the drift flux model (see Section 6.1), one may construct a graph of the countercurrent flows in the coordinate system of these variables, as shown in Figure 7.3-1. It may be observed that the CCFL situations are encountered only in the quadrant of $j_f < 0.0$ and $j_g > 0.0$. This explains the necessity of the negative sign of K_f in Equation (7.3-1).

According to Reference 7.3-2, a combination of CCFL and drift flux principles requires that the drift flux equation be a tangent to the CCFL curve in the j_g - j_f plane. The drift flux equation is given by

$$j_g = \frac{\alpha C_o}{1 - \alpha C_o} j_f + \frac{\alpha}{1 - \alpha C_o} \bar{V}_{gj} \quad . \tag{7.3-4}$$

(Derivation of this equation is shown in Appendix F.) The necessity of this requirement is obvious from the fact that the relationship between j_g and j_f must satisfy both Equations (7.3-1) and (7.3-4) and that the linear relation may not be applied to any point inside the CCFL curve. Hence, both intercepts of Equations (7.3-1) and (7.3-4) must coincide at one point on the curve, regardless of the actual values of j_g and j_f. The necessary mathematical condition is obtained by setting the Δ (i.e., $b^2 - 4ac$ term) in the solution of the intercept equation equal to zero. This gives the following relation between $\bar{V}_{gj}$ and C_o for the CCFL situations:

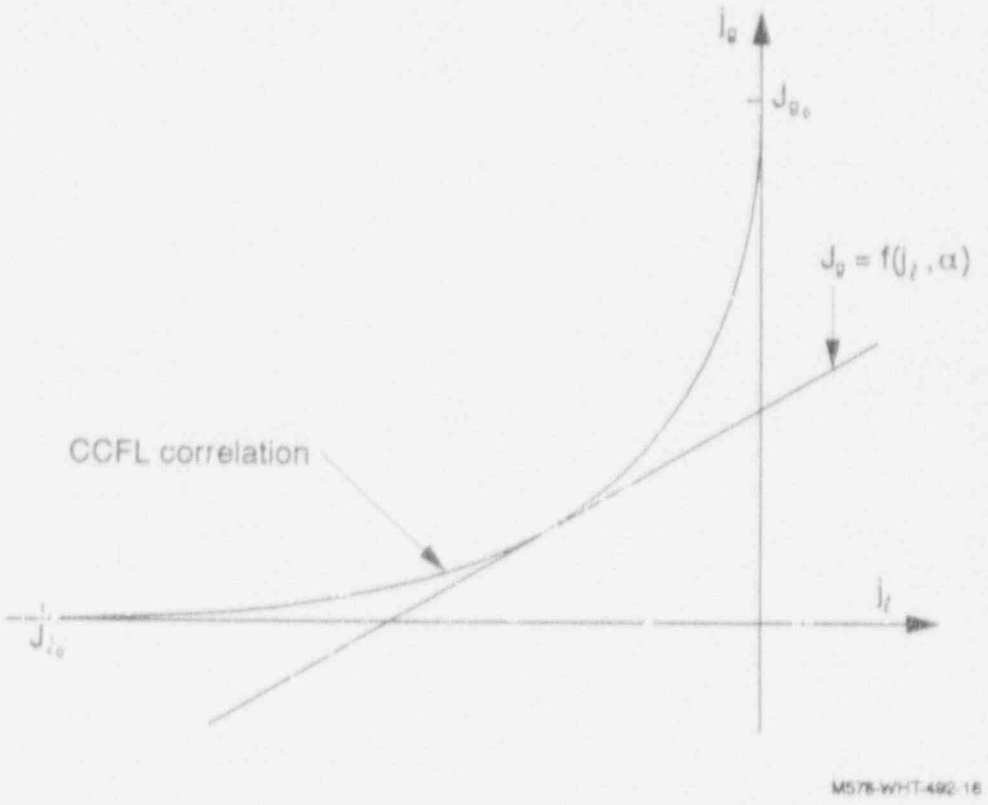

Figure 7.3-1. Drift flux correlation and CCFL.

$$\frac{\bar{V}_{gj}}{j_{\ell_0}} = \frac{KC_0(1 - \alpha C_0)}{\frac{j_{\ell^0}}{j_{g0}}\alpha C_0 + m^2(1 - \alpha C_0)} \quad . \tag{7.3-5}$$

This equation is solved for C_0 in terms of $\bar{V}_{gj}$ in CCFL situations. Solution of this equation provides

$$(C_0)_{ccfl} = A_0 \pm \sqrt{A_0^2 - \frac{rm^2}{\alpha}} \tag{7.3-6}$$

in which

$$A_o = 0.5 \left| \frac{1}{\alpha} + F \left(m^2 - \sqrt{\frac{\rho_g}{\rho_\ell}} \right) \right| \tag{7.3-7}$$

and

$$F = \frac{\bar{V}_{gj}}{K j_{\ell o}} \, . \tag{7.3-8}$$

The term $\left(\frac{\rho_g}{\rho_\ell} \right)^{0.5}$ in Equation (7.3-7) is the ratio of $\frac{j_{\ell o}}{j_{go}}$.

In order to avoid imaginary solutions of Equation (7.3-6), the value of F is limited to an F_{max} which reduces the square root in Equation (7.3-6) to zero. By setting $A_o^2 + \frac{Fm^2}{\alpha} = 0$ and doing some algebraic manipulations, one obtains

$$F = F_{max} = \frac{\gamma}{\alpha \left(1 + \sqrt{m^2 \gamma} \right)^2} \, . \tag{7.3-9}$$

As may be seen, in general, Equation (7.3-6) provides two solutions, depending on the sign to be used for the square root. However, instead of randomly choosing one of the two possible solutions, an interpolation routine is used that takes some fraction of each solution, depending on the local void fraction. The interpolation variable is based on $\chi 2$, which was defined by Equation (6.1-51) in Section 6.1

$$\chi 2 = \frac{\alpha - \alpha_{tran}}{0.25} \, . \tag{7.3-10}$$

The interpolated solution is

$$(C_o)_{ccfl} = A_o + (2\chi 2 - 1) \sqrt{A_o^2 - \frac{Fm^2}{\alpha}} \, . \tag{7.3-11}$$

For low void fractions, $\alpha < \alpha_{tran}$, $\chi 2$ is zero; hence, the negative root will be used. As α increases (with increasing j_g), $(C_o)_{ccfl}$ will include more and more of the positive root; and for $\alpha > (\alpha_{tran} + 0.25)$, where $\chi 2$ is 1, the positive root will apply completely.

As stated earlier, the CCFL constants m and K are dependent on geometry and flow properties. TRAC-BF1/MOD1 employs two sets of default values of m and K, one set for the upper tie-plate and another set for the side entry orifice. These sets, which are recommended for BWR geometry according to Reference 7.3-9, are;

For the upper tie-plate: m = 1.0 and K = 4.2
For the side entry orifice: m = 0.59, and

$$K = [A - B P_w^*]^2 \tag{7.3-12}$$

where A = 2.14, B = 0.008, and

$$P_w^* = \frac{P_w}{\left[\frac{\sigma}{g(\rho_\ell - \rho_g)}\right]^{0.5}} , \tag{7.3-13}$$

The data base for extracting these constants and relations is summarized in the next section.

In CCFL situations, the C_1 factor, according to Equation (6.1-30) of Section 6.1, is calculated with the following formula:

$$(C_1)_{ccfl} = \frac{1 - \alpha(C_0)_{ccfl}}{1 - \alpha} . \tag{7.3-14}$$

Equations (7.3-7), (7.3-8), (7.3-9), (7.3-11), and (7.3-14) are implemented as a part of the interfacial shear model in the FRCIF subroutine (see Section 6.1).

7.3.3 Data Base for the CCFL Model

The suggested correlations for countercurrent flow, or flooding, which appear in the technical literature[7.3-3,4,5] are based on data from a variety of geometries and flow conditions. It is not within the scope of this report to enumerate the basic data that have led to the development of generic flooding correlations by Wallis[7.3-3] or its modified version based on Kutateladze numbers.[7.3-4] However, some test data from BWR-specific geometries have been used to obtain the above mentioned empirical relation and constants for the Kutateladze type flooding correlations in those geometries. The sources of these data and the range of their variables are given in Table 7.3-1. A collected reference to the BWR related data, their analysis, and the resulting empirical constants is given by Sun in Reference 7.3-4.

Table 7.3-1. BWR fuel bundle flooding data base.

Test Geometry	Range of Variables	Reference
Upper tie plate[a] 7 x 7 bundle, simulated actual BWR tie plate flow area.	0.11376 < P < 0.14961 MPa 374 < Tg < 385 K 365 < Tℓ < 370 K 5.48 < j_g < 11.1 m/s 0.0068 < $-j_ℓ$ < 0.0656 m/s	Tobin[7.3-6]
Upper tie plate[a] 8 x 8 bundle, simulated actual BWR tie plate flow area.	0.10066 < P < 0.13789 MPa 373 < T_g < 382 K 350 < $T_ℓ$ < 370 K 3.25 < j_g < 12.04 m/s 0.0004 < $0j_ℓ$ < 0.126 m/s	Jones[7.3-7]
Upper tie plate[a] 8 x 8 bundle, 92% of the flow area of an actual 8 x 8 BWR tie plate.	0.101 < P < 0.120 MPa 373 < T_g < 378 K 304 < $T_ℓ$ < 374 K 9.74 < j_g < 18.88 m/s 0.007 < $-j_ℓ$ < 0.117 m/s	Naitoh et al.[7.3-8] (approximate)
Bundle bottom,[b] three side-entry orifices with D_i = 31.9, 37.6, and 61.7 mm.	0.0993 < P < 1.021 MPa 372.5 < T_g < 388.1 K 372.5 < $T_ℓ$ < 388.1 K 0.1436 < j_g < 25.79 m/s 0.00035 < $j_ℓ$ < 0.5097 m/s	Jones[7.3-9]

a. Data used for extracting the constants m and K for BWR upper tie plate.

b. Data used to derive the geometry and pressure-dependent correlation for K and the constant m for the side entry orifice of BWR fuel bundles.

As may be observed in Table 7.3-1, most of the BWR relevant data are taken at near atmospheric pressure. No comparison of the constants, m and K, has been made with data from higher pressures. However, since the CCFL correlation is based on non-dimensional variable groups, no major deviations are anticipated at higher pressures.

7.3.4 User-Defined CCFL Applications

Apart from the regular application of the CCFL correlation in the interfacial shear routine, TRAC-BF1/MOD1 provides a separate option for using the CCFL model at any specified junction. This option checks the flow situation at the specified junctions and calculates a liquid downflow velocity, according to Equation (7.3-1), for a given vapor velocity and the specified CCFL constants for that junction. These calculations are done in

the CCFLCK subroutine, and the input constants are A and B in Equation (7.3.-12) and m in Equation (7.3-1). A description of the CCFLCK subroutine is given below.

7.3.5 Description of the CCFLCK Subroutine

CCFLCK is a small subroutine that is called by the TF1DE and TF3DE subroutines for each hydraulic junction. The void fractions of the hydraulic volumes before and after the junction (α_1 and α_2, respectively), as well as the liquid and vapor velocities, $\bar{V}_\ell$ and $\bar{V}_g$, at the junction are among the arguments that are passed from the calling routine to CCFLCK in each case.

The computations within the CCFLCK subroutine are straightforward according to Equation (7.3-1). In the beginning, the absolute value of the incoming vapor velocity and the negative value of the incoming liquid velocity ($\bar{V}_{\ell n} = -|\bar{V}_\ell|$) are calculated for logical operations, and a check is made on the junction number to identify the proper set of the CCFL constants to be applied for that junction. Once K and m are defined, Equation (7.3-1) is used to calculate a liquid velocity, V_{lx}, for the given vapor velocity, $\bar{V}_g$, at the junction. Also, Equation (7.3-2) is used to calculate K_g for the given vapor velocity. The logic diagram of the CCFLCK subroutine is shown in Figure 7.3-2.

If K_g is larger than K, (vapor Kutateladze number above the cut-off value) there is no countercurrent flow; $\bar{V}_\ell$ is set equal to $\bar{V}_{lx}$ with the sign of the original V_g and returned to the calling routine. However, if K_g is smaller than K and $\bar{V}_{lx}$ is equal or smaller than $\bar{V}_{\ell n}$, the liquid velocity, $\bar{V}_\ell$, is returned to the calling routine with no alteration. Finally, if $\bar{V}_{lx}$ is larger than $\bar{V}_{\ell n}$, then $\bar{V}_\ell$ is set equal to $\bar{V}_{lx}$ with a sign that is the negative of the original liquid velocity $\left[\bar{V}_\ell = \bar{V}_{lx}\left(\frac{-\bar{V}_\ell}{|\bar{V}_\ell|}\right)\right]$, and this $\bar{V}_\ell$ is returned to the calling subroutine.

In the final part of the CCFLCK subroutine, one calculates the derivative of $\bar{V}_{lx}$ with respect to pressure difference, $\frac{DV_{lx}}{D(\Delta P)}$. This is done by using

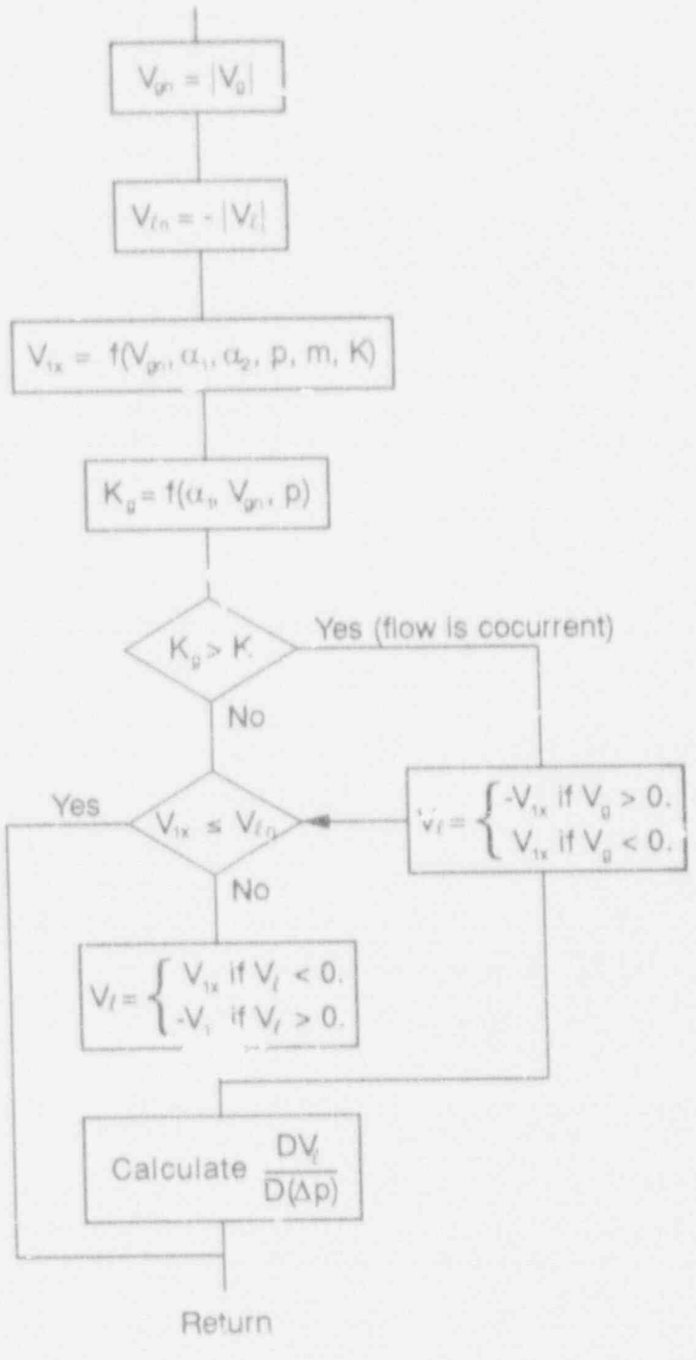

Figure 7.3-2. The logic diagram of the CCFLCK subroutine.

the analytically derived partial derivative of $\frac{\delta \bar{V}_\ell}{\delta \bar{V}_g}$ from Equation (7.3-1) and $\frac{D\bar{V}_g}{D(\Delta P)}$, which is brought in among the calling arguments.

$$\frac{D\bar{V}_{1x}}{D(\Delta P)} = \frac{1}{m^2}\left[\frac{\sqrt{\alpha_1 K \sqrt{\rho_g}\,(g\sigma\Delta\rho)^{0.25}}}{(1-\alpha_2)\left(\bar{V}_g\rho_\ell\right)^{0.5}} - \frac{\alpha_1\sqrt{\rho_g}}{(1-\alpha_2)\sqrt{\rho_\ell}}\right]\frac{D\bar{V}_g}{D(\Delta P)} \quad *, \text{ DL (7.3-15)}$$

7.3.6 References

7.3-1. J. G. M. Andersen and K. H. Chu, *BWR Refill-Reflood Program, Task 4.7 - Constitutive Correlations for Shear and Heat Transfer for the BWR Version of TRAC*, NUREG/CR-2134, EPRI NP-1582, GEAP-24940, December 1981.

7.3-2. J. G. M. Andersen, K. H. Chu, and J. C. Shaug, *BWR Refill-Reflood Program, Task 4.7 - Model Development. Basic Models for the BWR Version of TRAC*, NUREG/CR-2573, EPRI NP-2375, GEAP-22051, September 1983.

7.3-3. G. B. Wallis et al., *Countercurrent Annular Flow Regimes for Steam and Subcooled Water in a Vertical Tube*, EPRI NP-1336, January 1980.

7.3-4. K. H. Sun, "Flooding Correlations for BWR Bundle Tieplate and Bottom Side-Entry Orifices," *Second Multi-Phase Flow and Heat Transfer Symposium - Workshop, Miami Beach, FL, April 16-19, 1979.*

7.3-5. G. B. Wallis, *One-Dimensional, Two-Phase Flow*, New York: McGraw-Hill Book Company, 1969, pp. 336-345.

7.3-6. R. Tobin, *CCFL Test Results, Phase 1 - TLTA 7x7 Bundle*, GEAP-21304-5, 1977, Appendix C.

7.3-7. D. D. Jones, *Subcooled Counter-Current Flow Limiting Characteristics of the Upper Region of a BWR Fuel Bundle*, NEDG-NUREG-23549, 1977.

7.3-8. M. Naitoh, K. Chino, and R. Kawabe, "Restrictive Effect of Ascending Steam on Falling Water During Top Spray Emergency Core Cooling," *Journal of Nuclear Science and Technology, 15*, 11, 1978, p. 806.

7.3-9. D. D. Jones, *Test Report TLTA Components CCFL Tests*, NEDG-NUREG-23732, 1977.

8. SPECIAL COMPONENT MODELS

Some of the one-dimensional components in TRAC-BF1/MOD1 perform functions that alter the way in which one-dimensional fluid equations are normally solved. These functions are more than simply altering the normal closure relations that have been discussed in Chapters 4 and 6; these components either alter the normal finite differencing of the fluid equations, introduce source terms to the equations, or use complex logic to alter the closure relations to accomplish a specific modeling requirement. The PUMP component produces a momentum source term in the form of an additional Δp on the right-hand side of the momentum equation to model the pressure rise across the pump impeller. The steam/water separator-dryer component (SEPD) permits the user to model the swirl separators and chevron dryers in a BWR reactor. The VALVE component provides a variable flow area to model the action of various types of valves. The HEATR component models the shell side of both vertical and horizontal feedwater heaters as well as the shell side of condensers, including the phase separation due to drain cooler regions or hot wells. The JETP component models the jet pumps found in BWR systems by use of the TEE component momentum source in the TEE joining cell and jet pump specific singular loss coefficients. The TURB component models the energy extraction (and associated pressure and enthalpy drops) across the blade cascade of turbines, as well as the phase separation in moisture separators and steam extraction for feedwater heating. The CONTAN component models the BWR containment, using a separate lumped parameter formulation that provides boundary conditions to the remainder of the BWR reactor system. The FILL and BREAK components provide boundary conditions to the normal one-dimensional components by allowing the user to specify either flows (FILL) or pressures (BREAK) at the boundary, together with the fluid state if an inflow condition exists. Most of these component models have been described in Volume 1 of the TRAC-BF1/MOD1 Manual,[8.1-1] and the following sections are reproductions of the model descriptions from the Manual, with some additions and modifications.

8.1 PUMP COMPONENT

The PUMP model was developed at LANL and was included in the code from which TRAC-BWR was developed. The PUMP component describes the interaction of the system fluid with a centrifugal pump. The model calculates the pressure differential across the pump and its angular velocity as a function of the fluid flow rate and the fluid properties. The model can treat any centrifugal pump and allows for the inclusion of two-phase effects.

The pump model is represented by a one-dimensional component with N cells ($N > 1$). The pump momentum is modeled as a source at the user-specified interface between cells; this interface will be referred to as the pump interface for the remainder of this discussion. The source is positive for normal operation, so that a pressure rise occurs in the direction of increasing cell index. Therefore, it is necessary to construct the cell

noding such that the cell number increases in the normal flow direction. This latter requirement is equivalent to requiring the first cell of the component to be in the pump suction and the second cell in the pump discharge for normal operation.

The following considerations were important in creating the PUMP component:

1. Compatibility with adjacent components should be maximized,
2. Choking at the pump inlet or outlet should be predicted automatically, and
3. The calculated pressure rise across the pump should agree with that measured at steady-state conditions.

The first two criteria precluded the use of a lumped-parameter model. The PUMP component, therefore, combines the PIPE component with pump correlations.

The pump model that is in TRAC-BF1-MOD1 is very similar to that included in RELAP4/MOD5,[8.1-2] although some additional assumptions were made to incorporate the momentum source into the momentum equations. Also, the details of the input for the homologous curves are somewhat different in that the eight curve segments defined in RELAP4/MOD5 are combined into only four segments in TRAC-BF1/MOD1. Reference 8.1-3 (Chapter 9) provides a good discussion of pump operation, and Section 9.2 of the same reference describes the single-phase homologous curve description of a pump. Reference 8.1-4 is a general text on pumps and provides much information about pumps and their operating characteristics. Runstadler[8.1-5] provides an overview of the state of the art in pump modeling in the mid-1970s, about the time that work began on TRAC-BD1 and there was a need for a pump model in the code. Several organizations worked on pump models during the late 1970s, and the work continued through the 1980s. Furuya[8.1-6] developed an analytical pump model that yields the two-phase performance characteristics based on single-phase characteristics and the details of the pump geometry.

The similarity factor for pumps that is most often discussed is the specific speed ω_s defined in the following equation [Reference 8.1-4, Equation (5.9)]:

$$\omega_s = \frac{\omega Q^{1/2}}{(gH)^{3/4}} \qquad (8.1\text{-}1)$$

where

n = pump speed (rad/s, rev/s)

Q = volumetric flow (m^3/s, ft^3/s)

g = acceleration of gravity (m/s^2, ft/s^2)

H = pump head (m, ft).

This specific speed ω_s is dimensionless only if the units of the other parameters are consistent, as noted above. Stepanoff (Reference 8.1-4) points out that ω_s is constant for all similar pumps and ideally does not change with speed for a given pump; however, when it is used as a similarity parameter, ω_s should be calculated at the highest efficiency point of operation. Stepanoff also casts ω_s in another dimensionless form (Reference 8.1-4, Equation 5.35), which shows the importance of maintaining certain geometric ratios in similar pumps. All of this discussion really is intended to provide a guide to help the code user determine if a set of homologous curves can be used to describe this pump.

8.1.1 Pump Governing Equations

The pump model is identical to the one-dimensional pipe model except that the momentum equations between cells where the impeller is located are rewritten as

$$\frac{V_g^{n+1} - V_g^n}{\Delta t} = \frac{P_j^{n+1} - P_{j+1}^{n+1} + \Delta P^n + \left(\frac{\partial \Delta P}{\partial V}\right)^n V_g^{n+1} - V_g^n}{(\bar{\rho}_m)^n \Delta x} - g \cos\theta \qquad (8.1\text{-}2)$$

and

$$V_\ell = V_g \,, \qquad (8.1\text{-}3)$$

where ΔP is the pressure rise through the pump evaluated from the pump correlation. Equation (8.1-2) is implemented in subroutine TF1E. The steady-state solution of Equation (8.1-2) is

$$\Delta P = P_{j+1} - P_j + g \cos\theta \,, \qquad (8.1\text{-}4)$$

which is the desired result. Friction does not enter explicitly into the pump motion equation, because we assume that the friction effects are normally included in the homologous curves defining the pump head. Therefore, additive friction is not allowed at the impeller location.

It is necessary to evaluate ΔP and its derivative with respect to velocity for a pump cell only once each time step. The source is needed only in routine TF1E. This evaluation is performed by subroutine PUMPSR.

8.1.2 Pump Head and Torque from Homologous Curves

The pump correlation curves describe the pump head and torque response as a function of fluid volumetric flow rate and pump speed. Homologous curves (one curve segment represents a family of curves) are used for this description because of their simplicity. These curves describe, in a compact manner, all operating states of the pump obtained by combining positive or negative impeller velocities with positive or negative flow rates.

The following definitions are used in the subsequent development:

H = the pump head = $\Delta P/\rho_m$

Q = the pump volumetric flow, and

Ω = the pump impeller angular velocity,

where ΔP is the pressure rise across the pump and ρ_m is the pump average mixture density in the cells immediately adjacent to the pump interface. The code user should note that the definition of pump head H above differs from the standard definition by a factor g, the acceleration due to gravity. To allow one set of curves to be used for a variety of pumps, the following normalized quantities are used:

$$h = \frac{H}{H_R} , \tag{8.1-5}$$

$$q = \frac{Q}{Q_R} , \tag{8.1-6}$$

and

$$\omega = \frac{\Omega}{\Omega_R} , \tag{8.1-7}$$

where H_R is the rated head (RHEAD) for the pump, Q_R is the rated volumetric flow (RFLOW), and Ω_R is the rated pump speed (ROMEGA). The pump similarity relations[8.1-3] show that

$$\frac{h}{\omega^2} = f\left(\frac{q}{\omega}\right) . \tag{8.1-8}$$

For small ω, this correlation is not satisfactory, and the following combination of variables is used

$$\frac{h}{q^2} = f\left(\frac{\omega}{q}\right) . \qquad (8.1\text{-}9)$$

Equation (8.1-8) is used in the range $0 \le |q/\omega| \le 1$ and results in two separate curves, one for $\omega > 0$ and one for $\omega < 0$. Equation (8.1-9) is used in the range $0 \le |\omega/q| \le 1$ and yields two separate curves, one for $q > 0$ and one for $q < 0$. The four resulting curve segments, as well as the curve selection logic used in TRAC-BF1/MOD1, are shown in Table 8.1-1.

Table 8.1-1. Definitions of the four curve segments that describe the homologous pump head curves[a]

Curve segment	$\lvert q/\omega \rvert$	ω	q	Correlation
1	≤ 1	> 0	--	$h/\omega^2 = f(q/\omega)$
4	≤ 1	< 0	--	
2	> 1	--	> 0	$= f(\omega/q)$
3	> 1	--	< 0	

a. For the special case of both $\omega = 0.0$ and $q = 0.0$, the code sets $h = 0.0$.

To account for two-phase effects on pump performance, the pump curves are divided into two separate regimes. Data indicate that two-phase pump performance in the vapor-fraction range of 20%-80% is degraded significantly in comparison with its performance at vapor fractions outside of this range. One set of curves describes the pump performance for single-phase fluid (0 or 100% vapor fraction), and another set describes the two-phase, fully degraded performance at some void fraction between 0 and 100%. For single-phase conditions, the curve segments for Equation (8.1-8) are input as HSP1 for $\omega > 0$ and HSP4 for $\omega < 0$, and Equation (8.1-9) curve segments are input as HSP2 for $q > 0$ and HSP3 for $q < 0$. The fully degraded version of Equation (8.1-8) is input as curve HTP1 for $\omega > 0$ and HTP4 for $\omega < 0$. The fully degraded version of Equation (8.1-9) is input as HTP2 for $q > 0$ and HTP3 for $q < 0$.

The pump head at any vapor fraction is calculated from the relationship,

$$H = H_1 - M(\alpha)(H_1 - H_2) , \qquad (8.1\text{-}10)$$

where

H = the total pump head

H_1 = the single-phase pump head = $h_1 H_R$ where h_1 is the

nondimensional head from the single-phase homologous head curves

H_2 = the fully degraded pump head = $h_2 H_R$ where h_2 is the nondimensional head from the fully degraded homologous head curves

m = the head degradation multiplier (input as HDM), and

α = the donor-cell void fraction.

To this point, no knowledge of density is required to calculate H from the homologous head curves. The average mixture density in the cells immediately adjacent to the pump interfaces is always used to convert the total pump head H to ΔP, the pressure rise through the pump, by the definition $\Delta P = \rho_m H$.

The development of homologous torque curves parallels the previous development for homologous head curves. The dimensionless hydraulic torque is defined by

$$\beta = \frac{T_{hy}}{T_R} , \qquad (8.1\text{-}11)$$

where

T_{hy} = hydraulic torque

T_R = rated torque (RTORK).

The convention used is that a positive T_{hy} works to retard positive pump angular velocity. The dimensionless torque β is correlated as either β/ω or β/q just as the dimensionless head was correlated. For single-phase conditions, the correlations yield the corresponding four curve segments--TSP1, TSP2, TSP3, and TSP4. The fully degraded correlations produce four corresponding curves--TTP1, TTP2, TTP3, and TTP4. The homologous torque curve segments are correlated in the same manner as the head curve segments shown in Table 8.1-1 (replace h with β). For the special case of $\omega = q = 0.0$, the code sets $\beta_1 = \beta_2 = 0.0$.

The single-phase torque T_1 is dependent upon the fluid density and is calculated from

$$T_1 = \beta_1 T_R \left(\frac{\rho_m}{\rho_R} \right) , \qquad (8.1\text{-}12)$$

where

β_1 = dimensionless hydraulic torque from the single-phase homologous torque curves

ρ_m = pump average mixture density in the cells immediately adjacent to the pump interface

ρ_R = rated density (RRHO).

The density ratio is needed to correct for the density difference between the pumped fluid and the rated condition. Similarly, the fully degraded torque T_2 is obtained from

$$T_2 = \beta_2 T_R \left(\frac{\rho_m}{\rho_R} \right) , \qquad (8.1\text{-}13)$$

where β_2 is the dimensionless hydraulic torque from the fully degraded homologous torque curves. For two-phase conditions, the impeller torque is calculated from

$$T = T_1 - N(\alpha)(T_1 - T_2) , \qquad (8.1\text{-}14)$$

where

T = total impeller torque

$N(\alpha)$ = torque degradation multiplier (input as TDM).

In addition to the homologous head and torque curves, the head and torque degradation multipliers defined in Equations (8.1-10) and (8.1-14) are required. These functions of void fraction are nonzero only in the vapor-fraction range where the pump head and torque are either partially or fully degraded.

8.1.3 Pump Speed

The pump component treats the pump angular velocity as a constant (input) while the motor is energized. After a drive motor trip, the time rate of change for the pump angular velocity Ω is proportional to the sum of the moments acting on it and is calculated from the equation,

$$I \frac{d\Omega}{dt} = - \sum_i T_i = - (T + T_f + T_b + T_m) , \qquad (8.1\text{-}15)$$

where

I = combined impeller, shaft, and motor assembly moment of inertia (EFFMI)

T = hydraulic torque on the impelle

T_f = the torque caused by friction

T_b = bearing and windage torque

T_m = driving (or motor) torque computed by he turbine model or the control systems model.

We assume that T_f and T_b are

$$T_f = C_1 \left(\frac{\Omega|\Omega|}{\Omega_R^2} \right) \tag{8.1-16}$$

and

$$T_b = C_2 \left(\frac{\Omega|\Omega|}{\Omega_R^2} \right) , \tag{8.1-17}$$

where C_1 and C_2 are input constants (TFR1 and TFR2, respectively). The hydraulic torque T is evaluated using the homologous torque curves and Equation (8.1-14); it is a function of the volumetric flow, the upstream void fraction, the average density in the cells immediately adjacent to the pump interface, and the pump angular velocity. For time step n+1, Equation (8.1-15) is evaluated explicitly

$$\Omega^{n+1} = \Omega^n - \frac{\Delta t}{I} T(Q, \alpha, \rho_m, \Omega) + (C_1 + C_2) \frac{\Omega^n|\Omega^n|}{\Omega_R^2} + T_m . \tag{8.1-18}$$

8.1.4 Pump Homologous Curves

The user may specify pump homologous curves in the input or alternately may use the built-in pump curves. The set of built-in pump curves is based on the Semiscale Mod-1 system pump.[8.1-2,7,8,9] The Semiscale pump curves for single-phase homologous head (HSP), fully degraded two-phase homologous head (HTP), head degradation multiplier (HDM), single-phase homologous torque (TSP), and torque degradation multiplier (TDM) are provided in Figures 8.1-1 through 8.1-5, respectively. The fully degraded two-phase homologous torque curves (TTP) for the Semiscale pump is zero. Where applicable, the curves are numbered corresponding to the conditions provided in Table 8.1-1.

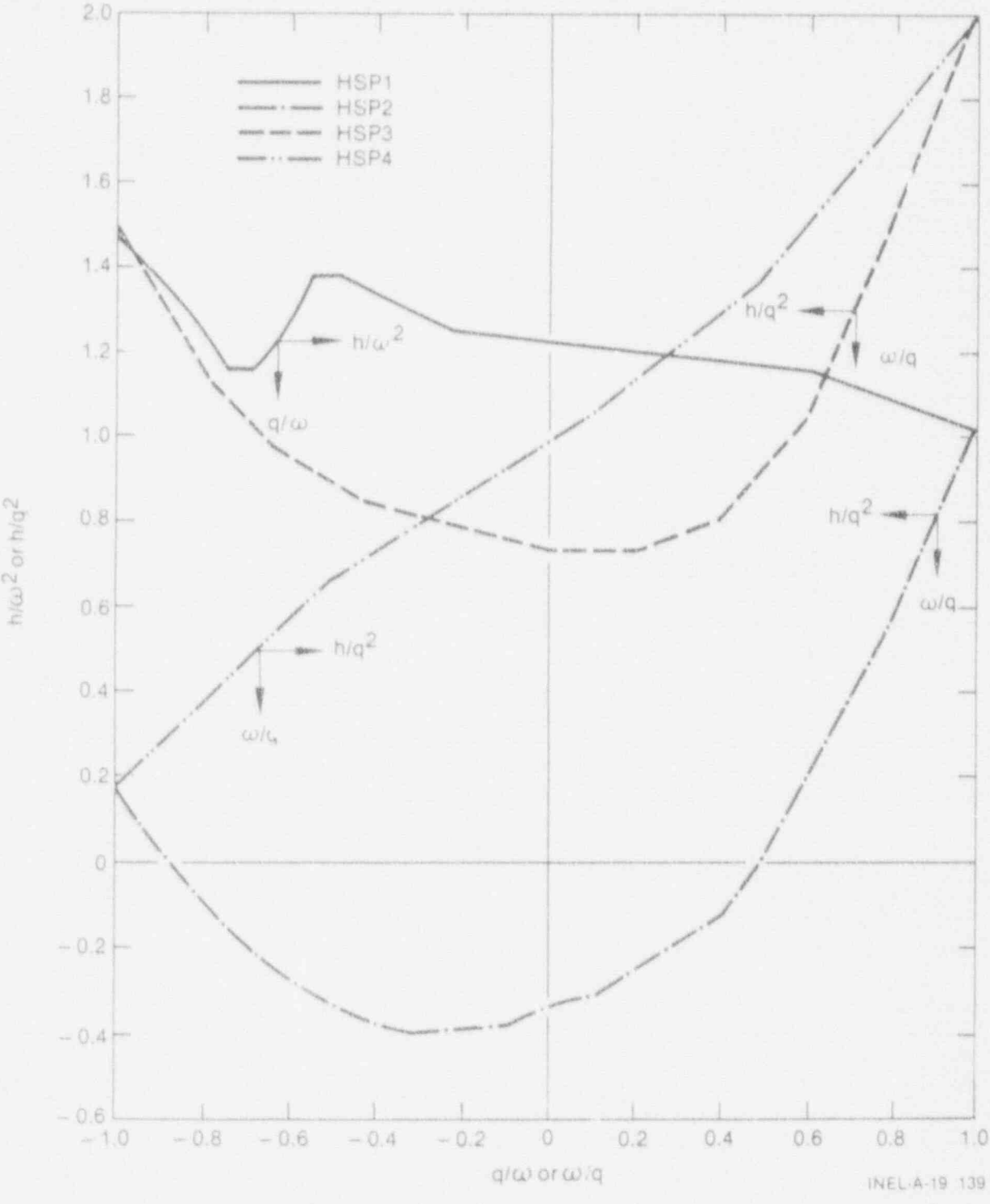

Figure 8.1-1. Semiscale single-phase homologous head curves.

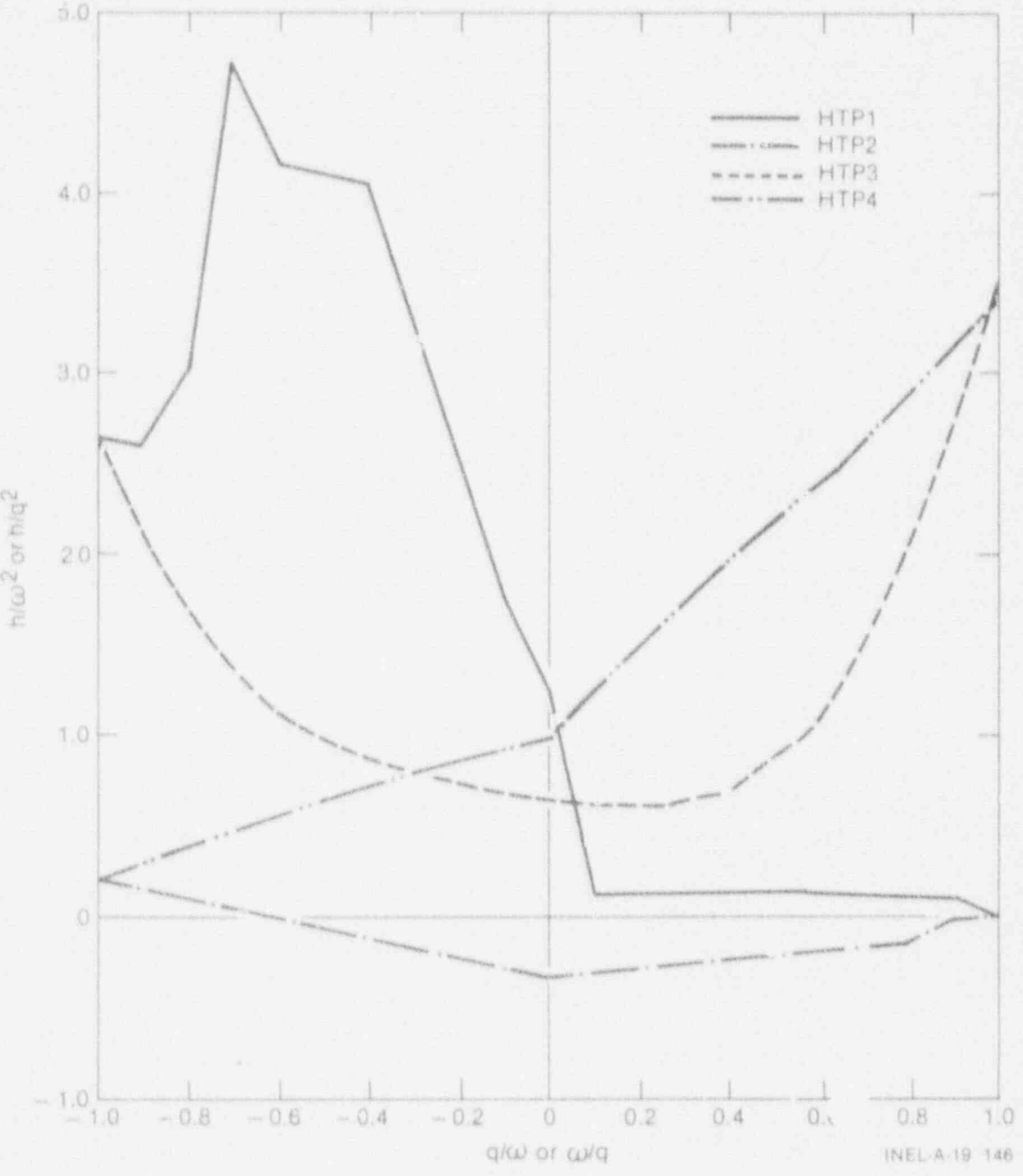

Figure 8.1-2. Semiscale fully degraded homologous head curves.

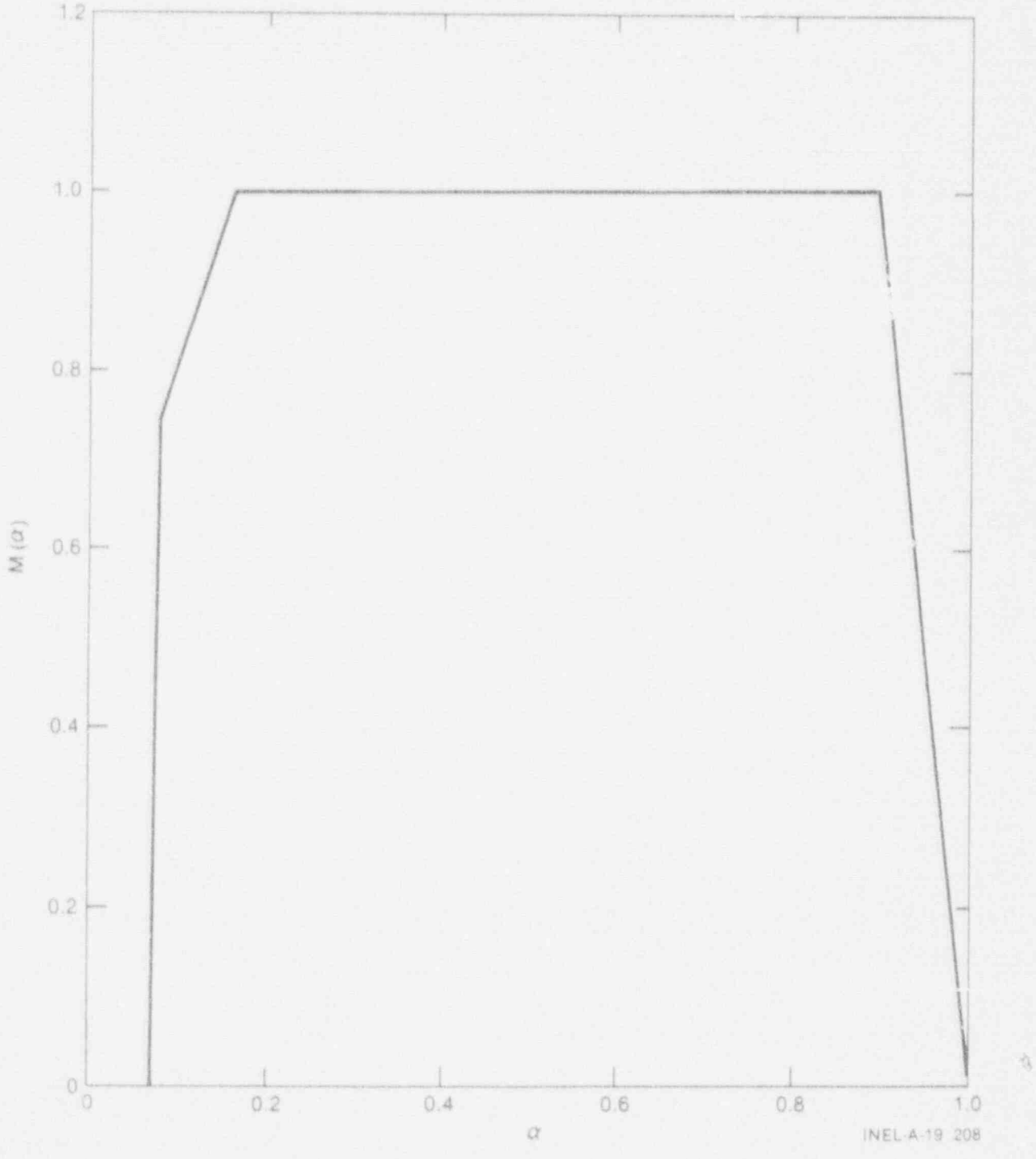

Figure 8.1-3. Semiscale head degradation multiplier curve.

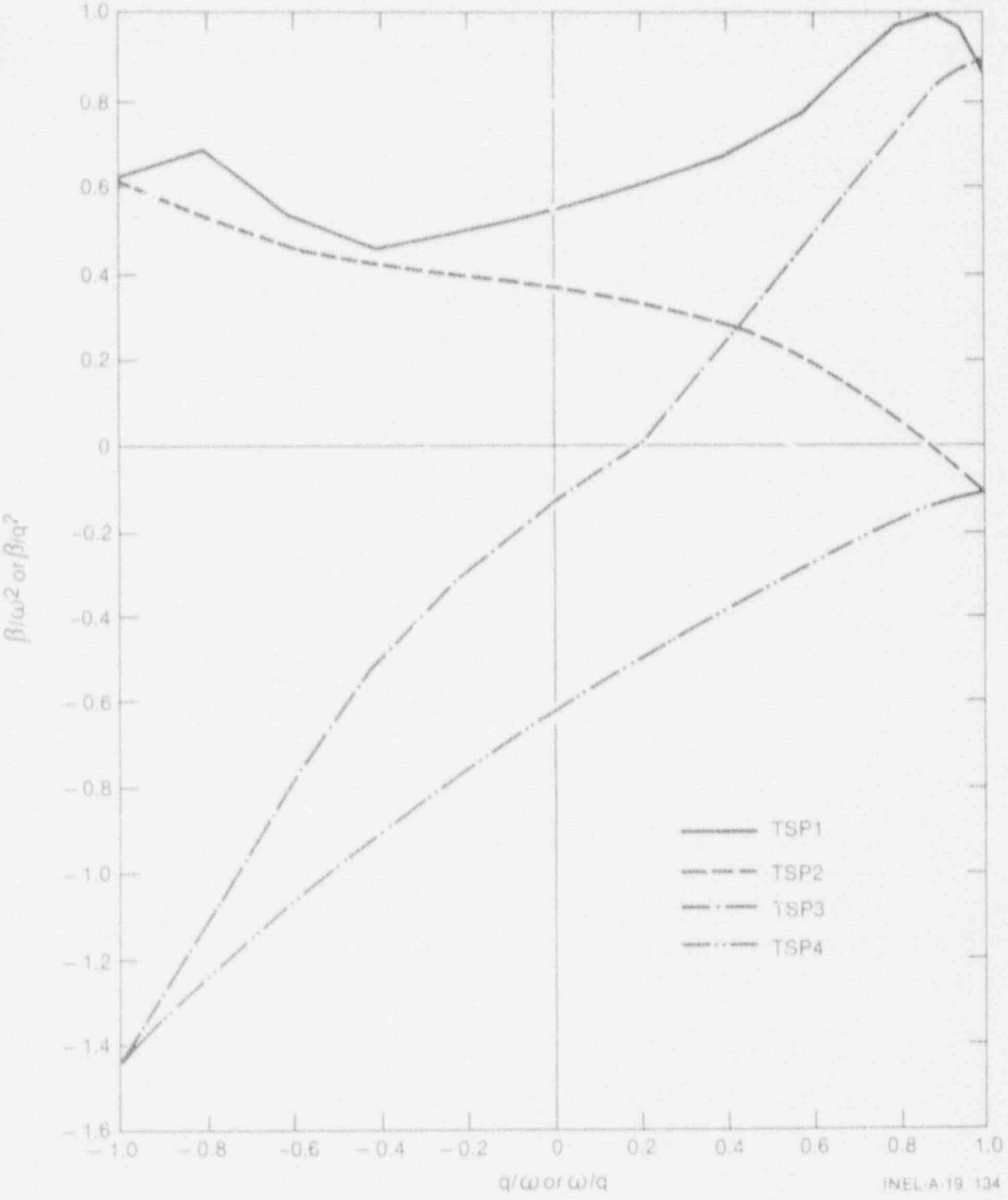

Figure 8.1-4. Semiscale single-phase homologous torque curves.

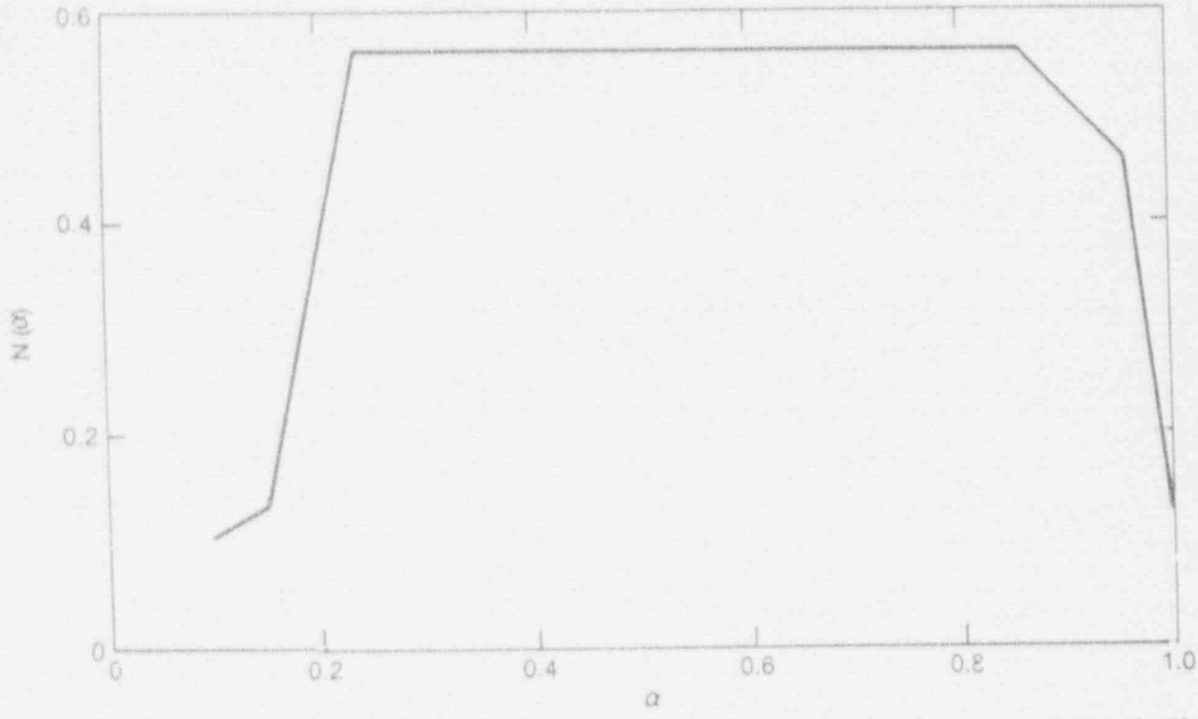

Figure 8.1-5. Semiscale torque degradation multiplier curve.

Because these homologous curves are dimensionless, they can describe a variety of pumps by specifying the desired rated density, head, torque, volumetric flow, and angular velocity as input.

There are restrictions and limitations in the current version of the PUMP component. A flow area change should not be modeled at the impeller location. Additionally, the head degradation multiplier $M(\alpha)$ and the torque degradation multiplier $N(\alpha)$ are assumed to apply to all operating states of the pump.

The PUMP component input consists of the same geometric and hydrodynamic data and initial conditions that are required for the PIPE component. In addition, information specific to the PUMP is required, as described in the input specifications. The speed table (SPTBL) as well as the homologous pump curve arrays must be input in the following order:

$x(1), y(1), x(2), y(2), \ldots, x(n), y(n)$.

Here, x is the independent variable and y is the dependent variable. Furthermore, the independent variables must increase monotonically on input, that is,

$x(1) < x(2) < \ldots < x(n-1), x(n)$.

Linear interpolation is used within the arrays.

8.1.5 PUMP Conclusions

The pump model included in the TRAC-BF1/MOD1 code has demonstrated a remarkable capability to model reactor pumps under many conditions. Obviously, the quality of the pump simulation is very dependent on the quality of the homologous curves used to describe the pump, and we recommend that whenever the data are available, the user input specific curves for the pump under consideration instead of using the built-in curves. An alternative is to use the Tetra Tech model (Reference 8.1-6) to generate the fully degraded nomol gous curves and associated two-phase multiplier curves from the pump geometry and the published single-phase performance curves from the manufacturer. Unless the pump to be modeled is similar to the Semiscale pump, the least desirable option is to select one of the sets of built-in curves.

From a code viewpoint, there are two deficiencies regarding the pump model. First, the assumed treatment of frictional torques in calculating the pump coastdown is limited at best and should be generalized. Second, the assumption of equal phase velocities at the pump interface, while a reasonably good assumption when the pump is operating at a significant rotational speed, breaks down as the pump speed approaches zero. At this point, the homogeneous flow assumption prevents unequal phase velocities and, in particular, prevents countercurrent flow at that one interface. The lack of phase slip can affect the separation of liquid and vapor in the pump suction and discharge. This effect could result in oscillatory flow to approximate the net effect of countercurrent flow. Under the current coding, the only solution to the second problem available to the code user is to replace the PUMP component with an equivalent PIPE component when the pump speed is near zero and the fluid velocities are low.

8.1.6 References

8.1-1. D. D. Taylor et al., *TRAC-BD1/MOD1: An Advanced Best Estimate Computer Program for Boiling Water Reactor Transient Analysis, Volume 1: Model Description*, NUREG/CR-3633, EGG-2294, April 1984.

8.1-2. *RELAP4/MOD5--A Computer Program for Trarsient Thermal-Hydraulic Analysis of Nuclear Reactors and Related Systems, Vol. 1*, ANCR-NUREG-1335, September 1976.

8.1-3. V. L. Streeter and E. B. Wylie, *Hydraulic Transients*, New York: McGraw-Hill Book Company, 1967.

8.1-4. A. J. Stepanoff, *Centrifugal and Axial Flow Pumps, 2nd edition*, New York: John Wiley & Sons, Inc., 1957.

8.1-5. P. W. Runstadler. *Review and Analysis of State-of-the-Art of Multiphase Pump Technology*, EPRI/NP-159, February 1976.

8.1-6. O. Furuya, *Development,of an Analytic Model to Determine Pump Performance Under Two-Phase Flow Conditions*, EPRI/NP-3519, May 1984.

8.1-7. D. J. Olson, *Experiment Data Report for Single- and Two-Phase Steady-State Tests of the 1-1/2-Loop MOD-1 Semiscale System Pump*, ANCR-1150, May 1974.

8.1-8. G. G. Loomis, *Intact Loop Pump Performance during the Semiscale MOD-1 Isothermal Test Series*, ANCR-1240, October 1975.

8.1-9. D. J. Olson, *Single- and Two-Phase Performance Characteristics of the MOD-1 Semiscale Pump Under Steady-State and Transient Fluid Conditions*, ANCR-1165, October 1974.

8.1-10. D. L. Reeder, *LOFT System and Test Description (5.5-Ft. Nuclear Core 1 LOCES)*, TREE-1208, NUREG/CR-0247, July 1978.

8.2 JET PUMP MODEL

The jet pump model in TRAC-BF1/MOD1 is based on the TEE component; the primary arm of the TEE component models the jet pump suction, mixing region, diffuser and discharge passage, and the TEE side arm models the drive line and drive nozzles. The regular continuity and energy equations are used in the jet pump component, but an additional term is included in the momentum equation for the mixing region of the jet pump. Singular loss (irreversible) coefficients based on data, jet pump geometry, and flow conditions in the jet pump are also used in the jet pump component. The additional term in the momentum equation represents the momentum gained in the mixing region as a result of the dissipation of the momentum of the high-speed drive line flow as it merges with the suction flow.

8.2.1 Jet Pump Momentum Source Term

The jet pump momentum source term was derived for each phase by performing a steady-state phasic momentum balance across the mixing region and comparing the resulting expression with the regular momentum equation for the mixing region. The comparison between the two formulations of the momentum equation is complicated by the fact that the regular momentum solution is performed on a staggered mesh and the velocity divergence operator is written as a backward spatial difference.

The momentum and continuity equations for the mixing cell of the jet pump are (see Figure 8.2-1)

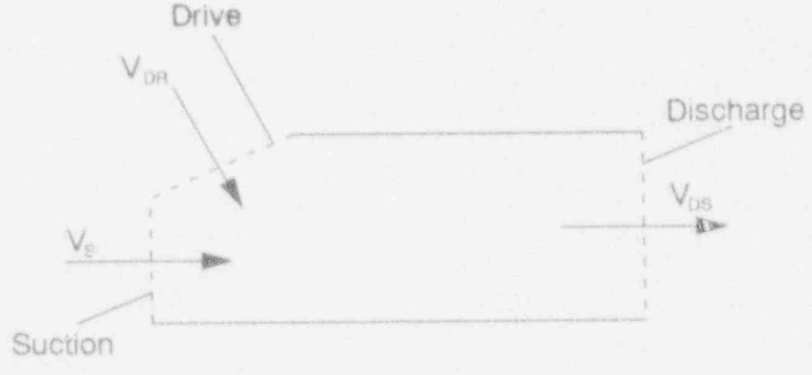

Figure 8.2-1. Jet pump mixing cell.

Jet Pump Model

Continuity:

$$\alpha_{DR}\rho_{DR}A_{DR}V_{DR} + \alpha_S\rho_S A_S V_S = \alpha_{DS}\rho_{DS}A_{DS}V_{DS} \tag{8.2-1}$$

Momentum:

$$\alpha_{DR}\rho_{DR}A_{DR}V_{DR}^2 + \alpha_S\rho_S A_S V_S^2 - \alpha_{DS}\rho_{DS}A_{DS}V_{DS}^2 = (P_{DS} - P_S)A_{DS}\alpha_{DS} \tag{8.2-2}$$

where

$$P_S = P_{DR} \tag{8.2-3}$$

$$\alpha_S = \alpha_{DS} \tag{8.2-4}$$

$$A_S + A_{DR} = A_{DS} \tag{8.2-5}$$

and all quantities are defined on the cell faces. The assumptions as given by the first two equalities are that the static pressures are equal on the suction and drive nozzle exit planes and that the change in phasic void fraction are small between the suction and discharge planes (planes S and DS). Multiplying the continuity equation by V and subtracting from the momentum equation gives

$$\alpha_{DR}\rho_{DR}A_{DR}\left(V_{DR}^2 - V_{DR}V_S\right) - \alpha_{DS}\rho_{DS}A_{DS}\left(V_{DS}^2 - V_{DS}V_S\right) = (P_S - P_{DS})A_{DS}\alpha_{DS} \tag{8.2-6}$$

or

$$\frac{P_S - P_{DS}}{\rho_{DS}} = \frac{\alpha_{DR}\rho_{DR}A_{DR}}{\alpha_{DS}\rho_{DS}A_{DS}} V_{DR}\left(V_{DR} - V_S\right) - V_{DS}\left(V_{DS} - V_S\right) . \tag{8.2-7}$$

Now the regular steady-state TRAC-BF1/MOD1 momentum equation is written as (see Figure 8.2-2)

$$-\frac{1}{\rho}\frac{\partial P}{\partial Z} - S = V\frac{\partial V}{\partial Z} + losses \tag{8.2-8}$$

or

$$-\frac{1}{\rho}\frac{P_2 - P_1}{\frac{1}{2}(\Delta Y_1 + \Delta Y_2)} - S = \frac{V_2\left(V_2 - V_1\right)}{\Delta Y_1} + losses \tag{8.2-9}$$

where

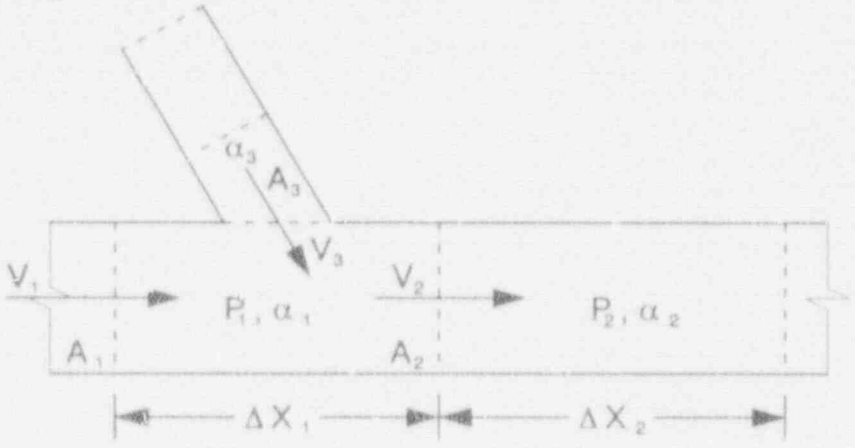

M578-WHT-492-18

Figure 8.2-2. Jet pump model momentum equation diagram.

$$\bar{\rho} = \frac{\Delta X_1 \rho_1 + \Delta X_2 \rho_2}{\Delta X_1 + \Delta X_2} \tag{8.2-10}$$

and the loss terms include wall friction, interphase friction and gravity head. Comparing these two formulations, the momentum source term, S is given by

$$S = \frac{\alpha_3 \rho_3 A_3}{\alpha_1 \rho_1 A_1} \frac{V_3 (V_3 - V_1)}{\frac{1}{2}(\Delta X_1 + \Delta X_2)} \tag{8.2-11}$$

where the donor convention has been used for all convected properties and the cell face pressures have been staggered with respect to the cell faces to give a form that corresponds to the regular momentum equation with its backward spatial difference approximation to the velocity divergence terms. These relations are summarized as

$$\alpha_1 = \alpha_S \tag{8.2-12}$$

$$\alpha_2 = \alpha_{DS} \tag{8.2-13}$$

$$\alpha_3 = \alpha_{DR} \tag{8.2-14}$$

$$P_1 = P_S \tag{8.2-15}$$

$$P_2 = P_{DS} \tag{8.2-16}$$

$$P_3 = P_{DR} \tag{8.2-17}$$

$$A_1 = A_S \tag{8.2-18}$$

$$A_2 = A_{DS} \tag{8.2-19}$$

$$A_3 = A_{DR} \tag{8.2-20}$$

$$V_1 = V_S \tag{8.2-21}$$

$$V_2 = V_{DS} \tag{8.2-22}$$

$$V_3 = V_{DR} \tag{8.2-23}$$

$$P_1 = P_e \tag{8.2-24}$$

$$P_2 = P_{DS} \cdot \tag{8.2-25}$$

Several additional assumptions are implicit in the derivation of the momentum source term as given by Equation (8.2-11) to establish the equivalence of the velocity divergence terms between the two forms of the momentum equation. First, the lengths of the two cells on either side of the discharge face must be the same

$$\frac{1}{2}(\Delta X_1 + \Delta X_2) = \Delta X_1 \qquad (8.2\text{-}26)$$

so that the velocity divergence terms are the same. Second,

$$\bar{\rho} = \frac{\Delta X_1 \rho_1 + \Delta X_2 \rho_2}{\Delta X_1 + \Delta X_2} = \rho_{bs} = \rho_1 \,. \qquad (8.2\text{-}27)$$

The second assumption is closely approximated by the code in that the changes in the phasic density between adjacent cells are usually quite small. However, the assumption of equal cell lengths is rarely satisfied by the code user, and the error in the assumed form of the momentum source term must be compensated for by the singular loss terms that are derived from data. The singular losses are derived using an assumed geometric representation of the actual jet pump. If the code user uses a different nodalization than that used to derive the singular losses, the compensation is not complete and the jet pump model will not perform as well as if the user had used the same geometric representation as was used when the singular losses were derived.

The momentum source term, as shown in Equation (8.2-11), was derived assuming that the nonconservative form of the velocity divergence operator was being used in the regular TRAC-BF1/MOD1 momentum solution. With the modification of the velocity difference to an approximate conservative form (see Section 7.1.1), the momentum source term had to be modified. The velocity divergence in the regular momentum solution is written as

$$\nabla\cdot\mathbf{V} = \left(\frac{A_2}{A_1} + \frac{A_2}{A_2}\right)V_2 \left(\frac{A_2}{A_1}V_2 - \frac{A_2}{A_1}V_1\right)\frac{1}{2\Delta X} \qquad (8.2\text{-}28)$$

where

$$\bar{A}_1 = \frac{Vol_1}{\Delta X_1} \qquad (8.2\text{-}29)$$

$$\bar{A}_2 = \frac{Vol_2}{\Delta X_2} \qquad (8.2\text{-}30)$$

and the areas with the overbar represent the flow area in the center of the cell. Assuming for the moment that

$$\bar{A}_2 = A_2 \qquad (8.2\text{-}31)$$

$$\bar{A}_1 = A_2 \tag{8.2-32}$$

we obtain

$$\bar{V}\nabla W = V_2 \nabla W_2 \ , \tag{8.2-33}$$

which differs from the velocity divergence term in the original derivation [Equation (8.2-9)] by

$$V\nabla W = \left[V_2(V_2 - V_1) + \frac{A_2 - A_1}{A_2}(V_2 V_1) \right] \frac{1}{\Delta X} \tag{8.2-34}$$

or

$$V\nabla W = \left[V_2(V_2 - V_1) + \frac{A_3}{A_2}(V_2 V_1) \right] \frac{1}{\Delta X} \tag{8.2-35}$$

where

$$A_3 = A_2 - A_1 \ . \tag{8.2-36}$$

Substituting this expression for the velocity divergence term into the regular momentum solution and eliminating the corresponding terms, the momentum source term becomes

$$S = \frac{\alpha_3 \rho_3 A_3}{\alpha_1 \rho_1 A_1} \left[\frac{V_3(V_3 - V_1)}{\frac{1}{2}(\Delta X_1 + \Delta X_2)} \right] = \frac{A_3}{A_1} \left[\frac{V_2 V_1}{\frac{1}{2}(\Delta X_1 + \Delta X_2)} \right] \ . \tag{8.2-37}$$

This deviation is based on the equivalence of the cell-centered flow areas to the discharge flow area as given by Equations (8.2-31) and (8.2-32). The second relation should always be satisfied by the jet pump geometry in that the mixing region in an actual jet pump is a straight section of constant flow area, whereas the first relation may be satisfied if the user divides the mixing region into at least two computation cells, each of which models a straight constant flow area section. If the user employs a coarse nodalization in which the first cell models the mixing region and the second cell models the jet pump diffusor, the first relation will not be satisfied. The performance of the jet pump will suffer unless the singular losses compensate for the error in modeling the geometry of the jet pump.

The momentum source term as given by Equation (8.2-37) is added to the

right-hand side of the regular TRAC-BF1/MOD1 phasic momentum equations for positive drive flow (drive flow into mixing cell) and is identically zero for reversed flow in the drive line.

In addition, a limit is placed on the numerical value of the macroscopic density ratio in the momentum source term so that the source term does not cause unrealistic phasic velocities. This limit is given by

$$\frac{\alpha_3 \rho_3}{\alpha_1 \rho_1} \geq 1 \qquad (8.2\text{-}38)$$

and arises form the observation that if the quantity in the denominator becomes smaller than the numerator, the value of the momentum source term becomes large relative to the phasic inertia (represented by the denominator) and "unrealistically" large values of the phasic velocity can result. This is a cosmetic problem in that the user can be mislead by a large value of the phasic velocity at small phasic void fractions into thinking that something is wrong where in reality, the momentum represented by the large velocity and low void fraction is correct and has a small value. The limitation also protects against a divide by zero in the single phase limits.

Finally, there is subtle error in the jet pump, which results from the implementation of the approximate conserving form of the velocity divergence term. The singular losses as explained in subsequent sections were derived using a code version without the modifications to the velocity divergence and are now being used in a code which has these modifications. The momentum source term was modified to compensate for the different form of the divergence term for the momentum solution at the discharge face. The momentum equations for the suction face and the drive face, however, use the new form of the velocity divergence terms and are now inconsistent with the singular losses as derived from data using an unmodified code version. These inconsistencies result in a slight degradation of the jet pump performance in TRAC-BF1-MOD1 (Figure 8.2-3) as compared to the performance as reported by General Electric (Figure 8.2-4) where the singular losses were derived.

8.2.3 Jet Pump Singular Loss Coefficients

In addition to the momentum source due to the high-speed drive line flow, there are pressure losses associated with the jet pump geometry. These include diffuser (expansion) and nozzle (contraction) losses, losses due to incomplete mixing of the drive and suction flows, and inlet and outlet losses where the jet pump connects to the BWR downcomer and lower plenum, respectively. The losses due to the jet pump and reactor vessel geometry are developed from handbook values as well as from analysis of data obtained from testing of a subscale jet pump mocel.[8.2-1]

The mixing and nozzle losses were developed from the analysis of the subscale data. These loss coefficients were developed by the General Electric

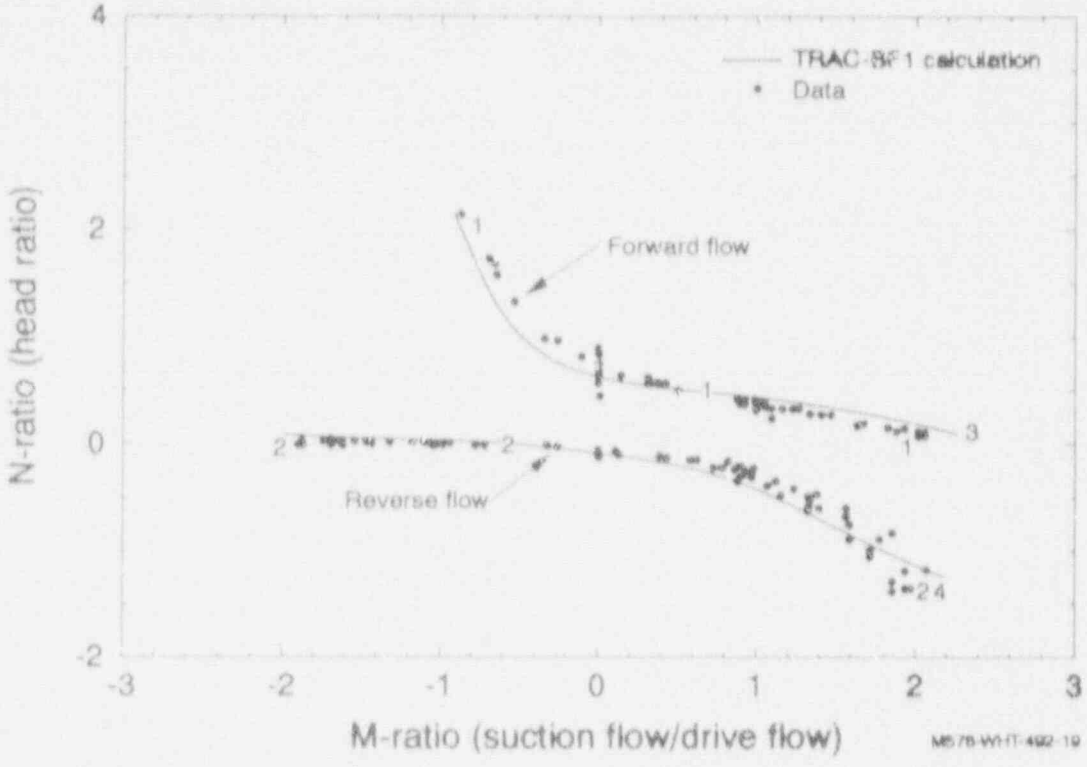

Figure 8.2-3. TRAC-BF1/MOD1 jet pump results compared to data for 1/6 scale INEL test.

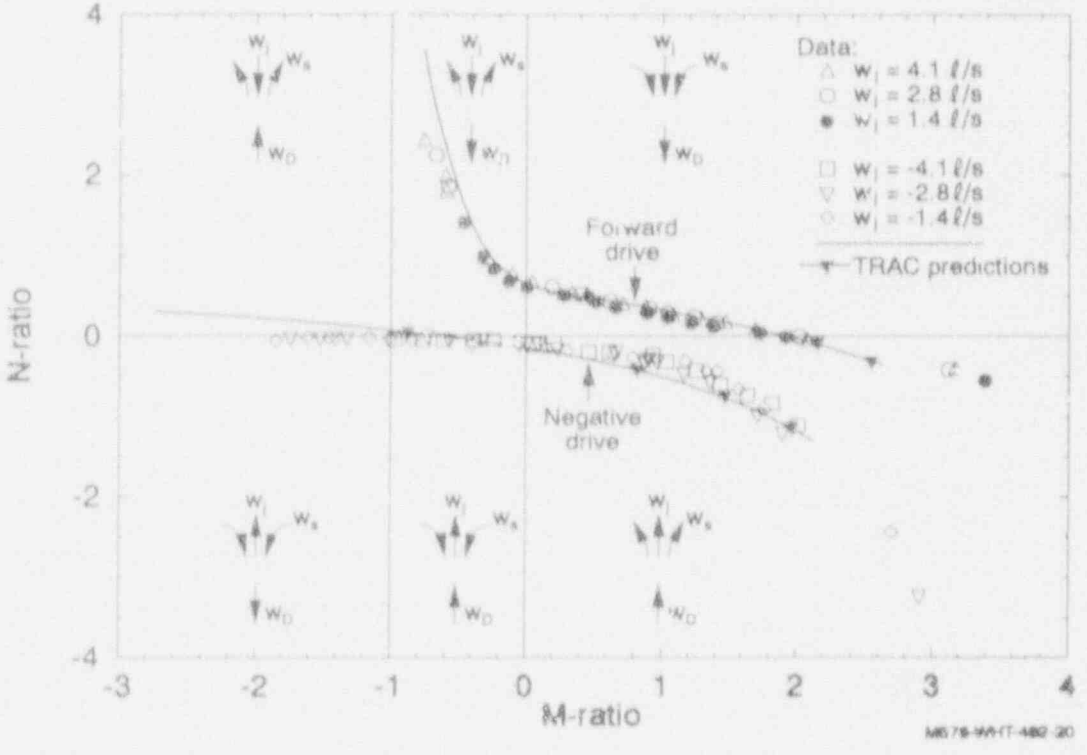

Figure 8.2-4. Comparisons of predicted versus measured MN curves for INEL jet pump.

Company (GE) as part of the BWR Refill-Reflood and FIST programs jointly sponsored by GE, EPRI, and the USNRC.[8.2-1] This model was developed by Andersen et al.[8.2-1] and was made available to the TRAC-BF1 project.

8.2.3.1 Diffuser (Expansion) Losses. The loss coefficient for the irreversible pressure loss for flow through a diffuser is given by Idelchik[8.2-2] as

$$K_e = C_e \tan \alpha^{1.5}(1 - A^*)^2 \qquad (8.2\text{-}39)$$

where

α = diffuser angle

A^* = area ratio of outlet to inlet

C_e = constant.

The recommended value of C_e is 5.5 and is the default value in TRAC-BF1/MOD1. The user may input the value of C_e if he so desires.

This pressure loss coefficient is used at every cell face of the jet pump where the flow areas at the cell centers on either side of the face increase in the direction of flow.

8.2.3.2 Nozzle (Contraction) Losses. The loss coefficient for the irreversible pressure loss for flow through a nozzle due to the contraction is given by Idelchik[8.2-2]

$$K_c = C_c \sin \alpha(1 - A^*) \qquad (8.2\text{-}40)$$

where

α = contraction angle

A^* = area ratio of outlet to inlet of contraction

C_c = constant.

The recommended value of C_c is 0.38 and is the default value in TRAC-BF1/MOD1. The user has the option to input his own value of C_c. This pressure loss coefficient is used at every face in the jet pump where the flow area at the cell centers on either side of the face decrease in the direction of flow.

8.2.3.3 Inlet Losses. There is an irreversible pressure loss at the jet pump suction inlet due to the contraction of the suction flow from the

downcomer to the jet pump. The loss coefficient for this loss has been estimated to be 0.04 from data obtained at the INEL using 1/6 scale jet pumps.[8.2-3] When the flow at the jet pump diffuser outlet reverses, there is a contraction loss from the lower plenum into the jet pump diffuser. The loss coefficient for this loss has been estimated from data to be 0.45. These values are in the TRAC-BF1/MOD1 code as default values, but the user may change them.

8.2.3.4 Outlet Losses. There is a loss at the diffuser outlet due to the flow expansion from the diffuser outlet into the lower plenum for normal operating conditions in the jet pump. The loss coefficient for this loss is estimated to be 1.0 and is implemented into the TRAC-BF1/MOD1 code at the diffuser outlet for forward flow in the diffuser.

8.2.3.5 Mixing Losses. There are irreversible pressure losses in the mixing region of the jet pump where the high-velocity drive flow mixes with the low-velocity suction flow. These losses have been estimated from the 1/6 scale jet pump data and have been correlated in terms of the drive velocity (V_{DR}), the ratio of suction mass flow rate to drive mass flow rate (M ratio), and the flow regime. The flow regimes are defined for various combinations of positive and negative suction flow, drive flow, discharge flow, and M ratio. The definitions of the flow regimes are shown schematically in Figure 8.2-5 and listed in Table 8.2-1. The loss coefficients in the various flow regimes for mixing losses are given in Table 8.2-2.

8.2.3.6 Nozzle Losses. In addition to the pressure losses in the drive nozzles caused by the contraction of the flow, there are additional losses because of the unique geometry of the drive nozzle. These losses have been estimated from the 1/6 scale jet pump data[8.2-3] and have been correlated in terms of the M ratio for the various flow regimes. These loss coefficients are listed in Table 8.2-2.

The accuracy of the jet pump model in TRAC-BF1/MOD1 was assessed by simulating the experiment used to obtain the data from which the loss coefficients were obtained. Figure 8.2-3 shows the comparison between the measured data and the TRAC-BF1/MOD1 computed results in terms of the N ratio versus the M ratio. The N ratio is defined as the rise in total head of the suction flow as it moves from the entrance to the exit of the jet pump divided by the difference in the total heads between the drive flow and the suction flow. The total head includes the pressure head, velocity head, and gravity head contributions. The M ratio is the ratio of total discharge flow rate divided by the drive flow rate. Figure 8.2-3 shows that quite good agreement is obtained between the measured data and the simulation.

(a) Positive drive line flow

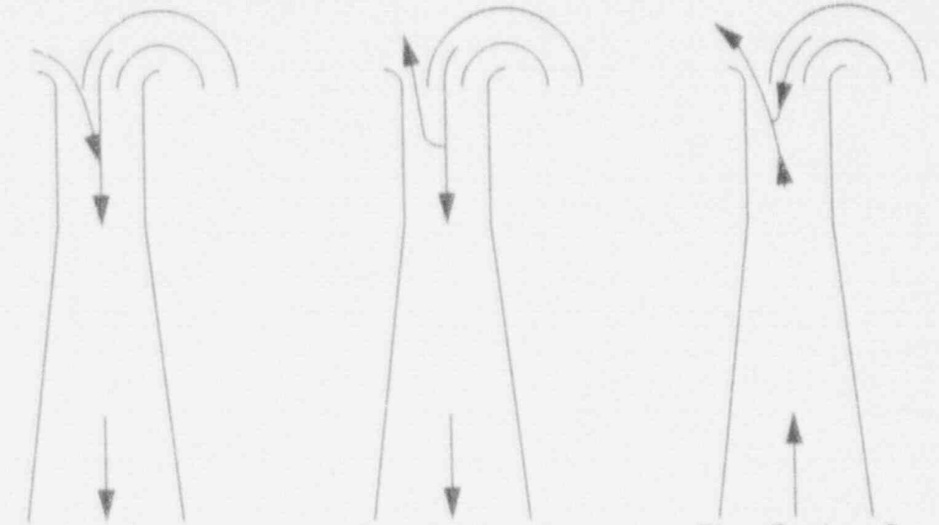

(b) Negative drive line flow

M578-WHT-492-21

Figure 8.2-5. Jet pump flow regimes.

Table 8.2-1. Jet pump flow regimes.

Regime	Drive flow	Suction flow	Discharge flow	M ratio
1[a]	Positive	Positive	Positive	$M > 0$
2	Positive	Negative	Positive	$0 > M > -1$
3	Positive	Negative	Negative	$M < -1$
4	Negative	Negative	Negative	$M > 0$
5	Negative	Positive	Negative	$0 > M > -1$
6	Negative	Positive	Positive	$M < -1$

a. Flow regime 1 is the normal operating regime.

Table 8.2-2. Flow-regime-dependent loss coefficients.

Regime	Mixing loss coefficient	Nozzle loss coefficient
1	0	0
2	$-0.134\ M^2 V_{DR}^2$	Min [2.5, M(0.08M - 0.06)]
3	$-(0.1 - 0.0333M)\ V_{DR}^2$	Min [2.5, M(0.08M - 0.06)]
4	0	Max [0.0, 0.48 - M (0.33 - 0.055M)]
5	0	Max [0.0, 0.48 - M (0.33 - 0.055M)]
6	0	2.55

8.2.3 References

8.2-1. Y. K. Cheung, V. Parameswaran, and J. C. Shaug, *BWR Refill-Reflood Program Task 4.7-Model Development: TRAC-BWR Component Models*, NUREG/CR-2457, GEAP-22052, April 1983.

8.2-2. Idelchik, *Handbook of Hydraulic Resistance Coefficients of Local Resistance and Friction*, AEC-TR-6630, 1966.

8.2-3. G. E. Wilson, *INEL One-Sixth Scale Jet Pump Data Analysis*, EGG-CAAD-5357, February 1981.

8.3. STEAM/WATER SEPARATOR AND DRYER

8.3.1 Model Description

The model used in TRAC-BF1-MOD1 utilizes the TEE component. Both the separator and steam dryer components of a BWR have a single inlet, which accepts two-phase fluid, and two outlets discharging nearly single phase fluid through each path. The separator accepts moderate-quality two-phase fluid from the mixing plenum and directs high-quality fluid to the steam dryer and low-quality fluid to the downcomer. The steam dryer accepts the high-quality fluid from the separator and removes the residual moisture to provide nearly single-phase steam to the steam dome. The separated liquid is directed back to the liquid pool surrounding the separators.

Each of these components can be represented by a TRAC-BF1/MOD1 TEE component that has three flow paths. The model as developed can be used to represent a separator (or a number of separators), the steam dryer, or both the multiple separators and the steam dryer.

Furthermore, there are two different separator options for determining the liquid carryover and the vapor carryunder qualities--a simple separator option where the user specifies constant carryover and carryunder qualities and a mechanistic separator option in which the carryover and carryunder qualities are computed as functions of the local conditions in the separator. The mechanistic separator methodology and coding implementing the methodology were developed by the General Electric Company (GE).[8.3-1].

The steam dryer also has two options, a prefect separator option in which all liquid is separated regardless of the local conditions and a more mechanistic model in which the dryer efficiency decreases as the vapor velocity increases above a critical dryer inlet velocity. The more mechanistic dryer model was developed by GE[8.3-1] and is adapted from their version of the TRAC-BWR code.

Figure 8.3-1 is a diagram of a combined separator/dryer component. The portion of the primary tube from the inlet to the joining cell represents the separator standpipe and barrel, the joining cell represents the volume between the separator discharge and dryer inlet, and the portion of the primary tube above the joining cell represents the dryer.

The TEE side arm represents the separator shroud. The separated liquid from the dryer flows down along the dryer skirt; this flow path is not explicitly modeled, since it occupies a negligible volume. The separator function occurs across the inlet face of the joining cell where the two-phase mixture leaves the stand pipe and barrel to appear at the inlet to the side arm rather than in the joining cell. The dryer function occurs at the outlet face of the joining cell where the convected void fraction is computed from the dryer efficiency. The phase separation is accomplished by adjusting the void fraction convected across the several faces of the joining cell and by

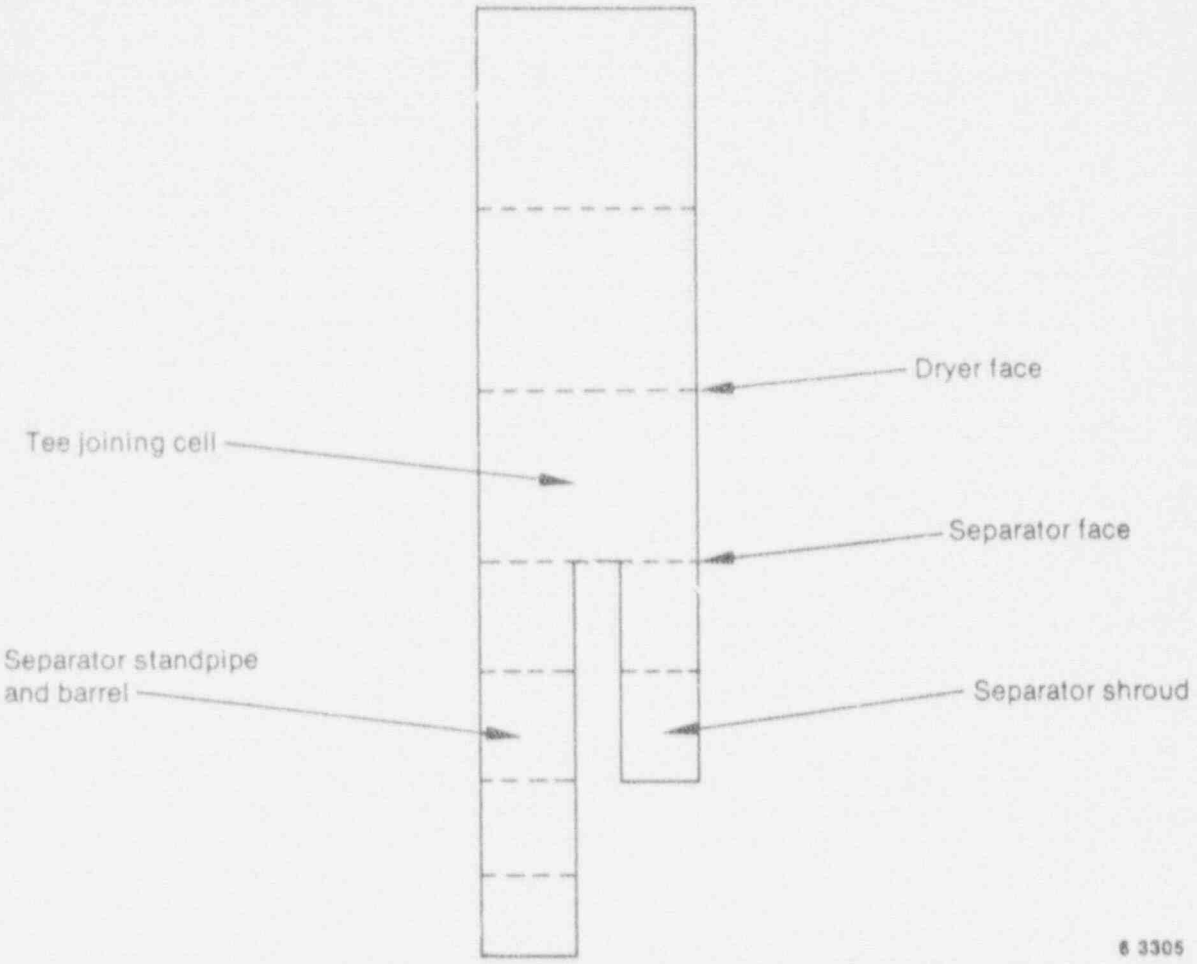

Figure 8.3-1. Diagram of combined separator-dryer.

adjusting the flow velocities at the inlet to the TEE side arm. The separator/dryer component thus uses the same methodology as the two-phase level model in which convected void fractions are different than the cell average value. The analogy may be carried further by reference to Figure 8.3-2, in which the phase separation is accomplished by the use of the two-phase level model in the joining cell. The above-level void fraction (void fraction convected across the dryer face) is determined by the dryer efficiency and the below-level void fraction is determined from the vapor carryunder mass flow rate. The phase velocities at the inlet to the TEE side arm are adjusted such that the desired cell average void fraction is maintained in the joining cell of the TEE. The side arm velocities are determined by adjusting the loss coefficient at the inlet to the side arm so that the velocity solution is sufficiently implicit to allow large time steps to be taken with the new model.

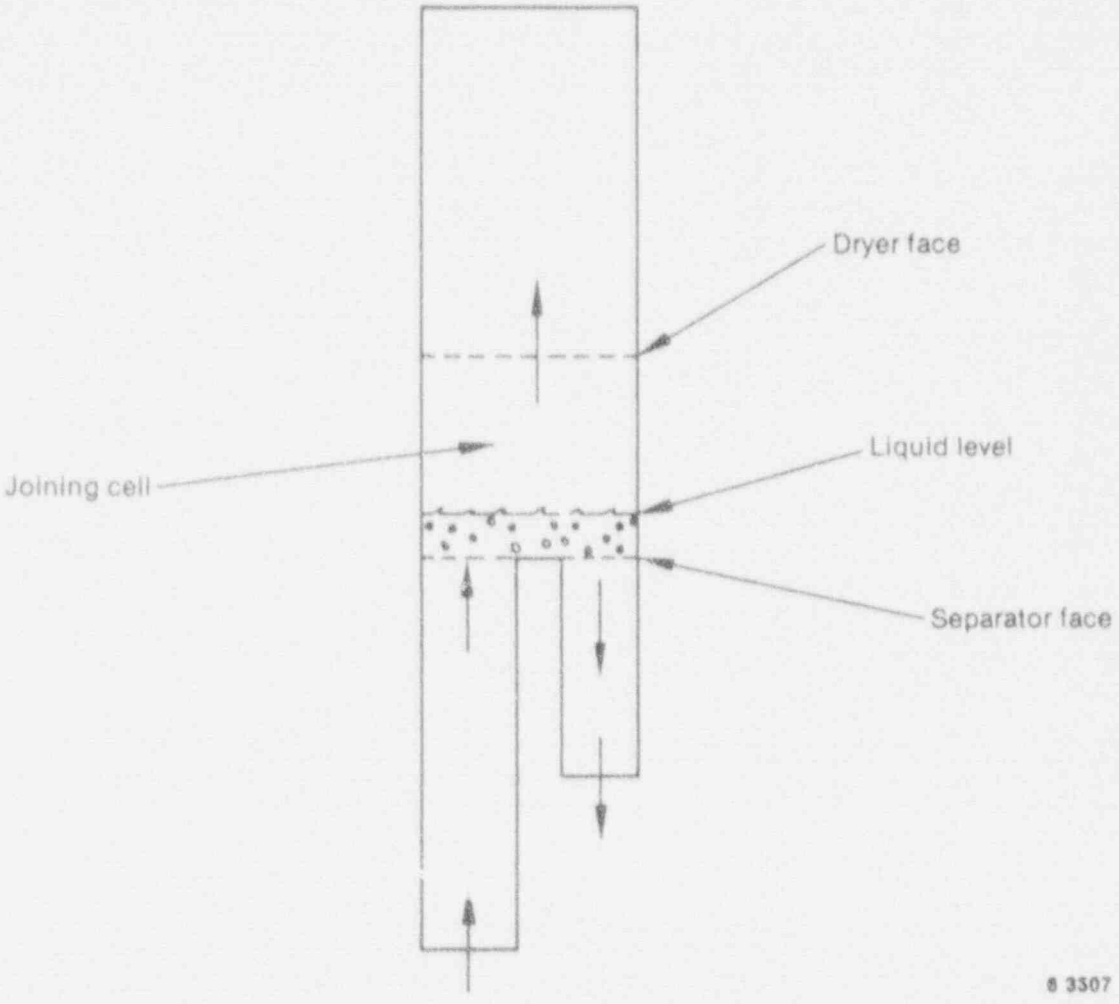

Figure 8.3-2. Separator phase separation.

8.3.2 Model Equations

The phase separation in the separator/dryer component is accomplished by determining the void fractions convected across the two outlet faces of the joining cell and by adjusting the loss coefficient at the inlet of the TEE side arm.

8.3.3 Dryer Void Fraction

The void fraction convected across the dryer face is determined by the dryer efficiency. If the simple dryer option is chosen, the dryer efficiency is assumed to be 100%. If the more

mechanistic dryer option is chosen, the dryer efficiency is computed from the vapor velocity across the dryer face and the dryer inlet liquid quality.

Once the dryer efficiency has been computed, the void fraction convected across the dryer face is computed. The convected void fraction is 1 for a dryer efficiency of 100% and is the donor void fraction for a dryer efficiency of 0.0%. For dryer efficiencies between 100% and 0%, the convected void fraction is linearly interpolated between the void fractions corresponding to values obtained for efficiencies of 100% and 0%, respectively

This relation is summarized in Equation (8.3-1) as

$$\alpha_D = \eta_D + (1 - \eta_D)\alpha_f \qquad (8.3\text{-}1)$$

where

α_D = convected void fraction at dryer face

η_D = dryer efficiency

α_f = donor void fraction at dryer face.

The dryer efficiency is computed by comparing the dryer inlet liquid quality to a critical dryer inlet liquid quality. The dryer efficiency is 100% if the dryer inlet liquid quality is below the critical dryer inlet liquid quality and is zero if the dryer inlet liquid quality exceeds the critical inlet liquid quality by a user-defined amount, ΔX_d. The dryer efficiency is linearly interpolated between these two extremes based on the dryer inlet liquid quality. The dryer efficiency is given by

$$\eta_D = \begin{cases} 1.0 \text{ for } X_i < X_{i,crit} \\ 1.0 + \dfrac{X_{i,crit} - X_i}{\Delta X_d} \text{ for } X_{i,crit} < X_i < X_{i,crit} + \Delta X_d \\ 0.0 \text{ for } X_i > X_{i,crit} + \Delta X_d \end{cases} \qquad (8.3\text{-}2)$$

where

η_D = dryer efficiency

X_i = dryer inlet liquid quality

$X_{i,crit}$ = critical dryer inlet liquid quality, and

ΔX_d = range of dryer inlet liquid quality over which efficiency degrades from 100% to 0%.

The range of dryer inlet liquid quality over which the dryer efficiency degrades is a user-input constant.

The dryer inlet liquid quality is determined from the donor void fraction assuming homogeneous flow at the dryer face and is given by

$$X_i = 1 - \frac{\alpha_f}{\alpha_f + (1 - \alpha_f)\left(\frac{\rho_\ell}{\rho_v}\right)} \tag{8.3-3}$$

where ρ_ℓ and ρ_v are the donor liquid and vapor densities, respectively.

Finally, the critical dryer inlet liquid quality is given as a linear function of the vapor velocity at the dryer face and is given by

$$X_i = \begin{cases} 1.0 \text{ for } V_{vd} < V_{vd,\ell} \\ 1.0 - \left(\dfrac{V_{vd} - V_{vd,\ell}}{V_{vd,u} - V_{vd,\ell}}\right) \text{ for } V_{vd,\ell} < V_{vd} < V_{vd,u} \\ 0.0 \text{ for } V_{vd,u} < V_{vd} \end{cases} \tag{8.3-4}$$

where

V_{vd} = vapor velocity at dryer face

$V_{vd,\ell}$ = lower dryer vapor velocity

$V_{vd,u}$ = upper dryer vapor velocity.

The lower dryer vapor velocity is the dryer inlet vapor velocity below which the dryer efficiency is 100% regardless of dryer inlet liquid quality. The upper dryer vapor velocity is the dryer inlet vapor velocity above which the dryer efficiency is less than 100% regardless of dryer inlet liquid quality. The dryer efficiency relationships are summarized in Figure 8.3-3.

8.2.4 Separator Void Fraction

The computation of the separator void fraction is much more complicated and is divided into two phases. The first phase of the calculation is the determination of the liquid carryover and vapor carryunder qualities. This calculation is performed once per time step in the prepass phase of the TRAC-BF1/MOD1 numerical integration scheme. If the simple separator option is used, the user-input values of liquid carryunder quality X_{cd} and vapor carryunder quality X_{cu} are used. If the mechanistic separator option has been selected by the user, X_{cd} and X_{cu} are determined by a call to subroutine SSEPOR, which computes the phasic flow rates of liquid and vapor at the two outlet ports of the separator using the separator geometric data and the local

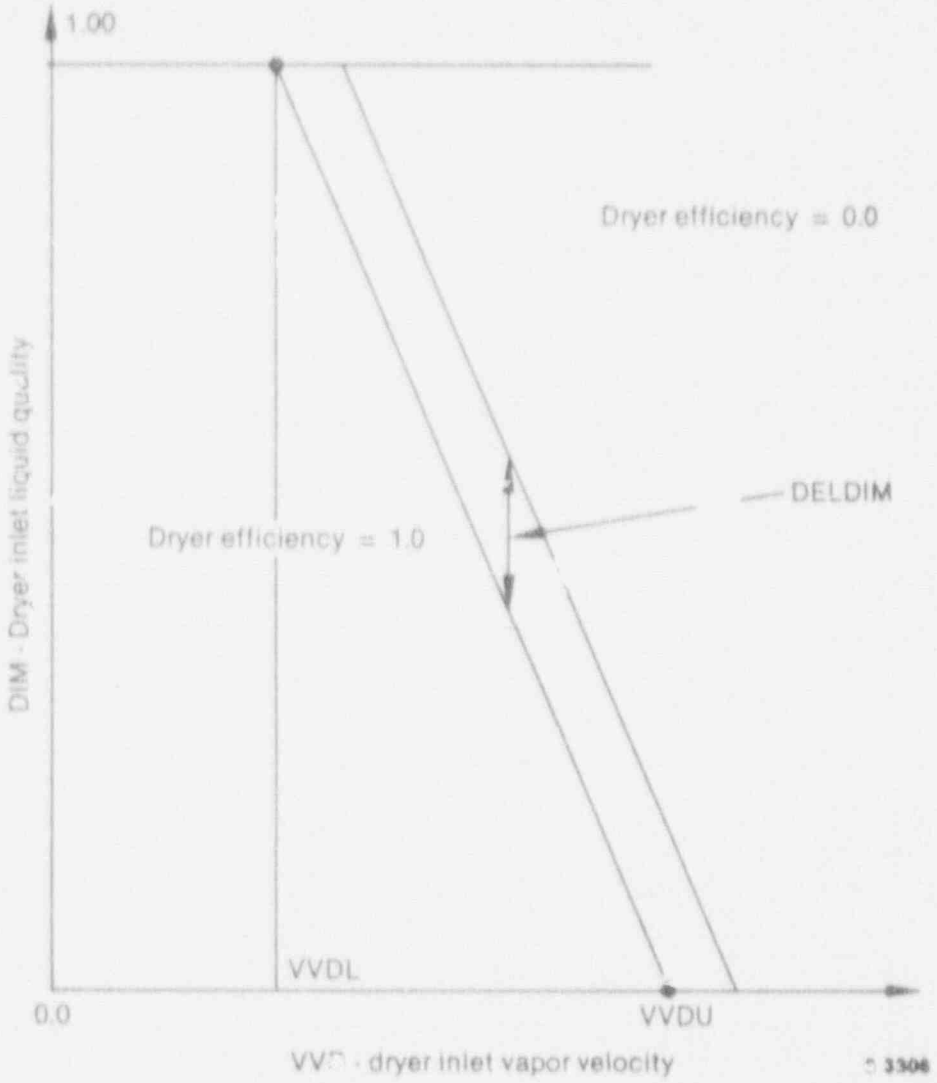

Figure 8.3-3. Dryer efficiency summary.

conditions at the separator inlet. (See Reference 3.9-2 for the details of calculation.) The carryover liquid quality X_{co} and the vapor carryunder quality X_{cu} are assumed to remain constant during the iterations used to update the TRAC-BF1/MOD1 hydrodynamic variables.

8.3.5 Implicit Portion of Separator Solution

Once the liquid carryover quality X_{co} and the vapor carryunder quality X_{cu} have been determined, the joining cell target void fraction α_o and the vapor carryunder mass flow rate $\dot{M}_{v,cu}$ are determined. This calculation is performed

once per iteration to prevent the overextraction of mass from the joining cell. The joining cell void fraction is determined from the liquid carryover quality assuming homogeneous flow at the exit of the separator and is given by

$$\alpha_0 = \frac{1 - X_{co}}{1 - X_{co} + \left(\frac{\rho_v}{\rho_\ell}\right) X_{co}} \tag{8.3-5}$$

$$\alpha_0 = Min\,[\alpha_0,\ 0.995]\ . \tag{8.3-6}$$

The vapor carryunder mass flow rate is computed from a steady-state vapor mass balance on the joining cell and is given by

$$\dot{M}_{v,cu} = \frac{\dot{M}_{v,i} - \left(\frac{1 - X_{co}}{X_{co}}\right) \dot{M}_{\ell,i}}{1 - \left(\frac{1 - X_{cu}}{X_{cu}}\right)\left(\frac{1 - X_{co}}{X_{co}}\right)} \tag{8.3-7}$$

where

$\dot{M}_{v,i}$ = vapor mass flow rate into joining cell

$\dot{M}_{\ell,i}$ = liquid mass flow rate into joining cell.

Once the target joining cell void fraction α_0 and the vapor carryunder mass flow rate $\dot{M}_{v,cu}$ have been computed, the separator void fraction and side arm fluid velocity can be computed.

The liquid mass flow rate out of the side arm is computed from a steady-state liquid mass balance on the joining cell

$$\dot{M}_{\ell,s} = \dot{M}_{\ell,x} - \Gamma - \dot{M}_{\ell,c} - \frac{F(\alpha_0 - \alpha)\rho_\ell}{\Delta t} Vol \tag{8.3-8}$$

where

$\dot{M}_{\ell,s}$ = liquid flow rate in side arm

$\dot{M}_{\ell,x}$ = extrapolated liquid inlet mass flow rate

$\dot{M}_{\ell,o}$ = dryer liquid flow rate.

The last term represents the liquid mass flow rate needed to remove the excess liquid in the joining cell and return the joining cell void fraction to the target value during the current time step. The attempt to return the joining cell void fraction to the target value sometimes leads to overextraction of mass from the joining cell. The factor F varies inversely with the number of iterations being used during this time step to attempt to prevent this overextraction and is given by

$$F = \begin{cases} 1.0 \text{ for } OITNO \leq 2 \\ 1.0 - 0.25\ (OITNO - 2) \text{ for } 2 < OITNO \leq 5 \\ 0.25 \text{ for } 5 < OITNO \end{cases} \tag{8.3-9}$$

where OITNO is the number of iterations. At steady state, when the joining cell void fraction is equal to the desired value, this term is identically zero. The extrapolated liquid mass flow rate is given by

$$\dot{M}^n_{\ell,x} + \dot{M}^n_{\ell,i} + \left(\dot{M}^n_{\ell,i} - \dot{M}^{n-1}_{\ell,i}\right)\frac{\Delta t^n}{\Delta t^{n-1}} \tag{8.3-10}$$

where

$\dot{M}^{n-1}_{\ell,i}$ = liquid mass flow rate from previous time step, and

Δt^{n-1} = previous time step size.

The liquid mass flow rate at the dryer face is computed using the current dryer void fraction.

The side arm fluid velocity can now be computed assuming homogeneous flow as

$$V_s = \frac{1}{A}\left(\frac{\dot{M}_{\ell,s}}{\rho_\ell} + \frac{\dot{M}_{v,cu}}{\rho_v}\right) \tag{8.3-11}$$

where A is the side arm flow area. The separator void fraction is then computed from

$$\alpha_s = \begin{cases} \alpha \text{ for } V_s < 0.0 \\ \dfrac{\dot{M}_{v,cu}}{\rho_v V_s A} \text{ for } V_s > 0.0 \end{cases} \qquad (8.3\text{-}12)$$

which means that the actual donor void fraction is used if reverse flow in the side arm is indicated.

8.3.6 Separator Velocity Solution

If reverse flow in the side arm is indicated by Equation (8.3-11), the side arm loss coefficient from the previous time step is used. If positive velocity in the side arm is indicated by Equation (8.3-11), then a new side arm loss coefficient is computed.

8.3.6.1 Side Arm Loss Coefficient. The side arm loss coefficient needed to balance the imposed pressure gradient is computed from a simplified steady-state momentum equation across the side arm face. This simplified momentum equation includes pressure drop, form losses, and gravity lead across the side arm face and is given by

$$\Delta P = \frac{1}{2} K \rho_m V_s^2 - g \rho_m \Delta X \qquad (8.3\text{-}13)$$

where

ΔP = pressure drop from center of joining cell to center of first side arm cell

K = side arm loss coefficient

ρ_m = average mixture density

g = gravitational constant

ΔX = distance from cell center to cell center.

The gravity head term assumes that the side arm is directed downward, and the input processor flags an error if the user does not specify a vertically directed side arm. This equation is solved for the side arm loss coefficient. The value computed is averaged with the value from the previous time step, and the averaged value is restricted to be within a factor of two of the previous value.

8.3.6.2 Side Arm Velocity Solution. The side arm loss coefficient is used in the time-dependent form of the simplified momentum equation to determine the predicted side arm fluid velocity and its derivative with respect to pressure gradient. The predicted fluid velocity is given by

$$V_s^n = \frac{V_s^{n-1} + \Delta t \left(\frac{\Delta P}{\rho_m \Delta X} + g \right)}{1 + \frac{1}{2} \frac{\Delta t}{\Delta X} K \left| V_s^{n-1} \right|} \qquad (8.3\text{-}14)$$

where

V_s^n = predicted side arm velocity

V_s^{n-1} = beginning of time step side arm velocity

and the other terms have been defined previously.

The derivative of the side arm velocity with respect to pressure gradient is given by

$$\frac{\partial V}{\partial P} \quad \frac{\Delta t}{\Delta X \rho_m \left(1 + \frac{1}{2} \frac{\Delta t}{\Delta X} K \left| V_s^{n-1} \right| \right)} \qquad (8.3\text{-}15)$$

where $\frac{\partial V}{\partial P}$ is the derivative of the side arm velocity with respect to the pressure gradient. These two values are used in the solution of the continuity and energy equations in place of the regular momentum solution for the first side arm face.

8.3.7 References

8.3-1. Y. K. Cheung, V. Parameswaran, and J. C. Shaug, *BWR Refill-Reflood Program Task 4.7-Model Development: TRAC-BWR Component Models*, NUREG/CR-2457, GEAP-22052, April 1983.

8.3-2. M. J. Thurgood et al., *COBRA-TRAC-A Thermal-Hydraulics Code for Transient Analysis of Nuclear Reactor Vessels and Primary Coolant Systems, Volume 1*, NUREC/CR-3046, PNL-4385, March 1983..

8.4 IMPLICIT TURBINE MODEL

The turbine model in TRAC-BD1/MOD1 was designed to provide a basic capability for modeling BWR main steam turbines and for modeling smaller turbines, such as those used for driving feedwater pumps. The turbine model is based on a simple thermodynamic description of flow through a turbine with user-specified performance parameters, such as mass flow rate and thermodynamic stage efficiency.

8.4.1 Physical Model of Turbine

The turbine is modeled as a one-dimensional branching flow component or tee. The principal branch represents the turbine inlet and outlet, and the turbine nozzles, rotor blades, stator blades and internal flow passages (hereafter referred to as turbine internals). The secondary branch, or side arm, represents either a liquid drain or a steam tap for driving a feedwater heater. Consistent with the modeling philosophy used to develop the original model in TRAC-BD1/MOD1,[8.4-1] the flow through the turbine internals is not treated in detail from first principles. Instead, the processes of momentum and energy exchange are lumped into source terms in the one-dimensional conservation equations. The idealized physical model is illustrated schematically in Figure 8.4-1. The assumed characteristics of this model are summarized below.

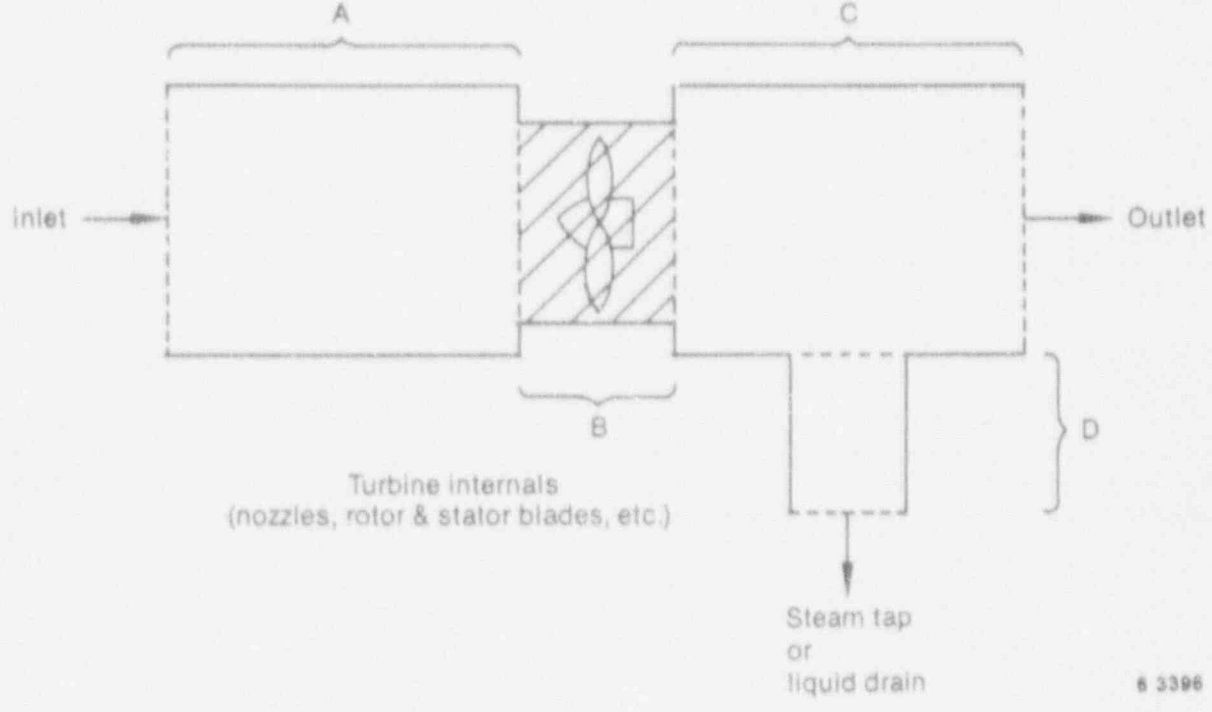

Figure 8.4-1. Idealized turbine model.

The two-phase inlet flow enters from the left and is homogenized in Region A prior to entry into the turbine internals (Region B). Heat exchange with the walls may occur in Region A, but all fluid dynamic processes associated with the internals are lumped into Region B. In this region, the fluid state is changed and momentum and energy are extracted by the turbine rotor. The net effect is that (a) the fluid pressure drops; (b) the total energy flow rate of the working fluid drops by an amount equal to the mechanical power output of the turbine rotor; (c) a saturated mixture is achieved, corresponding to the steam partial pressure in Region C; and (d) the velocity of the fluid changes due to density and/or flow area changes between entry to and exit from Region B. The flow area at the entrance to Region B is assumed equal to that at the inlet to Region A and the flow area at the exit from Region B is assumed equal to that at the exit from Region C.

The flows through Regions A and C are determined by the pressure gradient, the inertia of the fluid, and the wall friction losses (including form loss factors at the turbine entrance and exit). The flow through Region B is determined by the pressure gradient, the fluid inertia, and an effective form loss factor chosen to give the correct steady-state mass flow rate through the first turbine stage.[8.4-2]

The flow through Region D depends on whether the side arm represents a steam tap or a liquid drain. If it is a steam tap, the flow is determined in the same manner as for Regions A and C. If it is a liquid drain, it is determined from the user-input liquid separation efficiency (SEPEF). In this case, the vapor velocity is set to zero and the liquid velocity is set to the value required to extract (SEPEF) times (the total liquid mass in Region C) in a single computational time step.

Region B is assumed to have zero volume. Thus, the mass flow rate into the region is identically equal to the flow rate out, and the only effect of the region is to change the state of the working fluid and to transfer energy from the fluid to the turbine rotor.

8.4.2 Numerical Model

The conservation equations for momentum, mass, and energy used in TRAC-BF1/MOD1 are given in Sections 2.1.2 and 2.1.3. The semi-implicit finite-difference form of these equations used in the TRAC-BF1/MOD1 numerical scheme are given in Section 2.1.5. The original turbine model has been reformulated as a standard TRAC-BF1/MOD1 TEE and thus makes use of the above semi-implicit formulation of the fluid dynamic equations. The necessary modifications to the numerical model for the TEE component to achieve this objective are explained with the aid of Figure 8.4-2.

The turbine TEE consists of two cells in the primary tube and N cells in the side arm, where N is specified by the user. Since all side arm cells except the first are treated exactly like a normal TEE component, only the

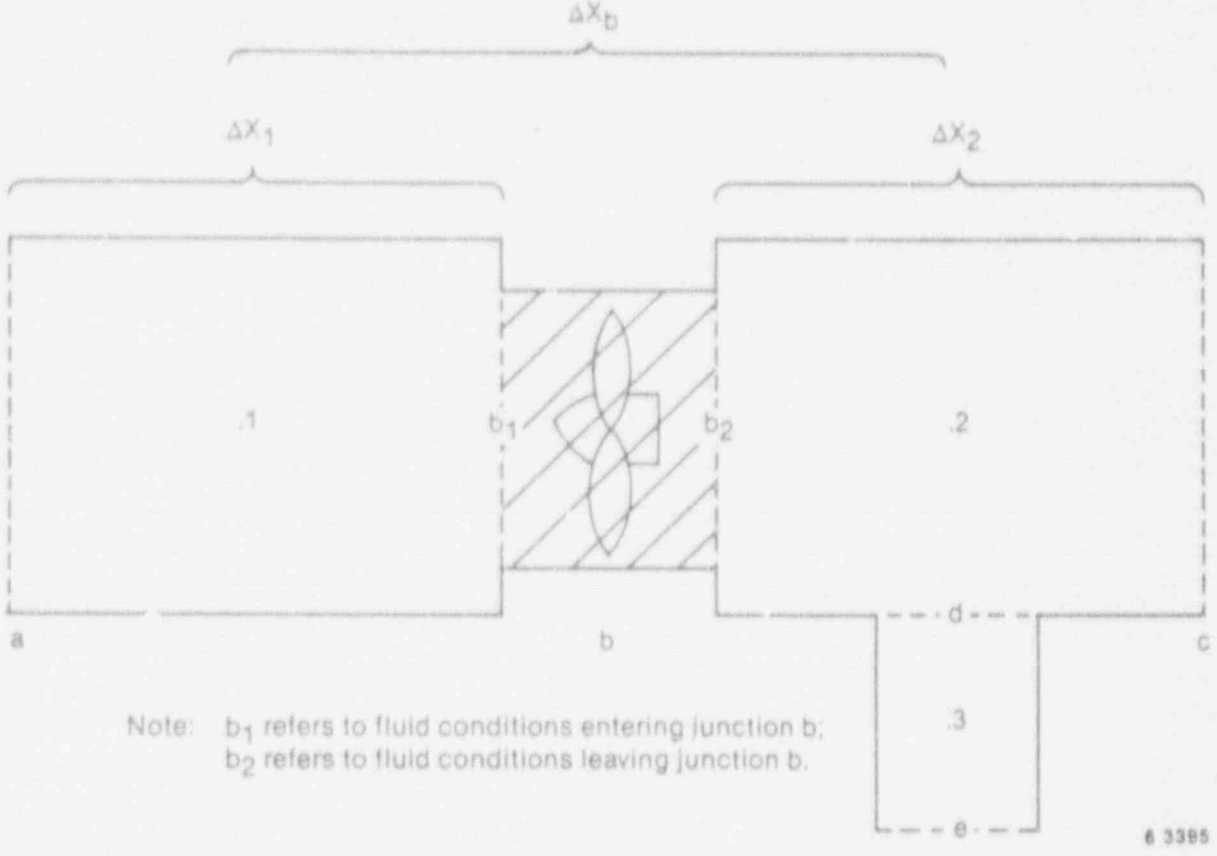

Figure 8.4-2 Schematic of numerical model for turbine.

first cell is indicated in Figure 8.4-2. The lumped effects of the turbine internals are felt at Junction b (hereafter referred to as the turbine membrane). As explained previously, the working fluid enters Junction b at the conditions prevailing at the center of Cell 1 and leaves as a saturated mixture at the pressure of Cell 2. The turbine membrane is assumed to possess zero volume, so the mass flow rate into Junction b is identically equal to the mass flow rate out of the junction.

The normal flow conditions for the turbine are into Cell 1 at Junction a, from Cell 1 to Cell 2 at Junction b, out of Cell 2 at Junction c and d, and toward the exit of the side arm at all other side arm junctions. The modifications explained below are applicable only for the case of normal flow and positive pressure gradient at Junction b (i.e., $p_2 < p_1$). For other flow conditions the described modifications do not apply and the fluid equations are solved by the unmodified TRAC-BF1/MOD1 semi-implicit scheme.

8.4.3 Momentum Equation

The normal TRAC-BF1/MOD1 momentum equations are written as velocity

equations for the liquid and vapor phases. Solution of the linearized equations yields expressions for the explicit new time junction phase velocities, V_g^{n+1} and V_ℓ^{n+1}, assuming no change in the pressure drop across the junction and implicit correction term, $\frac{\partial V_g^{n+1}}{\partial(\Delta P)}$ and $\frac{\partial V_\ell^{n+1}}{\partial(\Delta P)}$ for each phase velocity due to variation in the junction pressure drop during the time step. There is no change to the normal TRAC-BF1/MOD1 scheme for obtaining these terms at Junctions a and e.

The momentum (or velocity) equation used at Junction b is obtained by assuming the flow is homogeneous, and the total pressure drop between Cells 1 and 2 is lumped in a single form loss term characterized by the coefficient f_{turb}. Thus, the momentum equation solved at b is

$$\frac{\partial V_m}{\partial t} + V_m \frac{\partial V_m}{\partial X} = -\frac{1}{\rho_m}\frac{\partial P}{\partial X} - \frac{f_{turb} V_m^2}{\Delta X_b} . \qquad (8.4\text{-}1)$$

The form loss coefficient is obtained as follows. First, the steady- state turbine nozzle velocity[8.4-1] is computed.

$$V_{NOZ} = \left\{ \frac{2\gamma}{\gamma - 1}\frac{P_1}{\rho_1}\left[r_{b_1}^{2/\gamma} - r_{b_1}^{\gamma+1/\gamma} \right] \right\}^{1/2} , \qquad (8.4\text{-}2)$$

Next, the mass flow rate corresponding to this nozzle velocity is used to obtain the steady mixture velocity at b:

$$V_{m,b} = \frac{FA_{NOZ}}{FA_b} V_{NOZ} . \qquad (8.4\text{-}3)$$

Finally, f_{turb} is determined by substituting the velocity obtained from Equation (8.4-3) into the finite-difference approximation of the steady-state form of Equation (8.4-1)

$$f_{turb} = - \frac{V_{m,b_1}^n \left(V_{m,b_1}^n - V_{m,a}^n \right) \frac{\Delta X_b}{\Delta X_1} + \frac{1}{\rho_{m,1}^n}\left(P_2^n - P_1^n \right)}{\left(V_{m,b_1}^n \right)^2} . \qquad (8.4\text{-}4)$$

(To prevent numerical instabilities, a lower limit of 0.001 is placed on the numerical value of f_{turb}. With f_{turb} determined from the above explicit expression, the transient, semi-implicit, finite-difference approximation to Equation (8.4-1) becomes

$$\frac{V_{m,b_1}^{n+1} - V_{m,b_1}^{n}}{\Delta t} + V_{m,b}^{n}\left(\frac{V_{m,b_1}^{n} - V_{m,a}^{n}}{\Delta X_1}\right) = -\frac{1}{\rho_{m,1}^{n}}\left(\frac{P_2^{n+1} - P_1^{n+1}}{\Delta X_b}\right) - f_{turb}V_{m,b_1}^{n}V_{m,b_1}^{n+1} \quad . \quad (8.4\text{-}5)$$

Linearizing the pressure term in the above equation yields the following explicit values for $V_{m,b}^{n+1}$ and $\frac{\partial V_m^{n+1}}{\partial \Delta P}$:

$$V_{m,b}^{n+1} = \frac{-\frac{\Delta t}{\rho_1}\frac{P_2^{n} - P_1^{N}}{\Delta X_b} + V_{m,b_1}^{n} - V_{m,b_1}^{n}\left[V_{m,b_1}^{n}\left(\frac{V_{m,b_1}^{n} - V_{m,a}^{n}}{\Delta X}\right)\Delta T\right]}{1.0 + \frac{V_{m,b_1}^{n} f_{turb}\Delta t}{\Delta X_b}} \quad (8.4\text{-}6)$$

$$\frac{\partial V_{m,b_1}^{n+1}}{\partial \Delta P_b} = \frac{\frac{\Delta t}{\rho_1 \Delta X_b}}{1.0 \frac{V_{m,b_1}^{n} f_{turb}\Delta t}{\Delta X_b}} \quad . \quad (8.4\text{-}7)$$

Due to the assumption of homogeneous flow, V_{g,b_1}^{n+1} and V_{ℓ,b_1}^{n+1} are set equal to V_{m,b_1}^{n+1}; and $\frac{\partial V_{g,b_1}^{n+1}}{\partial \Delta P}$ and $\frac{\partial V_{\ell,b_1}^{n+1}}{\partial \Delta P}$ are set equal to $\frac{\partial V_{m,b_1}^{n+1}}{\partial \Delta P}$.

At Junction c, the only modification to the momentum equation is in the spatial acceleration terms. Since the phase velocities that are stored in the data base for Junction b are the phase velocities entering the turbine membrane (V_b), the spatial gradient terms in the momentum equations at Junction c must be altered to reflect the velocity differences between the exit of the turbine membrane and turbine exit. Thus, the spatial terms used in the vapor and liquid momentum solutions at Junction c are of the form

$$\frac{V_{p,c}^{n}\left(V_{p,c}^{n} - V_{m,v_2}^{n}\right)}{\Delta X_2}$$

where

$$V^{n}_{m,b_2} = V^{n}_{m,b_1}\left(\frac{FA_1}{FA_2}\right)\left(\frac{\rho^{n}_{m,b_1}}{\rho^{n}_{m,b_2}}\right) \qquad (8.4\text{-}8)$$

ρ^{n}_{m,b_1} = mixture density at entrance to turbine membrane cell (centered value in Cell 1)

ρ^{n}_{bi,b_2} = mixture density at exit of turbine membrane.

The momentum equation at Junction d is treated differently depending on whether the side arm represents a steam tap for feedwater heaters or a liquid separator drain. In the former case, the only modification to the normal TRAC-BF1/MOD1 momentum solution occurs when the control system is used to regulate the mass flow rate out the side arm. For this case, the side arm loss coefficients FKLOS and RKLOS are set each time step by the control system and are not directly controlled by the user.

In the case of the side arm representing a liquid separator drain, the momentum equations at Junction d are replaced with "pseudo momentum equations" designed to pull liquid only out of Cell 2 in a manner that approximates the effect of the true separation process. With the separator efficiency (SEPEF) set by the user, the explicit new time liquid velocity is defined as

$$V^{n+1}_{\ell,d} = SEPEF\left(\frac{1-\alpha^{n}_{2}}{FA_d\Delta t}\right). \qquad (8.4\text{-}9)$$

As previously discussed, this velocity is such that all the liquid present in Cell 2 at the end of the previous time step would leave through the side arm during the current time step if $V^{n+1}_{\ell,d}$ is not implicitly changed during the time step.

The implicit correction term $\frac{\partial V^{n+1}_{\ell,d}}{\partial(\Delta P_d)}$ is obtained by defining a "pseudo loss coefficient," f_{side}, as follows:

$$\Delta P_d = f_{side}\,\rho_\ell V^{n}_{\ell,d}\,. \qquad (8.4\text{-}10)$$

This expression is differentiated with respect to (ΔP_d) to obtain the following value for the implicit term:

$$\frac{\partial V_{\ell,d}^{n+1}}{\partial(\Delta P_d)} = \frac{1}{2} \frac{\bar{V}_{\ell,d}^{n+1}}{P_3^n - P_2^n} \quad . \tag{8.4-11}$$

When $P_3^n - P_2^n < 0$, both the explicit and implicit terms are set to zero. Also, to avoid numerical instability during startup, the maximum explicit velocity $V_{\ell,d}^{n+1}$ is limited to 50 m/s. The vapor velocity and its implicit correction term are both set to zero for the liquid separator option.

The above approach to computing the separator liquid velocity is not mathematically rigorous. The implicit correction term should clearly be tied to the change in the void fraction in Cell 2 and not to the pressure drop. However, the present approach is much simpler and has produced satisfactory results in test calculations to date.

8.4.4 Continuity Equation

The continuity equations for vapor and liquid mass are solved by the unmodified TRAC-BF1/MOD1 scheme in all cells of the turbine except Cell 2. For normal flow, the effect on the working fluid of passing through the turbine membrane is to lower the mixture enthalpy and pressure and change the mixture quality. This change in the mixture quality, together with the change in the specific internal energy of the steam and liquid after passing through Junction b, must be reflected in the continuity (and energy) equations for Cell 2.

The state of the mixture leaving Junction b is computed by assuming that the turbine membrane extracts adiabatically an amount of energy given by:

$$w_{turb} = \eta \Delta h_{ideal} \tag{8.4-12}$$

where

Δh_{ideal} = ideal enthalpy change of working fluid assuming an isentropic ideal gas expansion from pressure P_1 to pressure P_2.

Both η and Δh_{ideal} are computed explicitly, as described in Reference 8.4-2. Applying the 1st law, the enthalpy of the mixture on exit from Junction b is computed from the equation:

$$\frac{1}{2} V_{m,b_1}^2 + h_{b_1} = \frac{1}{2} V_{m,b_2}^2 + h_{b_2} + w_{turb} \quad . \tag{8.4-13}$$

Assuming that the working fluid leaves Junction b as a saturated mixture of vapor and liquid at pressure P_2, Equation (8.4-13) leads to the following expression to compute the homogeneous exit quality, x_{b2}, leaving Junction b:

$$x_{b2} = \frac{x_{b1} h^n_{g,b1} + (1 - x_{b1}) h^n_{\ell,b1} + \left(\frac{V^n_{m,b1}}{2}\right)^2 - w_{turb} - h^n_{\ell,b2} + \left(\frac{V^n_{\ell,c}}{2}\right)^2}{h^n_{g,b2} - h^n_{\ell,b2}} \quad . \tag{8.4-14}$$

with λ_{b2}, the explicit estimate for the homogeneous velocity at the turbine membrane exit may be computed from mass continuity as follows:

$$\bar{V}^{n+1}_{m,b2} = \frac{\rho^n_{m,b1}}{\rho^n_{m,b2}} \frac{FA_{b1}}{FA_{b2}} \bar{V}^{n+1}_{m,b1} \quad . \tag{8.4-15}$$

The implicit correction term is then

$$\frac{\partial \bar{V}^{n+1}_{m,b2}}{\partial(\Delta P_b)} = \frac{\rho^n_{m,b1}}{\rho^n_{m,b2}} \frac{FA_{b1}}{FA_{b2}} \frac{\partial \bar{V}^{n+1}_{m,b1}}{\partial(\Delta P_{b1})} \quad . \tag{8.4-16}$$

The explicit estimates for the integrated mass flux terms for vapor and liquid entering Cell 2 from Cell 1 are now computed from the corresponding terms representing mass flux out of Cell 1 together with the above value for x_{b2} as follows:

$$\bar{M}^{n+1}_{g,b2} = \bar{M}^{n+1}_{g,b1} + \bar{M}^{n+1}_{\ell,b1} x_{b2} \tag{8.4-17}$$

$$\bar{M}^{n+1}_{\ell,b2} = \bar{M}^{n+1}_{g,b1} + \bar{M}^{n+1}_{\ell,b1} - \bar{M}^{n+1}_{g,b2} \quad . \tag{8.4-18}$$

The terms $\bar{M}_{g,b}$ and $\bar{M}_{\ell,b}$ are computed by the normal TRAC-BF1/MOD1 numerical scheme. The implicit corrections to the integrated mass flux terms are also obtained from the corresponding terms computed for the mass flows out of Cell 1. Thus,

$$\frac{\partial M^{n+1}_{g,b2}}{\partial(\Delta P_b)} = \alpha_{b2} \rho_{g,b2} FA_{b1} \frac{\rho_{m,b2}}{\rho_{m,b1}} \frac{\partial V^{n+1}_{m,b1}}{\partial(\Delta P_b)} (\Delta t) \tag{8.4-19}$$

$$\frac{\partial M_{\ell,b_2}^{n+1}}{\partial(\Delta P_b)} = (1 - \alpha_{b_2})\,\rho_{\ell,b_2} FA_{b_1} \frac{\rho_{m,b_2}}{\rho_{m,b_1}} \frac{\partial V_{m,b_1}^{n+1}}{\partial(\Delta P_b)} (\Delta t). \qquad (8.4\text{-}20)$$

By formulating the mass flux terms and the implicit corrections in the above fashion, mass is identically conserved across Junction b.

8.4.5 Energy Equation

The energy equation has been modified from the normal scheme only in Cells 1 and 2 of the turbine. The modification for Cell 1 reflects the effect of frictional dissipation. At this point, it is noted that the energy equations used in the TRAC-BF1/MOD1 thermal-hydraulic solution[8.4-1] are thermal energy equations. They were obtained from the total energy (1st law) equations by subtracting out the volume integrals of the product of the respective phase volumetric fluxes ($FA \cdot V_p$) with their corresponding momentum equations. However, implicit in the form of the resulting energy equations is the assumption that frictional dissipation is zero. For most flow situations modeled with TRAC-BF1/MOD1, the dissipation terms are small and can be neglected. To account for the possibility of a large frictional (or form) loss through the turbine entrance (Junction a), the effect of dissipation has been added to the thermal energy equation for Cell 1.

By performing the above-mentioned operations on the one-dimensional momentum and energy equations, the following terms are added to the thermal energy equations:

$\alpha_p \rho_p V_p^3 \frac{d(FA)}{dx} dx$ is added to the left-hand side of the mixture energy equation (see Section 2.1.1) and $V_p(FA)f_p\,dx$ is added to the right-hand side of the vapor energy equation (see Section 2.1.1). In the mixture energy equation, both the vapor and liquid dissipation terms (p = g and ℓ) are added, while in the vapor energy equation, only the vapor terms are used (p = g). (Note that the above form of the dissipation terms neglects the effect of dissipation due to the interfacial shear.)

In the turbine energy equation modifications for Cell 1, the area change term above is neglected. The second term is evaluated assuming that all terms under the integral (8.4-11) are constant and equal to the values at Junction a. f_p is simply the total wall friction term in the momentum equation for Junction a and is a linear combination of V_g^2 and V_ℓ^2. Thus, the dissipation term for Cell 1 is approximated as

$$V_p(FA)f_p\,dx = V_p\left(A_pV_g^2 + B_pV_\ell^2\right) \tag{8.4-21}$$

and the term on the right-hand side is written semi-implicitly as

$$V_p\left(A_pV_g^2 + B_pV_\ell^2\right) = V_p^{n+1}A_p^n(V_g^n)^2 + B_p^n(V_\ell^n)^2 \,. \tag{8.4-22}$$

The coefficients A_p and B_p are simply products and quotients of volume fractions, phasic densities, and friction factors and are evaluated explicitly, as indicated. The fact that V_p^{n+1} appears in the above expression requires additions to both the explicit residual in the energy equation for Cell 1 and the implicit derivative of the residual with respect to the pressure drop across Junction a. These additions are, respectively

$$(DISS)_g^{n+1} = \bar{V}_{g,a}^{n+1}FA_a\alpha_{DC,a}\rho_{g,a}DX_a\alpha_{DC,a}WFV_a(V_{g,a}^n)^2 + (1-\alpha_{DC,a})WFL_a(V_{\ell,a}^n)^2\,\frac{\rho_{\ell,a}}{\rho_{g,a}} \tag{8.4-23}$$

$$(DISS)_\ell^{n+1} = \bar{V}_{\ell,a}^{n+1}FA_a(1-\alpha_{DC,a})\rho_{\ell,a}DX_a\alpha_{DC,a}WFV_a(V_{g,a}^n)^2\,\frac{\rho_{g,a}}{\rho_{\ell,a}} + (1-\alpha_{DC,a})WFL_a(V_{\ell,a}^n)^2 \tag{8.4-24}$$

$$\frac{\partial(DISS)_g^{n+1}}{\partial(\Delta P_a)} = \frac{\partial V_{g,a}^{n+1}}{\partial(\Delta P_a)}\,\frac{(DISS)_g^{n+1}}{\bar{V}_{g,a}^{n+1}} \tag{8.4-25}$$

$$\frac{\partial(DISS)_p^{n+1}}{\partial(\Delta P_a)} = \frac{\partial V_{\ell,a}^{n+1}}{\partial(\Delta P_a)}\,\frac{(DISS)_g^{n+1}}{\bar{V}_{g,a}^{n+1}} \,. \tag{8.4-26}$$

The effects of friction in the turbine internals are presumably accounted for in the turbine stage efficiency η and the pressure drop, and thus the addition of dissipation to the thermal energy equation is performed only in Cell 1 to reflect the effect of wall friction and form loss at the turbine entrance.

The energy equation for Cell 2 must be modified to reflect the altered specific enthalpies and phasic mass flows at the exit of the turbine membrane. This is done by altering the energy flux terms due to vapor and liquid flow into the cell at b_2 in the same manner as was done for the mass flux terms.

Thus,

$$E_{p,b_2} = M_{p,b_2} e_{p,b_2} \quad . \tag{8.4-27}$$

In addition to the above correction, the dilatation terms $[P_k^{n+1}\nabla_k(\alpha^n V_g^{n+1})$ and $P^{n+1}\nabla_k(\alpha^n V_g^{n+1} + (1-\alpha^n)V_\ell^{n+1})]$ must be altered to reflect the change in void fraction, mixture velocity, and flow area as the working fluid crosses the turbine membrane. The modified terms for the vapor and mixture energy equations for Cell 2 are, respectively,

$$P_2^{n+1}\left(\frac{\alpha_{b_2}^n V_{g,b_2}^{n+1} - \alpha_2^n V_{g,c}^{n+1}}{\Delta x_2}\right)$$

and

$$P_2^{n+1}\left(\frac{\alpha^- V_{g,b_2}^{n+1} + (1-\alpha_{b_2}^n)V_{\ell,b_2}^{n+1} - \alpha_2^n V_{g,c}^{n+1} + (1-\alpha_2^n)V_{\ell,c}^{n+1}}{\Delta x_2}\right) .$$

(Again, note that junction properties such as velocity and flow area that are stored in the data base for Junction b are those appropriate at the upstream side of the turbine membrane, b_1, in Figure 8.4-2.)

8.4.6 Critical Flow

The criterion for critical or choked flow at the turbine membrane is the same as was used in the previous model.[8.4-1] When the pressure ratio P_2/P_1 exceeds the critical value, the explicit new time velocity is computed as follows:

$$\bar{V}_{NO2}^{n+1} = \left(\frac{2\gamma}{\gamma-1}\,\frac{P_1^n}{\rho_{m,1}^n}\,r_{crit}^{2/\gamma} - r_{crit}^{\gamma+1/\gamma}\right)^{1/2} \quad . \tag{8.4-28}$$

The implicit correction to the choked velocity arises due to changes in the upstream pressure (P_1) only. However, since the TRAC-BF1/MOD1 network solution is based on pressure differences across junctions rather than cell pressures, it is assumed that

$$\frac{\partial V_{NOZ}^{n+1}}{\partial(\Delta P_b)} = \frac{\gamma}{\gamma - 1} \frac{1}{\rho_{N,1}^{n}} r_{crit}^{2/\gamma} - r_{crit}^{\gamma+1/\gamma} \left(V_{NOZ}^{n+1}\right)^{-1} . \qquad (8.4\text{-}29)$$

Choking at all turbine junctions other than b is treated by the normal critical flow model in TRAC-BD1,[8.4-1] with the single exception of Junction d when the side arm is treated as a liquid separator drain. In this case, a critical flow model is clearly not applicable.

8.4.7 References

8.4-1. D. D. Taylor et al., *TRAC-BD1/MOD1: An Advanced Best Estimate Computer Program for Boiling Water Reactor Transient Analysis*, Volume 1, NUREG/CR-3633, EGG-2994, April 1984.

8.4-2. M. M. Giles, *TRAC-BD1 Turbine Model*, EGG-CBB-6029, September 1982.

9. HEAT STRUCTURE PROCESS MODELS

Four fundamental heat structure process models are modeled by the TRAC-BF1/MOD1 code. They include the interfacial heat transfer between the vapor and liquid phases, conduction within structural components, heat transfer between the structures and the fluid, and internal fuel rod power generation. Interfacial heat transfer has been addressed in development of the fluid-dynamics equations. The remaining three mechanisms are discussed below.

The thermal history of the structural reactor materials is obtained from a solution of the heat-conduction equation. The energy exchange between the structures and the fluid is modeled using Newton's law of cooling. The coupling algorithm is semi-implicit. For each new time step (Figure 9-1), the fluid-dynamics equations are solved based on previous values for the wall heat-transfer coefficient (h) and surface wall temperatures (T_{wall}). The expressions can be written as

$$q_w^{n+1} = h^n \left(T_w^n - T_f^{n+1} \right) . \qquad (9\text{-}1)$$

Once the fluid-dynamics equations are solved, the wall temperature distributions are deduced from the conduction equation.

For simplicity as well as computing efficiency, the conduction models are separated according to their geometric function. They include conduction within cylindrical walls, slabs, core rods, and flat channel walls. The first model analyzes heat conduction within the pipe walls of loop components and of internal vessel components (control guide tubes and vessel wall). The second model is used to represent vessel internal structures that cannot be characterized by a cylindrical conduction model. The third model is used to represent the heat transfer in a fuel rod. The fourth model is used to represent heat conduction within the walls of the BWR fuel bundle or channel. The fifth model is used to model the fuel rod power density distribution. These walls are assumed to be flat, rather than cylindrical. Each of these five models is discussed in detail.

In addition, the TRAC-BF1/MOD1 model for the zirconium-steam oxidation reaction is discussed, together with its effect on outer fuel rod cladding radius and internal heat generation rate used in the conduction equations for the fuel rods.

The remainder of this chapter is outlined as follows. Section 9.1 documents cylindrical heat conduction in one-dimensional components, 9.2 documents the Cartesian heat conduction for VESSEL slabs, 9.3 documents fuel-rod heat conduction, and Section 9.4 documents the reactor core power model.

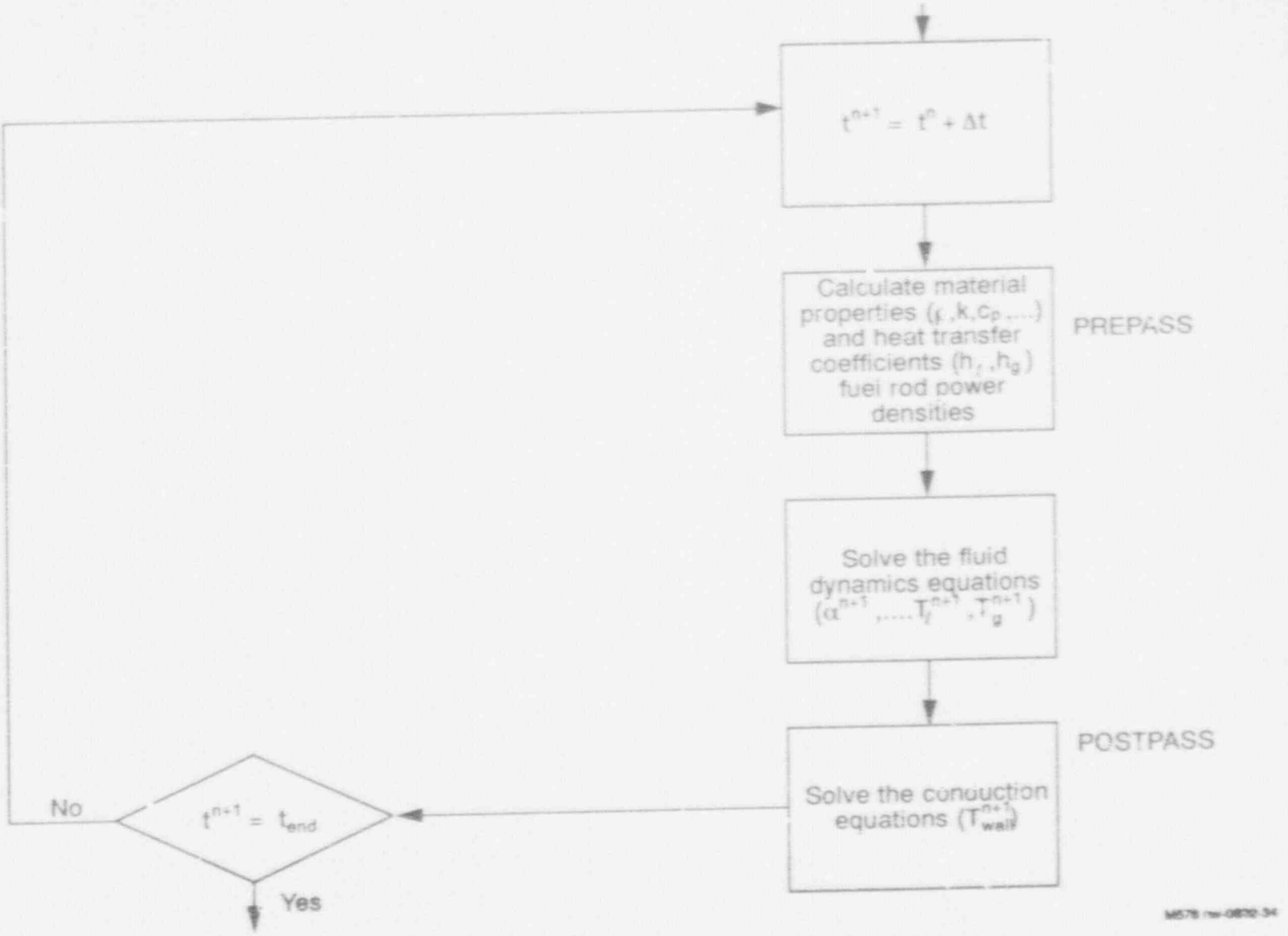

Figure 9-1. Semi-implicit coupling between hydrodynamics and structural heat transfer.

9.1 CYLINDRICAL WALL HEAT CONDUCTION

The temperature distribution within the walls of a component is determined by Subroutine CYLHT. A solution is obtained from a finite difference approximation to the one-dimensional conduction equation

$$\rho c_p \frac{\partial T}{\partial t} = \frac{1}{r} \frac{\partial}{\partial r}\left(rk \frac{\partial T}{\partial r}\right) + \dot{q}''' \quad . \tag{9.1-1}$$

The finite difference equations are derived by applying an integral method[9.1-1] to the elemental volumes shown in Figure 9.1-1. The general form for the ith volume ($1 < i < n$) is

$$\frac{r_{i-1/2}k_{i-1/2}}{\Delta r_{i-1}} T_{i-1}^{n+1} - \left\{ \frac{r_{i-1/2}k_{i-1/2}}{\Delta r_{i-1}} + \frac{r_{i+1/2}k_{i+1/2}}{\Delta r_i} + \frac{1}{2\Delta t}\left[\left(r_i\Delta r_{i-1} - \frac{\Delta r_{i-1}^2}{4}\right)(\rho c_p)_{i-1/2}\right.\right.$$

$$\left.\left. + \left(r_i\Delta r_i + \frac{\Delta r_i^2}{4}\right)(\rho c_p)_{i+1/2}\right]\right\} T_i^{n+1} + \frac{r_{i+1/2}k_{i+1/2}}{\Delta r_i} T_{i+1}^{n+1}$$

$$= -\frac{1}{2}\left(r_i\Delta r_{i-1} - \frac{\Delta r_{i-1}^2}{4}\right)\left[\frac{(\rho c_p)_{i-1/2}}{\Delta t} T_i^n + q'''\right] + \left(r_i\Delta r_i - \frac{\Delta r_i^2}{4}\right)\left[\frac{(\rho c_p)_{i+1/2}}{\Delta t} T_i^n + \dot{q}'''\right] \tag{9.1-2}$$

where

$$T_i^n = T(t^n, r_i) \quad . \tag{9.1-3}$$

The boundary conditions applied to the inner ($i = 1$) and outer ($i = N$) surfaces are

$$-k\frac{\partial T}{\partial r}\bigg|_{i=1,N} = h_\ell(T_\ell - T_i) + h_g(T_g - T_i) - q_{r_i} \quad . \tag{9.1-4}$$

Applying this boundary condition to the inner surface ($i = 1$), the above finite difference equation becomes

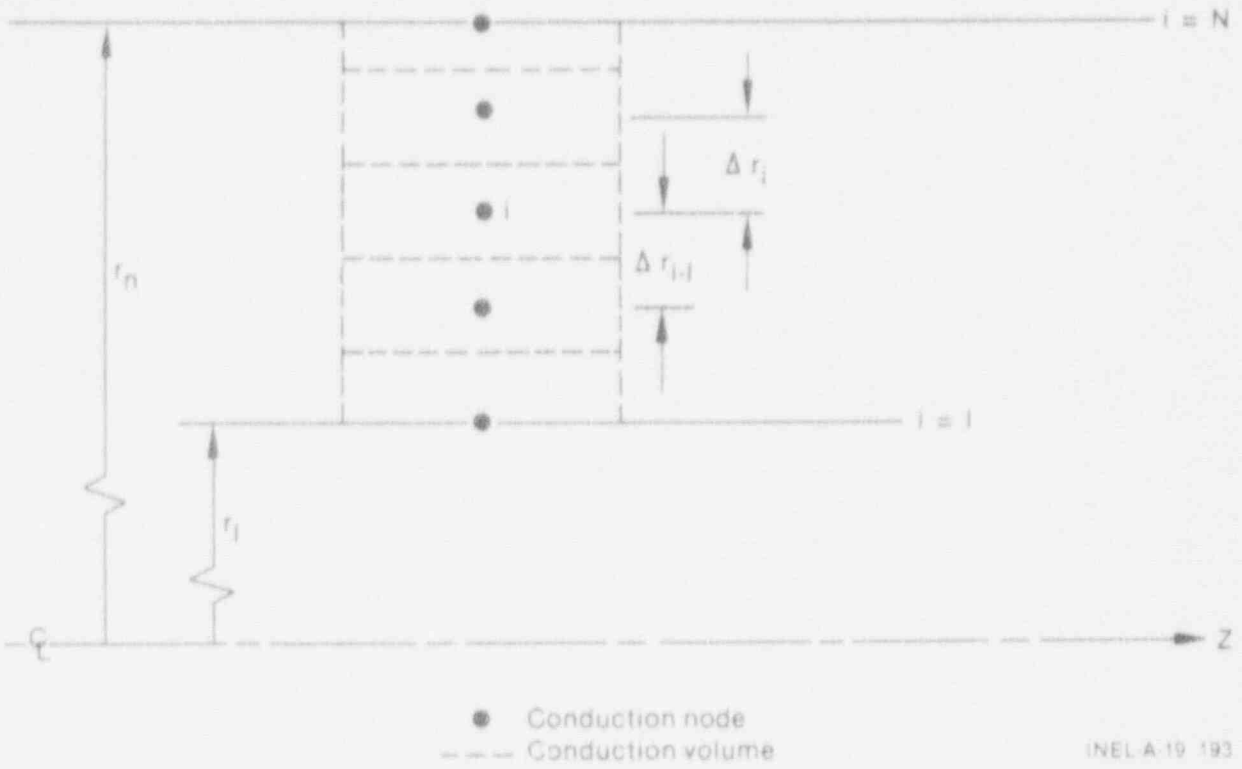

Figure 9.1-1. Cylindrical wall geometry.

$$-\left[\frac{r_{3/2}k_{3/2}}{\Delta r_1} + \frac{1}{2}\left(r_1\Delta r_1 + \frac{\Delta r_1^2}{r}\right)\frac{(\rho c_p)_{3/2}}{\Delta t} + f_{ss}r_1(h_\ell + h_g)\right]T_1^{n+1} + \frac{r_{3/2}k_{3/2}}{\Delta r_1}T_2^{n+1}$$

$$= -\frac{1}{2}\left(r_1\Delta r_1 - \frac{\Delta r_1^2}{4}\right)\left[\frac{(\rho c_p)_{3/2}}{\Delta t}T_1^n + \dot{q}'''\right] + r_1\left[h_\ell\left(f_t T_1^n - T_\ell^{n+1}\right) + h_g\left(f_t T_1^n - T_g^{n+1}\right)\right] + q_{r_1} \quad (9.1\text{-}5)$$

In this equation, f_{ss} and f_t are *implicitness* parameters. Because of the semi-implicit coupling with the fluid equations, f_{ss} and f_t take on the values of 0 and 1, respectively, for transient calculations. This ensures that both sets of equations use identical surface heat fluxes as boundary conditions for each time step. When a steady-state solution is required, however, large time steps are desirable. Therefore, the conduction equation is written in a fully implicit form and $f_{ss} = 1$ and $f_t = 0$.

Note that the above formulation conveniently positions nodal points on material interfaces. Material properties are evaluated between nodes.

The resulting linear equations are solved in a sequential fashion in the axial (z) direction. For each axial position, a solution is achieved using Gaussian elimination. A lumped parameter solution is available if the number of nodes is one (NODES = 1). For this option, the wall temperature is obtained from

$$T^{n+1} = \left\{ \frac{1}{2}\left(2\Delta r + \frac{\Delta r^2}{R_i}\right)\left(\frac{\rho C_p}{\Delta t}T^n + \dot{q}'''\right) + h_{\ell_i}\left(T_\ell^{n+1} - f_t T^n\right) + h_{g_i}\left(T_{g_i}^{n+1} - f_t T^n\right) \right.$$

$$\left. - \left(1 + \frac{\Delta r}{R_i}\right)\left[h_{\ell_o}\left(f_t T^n - T_{\ell_o}^{n+1}\right) + h_{g_o}\left(f_t T^n - T_{g_o}^{n+1}\right)\right] \right\} \Bigg/$$

$$\left\{ \frac{1}{2}\left(2\Delta t + \frac{\Delta r^2}{R_i}\right)\left(\frac{\rho C_p}{\Delta t}\right) + f_{ss}\left[h_{\ell_i} + h_{g_i} + \left(1 + \frac{\Delta r}{R_i}\right)\left(h_{\ell_o} + h_{g_o}\right)\right] \right\} . \qquad (9.1\text{-}6)$$

The subscripts i and o refer to the inner and outer radii, respectively.

Note that the present coding does not allow for radiation heat-transfer boundary conditions when NODES = 1.

The boundary condition at the inside surface is inferred from the hydraulic conditions inside the component. The outer boundary condition is normally constant, with user-specified values for the heat transfer coefficient and fluid temperatures. Alternately, the user may utilize a generalized heat transfer capability whereby the outer surface of any one-dimensional component may be thermally coupled to the fluid inside any other component (including the vessel) in the model.

TRAC-BF1/MOD1 also can be used to model the conduction heat transfer with the preceding cylindrical conduction solution within any double-sided heat slab surface within the vessel. Examples of such heat structures are the core barrel, which sees fluid conditions in both the downcomer and the core bypass, and the vessel wall, which sees ambient fluid conditions as well as downcomer fluid conditions.

9.1.1 Reference

9.1-1. P. O. Roache, *Computational Fluid Dynamics*, Albuquerque: Hemosa Publishers, 1972.

9.2 CARTESIAN HEAT CONDUCTION FOR VESSEL SLABS

Conduction within vessel structures such as downcomer walls and support plates is modeled in Subroutine SLABHT. A lumped parameter solution is available. Through input, the user must supply the slab mass, m, surface area, A, and material properties, c_p and k, for heat slabs in each fluid-dynamic volume. The lumped parameter temperature is obtained from

$$T^{n+1} = \frac{\frac{\rho C_p}{\Delta t} x T^n - h_\ell \left(f_t T^n - T_\ell^{n+1}\right) - h_g \left(f_t T^n - T_g^{n+1}\right)}{\frac{\rho C_p}{\Delta t} x + f_{ss}(h_\ell + h_g)} \qquad (9.2\text{-}1)$$

where x is an effective slab thickness (m/2ρA). The steady-state (f_{ss}) and transient (f_t) flags were discussed in the previous section.

9.3 FUEL ROD HEAT CONDUCTION

9.3.1 Cylindrical Model

Subroutine RODHT analyzes the conduction of reactor rods on a rod-by-rod basis. The formulation can model diverse rod geometries. Both nuclear and electrically heated rods can be analyzed. The effects of internal heat generation, gap conduction, metal-water reaction, and variable rod properties are included. The numerical procedures are capable of modeling the entire LOCA scenario in a consistent and mechanistic fashion. The model can also resolve large axial (z) gradients characteristic of the reflood phase.

The rod conduction solution is obtained for each rod group within each fuel bundle component specified by the user. The number of rod groups required to represent the radiation heat transfer within the bundle is optional. However, for each rod group, a conduction solution is obtained and coupling of the rod heat transfer with the hydraulics is modeled with Newton's law of cooling. Power distributions from bundle to bundle, from rod to rod, and from node to node within the rod are modeled.

The fuel rod conduction solution method is similar to that described in the cylindrical geometry section. The major differences pertain to treatment of boundary conditions, user selection of composite material structure, and provision for spatial and time-dependent internal heat generation.

The fuel rod conduction model has two significant features not found in the previous code versions. First, axial conduction is included in the finite-difference equations. Second, the nodes are defined as centered at material boundaries, and the code calculates and stores special *interface* material properties that are used in the conduction solutions. Referring to Figure 9.3-1, the finite-difference equation for conduction at an interior node (i,j) is identical to that found in References 9.3-1 and 9.3-2 except that axial conduction is included and written as

$$\frac{1}{2}(\Delta Z_u + \Delta Z_\ell)\left[\frac{1}{4}(r + r_+)^2 - \frac{1}{4}(r + r_-)^2\right]\rho C_p \frac{T^{n+1} - T^n}{\Delta t}$$

$$= [\textit{volumetric source terms}] + [\textit{normal radial conduction terms}] \qquad (9.3\text{-}1)$$

$$+ \left[\frac{1}{4}(r + r_+)^2 - \frac{1}{4}(r + r_-)^2\right]\left[\frac{1}{2}(k_u + k)\frac{T_u^n - T^{n+1}}{\Delta Z_u} + \frac{1}{2}(k_\ell + k)\frac{T_\ell^n - T^{n+1}}{\Delta Z_\ell}\right]$$

At the top and bottom of the heated length, the axial conduction terms are modified; while at the rod axis, material interfaces, and rod surface, the

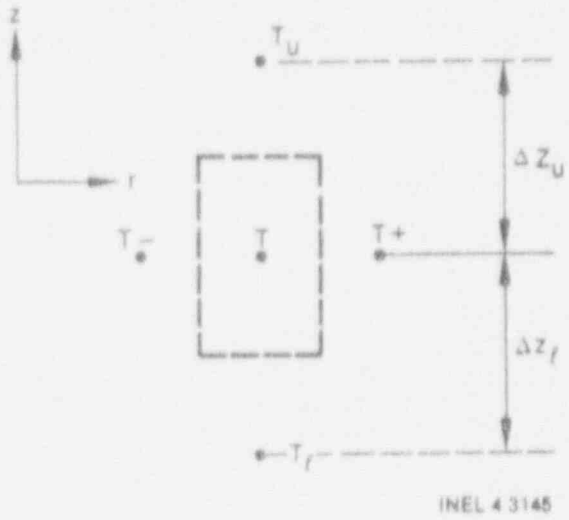

Figure 9.3-1. Nodalization for fuel rod heat conduction.

radial conduction terms are modified (as specified in References 9.3-1 and 9.3-2). NOTE: For each row of nodes across a rod, these finite-difference equations form a tridiagonal system of linear equations in terms of the new-time node temperatures T_-^{n+1}, T^{n+1}, and T_+^{n+1}. These linear systems are solved row by row (ascending the rod) for each rod group. Because the axial conduction terms are explicit, involving old-time temperatures T_ℓ^n and T_U^n, this row-by-row scheme may be used instead of solving for the temperature field for the whole rod at once, which would require inverting a large (although sparse) matrix (perhaps 200 x 200 or more).

The gap between the fuel and cladding of fuel rods is treated by explicit noding on fuel and cladding surfaces with a heat-transfer coefficient between these nodes. Stored energy and internal heat generation in the gap region are neglected. The finite-difference equation for the outermost fuel pellet node is

$$\frac{\rho C_p}{\Delta t}\left(T^{n+1} - T^n\right) = \frac{1}{2}\,\frac{(r + r_-)\,(k + k_-)}{\left[r - \frac{1}{4}\,(r - r_-)\right](r - r_-)^2}\,(T^{n+1} - T_-^{n+1})$$

$$+\,\frac{r h_{gap}}{\frac{1}{2}\left[r - \frac{1}{4}\,(r - r_-)\right](r - r_-)}\,(T_+^{n+1} - T^{n+1})$$

$$+\,(\textit{axial conduction terms}) + (\textit{volumetric heat source})\,. \qquad (9.3\text{-}2)$$

For the innermost cladding node, the finite-difference equation is

$$\frac{\rho C_p}{\Delta t}\left(T^{n+1} - T^{n}\right) = \frac{1}{2}\,\frac{(r_o + r)\,(k_{\cdot\cdot\cdot})}{\left[r - \frac{1}{4}\,(r_+ - r)\right](r_+ - r)^2}\left(T_+^{n+1} - T^{n+1}\right)$$

$$+\,\frac{r\,h_{gap}}{\frac{1}{2}\left[r + \frac{1}{4}\,(r_+ - r)\right](r_+ - r)}\left(T^{n+1} - T^{n+1}\right)$$

+ (*axial conduction terms*) + (*volumetric heat sources*)

+ (*metal-water reaction source*) .

The equation used for the outside of the cladding is similar to equation (9.3-2) (outside surface node of the fuel region) except that the radiative heat flux and metal-water reaction are included. This equation is

$$\left(T^{n+1} - T^{n}\right) = \frac{1}{2}\,\frac{(r + r_-)\,(k + k_-)}{\left[r - \frac{1}{4}\,(r - r_-)\right](r - r_-)^2}\left(T_-^{n+1} - T^{n+1}\right)$$

$$+\,\frac{r\left[h_\ell\left(T_\ell - T^{n+1}\right) + h_v\left(T_v - T^{n+1}\right)\right]}{\frac{1}{2}\left[r - \frac{1}{4}\,(r - r_-)\right](r - r_-)}$$

+ (*axial conduction, metal-water reaction, and radiation terms*) . (9.3-4)

9.3.2 Rectangular Model

The walls of CHAN components are modeled as flat plates rather than cylinders. In addition, axial conduction is included in the difference equations when the reflood model is activated. For the nodalization conventions used in Figure 9.3-2, the finite-difference form of the conduction equations used in TRAC-BF1/MOD1 are

1. For an inside surface node

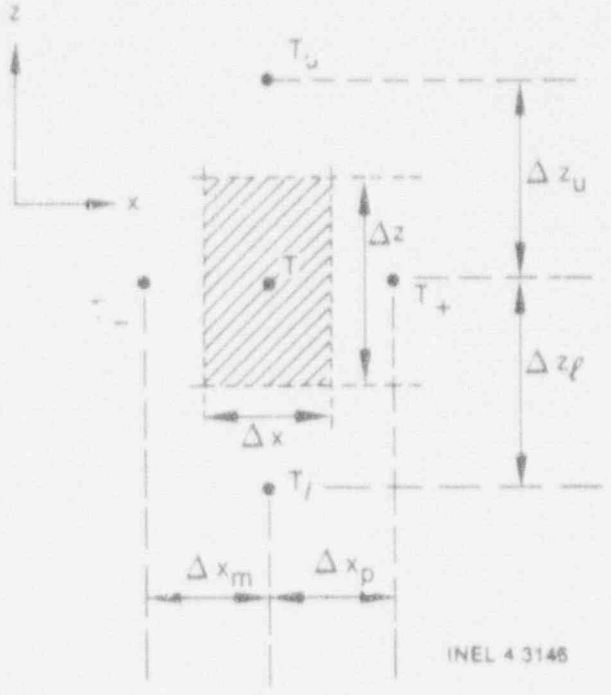

Figure 9.3-2. Nodalization for CHAN wall heat conduction.

$$\Delta z \Delta x \frac{\rho C_p}{\Delta t}\left(T^{n+1} - T^n\right) = \Delta z\left[h_{i,v}\left(T_{i,v}^{n+1} - T^{n+1}\right) + h_{i,\ell}\left(T_{i,\ell}^{n+1} - T^{n+1}\right)\right] + \Delta z k_+ \frac{T_+^{n+1} - T^{n+1}}{\Delta x_p}$$

$$+ \Delta x\left[k_u \frac{T_u^n - T^{n+1}}{\Delta z_u} + k_\ell \frac{T_\ell^n - T^{n+1}}{\Delta z_\ell}\right] + \Delta z q_{rad} + \Delta z \Delta x q''' \,. \qquad (9.3\text{-}5)$$

Here $T_{i,v}$ and $T_{i,\ell}$ refer to the vapor and liquid fluid temperatures, respectively, at the inner wall surface. $h_{i,v}$ and $h_{i,\ell}$ are the corresponding heat transfer coefficients.

2. For an outside surface node

$$\Delta z \Delta x \frac{\rho C_p}{\Delta t}\left(T^{n+1} - T^n\right) = \Delta z\left[h_{o,v}\left(T_{o,v}^{n+1} - T^{n+1}\right) + h_{c,\ell}\left(T_{i,\ell}^{n+1} - T^{n+1}\right)\right] + \Delta z k_- \frac{T_-^{n+1} - T^{n+1}}{\Delta x_m}$$

$$+ \Delta x \left[k_u \frac{T_u^n - T^{n+1}}{\Delta z_u} + k_\ell \frac{T_\ell^n - T^{n+1}}{\Delta z_\ell} \right] + \Delta z \Delta x q''' \quad . \tag{9.3-6}$$

3. For an interior node

$$\Delta z \Delta x \frac{\rho C_p}{\Delta t} (T^{n+1} - T^n) = \Delta z k_- \frac{\left(T_-^{n+1} - T^{n+1}\right)}{\Delta x_m} + \Delta z \frac{\left(T_+^{n+1} - T^{n+1}\right)}{\Delta x_p}$$

$$+ \Delta x \left[k_u \frac{T_u^n - T^{n+1}}{\Delta z_u} + k_\ell \frac{T_\ell^n - T^{n+1}}{\Delta z_\ell} \right] + \Delta z \Delta x q''' \quad . \tag{9.3-7}$$

It will be noted that the right-hand side of the above equations includes terms for surface convection, axial and transverse conduction, surface radiation, and internal heat generation. The four conductivities used in these equations (k_ℓ, k_u, k_+, k_-) are linear averages between the conductivity of the central node and the appropriate outer node.

The channel wall surface boundary conditions are determined from the same heat transfer correlations package as is used for other components.

Additional information relative to the rod heat transfer package is supplied in Appendix G, which documents the moving mesh model for reflood.

9.3.3 Metal-Water Reaction

When sufficiently high temperatures are reached by zircaloy in a steam environment, an exothermic reaction may occur that will influence the peak cladding temperatures attained. The zirconium-steam reaction equation is

$$Zr + 2H_2O \rightarrow ZrO_2 + 2H_2 + Heat \quad . \tag{9.3-8}$$

In the presence of sufficient steam, the reaction rate expression of Reference 9.3-3 is written as

$$-\frac{dr}{dt} = \frac{1.126 \times 10^{-6}}{R_o - r} \exp\left(\frac{18062}{T}\right) \qquad (9.3\text{-}9)$$

where

r = reacting surface radius (m)

R_o = cladding outer radius (m)

T = cladding surface temperature

and is assumed to be valid.

The method outlined in Reference 9.3-4 is used to calculate the zirconium-oxide penetration depth and associated heat source. The mass of zirconium per unit cladding length (m_{Zr}) consumed by the reaction in one time step is

$$m_{Zr} = \pi\rho_{Zr}\left[(r^n)^2 - (r^{n+1})^2\right] . \qquad (9.3\text{-}10)$$

Equation (9.3-10) is used to calculate r^{n+1}, yielding

$$r^{n+1} = R_o - \left[(r^n)^2 + 2.252 \times 10^{-6}\,\Delta t \exp\left(\frac{18062}{T}\right)\right]^{1/2} . \qquad (9.3\text{-}11)$$

The heat source (q'''_{mw}) added to the conduction equations, assuming a one-region cladding, is

$$q'''_{mw} = 6.513 \times 10^6 m_{Zr}\left[\Delta t\left(R_o^2 - R_i^2\right)\right]^{-1} \qquad (9.3\text{-}12)$$

where R_i is the inner cladding radius and 6.513×10^6 J/kg corresponds to the energy release per kilogram of zirconium oxidized.

9.3 References

9.3-1. J. Spore et al., *TRAC-BD1: An Advanced Best Estimate Computer Program for Boiling Water Reactor Loss-of-Coolant Analysis*, NUREG/CR-2178, October 1981.

9.3-2. Los Alamos National Laboratory Safety Code Development Group, *TRAC-PD2, An Advanced Best Estimate Computer Program for Pressurized Water Reactor Loss-of-Coolant Accident Analysis*, NUREG/CR-2054, LA-8709-MS,

April 1981.

9.3-3. J. V. Cathcart, *Quarterly Progress Report on the Zirconium Metal-Water Oxidation Kinetics Program*, ORNL/NUREG/TM-41, August 1976.

9.3-4. *RELAP4/MOD5: A Computer Program for Transient Thermal-Hydraulic Analysis of Nuclear Reactors and Related Systems, Volume 1*, ANCR-NUREG-1335, September 1976,

9.4 CORE POWER MODELS

In general, the requirements for simulating reactor core neutronics during a postulated transient entails the use of a space-time-dependent multi-group neutron transport model. However, the computational solution for a detailed space-time neutron transport calculation is generally cost prohibitive. Consequently, the core power response models employed in TRAC-BF1/MOD1 have a number of simplifications to the generalized neutron transport formulation.

The TRAC-BF1/MOD1 code has three methods of simulating core power response. The first method is simply a user-supplied table lookup scheme. The supplied table is a power-versus-time input. The second method employs a space-independent reactor kinetics model with reactivity feedback. The second model is useful for simulating transients where time-dependent spatial variations in the core power distribution are not significant. The third method employs a one-dimensional, two-group, neutron transport model. The third model solves the one-dimensional steady-state and time-dependent neutron diffusion equations in a rectangular geometry.

The remainder of Section 9.4 is outlined as follows. Section 9.4.1 will define and discuss several key parameters that are used in the formulation of the point kinetics and one-dimensional diffusion neutronics models. Section 9.4.2 will detail the space-independent kinetics formulation, numerical approximations to the point kinetics formulation in TRAC-BF1/MOD1, and implementation of the point kinetics model into the code. Section 9.4.3 will detail the one-dimensional neutron diffusion model formulation, numerical approximations to this formulation, and implementation into the TRAC-BF1/MOD1 code. Section 9.4.4 will give conclusions relative to applicability of the above models.

9.4.1 Preliminary Definitions

This section details several key definitions needed to understand the formulation for the space independent and one-dimensional neutron kinetics models. For a comprehensive overview of the fundamentals for neutron transport and kinetics, see References 9.4-1 through 9.4-5.

Power in a nuclear reactor is generated by approximately 200 MeV of energy each time a neutron causes a nucleus to fission. The rate at which this energy is released is determined by the state of the neutron chain reaction. The behavior of such neutron chain reactions is most easily understood in terms of the populations of neutrons in successive generations. The key parameter involved here is denoted by k and is defined in terms of the neutron population of successive generations.

$$k = \frac{\text{number of neutrons in } (n+1)\text{th generation}}{\text{number of neutrons in nth generation}} \quad . \tag{9.4-1}$$

If we had a system in which the only mechanism for neutron production was fission without external sources, the nth generation would produce

$$N_n = N_1 k^{n-1} \tag{9.4-2}$$

neutrons, where N_1 is the number of neutrons in the first generation. When treated precisely, the kinetic behavior of the above chain reaction is far more complex.

Complications arise from the fact that small fractions of neutrons are not instantaneously produced by fission but result from the decay of certain fission products. A chain reaction is said to be subcritical, critical, or supercritical at time t depending on whether $k(t) < 1$, $k(t) = 1$, or $k(t) > 1$, respectively.

Often it is more convenient to deal with the reactivity $\rho(t)$ at some time t which is defined in terms of the $k(t)$ as

$$\rho(t) = \frac{k(t) - 1}{k(t)} \quad . \tag{9.4-3}$$

Clearly, the subcritical, critical, and supercritical states correspond to $\rho < 0$, $\rho = 0$, and $\rho > 0$, respectively.

We now turn briefly to definitions needed to describe spatial as well as time effects in neutron transport theory. In a reactor, the neutron flux is a function of space, time, and energy and can be denoted as

$$\Phi = \Phi(E,r,t) = v(E,r,t)n(E,r,t) \tag{9.4-4}$$

where

E = neutron energy

r = location of neutron at position (x,y,z)

v = neutron speed

n = neutron density.

The probability that a neutron with a given energy E will undergo a collision travelling a unit distance ρ with a nucleus is defined as

$$\Sigma(E,r,t) = \bar{n}(r,t)\sigma(E) \quad . \tag{9.4-5}$$

where

$\bar{n}(r,t)$ = the atomic density of reactor nuclei at position r at time t

$\Sigma(E,r,t)$ = macroscopic cross section

$\sigma(E)$ = microscopic cross section.

The above units are generally given in centimeters. A neutron that undergoes a collision is scattered, captured, or causes a fission.

The expression $\sigma(E)$ is generally referred to as the total cross section and is written as

$$\sigma_t(E) = \sigma_s(E) + \sigma_c(E) + \sigma_f(E) \tag{9.4-6}$$

where the subscripts t, s, c, and f refer to total, scattering, capture, and fission. At times it is convenient to group fission and capture cross sections together. Thus, an absorption cross section is defined by

$$\sigma_a(E) = \sigma_c(E) + \sigma_f(E) \tag{9.4-7}$$

for each reaction type. A macroscopic cross section is defined as

$$\Sigma_x(E,r,t) = \bar{n}\sigma_x(E) \tag{9.4-8}$$

where the subscript x refers to the reaction type.

9.4.2 Space-Independent Reactor Kinetics and Core Decay Models

Even the one-dimensional, two-group approximation discussed in Section 9.4.3 requires extensive numerical calculations. Consequently, it is often desirable to solve the reactor power only as a function of time. Although this approach is not as accurate, such simplifications may provide a great deal of insight into the nature of reactor transients. The derivation of the space-independent or point reactor kinetics equation begins with the more generalized space- and energy-dependent neutron transport equation. The general diffusion equation is collapsed into a single energy group diffusion equation. By assuming that the power distribution can be separated into separate spatial and time-dependent functions, the point kinetics equation can be derived using spatial averaging techniques. This approximation is adequate for cases in which the core spatial distribution remains nearly constant.

Accurately modeling a rod withdrawal accident or similar scenario is an example of a case where the above approximation would not be appropriate.

9.4.2.1 Formulation of Point Kinetics Equations. In the space-independent formulation employed in TRAC-BF1/MOD1, the decay heat equation that describes the energy release from fission decay products is solved after the point kinetics equation is solved. Moreover, in this formulation, allowances for direct moderator heating have been made. The point kinetics and decay heat equations are as given in Reference 9.4-6.

$$\frac{dP}{dt} = \frac{1-\beta}{\Lambda}(\rho - 1)P + \sum_{i=1}^{n} \lambda_i C_i \qquad (9.4\text{-}9)$$

$$\frac{dC_i}{dt} = -\lambda_i C_i + \frac{\beta_i}{\Lambda} P \text{ for } i = 1,2,\ldots n \qquad (9.4\text{-}10)$$

$$\frac{dH_{\ell k}}{dt} = -\lambda''_{\ell k} H_{\ell k} + \frac{E_{\ell k} P_\ell}{Q} \text{ for } \ell = 1,2,\ldots m + k = 1,2\ldots n_f \qquad (9.4\text{-}11)$$

where

β_i = effective delayed neutron fraction of delayed group i

β = total effective delayed neutron fraction = $\sum_{i=1}^{n} \beta_i$

C_i = fission power of delayed neutron group i (W)

$E_{\ell k}$ = effective energy input to decay group k from fission of isotope ℓ (MeV/fission-s)

$H_{\ell k}$ = decay power of decay heat group k from fissile isotope ℓ (W)

Λ = prompt neutron generation time (s)

λ_i = decay constant of delayed neutron group i (1/s)

$\lambda''_{\ell k}$ = decay constant for decay heat group k from fissile isotope ℓ (1/s)

m = number of decay heat groups

n = number of delayed neutron groups

n_f = number of fissile isotopes

P_ℓ = instantaneous fission power of isotope ℓ (W)

P = instantaneous total fission power (W) = $\sum_{k=1}^{n_f} P_k$

Q = total energy release per fission (MeV/fission)

ρ = total feedback reactivity ($).

Equations (9.4-9) and (9.4-10) constitute the point kinetics equations. Equation (9.4-9) describes the time rate of change of total instantaneous fission power. The first and second terms on the right-hand side of Equation (9.4-9) comprise the neutrons directly generated by the fissile fuel and neutrons generated by fissile product precursors, respectively.

Equation (9.4-10) describes the rate of change of the delayed neutron concentrations. The first term on the right-hand side of Equation (9.4-10) describes the rate of decay, while the second describes the rate of production from fissioning isotopes. Table 9.4-1 lists the values for β_i and λ_i presently employed in the code. The β_i's are default values and can be changed by the code user. The value of Λ has a default value of 4.754 E-5 s if not specified by the user. Together, Equations (9.4-9) and (9.4-10) constitute 1+n equations in 1+n unknowns, where P(t) and $C_i(t)$ for i=1, 2, ..., n are to be solved for.

Table 9.4-1. Default values for key reactor kinetics constants.

Group i	β_i	λ_i
1	2.74 x 10-4	0.0127
2	1.38 x 10-3	0.0327
3	1.22 x 10-3	0.115
4	2.64 x 10-3	0.311
5	8.32 x 10-4	1.40
6	1.69 x 10-4	3.87

The reader is cautioned that the β_i's and Λ values are nominal values that may not characterize the fuel properties to be simulated. Since these parameters can differ depending on fuel burnup and enrichment, the use of separate neutronics calculations may have be to employed to calculate globally averaged values of the β_i's and Λ.

The decay heat equation [Equation (9.4-11)] quantifies thermal energy production of fission products that decay by emitting beta and gamma rays.

The beta and gamma radiation is subsequently absorbed as heat. The first term in Equation (9.4-11) is the loss rate due to decay of the various gamma and beta emitters, and the second term is the creation rate for new gamma and beta emitters from fission.

In the current formulation in TRAC-BF1/MOD1, the user specifies fission power fractions for three nuclides--^{235}U, ^{238}U, and ^{239}Pu. The default values for these power fractions are .71, .21, and .08 for ^{235}U, ^{239}Pu, and ^{238}U, respectively. The energy release rates $E_{\ell k}$ and associated decay constraints $\lambda_{\ell k}$ are given in References 9.4-6 and 9.4-7.

In order to better understand the energetics of Equations (9.4-9) through (9.4-11), consider the fissioning of ^{235}U, which is the principal fuel in most BWRs. A fissioning ^{235}U atom releases approximately 200 MeV of energy. Most of this energy (~93%) is promptly converted into thermal energy, while a small percentage (~7%) of the fission energy is stored in the fission products to be released at a later time. Similar energetics apply to ^{238}U and ^{239}Pu.

To calculate the effective instantaneous thermal power delivered to the reactor, Equations (9.4-9) and (9.4-10) must first be solved for P(t). Now, P(t) is the instantaneous fission power due to both prompt and delayed neutrons. Since some of the instantaneous fission power is stored in the fission decay products for later release and some of the previously stored energy is released, the instantaneous effective thermal power is the sum of instantaneous neutron power (less instantaneous neutron power deposited to decay products) and instantaneous power released by previously existing fission decay products. Once Equations (9.4-9) and (9.4-10) have been solved, instantaneous effective thermal power can be quantitatively expressed as

$$P_{eff} = P - \sum_{k=1}^{n_f} P_k \sum_{\ell=1}^{m} \frac{E_{\ell k}}{Q\lambda_{\ell k}^{H}} + \sum_{k=1}^{n_f} \sum_{\ell=1}^{m} H_{\ell k} \qquad (9.4\text{-}12)$$

where P_{eff} is the instantaneous thermal energy deposited into the reactor core.

The code user has the additional option of partitioning the fraction of fission power and decay heat for direct moderator heating. These fractions currently default to 0.0. Determining what this moderator deposition is depends on specific BWR system configuration. Most of this moderator energy deposition is due to gamma heating and may require a detailed core radiation transport simulation to give a good estimate. This modeling capability exists for the point kinetics model as well as the one-dimensional diffusion approximation.

In a BWR, direct moderator heating can be significant, because this causes an almost instantaneous void reactivity feedback during a reactor transient simulation. For example, this phenomenon may apply to severe BWR pressurization transients. If all power generated is assumed to be deposited only into the fuel and then transferred to the moderator/coolant, the void

generation and associated reactivity feedback are delayed. This delay may artificially distort the character of the transient.

The formulation of direct moderator heating in TRAC-BF1/MOD1 for a given cell is density-weighted and is assumed to be directly proportional to the power[9.4-8]

$$P_{DMH} = \frac{\rho_m}{1000}(F_f P_f + f_d P_d) \qquad (9.4\text{-}13)$$

where

P_f = instantaneous fission power (W)

F_f = direct moderator heating power fraction for P_f

P_d = instantaneous decay power (W)

f_d = direct moderator heating power fraction for P_d

ρ_m = cell-average moderator density (kg/m3).

The F_f and f_d coefficients are user-specified fractions. The rate of thermal energy deposition into the fuel then becomes

$$P_{fuel} = (P_f + P_d) - P_{DMH} . \qquad (9.4\text{-}14)$$

The next two subsections will detail the feedback reactivity model presently employed in TRAC-BF1/MOD1 and additional details for approximating the core power decay model.

9.4.2.2 Reactivity Feedback Model. The reactivity parameter ρ in Equation (9.4-9) consists of a user-input control reactivity and a code-calculated feedback (fb) reactivity. We can express the total reactivity as

$$\rho = \rho_{prog} + \rho_{fb} \qquad (9.4\text{-}15)$$

$$\rho_{prog} = \frac{k_{prog} - 1}{k_{prog}} , \qquad (9.4\text{-}16)$$

The control reactivity is computed from a table lookup scheme or is driven by user-modeled control variables. The control reactivity is intended to model reactivity associated with control rod motion or any other external changes that might effect the core neutronics during a transient. The feedback reactivity is assumed to be decoupled from the control reactivity. Furthermore, in formulating the feedback reactivity, it is assumed that each

phenomenon driving feedback is mutually decoupled. The controlling phenomena driving reactivity feedback presently modeled with TRAC-BF1/MOD1 are:

- moderator void (VD)
- moderator temperature (TM)
- fuel temperature (TF)
- boron injection (B).

For any of the above four controlling phenomena, the general form of the reactivity coefficient is given as

$$C_q = \frac{1}{k}\frac{\partial k}{\partial q} \tag{9.4-17}$$

for the core property parameter q. The feedback reactivity for a small change in q is expressed as

$$\frac{\Delta k}{k} = C_q \, \Delta q \ . \tag{9.4-18}$$

Since it is assumed that the reactivities for each q variation can be calculated independently, the total feedback reactivity becomes

$$\rho_{fb} = \sum_{q=1}^{4} C_q \, \Delta q \ . \tag{9.4-19}$$

In a typical BWR reactor core, the thermal-hydraulic properties are not spatially uniform. Consequently, in the formulation of Equation (9.4-19), a spatially dependent weighting scheme is employed to calculate the global behavior of ρ_{fb}. For a nonuniform reactor with spatially varying core properties, the total feedback reactivity is

$$\rho_{fb} = \int dv \sum_{q=1}^{4} \rho_q(\bar{r}) W_q(\bar{r}) \Delta q(\bar{r}) \tag{9.4-20}$$

where the control volume integrated over is the reactor core and W_q are spatially varying weighting functions. The present TRAC-BF1/MOD1 modeling options allow the user to either employ a volume or a power-squared weighting scheme.[9.4-7] The power-squared weighting scheme is formulated so that

$$W_{TM}(\bar{r}) = W_{VD}(\bar{r}) = W_B(\bar{r}) = W_{TF}(\bar{r}) \alpha P^2(\bar{r}) \tag{9.4-21}$$

where $P(\bar{r})$ is a normalized power distribution. Equation (9.4-21) has a

theoretical basis and can be found in References 9.4-6 and 9.4-8.

The reactivity feedback model for void, boron, moderator, and fuel temperature currently employs reactivity coefficients that are polynomial approximations using core-averaged properties. The polynomial approximations to the reactivity coefficients are functions of local thermal-hydraulic conditions. However, the polynomial coefficients themselves are spatially invariant and are globally averaged parameters. The invariance assumption is reasonable if core fuel properties are approximately uniform at different power densities.

The Doppler reactivity variation induces a change in k, which is due to variations in fuel temperature and moderator voiding around the fuel. The Doppler reactivity change is formulated as

$$\rho_{TF} = C_{TF}\left(\sqrt{T_f} - \sqrt{T_{fo}}\right) \qquad (9.4\text{-}22)$$

where T_f is the final average fuel temperature and T_{fo} is the reference average fuel temperature. The coefficient C_{TF} is a polynomial function of the local moderator void fraction and is given as

$$a_{TF} + b_{TF}\alpha + C_{TF}\alpha^2 \ . \qquad (9.4\text{-}23)$$

The Doppler coefficient in a BWR is a function of α because the channel void fraction strongly affects the fuel resonance escape probability behavior.

The change in moderator void reactivity feedback driven by a small change in α is calculated as

$$\rho_{VD} = C_{VD}\,\Delta\alpha \ . \qquad (9.4\text{-}24)$$

The void reactivity coefficient C_{VD} is also expressed as a quadratic power series expansion in the fuel channel void fraction.

$$C_{VD} = a_{VD} + b_{VD}\alpha + C_{VD}\alpha^2 \ . \qquad (9.4\text{-}25)$$

Fuel channel void collapse or generation is the dominant feedback mechanism during most postulated BWR operational transients.

During normal operating conditions, the moderator temperature reactivity feedback is small compared to void reactivity feedback. However, moderator feedback effects are important during cold standup and hot standby conditions where moderator void generation conditions are nonexistant or small. For a small variation in moderator temperature, the moderator reactivity feedback is expressed as

$$\rho_{TM} = C_{TM}\,\Delta T_M \tag{9.4-26}$$

where T_M is the fuel channel liquid moderator temperature. The moderator temperature coefficient is expressed as a power series function of moderator temperature

$$C_{TM} = a_{TM} + B_{TM}T_M + C_{TM}T_M^2 . \tag{9.4-27}$$

The boron feedback reactivity is assumed to be

$$\rho_m = C_{BC}\,\Delta B \tag{9.4-28}$$

where B is the boron concentration in ppm. The boron concentration feedback coefficient C_{BC} is modeled as a quadratic function of the moderator density ρ_m, so that

$$C_{BC} = a_B + b_B\rho_m + C_B\rho_m^2 . \tag{9.4-29}$$

A set of default coefficients for the various feedback phenomena is listed in Table 9.4-2. The reactivity quadratic curves were obtained from curve fitting data.[9.4-9] The default values are nominally for a fresh BWR core; however, the default values are only recommended if a code user does not have data that are BWR plant-specific. Reactivity parameters are dependent on fuel geometry, burnup, and other considerations. The actual coefficient values may require the use of multidimensional neutronics simulation.

9.4.2.3 Solution Approximation to the Point Kinetics Equations. The present strategy for integrating the point kinetics equations to advance the fission power and delayed neutron precursors to new time values requires the following input:

1. old-time fission power
2. old-time delayed neutron precursor concentrations
3. new-time feedback reactivity change calculated from new-time thermal-hydraulic input parameters and/or user-supplied control variables or tables.

The solution scheme used in TRAC-BF1/MOD1 employs a fourth-order Runge-Kutta integration method developed by Gill.[9.4-10,11] This technique was found to be very fast with excellent round-off error-limiting characteristics. Unless the thermal-hydraulic time step is small, it is generally necessary to solve the point kinetics equation over a series of time step subintervals.

Table 9.4-2. Default values for key feedback phenomena.

Parameter	Constant	Value
Neutron generation time (s)	TNEUT	4.754×10^{-5}
Fuel reactivity coefficients	C_1^{TF}	-8.44×10^{-4}
	C_2^{TF}	-3.95×10^{-4}
	C_3^{TF}	0.00
Moderator temperature	C_1^{TM}	-1.158×10^{-4}
Reactivity coefficients	C_2^{TM}	4.63×10^{-7}
	C_3^{TM}	-9.69×10^{-10}
Void reactivity coefficients	C_1^{VD}	-4.78×10^{-2}
	C_2^{VD}	-2.748×10^{-1}
	C_3^{VD}	1.911×10^{-1}
Boron reactivity coefficients	C_1^{B}	3.6×10^{-5}
	C_2^{B}	-2.23×10^{-7}
	C_3^{B}	0.0

This is borne out by the physical observation that the characteristic time constants connected with the neutron kinetics time scales can be very small relative to hydrodynamic time scales. This is especially true for severe transients where there is a very large reactivity insertion. The maximum solution time step subinterval for the point kinetics equations scales with the prompt neutron generation time and is given by

$$\delta t_n = \frac{0.8\Lambda}{\beta \, Max \, [\rho - 1, 1]} \qquad (9.4\text{-}30)$$

where ρ is the old-time reactivity. From the above expression, it is also clear that, for large ($\rho \gg 1$) reactivity insertions, δt_n varies inversely with ρ. Thus, the more severe the transient, the smaller δt_n becomes. The approximation for the total global change in core reactivity is detailed in Section 9.4.3.3. With respect to TRAC-BF1/MOD1, the solution algorithm time step size is limited by the hydraulic time step size Δt_H. If $\delta t_n < \Delta t_H$, the kinetics equations are integrated over J equal subintervals where

$$J = \frac{\Delta t_H}{\delta t_n} + 1 \, . \tag{9.4-31}$$

The total reactivity increment that was calculated as a function of the last hydraulic time step is split into $\frac{\Delta \rho_T}{J}$ increments. Thus, when the kinetics equations are integrated, the reactivity change is approximated as a time-dependent ramp change split up into J equal increments of magnitude $\frac{\Delta \rho_T}{J}$. The linear assumption may break down, however, if there is a very large initial reactivity change coincident with the situation $\Delta t_H >> \delta t_n$. Under these circumstances, some nonlinear reactivity insertion rate may be a better approximation to integrate the point kinetics equation.[9.4-8,9] If $\delta t_n > \Delta t_H$, only one integration of the point kinetics equation is done. Under these circumstances, the new-time reactivity change can be thought of as a step change approximation.

It should be noted that the decay heat equation [Equation (9.4-11)] is solved using the same Runge-Kutta algorithm and the same time subinterval δt_n. However, the numerical solution to Equation (9.4-11) is further modified after the $H_{\ell k}$'s have been solved to account for[9.4-6]

1. Heavy element decay heat (from ^{239}U and ^{239}Np) and
2. Inclusion of the effect of fission product neutron capture.

If the above two phenomena were not accounted for, the instantaneous fission decay energy would be

$$P_{DINT} = \sum_{k=1}^{n_f} \sum_{\ell=1}^{m} H_{\ell k} \, . \tag{9.4-32}$$

In fact, the user does not have to model these phenomena; the code decay heat will default to Equation (9.4-32). With the above two phenomena accounted for, the actual instantaneous decay power is written as

$$P'_{DINT} = G \, P_{DINT} + P_{HE} \tag{9.4-33}$$

where P_{HE} accounts for heavy element decay heat and G accounts for fission product neutron capture. The expressions for G and P_{HE} are rather complex expressions and are given in Reference 9.4-6.

9.4.2.4 Approximations of Reactivity Feedback for the Point Reactor Kinetics Equations. The calculation of reactivity feedback (not including

user-supplied reactivity insertion tables or control variables) is initially done on a cell-by-cell basis. The reactor core is partitioned into channel regions (using CHAN components) and bypass regions (using VESSEL component). Contributions for the moderator, Doppler, void, and boron feedback coefficients are globally summed over all CHAN and VESSEL cells. The same reactivity coefficient polynomial curve fits are used for the CHAN and bypass VESSEL cells. The user has the option to specify what fraction of the reactivity contribution is from the VESSEL bypass and CHAN components.

After the new-time thermal-hydraulic calculations are done, the total reactivity change is calculated from the individual changes in reactivity for the moderator, boron, Doppler, and void contributions. The total change in feedback reactivity is written as

$$\rho_{FB}^{n+1} = \rho_{FB}^{n} + \Delta\rho_{FB}^{n+1} \tag{9.4-34}$$

where

$$\Delta\rho_{FB}^{n+1} = \Delta\rho_{TF}^{n+1} + \Delta\rho_{TM}^{n+1} + \Delta\rho_{VD}^{n+1} + \Delta\rho_{B}^{n+1} \tag{9.4-35}$$

and where n and n+1 indicate old and new time values.

The individual reactivity contributions are computed from

$$\Delta\rho_{TF}^{n+1} = \sum_{i} \rho_{TF,i}^{n+1} \left(\sqrt{T_{F,i}^{n+1}} - \sqrt{T_{F,i}^{n}} \right) W_{TF,i} \tag{9.4-36}$$

$$\Delta\rho_{VD}^{n+1} = \sum_{i} \rho_{VD,i}^{n+1} \left(\alpha_{i}^{n+1} - \alpha_{i}^{n} \right) W_{VD,i} \tag{9.4-37}$$

$$\Delta\rho_{TM} = \frac{\sum_{i} W_{TM,i} \rho_{TM,i}^{n+1} \left[\left(1 - \alpha_{i}^{n+1}\right) \rho_{\ell}^{n+1} T_{M,i}^{n+1} - \left(1 - \alpha_{i}^{n}\right) \rho_{\ell}^{n} T_{M,i}^{n} \right]}{\sum_{i} \left(1 - \alpha_{i}^{n+1}\right) \rho_{\ell}^{n+1} W_{TM,i}} \tag{9.4-38}$$

$$\Delta\rho_B^{n+1} = \frac{\sum_i W_{B,i}\rho_{B,i}^{n+1}\left[\left(1-\alpha_i^{n+1}\right)\rho_{\ell,i}^{n+1}B_i^{n+1} - \left(1-\alpha_i^{n}\right)\rho_{\ell}^{n}B_i^{n}\right]}{\sum_i \left(1-\alpha_i^{n+1}\right)\rho_{\ell}^{n+1}W_{B,i}} \quad (9.4\text{-}39)$$

where i is the cell index and the summation is over all cells in the reactor core region. The reactivity coefficients are computed using the new-time conditions in each cell. The moderator temperature and boron feedback contributions are normalized by the amount of liquid in the cells. This is because the property is connected with the liquid phase and cannot exist apart from the presence of liquid.

As previously mentioned as an option, the user is allowed to choose for each feedback reactivity component whether the power-squared weighting is to be applied or not. When the power-squared weighting is not chosen for a given feedback reactivity component, the simple volume average is used.

In addition to the feedback, the explicit reactivity (control rod) insertion is modeled as a user-input reactivity-versus-time table. This reactivity table represents the additional control rod reactivity worth inserted from steady state. At the beginning of the transient, this reactivity value is therefore zero. The control rod reactivity, ρ_{CR}, inserted in each time step is found from this reactivity table. The total reactivity inserted into each time step is the sum of the feedback reactivity and the control rod reactivity. The neutron multiplication factor at the new time is updated as

$$k^{n+1} = k^n + k^n\left(\rho_{FB}^{n+1} + \rho_{CR}^{n+1}\right) \quad (9.4\text{-}40)$$

where k^{n+1} and k^n are the neutron multiplication factors at the new and old times, respectively. At the beginning of a transient, k = 1 is assumed. The new-time reactivity ρ is

$$\rho^{n+1} = \frac{k^{n+1}-1}{k^{n+1}} \quad (9.4\text{-}41)$$

where ρ^{n+1} is then used in the point kinetics equation to solve for the new-time fission power.

9.4.2.5 Implementation of the Space-Independent Reactor Kinetics Model. The user input requirements for the TRAC-BF1/MOD1 core power model are presently inputted into the code using the one-dimensional CHAN and three-dimensional VESSEL components and auxiliary POWER cards to define additional input data. The subroutine FPOW is the principal input processor of the user-supplied kinetics parameters. If the user specifies a spatially independent

model, the subroutine FPOW calls FPPT, which processes only spatially independent kinetics input models. The decay heat and delayed neutron constants are stored in block data with the name BLOCKDATA. The subroutine POWER controls the overall solution logic for the space-independent core power solution. This subroutine employs user inputted options to branch to other subroutines depending on what options have been invoked. Relative to space-independent models, the following options can be invoked:

1. Constant power
2. Table lookup power
3. Trip-initiated power
4. Point kinetics with table lookup reactivity
5. Point kinetics with trip-initiated table lookup
6. Point kinetics with reactivity feedback
7. Point kinetics with trip-initiated table lookup, reactivity feedback, and scram insertion.

It should be pointed out that the one-dimensional kinetics model can also be invoked by the subroutine POWER. Discussion of this model is deferred until Section 9.4.3.

If the user employs option 1, the code will either use a constant core Power specified by the user or employ a user-specified control system to drive the core power. In the event that the user employs lookup tables (options 2 or 3), the code employs a linear interpolation scheme to find power or reactivity at a particular time step. The subroutine LININT is employed to do this interpolation. The use of option 1, 2, or 3 precludes the use of the reactor physics models supplied in the code.

If the kinetics space-independent solution scheme is employed (options 4 through 7), POWER calls the subroutine POWPT, which solves the point kinetics Equations (9.4-9) and (9.4-10). Once the prompt fission power has been calculated, POWER calls POWDK, which uses the numerical results from POWPT to calculate the decay power fraction of the total power.

Relative to the reactivity feedback, the subroutine VSL calculates the VESSEL bypass moderator, boron, and void reactivity feedback contributions. The CHAN component Doppler feedback reactivity is calculated with subroutine COR3. The CHAN component moderator, void, and boron feedback reactivities are calculated with subroutine CHN3. It should be pointed out that subroutine CHN3 is run before COR3. COR3 uses new-time channel thermal-hydraulic conditions to calculate the new-time fuel temperature profile prior to calculating the Doppler reactivity feedback. If the user-specified time-versus-reactivity table is employed, ρ_{CR} is interpolated in the subroutine POWPT. If the control rod reactivity is modeled as a control variable, the

subroutines for the TRAC-BF1 control system are employed. The approximation model for direct moderator heating is done in subroutine TFIE.

9.4.3 One-Dimensional Kinetics Model

This section documents the one-dimensional diffusion model presently employed in the TRAC-BF1/MOD1 code. This model is a two-group kinetics scheme based on the Analytic Nodal Method (ANM).[9.4-12,13] The ANM can also be extended to two- or three-dimensional problems by making the appropriate programming modifications to TRAC-BF1/MOD1. The one-dimensional model assumes axial variation of the core neutronic properties but is assumed uniform in the radial direction. This assumption precludes detailed modeling transients with inherently three-dimensional characteristics. The one-dimensional diffusion approximation is applicable to a number of transient scenarios, including many types of anticipated transients without scram (ATWS). Control bank insertion or withdrawal events may also be applicable under certain circumstances where the radial flux profile can be approximated as being flat. ATWS applications using the TRAC ANM approximation can be found in Reference 9.4-13.

The one-dimensional TRAC-BF1/MOD1 model assumes that a parallel multi-channel core can be divided into a number of axial nodes. Each hydraulic node in the reactor core may be subdivided into multiple neutronic nodes, and each neutronic node may have separate fuel characteristics. The one-dimensional diffusion model can be thought of as working in three stages.

1. Radially averaged properties (state variables) for each axial hydraulic level are calculated (void fraction, moderator temperature, fuel rod temperature, boron concentration, and control rod fraction).

2. One-dimensional diffusion transport parameters for each axial node are calculated with the radially averaged properties from stage 1.

3. The transport coefficients from stage 2 are inserted into the two-group ANM diffusion approximation, and the core power distribution is calculated.

It should be noted that stages 1-3 apply to both steady-state and transient situations. In the transient mode, the core thermal-hydraulic properties are recalculated at each hydraulic time step so that the core properties, transport coefficients, and diffusion equation solution similarly have to be updated. We shall now detail each of the above three stages.

9.4.3.1 Radial Averaged-Thermal-Hydraulic Properties. In TRAC-BF1/MOD1, the core region can be represented by multiple CHAN components, each having different characteristics in the radial direction. Each CHAN component approximates a particular fuel bundle radial region. Because of radial variations in moderator temperatures, void fractions, etc., a radial averaging algorithm is employed to generate averaged core properties at a particular

axial level. These averaged properties are required to calculate transport coefficients used in the TRAC-BF1/MOD1 one-dimensional diffusion model. The radial cell averaging is done over both the CHAN and associated VESSEL bypass components.

The approximations used for the representative radially averaged thermal-hydraulic properties are given as follows:

$$\bar{a}_i = \sum_{n=1}^{N_c} \alpha_{i,n} R^c_{i,n} + \sum_{j \in i}^{N_v} \alpha_j r^v_{j,i} \tag{9.4-42}$$

$$\bar{T}_{mi} = \frac{\sum_{n=1}^{N_c} (1 - \alpha_{i,n}) T_{mi,n} R^c_{i,n} + \sum_{j \in i}^{N_v} (1 - \alpha_j) T_{mj} R^v_{j,i}}{1 - \bar{\alpha}_i} \tag{9.4-43}$$

$$\bar{T}_{fi} = \sum_{n=1}^{N_c} \bar{T}_{fi,n} R^c_{i,n} \tag{9.4-44}$$

$$\bar{T}_{fi,n} = \sum_{k=1}^{K_n} \sum_{\ell=1}^{L_{k,n}} T_{fi,n,k,\ell} R^f_{k,\ell} \tag{9.4-45}$$

$$\bar{B}_i = \frac{\sum_{n=1}^{N_c} (1 - \alpha_{i,n}) \rho_{\ell i,n} b_{i,n} R^c_{i,n} + \sum_{j \in i}^{N_v} (1 - \alpha_j) \rho_{\ell j} b_j R^v_{j,i}}{\sum_{n=1}^{N_c} (1 - \alpha_{i,n}) \rho_{\ell i,n} R^c_{i,n} + \sum_{j \in i}^{N_v} (1 - \alpha_j) \rho_{\ell j} R^v_{j,i}} \tag{9.4-46}$$

where

α = void fraction

R^c = CHAN weight factor

N_c = number of CHAN components

N_v = number of VESSEL cells corresponding to level i

T_m = moderator temperature (K)

T_f = fuel temperature (K)

$\mathcal{B}$ = boron density (kg/m3)

b = boron concentration (ppm)

K_n = number of rod groups in CHAN component n

$L_{k,n}$ = number of radial fuel nodes in fuel rod group k in CHAN component n

R^f = fuel temperature weight factor

R^v = VESSEL weight factor

ρ_ℓ = liquid density (kg/m^3)

i = core hydraulic level index

j = VESSEL cells on core level index

n = CHAN component index

κ = rod group index

l = fuel radial node index.

Each hydraulic parameter consists of a weighted average of CHAN and VESSEL component hydraulic variables. The VESSEL component portion of the hydraulic parameter represents the contribution of the bypass region surrounding each fuel bundle. Normally, the bypass region of the core is represented by fewer axial cells than the region within the CHAN component portion of the core; hence, the weight factors for the VESSEL portion of the weighted sums must take this into account. We shall now give further details to explain how the CHAN, VESSEL, and fuel weighting factors are defined.

The CHAN weight factor may be determined using one of three options--volume weighting, power-squared weighting, or user-input weighting. The general form of the weight factor is

$$R^c = A\,Vol \tag{9.4-47}$$

where

R^c = CHAN weight factor

A = option-dependent parameter

Vol = total CHAN cell volume which equals number of bundles represented by this CHAN component times the volume of one bundle axial section.

For volume weighting, A = 1; for power-squared weighting, A = P_c^2; and for

1

IMAGE EVALUATION
TEST TARGET (MT-3)

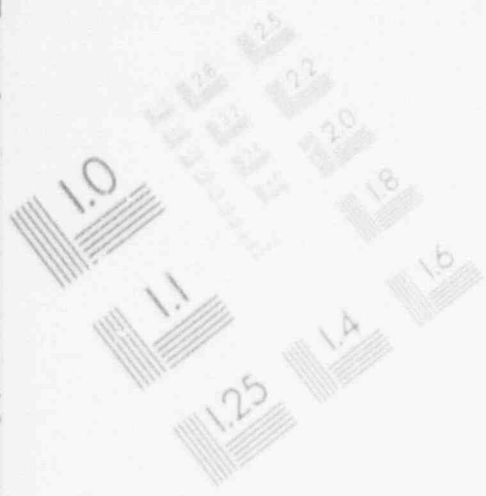

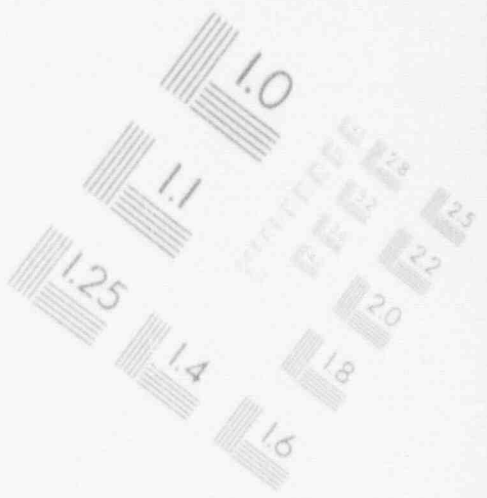

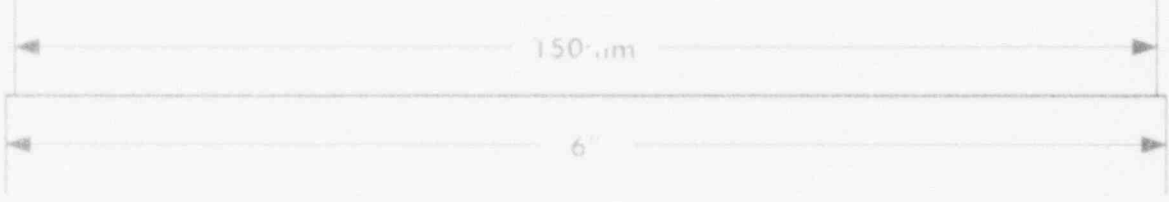

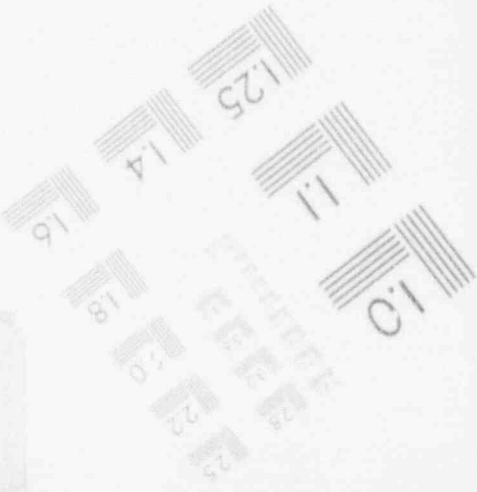

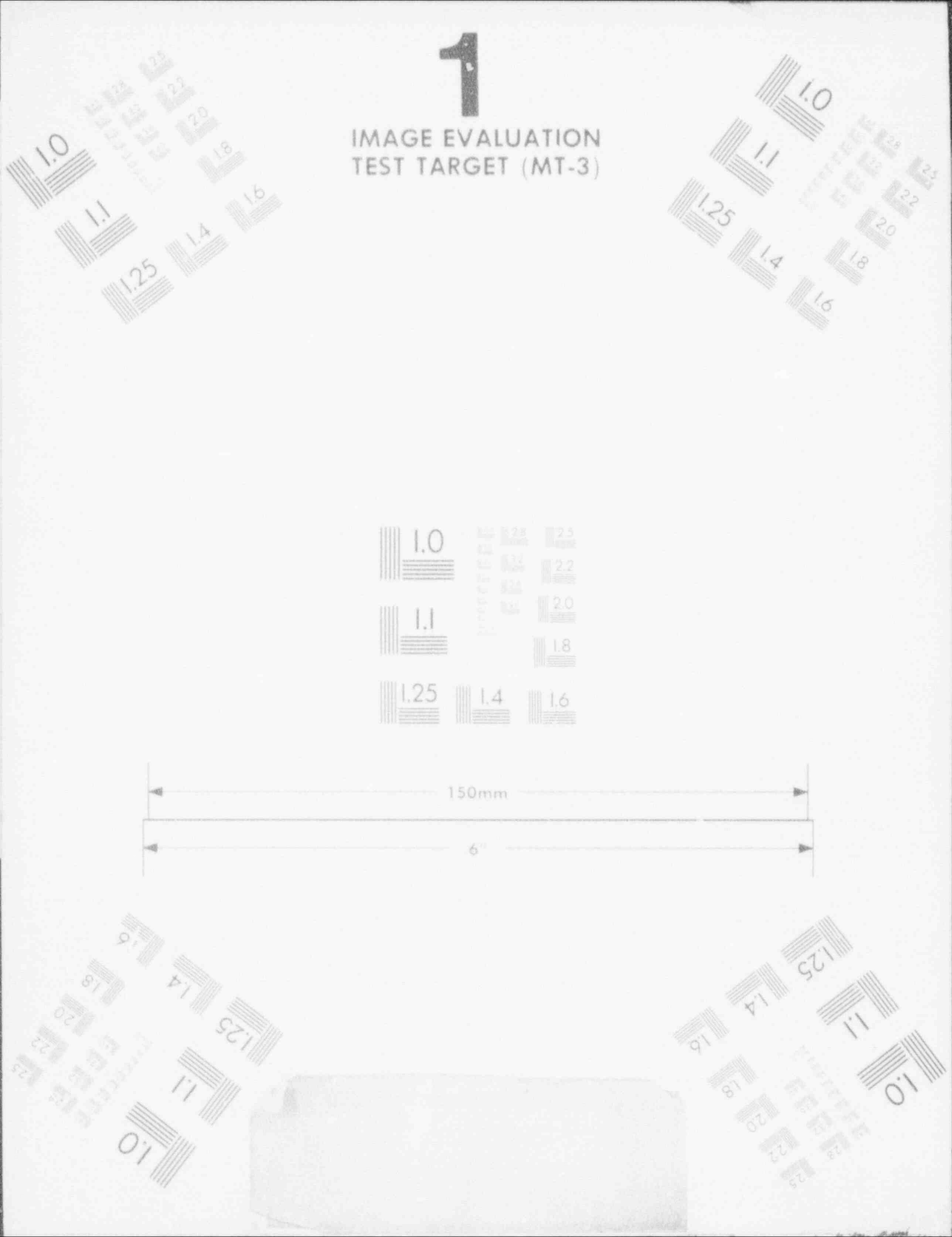
1
IMAGE EVALUATION
TEST TARGET (MT-3)
1.0
1.1
1.25
1.4
1.6
1.8
2.0
2.2
2.5
150mm
6"

1

IMAGE EVALUATION
TEST TARGET (MT-3)

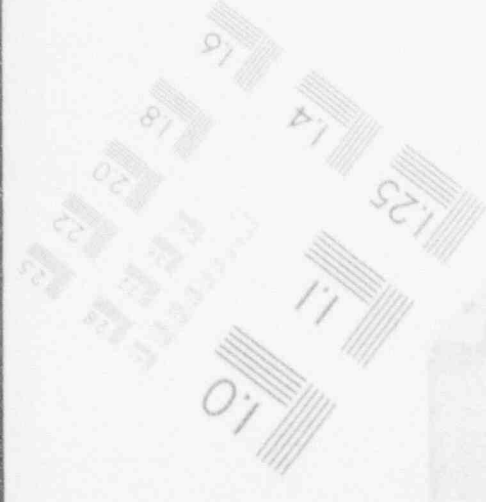

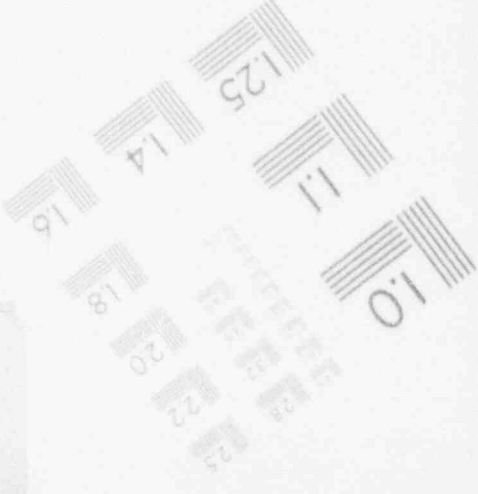

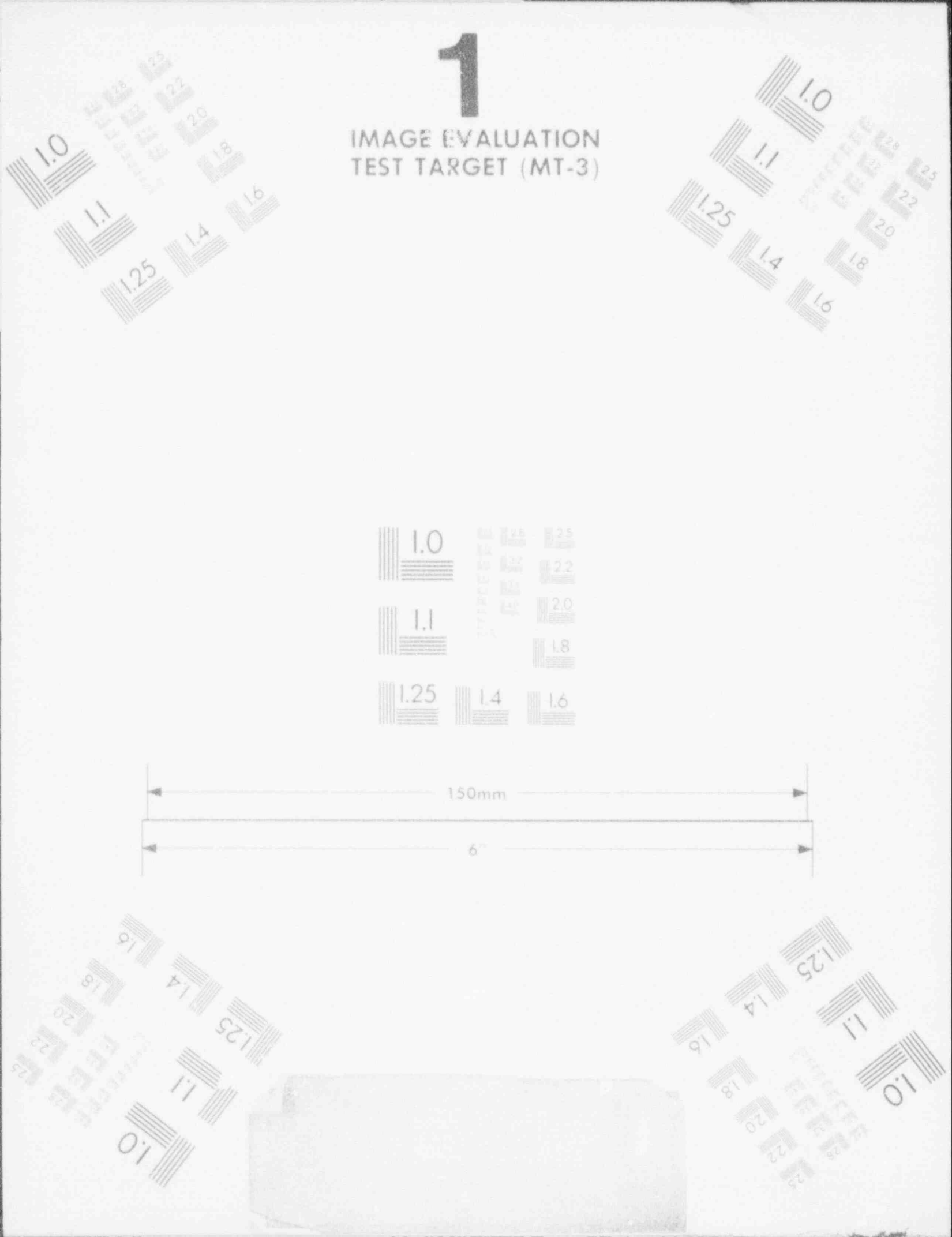
1
IMAGE EVALUATION
TEST TARGET (MT-3)
1.0
1.1
1.25
1.4
1.6
2.0
1.8
2.2
2.5
150mm
6"

1

IMAGE EVALUATION
TEST TARGET (MT-3)

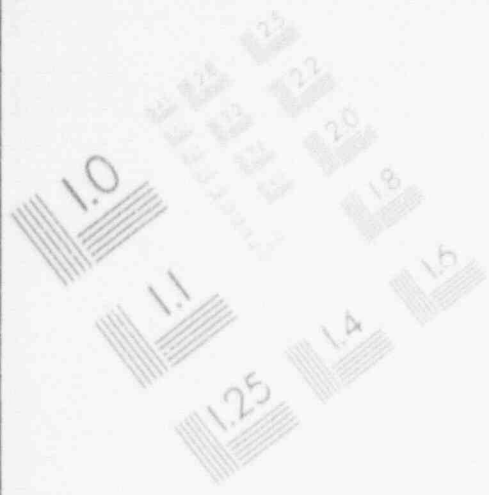

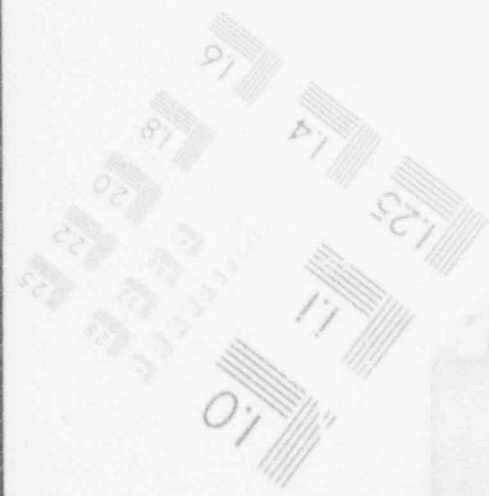

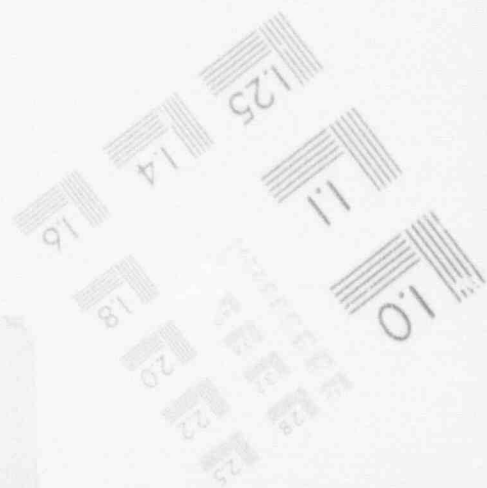

user-input weighting, A = U, where P_c is the power density in a particular CHAN cell.

Estimating the weight factors for the vessel region is complicated by the fact that the VESSEL cells and the CHAN cells do not generally span the same elevations. The weight factors for the VESSEL cells that represent the bypass region are computed from the weight factors in the CHAN cells. The weight factor for VESSEL cell j, which spans core hydraulic level i, is given by the weighted average of the weight factors for the CHAN cells inside VESSEL cell j on core hydraulic level i

$$R^v_{j,i} = W_f V^v_{j,i} \left(\frac{\sum_{k=1}^{k_j} R^c_k}{\sum_{k=1}^{k_j} V^c_k} \right) \qquad (9.4\text{-}48)$$

where

W_f = user-input VESSEL relative weight factor

$V^v_{j,i}$ = volume of VESSEL cell j on core hydraulic level i

R^c_k = CHAN weight factor

V^c_k = volume of CHAN cell

k_j = number of CHAN components in VESSEL cell j.

The formulation of the fuel weight factors are similar to the CHAN weight factors. The general form is given as

$$R^f = f(A, \text{Vol}) \qquad (9.4\text{-}49)$$

where

R^f = fuel temperature node weight factor

A = option-dependent parameter

Vol = total cylindrical shell fuel volume between two radial temperatures nodes for a particular rod group.

For volume weighting, A = 1; for power-squared weighting, $A = P_f^2$; and for user-input weighting, A = U, where P_f is the power density in a fuel rod temperature node.

9.4.3.2 Control Rod Model. The control rod model is incorporated into the one-dimensional kinetics model via a space-time dependent control rod fraction parameter C_f. This parameter drives the transport coefficients in the one-dimensional kinetics field equations.[9.4-15,16] (see Section 9.4.3.3 for more details).

The control rod model in TRAC-BF1/MOD1 consists of a user-specified number of control rod groups, each group containing a user-input number of individual control rods. A control rod group contains control rods having the same initial axial insertion and actuated by the same scram or trip signal. The user specifies the trip number for each control rod group and the insertion velocity of the rods in the group once the trip signal has occurred.

The control fraction on each core neutronic level is determined from the locations of all of the control rods and varies from zero to one for each core level. A value of zero means that there are no control rods at this level, and a value of one means that all control rods have been inserted completely through this core level. The control fraction is the average control rod position in the level and is given by

$$Cf_i = \frac{\sum_{k=1}^{N_g} N_k f_{k,i}}{N_{cr}} \qquad (9.4\text{-}50)$$

where

Cf_i = control fraction on core level i

N_g = number of control rod groups

N_k = number of control rods in control rod group k

N_{cr} = total number of control rods

$f_{k,i}$ = relative location of control rod group k on core level i.

The relative locations of the control rods on a core level are determined from the absolute axial location of each control rod and the top and bottom of each axial level in the core region. Figure 9.4.1 shows an example of control rod locations and the resulting control fraction for each core level. The absolute axial location is computed from the initial control rod positions and the distance the rod has moved since the scram or trip signal was received.

9.4.3.3 Generation of One-Dimensional Neutron Kinetics Transport Coefficients. Once the radially averaged parameters from Sections 9.4.3.1 and 9.4.3.2 have been calculated, the one-dimensional kinetics transport

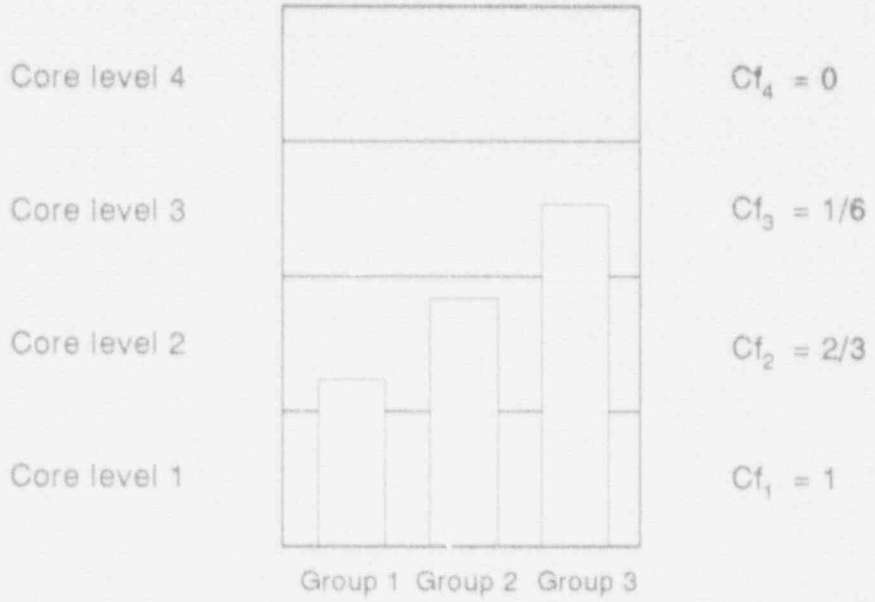

$$Cf_1 = \frac{1}{3}(f_{1,1} + f_{2,1} + f_{3,1}) = \frac{1}{3}(1+1+1) = 1$$

$$Cf_2 = \frac{1}{3}(f_{1,2} + f_{2,2} + f_{3,2}) = \frac{1}{3}(0.2+0.8+1.0) = \frac{2}{3}$$

$$Cf_3 = \frac{1}{3}(f_{1,3} + f_{2,3} + f_{3,3}) = \frac{1}{3}(0+0+0.5) = \frac{1}{6}$$

$$Cf_4 = \frac{1}{3}(f_{1,4} + f_{2,4} + f_{3,4}) = \frac{1}{3}(0+0+0) = 0$$

Figure 9.4-1. Control rod locations and corresponding control fractions.

coefficients can be determined using polynomial correlations. These correlations are determined with a separate detailed neutron transport calculation.[9.4-14,16] The form of this correlation for the jth transport parameter is

$$X_j = Cf_j(a_1 + a_2\alpha + a_3\alpha^2) + (1 - Cf_j)(a_4 + a_5\alpha + a_6\alpha^2)$$

$$+ a_7\left(\sqrt{T_{fj}} - \sqrt{T_{foj}}\right) + a_8(T_{mj} - T_{moj}) + a_9B_j \qquad (9.4\text{-}51)$$

where

X_j = specific transport coefficient

Cf_j = control fraction

α_j = radially averaged void fraction

T_{fj} = radially averaged fuel temperature (K)

T_{mj} = radially averaged moderator temperature (K)

B_j = radially averaged boron concentration (ppm)

a_i = user-defined coefficients (for i = 1, 2, ...9)

T_{foj} = user-defined fuel reference temperature (K)

T_{moj} = user-defined moderator reference temperature (K).

The nine user-defined coefficients and two reference temperatures equal 11 unknown coefficients per correlation. The transport parameters that are calculated with the above correlation include nine different variables:

1. The fast neutron group diffusion coefficients.
2. The thermal neutron group diffusion coefficient.
3. The fast group macroscopic absorption cross section.
4. The thermal group macroscopic absorption cross section.
5. Fast group macroscopic downscatter cross section.
6. Fast group transverse buckling squared.
7. Thermal group transverse buckling squared.
8. Fast group macroscopic fission cross section.
9. Thermal group macroscopic fission cross section.

Each transport parameter is described by the same functional relationship with different coefficients. Moreover, each 11 sets of coefficients will differ for different fuel types.

The polynomial coefficients in Equation (9.4-50) are generated using a three dimensional multi-group neutronics simulation code. Since there are nine transport parameters, each of which has 11 separate polynomial coefficients, a total of 99 independent coefficients must be generated per fuel type. Each axial level of the core may have different fuel types. For

instance, if the core were composed of a single fuel type and there were 10 neutronic levels, we would need 11·9 different coefficients in order to calculate all of the nine transport variables. If, on the other hand, all 10 levels were of different fuel types (different burnups for example), we would then need 10·11·9 different coefficients in order to calculate all transport parameters.

The neutron transport parameter coefficients are calculated using a least-squares fitting scheme to the information calculated from a three-dimensional neutronics calculation. In order to perform the least-squares fits, one must calculate transport parameters as functions of the following state variables:

- control rod fraction
- moderator temperature
- boron concentration
- fuel temperature
- void fraction

at a particular computational cell or cells. After the nine transport and five state variables have been calculated at each axial level, they are radially averaged using a weighting function scheme to produce one averaged value per level for each state and transport variable. At least 11 sets of data per fuel type must be generated to uniquely determine parameter fits for the transport variables. Also, the variations in the state variables should cover the range of parameter space expected to occur in the hypothetical transient being simulated. This will ensure that the transport variables are being interpolated between known regions of state space rather than extrapolating outside known state space boundaries.

The details of how TRAC-BF1/MOD1 interfaces with particular three-dimensional neutron transport codes are found in References 9.4-15 and 9.4-16. The reader is cautioned that using calculated data from a separate neutronics transport code for input into TRAC-BF1/MOD1 requires an understanding of the inherent differences in how TRAC-BF1/MOD1 and a three-dimensional neutronics code calculates core power. In particular, many advanced neutronics codes have a thermal-hydraulics package (RAMONA-3B for example) that solves field equations that are different than those in TRAC-BF1/MOD1.[9.4-17] For this reason, transport versus state variable correlations derived from a specific neutron transport code may require additional adjustments before being used as input to the TRAC-BF1/MOD1 one-dimensional kinetics model.

9.4.3.4 The One-Dimensional Two Group Neutron Diffusion Model. In the last two sections, we detailed how volume-averaged state and transport variables are calculated. These variables are substituted into the one-dimensional diffusion field equations to calculate the core power profile.

The one-dimensional kinetics model in TRAC-BF1/MOD1 is a two-group formulation based on the Analytic Nodal Method.[9.4-12,13] The advantage of the one-dimensional kinetics option over traditional point kinetics is that the axial flux profile is allowed to change as a function of time in response to changing thermal-hydraulic conditions and/or control system actions. However, considerably more user input is required in order to implement the one-dimensional kinetics model, as compared to the point kinetics model.

The two-group, one-dimensional, space- and time-dependent neutron diffusion equations can be written in matrix form as

$$\begin{bmatrix} \frac{1}{v_1} & 0 \\ 0 & \frac{1}{v_2} \end{bmatrix} \frac{\partial}{\partial t} \begin{bmatrix} \phi_1 \\ \phi_2 \end{bmatrix} = \frac{\partial}{\partial z} \begin{bmatrix} D_1 & 0 \\ 0 & D_2 \end{bmatrix} \frac{\partial}{\partial z} \begin{bmatrix} \phi_1 \\ \phi_2 \end{bmatrix} - \begin{bmatrix} \Sigma_{a1}+\Sigma_{r1}+D_1B_1^2 & 0 \\ -\Sigma_{r1} & \Sigma_{a2}+D_2B_2^2 \end{bmatrix} \begin{bmatrix} \phi_1 \\ \phi_2 \end{bmatrix}$$

$$+ \frac{1-\beta}{\lambda} \begin{bmatrix} \chi_1 \\ \chi_2 \end{bmatrix} \begin{bmatrix} \nu\Sigma_{f1} \\ \nu\Sigma_{f2} \end{bmatrix}^T \begin{bmatrix} \phi_1 \\ \phi_2 \end{bmatrix} + \sum_i^k \begin{bmatrix} \chi_1 \\ \chi_2 \end{bmatrix} \lambda_k C_k \qquad (9.4\text{-}52)$$

where the space- and time-dependence of all parameters except λ, λ_k, and β is implied and

D_1 = the group 1 diffusion coefficient

D_2 = the group 2 diffusion coefficient

Σ_{a1} = the group 1 macroscopic absorption cross section

Σ_{a2} = the group 2 macroscopic absorption cross section

Σ_{r1} = the group 1 macroscopic downscatter cross section

B_1^2 = the group 1 transverse buckling squared

B_2^2 = the group 2 transverse buckling squared

χ_1 = the fraction of fission neutrons released into group 1. (χ_1 is assumed to be a constant equal to 1.0; no distinction is made in this derivation between the prompt and delayed neutron emission spectra.)

χ_2 = the fraction of fission neutrons released into group 2. (χ_2 is assumed to be a constant equal to 0.0)

$\nu\Sigma_{f1}$ = the group 1 macroscopic production cross section

$\nu\Sigma_{f2}$ = the group 2 macroscopic production cross section

ϕ_1 = the group 1 scalar neutron flux

ϕ_2 = the group 2 scalar neutron flux

λ = a constant parameter used to force criticality for a particular set of input diffusion theory parameters

v_1 = the group 1 average neutron velocity

v_2 = the group 2 average neutron velocity

λ_k = the decay constant for delayed neutron precursor k

C_k = the concentration of delayed neutron precursor k

K = the number of delayed neutron precursor groups

β = the total effective delayed neutron fraction.

Equation (9.4-52) may be written in a more compact form

$$[v]^{-1}\frac{\partial}{\partial t}[\phi] = \frac{\partial}{\partial z}[D]\frac{\partial}{\partial z}[\phi] - [\Sigma_t][\phi] + [\chi](1-\beta)\left[\frac{\nu\Sigma_f}{\lambda}\right]^T[\phi]$$

$$+ \sum_i^K [\chi]\lambda_k C_k \qquad (9.4\text{-}53)$$

where all bracketed quantities denote matrices or vectors.

The region of interest (usually the entire reactor and possibly the axial reflectors) is now partitioned into an arbitrary number of subregions, or nodes. Each node, i, extends from interface i to interface i+1 and is of width h_i, where $h_i = z_{i+1} - z_i$. If it is assumed that suitably averaged, space-independent (within each node) neutron diffusion theory parameters are available for every node, then Equation (9.4-53) may be integrated over a typical node, i, to yield

$$h_i[v_i]^{-1}\frac{\partial}{\partial t}[\bar{\phi}_i] = -[J_{i+1}] + [J_i] - h_i[\Sigma_{ti}][\bar{\phi}_i]$$

$$+ h_i[\chi](1-\beta)\left[\frac{\nu\Sigma_{fi}}{\lambda}\right][\bar{\phi}_i] + \sum_1^K [\chi]\lambda_k \bar{C}_i \tag{9.4-54}$$

where

$$\bar{C}_{ki} = \int_{z_i}^{z_{i+1}} C_k \, dz \tag{9.4-55}$$

$$[\bar{\phi}_i] = \frac{1}{h_i}\int_{z_i}^{z_{i+1}} [\phi(z)] \, dz \text{ (node-average flux vector)} \tag{9.4-56}$$

$$[J_i] = [-D_i]\frac{d}{dz}[\phi(z_i)] \text{ (net current vector at } z_i) \tag{9.4-57}$$

The equation governing delayed neutron precursor k is given by

$$\frac{\partial C_k}{\partial t} = -\lambda_k C_k + \beta_k\left[\frac{\nu\Sigma_f}{\lambda}\right]^T[\phi] \tag{9.4-58}$$

where β_k is the partial effective delayed precursor fraction for precursor k and

$$\sum_1^K \beta_k = \beta \, . \tag{9.4-59}$$

Integration of Equation (9.4-58) over node i yields

$$\frac{d}{dt}\bar{C}_{ki} = -\lambda_k \bar{C}_{ki} + h_i\beta_k\left[\frac{\nu\Sigma_{fi}}{\lambda}\right]^T[\bar{\phi}_i] \, . \tag{9.4-60}$$

Additional relationships between the node-averaged fluxes and the interface currents are now required in order to allow the solution of the system of Equations (9.4-54) and (9.4-60) to be obtained for the node-average fluxes and the nodal precursor inventories, C_{ki}, as functions of time. The desired relationships may be obtained using the Analytic Nodal Method.[2.4-6,7] This method produces a flux-current relationship for node i of the form

$$[J_{i+1}] - [J_i] = [CL_i][\bar{\phi}_{i-1}] + [CC_i][\bar{\phi}_i] + [CR_i][\bar{\phi}_{i+1}] \tag{9.4-61}$$

where the coupling matrices $[CL_i]$, $[CC_i]$, and $[CR_i]$ are complicated functions of the nodal cross sections and dimensions.

Substituting Equation (9.4-61) into Equation (9.4-54) and rearranging yields

$$-h_i[v_i]^{-1}\frac{d}{dt}[\bar{\Phi}_i] = [CL_i][\bar{\Phi}_{i-1}] + [CC_i][\bar{\Phi}_i] + [CR_i][\bar{\Phi}_{i+1}] + h_i[\Sigma_{fi}][\bar{\Phi}_i]$$

$$- h_i[\chi](1-\beta)\left[\frac{\nu\Sigma_{fi}}{\lambda}\right]^T[\bar{\Phi}_i] - \sum_i^K [\chi]\lambda_k\bar{C}_{ki} \quad . \tag{9.4-62}$$

Equations (9.4-60) and (9.4-62) are the basic time-dependent nodal equations of interest. Note that Equation (9.4-62) is nonlinear because quantities proportional to the time derivatives of the fluxes and precursor concentrations appear in the coupling matrices. This is a consequence of the Analytic Nodal formulation.

The time-dependent nodal equations are usually initialized by assuming that the transient to be calculated starts from an equilibrium condition. Initial fluxes can thus be obtained by running a steady-state nodal calculation and using the resulting fluxes and eigenvalue to initialize Equation (9.4-62). In the TRAC-BF1/MOD1 program, the steady-state flux calculation would normally be run iteratively with the thermal-hydraulic initialization procedure, since the diffusion theory parameters are functions of the thermal-hydraulic state variables associated with each node and these state variables are, in turn, functions of the nodal fluxes and powers.

At every point in time, t_n, of interest, nodal powers are computed by the following formula:

$$PWR_i^n = (epf)\ h_i\left[\Sigma_{fi}^n\right]^T\left[\bar{\Phi}_i^n\right] \tag{9.4-63}$$

where

PWR_i = the total power in node i at time tn

epf = an input power normalization factor, usually equal to the user-specified prompt energy per fission times the reactor transverse area

h_i = the height of node i

$\left[\Sigma_{fi}^n\right]$ = the macroscopic fission cross section for node i at time t_n

$\left[\bar{\phi}_i^n\right]$ = the node average flux vector for node i at time t_n.

The total reactor power is then the sum of all the individual nodal powers.

For most transient situations, the neutron diffusion kinetics equations must be integrated over time intervals smaller than the TRAC-BF1/MOD1 thermal-hydraulic time step size Δt_n. One exception is the prompt jump approximation, which is available to the code user. This approximation assumes that reactivity is very small, so the kinetics equations can be integrated between thermal-hydraulic time steps.

The automatic time step control algorithm solves the neutron kinetics equations over a series of time subintervals between two thermal-hydraulic computational time steps. The derivation used to calculate the maximum size for the subinterval time step can be found in Reference 9.4-13. The time step partitioning between two thermal-hydraulic time steps is required for numerical stability. The physical basis is that the characteristic time constants associated with the nodal neutron kinetics equations can be much smaller than any thermal-hydraulic time scale. For severe transients, this time scale ordering regime exists.

If either of the automatic time step control algorithms is requested in the TRAC-BF1/MOD1 nodal routines, the fully implicit approximation ($\theta = 1$) is specified; and the subintervals δt_{jn} of the input time interval DT_j are currently set such that, at all times,

$$\frac{0.01}{|\omega_{pm}|} \geq \delta t_{jn} \geq \frac{0.005}{|\omega_{pm}|} \tag{9.4-64}$$

where

$$|\omega_{pm}| = \max_{i,g} |\omega_{pi}^g| \tag{9.4-65}$$

$$\omega_{pi}^{n+1} = \ln\left(\frac{\bar{\phi}_i^{gn+1}}{\bar{\phi}_i^{gn}}\right). \tag{9.4-66}$$

This constrains the flux that is changing the fastest during a transient to change by no more than approximately 1% but by at least .5% during each time subinterval. These limits can be changed easily as a programmer option. The relevant statements are flagged in the coding. The ω_p data used in Equations (9.4-61) and (9.4-62) are always the most recently available as the calculations progress across the time input interval DT_j. Thus, the subinterval estimate, δt_{jn}, is constantly updated across DT_j. For example, a typical calculation may require a few small subintervals near the beginning of a time step DT_j; but after a short time, it is usually possible to divide the

remaining portion of DT_j into much larger intervals, since the components of the nodal $[\omega_p]$ matrices ordinarily decrease in absolute magnitude as a calculation for an input interval DT_j progresses. This is a consequence of the assumption that the input nodal diffusion theory parameters are constant during each DT_j.

The two time step control algorithms differ only in the matter in which an estimate is made of the magnitudes of the components of the $[\omega_p]$ matrices at the beginning of each input time step DT_j. This estimate is used to set the first subinterval time step. Since no subinterval time steps have yet been taken, it is not possible to use Equation (9.4-66). It is also usually not sufficient to simply use the $[\omega_{pi}]$ matrices computed at the end of the previous TRAC-BF1/MOD1 time step DT_{j-1}. The nodal diffusion theory parameters will usually be different from one time step to the next, due to changing thermal-hydraulic conditions, control actions, and other time-dependent changes that can occur during a reactor transient.

The first time step control algorithm sets the starting subinterval on the basis of nodal k-infinity data, which are computed from the input nodal diffusion theory parameters for each time step. At the beginning of each time step, the following parameter is computed for each node:

$$\Omega_i^j = \frac{k_{\infty i}^j - k_{\infty i}^{j-1}}{k_{\infty i}^{j-1} l_{\infty i}^j} \tag{9.4-67}$$

where $k_{\infty i}^j$ is the k-infinity value for node i during time step DT_j, and $k_{\infty i}^{j-1}$ is the k-infinity value for the previous time step, DT_{j-1}. The parameter $l_{\infty i}^j$ is an approximate estimate of the infinite medium prompt neutron generation time for node i. The k_∞ and l_∞ data are computed for each node using the following expression:

$$k_{\infty i}^j = \frac{\nu\Sigma_{f1i}^j \left(\Sigma_{a2i}^j + D_{2i}^j B_{2i}^{2j}\right) + \nu\Sigma_{f2i}^j \Sigma_{r1i}^j}{\lambda \left(\Sigma_{a1i}^j + D_{1i}^j B_{1i}^2 + \Sigma_{r1i}^j\right)\left(\Sigma_{a2i}^j + D_{2i}^j B_{2i}^{2j}\right)} \tag{9.4-68}$$

for the case where $[\chi] = \begin{bmatrix} 1 \\ 0 \end{bmatrix}$ and

$$l_{\infty i}^j = \frac{k_{\infty i}^j - k_{\alpha i}^j}{k_{\infty i}^j k_{\alpha i}^j} \tag{9.4-69}$$

where $k_{\alpha i}^j$ is computed from Equation (9.4-64) with the absorption cross

sections increased by the input inverse velocity terms $[v_i]^{-1}$ for each group. The starting time step is then

$$\partial t_{j1} = \frac{0.01}{Max_i \left(\Omega_i'\right)} \quad . \tag{9.4-70}$$

This method of obtaining the starting subinterval requires very little computer time but can produce an undesirably large subinterval estimate if the neutron fluxes and precursors are not near equilibrium. It should be noted that if no diffusion transport parameter changes are made in any node between TRAC-BF1/MOD1 thermal-hydraulic time steps, then Equation (9.4-70) is not used. The starting time step is obtained from Equations (9.4-63) and (9.4-67) directly using the omega data computed at the end of the last Δt_H thermal-hydraulic time step.

With regard to the second initialization option, the algorithm sets the starting interval on the basis of the neutron kinetics equation itself. Substitution of Equation (9.4-61) into Equation (9.4-54) yields

$$-h_i[V_i]^{-1}[\omega_{ji}][\bar{\Phi}_i] = [CL_i][\bar{\Phi}_{i-1}] + [CT_i][\bar{\Phi}_i] + [CR_i][\bar{\Phi}_{i+1}]$$

$$- \sum_{1}^{k} [\chi]\lambda_k \bar{C}_{ki} \quad . \tag{9.4-71}$$

Rearranging this expression and solving for the omega matrix on the left-hand side (using the thermal-hydraulic time node-average fluxes, delay precursor inventories, and new-time diffusion theory transport parameters) provides estimates for the expected omega matrices for each node at the beginning neutronics time step. These are then used in Equation (9.4-63). The coupling matrices in Equation (9.4-70) are computed using the omega data from the end of the previous TRAC-BF1/MOD1 time interval but are based on new-time transport parameters. The estimated omega matrices on the left-hand side of Equation (9.4-70) are thus evaluated without iterations. Again, a check is made to determine whether any diffusion transport parameter changes were made from the previous TRAC-BF1/MOD1 time step (or from the assumed initial equilibrium condition when computing the estimated omegas for the first time step). If no changes were made, the omega data from the end of the previous time step are used in Equation (9.4-63) in order to estimate the starting interval.

The second time step initialization algorithm is very conservative and requires more computing time, since an extra set of omega matrices has to be evaluated for the conditions existing at the beginning of the time step. However, this algorithm appears to be applicable to a wider range of transients, and in addition it will detect and account for transport variable changes, if any, from one time step to the next.

9.4.3.5 Implementation of the One-Dimensional Diffusion Mode. The programming for the TRAC-BF1/MOD1 one-dimensional kinetics package is implemented in a number of subroutines in a way similar to the point kinetics model (see Section 9.3.2). However, the level of programming detail is significantly more complex.

As in the point kinetics package, the one-dimensional diffusion model is interfaced with the one-dimensional CHAN and three-dimensional VESSEL components. This allows the user to appropriately partition the fuel bundle and vessel bypass elements so that TRAC-BF1/MOD1 can correctly estimate macroscopic cross sections and other transport variables in the one-dimensional diffusion model. The subroutine FPOW is the master input processor of the user supplied kinetics data. FPOW will call the subroutine FP1D to process one-dimensional kinetics input if the one-dimensional kinetic option is on. Initialization of decay heat arrays, computation of weight factors, and the calculation of rod power distribution factors are controlled by the subroutines IPDK, IPRW, and IPFL, respectively. The one-dimensional model also uses the same data from BLOCKDATA to calculate the decay heat fraction of the total core power.

The key specifications and options that the TRAC-BF1/MOD1 user has when invoking the one-dimensional diffusion model are as follows:

1. Calculate either steady-state and/or transient diffusion equation solutions.

2. Specify source convergence options for steady-state solutions.

3. Specify time differencing and fractional nodal change parameters for time-dependent solutions.

4. Specify boundary conditions via albedo matrices.

5. Specify polynomial fit coefficients for the diffusion equation transport parameters.

It should be pointed out that the code will generally default to some value if the user has not chosen a particular parameter or parameters.

If the one-dimensional kinetics option is employed, the subroutine POWER passes control to the one-dimensional diffusion code package, which is composed of a number of different subroutines. A summary of these one-dimensional kinetics subroutines is given in Appendix H.

The kinetics subroutines are not self-contained but require thermal-hydraulic data calculated from other subroutines in order to solve the one-dimensional diffusion equation nodal finite-difference scheme. In particular, subroutines VSL3, CHN3, and COR3 calculate radially averaged hydraulic and fuel temperature data to subroutine NXSECT, which computes new time diffusion equation transport variables for the one-dimensional diffusion subroutines. Once the power distribution has been calculated by the one-

dimensional kinetics package, additional data processing is performed by TFIE to partition power between the modeled fuel bundles and moderator.

9.4.4 Conclusions

Both of the neutronics models documented in Section 9.4 were global approximations to the generalized three-dimensional neutron transport methodology. The global approximations were made on the assumption that the fuel and moderator properties were spatially homogenous (point kinetics model) or radially homogeneous at different axial locations (one-dimensional approximation). Relative to the point kinetics model, the following conclusions are made:

1. The point-kinetics model can provide quick estimates of reactor power when spatial effects are judged to be insignificant.

2. The TRAC-BF1/MOD1 user is cautioned that certain types of kinetics problems are inherently multi-dimensional, so the point kinetics approximation breaks down.

3. The present point kinetics model assumes linear variations in reactivity feedback for a given thermal-hydraulic time step. If the hydraulic time step is very large relative to the neutronics time scale, the linear assumption may become invalid.

4. The power-squared or volume-weighting reactivity feedback modeling in the point-kinetics formulation indirectly accounts for some spatial variation in reactor core state variables.

Conclusions relative to the one-dimensional nodal neutronics model are as follows:

1. The analytic nodal routines provide TRAC-BF1/MOD1 with an efficient one-dimensional neutronics capability.

2. The accuracy of this model is dependent on how well the modeled reactor can be represented in one dimension. In particular, calculations with a separate neutronics code must be performed to generate radially averaged transport coefficients.

3. The assumption of one-dimensional geometry can be eliminated by expanding the TRAC-BF1/MOD1 nodal routines to two or three dimensions.

Conclusions relevant to both TRAC-BF1/MOD1 models include:

1. Reactor kinetics constants such as delayed neutron fractions and neutron lifetimes should be chosen with great care. Supplied default values are nominal values and do not always characterize the

conditions peculiar to specific reactors.

2. The power fraction for direct moderator heating can be very important, depending on the transient scenario simulated. Moderator power deposition fractions should be carefully chosen under these conditions.

3. Wherever possible, the simplified models in TRAC-BF1/MOD1 should be benchmarked against more detailed three-dimensional neutronics codes.

9.4.5 References

9.4-1. A. F. Henry, *Nuclear-Reactor Analysis*, Cambridge, Massachusetts: M.I.T Press, 1975.

9.4-2. D. L. Hetrick, *Dynamics of Nuclear Reactors*, Chicago, Illinois: University of Chicago Press, 1971.

9.4-3. J. R. Lamarsh, *Introduction to Nuclear Reactor Theory*, Reading, Massachusetts: Addison-Wesley, 1966.

9.4-4. W. M. Stacey, *Space-time Nuclear Reactor Kinetics*, New York, New York: Academic Press, 1969.

9.4-5. M. Ash, *Nuclear Reactor Kinetics*, New York, New York: McGraw-Hill Book Company, 1979.

9.4-6. D. D. Taylor et. al., *TRAC-BD1/MOD1: An Advanced Best Estimate Computer Program for Boiling Water Reactor Transient Analysis*, NUREG/CR-3633, EGG-2294, April 1984.

9.4-7. ANS Standards Committee Working Group, "ANS-5.1: Decay Heat Power in Light Water Reactors," ANS, ANSI/ANS-5.1-1979, August 1979.

9.4-8. C. C. Tsai, *TRAC-BWR Completion Report, Power Squared Feedback-Reactivity Weighting and Direct Moderator Heating*, WR-CD-82-061, March 1982.

9.4-9. C. C. Tsai, *TRAC-BWR Completion Report, Implementation of Reactivity Feedback Model*, WR-CD-81-049, June 1981.

9.4-10. S. Gill, "A Process for the Step-by-Step Equation Integration of Differential Equations in an Automatic Digital Computer Machine, *Proceedings of the Cambridge Phitos. Society, 47*, 1951, pps. 96-108.

9.4-11. R. S. Thompson, "Improving Roundoff in Runge-Kutta Computations with Gill's Method," *Private Communication of the ACM L3*, 12, December 1970.

9.4-12. D. W. Nigg et. al., *An Improved Integration Method for the TRAC-BD1 Analytical Nodal Reactor Kinetics Equations*, EGG-PBS-6554, May 1984.

8-4-13. D. W. Nigg, *One-Dimensional Nodal Neutronics Routines for the TRAC-BD1 Thermal Hydraulics Program*, EGG-PBS-6379, Revision 1, July 1984.

9.4-14. W. L. Weaver, "One-Dimensional Kinetics in the TRAC-BF1 Code," *Proceedings of the ANS Topical Meeting on Anticipated and Abnormal Transients in Nuclear Power Plants, Volume 1, Atlanta, Georgia, April 1987.*

9.4-15. W. L. Weaver, *TRAC-BD1/MOD1 Completion Report: Implementation of One-Dimensional Neutron Kinetics*, SE-CMD-84-003, May 31, 1984.

9.4-16. W. L. Weaver, *TRAC-BWR Design Report: Generation of One-Dimensional Kinetics Input*, EGG-RTH-7528, January 1987.

9.4-17. W. Wulff et al., *A Description and Assessment of RAMONA-3B: A Computer Code with Three-Dimensional Neutron Kinetics for BWR System Transients*, BNL-NUREG-51746, NUREG/CR-3664, January 1984.

Appendix A

Thermodynamic Properties

APPENDIX A

THERMODYNAMIC PROPERTIES

The thermodynamic properties subroutines used in TRAC-BF1/MOD1 are based on polynomial fits to steam table data for water and ideal gas behavior for the noncondensable gas component. The thermodynamic property routines are used by all TRAC-BF1/MOD1 component modules. Tables A-1 through A-8 list the values of the constants.

Subroutine THERMO supplies thermodynamic properties for TRAC-BF1/MOD1. The input variables are the total pressure, the partial pressure of the noncondensable gas component, and the liquid and gas-phase temperatures. The output variables include the saturation temperature corresponding to total pressure; the saturation temperature corresponding to the partial pressure of steam; the specific internal energies of liquid, gas, and noncondensable; the saturated liquid and steam enthalpies corresponding to the partial pressure of steam; the liquid, gas, and noncondensable densities; the derivatives of saturation temperatures and enthalpies with respect to pressure; and, finally, the partial derivatives of liquid, steam, and noncondensable internal energies and densities with respect to pressure (at constant temperature) and with respect to temperature (at constant pressure).

The range of validity for the thermodynamic properties supplied by THERMO is

$273.15\ K \leq T_\ell \leq 713.94\ K$;

$273.15\ K \leq T_v \leq 3000.0\ K$; and

$1.0\ Pa \leq p \leq 450.0\ E5\ Pa$.

If THERMO is provided with data outside these ranges, it adjusts the data to the corresponding limit and issues a warning message.

A-1 SATURATION PROPERTIES

A-1.1 Relationship between Saturation Pressure and Temperature

The saturation line that lies between the triple point (273.15 K) and the critical point (647.3 K) is divided into two regions of temperature and pressure, and a separate correlation is used in each region.

A-1.1.1 First Region of Temperature and Pressure. The first region of temperature is defined by

APPENDIX A

Table A-1. Miscellaneous constants.

Constant	Value	Constant	Value
A_{11}	1.00008875 E-3	C_{19}	Not used
A_{12}	7.691625 E2	C_{20}	9.056466 E4
A_{13}	1.300115 E-3	C_{21}	370.4251
A_{14}	1. E-5	C_{22}	1004.832
C_1	- 2263.0	C_{23}	$C_{16} \cdot C_4$
C_2	0.434	C_{24}	4186.8
C_3	- 6 064	C_{25}	287.03
C_4	$C_{12}/(C_{16} - 1)$	C_{26}	$C_{24} (C_5 - C_{29})$
C_5	273.15	C_{27}	$C_{26} + C_{10}$
C_6	$C_{27} - C_{12} \cdot C_5$	C_{28}	$(C_{12} - C_{25})/C_{12}$
C_7	C_{24}	C_{29}	273.15
C_8	$- 0.61132 + C_7(C_5 - C_{29})$	C_{30}	1.0
C_9	990.0	C_{31}	450.0 E5
C_{10}	$h_{fg}(C_5)$	C_{32}	C_5
C_{11}	1. E5	C_{33}	713.94026
C_{12}	461.49	C_{34}	C_5
C_{13}	0.0228	C_{35}	3000.0
C_{14}	0.65141	C_{36}	610.8
C_{15}	0.0	C_{37}	221.2 E5
C_{16}	1.3	C_{38}	647.3
C_{17}	$C_{22} - C_{25}$	C_{39}	139.6997 E5
C_{18}	C_{22}/C_{17}	C_{40}	609.625

Ta'le A-2. Constants for steam internal energy function.[a]

Region	Maximum Pressure (Pa)	Ave	Bve	Cve	Dve
1	20 E5	2.49497 E6	2.08558 E-1	-1.35539 E-7	2.852268 E-14
2	50 E5	2.56008 E6	3.10861 E-2	-6.89888 E-9	4.32037 E-16
3	100 E5	2.59155 E6	8.77499 E-3	-1.794999 E-9	4.29999 E-17
4	150 E5	2.66060 E6	-1.3545 E-2	6.425 E-10	-4.21 E-17
5	200 E5	3.82016 E6	-2.30199 E-1	1.40689 E-8	-3.1786 E-16
6	220 E5	-1.21034 E8	1.80188 E1	-8.74424 E-7	1.40911 E-14
7	250 E5	2.20 E6	0.	0.	0.
8	300 E5	2.20 E6	0.	0.	0.
9	350 E5	2.20 E6	0.	0.	0.
10	400 E5	2.20 E6	0.	0.	0.
11	450 E5	2.20 E6	0	0.	0.

a. Constants in TRAC-BF1/MOD1 have 14 significant figures.

Table A-3. Constants for gamma function.[a]

Region	Maximum Pressure (Pa)	Avg	Bvg	Cvg	Dvg
1	20 E5	1.06668	2.83108 E-8	-2.1151 E-14	4.7404 E-21
2	50 E5	1.07354	2.651805 E-9	-6.3461 E-16	3.9824 E-23
3	100 E5	1.077773	-2.43 E-11	-7.19799 E-17	4.87999 E-25
4	150 E5	1.085113	-1.9307 E-9	8.91 E-17	-3.896 E-24
5	200 E5	1.16398	-1.63385 E-8	9.5856 E-16	-2.1194 E-23
6	220 E5	3.88988	-3.85959 E-7	1.74763 E-14	-2.6377 E-22
7	250 E5	2.71687	-2.28327 E-7	1.04173 E-14	-1.58428 E-22
8	300 E5	3.97498	-3.06571 E-7	1.063789 E-14	-1.22579 E-22
9	350 E5	1.29469	-2.48349 E-8	7.8979 E-16	-8.079 E-24
10	400 E5	1.05905	-2.46159 E-9	8.8399 E-17	-8.0799 E-25
11	450 E5	1.143019	-7.709599 E-9	1.933599 E-16	-1.46399 E-24

a. Constants in TRAC-BF1/MOD1 have 14 significant figures.

Table A-4. Constants for steam heat capacity function.[a]

Region	Maximum Temperature (K)	Acp	Bcp	Ccp	Dcp
1	323.15	-7.9678 E2	2.81876 E1	-1.01806 E-1	1.2499 E-4
2	373.15	-9.70826 E2	2.8325 E1	-9.76562 E-2	1.16 E-4
3	423.15	-1.66497 E3	3.315936 E1	-1.0861179 E-1	1.2399 E-4
4	473.15	-6.142048 E3	6.363098 E1	-1.77623 E-1	1.7599 E-4
5	523.15	-8.228995 E4	5.377395 E2	-1.16125	8.5599 E-4
6	573.15	-6.5842 E5	3.79343 E3	-7.29249	4.704 E-3
7	623.15	3.45616 E5	-2.2129 E2	-2.4524	3.14799 E-3
8	647.3	1.979837 E6	-1.478255 E4	3.16564 E1	-2.08433 E-2
9	673.3	-9.62493 E7	4.363367 E5	-6.58876 E2	3.31461 E-1
10	723.3	-1.10749 E7	4.80737 E4	-6.9212 E1	3.30917 E-2

a. Constants in TRAC-BF1/MOD1 have 14 significant figures.

Table A-5. Constants for liquid internal energy function.[a]

Region	Maximum Temperature (K)	Af	Bfe	Cfe	Dfe
1	423.15	-1.14367 E6	4.1868 E3	0	0
2	473.15	8.09575 E6	-5.70088 E4	1.34436 E2	-9.78797 E-2
3	523.15	-1.93739 E6	9.74928 E3	-1.32996 E1	1.08799 E-2
4	573.15	-5.32458 E6	2.91794 E4	-5.04522 E1	3.456 E-2
5	623.15	-6.35835 E7	3.2873 E5	-5.63712 E2	3.276 E-1
6	645.15	-6.62391 E9	3.16056 E7	-5.02637 E4	2.665 E1
7	673.15	-5.4759 E9	2.46356 E7	-3.6931 E4	1.84547 E1
8	713.94	-7.15364 E7	3.05608 E5	-4.24245 E2	1.97199 E-1

a. Constants in TRAC-BF1/MOD1 have 14 significant figures.

Table A-6. Miscellaneous liquid property constants.[a]

Constant	Value
C_{k0}	-8.329 E-4
C_{k2}	-2.2458 E-17
C_{k4}	-1.4504 D-16
a_{ℓ}	7.146

a. Constants in TRAC-BF1/MOD1 have 14 significant figures.

Table A-7. Constants in liquid specific volume function.[a]

Region	Maximum Temperature (K)	Avo	Bvo	Cvo	Dvo
1	373.15	1.705767 E-3	-6.03208 E-6	1.5944 E-8	-1.2149 E-11
2	473.15	5.21459 E-4	3.518922 E-6	-9.73048 E-9	1.085668 E-11
3	573.15	-1.493186 E-2	9.793156 E-5	-2.01728 E-7	1.40804 E-10
4	603.15	-4.93342 E-1	2.59285 E-3	-4.53871 E-6	2.65379 E-9
5	613.15	-3.45589	1.735179 E-2	-2.90474 E-5	1.62202 E-8
6	623.15	-1.19525 E1	5.89049 E-2	-9.67866 E-5	5.30292 E-8
7	633.15	-3.74466 E1	1.81734 E-1	-2.940499 E-4	1.5863 E-7
8	643.15	-3.97132 E2	1.88018	-2.96739 E-3	1.561217 E-6
9	653.15	-2.31427 E3	1.07102 E1	-1.65217 E-2	8.49552 E-6
10	663.15	2.048156 E3	-9.345278	1.4212 E-2	-7.2037 E-6
11	673.15	-7.38647 E1	3.31449 E-1	-4.96087 E-4	2.477179 E-7
12	713.94	-2.189132 E1	9.67584 E-2	-1.14289 E-4	7.05672 E-8

a. Constants in TRAC-BF1/MOD1 have 14 significant figures.

Table A-8. Constants in liquid specific volume correction factor.[a]

Region	Maximum Temperature (K)	Afn	Bfn	Cfn	Dfn
1	373.15	-4.24863 E9	3.75167 E7	-1.00649 E5	8.75972 E1
2	473.15	-2.79363 E8	5.566317 E6	-1.49217 E4	1.0834095 E1
3	573.15	-1.17612 E8	4.38322 E6	-1.208837 E4	8.60345
4	603.15	-4.54151 E9	2.73686 E7	-5.18947 E4	3.15812 E1
5	613.15	-4.01043 E10	2.029257 E8	-3.40759 E5	1.900066 E2
6	623.15	-6.01738 E10	2.99849 E8	-4.96759 E5	2.73686 E2
7	633.15	2.06788 E10	-8.95038 E7	1.282278 E5	-6.072229 E1
8	643.15	8.379355 E10	-3.899718 E8	6.050262 E5	-3.129196 E2
9	653.15	9.240237 E10	-4.267492 E8	6.569561 E5	-3.371112 E2
10	663.15	-2.75477 E10	1.2580004 E8	-1.914749 E5	9.713614 E1
11	673.15	6.860819 E8	-3.063602 E6	4.561362 E3	-2.264207
12	713.94	4.34584 E7	-1.83799 E5	2.59716 E2	-1.224404 E-1

a. Constants in TRAC-BF1/MOD1 have 14 significant figures.

$273.15\ K \leq T_s \leq 370.4251\ K$

$1\ Pa < p_s < 90564.66\ Pa.$

In this region, thermodynamic relations are used to define the saturation properties. The enthalpy of vaporization, $h_{\ell v}$, is represented as a linear function of temperature

$$h_{\ell v} = 3180619.59 - 2470.2120\ T_s\ . \tag{A-1}$$

The Clausius-Clapeyron equation, which assumes that steam is an ideal gas and neglects liquid volume compared to steam volume, can be written as

$$\frac{dp_s}{dT_s} = \frac{h_{\ell v} p_s}{R_v T_s^2} \tag{A-2}$$

where R_v is the gas constant for steam. Substituting for $h_{\ell v}$ and integrating, using the boundary condition $p_s = 24821$ Pa at $T_s = 338$ K, gives

$$p_s = 24821 \left(\frac{T_s}{338}\right)^{-5.3512} \exp\left[\frac{20.387\ (T_s - 338)}{T_s}\right]\ . \tag{A-3}$$

To compute the saturation temperature for a given pressure, this equation must be solved iteratively. To simplify the solution and avoid iteration, an approximate solution is used that gives the value of saturation temperature to within a fraction of a percent error. First, an approximate value of saturation temperature is determined from

$$T_{s,ap} = \frac{2263}{6.064 - 0.434 \ln\left(\frac{p_s}{100000}\right)} \tag{A-4}$$

which gives the saturation temperature within a few degrees of its correct value. This value is corrected by integrating the Clausius-Clapeyron equation, assuming constant $h_{\ell v}$ between $T_{s,ap}$ and T_s, which gives

$$T_s = \frac{T_{s,ap}}{1 - \left[\frac{R_v T_{s,ap}}{h_{\ell v}(T_{s,ap})}\right] \ln\left[\frac{p_s}{p_{s,a}(T_{s,ap})}\right]} \tag{A-5}$$

where $h_{\ell v}(T_{s,ap})$ and $p_s(T_{s,ap})$ are calculated using the equations above at $T_{s,ap}$. The derivative along the saturation line is also needed and is given by

$$\frac{\partial T_s}{\partial p_s} = \frac{R_v T_s^2}{p_s h_{fv}(T_s)} \quad . \tag{A-6}$$

A-1.1.2 Second Region of Temperature and Pressure. The second region of temperature is given by

$T_s \geq 370.4251$ K

$p_s \geq 9.056466$ E4 Pa.

In this range of temperature and pressure, a simpler functional form is used and is written

$$p_s = \frac{1}{A_{14}} \left(\frac{T_s - C_3}{C_1} \right)^{\frac{1}{C_2}} \tag{A-7}$$

$$T_s = C_1 (A_{14} p_s)^{C_2} + C_3 \tag{A-8}$$

$$\frac{dT_s}{dp_s} = \frac{C_2 (T_s - C_3)}{p_s} \quad . \tag{A-9}$$

Los Alamos National Laboratory has since modified the high-pressure range calculation. Those modifications have not as yet been incorporated into TRAC-BF1/MOD1.

A-1.2 Internal Energy of Saturated Steam

There are 12 pressure ranges in which the saturated vapor internal energy and the derivatives of the saturation enthalpy with respect to pressure and temperature are evaluated. The lowest pressure range uses one functional form, while the 11 highest pressure ranges use another functional form with different sets of constants. The two functional forms are given, along with the sets of constants and pressure ranges.

A-1.2.1 Lowest Pressure Range. The lowest pressure range is given by $p_v < 5.0$ E5 Pa, where p_v is the partial pressure of steam. In this pressure range, the internal energy is given by

$$e_{vs} = u_{vs} - \frac{p_v}{\rho_{vs}} = h_{vs} - R_v T_s \tag{A-10}$$

and

$$\frac{de_{vs}}{dp_v} = \frac{dh_{vs}}{dp_v} - R_v \frac{dT_s}{dp_v} . \tag{A-11}$$

The quantities have been determined by fitting the saturated vapor enthalpy and its derivative with respect to pressure as

$$h_{vs} = C_8 + C_7[T_s(p_v) - C_5] + h_{fv}[T_s(p_v)] \tag{A-12}$$

$$\frac{dh_{vs}}{dp_v} = C_7 - 2470.212 \frac{dT_s}{dp_v} . \tag{A-13}$$

Other quantities that will be needed later are γ_{vs}, the ratio of vapor specific heats along the saturation line, and its derivative along the saturation line with respect to pressure. These quantities are given by

$$\gamma_{vs} = \frac{h_{vs}}{e_{vs}} \tag{A-14}$$

$$\frac{d\gamma_{vs}}{dp_v} = \frac{dh_{vs}}{dp_v} - \frac{\gamma_{vs}}{e_{vs}} \frac{de_{vs}}{dp_v} . \tag{A-15}$$

A-1.2.2 Higher-Pressure Ranges. In the high-pressure ranges, the quantities of interest are determined from polynomials. These polynomials have different coefficients for the different pressure ranges. The pressures ranges and coefficients are given in Tables A-2 and A-3. The functions for pressure range j are

$$e_{vs}(j) = Ave(j) + p_v(Bve(j) + p_v[Cve(j) + p_v Dve(j)]) \tag{A-16}$$

$$\frac{de_{vs}(j)}{dp_v} = Bve(j) + p_v[2.0\ Cve(j) + p_v 3.0\ Dve(j)] \tag{A-17}$$

$$\gamma_{vs}(j) = Avg(j) + p_v(Bvg(j) + p_v[Cvg(j) + p_v Dvg(j)]) \quad \text{(A-18)}$$

$$\frac{d\gamma_{vs}(j)}{dp_v} = Bvg(j) + p_v[2.0\ Cvg(j) + p_v 3.0\ Dvg(j)] \quad \text{(A-19)}$$

$$h_{vs}(j) = e_{vs}(j)\gamma_{vs}(j) \quad \text{(A-20)}$$

$$\frac{dh_{vs}(j)}{dp_v} = \gamma_{vs}(j)\frac{de_{vs}(j)}{dp_v} + e_{vs}(j)\frac{d\gamma_{vs}(j)}{dp_v} . \quad \text{(A-21)}$$

A-1.3 Heat Capacity of Saturated Steam at Constant Pressure

Although the heat capacity of steam is not an output variable of the THERMO subroutine, it is used in subsequent calculations. The temperature is divided into 10 regions, with the heat capacity and its derivative with respect to pressure being determined from the same polynomial function in each temperature range with different coefficients. The polynomial function is given by

$$Cps(j) = Acp(j) + T_s(Bcp(j) + T_s[Ccp(j) + T_s Dcp(j)]) \quad \text{(A-22)}$$

$$\frac{dCps(j)}{dp_v} = (Bcp(j) + T_s[2.0\ Ccp(j) + 3.0\ T_s Dcp(j)])\frac{dT_s}{dp_v} . \quad \text{(A-23)}$$

A-2 LIQUID PROPERTIES

A-2.1 Liquid Internal Energy

The liquid internal energy is computed by adding a correction term to the internal energy at saturation (corresponding to saturation pressure at the liquid temperature), that is

$$e_\ell(T_\ell,p) = e_\ell(T_\ell,PSL) + ELP \tag{A-24}$$

where PSL is the saturation pressure corresponding to T_ℓ and

$$ELP = (p - PSL)\left(\frac{\partial e_\ell}{\partial p}\right)_{T_\ell} \tag{A-25}$$

where the derivative of liquid internal energy with respect to pressure at constant temperature is given by

$$\left(\frac{\partial e_\ell}{\partial p}\right)_{T_\ell} = C_{k0}\left[1 - \exp\left(C_{k4}PSL\right)\right] + C_{k2}PSL^2 \ . \tag{A-26}$$

The derivative of the liquid internal energy is calculated from

$$\left(\frac{\partial e_\ell}{\partial T_\ell}\right)_p = \frac{\partial}{\partial T_\ell} e_\ell(T_\ell,PSL)_p + ERT \tag{A-27}$$

where

$$ERT = \frac{\partial}{\partial T_\ell}(ELP)_p$$

$$= \left\{C_{k0}\left[1 - (C_{k4}p + C_{k4}PSL)\exp\left(C_{k4}PSL\right) - 1\right] + C_{k2}\left[2p\ PSL - 3PSL^2\right]\right\}\frac{dPSL}{dT_\ell} \ . \tag{A-28}$$

The liquid internal energy at saturation is computed from a third-order polynomial in each of eight temperature ranges. The polynomial coefficients are different in each temperature range. The temperature ranges and the coefficients for each range are given in Table A-5. The polynomial function is given by

$$e_\ell(T_\ell,PSL) = Ale(j) + T_\ell(Ble(j) + T_\ell[Cle(j) + T_\ell Dle(j)]) \tag{A-29}$$

for each temperature range j.

A-2.2 Liquid Density

The liquid density is computed in two steps. The density is computed from the primary liquid density function to which a residual void correction is applied.

A-2.2.1 Primary Liquid Density Correlation. The primary liquid density is computed from a correlation for the liquid specific volume as a function of liquid temperature, to which a pressure-dependent correction factor is applied, and is

$$\rho_\ell(T_\ell,p) = \frac{1}{v_\ell(T_\ell)\left[1 - \frac{\ln\left(1 + \frac{p}{F(T_\ell)}\right)}{a_\ell}\right]} \qquad \text{(A-30)}$$

where

$$v_\ell(T_\ell) = Avo + T_\ell[Bvo + T_\ell(Cvo + T_\ell Dvo)] \qquad \text{(A-31)}$$

and

$$F(T_\ell) = Afn + T_\ell[Bfn + T_\ell(Cfn + T_\ell Dfn)] \; . \qquad \text{(A-32)}$$

The temperature range is broken up into 12 temperature regions, and the polynomial coefficients are different in each region. The temperature regions and the coefficients for each region are listed in Tables A-7 and A-8.

The derivatives of the liquid density with respect to pressure and temperature are found by differentiation of the liquid density function.

A-2.2.2 Residual Void Correction. After evaluation of the functions described above, the liquid density and its derivatives are modified to reflect a residual void fraction. In the following, the unmodified values computed by the formulas described above are denoted by a tilde (~). There are two pressure ranges for the residual void correction.

A-2.2.2.1 High-Pressure Residual Void Correction--The high-pressure range for the residual void correction is given by

P > 4. E5 Pa.

In the high-pressure region, the corrected liquid density and its derivatives are given by

$$\rho_\ell(T_\ell,p) = \left(1 - \frac{1000}{p}\right) \tilde{\rho}_\ell(T_\ell,p) \tag{A-33}$$

$$\left[\frac{\partial \rho_\ell(T_\ell,p)}{\partial T_\ell}\right]_p = \left(1 - \frac{1000}{p}\right) \left[\frac{\partial \tilde{\rho}_\ell(T_\ell,p)}{\partial T_\ell}\right]_p \tag{A-34}$$

$$\left[\frac{\partial \rho_\ell(T_\ell,p)}{\partial p}\right]_{T_\ell} = \left(1 - \frac{1000}{p}\right) \left[\frac{\partial \tilde{\rho}_\ell(T_\ell,p)}{\partial p}\right]_T + \frac{1000\ \tilde{\rho}_\ell(T_\ell,p)}{p^2} \ . \tag{A-35}$$

A-2.2.2.2 Low-Pressure Residual Void Correction--The low-pressure region for the residual void correction is given by

$P < 4.0$ E5 Pa.

In this region of pressure, the corrected liquid density and its derivatives are given by

$$Alf = 6.25\ E\text{-}9\ p + 0.005 \tag{A-36}$$

$$\rho_\ell(T_\ell,p) = Alf\ \tilde{\rho}_\ell(T_\ell,p) \tag{A-37}$$

$$\left[\frac{\partial \rho_\ell(T_\ell,p)}{\partial p}\right]_{T_\ell} = (1 - Alf) \left[\frac{\partial \tilde{\rho}_\ell(T_\ell,p)}{\partial p}\right]_{T_\ell} + 6.25\ E\text{-}9\ \tilde{\rho}_\ell \tag{A-38}$$

$$\left[\frac{\partial \rho_\ell(T_\ell,p)}{\partial T_\ell}\right]_p = (1 - Alf) \left[\frac{\partial \tilde{\rho}_\ell(T_\ell,p)}{\partial T_\ell}\right]_p \ . \tag{A-39}$$

A-3 VAPOR PROPERTIES

There are two vapor species in TRAC-BF1/MOD1, steam and noncondensable gas. Correlations are provided for the properties of each of these species.

A-3.1 Steam Properties

Steam properties are computed from different correlating functions, depending upon whether the steam is superheated or subcooled.

A-3.1.1 Superheated Steam ($T_v > T_s(p_v)$). Superheated steam is defined as steam whose temperature is greater than the saturation temperature based on the partial pressure of steam.

A-3.1.1.1 Internal Energy of Superheated Steam.--The internal energy of steam is computed by integrating the enthalpy from the saturated state to the temperature of interest along a line of constant pressure to give

$$e_v(T_{v,p}) = e_v[T_s(p_v), p_v] + A_{12}\left\{[T_v - T_s(p_v)] + (T_v^2 - \beta)^{1/2} - \frac{T_s(p_v)}{A_{11}C_{ps} - 1}\right\} \qquad \text{(A-40)}$$

and

$$\beta = T_s^2(p_v)\left[1 - \frac{1}{(A_{11}C_{ps} - 1)^2}\right] \qquad \text{(A-41)}$$

where β is the isobaric thermal expansion coefficient.

The saturated vapor enthalpy function was described in Section A-1.2, and the other constants are listed in Table A-1.

The derivative of vapor internal energy with respect to temperature at constant pressure is given by

$$\left(\frac{\partial e_v}{\partial T_v}\right)_{p_v} = \frac{C_4}{1 - \frac{\beta}{\kappa^2}} \qquad \text{(A-42)}$$

and

$$\kappa = A_{13}(e_v - e_{vs}) + T_s\left(1 + \frac{1}{A_{11}C_{ps} - 1}\right) \qquad \text{(A-43)}$$

where κ is the isothermal compressibility.

The derivative of vapor internal energy with respect to pressure at constant temperature is given by

$$\left(\frac{\partial e_v}{\partial p}\right)_{T_v} = -1/2\left(\frac{\partial e_v}{\partial T_v}\right)_p \left[\left(1 - \frac{\beta}{\kappa^2}\right)\kappa_p' + \frac{1}{\kappa}\frac{d\beta}{dp}\right] \tag{A-44}$$

$$\kappa_p' = \left(\frac{\partial \kappa}{\partial p_v}\right)_{T_v} = A_{13}\left(\frac{\partial e_v}{\partial p_v}\right)_{T_v}$$

$$= -A_{13}\left(\frac{de_{vs}}{dp_v}\right) + \left(1 + \frac{1}{A_{11}C_{ps} - 1}\right)\left(\frac{dT_s}{dp_v}\right) - \frac{A_{11}T_s}{(A_{11}C_{ps} - 1)^2}\left(\frac{dC_{ps}}{dp_v}\right) \tag{A-45}$$

$$\frac{d\beta}{d\kappa} = \frac{2}{T_s}\left[\beta\frac{dT_s}{dp_v} + A_{11}\frac{dC_{ps}}{dp_v}\left(\frac{T_s}{A_{11}C_{ps} - 1}\right)^3\right]. \tag{A-46}$$

A-3.1.1.2 Density of Superheated Steam. The density of superheated steam is given by

$$\rho_v(T_v, p) = \frac{p_v}{(\gamma_{vs} - 1)e_{vs} + 0.3D_e} \tag{A-47}$$

and

$$D_e = A_{12}\left[T_v - T_s + \left(T_v^2 - \beta\right)^{1/2} - \frac{t_s}{A_{11}C_{ps} - 1}\right]. \tag{A-48}$$

The derivative of steam density with respect to temperature at constant pressure is given by

$$\left(\frac{\partial \rho_v}{\partial T_v}\right)_p = \frac{-0.3\ \rho_v(T_v, p_v)}{(\gamma_{vs} - 1)e_{vs} + 0.3D_e}\left(\frac{\partial e_v}{\partial T_v}\right)_p. \tag{A-49}$$

The derivative of steam density with respect to pressure at constant temperature is given by

$$\left(\frac{\partial \rho_v}{\partial p_v}\right)_{T_v} = \frac{1 - \rho_v(T_v,p_v)\left[e_{vs}\frac{\partial \gamma_{vs}}{\partial p_v} + (\gamma_{vs} - 1.3)\frac{\partial e_{vs}}{\partial p_v}\right]}{(\gamma_{vs} - 1)e_{vs} + 0.3\ D_e}$$

$$- \frac{0.3\ \rho_v(T_v,p_v)}{(\gamma_{vs} - 1)e_{vs} + 0.3\ D_e}\left(\frac{\partial e_v}{\partial p_v}\right)_{T_v} . \qquad \text{(A-50)}$$

A-3.1.2 Subcooled Steam [$T_v < T_s(p_v)$]. Subcooled steam is defined as steam whose temperature is less than the saturation temperature based on the partial pressure of steam.

A-3.1.2.1 Internal Energy of Subcooled Steam--The internal energy of steam is computed by integrating the internal energy from the saturated state to the temperature of interest along a line of constant pressure, assuming that the heat capacity at constant volume remains constant at its value on the saturation line. This gives

$$e_v(T_v,p) = e_v[T_s(p_v),p_v] + [T_v - T_s(p_v)]\frac{C_{ps}[T_s(p_v)]}{C_{16}} \qquad \text{(A-51)}$$

$$\left[\frac{\partial e_v(T_v,p_v)}{\partial T_v}\right]_{p_v} = \frac{C_{ps}[T_s(p_v)]}{C_{16}} \qquad \text{(A-52)}$$

$$\left(\frac{\partial e_v(T_v,p_v)}{\partial p_v}\right)_{T_v} = \left\{\frac{\partial e_v[T_s(p_v),p_v]}{\partial p_v}\right\}_{T_v} + \left\{\frac{\partial C_{ps}[T_s(p_v),p_v]}{\partial p_v}\right\}_{T_v}\left[\frac{T_v - T_s(p_v)}{C_{16}}\right]$$

$$- \frac{C_{ps}[T_s(p_v),p_v]}{C_{16}}\left[\frac{\partial T_s(p_v)}{\partial p_v}\right] \qquad \text{(A-53)}$$

where the derivatives and heat capacity of saturated steam were described in Section A-1.

A-3.1.2.2 Density of Subcooled Steam--The density of subcooled steam is computed using the same correlating functions as for superheated steam (as described in Section A-3.1.1.2) except that the correlating parameter, D_v, is given by

$$D_v = \frac{C_{15}[T_s(p_v), p_v]}{C_{16}} [T_v - T_s(p_v)] \quad . \tag{A-54}$$

A-3.1.3 Steam Density Corrections. There are two separate corrections applied to the steam density as computed from the formulation described in the previous sections. If the computed density is negative, then the steam density and its derivatives with respect to pressure and temperature are recomputed assuming that steam is a perfect gas. These relations are

$$\rho_v(T_v, p) = \frac{p_v}{C_{12} T_v} \tag{A-55}$$

$$\left(\frac{\partial \rho_v}{\partial T_v}\right)_{p_v} = -\frac{\rho_v(T_v, p)}{T_v} \tag{A-56}$$

$$\left(\frac{\partial \rho_v}{\partial p}\right)_{T_v} = \frac{\rho_v(T_v, p)}{p_v} \quad . \tag{A-57}$$

The second correction is used whenever the computed steam density is greater than the computed liquid density. In this case, the vapor density and its derivatives with respect to pressure and temperature are set approximately equal to their corresponding liquid properties. Thus,

if $\rho_v(T_v, p_v) \geq 0.999\ \rho_\ell(T_\ell, p)$, then

$$\rho_v(T_v, p_v) = 0.999\ \rho_\ell(T_\ell, p) \tag{A-58}$$

$$\left[\frac{\partial \rho_v(T_v, p_v)}{\partial p_v}\right]_{T_v} = 0.999 \left[\frac{\partial \rho_\ell(T_\ell, p)}{\partial p_v}\right]_{T_\ell} \tag{A-59}$$

$$\left[\frac{\partial \rho_v(T_v,p_v)}{\partial T_v}\right]_{p_v} = 0.999\left[\frac{\partial \rho_\ell(T_\ell,p)}{\partial T_\ell}\right]_{p_v} \quad (A\text{-}60)$$

A-3.2 Noncondensable Gas Properties

The density and internal energy of the noncondensable gas are computed from the perfect gas law and are given by

$$e_a(T_v,\rho_a) = C_{17}T_v \quad (A\text{-}61)$$

$$\left[\frac{\partial e_a(T_v,\rho_a)}{\partial T_v}\right]_p = C_{17} \quad (A\text{-}62)$$

$$\left[\frac{\partial e_a(T_v,\rho_a)}{\partial \rho_a}\right]_{T_v} = 0 \quad (A\text{-}63)$$

$$\left[\frac{\partial \rho_a(T_v,p_a)}{\partial p_a}\right]_{T_v} = \frac{1}{C_{25}T_v} \quad (A\text{-}64)$$

$$\left[\frac{\partial \rho_a(T_v,p_a)}{\partial T_v}\right]_{p_a} = -C_{25}\rho_a(T_v,p_a)\left[\frac{\partial \rho_a(T_v,p_a)}{\partial p_a}\right]_{T_v} \quad (A\text{-}65)$$

$$\rho_a = (T_v,p_a) = p_a\left[\frac{\partial \rho_a(T_v,p_a)}{\partial p_a}\right]_{T_v} . \quad (A\text{-}66)$$

A-3.3 Properties of Water Mixtures

The internal energy of a mixture of steam and noncondensable gas is given by the density-weighted average of the internal energies of the two species

$$e_m(T_{v,p}) = \frac{\rho_v(T_v,p_v)e_v(T_v,p_v) + \rho_a(T_v,p_a)e_a(T_v,p_a)}{\rho_v(T_v,p_v) + \rho_a(T_v,p_a)} \quad . \tag{A-67}$$

The density of a mixture of steam and noncondensable gas is the sum of the densities of the two species.

APPENDIX B

MATERIAL PROPERTIES

APPENDIX B

MATERIAL PROPERTIES

An extensive library of temperature-dependent material properties is incorporated in the TRAC-BF1/MOD1 code. The entire library is accessible by the CHAN fuel rod components, while component walls and VESSEL double-sided heat slabs have access to structural material property sets only. There are 10 sets of materials properties that comprise the library, each set supplying values for thermal conductivity, specific heat, density, and spectral emissivity for use in heat transfer calculations. The first five sets contain properties for nuclear-heated or electrically heated fuel rod simulation. Included are nuclear fuels, zircaloy cladding, fuel-cladding gap gases, electrical heater rod filaments, and electrical heater rod insulating material. The last five sets are for structural materials, including stainless steels, carbon steel, and Inconel. The material indices used in the library are:

1. mixed-oxide fuel
2. zircaloy
3. gas gases
4. boron nitride insulation
5. constantan/nichrome heater
6. stainless steel, Type 304
7. stainless steel, Type 316
8. stainless steel, Type 347
9. carbon steel, Type A508
10. Inconel, Type 718.

In addition to the library of built-in material properties, the code provides for user-supplied tables of materials properties.

Figure B-1 illustrates the calling tree for obtaining the property values. Subroutines MFROD and MPROP are simple processors for calculating the average temperature and calling the appropriate subroutine based on the user-supplied material index. Subroutine FROD controls the fuel-cladding gap conductance and fuel rod thermal conduction calculations. Gap gas properties are calculated only when the dynamic fuel-cladding gap heat transfer coefficient option is used.

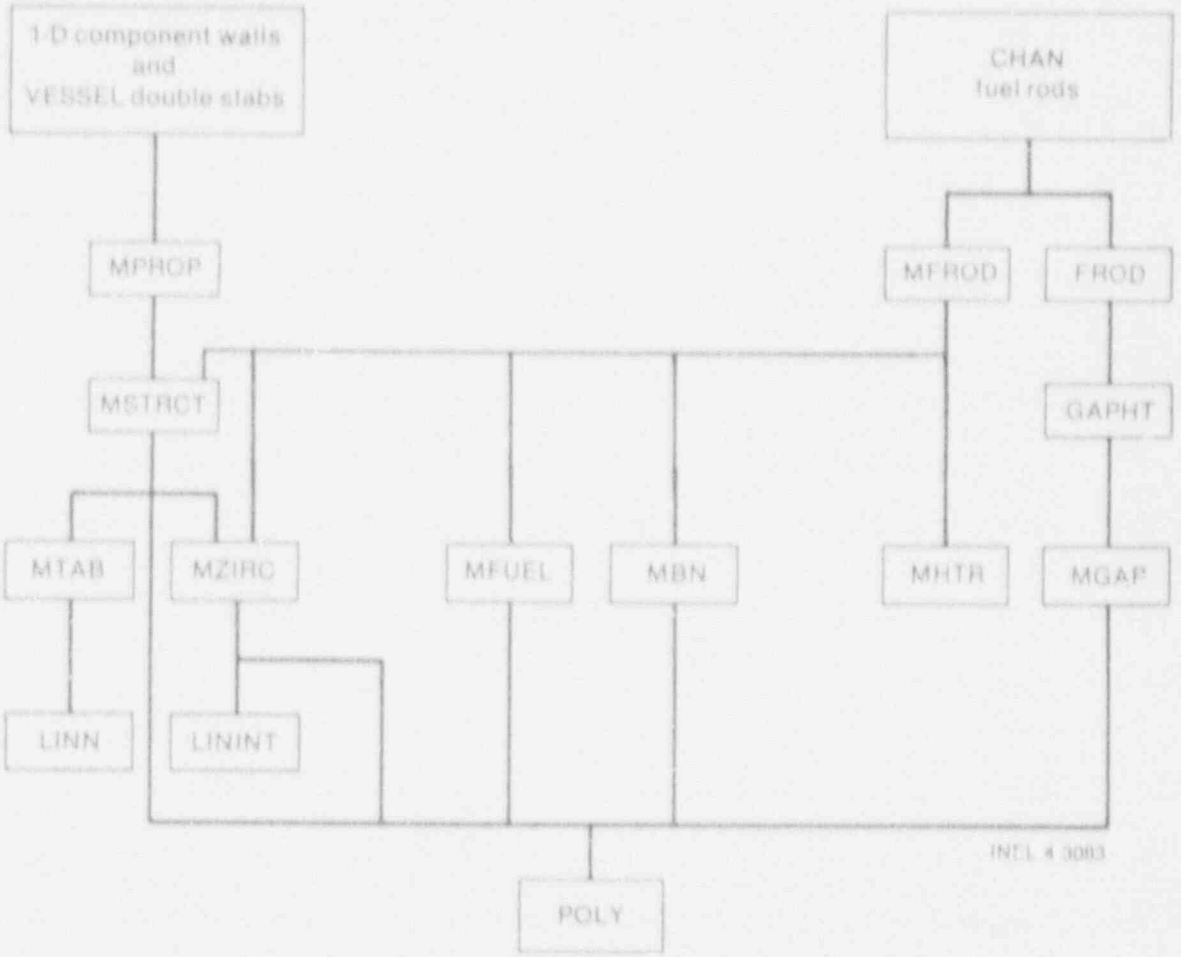

Figure B-1. Material properties code organization.

Density variation with thermal expansion is currently suppressed, because it is inconsistent with the fixed-node conduction solution. When node spacing changes are implemented, the expansion calculation may be activated.

B-1. NUCLEAR FUEL (UO_2-PuO_2) PROPERTIES

Subroutine MFUEL calculates the properties for mixed-oxide nuclear fuels. Values obtained are influenced by three user-supplied input variables: fraction of theoretical density, fraction of plutonium oxide in the fuel, and fuel burnup. Property changes upon melting are not included in this code version.

B-1.1 Density

A constant value is used;

$$\rho = f_{TD}\left[(1 - f_{PuO_2})\rho_{UO_2} + f_{PuO_2}\rho_{PuO_2}\right] \quad \text{(B-1)}$$

where

fTD = fraction of theoretical fuel density

f_{PuO_2} = weight fraction of PuO_2 in fuel

ρ_{UO_2} = 1.097 E4

ρ_{PuO_2} = 1.146 E4.

B-1.2 Specific Heat

The mixed-oxide fuel specific heat correlations ar taken from the MATPRO report[B-1]

$$c_p = 15.496\,\frac{b_1 b_4^2 \exp\left(\frac{b_4}{T}\right)}{T^2\left[\exp\left(\frac{b_4}{T}\right) - 1\right]^2} + 25_2 T + \frac{b_3 b_5}{b_6 T^2}\exp\left(\frac{-b_5}{b_6 T}\right) \quad \text{(B-2)}$$

where

c_p = specific heat capacity (J/kg·K)

T = fuel temperature (K)

and

b_1 = 19.145 for UO_2; 19.53 for UO_2-PuO_2

b_2 = 7.8473 E-4 for UO_2; 9.25 E-4 for UO_2-PuO_2

b_3 = 5.6437 E6 for UO_2; 6.02 E6 for UO_2-PuO_2

b_4 = 535.285 for UO_2; 539.0 for UO_2-PuO_2

b_5 = 37694.6 for UO_2; 40100.0 for UO_2-PuO_2

b_6 = 1.987 for UO_2; 1.987 for UO_2-PuO_2.

B-1.3 Thermal Conductivity

The mixed-oxide fuel thermal conductivity correlations are taken from the MATPRO report[B-1] and include porosity and density correction factors.

For $T_c \leq T_1$,

$$k = \left[c \frac{c_1}{c_2 + T_c} + c_3 \exp (c_4 T_c) \right] \quad \text{(B-3)}$$

For $T_c > T_1$,

$$k = c\, c_5 + c_3 \exp (c_4 T_c) \quad \text{(B-4)}$$

where

T_c = temperature (°C)

f_{TD} = fraction of theoretical density

$$c = 100.0 \left[\frac{1 - \beta(1 - f_{TD})}{1 - 0.05\beta} \right] \quad \text{(B-5)}$$

$$\beta = c_6 + c_7 T_c \quad \text{(B-6)}$$

and

c_1 = 40.4 for UO_2; 33.3 for UO_2-PuO_2

c_2 = 464.0 for UO_2; 375.0 for UO_2-PuO_2

c_3 = 1.216 E-4 for UO_2; 1.54 E-4 for UO_2-PuO_2

c_4 = 1.867 E-3 for UO_2; 1.71 E-3 for UO_2-PuO_2

c_5 = 0.0191 for UO_2; 0.0171 for UO_2-PuO_2

c_6 = 2.58 for UO_2; 1.43 for UO_2-PuO_2

c_7 = -5.8 E-4 for UO_2; 0.0 for UO_2-PuO_2

T_1 = 1650.0 for UO_2; 1550.0 for UO_2-PuO_2.

B-1.4 Spectral Emissivity

The mixed-oxide spectral emissivity is calculated as a function of temperature based on MATPRO correlations. The values for UO_2 fuel and UO_2-PuO_2 fuel are assumed to be equivalent.

For $T \leq 1000°C$,

$$\varepsilon = 0.8707 \tag{B-7}$$

For $1000 < T \leq 2050°C$,

$$\varepsilon = 1.311 - 4.404\ E{-}4\ T \tag{B-8}$$

For $T > 2050°C$,

$$\varepsilon = 0.4083\ . \tag{B-9}$$

B-2. ZIRCALOY CLADDING PROPERTIES

Subroutine MZIRC calculates the properties for zircaloy and oxidized zircaloy cladding. The values obtained are for zircaloy-4. Zircaloy-2 properties are assumed to be identical. The equations used are based on the correlations in the MATPRO report.[B-1]

B-2.1 Density

A constant value is used;

$$\rho = 6551.4\ . \tag{B-10}$$

B-2.2 Specific Heat

Since zircaloy undergoes a phase change (alpha to beta) from 1090 to 1248 K, with a resultant sharp spike in the specific heat value during the transition, the specific heat is calculated by linear interpolation. Table B-1 provides the values of specific heat versus temperature that are used for $T \leq 1248$ K.

For $T > 1248$ K, $C_p = 356$ J/kg·K.

Table B-1. Specific heat versus temperature for T ≤ 1248 K.

T (K)	C_p (J/kg·K)
300	281
400	302
640	381
1090	375
1093	502
1113	590
1133	615
1153	719
.173	816
1193	770
1213	619
1233	469
1248	356

B-2.3 Thermal Conductivity

Four-term polynomials are used to calculate the zircaloy and oxidized zircaloy thermal conductivities. Kelvin temperature is the independent variable, and the polynomial constants are

a_0 = 7.51 for Zr; 1.96 for ZrO_2

a_1 = 2.09 E-2 for Zr; -2.41 E-4 for ZrO_2

a_2 = -1.45 E-5 for Zr; 6.43 E-7 for ZrO_2

a_3 = 7.67 E-9 for Zr; 1.95 E-10 for ZrO_2.

The form of the polynomial used in this section and the subsequent materials properties sections is

$$Y = a_0 + a_1 x + a_2 x^2 + \ldots + a_m x^m . \qquad (B\text{-}1)$$

B-2.4 Spectral Emissivity

The emissivity of zircaloy is temperature-dependent, and the emissivity of zircaloy oxide is temperature- and time-dependent. For simplicity, a constant value of $\varepsilon = 0.75$ is currently used.

B-3. FUEL-CLADDING GAP GAS PROPERTIES

Subroutine MGAP calculates values for the gap gas mixture thermal conductivity used in predicting gap heat-transfer coefficients. The method is taken from MATPRO[B-1] and is based on calculating mixture values for a possible seven constituent gases

$$k_{gap} = \sum_{i=1}^{n} \left(\frac{k_i x_i}{x_i + \sum_{\substack{j=1 \\ j \neq i}}^{n} \Psi_{ij} x_j} \right) \tag{B-12}$$

where

k_{gap} = gap mixture thermal conductivity (W/m·K)

$$\Psi_{ij} = \Phi_{ij} \left[1 + 2.41 \frac{(M_i - M_j)(M_i - 0.142\, M_j)}{(M_i + M_j)^2} \right] \tag{B-13}$$

$$\Phi_{ij} = \frac{\left[1 + \left(\frac{k_i}{k_j} \right)^{1/2} \left(\frac{M_j}{M_i} \right)^{1/4} \right]^2}{2^{3/2} \left(1 + \frac{M_i}{M_j} \right)^{1/2}} \tag{B-14}$$

k_i = constituent gas thermal conductivity (W/m·K)

M_i = constituent gas molecular weight

x_i = constituent gas mole fraction.

The seven constituent gases considered are helium, argon, xenon, krypton, hydrogen, air/nitrogen, and water/vapor. Except for water/vapor, their thermal conductivities are defined as

$$k = aT^b \tag{B-15}$$

where

T = temperature (K)

a = 3.36 E-3 for He; 3.421 E-4 for Ar; 4.0288 E-5 for Xe; 4.726 E-5 for Kr; 1.6355 E-4 for H; and 2.091 E-4 for air/N

b = 0.668 for He; 0.701 for Ar; 0.872 for Xe; 0.923 for Kr; 0.8213 for H; and 0.846 for air/N.

For water/vapor, the correlation is

$$k = (2.2428\ E\text{-}7 + 5.0534\ E\text{-}10\ T - 1.853\ E\text{-}14\ T^2)\frac{P_g}{T} + \frac{1.0086\ p_g^2}{T^2(T - 273)^{4.2}}$$

$$+ 1.76\ E\text{-}4 + 3.261\ E\text{-}5\ T + 3.209\ E\text{-}8\ T^2 - 7.733\ E\text{-}12\ T^3 \qquad \text{(B-16)}$$

where p is the gap gas pressure (N/m^2).

When the gap dimension shrinks to the order of the gas mean free path, a correction factor is applied to the light gas thermal conductivities to account for the change in energy exchange between gas and surface. Once again utilizing the MATPRO recommendations,[B-1] the correction factor for hydrogen and helium is

$$k = \frac{k_i}{1 + fk_i} \qquad \text{(B-17)}$$

where

$$f = \frac{0.2103\sqrt{T_g}}{P_g\lambda} \qquad \text{(B-18)}$$

T_g = average gap gas temperature (K)

λ = characteristic fuel RMS roughness (4.389 E-6 m).

B-4. Electrical Fuel Rod Insulator (BN) Properties

Subroutine MBN calculates values for boron nitride insulators used in electrically heated nuclear fuel rod simulators. Magnesium oxide insulators are assumed to have roughly equivalent values.

B-4.1 Density

A constant value of 2002 kg/m^3 from Reference B-2 is used.

B-4.2 Specific Heat

A four-term polynomial is used to calculate the specific heat. The independent variable is temperature (°F), and the constants are modifications of those reported in Reference B-3: a_0 = 760.59; a_1 = 1.7955; a_2 = -8.6704 E-4; and a_3 = 1.5896 E-7.

B-4.3 Thermal Conductivity

The boron nitride thermal conductivity[B-4] is calculated based on a conversion to SI units of a curve fit

$$k = 25.27 - 1.365\ E\text{-}3\ T_f \qquad \text{(B-19)}$$

where

k = thermal conductivity (W/m·K)

T_f = temperature (°F).

B-4.4 Spectral Emissivity

A constant value of unity is used for the boron nitride spectral emissivity.

B-5. ELECTRICAL FUEL ROD HEATER COIL (CONSTANTAN) PROPERTIES

Subroutine MHTR calculates property values for constantan heater coils as used in electrically heated nuclear fuel rod simulators. Nichrome coils, used in some installations in place of constantan, are assumed to have similar properties. The correlations used are from Reference B-4.

B-5.1 Density

A constant value of 8393.4 kg/m^3 is used.

B-5.2 Specific Heat

$$c_p = 110\ T^{0.2075} \qquad \text{(B-20)}$$

where

c_p = specific heat (J/kg·K)

T_f = temperature (°F).

B-5.3 Thermal Conductivity

$$k = 29.18 + 2.683\ E\text{-}3\ (T_f - 100) \qquad \text{(B-21)}$$

where

k = thermal conductivity (W/m·K)

T_f = temperature (°F).

B-5.4 Spectral Emissivity

A constant value of unity is used.

B-6. STRUCTURAL MATERIAL PROPERTIES

Subroutine MSTRCT supplies property values for five types of structural materials normally used in light water power reactor plants: stainless steel, Type 304; stainless steel, Type 316; stainless steel, Type 347; carbon steel, Type A508; and Inconel, Type 718. A tabulation of the correlations used and a list of associated references are given in Table B-2.

B-7. USER-SUPPLIED MATERIAL PROPERTIES

At the option of the user, Subroutine MTAB gets property values from the user-supplied material property table, using straight-line interpolation.

B-8. REFERENCES

B-1. J. K. Hohorst, Ed., *SCDAP/RELAP5/MOD2 Code Manual, Volume 4: MATPRO--A Library of Materials Properties for Light-Water-Reactor Accident Analysis*, NUREG/CR-5273, EGG-2555, February 1990.

B-2. Y. S. Touloukian, Ed., *Thermophysical Properties of High Temperature Solid Materials*, New York: MacMillan Co., 1967.

B-3. Electric Power Research Institute, *A Prediction of the Semiscale Blowdown Heat Transfer Test S-02-8 (NRC Standard Problem Five)*, EPRI NP-212, October 1976.

B-4. W. L. Kirchner, *Reflood Heat Transfer in a Light Water Reactor, Volumes I and II*, NUREG-0106, August 1976.

B-5. Argonne National Laboratory, *Properties for LMFBR Safety Analysis*, ANL-CEN-RSD-76-1, 1976.

B-6. J. C. Spanner, Ed., *Nuclear Systems Materials Handbook--Volume 1, Design Data*, TID-26666, 1976.

Table B-2. Structural materials properties.

Appendix C

Data Base Used by M. Ishii for Verification of Drift Flux Models

APPENDIX C

DATA BASE USED BY M. ISHII FOR VERIFICATION OF DRIFT FLUX MODELS

In the derivation of drift flux formulas, for variables such as the distribution parameter, C_o, and phasic drift velocity, V_{gj}, in different flow regimes, Ishii has used a variety of data from different sources.[C-1,2,3] It should be noted that, with the exception of correlations given for C_∞, there are no empirical correlations in the drift flux model that are generated only from data. The mathematical relations for different variables, such as C_o and V_{gj}, have been derived on mechanistic principles first and then compared with a collection of data to ascertain their validity. In some cases, however, a body of experimental data has been used to determine the leading constant or an exponent in formulations. In the same manner, additional sets of data were employed by Andersen and Chu[C-4,5] in developing some improved correlations for V_{gj} and C_o that were addressed in the text. The source, nature and the range of variables of those data are summarized here in Tables C-1 and C-2.

REFERENCES

C-1. M. Ishii, *One-Dimensional Drift-Flux Model and Constitutive Equations for Relative Motion Between Phases in Various Two-Phase Flow Regimes*, ANL-77-47, October 1977.

C-2. M. Ishii, "Recommended Correlations for Interfacial Shear in Post CHF Regime," letter to Dr. M. W. Young, of U.S. Nuclear Regulatory Commission, from Argonne National Laboratory, May 12, 1983.

C-3. M. Ishii and K. Mishima, *Correlation for Liquid Entrainment in Annular Two-Phase Flow of Low Viscous Fluid*, ANL/RAS/LWR 81-2, March 1981.

C-4. J. G. M. Andersen and K. H. Chu, *BWR Refill-Reflood Program, Task 4.7 - Constitutive Correlations for Shear and Heat Transfer for the BWR Version of TRAC*, NUREG/CR-2134, EPRI NP-1582, GEAP-24940, December 1981.

C-5. J. G. M. Andersen, K. H. Chu, and J. C. Shaug, *BWR Refill-Reflood Program, Task 4.7 - Model Development. Basic Models for the BWR Version of TRAC*, *NUREG/CR-2573*, EPRI NP-2375, GEAP-22051, September 1983.

C-6. J. Nikuradse, "Gesetzmasigkeit der turbulenten stromung in glatten Rohren," *Forsch. Arb. Ing.-Wes. 356*, 1932.

C-7 K. Schwartz, "Investigation of Distribution of Density, Water and Steam

Velocity and of the Pressure Drop in Vertical Tubes," *VDI Forschungsh. 20*, Series B, 445, 1945.

C-8. J. F. Marchaterre, *The Effect of Pressure on Boiling Density in Multiple Rectangular Channels*, ANL-5522, February 1956.

C-9. T. A. Hughes, *Steam-Water Mixture Density Studies in a Natural Circulation High Pressure System*, Babcock and Wilcox, G. Report No. 5435, 1958.

C-10. S. Z. Rouhani and K. M. Becker, *Measurement of Void Fraction for Flow of Boiling Heavy Water in a Vertical Round Duct*, AE-106, Aktiebolaget Atomenergi, Studsvik, Sweden, 1963.

C-11. G. E. Semissaert, *Two-Component Two-Phase Flow Parameters for Low Circulation Rates*, ANL-6755, July 1963.

C-12. N. Adorni, G. Peterlongo, R. Ravetta, and F. A. Tacconi, *Large Scale Experiments on Heat Transfer and Hydrodynamics with Steam-Water Mixtures*, CISE Report R-91, Italy, 1964.

C-13. R. J. Thome, *Effect of a Transverse Magnetic Field on Vertical Two-Phase Flow through a Rectangular Channel*, ANL-6854, 1964.

C-14. G. B. Wallis, D. A. Steen, S. N. Brenner, and T. M. Turner, *Joint U. S.-Euratom Research and Development Program, Quarterly Progress Report*, January, Dartmouth College, 1964.

C-15. J. L. L. Baker, *Flow-Regime Transition at Elevated Pressures in Vertical Two-Phase Flow*, ANL-7093, September 1965.

C-16. C. C. St. Pierre, *Freguency-Response Analysis of Steam Voids to Sinusoidal Power Modulation in a Thin-Walled Boiling Water Coolant Channel*, ANL-7041, May 1965.

C-17. N. Zuber, "Flow Excursions and Oscillations in Boiling, Two-phase Flow Systems with Heat Addition," *Proceedings of the Symposium on Two-Phase Flow Dynamics, 1, 1967*, p. 1071.

C-18. M. Petrick, *A Study of Vapor Carryunder and Associated Problems*, ANL-6581, July 1982.

C-19. F. Bergonzoli and F. J. Halfen, *Heat Transfer and Void Formation during Forced Circulation Boiling of Organic Coolants*, NNC-SR-8906, 1964.

C-20. L. E. Gill and G. F. Hewitt, *Further Data on the Upwards Annular Flow of Air-water Mixtures*, AERE-R3935, 1962.

C-21. P. Alia, L. Cravarolo, A. Hassid, and E. Pedrocchi, *Liquid Volume Fraction in Adiabatic Two-phase Vertical Upflow Round Conduit*, CISE Report-105, Italy, 1965.

C-22. L. Cavarolo, A. Georgini, A. Hassid, and E. Pedrocchini, *A Device for the Measurement of Shear Stress on the Wall of a Conduit, Its Application in Mean Density Determination in Two-phase Flow: Shear Stress Data in Two-phase Adiabatic Vertical Flow*, CISE Report-82, Italy, 1964.

Table C-1. Experiments used to check the distribution parameter

Reference	Flow medium and test geometry	Range of variables
Nikuradse[C-6]	Single-phase water. Round Tubes, D_i = 0.025, 0.050, and 0.10 m	Reynolds numbers from 600 to 10^6
Schwartz[C-7]	Steam-water. Round tube, D = 0.0596 m L = 6.350 m	Pressure = 2.11 to 8.10 MPa G = 577.8 to 608.6 kg/m^2·s X = 2.8% to 5.85%
Marchaterre[C-8]	Boiling water. Parallel rectangular channels, 0.011x0.094 m^2 (3) 0.056x0.094 m^2 (2) L = 1.22 m	Pressure = 0.78 to 4.18 MPa Mass velocity, G = 365.46 to 499.88 kg/m^2·s Exit steam quality, X = 1.9% to 8.2%
Hughes[C-9]	Steam-water. Round Tube, D_i = 0.168 m L = 3.105 m	Pressure = 6.8 to 16.32 MPa G = 118.8 to 362.6 kg/m^2·s X = 3.22% to 22.77%
Rouhani and Becker[C-10]	Boiling heavy-water. Round tube, D_i = 0.006 m L = 2.50 m	Pressure = 0.7 to 6.0 MPa G = 650 to 2050 kg/m^2·s X = 0.0 to 38%
Semissaert[C-11]	Air-water. Round tube, D_i = 0.07 m, L = 3.19 m	Pressure = 0.1 MPa j_g = 0.0 to 11.0 m/s j_ℓ = 0.0 to 0.305 m/s
Adorni[C-12]	Boiling water. Round tube, D_i = 0.0251 m L = 1.661 m	Pressure = 5.1 MPa G = 1500 to 3800 kg/m^2·s X = 5% to 70.4%
Thome[C-13]	NaK-N_2 mixture. Rectangular Channel 0.0064x0.516 m^2 L = 0.762 m	Pressure = 0.107 to 0.16 MPa j_g = 0.078 to 3.89 m/s j_ℓ = 0.39 and 1.36 m/s
Wallis[C-14] (Appendix)	Air-water. Round tube, D_i = 0.0248 m L = 1.778 m	Pressure = 0.1 MPa j_g = 0.539 to 11.46 m/s j_ℓ = 0.0285 to 1.384 m/s
Baker[C-15]	Freon-11. Rectangular channel 0.0097x0.0267 m^2 L = 1.130 m	Pressure = 0.411 to 2.492 MPa j_g = 0.021 to 2.05 m/s j_ℓ = 0.024 to 15.4 m/s

Table C-1. (continued)

Reference	Flow medium and test geometry	Range of variables
St. Pierre[C-16]	Boiling water. Rectangular channel 0.011x0.0445 m^2 L = 1.55 m	Pressure = 1.36 to 5.44 MPa j_g = 0.0 to 1.93 m/s j_ℓ = 0.77 to 1.15 m/s
Semissaert[C-11]	Air-water. Round tube, D_i = 0.07 m, L = 3.19 m	Pressure = 0.1 MPa j_g = 0.0 to 11.0 m/s j_ℓ = 0.0 to 0.305 m/s
Adorni[C-12]	Boiling water. Round tube, D_i = 0.0251 m L = 1.66i m	Pressure = 5.1 MPa G = 1500 to 3800 $kg/m^2 \cdot s$ X = 5% to 70.4%
Thome[C-13]	Nak-N_2 mixture. Rectangular channel 0.0064 x 0.0516 m^2 L = 0.762 m	Pressure = 0.107 to 0.16 MPa j_g = 0.078 to 3.89 m/s j_ℓ = 0.39 and 1.36 m/s
Wallis[C-14] (Appendix)	Air-water. Round tube, D_i = 0.0248 m L = 1.778 m	Pressure = 0.1 MPa j_g = 0.539 to 11.46 m/s j_ℓ = 0.0285 to 1.384 m/s
Baker[C-15]	Freon-11. Rectangular channel 0.0097x0.0267 m^2 L = 1.130 m	Pressure = 0.411 to 2.492 MPa j_g = 0.021 to 2.05 m/s j_ℓ = 0.024 to 15.4 m/s
St. Pierre[C-16]	Boiling water. Rectangular channel 0.011x0.0445 m^2 L = 1.55 m	Pressure = 1.36 to 5.44 MPa j_g = 0.0 to 1.93 m/s j_ℓ = 0.77 to 1.15 m/s
Zuber[C-17]	Boiling freon-22. Round tube, D_i = 0.01 m L = 1.54 m	Pressure = 0.61 to 3.3 MPa G = 81.16 to 8116 $kg/m^2 \cdot s$ X = 0.0 to 60%
Petrick[C-18]	Boiling water. Round tube riser: D_i = 0.067 m and annular downcomer: D_i = 0.089 m D_o = 0.132 m L = unspecified	Pressure = 4.8 MPa Upflow, G = 739 to 1276 $kg/m^2 \cdot s$ X = 2.1% to 6.5% Downflow, G = 347 to 600 $kg/m^2 \cdot s$ X = 0.0% to 3.4%

Table C-1. (continued)

Reference	Flow medium and test geometry	Range of variables
Bergonzoli and Halfen[C-19]	Boiling Santowax-R Round tube, D_i = 0.0122 m L = 3.66 m	Pressure = 0.102 to 0.238 MPa G = 1400 to 3141 kg/m^2·s X = 0.0% to 8.5% in upflow X = 0.0% to 17% in downflow

Table C-2. Experiments used to check drift velocity formulas

Reference	Flow medium and test geometry	Range of variables
Gill and Hewitt[C-20]	Air-water, Round tube, D_i = 0.0318 m L = 3.66 m	Pressure = unspecified ρ_g = 1.18 to 1.83 kg/m^3 ρ_ℓ = 1012.4 to 1014.0 kg/m^3 j_g = 12.96 to 89.9 m/s j_ℓ = 0.0031 to 0.47 m/s
Alia et al.[C-21]	Argon-water and argon-ethyl alcohol Round tubes, D_i = 0.015 m and 0.025 m L = 4.0 m	Pressure = 0.1 to 2.2 MPa j_g = 4.43 to 55.4 m/s j_ℓ = 0.221 to 1.772 m/s
Cavarolo[C-22]	Argon-water and argon-ethyl alcohol Round tube, D_i = 0.025 m L = 3.0 m	Pressure = 0.1 to 2.2 MPa j_g = 0.693 to 26.32 m/s j_ℓ = 0.075 to 2.063 m/s

APPENDIX D

DERIVATION OF THE ISENTROPIC SOUND SPEED AS A FUNCTION OF PRESSURE AND TEMPERATURE FOR A SINGLE-COMPONENT, SINGLE-PHASE SUBSTANCE

APPENDIX D

DERIVATION OF THE ISENTROPIC SOUND SPEED AS A FUNCTION OF PRESSURE AND TEMPERATURE FOR A SINGLE-COMPONENT, SINGLE-PHASE SUBSTANCE

To begin, let us consider the following expressions for the differential change in entropy.

$$ds = C_v \frac{dT}{T} + \left.\frac{\partial P}{\partial T}\right|_\rho \frac{-d\rho}{\rho^2} \tag{D-1}$$

and

$$ds = C_p \frac{dT}{T} + \left.\frac{1}{\rho^2}\frac{\partial \rho}{\partial T}\right|_\rho dp \ . \tag{D-2}$$

For isentropic systems, ds = 0, so

$$C_v = \frac{T}{\rho^2}\left(\frac{\partial P}{\partial T}\right)_\rho \left(\frac{\partial \rho}{\partial T}\right)_s \tag{D-3}$$

and

$$C_p = \frac{-T}{\rho^2}\left(\frac{\partial \rho}{\partial T}\right)_\rho \left(\frac{\partial P}{\partial T}\right)_s \ . \tag{D-4}$$

Thus,

$$\frac{C_v}{C_p} = \frac{-\left(\frac{\partial P}{\partial T}\right)_\rho \left(\frac{\partial \rho}{\partial T}\right)_s}{\left(\frac{\partial \rho}{\partial T}\right)_p \left(\frac{\partial P}{\partial T}\right)_s} \ . \tag{D-5}$$

From the cyclical relationships,

$$\left(\frac{\partial P}{\partial T}\right)_\rho \left(\frac{\partial T}{\partial \rho}\right)_p \left(\frac{\partial \rho}{\partial P}\right)_T = -1 \tag{D-6}$$

also

$$\left[\left(\frac{\partial T}{\partial \rho}\right)\left(\frac{\partial P}{\partial T}\right)\right]_s = \left(\frac{\partial P}{\partial \rho}\right)_s . \tag{D-7}$$

Therefore, substituting gives

$$\frac{C_v}{C_p} = \frac{\left(\frac{\partial \rho}{\partial P}\right)_s}{\left(\frac{\partial \rho}{\partial P}\right)_T} . \tag{D-8}$$

This means that calculating C_v and C_p is sufficient to specify $\left(\frac{\partial \rho}{\partial P}\right)_s$.

Now, for any gaseous substance,

$$C_p - C_v = \frac{T\left(\frac{\partial \rho}{\partial T}\right)_p^2}{\rho^2\left(\frac{\partial \rho}{\partial P}\right)_T} \tag{D-9}$$

and

$$\frac{C_v}{C_p} = 1 - \frac{T\left(\frac{\partial \rho}{\partial T}\right)_p^2}{\rho^2\left(\frac{\partial \rho}{\partial P}\right)_T\left[\left(\frac{\partial e}{\partial T}\right)_\rho - \frac{P}{\rho^2}\left(\frac{\partial \rho}{\partial T}\right)_\rho\right]} . \tag{D-10}$$

The isentropic sound speed is then

$$\left(\frac{\partial P}{\partial \rho}\right)_s^{1/2} = \left\{\left(\frac{\partial \rho}{\partial P}\right)_T - \frac{T\left(\frac{\partial \rho}{\partial T}\right)_p^2}{\rho^2\left[\left(\frac{\partial e}{\partial T}\right)_\rho - \frac{P}{\rho^2}\left(\frac{\partial \rho}{\partial T}\right)_\rho\right]}\right\}^{-1/2} . \tag{D-11}$$

Appendix E

Derivation of the Two-Phase, Two-Component HEM Sonic Velocity

APPENDIX E

DERIVATION OF THE TWO-PHASE, TWO-COMPONENT HEM SONIC VELOCITY

Following the analysis of Ransom, the sonic velocity for a homogeneous equilibrium mixture is given as

$$a = \left(\frac{\partial P}{\partial \rho}\right)^{1/2} . \tag{E-1}$$

Assuming that one phase is a steam-liquid mixture and the other is an imiscible component such that the gaseous phase is a Gibbs-Dalton mixture, the density of the mixture may be expressed as

$$\rho = \alpha(\rho_g + \rho_{NC}) + (1 - \alpha)\rho_\ell . \tag{E-2}$$

Taking the derivative of this mixture density with respect to pressure at constant entropy gives

$$\left(\frac{\partial \rho}{\partial P}\right)_s = \alpha\left(\frac{\partial \rho_g}{\partial P}\right)_s + \alpha\left(\frac{\partial \rho_{NC}}{\partial P}\right)_s + (1 - \alpha)\left(\frac{\partial \rho_\ell}{\partial P}\right)_s + (\rho_g + \rho_{NC} - \rho_\ell)\left(\frac{\partial \alpha}{\partial P}\right)_s . \tag{E-3}$$

To evaluate $\left(\frac{\partial \alpha}{\partial P}\right)_s$, consider the mixture specific entropy,

$$S = X_g S_g + X_{NC} S_{NC} + (1 - X_g - X_{NC}) S_\ell \tag{E-4}$$

where

$$X_g = \frac{\alpha \rho_g}{\rho} \tag{E-5}$$

$$X_{NC} = \frac{\alpha \rho_{NC}}{\rho} . \tag{E-6}$$

In an isentropic system,

$$\left(\frac{\partial S}{\partial P}\right)_s = 0 = X_{NC}\left(\frac{\partial S_{NC}}{\partial P}\right)_s + X_g\left(\frac{\partial S_g}{\partial P}\right)_s + (1 - X_{NC} - X_g)\left(\frac{\partial S_\ell}{\partial P}\right)_s + (S_g - S_\ell)\left(\frac{\partial X_g}{\partial P}\right)_s + (S_{NC} - S_\ell)\left(\frac{\partial X_{NC}}{\partial P}\right)_s . \quad \text{(E-7)}$$

Since the noncondensible is assumed to be immiscible in the liquid-vapor mixture,

$$\left(\frac{\partial X_{NC}}{\partial P}\right)_s = 0 . \quad \text{(E-8)}$$

From Equation (E-5),

$$\left(\frac{\partial X_g}{\partial P}\right)_s = \frac{\alpha}{\rho}\left(\frac{\partial \rho_g}{\partial P}\right)_s + \frac{\rho_g}{\rho}\left(\frac{\partial \alpha}{\partial P}\right)_s - \frac{\alpha\rho_g}{\rho^2}\left(\frac{\partial \rho}{\partial P}\right)_s . \quad \text{(E-9)}$$

If we substitute Equation (E-9) into Equation (E-7) and rearrange terms, we get

$$\left(\frac{\partial \alpha}{\partial P}\right)_s = \frac{\Sigma_1}{\rho_g}(S_g - S_\ell) - \frac{\alpha}{\rho_g}\left(\frac{\partial \rho_g}{\partial P}\right)_s + \frac{\alpha}{\rho}\left(\frac{\partial \rho}{\partial P}\right)_s \quad \text{(E-10)}$$

where

$$\Sigma_1 = -\left[\alpha\rho_{NC}\left(\frac{\partial S_{NC}}{\partial P}\right)_s + \alpha\rho_g\left(\frac{\partial S_g}{\partial P}\right)_s + (1 - \alpha)\rho_\ell\left(\frac{\partial S_\ell}{\partial P}\right)_s\right] . \quad \text{(E-11)}$$

If Equation (E-11) is substituted into Equation (E-3), we have

$$\left[1 - \alpha\left(\frac{\rho_{NC} + \rho_g - \rho_\ell}{\rho}\right)\right]\left(\frac{\partial \rho}{\partial P}\right)_s = \alpha\left[1 - \left(\frac{\rho_g + \rho_{NC} - \rho_\ell}{\rho_g}\right)\right]\left(\frac{\partial \rho_g}{\partial P}\right)_s + \alpha\left(\frac{\partial \rho_{NC}}{\partial P}\right)_s + (1 - \alpha)\left(\frac{\partial \rho_\ell}{\partial P}\right)_s + \Sigma_2 \quad \text{(E-12)}$$

where

$$\Sigma_2 = \frac{(\rho_g + \rho_{NC} - \rho_\ell)\Sigma_1}{\rho_g(S_g - S_\ell)} \tag{E-13}$$

so that

$$\left(\frac{\partial \rho}{\partial P}\right)_s = \frac{\rho}{\rho_g \rho_\ell}\left[\alpha\rho_g\left(\frac{\partial \rho_{NC}}{\partial P}\right)_s + \alpha(\rho_\ell - \rho_{NC})\left(\frac{\partial \rho_g}{\partial P}\right)_s \rho_g(1-\alpha)\left(\frac{\partial \rho_\ell}{\partial P}\right)_s + (\rho_{NC} + \rho_g - \rho_\ell)\Sigma_1\right] . \tag{E-14}$$

Having defined an expression for $\left(\frac{\partial \rho}{\partial P}\right)_s$, the next step is to define the property derivatives. Recall that the thermodynamic variables are defined as

$$f_{NC} = f_{NC}(P_{NC}, T) \tag{E-15}$$

$$f_g = f_g(P_g, T) \tag{E-16}$$

and

$$f_\ell = f_\ell(P, T) \tag{E-17}$$

where

$$P = P_{NC} + P_g \tag{E-18}$$

since we are dealing with a Gibbs-Dalton mixture. The result of this is that

$$\left(\frac{\partial P_{NC}}{\partial P}\right)_s = 1 - \left(\frac{\partial P_g}{\partial T}\right)\left(\frac{\partial T}{\partial P}\right)_s \tag{E-19}$$

and

$$\left(\frac{\partial P_g}{\partial P}\right)_s = \left(\frac{\partial P_g}{\partial T}\right)\left(\frac{\partial T}{\partial P}\right)_s \quad . \tag{E-20}$$

Here, the assumption has been made that the equilibrium partial steam pressure is that which corresponds to the equilibrium temperature. Thus,

$$P_g = P_g(T) \quad . \tag{E-21}$$

From this knowledge, the basic derivative properties may be defined as from the chain rule as

$$\left(\frac{\partial \rho_{NC}}{\partial P}\right)_s = \left(\frac{\partial \rho_{NC}}{\partial P_{NC}}\right)_T + \left[\left(\frac{\partial \rho_{NC}}{\partial T}\right)_{P_{NC}} - \left(\frac{\partial \rho_A}{\partial P_A}\right)_T\left(\frac{\partial P_g}{\partial T}\right)\right]\left(\frac{\partial T}{\partial \rho}\right)_s \tag{E-22}$$

$$\left(\frac{\partial \rho_g}{\partial P}\right)_s = \left[\left(\frac{\partial \rho_g}{\partial \rho_s}\right)_T\left(\frac{\partial P_g}{\partial T}\right) + \left(\frac{\partial \rho_g}{\partial T}\right)_{P_g}\right]\left(\frac{\partial T}{\partial \rho}\right)_s \tag{E-23}$$

$$\left(\frac{\partial \rho_\ell}{\partial P}\right)_s = \left(\frac{\partial \rho_\ell}{\partial P}\right)_T + \left(\frac{\partial \rho_\ell}{\partial T}\right)_{P_\ell}\left(\frac{\partial T}{\partial P}\right)_s \tag{E-24}$$

$$\left(\frac{\partial S_{NC}}{\partial P}\right)_s = \frac{1}{\rho_{NC}^2}\left(\frac{\partial \rho_{NC}}{\partial T}\right)_{P_{NC}} + \left[\frac{C_{P_{NC}}}{T} - \frac{1}{\rho_{NC}^2}\left(\frac{\partial \rho_{NC}}{\partial T}\right)_{P_{NC}}\left(\frac{\partial P_g}{\partial T}\right)\right]\left(\frac{\partial T}{\partial \rho}\right)_s \tag{E-25}$$

$$\left(\frac{\partial S_g}{\partial P}\right)_s = \left[\frac{C_{P_g}}{T} + \frac{1}{\rho_g^2}\left(\frac{\partial \rho_g}{\partial T}\right)_{P_g}\left(\frac{\partial P_g}{\partial T}\right)\right]\left(\frac{\partial T}{\partial \rho}\right)_s \tag{E-26}$$

$$\left(\frac{\partial S_\ell}{\partial P}\right)_s = \frac{1}{\rho_\ell^2}\left(\frac{\partial \rho_\ell}{\partial T}\right)_p + \frac{C_{P_\ell}}{T}\left(\frac{\partial T}{\partial P}\right)_s \tag{E-27}$$

where

$$C_{P_{NC}} = \left(\frac{\partial e_{NC}}{\partial T}\right)_{P_{NC}} - \frac{P_{NC}}{\rho_{NC}^2}\left(\frac{\partial \rho_{NC}}{\partial T}\right)_{P_{NC}} \tag{E-28}$$

$$C_{P_g} = \left(\frac{\partial e_g}{\partial T}\right)_{P_g} - \frac{P_g}{\rho_g^2}\left(\frac{\partial \rho_{NC}}{\partial T}\right)_{P_g} \tag{E-29}$$

$$C_{P_\ell} = \left(\frac{\partial e_\ell}{\partial T}\right)_{P_\ell} - \frac{P_\ell}{\rho_\ell^2}\left(\frac{\partial \rho_\ell}{\partial T}\right)_{P_\ell} . \tag{E-30}$$

This leaves the specification of $\left(\frac{\partial T}{\partial P}\right)_s$. To this, consider the identity

$$X_{NC}\rho_g = X_g\rho_{NC} . \tag{E-31}$$

Differentiating with respect to pressure gives

$$X_{NC}\left(\frac{\partial \rho_g}{\partial P}\right)_s = X_g\left(\frac{\partial \rho_{NC}}{\partial P}\right)_s + \rho_{NC}\left(\frac{\partial X_g}{\partial P}\right)_s . \tag{E-32}$$

Using the result from Equation (E-7) gives

$$X_{NC}\left(\frac{\partial \rho_g}{\partial P}\right)_s = X_g\left(\frac{\partial \rho_{NC}}{\partial P}\right)_s - \frac{\rho_{NC}}{S_g - S_\ell} \left[X_{NC}\left(\frac{\partial S_{NC}}{\partial P}\right)_s + X_g\left(\frac{\partial S_{NC}}{\partial P}\right)_s + (1 - X_{NC} - X_g)\left(\frac{\partial S_\ell}{\partial P}\right)_s\right] . \tag{E-33}$$

Substituting the relations defined above,

$$\alpha\rho_{NC}\left(\frac{-\partial \rho_g}{\partial T} + \frac{\partial \rho_g}{\partial P_g}\frac{\partial P_g}{\partial T}\right)\left(\frac{\partial T}{\partial P}\right)_s = \alpha\rho_g\left[\frac{\partial \rho_{NC}}{\partial P_{NC}} + \left(\frac{\partial \rho_{NC}}{\partial T} - \frac{\partial \rho_{NC}}{\partial P_{NC}}\frac{\partial P_g}{\partial T}\right)\left(\frac{\partial T}{\partial P}\right)_s\right]$$

$$- \frac{\rho_{NC}}{S_g - S_\ell} \left\{ \alpha \rho_{NC} \left[\frac{1}{\rho_{NC}^2} \frac{\partial \rho_{NC}}{\partial T} + \left(\frac{C_{P_{NC}}}{T} - \frac{1}{\rho_{NC}^2} \frac{\partial \rho_{NC}}{\partial T} \frac{\partial P_g}{\partial T} \right) \left(\frac{\partial T}{\partial P} \right)_s \right] \right.$$

$$\left. + \alpha \rho_g \left[\frac{C_{P_g}}{T} + \frac{1}{\rho_g^2} \frac{\partial \rho_g}{\partial T} \frac{\partial P_g}{\partial T} \right] \left(\frac{\partial T}{\partial P} \right)_s + (1 - \alpha) \rho_\ell \left[\frac{1}{\rho_\ell^2} \frac{\partial \rho_\ell}{\partial T} + \frac{C_{P_\ell}}{T} \left(\frac{\partial T}{\partial P} \right)_s \right] \right\} . \quad \text{(E-34)}$$

Solving for $\left(\frac{\partial T}{\partial P} \right)_s$ then gives the result

$$\left(\frac{\partial T}{\partial P} \right)_s = \left[\alpha \rho_g \frac{\partial \rho_{NC}}{\partial P_{NC}} - \frac{1}{S_g - S_\ell} \left(\alpha \frac{\partial \rho_{NC}}{\partial T} + \frac{(1 - \alpha) \rho_{NC}}{\rho_\ell} \frac{\partial \rho_\ell}{\partial T} \right) \right]$$

$$\left\{ \alpha \rho_{NC} \left(\frac{\partial \rho_g}{\partial P_{NC}} \frac{\partial P_g}{\partial T} - \frac{\partial \rho_g}{\partial T} \right) + \alpha \rho_g \left(\frac{\partial \rho_{NC}}{\partial P_{NC}} \frac{\partial P_g}{\partial T} - \frac{\partial \rho_{NC}}{\partial T} \right) \right.$$

$$+ \frac{1}{S_s - S_\ell} \left[\alpha \left(\frac{\rho_{NC}^2 C_{P_{NC}}}{T} - \frac{\partial \rho_{NC}}{\partial T} \frac{\partial P_g}{\partial T} \right) \right.$$

$$\left. \left. + \alpha \left(\rho_{NC} \rho_g \frac{C_{P_g}}{T} + \frac{\rho_{NC}^2}{\rho_g} \frac{\partial \rho_g}{\partial T} \frac{\partial P_g}{\partial T} \right) + (1 - \alpha) \rho_{NC} \rho_\ell \frac{C_{P_\ell}}{T} \right] \right\} . \quad \text{(E-35)}$$

Finally, at saturation conditions, this Clasius-Clapyron equation gives

$$\frac{\partial P_g}{\partial T} = \left(\frac{S_g(P_g, T) - S_\ell(P_g, T)}{\rho_\ell(P_g, T) - \rho_g(P_g, T)} \right) \rho_\ell(P_g, T) \rho_g(P_g, T) . \quad \text{(E-36)}$$

Assuming that the approximation is valid in the presence of a NC gas,

$$\left(\frac{S_g(P_g,T) - S_\ell(P_g,T)}{\rho_\ell(P,T) - \rho_g(P_g,T)}\right)\rho_\ell(P,T) = \left(\frac{S_g(P_g,T) - S_\ell(P_g,T)}{\rho_\ell(P_g,T) - \rho_s(P_g,T)}\right)\rho_\ell(P_g,T) \tag{E-37}$$

allows for $(S_g - S_\ell)$ to be expressed as

$$S_g - S_\ell = \frac{\partial P_s}{\partial T}\frac{\rho_\ell - \rho_g}{\rho_\ell \rho_g} \; . \tag{E-39}$$

Equations (E-5), (E-7), and (E-8) thus provide complete closure for the two-phase, two-component HEM sonic velocity. It is interesting to examine the limit of no air in $\rho_A \to 0$. In this case,

$$\lim_{\rho_{NC}\to 0}\left(\frac{\partial T}{\partial P}\right)_s = \left(\frac{\partial P_g}{\partial T}\right)^{-1} \tag{E-39}$$

and

$$\lim_{\rho_{NC}\to 0}\left(\frac{\partial \rho}{\partial P}\right)_s = \frac{\rho}{\rho_\ell \rho_g}\left\{\alpha\rho_\ell\left(\frac{\partial \rho_g}{\partial P}\right)_s + (1-\alpha)\rho_g\left(\frac{\partial \rho_\ell}{\partial P}\right)_s - \frac{\rho_g - \rho_\ell}{S_g - S_\ell}\left[\alpha\rho_g\left(\frac{\partial S_g}{\partial P}\right)_s + (1-\alpha)\rho_\ell\left(\frac{\partial S_\ell}{\partial P}\right)_s\right]\right\} \; . \tag{E-40}$$

This result is in agreement with that prescribed by Free and Spore in the original choking model.

Appendix F

Derivation of the Drift Flux Equation

APPENDIX F

DERIVATION OF THE DRIFT FLUX EQUATION

The basic definitions of the drift flux formulation of two-phase flow were given in Section 6.1 of this report. However, for a quick reference, a simple derivation of Equation (7.3-4) is given below.

According to the definitions given by Wallis (see Chapters 1 and 4 of Reference F-1), the overall volumetric flow equation for vapor and liquid may be written as

$$\frac{Q_g}{\alpha A} = C_o \frac{Q_\ell + Q_g}{A} + \frac{J_{g\ell}}{\alpha} \tag{F-1}$$

where Q_g and Q_ℓ are the total volumetric flow rates of vapor and liquid, respectively, α is the vapor volume fraction, A is the total flow area, and C_o is the distribution parameter defined by

$$C_o = \frac{\frac{1}{A}\int \alpha^2 J \, dA}{\left(\frac{1}{A}\int \alpha \, dA\right)\frac{1}{A}\int \alpha J \, dA} \tag{F-2}$$

in which, according to definitions (see Chapter 1 of Reference F-1),

$$J = J_g + J_\ell \tag{F-3}$$

$$J_g = \frac{Q_g}{A} = \frac{1}{A}\int \alpha V_g \, dA \tag{F-4}$$

$$J_\ell = \frac{Q_\ell}{A} = \frac{1}{A}\int (1 - \alpha) V_\ell \, dA \tag{F-5}$$

and

$$J_{g\ell} = \alpha(1 - \alpha)\frac{Q_g - Q_\ell}{A} = \alpha(1 - \alpha)(J_g - J_\ell) \tag{F-6}$$

$$V_{gj} = V_g - (J_g + J_\ell) = (1 - \alpha)(V_g - V_\ell) \quad . \tag{F-7}$$

Substituting $J_{g\ell}$ in Equation (F-1) by Equation (F-3), eliminating Q_g and Q_ℓ between these relations, and using V_{gj} instead of $(1 - \alpha)(V_g - V_\ell)$ converts Equation (F-1) into the following form:

$$\frac{J_g}{\alpha} = C_o(J_g + J_\ell) + V_{gj} \quad . \tag{F-9}$$

This equation may be rearranged to give Equation (7.3-4) that reads

$$J_g = \frac{\alpha C_o}{1 - \alpha C_o} J_\ell + \frac{\alpha}{1 - \alpha C_o} V_{gj} \quad . \tag{F-9}$$

Reference

F-1. G. B. Wallis, *One-Dimensional, Two-Phase Flow*, New York: McGraw-Hill Book Company, 1969, pp. 336-345.

Appendix G

Moving Mesh Reflood Model

APPENDIX G

MOVING MESH REFLOOD MODEL

This model incorporates into TRAC-BF1/MOD1 the moving-mesh reflood core heat transfer model originally developed by the Los Alamos National Laboratory Safety Code Development Group for TRAC-PD2. In addition, a similar moving-mesh upgrade was developed for the CHAN (BWR fuel element component) wall heat transfer. The CHAN wall model tracks both rising and falling quench fronts on the inside and outside of the wall and allows inter-component heat transfer from the outside wall surface to the fluid of an outside component.

These models were originally documented in the following EG&G internal report: C. M. Mohr, *Moving Mesh Reflood Heat Transfer Model*, IS-NSMD-83-013, May 1983.

G-1. NOMENCLATURE

C_p	Specific heat (J/kg·K)
h_ℓ, h_v	Liquid and vapor heat transfer coefficients (W/m^2·K)
$\bar{h}_\ell$, $\bar{h}_v$	Average liquid and vapor heat transfer coefficients (W/m^2·K)
k, k_i	Thermal conductivity (W/m·K)
ℓ_j	Axial level of outside component associated with wall node j
QPPP	Volumetric heat source in channel wall (W/m^3)
QRAD	Surface heat flux on inside channel wall due to radiation (W/m^2)
QTOT	Total heat flux to a wall node or fluid cell (W/m^2)
r_i	Rod radius at node i (m)
T_ℓ, T_v	Fluid cell liquid and vapor temperatures (K)
T_j, TW_j	Local and average wall surface temperature at node j (K)
Δt	Time step size (s)
W.P.	Wetted perimeter of heat transfer surface (wall or rods) (m)

X	Fraction of node rewetted
$X_{f,j}$	Overlap fraction of wall node j on outer cell ℓ_j
Δx	Radial node spacing in wall (m)
Z_j	Elevation of node row j (m)
ZQF	Elevation of quench front (m)
α_k	Void fraction in fluid cell k
ρ	Wall or rod local density (kg/m^3)
δ_m, δ_p, δ_u, δ_ℓ	Flag for node location at inside, outside, top, and bottom of CHAN wall (=1 if located there, =0 otherwise)

G-2. MODEL REQUIREMENTS

The fuel rod and channel wall models are discussed in this section.

G-2.1 FUEL ROD MODEL (TRAC-PD2 REFLOOD MODEL)

The original reflood fine-mesh model in TRAC-BD1 had the following features:

1. A fixed fine-mesh array, with node locations input at the start of reflood and kept throughout the rest of the transient.

2. The same fine-mesh spacing for each rod group.

These features limited code efficiency, since fine-mesh nodes cannot be clustered about a moving quench front without so nodalizing the whole rod, causing excessive heat transfer calculations in regions of the rod (far from the quench front) where they are not needed. In order to eliminate this problem and still permit fine nodalization where needed, a moving-mesh reflood model developed at Los Alamos National Laboratory for TRAC-PD2 was adapted for use in the TRAC-BF1/MOD1 code.

G-2.2 CHANNEL WALL MODEL

The same limitations that applied to the original TRAC-BD1 fuel rod model applied to the channel wall quench model as well. In addition:

1. Falling-film and bottom-flood quench fronts were not tracked on the outside of the CHAN wall.

2. Each node in the CHAN wall could transfer heat to only one outer component cell.

3. The heat transfer regimes permitted on the outside of the channel wall were restricted.

The present model addresses these limitations by:

1. Tracking quench fronts on the outside of the channel wall.

2. Partitioning heat transfer from a node according to the wall area associated with each outer cell.

3. Allowing a full range of heat transfer modes on the outside of the channel wall.

The scheme followed for the CHAN wall fine-mesh model closely follows that used for the rod model.

G-3. MODEL DESIGN

Models for heat transfer from the fuel rod surface, heat conduction within the rod, heat transfer from inner and outer walls of the channel, and heat conduction within the channel are described in this section.

G-3.1 FUEL ROD-SURFACE HEAT TRANSFER MODEL

In the original TRAC-BD1 fuel rod model, heat transfer coarse-mesh nodes were centered in the hydrodynamic cell, as shown in Figure G-1, which depicts a typical fuel rod and several associated hydrodynamic cells. When the reflood fine-mesh model is invoked, each coarse-mesh node is divided into n equal-length fine-mesh nodes ("n" is user-input for each coarse-mesh row), as shown in Figure G-2, where the coarse-mesh node has been divided into five fine-mesh nodes. In neither instance does a fuel rod heat transfer node overlap two adjacent hydrodynamic cells. The new model, however, places the coarse-mesh nodes at hydrodynamic cell boundaries, where each transfers heat into two hydrodynamic cells, as shown in Figure G-3. The upper and lower elevations of each node are taken as the midpoints between the center node and the nodes above and below. In order to maintain equality between the heat transfer out of the wall nodes and the heat received by the fluid cells, average heat transfer coefficients (and associated wall or fluid temperature) must be defined for each fluid cell and each fuel rod node. Figure G-4 shows portions of three fluid cells and two associated coarse-mesh nodes. Note that

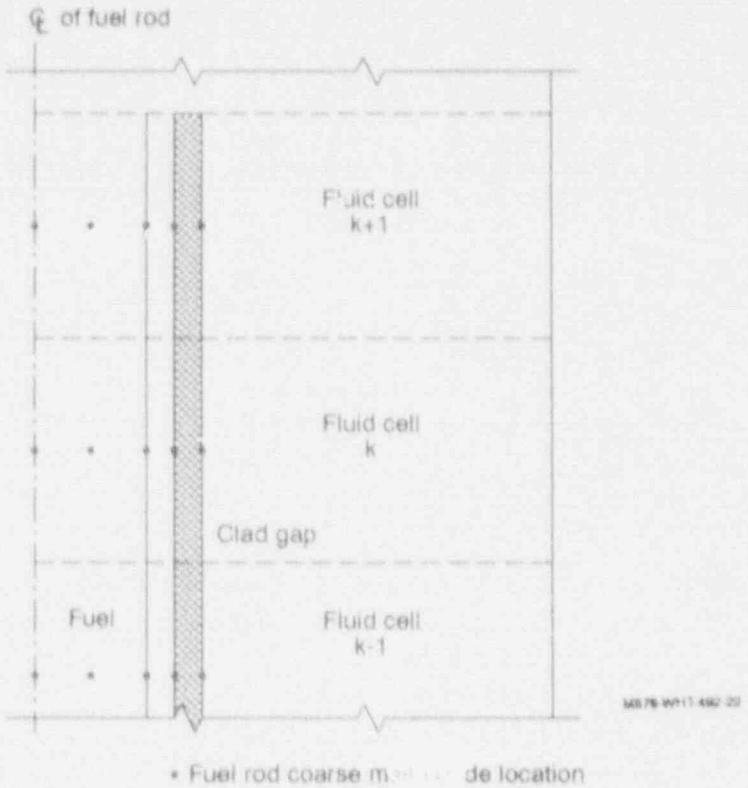

Figure G-1. Previous fuel rod coarse-mesh nodalization.

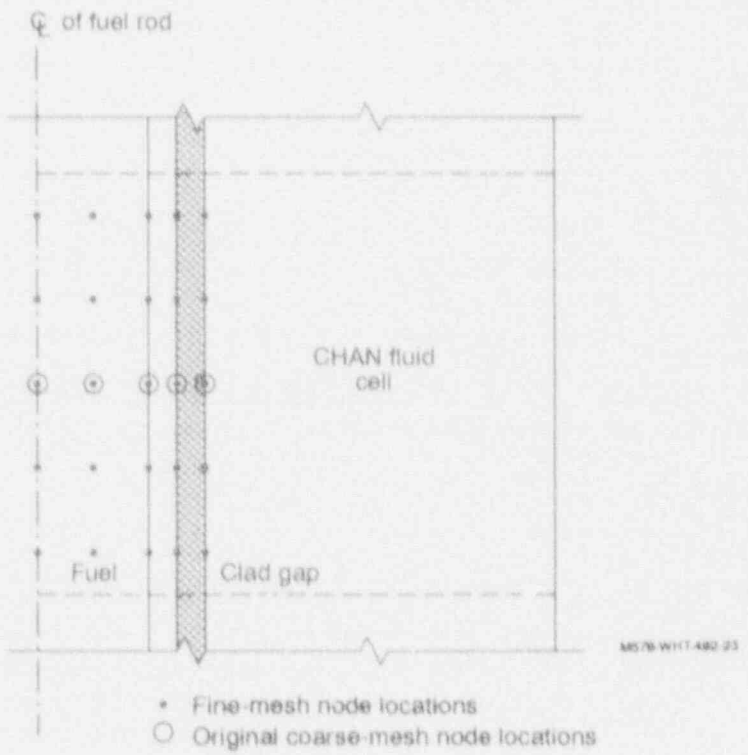

Figure G-2. Previous fuel rod fine-mesh nodalization.

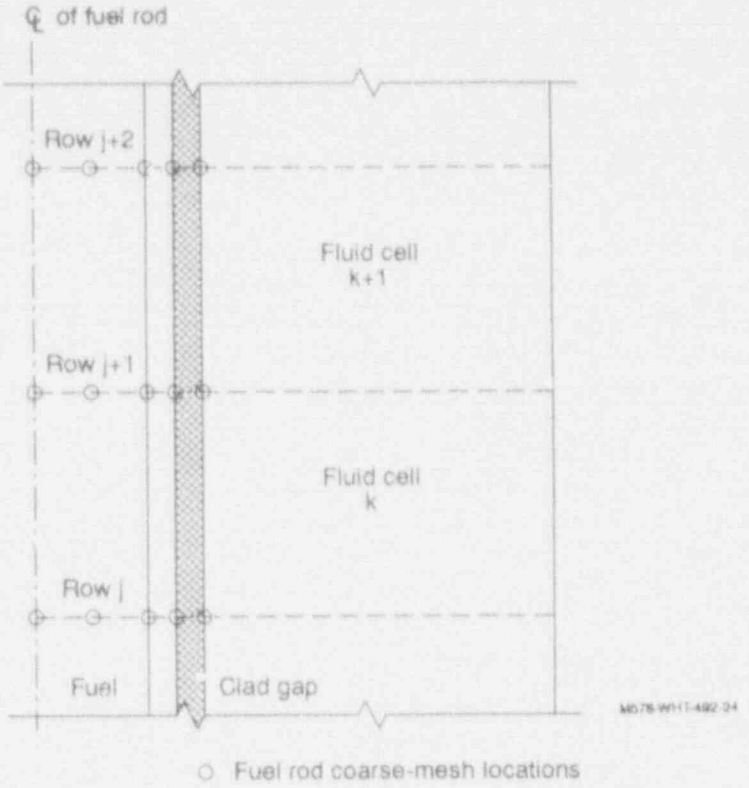

Figure G-3. Revised fuel rod coarse-mesh nodalization.

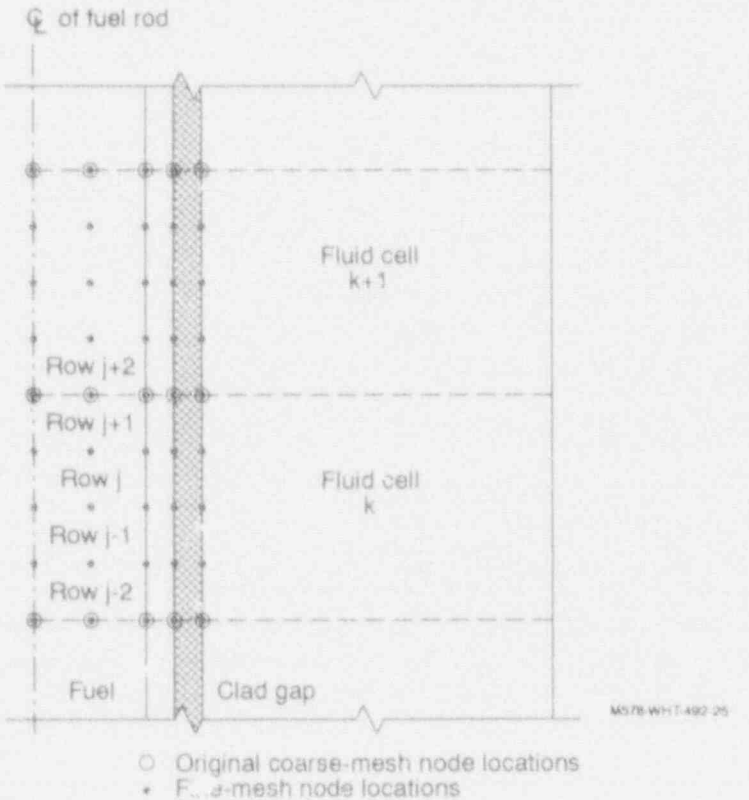

Figure G-4. Revised fuel rod fine-mesh nodalization.

each coarse-mesh node transfers heat to two fluid cells. For the situation shown in Figure G-3, the total heat transfer to liquid in fluid cell k is

$$Q_{TOT,\ell,k} = W.P. \left[Z_{j+1} - \frac{1}{2}(Z_{j+1} + Z_j) \right] h_{\ell,j+1\to k}(TW_{j+1} - T_{\ell,k})$$

$$+ W.P. \left[\frac{1}{2}(Z_{j+1} + Z_j) - Z_j \right] h_{\ell,j\to k}(TW_j - T_{\ell,k}) \quad . \tag{G-1}$$

We define an appropriate average wall temperature and heat transfer coefficient as follows:

$$\hat{T}W_{\ell,k} = \frac{\frac{1}{2}(Z_{j+1} - Z_j)h_{\ell,j+1}TW_{j+1} + \frac{1}{2}(Z_{j+1} - Z_j)h_{\ell,j}TW_j}{\frac{1}{2}(Z_{j+1} - Z_j)h_{\ell,j+1} + \frac{1}{2}(Z_{j+1} - Z_j)h_{\ell,j}} \tag{G-2}$$

$$\hat{h}_{\ell,w\to k} = \frac{\frac{1}{2}(Z_{j+1} - Z_j)h_{\ell,j+1} + \frac{1}{2}(Z_{j+1} - Z_j)h_{\ell,j}}{Z_{j+1} - Z_j} \quad . \tag{G-3}$$

Analogous expressions for vapor TW_v and $h_{v,w\to k}$ may be derived.

Close inspection shows that, indeed,

$$Q_{TOT,\ell,k} = \hat{h}_{\ell,w\to k}\hat{T}W_{\ell,k}(Z_{j+1} - Z_j)W.P. \quad . \tag{G-4}$$

A similar average must be derived for the wall nodes that are in thermal contact with two fluid cells. These averages become more complicated when fine-mesh nodes are introduced, but the general form remains similar.

Another feature unique to the reflood package is the adjustment of the void fraction used in calculating heat transfer coefficients if the quench front is near the node. Referring to Figure G-4, the void fraction, α_j, used at node j is:

$$\bar{\alpha}_j = \begin{cases} \alpha_\ell \text{ when } ZQF > Z_{j+1} \\ \alpha_v \text{ when } ZQF < Z_j \end{cases} \tag{G-5}$$

$$\bar{\alpha}_j = \frac{1}{2}\left[\alpha_k + X\alpha_{k+1} + (1 - X)\alpha_{k-1}\right] \quad \text{(G-6)}$$

where

$$\alpha_L = \frac{1}{2}(\alpha_k + \alpha_{k-1}) \quad \text{(G-7)}$$

$$\alpha_V = \frac{1}{2}(\alpha_{k+1} + \alpha_k) \quad \text{(G-8)}$$

$$X = \frac{Z_{j+1} - ZQF}{Z_{j+1} - Z_j} \quad \text{(G-9)}$$

and ZQF, the elevation of the quench front, is in node j. This adjustment permits a smooth void fraction transition as the quench front moves up in the node.

The model has three distinct types of heat transfer nodes. The coarse-mesh nodes, used before reflood is specified, are centered on fluid cell boundaries as previously illustrated. The fixed fine-mesh nodes are introduced at the beginning of reflood and do not "move." These are similar to the fine-mesh nodes in earlier versions of the code. The user specifies in input how many of these nodes should be introduced between each pair of adjacent coarse-mesh nodes. Finally, the third kind of nodes are the "moving" nodes. The placement of these nodes is up to the computer, subject to limitations imposed by user input. These limitations are:

1. Maximum total number of heat transfer nodes per rod group.

2. Minimum spacing between heat transfer nodes (required for stability).

3. Minimum surface temperature difference between adjacent existing nodes. If this temperature difference is exceeded, the code will attempt to insert another row of fine-mesh nodes between the two nodes that have the excessive temperature difference.

Nodes are inserted in such a manner as to minimize disruption of energy conservation. When rows are deleted, however, the temperatures of the nodes above and below are not adjusted, so that some minor energy loss (or gain) may occur. The algorithm for calculating the temperature of an inserted node is

where ρ_{j-1}, C_{pj-1}, ρ_{j+1}, and C_{pj+1} are the density and specific heat for the nodes below and above the inserted node, and

$$T_j = \frac{\rho_{j-1}C_{pj-1}T_{j-1} + \rho_{j+1}C_{pj+1}T_{j+1}}{2\rho_j C_{pj}} \qquad \text{(G-10)}$$

$$\rho_j = \frac{\rho_{j-1} + \rho_{j+1}}{2} \qquad \text{(G-11)}$$

$$C_{pj} = \frac{C_{pj-1} + C_{pj+1}}{2} \, . \qquad \text{(G-12)}$$

In general, T_j would be very close to 1/2 ($T_{j+1} + T_{j-1}$), and energy conservation should not be seriously violated for addition or deletion of rows of nodes.

Falling film and bottom flood quench fronts are tracked on each rod group. While the previous code versions had an explicit calculation of quench front velocity, this package considers a node quenched whenever the node is in heat transfer mode 1, 2, 3, 11, or 12. The quench front positions are taken as the lowermost consecutive quenched node for the falling film and the uppermost consecutive quenched node for the bottom flood position. While this method could permit isolated patches of quenched nodes, this has not yet been observed in any sample test cases.

G-3.2 FUEL ROD CONDUCTION MODEL

The fuel rod conduction model has two significant differences from that found in previous code versions. First, axial conduction is included in the finite-difference equations. Second, the nodes are defined as centered at material boundaries, and the code calculates and stores special "interface" material properties, which are used in the conduction solutions. Referring to Figure G-5, the finite-difference equation for conduction at an interior node (i,j) is identical to that found in References G-1 and G-2 except that axial conduction is included.

$$\frac{1}{2}(\Delta Z_u + \Delta Z_\ell)\left[\frac{1}{4}(r_i + r_{i+1})^2 - \frac{1}{4}(r_i + r_{i-1})^2\right]\rho_{i,j}C_{pi,j}\frac{T_{i,j}^{n+1} - T_{i,j}^{n}}{\Delta t}$$

$$= [\textit{volumetric source terms}] + [\textit{normal radial conduction terms}]$$

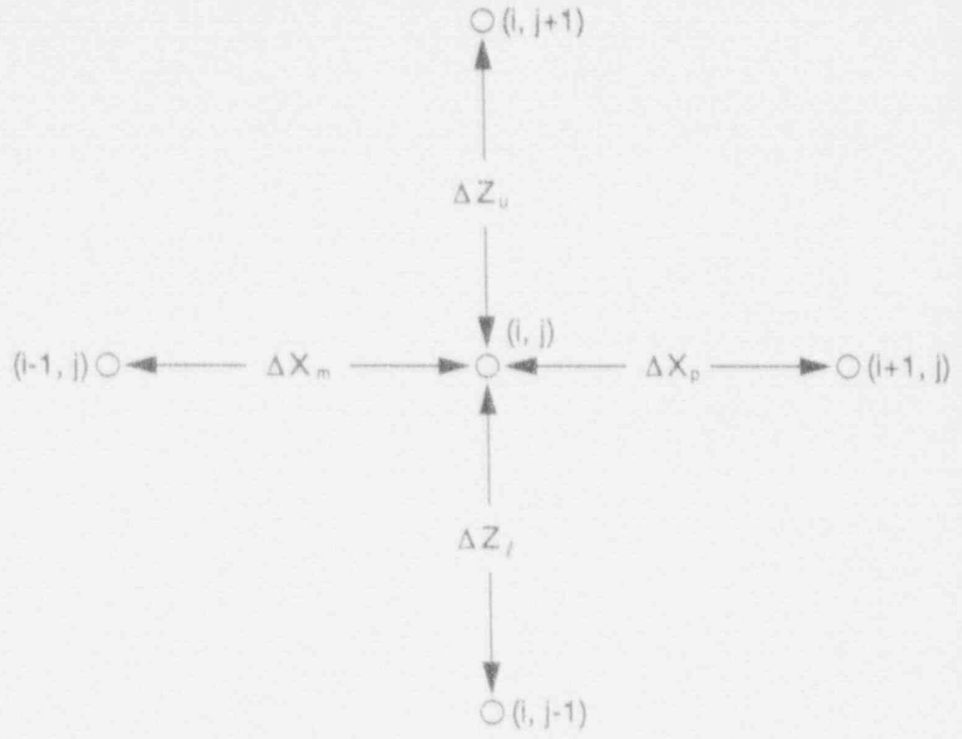

Figure G-5. Nodalization for fuel rod conduction equations.

$$+\left[\frac{1}{4}(r_i + r_{i+1})^2 - \frac{1}{4}(r_i + r_{i-1})^2\right]\left[\frac{1}{2}(k_{i,j+1} + k_{i,j})\frac{T^n_{i,j+1} - T^{n+1}_{i,j}}{\Delta Z_p}\right.$$

$$\left. + \frac{1}{2}(k_{i,j-1} + k_{i,j})\frac{T^n_{i,j-1} - T^{n+1}_{i,j-1}}{\Delta Z_m}\right], \qquad \text{(G-13)}$$

At the top and bottom of the heated length, the axial conduction terms are modified, while at the rod axis, material interfaces, and rod surface, the radial conduction terms are modified (as specified in References G-1 and G-2). Note that for each row of nodes across a rod these finite-difference equations form a tridiagonal system of linear equations in terms of the new-time node temperatures $T^{n+1}_{i-1,j}$, $T^{n+1}_{i,j}$, and $T^{n+1}_{i+1,j}$. These linear systems are solved row by row (ascending the rod) for each rod group. Because the axial conduction terms are explicit, involving old-time te atures $T^n_{i,j-1}$ and $T^n_{i,j+1}$, this row-by-row scheme may be used instead of g for the temperature field for

the whole rod at once, which would require inverting a large (although sparse) matrix (perhaps 200 x 200 or more).

G-3.3 CHANNEL WALL INSIDE SURFACE

The surface heat transfer on the inside of the channel wall is analogous to the rod surface heat transfer. Coarse mesh nodes are located at cell boundaries, and the same temperature and heat-transfer coefficient averaging schemes are used. Volumetric heat sources and radiation are included, and the same method for averaging void fractions near a quench front is employed.

G-3.4 CHANNEL WALL OUTSIDE SURFACE HEAT TRANSFER

The heat transfer situation on the outside of the channel wall is complicated by the fact that the coarse-mesh nodes may not be located at fluid cell boundaries. Previous versions of the code handled this by assuming that all the heat transfer from a wall node went into the fluid cell that overlapped most of the node. The present model partitions the heat transfer according to the fraction of overlap with each fluid cell. The model is limited, however, since it only permits a wall node to contact one or two fluid cells. This places some burden on the user to ensure proper alignment of channel and outside-component cells in order to comply with this rule, but, in general, the restriction is reasonable, since channels are always noded much finer than the surrounding bypass region. Figure G-6 shows several fluid cells (both CHAN and outside component) and associated wall heat transfer nodes (both fine and coarse mesh).

A new variable, X_f, has been defined for each wall node, which is fraction of the node that transfers heat to the lowest outer cell which overlaps. Referring to Figure G-6,

$$(X_f)_{k+1} = \frac{Z_{j-1} - \frac{1}{2}(Z_k + Z_{k+1})}{\frac{1}{2}(Z_{k+2} - Z_k)} \qquad (G\text{-}14)$$

$$(X_j)_{k+2} = 1 \qquad (G\text{-}15)$$

$$(X_j)_{k+3} = 1 \qquad (G\text{-}16)$$

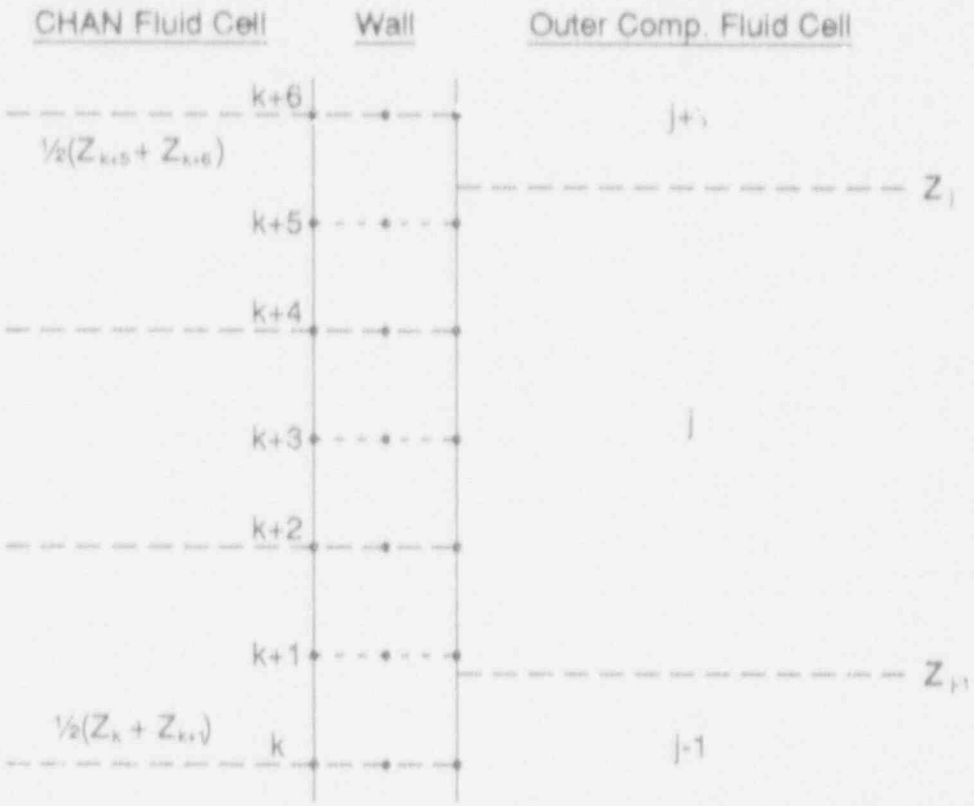

Figure G-6. CHAN wall fine-mesh nodalization scheme and relationship to adjacent fluid cells.

$$(X_j)_{k+4} = 1 \tag{G-17}$$

$$(X_f)_{k+5} = \frac{Z_j - \frac{1}{2}(Z_{k+5} + Z_{k+6})}{\frac{1}{2}(Z_{k+6} - Z_{k+4})} \,. \tag{G-18}$$

Previous code versions contained a variable defined on the fine-mesh nodes that stored the outer component cell number that most overlaps the wall node. This variable has been changed to store the lowest outer component cell that the node overlaps. Combined with X_f and the rule that only two cells may overlap a node, the fraction of each node in contact with each cell is completely defined. However, since this model can add and delete fine-mesh nodes according to the wall temperature profile, these two values need to be

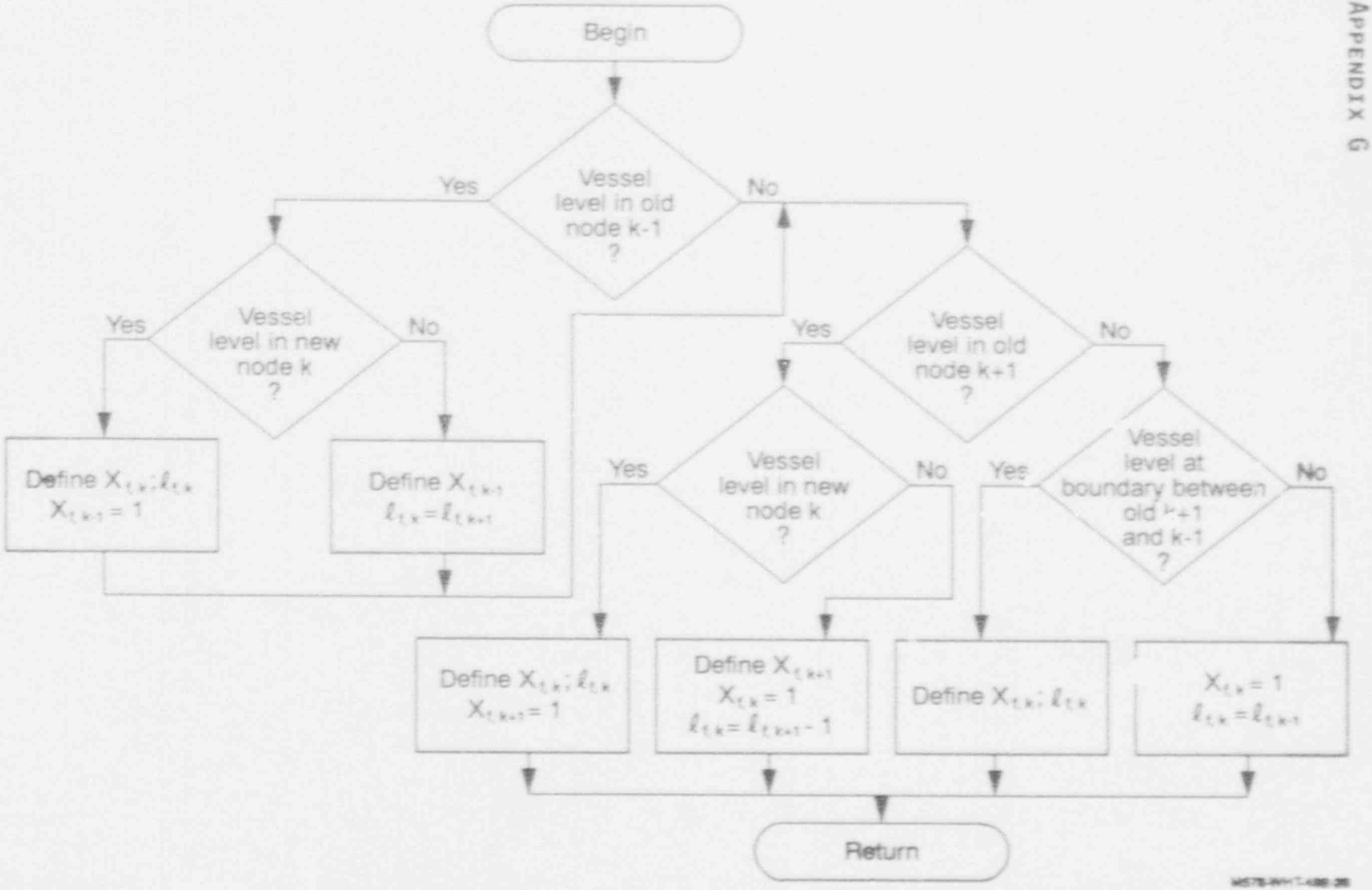

Figure G-7. Logic for addition of a fine-mesh channel wall node and redefinition of node overlap parameters.

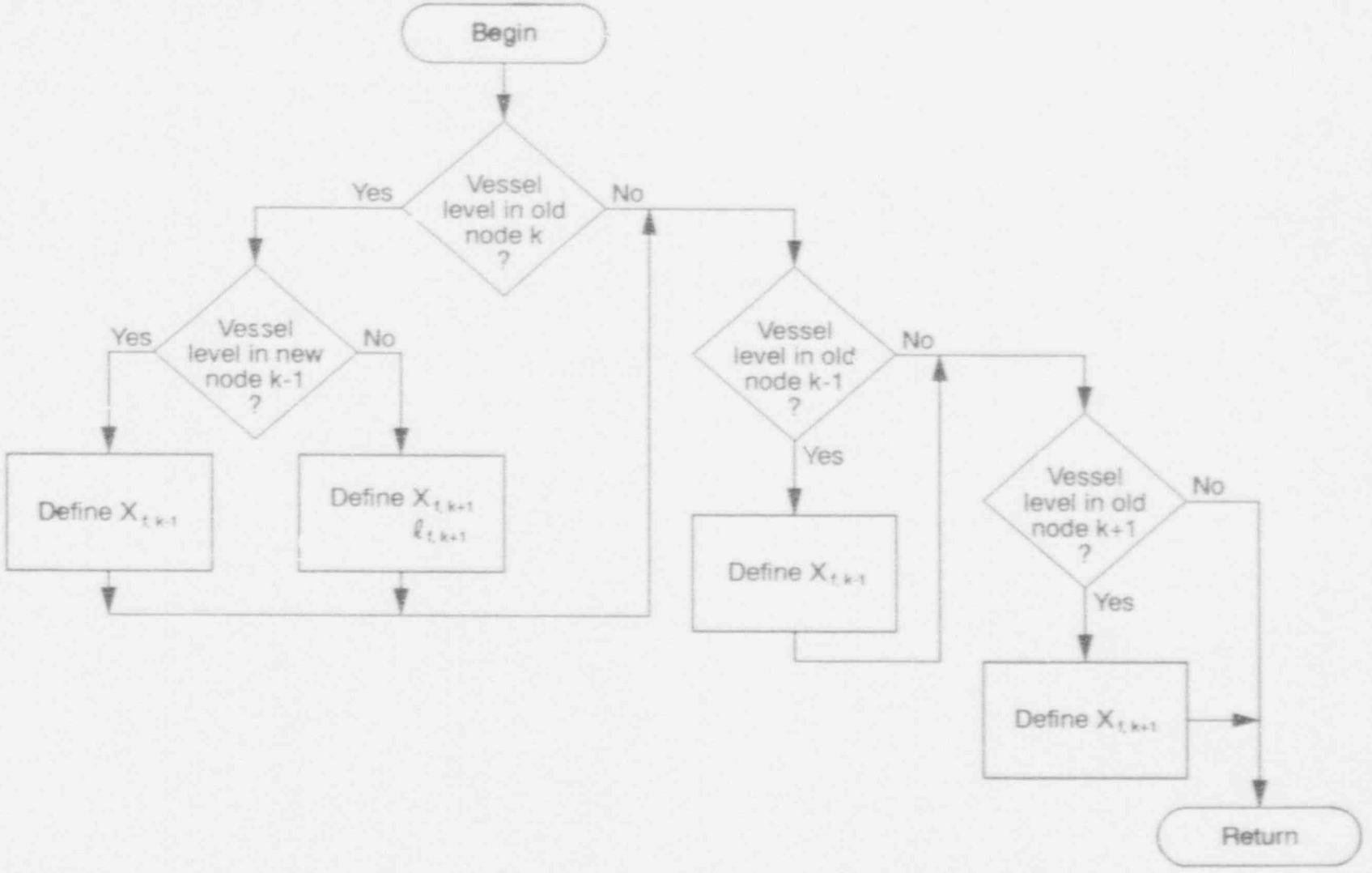

Figure G-8. Logic for removal of a fine-mesh channel wall node and redefinition of node overlap parameters.

redefined each time node spacing is altered. A flow chart showing the logic used for different situations when a node is added is given in Figure G-7. A similar chart for the deletion of a node is given in Figure G-8. When a vessel (or other outer component) cell boundary is near the added or deleted node, the boundary location is determined using the previous X_ℓ's and l_ℓ's, and this information is combined with the new H.T. node boundary elevations to calculate the new Z_ℓ's and l_ℓ's using Equations (G-14) through (G-18).

G-3.5 CHANNEL WALL CONDUCTION

Previous code versions considered the channel wall to be cylindrical, ignored axial conduction, and tracked quench fronts only on the inside surface, using explicit quench-front velocity correlations. This model pictures the channel wall as flat rather than cylindrical, includes axial conduction, calculates quench front locations on the outside of the wall, and omits the explicit calculation of quench front velocity. The quench front location is taken to be the uppermost (r lowermost, for top flood) wetted node, the criteria for wettedness being identical to that for the fuel rod model.

The equation used for the conduction solution is quite similar to Equation (G-13) but is written in Cartesian coordinates. Referring to Figure G-5, the equation is

$$\left[\frac{(1-\delta_m)\Delta X_m + (1-\delta_p)\Delta X_p}{2}\right]\left[\frac{(1-\delta_u)\Delta Z_u + (1-\delta_\ell)\Delta Z_\ell}{2}\right]\rho_{i,j}C_{pi,j}\frac{T^{n+1}_{i,j} - T^{n}_{i,j}}{\Delta t}$$

$$= (1-\delta_u)\left[\frac{(1-\delta_m)\Delta X_m + (1-\delta_p)\Delta X_p}{2\Delta Z_u}\right]k_{i,j+1/2}(T^{n}_{i,j+1} - T^{n+1}_{i,j})$$

$$+ (1-\delta)\left[\frac{(1-\delta_m)\Delta X_m + (1-\delta_p)\Delta X_p}{2\Delta X_\ell}\right]k_{i,j-1/2}(T^{n}_{i,j-1} - T^{n+1}_{i,j})$$

$$+ (1-\delta_p)\left[\frac{(1-\delta_u)\Delta Z_u + (1-\delta_\ell)\Delta Z_\ell}{2\Delta X_p}\right]k_{i+1/2,j}(T^{n+1}_{i,j} - T^{n+1}_{i,j})$$

$$+ (1 - \delta_m) \left[\frac{(1 - \delta_u)\Delta Y_u + (1 - \delta_\ell)\Delta Y_\ell}{2\Delta Y_m} \right] k_{i-1/2,j} (T^{n+1}_{i-1,j} - T^{n+1}_{i,j})$$

$$+ \delta_m \left[h_{m,\ell} (T_{m,\ell} - T^{n+1}_{i,j}) + h_{m,v} (T_{m,r} - T^{n+1}_{i,j}) \right] \left[\frac{(1 - \delta_u)\Delta Y_u + (1 - \delta_\ell)\Delta Y_\ell}{2} \right]$$

$$+ \delta_p \left[h_{p,\ell} (T_{p,\ell} - T^{n+1}_{i,j}) + h_{p,v} (T_{p,v} - T^{n+1}_{i,j}) \right] \left[\frac{(1 - \delta_n)\Delta Y_u + (1 - \delta_\ell)\Delta Y_\ell}{2} \right]$$

$$+ \delta_m \left[\frac{(1 - \delta_n)\Delta Y_u + (1 - \delta_\ell)\Delta Y_\ell}{2} \right] QRAD\ (j)$$

$$+ \left[\frac{(1 - \delta_u)\Delta Y_u + (1 - \delta_\ell)\Delta Y_\ell}{2} \right] \left[\frac{(1 - \delta_m)\Delta Y_m + (1 - \delta_p)\Delta Y_p}{2} \right] QPPP\ (i,j) \qquad \text{(G-19)}$$

where

δ_u = 1 at top nodes, 0 elsewhere

δ_ℓ = 1 at bottom nodes, 0 elsewhere

δ_m = 1 at inside surface nodes, 0 elsewhere

δ_p = 1 at outside surface nodes, 0 elsewhere

$\rho_{i,j}$ = density at node (i,j)

$C_{pi,j}$ = specific heat at node (i,j)

$k_{i,j}$ = conductivity at node (i,j)

$k_{i,j+1/2}$ = 1/2 ($k_{i,j}$ + $k_{i,j+1}$) = average k between nodes

n = old-time value

n+1 = new-time value (being calculated).

The first two terms after the equals sign are the explicit axial conduction terms; the next two terms are the implicit transverse conduction terms; the next two terms are the surface heat transfer terms; the next term is the inner surface radiation term; and the final term is the volumetric heat source term.

G-4. REFERENCES

G-1. J. Spore et al., *TRAC-BD1: An Advanced Best-Estimate Computer Program for Boiling Water Reactor Loss-of-Coolant Accident Analysis*, EGG-2109, NUREG/CR-2178, October 1981.

G-2. Los Alamos National Laboratory Safety Code Development Group, *TRAC-PD2, An Advanced Best Estimate Computer Program for Pressurized Water Reactor Loss-of-Coolant Accident Analysis*, LA-8709-MS, NUREG/CR-2054, April 1981.

APPENDIX H

ANALYTIC NODAL MODEL ROUTINES IN TRAC-BF1/MOD1

APPENDIX H

ANALYTIC NODAL MODEL ROUTINES IN TRAC-BF1/MOD1

This appendix describes the Analytic Nodal Model routines presently employed in the TRAC-BF1/MOD1 code. TRAC-BF1/MOD1 will call three subroutines at various times during reactor simulation.

K1DSS: This is the control routine for steady-state (eigenvalue) calculations. A set of nodal cross sections and the necessary geometry information for the reactor being modeled are input. Output consists of a set of two-group node-averaged fluxes normalized to a user-specified power. These, plus the output global eigenvalue, constitute the solution for the given reactor conditions. Nodal powers and relative power distributions are also output. K1DSS should be used to compute an initial condition for a transient. It can be called repeatedly during the thermal-hydraulics initialization procedure in order to iteratively generate an initial reactor power distribution that is consistent with the initial reactor thermal-hydraulic conditions which, in turn, should be consistent with the initial power distribution.

K1FLUX: The subroutine is called one time, after initial condition nodal fluxes have been determined. K1FLUX initializes the delayed neutron precursor inventories in each node so that they are consistent with the initial flux distribution, assumed to be a steady-state flux distribution. K1FLUX also initializes the power and omega arrays.

K1DTR: This is the control routine for time-dependent calculations. Each time K1DTR is called, the fluxes, powers, omegas, and precursor inventories are advanced forward in time. Input consists of the fluxes, precursor inventories, and their associated omega arrays as they stand at the beginning of a time step, along with a set of nodal cross sections and albedos presumed to exist during Δt_H. Fluxes, powers, omegas, and precursor inventories at the end of Δt_H are output. In addition, the total energy deposited in each node during Δt_H is output. If automatic time step control is requested, K1DTR breaks Δt_H up into subintervals, as described in Section 9.4.3. If automatic time step control is not requested, all data are advanced forward over Δt_H in one step. In addition, if inverse velocity terms equal to zero are detected in the input data, Δt_H is not subdivided, even if automatic time step control is requested. For this reason, caution should be used when running special problems having inverse velocity terms equal to zero.

The three subroutines described above call several other subroutines in order to solve the steady-state and time-dependent equations. These subroutines, shown in Figure H-1, are described below:

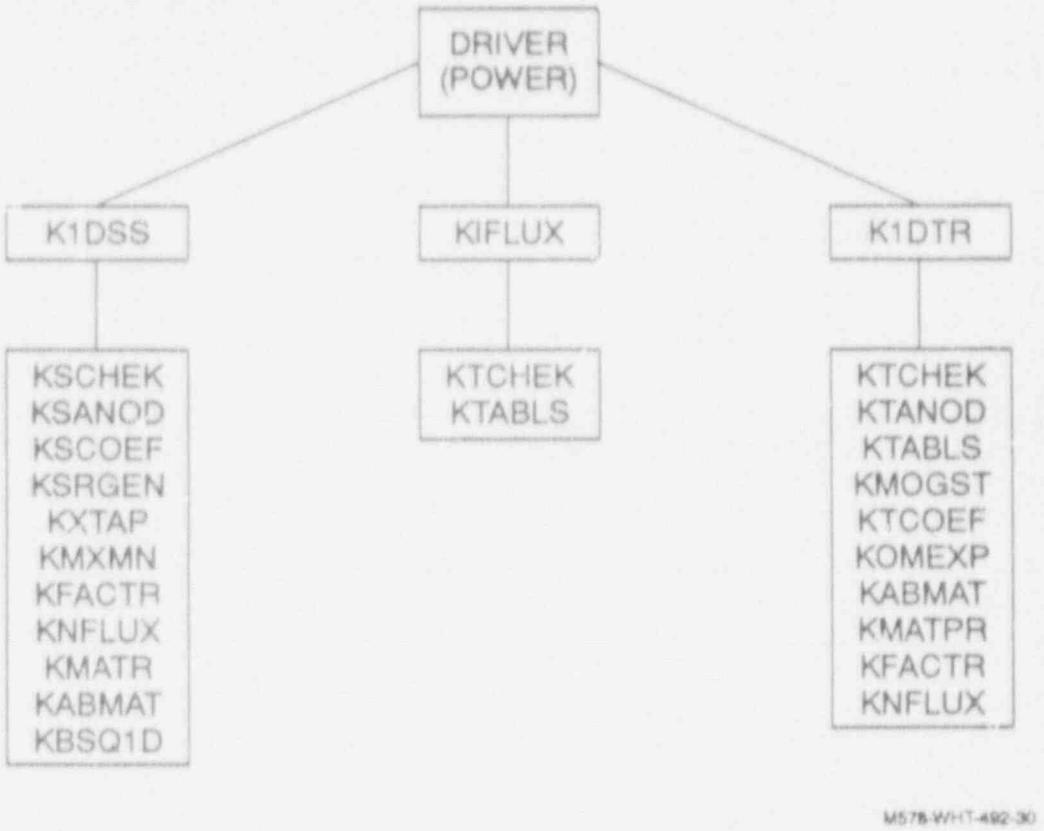

Figure H-1. Subroutine diagram for the TRAC-BF1/MOD1 Analytic Nodal neutronics routines.

KSCHEK: Checks the input steady-state cross section vector fo data that are not physically realistic. Computes nodal k-infinity data. Prepares a printed cross section table if requested.

KSANOD: Solves the steady-state, one-dimensional Analytic Nodal equations using the source iteration method. KSANOD performs outer iterations until the global eigenvalue and the nodal source distribution are converged to some arbitrary criterion. During each outer iteration, the nodal flux vector is computed using Gaussian elimination.

KSCOEF: Assembles the steady-state global nodal coefficient matrix. The non-zero elements of this matrix are returned in three arrays containing, respectively, the below-diagonal terms, the diagonal terms, and the above-diagonal terms.

KSRGEN: Generates a nodal fission source vector for steady-state problems using the latest flux estimate.

EXTAP: Extrapolates the latest nodal source iterate using Chebyshev polynomials, if requested.

KMXMN: Computes source convergence data.

KFACTR: Factors the global nodal coefficient matrix using Gaussian elimination. The below-diagonal elements of the factored matrix are written in elementary form into the same locations where the below-diagonal elements of the unfactored matrix were originally stored.

KNFLUX: Given a factored global nodal coefficient matrix and a global source vector, KNFLUX computes the global flux vector by back-substitution. The input source vector is destroyed.

KMATPR: Performs various submatrix manipulations (multiplication, inversion, etc.) required during assembly of a global nodal coefficient matrix.

KABMAT: Generates the necessary data for each node for use in assembly the global nodal coefficient coupling matrices. For time-dependent problems, these are also used during assembly of the global source vector.

KTCHEK: Checks the input time-dependent cross section vector for data that are not physically realistic. Computes nodal k-infinity and generation time data. Estimates the maximum expected omega if automatic time step control is requested. Prepares a printed cross section table if requested. KTCHEK is called at the beginning of each time step, since, in the general case, the input cross sections will be different for each time step.

KTANOD: Advances the nodal fluxes, powers, precursor inventories and omega data forward over time interval δt_n. δt_n may be a subinterval of the time interval Δt_H input to Subroutine KLDTR. If so, KTANOD is repeatedly called to march across Δt_H. If, as is recommended, an option to compute the delayed portion of the total reactor power separately is included in TRAC-BF1/MOD1 with space-dependent kinetics, this could logically be done in Subroutine KTANOD.

KTABLS: Prints a table of nodal fluxes, powers, and other data whenever called. KTABLS simply edits the current information in the nodal arrays.

KOMGST: KOMGST evaluates the kinetics equation at the beginning of each time step I&tH in order to estimate the maximum expected omega.

KTCOEF: Assembles the global time-dependent nodal coefficient matrix and the global time-dependent nodal source vector. These are input to KFACTR and KNFLUX to step the fluxes forward

KOMEXP: The delayed precursor formulation contains several terms of the form [1-exp(-x)]. This expression is subject to round-off error if x is small. KOMEXP computes [1-exp(-x)] using an x-dependent number of terms of an infinite series in order to avoid round-off error.

KSSQID: Performs one-dimensional thermal buckling search using Crowther's method prior to a steady-state calculation.

NRC FORM 335
(2-89)
NRCM 1102
3201, 3202

U.S. NUCLEAR REGULATORY COMMISSION

BIBLIOGRAPHIC DATA SHEET

(See instructions on the reverse)

1. REPORT NUMBER
(Assigned by NRC, Add Vol., Supp., Rev., and Addendum Numbers, if any.)

NUREG/CR-4391
EGG-2680

2. TITLE AND SUBTITLE

TRAC/BF1-MOD1 Models and Correlations

3. DATE REPORT PUBLISHED

MONTH	YEAR
August	1992

4. FIN OR GRANT NUMBER

L2031

5. AUTHOR(S)

Edited by
J. A. Borkowski, N. L. Wade

Contributing Authors
S. Z. Rouhani, F. W. Shumway, W. L. Weaver, W. H. Rettig*, C. L. Kullberg

6. TYPE OF REPORT

Technical

7. PERIOD COVERED *(Inclusive Dates)*

8. PERFORMING ORGANIZATION — NAME AND ADDRESS *(If NRC, provide Division, Office or Region, U.S. Nuclear Regulatory Commission, and mailing address; if contractor, provide name and mailing address.)*

Idaho National Engineering Laboratory
EG&G Idaho, Inc.
Idaho Falls, ID 83415

*Presently with the
Department of Energy
Idaho Field Office
Idaho Falls, ID 83401

9. SPONSORING ORGANIZATION — NAME AND ADDRESS *(If NRC, type "Same as above"; if contractor, provide NRC Division, Office or Region, U.S. Nuclear Regulatory Commission, and mailing address.)*

Division of Systems Research
Office of Nuclear Regulatory Research
U.S. Nuclear Regulatory Commission
Washington, D.C. 20555

10. SUPPLEMENTARY NOTES

13. ABSTRACT (200 words or less)

The TRAC-BWR code development program at the Idaho National Engineering Laboratory has developed versions of the Transient Reactor Analysis Code (TRAC) for the U.S. Nuclear Regulatory Commission and the public. The TRAC-BF1/MOD1 version of the computer code provides a best-estimate analysis capability for analyzing the full range of postulated accidents in boiling water reactor (BWR) systems and related facilities. This version provides a consistent and unified analysis capability for analyzing all areas of a large- or small-break loss-of-coolant accident (LOCA), beginning with the blowdown phase and continuing through reatup, reflood with quenching, and, finally, the refill phase of the accident. Also provided is a basic capability for the analysis of operational transients up to and including anticipated transients without scram (ATWS). The TRAC-BF1/MOD1 version produces results consistent with previous versions. Assessment calculations using the two TRAC-BF1 versions show overall improvements in agreement with data and computation times as compared to earlier versions of the TRAC-BWR series of computer codes.

12. KEY WORDS/DESCRIPTORS *(List words or phrases that will assist researchers in locating the report.)*

TRAC, BWR safety analysis

13. AVAILABILITY STATEMENT

Unlimited

14. SECURITY CLASSIFICATION

(This Page)
Unclassified

(This Report)
Unclassified

15. NUMBER OF PAGES

16. PRICE